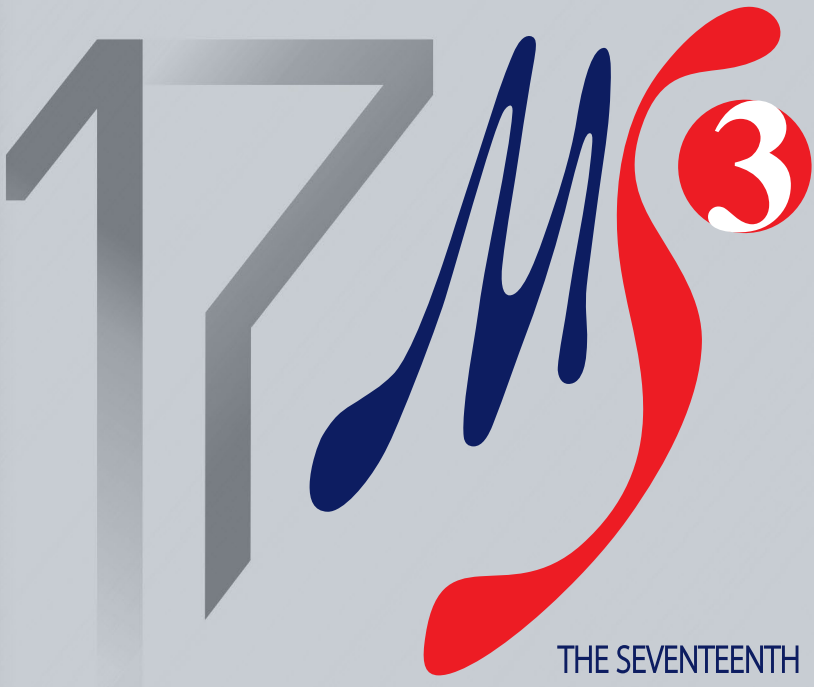


THE SEVENTEENTH
MOSCOW
SOLAR SYSTEM
SYMPOSIUM

OCTOBER 12-16, 2026
SPACE RESEARCH
INSTITUTE
MOSCOW

СЕМНАДЦАТЫЙ
МОСКОВСКИЙ
СИМПОЗИУМ
ПО ИССЛЕДОВАНИЯМ
СОЛНЕЧНОЙ СИСТЕМЫ

12-16 ОКТЯБРЯ 2026
ИНСТИТУТ
КОСМИЧЕСКИХ
ИССЛЕДОВАНИЙ
МОСКВА

ИКИ
ИНСТИТУТ КОСМИЧЕСКИХ ИССЛЕДОВАНИЙ РАН

ГЕОХИ

BROWN

СЕМНАДЦАТЫЙ МОСКОВСКИЙ СИМПОЗИУМ ПО ИССЛЕДОВАНИЯМ СОЛНЕЧНОЙ СИСТЕМЫ 17M-S^3

октябрь 12–16, 2026
ИНСТИТУТ КОСМИЧЕСКИХ ИССЛЕДОВАНИЙ РОССИЙСКОЙ АКАДЕМИИ НАУК
МОСКВА, РОССИЯ

THE SEVENTEENTH MOSCOW SOLAR SYSTEM SYMPOSIUM 17M-S^3

october 12–16, 2026
SPACE RESEARCH INSTITUTE OF RUSSIAN ACADEMY OF SCIENCES
MOSCOW, RUSSIA

спонсоры:
- Институт космических исследований РАН
- Институт геохимии и аналитической химии им. Вернадского РАН
- Брауновский университет (США)

sponsored by:
- Space Research Institute RAS
- Vernadsky Institute of Geochemistry and Analytical Chemistry RAS
- Brown University, USA

ISBN: 978-5-00015-089-4
DOI: 10.21046/17MS3-2026
© Федеральное Государственное Бюджетное Учреждение Науки
ИНСТИТУТ КОСМИЧЕСКИХ ИССЛЕДОВАНИЙ РОССИЙСКОЙ АКАДЕМИИ НАУК (ИКИ РАН)
2026

TABLE OF CONTENT

INTRODUCTION

PROGRAM COMMITTEE

PROGRAM
overview PROGRAM
scientific PROGRAM

ABSTRACTS

INFORMATION
ADDRESS
METRO MAP
REGISTRATION AND INFORMATION DESK
ORAL SESSIONS, location
POSTER SESSIONS, location
INTERNET ACCESS AND WiFi
SOCIAL PROGRAM
LUNCH POINTS

THE SEVENTEENTH MOSCOW SOLAR SYSTEM SYMPOSIUM 17M-S^3

SPACE RESEARCH INSTITUTE MOSCOW, RUSSIA october 12–16, 2026

Starting from 2010, the Space Research Institute holds annual international symposia on Solar system exploration. Main topics of these symposia include wide range of problems related to formation and evolution of Solar system, planetary systems of other stars; exploration of Solar system planets, their moons, small bodies; interplanetary environment, astrobiology problems. Experimental planetary studies, science instruments and preparation for space missions are also considered at these symposia.

The Seventeenth Moscow international Solar System Symposium (17M-S^3) will be held from October 12 till 16, 2026

THE FOLLOWING SESSIONS WILL BE HELD DURING THE SYMPOSIUM:

OPENING SESSION

- Session. ATMOSPHERES OF PLANETS
- Session. INTERNAL STRUCTURE OF PLANETS AND MOONS
- Session. SURFACES OF PLANETS AND MOONS
- Session. EXTRASOLAR PLANETS
- Session. SOLAR SYSTEM IN THE LAB
- Session. EXOSPHERES OF AIRLESS BODIES
- Session. ASTROBIOLOGY
- Session. SMALL BODIES INCLUDING SPACE DUST
- Session. PLANETARY MISSIONS AND SCIENTIFIC INSTRUMENTATION

POSTER SESSION

Space Research Institute holds this symposium with participation of the following organizations:

- Vernadsky Institute of Geochemistry and Analytical Chemistry RAS, Russia
- Brown University, USA
- Schmidt Institute of Physics of the Earth RAS, Russia
- Keldysh Institute of Applied Mathematics RAS, Russia
- Kotelnikov Institute of Radio-engineering and Electronics RAS, Russia
- Sternberg Astronomical institute, Moscow State University, Russia

Symposium website: **https://ms2026.cosmos.ru**

Contact email address: **ms2026@cosmos.ru**

PROGRAM COMMITTEE

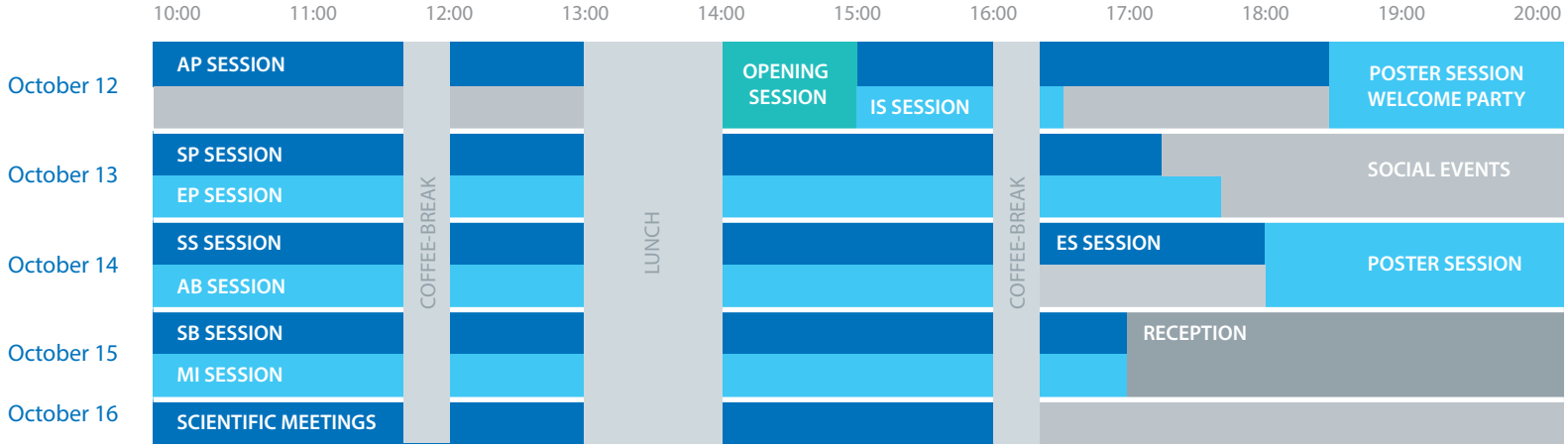
chair:
acad. **ZELENYI L.M.** IKI RAS

members:
BAZILEVSKIY A.T. GEOHI RAS
GUDKOVA T.V. IFZ RAS
HEAD III J. Brown University, USA
IVANOV M.A. GEOHI RAS
JHEETA S. NoRCEL, United Kingdom
KORABLEV O.I. IKI RAS
KOSTITSYN Y.A. GEOHI RAS
KOTSYURBENKO O.R. Yugra State University
KUZNETSOVA I.E. IRE RAS
MITROFANOV I.G. IKI RAS
RODIONOVA Z.F. GAISH MSU
SHEMATOVICH V.I. INASAN RAS
SIDORENKO V.V. IPM RAS
TAVROV A.V. IKI RAS
TITOV D. Sun Yat-sen University, China
ZAKHAROV A.V. IKI RAS
ZASOVA L.V. IKI RAS

secretary:
ROSTE O.Z. IKI RAS

PROGRAM

overview 17M-S³ program
THE SEVENTEENTH MOSCOW SOLAR SYSTEM SYMPOSIUM
IKI RAS, 12–16 October 2026



	OPENING SESSION/ IKI CONFERENCE HALL
AP SESSION	ATMOSPHERES OF PLANETS SESSION/ IKI CONFERENCE HALL
IS SESSION	INTERNAL STRUCTURE OF PLANETS AND MOONS SESSION/ IKI EXHIBITION HALL
SP SESSION	SURFACES OF PLANETS AND MOONS SESSION/ IKI CONFERENCE HALL
EP SESSION	EXTRASOLAR PLANETS SESSION/ IKI EXHIBITION HALL
SS SESSION	SOLAR SYSTEM IN THE LAB SESSION/ IKI CONFERENCE HALL

ES SESSION	EXOSPHERES OF AIRLESS BODIES SESSION/ IKI CONFERENCE HALL
AB SESSION	ASTROBIOLOGY SESSION/ IKI EXHIBITION HALL
SB SESSION	SMALL BODIES INCLUDING SPACE DUST SESSION/ IKI CONFERENCE HALL
MI SESSION	PLANETARY MISSIONS AND SCIENTIFIC INSTRUMENTATION SESSION/ IKI EXHIBITION HALL
	SCIENTIFIC MEETINGS/ IKI CONFERENCE HALL
	POSTER SESSION/ IKI EXHIBITION HALL

14:00–15:00

OPENING SESSION

Convener: **Lev ZELENYI**
conference hall, second floor

Opening Remarks

Dr. Ulpia-Elena BOTEZATU (Romania), Co-Chair ATLAC
Mr. Hasan ABBAS (Pakistan), Co-Chair ATLAC

Action Team on Lunar Activities Consultation (ATLAC), UN COPUOS

10:00–13:00

1 SESSION ATMOSPHERES OF PLANETS

Conveners: **Oleg KORABLEV, Anna FEDOROVA**
conference hall, second floor

10:00–10:20	**Hiroki ANDO et al.**	Long-term variability of the Venusian atmosphere studied with Venus Express and Akatsuki radio occultation measurements /***Invited talk***/	17MS3-AP-01
10:20–10:40	**Dmitrij TITOV and Z. WANG**	Venus cloud top morphology: from VMC/ Venus Express to UVI/ Akatsuki	17MS3-AP-02
10:40–11:00	**Dmitry GORINOV et al.**	Venus Nightside Lower and Middle Cloud Atmospheric Circulation from IR2/Akatsuki Data	17MS3-AP-03
11:00–11:20	**Jinjin ZHAO and Dmitrij TITOV**	Venus Cloud Morphology: Vertical Coupling and Temporal Evolution from Venus Express Multispectral Imaging	17MS3-AP-04
11:20–11:40	**Masahiro TAKAGI et al.**	Angular momentum balance of the Venus atmospheric superrotation in and above the cloud layer /***Invited talk***/	17MS3-AP-05
11:40–12:00		COFFEE-BREAK	
12:00–12:20	**Mikhail RAZUMOVSKIY and B. FOMIN**	Compact flux-fitting k-distribution parameterizations suitable for radiation blocks in Venus climate models	17MS3-AP-06*
12:20–12:40	**Andrey KIRILLOV et al.**	Electronic kinetics and emissions of carbon monoxide in discharges in CO_2-N_2-CO atmospheres	17MS3-AP-07
12:40–13:00	**Anastasiia IVANOVA et al.**	Studies of the atmospheres of giant planets based on data obtained at the SAO RAS	17MS3-AP-08
13:00–14:00		LUNCH	

* Participant in the Early Career Researcher Contest

15:00–18:20

1 SESSION (CONTINUATION) ATMOSPHERES OF PLANETS

Conveners: **Oleg KORABLEV, Anna FEDOROVA**
conference hall, second floor

15:00–15:20	**Denis BELYAEV et al.**	Martian neutral atmosphere from the mesosphere to CO_2 exobase: a multi-mission climatology from occultation experiments	17MS3-AP-09
15:20–15:40	**Anna FEDOROVA et al.**	Non-migrating tides in the Martian mesosphere from temperature measurements of TGO and IUVS/MAVEN	17MS3-AP-10
15:40–16:00	**Anastasia ROMANOVA et al.**	Interannual variations of the Martian seasonal cycle based on data from the HEND/Odyssey experiment	17MS3-AP-11*
16:00–16:20		COFFEE-BREAK	
16:20–16:40	**Anatoliy PAVLOV and A. A. GOROKHOV**	Destruction of methane by negative ions in the lower atmosphere of Mars: A possible solution to the methane problem	17MS3-AP-12
16:40–17:00	**Hanlin YE and Jinsong PING**	Terrain-Modulated Illumination and Incoming Solar Radiation on Mars: Implications for Atmospheric Simulation Models and Mission Planning	17MS3-AP-13
17:00–17:20	**Tatiana ERMAKOVA et al.**	The Northern Hemisphere Stratosphere in the Past and Future: A Comparative Analysis of Temperature, Vertical Velocity, and Heat Transport	17MS3-AP-14
17:20–17:40	**Andrey KOVAL et al.**	The Impact of Solar Activity on Global Wave Processes in the Middle and Upper Atmosphere: Numerical Modeling	17MS3-AP-15
17:40–18:00	**Grigory TSURIKOV et al.**	Analysis of Earth's polar thermosphere overcooling during geomagnetic storms	17MS3-AP-16
18:00–18:20	**Sofiia BLAZHNOVA et al.**	Temporal and spatial characteristics of sporadic charged particle fluxes in the orbit around Mars, as measured by the HEND instrument onboard Mars Odyssey	17MS3-AP-17*

18:30–20:30

POSTER SESSION, WELCOME PARTY

exhibition hall, ground floor

* Participant in the Early Career Researcher Contest

15:00–16:30

2 SESSION
INTERNAL STRUCTURE OF PLANETS AND MOONS

Convener: **Tamara GUDKOVA**
exibition hall, ground floor

15:00–15:15	**Ekaterina KRONROD et al.**	A physically based stratified model of the lunar crust: comparison with an exponential compaction model	17MS3-IS-01
15:15–15:30	**Alexey BATOV et al.**	Tectonic stresses in the Cerberus region on Mars according to the analysis of digital relief models	17MS3-IS-02
15:30–15:45	**Egor KULIK and Tamara GUDKOVA**	On the dependence of the value of the Chandler period of Mars on the mineralogy and temperature of the mantle	17MS3-IS-03
15:45–16:20		COFFEE-BREAK	
16:00–16:15	**Anton SALNIKOV et al.**	Toward a global model of the Martian crustal magnetic field using legacy orbital magnetic observations	17MS3-IS-04
16:15–16:30	**Ivan BORONIN and Tamara GUDKOVA**	Inversion Results for Venus' Internal Structure with Probabilistic Approach: Elastic and Inelastic Models	17MS3-IS-05

18:30–20:30

POSTER SESSION, WELCOME PARTY

exhibition hall, ground floor

* Participant in the Early Career Researcher Contest

10:00–17:15

3 SESSION SURFACES OF PLANETS AND MOONS

Convener: **Mikhail IVANOV**
conference hall, second floor

10:00–10:15	**Svetlana DEMIDOVA**	Ancient magmatism of the eastern part of the lunar nearside as recorded in Luna-16 soil sample	17MS3-SP-01
10:15–10:30	**Artem LYSENKO et al.**	Thermal-cycling resistance of lunar regolith simulant samples produced by selective laser melting	17MS3-SP-02*
10:30–10:45	**Nikita SHANDROV et al.**	Local water-rich regions in the lunar south polar area from LEND data	17MS3-SP-03
10:45–11:00	**Zhiguo MENG et al.**	Retrieving Geothermal Heat Flow of the Moon Using Onboard Passive Microwave Remote Sensing Data	17MS3-SP-04
11:00–11:15	**Sergey KRASILNIKOV**	Small-scale crater morphology on the Moon	17MS3-SP-05
11:15–11:30		COFFEE-BREAK	
11:30–11:45	**Jun HUANG et al.**	Geology of Rimae Bode region as priority site candidate for China's first crewed lunar mission	17MS3-SP-06
11:45–12:00	**Zhanna RODIONOVA et al.**	Some Features of Crater Distribution in the Polar Regions of the Moon	17MS3-SP-07
12:00–12:15	**Ekaterina FEOKTISTOVA et al.**	The De Gerlach-Shackleton Crater Region as a Potential Landing Site for Future Lunar Missions	17MS3-SP-08
12:15–12:30	**Olga CHERNENKO et al.**	Design of a Small-Scale Capsule's Return from the Lunar Surface	17MS3-SP-09*
12:30–12:45	**Alexey ANDREEV et al.**	Development of a Lunar Observation System for the Determination of the Moon's Rotation Parameters	17MS3-SP-10
12:45–13:00	**Alexander BASILEVSKY et al.**	Geologic-morphologic analysis of Malapert Mons on the Moon	17MS3-SP-11
13:00–14:00		LUNCH	
14:00–14:15	**Alexander GUSEV**	Geological exploring of the Moon: rare earth elements	17MS3-SP-12
14:15–14:30	**Mikhail IVANOV et al.**	Geology of the western portion of Noachis Terra on Mars	17MS3-SP-13
14:30–14:45	**Ekaterina CHOLOVSKAIA and Mikhail IVANOV**	Geological settings of clay minerals in the western Noachis Terra, Mars	17MS3-SP-14

* Participant in the Early Career Researcher Contest

14:45–15:00	**Dmitry GOLOVIN et al.**	Local water rich regions in the equatorial area of Mars by FREND/TGO data	17MS3-SP-15
15:00–15:15	**George BAROEV et al.**	Investigation of seasonal variability in passive measurements of the DAN instrument onboard the Curiosity rover	17MS3-SP-16*
15:15–15:30	**Daria EVDOKIMOVA et al.**	SPICAV IR and VMC collocated observations to explore the Venus surface properties	17MS3-SP-17
15:30–15:45	**Mikhail IVANOV et al.**	Emissivity variations of extensive rock units on Venus from the VMC data	17MS3-SP-18
15:45–16:00		COFFEE-BREAK	
16:00–16:15	**Mikhail IVANOV et al.**	Selection of landing sites of the Venera-D mission	17MS3-SP-19
16:15–16:30	**Danil MALYSHEV and Mikhail IVANOV**	Spatial distribution and evolution of coronae and large volcanoes in Ulfrun and Beta Regiones, Venus	17MS3-SP-20*
16:30–16:45	**Victor GUBAREV et al.**	Results of gamma-ray measurements performed by the MGNS instrument during the cruise phase of the BepiColombo mission to Mercury	17MS3-SP-21
16:45–17:00	**Askaniy ANPILOGOV**	A unified approach to photometric transformations and celestial object color determination	17MS3-SP-22*
17:00–17:15	**Yaroslaw ILYUSHIN and Hongli ZHAO**	Calculation of Radar Reflections from Relief Surfaces of Celestial Bodies	17MS3-SP-23*

* Participant in the Early Career Researcher Contest

10:00–17:40

4 SESSION EXTRASOLAR PLANETS

Convener: **Alexander TAVROV**
exhibition hall, ground floor

10:00–10:20	**Piero D'INCECCO et al.**	Using Venus and Terrestrial Volcanic Analogs to Interpret Rocky Exoplanets	17MS3-EP-01
10:20–10:40	**Grigory MOROZOV and Elena BELENKAYA**	Dependence of Exoplanet Properties on Their Location Relative to the Habitable Zone	17MS3-EP-02*
10:40–11:00	**Vladislava ANANYEVA and Alexander TAVROV**	Dependences of the Mass Distribution of TESS Transiting Giant Planets on Planetary Orbital Periods and on Host Star Masses	17MS3-EP-03
11:00–11:20	**Anastasiia IVANOVA et al.**	Photometric observations of exoplanets by the SAO RAS	17MS3-EP-04
11:20–11:40	**Elza BUSLAEVA and Elena BELENKAYA**	Comparison of exoplanet characteristics in single and multi-star systems	17MS3-EP-05
11:40–12:00		COFFEE-BREAK	
12:00–12:20	**Grigory TSURIKOV et al.**	The Spektr-UF space telescope as a tool for studying exoplanet atmospheres	17MS3-EP-06
12:20–12:40	**Alexander TAVROV et al.**	Progress in stellar coronagraphy for exoplanet imaging in IKI RAS	17MS3-EP-07
12:40–14:00		LUNCH	
14:00–14:20	**Marina RUMENSKIKH et al.**	Improving exoplanetary magnetic field determination via atomic alignment with inhomogeneous stellar spectra	17MS3-EP-08*
14:20–14:40	**Roman KISLOV et al.**	Structure of the planetary wind flow of hot Jupiters with their own magnetic field at different positions of the Alfvén critical surface	17MS3-EP-09
14:40–15:00	**Stanislav SHARIPOV et al.**	Three-Dimensional Modeling of the Atomic Alignment Effect as a Diagnostic of Magnetic Fields in Hot Exoplanets	17MS3-EP-10
15:00–15:20	**Gleb MALYGIN and Elena BELENKAYA**	Magnetosphere of the brown dwarf 15 Sge b in a system with a solar-type central star	17MS3-EP-11*
15:20–15:40	**Anton KROTOV and Elena BELENKAYA**	Magnetosphere of Tau Bootis b in the paraboloid and MHD models	17MS3-EP-12*
15:40–16:00	**Eduard KUZNETSOV**	Resonance properties of the compact four-planet system Kepler-51	17MS3-EP-13

* Participant in the Early Career Researcher Contest

16:00–16:20		COFFEE-BREAK	
16:20–16:40	**Ildar SHAIKHISLAMOV et al.**	Modeling transit absorption in HI and HeI lines at atmospheres of hot exoplanets following super-flare	17MS3-EP-14
16:40–17:00	**Roman EVDOKIMOV and Valery SHEMATOVICH**	Residual hydrogen-helium atmospheres of mini-Neptunes: the possibility of formation and stability with taking into account various thermal loss mechanisms and the interior composition	17MS3-EP-15
17:00–17:20	**Roman EVDOKIMOV and Valery SHEMATOVICH**	Estimate of the influence of interior composition on the thermal atmospheric mass-loss for mini-Neptunes	17MS3-EP-16
17:20–17:30	**Danial RAHBARMAH**	Ground-Based Spectroscopic Detection of Jupiter-like Planets Orbiting Contact Binary Stars: Minimum Instrumental Requirements and Observational Constraints	17MS3-EP-PS-13
17:30–17:40	**Aida RAKIAN**	Searching for Circumbinary Planets Around Contact Binary Stars: Methodology, Challenges, and Detection Limits	17MS3-EP-PS-14

* Participant in the Early Career Researcher Contest

10:00–15:40

5 SESSION SOLAR SYSTEM IN THE LAB

Convener: **Mikhail GERASIMOV**
conference hall, second floor

10:00–10:20	**Ivan AGAPKIN et al.**	Microwave sintering of lunar soil analogue VI-LH1	17MS3-SS-01*
10:20–10:40	**Nina SKVORTSOVA et al.**	Simulation experiments using powerful pulsed gyrotrons for the deposition of lunar dust on metal plates	17MS3-SS-02
10:40–11:00	**Sergey VOROPAEV et al.**	Evaluation of mid-IR spectra of natural silicates for remote sensing of the Moon	17MS3-SS-03
11:00–11:30	**Vladimir SHKLOVER and Mikhail GERASIMOV**	New frontiers in the microstructural studies of lunar regolith /***Invited talk***/	17MS3-SS-04
11:30–12:00		COFFEE-BREAK	
12:00–12:20	**Valery SHUVALOV and Boris IVANOV**	Impact structures on Venus as a result of asteroid destruction in the atmosphere	17MS3-SS-05
12:20–12:40	**Vladimir SVETSOV**	Impact erosion of ocean on early Earth	17MS3-SS-06
12:40–13:00	**Egor SOROKIN**	Mathematical Modeling of a Micrometeorite Impact	17MS3-SS-07
13:00–14:00		LUNCH	
14:00–14:20	**Evgeniya PETROVA et al.**	Experimental modeling of the formation of the fusion crust of stony meteorites	17MS3-SS-08
14:20–14:40	**Maxim ZAITSEV et al.**	On organic compounds formation induced by the microwave breakdown and plasma-dust clouds generated from nitrogen – carbon dioxide atmospheres and peridotite	17MS3-SS-09
14:40–15:00	**Anna KUZOVCHIKOVA et al.**	Selection of mineral supplements for lunar regolith simulants improving the conditions of microwave breakdown and the formation of plasma-dust clouds	17MS3-SS-10*
15:00–15:20	**Anastasia BAKHMUTOVA et al.**	Synthesis of carbon nanotubes on meteorite metal via alcohol decomposition	17MS3-SS-11
15:20–15:40	**Alexander LAVRUKHIN et al.**	Mercury's magnetospheric magnetic field after the six BepiColombo flybys	17MS3-SS-12
15:40–16:20		COFFEE-BREAK	

* Participant in the Early Career Researcher Contest

16:20–18:00

6 SESSION EXOSPHERES OF AIRLESS BODIES

Convener: **Alexander ZAKHAROV**
conference hall, second floor

16:20–16:40	**Alexey BEREZHNOY et al.**	About initial conditions of expansion of impact-produced clouds	17MS3-ES-01
16:40–17:00	**Vladimir BUSAREV et al.**	Further evidence of dust activity of main-belt asteroids from their reflectance spectra	17MS3-ES-02
17:00–17:20	**Alexandr SOKOLOV et al.**	Simulation experiments on deposition of LMS-1D regolith particles on the surface of solar panels in gyrotron discharge	17MS3-ES-03
17:20–17:40	**Ilia KUZNETSOV et al.**	Lunar dust activation processes: Experimental approach	17MS3-ES-04
17:40–18:00	**Stanislav KUZNETSOV and Vladimir BUSAREV**	Application of the Particle-in-Cell method to model electrostatic field near airless bodies	17MS3-ES-05*

18:00–20:00

POSTER SESSION

exhibition hall, ground floor

* Participant in the Early Career Researcher Contest

10:00–15:20

7 SESSION ASTROBIOLOGY

Convener: **Oleg KOTSYURBENKO**
exhibition hall, ground floor

10:00–10:40	**Oleg GUSEV**	Single-cell level mechanisms of tolerance to extreme desiccation: how a midge can fly to Mars /***Invited talk***/	17MS3-AB-01
10:40–11:00	**Alexander GURIDOV and S. PODDUBKO**	Survival of archaea and bacteria under outer space conditions of a polar Earth orbit on the exterior of the BION-M No: 2 spacecraft	17MS3-AB-02
11:00–11:20	**Mikhail KARGANOV et al.**	Fragmentation of Lambda phage dry DNA during exposure outside and inside the Bion-M no: 2 satellite	17MS3-AB-03
11:20–11:40	**Daniil BARBASHIN et al.**	Preliminary Results of GEOHI RAS Experiments Aboard Bion-M No: 2	17MS3-AB-04
11:40–12:00		COFFEE-BREAK	
12:00–12:20	**Yuming FU et al.**	Sequential exposure reveals stage-specific effects of simulated microgravity and X-ray irradiation on *Bacillus mojavensis* spore revival	17MS3-AB-05
12:20–12:40	**Petar EFTIMOV and N. STEFANOVA**	Early embryogenesis in microgravity conditions – from biophysics to signal pathways	17MS3-AB-06
12:40–13:00	**Mikhail ZARUBIN and E. KRAVCHENKO**	Tardigrade extreme stress tolerance: implications for radiation biophysics and spaceflight studies	17MS3-AB-07*
13:00–14:00		LUNCH	
14:00–14:20	**Sergey BULAT et al.**	Questioned microbial communities of the subglacial Antarctic Lake Vostok water following 1st lake unsealing: Re-evaluation of previous finds and discovering new ones using nanopore sequencing	17MS3-AB-08
14:20–14:40	**Oleg KOTSYURBENKO et al.**	Astrobiological Research as Part of the Venera-D Space Mission	17MS3-AB-09
14:40–15:00	**Alexander SAFRONOV**	Space mission: From developing the basic principles of creating habitable planets to the search for intelligent worlds	17MS3-AB-10
15:00–15:20	**Elena KADYSHEVICH and Victor OSTROVSKII**	Life Origination Hydrate Theory: living-matter origination and development and possible signatures of planetary habitability	17MS3-AB-11
15:40–16:20		COFFEE-BREAK	

18:00–20:00

POSTER SESSION

exhibition hall, ground floor

* Participant in the Early Career Researcher Contest

10:00–17:00

8 SESSION SMALL BODIES INCLUDING SPACE DUST

Conveners: **Alexander BASILEVSKY, Alexander ZAKHAROV**
conference hall, second floor

10:00–10:15	**Marina SHCHERBINA and N. KISELEV**	New Public Database of Asteroid Polarimetric Observations: Structure, Content, and Scientific Application	17MS3-SB-01*
10:15–10:30	**Olga TURCHINSKAYA et al.**	Multiscale 3d modelling of tension-fracture and shear deformation systems on the surface of 67P comet	17MS3-SB-02
10:30–10:45	**Maria KIRSANOVA et al.**	Modeling of H_2O and CH_3OH Emission Lines in the Coma of a Comet for the Submillimeter Wavelength Range	17MS3-SB-03
10:45–11:00	**Sergey POPEL et al.**	Dusty plasmas at comet nucleus: specific dusty plasma effects and influence of dust particle chemical composition	17MS3-SB-04
11:00–11:15	**Maryan NASTARAN et al.**	Investigating the structure, microstructure and shock characteristics in the Lut desert chondrite meteorite	17MS3-SB-05*
11:15–11:30	**Anna KARTASHOVA et al.**	Observations of Small Bodies of the Solar System at the Terskol and Sanglokh Observatories	17MS3-SB-06
11:30–12:00		COFFEE-BREAK	
12:00–12:15	**Olga POPOVA and D. GLAZACHEV**	Classification of UGS-observed fireballs	17MS3-SB-07
12:15–12:30	**Olga CHERNENKO et al.**	Trajectory Design for the Application of Earth-Resonant Asteroids in Planetary Defense	17MS3-SB-08*
12:30–12:45	**Maryan NASTARAN et al.**	Asteroid Rotation Periods: Statistical Analysis in the Diameter-Spin Distribution	17MS3-SB-09*
12:45–13:00	**Marina SHCHERBINA et al.**	Polarimetric and Photometric Characteristics of the Interstellar Comet 3I/ATLAS: Key Features /***Invited talk***/	17MS3-SB-10
13:00–14:00		LUNCH	

* Participant in the Early Career Researcher Contest

14:00–14:15	**Boris SHUSTOV et al.**	On detection strategy of dangerous asteroids	17MS3-SB-11
14:15–14:30	**Maria SERGIENKO et al.**	The Southern Delta Aquariids Meteoroid Stream	17MS3-SB-12
14:30–14:45	**Elena PODOBNAYA et al.**	Size frequency distribution of fresh impact clusters on Mars	17MS3-SB-13
14:45–15:00	**Gleb KUCHEROV et al.**	On the origin of the discovered 250-km-radius plutino atmosphere	17MS3-SB-14*
15:00–15:15	**Maxim NYRTSOV et al.**	Measuring Crater Morphometry on Irregular Bodies: Reference Surfaces, Projections, and Distortion	17MS3-SB-15
15:15–15:30	**Sergei IPATOV**	Migration of bodies from the zone of the giant planets to the terrestrial planets and the Moon	17MS3-SB-16
15:30–15:45	**Nadezhda LYASHENKO et al.**	Dust migration from the outer Solar System under the interstellar gas cloud encounter	17MS3-SB-17
15:45–16:00	**Yulia REZNICHENKO et al.**	Dusty plasma clouds on Venus, the Earth and Mars	17MS3-SB-18
16:00–16:30	COFFEE-BREAK		
16:30–16:45	**Yuriy CHETVERIKOV et al.**	Monitoring of cosmic dust fallout in Antarctica and global dust emissions	17MS3-SB-19
16:45–17:00	**Nuraddin ADIGOZALOV and Vladislav SIDORENKO**	Co-orbital population of Venus: presumed members and their possible secular evolution	17MS3-SB-20
17:00–20:00	**RECEPTION**		

* Participant in the Early Career Researcher Contest

10:00–17:00

9 SESSION PLANETARY MISSIONS AND SCIENTIFIC INSTRUMENTATION

Convener: **Oleg KORABLEV**
exhibition hall, ground floor

10:00–10:20	**Hanlin YE and Jinsong PING**	New Window of Earth Monitoring from Lunar North Pole	17MS3-MI-01
10:20–10:40	**Ekaterina KAZANTSEVA et al.**	Locating the Blue Ghost M1 Lander on the Lunar Surface Using Radio Interferometric Measurements	17MS3-MI-02*
10:40–11:00	**Olga TURCHINSKAYA et al.**	Proposed Route for a Heavy Scientific Rover at the Lunar South Pole: Travel-Time Assessment and Preliminary Operational Timeline	17MS3-MI-03
11:00–11:20	**Andrey SHUGAROV et al.**	Lightweight Lunar Ultraviolet Telescope (LLUT-150) project	17MS3-MI-04
11:20–11:40	**Andrey GAROV et al.**	Joint Luna Data Centre (JLDC): Processing and Visualization of Topographic Information of the Celestial Bodies of the Solar System in Planetary Data Geoportal	17MS3-MI-05
11:40–12:00		COFFEE-BREAK	
12:00–12:20	**Jordanka SEMKOVA et al.**	Summary of 10-years observation of the radiation environment onboard ExoMars TGO	17MS3-MI-06
12:20–12:40	**Kullapha CHAIWONGKHOT et al.**	Geant4-Based Design Optimization and Performance Estimation of the Sino-Thai Energetic Photon Survey (STEPS) Compact Gamma-Ray Spectrometer Payload for the Chinese Space Station Mission	17MS3-MI-07
12:40–13:00	**Thanayuth PANYALERT et al.**	Environment Characterization for a Gamma-Ray Detector Payload on the China Space Station	17MS3-MI-08
13:00–14:00		LUNCH	
14:00–14:20	**Lev ZELENYI et al.**	The Venera-D Mission to Venus	17MS3-MI-09
14:20–14:40	**Evgeny NIKOLAEV et al.**	Feasibility of Using the Multi-Electrode Harmonized Kingdon Trap as a Mass Spectrometer for Planetary Research	17MS3-MI-10
14:40–15:00	**Mikhail LUGININ et al.**	Nephelometers for Venus: a Review in the Context of the Upcoming Venera-D Mission	17MS3-MI-11
15:00–15:20	**Alexander TROKHIMOVSKIY et al.**	Infrared Studies of the Venusian Atmosphere Using the VIKA and VIRAL Instruments	17MS3-MI-12
15:20–15:40	**Zhiquan YUAN**	Microcomb-based mid-infrared dual-comb spectroscopy with GHz resolution	17MS3-MI-13*
15:40–16:20		COFFEE-BREAK	
16:20–17:00		DISCUSSION	
17:00–20:00		**RECEPTION**	

* Participant in the Early Career Researcher Contest

11:00–13:00	**ROUND TABLE:** **VENERA-D: OPTIMAL ENTRY COORDINATES OF THE DESCENT**** Convener: **Dmitry GORINOV** conference hall, second floor
11:40–12:00	COFFEE-BREAK
	ROUND TABLE (CONTINUATION)) **VENERA-D: OPTIMAL ENTRY COORDINATES OF THE DESCENT****
13:00–14:00	LUNCH
14:00–16:00	**ROUND TABLE:** **ASTROBIOLOGY IN RUSSIA: PROSPECTS FOR DEVELOPMENT**** Convener: **Oleg KOTSYURBENKO** conference hall, second floor
16:00–16:20	COFFEE-BREAK

* Participant in the Early Career Researcher Contest

12 October 18:30–20:30
14 October 18:00–20:00

POSTER SESSION

exhibition hall, ground floor

ATMOSPHERES OF PLANETS

Aliaksei SVIACHKO et al.	Detection Limits of Trace Gas Constituents in Venus Mesosphere modeled for a Solar Occultation Experiment in the Infrared	17MS3-PS-01*
Alexander TERTYSHNIKOV	Hydrogen density field at the altitude of the Meteor-2-4 spacecraft in January 2025	17MS3-PS-02
Vladimir VDOVICHENKO et al.	Spectral observations of Titan and Saturn in 2024	17MS3-PS-03
Vladimir VDOVICHENKO et al.	Features of Methane and Ammonia Absorption along Jupiter's Central Meridian and in the Great Red Spot in 2014–2024	17MS3-PS-04
Vladimir OGIBALOV	Influence of the redistribution of aerosols in altitude within the radiative transfer problem in the NIR bands of CO_2 and CO molecules under breakdown of vibrational LTE in the daytime Martian atmosphere	17MS3-PS-05
Vladimir OGIBALOV	Method for solution of the radiative transfer problem in the rovibrational bands of the CO_2 and CO molecules under breakdown of vibrational LTE in the Martian atmosphere with taking account of radiation extinction by aerosols	17MS3-PS-06

INTERNAL STRUCTURE OF PLANETS AND MOONS

Tamara GUDKOVA et al.	Search for seismic activity on Venus by pressure perturbations in the atmosphere	17MS3-PS-07

SURFACES OF PLANETS AND MOONS

Alexander KRASILNIKOV and Mikhail IVANOV	Determination of the mixing factor of local and foreign material in the Langrenus, Cavalerius and Theophilus crater ejecta	17MS3-PS-08
Alexander VOZISOV and Mikhail IVANOV	Morphology and topographic configuration of the Pallacopas Vallis fluvial system, Mars: Preliminary results	17MS3-PS-09*
Alexander KOSOV et al.	Radio science experiment on Luna-26 orbiter, Methods and accuracy of gravitation field measurements	17MS3-PS-10
Yury NEFEDYEV et al.	Multiparameter harmonic model of asteroid Ryugu using data from the «Hayabusa2» space mission	17MS3-PS-11
Changqing DING et al.	Lunar Near-Surface Radar Sounding Using Ballistic Hopper Trajectories	17MS3-PS-12*

* Participant in the Early Career Researcher Contest

EXTRASOLAR PLANETS

Danial RAHBARMAH	Ground-Based Spectroscopic Detection of Jupiter-like Planets Orbiting Contact Binary Stars: Minimum Instrumental Requirements and Observational Constraints	17MS3-PS-13
Aida RAKIAN	Searching for Circumbinary Planets Around Contact Binary Stars: Methodology, Challenges, and Detection Limits	17MS3-PS-14

SOLAR SYSTEM IN THE LAB

Victor GROKHOVSKY et al.	Comparison of the metal structure in the mesosiderites Catalina 500 (A3) and Vaca Muerta (B1)	17MS3-PS-15
Dmitry MOISEENKO et al.	Laboratory simulation of ions and neutral particles interaction with different materials	17MS3-PS-16
Razilia MUFTAKHETDINOVA et al.	On the dynamic strength of meteorites	17MS3-PS-17*
Ivan AGAPKIN et al.	Concentrated solar-simulated sintering of lunar soil analogue VI-LH1	17MS3-PS-18*

SMALL BODIES INCLUDING SPACE DUST

Alberto VODNIZA and L. CHAVES	Study of comet 3I/Atlas	17MS3-PS-19
Sergey KOPNIN and Sergey POPEL	Dust particle charging in Jovian magnetospheric plasmas	17MS3-PS-20
Yuri BONDARENKO and D. MARSHALOV	Physical characterization of Near-Earth Asteroid (163899) 2003 SD220 from bistatic radar observations	17MS3-PS-21
Elena BAKANAS et al.	Photometric observations of comet C/2022 N2 (PANSTARRS)	17MS3-PS-22

PLANETARY MISSIONS AND SCIENTIFIC INSTRUMENTATION

Egor TARASOV et al.	Hardware-Software Complex of the Check-Out Equipment for Ground Testing of the Sampling Device of the Luna-27 Lunar Lander	17MS3-PS-23*
Daniil BARBASHIN et al.	Development of Fungal Biotechnologies for Lunar Exploration	17MS3-PS-24
Sergei KULIKOV et al.	The VAMP experiment: Magnetic field measurements onboard the Venus-D orbiter	17MS3-PS-25
Vladislav ZUBKO et al.	Feasibility of Reaching Extreme Trans Neptunian Objects Using Multi-Planet Gravity Assists	17MS3-PS-26*
Vladislav ZUBKO et al.	Low-Energy Multi-Asteroid Missions Using Resonant Orbits, Venus Gravity Assists and Split-Probe Deployment	17MS3-PS-27*
Jiangchao YUAN and Ge DONG	Low-Altitude Rapid Terrain Exploration: A Portable Jetpack Platform with Adaptive Propulsion Control	17MS3-PS-28*
Paparin JAMLONGKUL et al.	Preliminary Geant4 simulation study of gamma-ray responses in lunar environment using the MATCH detector onboard Chang'E-7 orbiter	17MS3-PS-29*
Pradiphat MUANGHA et al.	Simulation of the ALIGN Payload for Chang'E-8: Neutron-Gamma Discrimination and Background Effects from a Radioisotope Heater Units	17MS3-PS-30*

* Participant in the Early Career Researcher Contest

ABSTRACTS

Session 1.
ATMOSPHERES OF PLANETS (AP)
Oral Session

LONG-TERM VARIABILITY OF THE VENUSIAN ATMOSPHERE STUDIED WITH VENUS EXPRESS AND AKATSUKI RADIO OCCULTATION MEASUREMENTS

H. Ando[1], K. Noguchi[2], T. Imamura[3], M. Takagi[1], H. Sagawa[1], A. Yamazaki[4], J. Oschlisniok[5], S. Tellmann[5], M. Pätzold[5], B. Häusler[6], R. K. Choudhary[7], M. Antonita[8]

[1] *Faculty of Science, Kyoto Sangyo University, Kyoto, Japan*
hando@cc.kyoto-su.ac.jp
[2] *Faculty of Science, Nara Women's University, Nara, Japan*
[3] *Department of Complexity Science and Engineering, The University of Tokyo, Chiba, Japan*
[4] *Institute of Space and Astronautical Science, Japan Aerospace Exploration Agency, Sagamihara, Japan*
[5] *Rheinisches Institut für Umweltforschung, Abteilung Planetenforschung, Universität zu Köln, Cologne, Germany*
[6] *Institut für Raumfahrttechnik und Weltraumnutzung, Universität der Bundeswehr München, Neubiberg, Germany*
[7] *Vikram Sarabhai Space Centre, Space Physics Laboratory, Thiruvananthapuram, India*
[8] *Indian Space Research Organization, Bengaluru, India*

KEYWORDS:
Venus, radio occultation, long-term variability

ABSTRACT:
Despite decades of exploration, Venus's climate system governing the atmosphere beneath the cloud top (~70 km altitude) remains poorly understood due to the persistent thick cloud cover. Here, we present the first detailed characterization of temporal variability in the thermal structure of Venus's low-latitude atmosphere from the sub-cloud region to the mesosphere (45–80 km), using 257 vertical temperature profiles obtained from Venus Express and Akatsuki radio occultation measurements in 2006–2023. Remarkable decadal temperature variations of ~10 K were observed below 55 km, far exceeding those of ~2 K seen at comparable pressure levels in Earth's tropics. The variation in temperature partly correlates with that in the ultraviolet albedo of Venus's cloud, suggesting potential links to the solar heating, cloud physics, and photochemistry. Furthermore, the variations in temperature and geopotential height are nearly in phase with those in zonal wind speed at the cloud top, indicating a strong coupling between the atmospheric dynamics in the upper cloud and the underlying thermal structure. While the mechanisms behind the observed variations remain elusive, our findings reveal that Venus has a more pronounced climate change than Earth. To elucidate Venus's climate system, we need long-term and continuous observations by successive future missions.

VENUS CLOUD TOP MORPHOLOGY: FROM VMC/ VENUS EXPRESS TO UVI/AKATSUKI

D.V. Titov, Z. Wang
School of Atmospheric Sciences, Planetary Environmental and Astrobiological Research Laboratory
Sun Yat-sen University, Zhuhai, China, titov5@mail.sysu.edu.cn

KEYWORDS:
Venus, cloud morphology, UV absorbers, imaging

INTRODUCTION:
Imaging of Venus in the ultraviolet-blue spectral range became a powerful tool to study the cloud top morphology, distribution of absorbing species and atmospheric dynamics [1]. Recent imaging by the UVI instrument onboard JAXA Akatsuki mission significantly extended the database of the planet UV images (Yamazaki et al. 2018). The mission monitored the Venus cloud tops from equatorial orbit thus complementing earlier Venus Express observations from the polar orbit [3]. Most importantly Akatsuki UVI camera had two narrow-band filters at 283 nm and 365 nm. The former was centred on the SO2 absorption feature with some contribution from the unknown UV absorber, while the latter sounded the spectral feature of the unknown UV absorber solely (Fig. 1). Iwanaka et al. [4] used these images to constrain the spatial and local time distribution of both absorbers at the cloud tops.

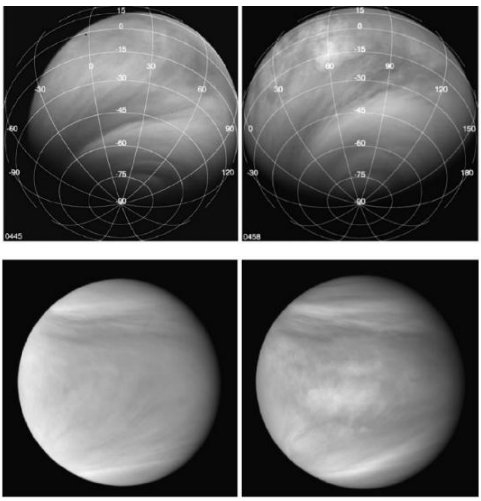


Fig. 1. Global views of Venus (adapted from [1])

METHOD AND RESULTS:
In this talk we will present preliminary qualitative analysis of the UVI/ Akatsuki images in two areas. Firstly, we will compare the global cloud top morphology seen by UVI/ Akatsuki and VMC/ Venus Express at 365 nm (see Fig. 1). The views of Venus captured by the two spacecraft are highly complementary due to different orbits. Secondly, we will present preliminary comparative analysis of 283/365 nm image pairs simultaneously captured by Akatsuki. This would allow to assess relative vertical distribution of sulfuric acid clouds, unknown UV absorber, and SO_2 gas.

Upper panel: VMC UV (365 nm) images taken from a distance of about 30,000 km with the sub-spacecraft point approximately in the middle latitudes of the Southern hemisphere [3]. Lower panel: examples of UVI/Akatsuki images in 0.283 nm (left) and 0.365 nm (right) filters [2]. The Southern pole is at the bottom of the images. The atmosphere super-rotates in the counter-clockwise direction (from right to left).

REFERENCES:

[1] Titov D.V. et al. Clouds and hazes of Venus // Space Sci Rev. 2018. V. 214. P. 126. DOI: 10.1007/s11214-018-0552-z.
[2] Yamazaki et al. Ultraviolet imager on Venus orbiter Akatsuki and its initial results // Earth Planets and Space. 2018. V. 70(1). Article 23. DOI: 10.1186/s40623-017-0772-6.
[3] Titov D.V. et al. Morphology of the cloud tops as observed by the Venus Express Monitoring Camera // Icarus. 2011. DOI: 10.1016/j.icarus.2011.06.020.
[4] Iwanaka T. et al. Sulfur dioxide distribution at the Venusian cloud top retrieved from Akatsuki UV images // JGR Planets. 2025. V. 130. DOI: 10.1029/2024JE008775.

VENUS NIGHTSIDE LOWER AND MIDDLE CLOUD ATMOSPHERIC CIRCULATION FROM IR2/AKATSUKI DATA

D. A. Gorinov, L. V. Zasova, I. V. Khatuntsev, M. V. Patsaeva
Space Research Institute RAS, Moscow 117997, Russia
dmitry_gorinov@cosmos.ru

KEYWORDS:
Venus, dynamics, infrared images, equatorial jet

INTRODUCTION:

This work presents the analysis of the atmospheric dynamics at the the lower and middle cloud layer on the nightside of Venus, using data from the Akatsuki spacecraft's IR2 camera at the wavelengths of 1.74, 2.26 and 2.32 μm. A total of approximately 70,000 vectors were obtained using a manual cloud tracking method, and approximately 150,000 using an automated correlation method. Comparison with VIRTIS-M/Venus Express results in 1.74 μm is also being made [1]. Global data shows dependence on local time and the presence of zonal velocity acceleration at the equatorial region (78±2 m/s, equatorial jet), as observed by previous researchers [2, 3], along with a change in the shape of the latitudinal profile of zonal velocity. Within 20–60° latitude range, the zonal velocity in both the Northern and Southern Hemispheres varies between –60 and –70 m/s, while the meridional velocity is 1–2 m/s in the Southern Hemisphere and 1–4 m/s in the Northern Hemisphere: the meridional flow in the lower directions is directed toward the equator, which is consistent with VIRTIS-M in the 1.74 μm channel. This result suggests that the IR2 camera can detect the upper branch of the "return" Hadley cell in the middle cloud layer.

The Akatsuki spacecraft's equatorial orbit allows for comparison of the dynamic characteristics of the Northern and Southern Hemispheres. This revealed a global asymmetry: at low and high latitudes (0–25 and 60–90°), zonal wind speed is higher in the Southern Hemisphere, while at mid-latitudes (30–45°), it is higher in the Northern Hemisphere.

The dramatic change in velocity from VIRTIS-M to IR2 may have correlation with the solar activity cycle and changes in solar energy influx. The IR2 measurements in 2016, which were carried out near the maximum of solar cycle No. 24 (April 2014), i.e. 1.5–2 years after the maximum, show zonal velocities that are 15–20 m/s higher than those measured by VIRTIS-M (2006–2008) at the minimum of solar cycle 24, i.e. 6–8 years before the maximum. A similar acceleration of the zonal flow by 15–20 m/s is also observed in the upper cloud layer between the UV measurements of the VMC cameras (2006–2008) of the Venus Express spacecraft and the UVI cameras of the Akatsuki spacecraft (2016) [4] during the same periods of the solar activity cycle. Thus, an increase in zonal velocity, correlated with the solar activity cycle, is observed in both the upper and lower cloud layers in the equatorial region. As solar activity increases, absorption in the UV range increases [5], resulting in the generation of thermal tides that supply energy to maintain superrotation.

REFERENCES:

[1] Gorinov D. A., Zasova L. V., Khatuntsev I. V. et al. Winds in the Lower Cloud Level on the Nightside of Venus from VIRTIS-M (Venus Express) 1.74 μm Images // Atmosphere. 2021. V. 12. No. 2. Article 186. https://doi.org/10.3390/atmos12020186.
[2] Horinouchi T. et al. Equatorial jet in the lower to middle cloud layer of Venus revealed by Akatsuki // Nature Geoscience. 2017. V. 10. No. 9. P. 646–651.
[3] Peralta J., Muto K., Hueso R. et al. Nightside Winds at the Lower Clouds of Venus with Akatsuki /IR2: Longitudinal, Local Time, and Decadal Variations from Comparison with Previous Measurements // The Astrophysical J. Supplement Series. 2018. V. 239. No. 2. Article 29. DOI: 10.3847/1538-4365/aae844.

[4] Khatuntsev I.V. et al. Twelve-Year Cycle in the Cloud Top Winds Derived from VMC/Venus Express and UVI/Akatsuki Imaging // Atmosphere. 2022. V. 13. No. 12. P. 2023.
[5] Lee Y.J. et al. Spatial and temporal variability of the 365-nm albedo of Venus observed by the camera on board Venus Express // J. Geophysical Research: Planets. 2020. V. 125. No. 6.

VENUS CLOUD MORPHOLOGY: VERTICAL COUPLING AND TEMPORAL EVOLUTION FROM VENUS EXPRESS MULTISPECTRAL IMAGING

J. Zhao, D. V. Titov
Planetary Environmental and Astrobiological Research Laboratory
zhaojj58@mail.sysu.edu.cn
School of Atmospheric Sciences, Sun Yat-sen University, Zhuhai Campus, Guangdong, China

KEYWORDS:
Venus, Venus atmosphere, Venus clouds, Venus Express

INTRODUCTION:
The atmosphere of Venus is entirely shrouded in a global, dense cloud deck with a vertical optical depth of 20–40 at visible wavelengths. This cloud system is the primary regulator of the planet's radiative energy budget, a key driver of its extreme atmospheric super-rotation, and hosts an as-yet unknown ultraviolet (UV) absorber in its upper layer. While numerous studies by early mission characterized the morphology of Venus's cloud tops, the structural properties of deep cloud layers, their vertical coupling with the upper cloud system, and their connection to large-scale atmospheric dynamics remain poorly constrained. This critical knowledge gap limits a holistic understanding of the Venusian atmospheric system.

In this work we present a preliminary analysis of Venus cloud morphology using multi-band observations by the European Space Agency (ESA) Venus Express mission. We employ a complementary dual-sounding approach to probe the vertical cloud structure.Daytime 0.35 μm UV images from the Venus Monitoring Camera (VMC) are used to map the spatial distribution of the unknown UV absorber at the cloud top (~65–70 km altitude), while nighttime observations in the 1.74 μm near-infrared (NIR) transparency window from the Visible and Infrared Thermal Imaging Spectrometer (VIRTIS) are used to characterize large scale morphology of the deep cloud (48-55 km altitude) and retrieve the total cloud opacity. Our analysis leverages full-orbit observations from the mission's 24-hour polar orbit.

This work aims at revealing spatial coupling between morphology of the cloud-top UV features and deep cloud, clarify the polar vortex's full-column vertical coherence, resolve the evolution of the global cloud morphology, and establish relation of the cloud morphology to the atmospheric circulation to further quantify cloud regulation of radiative energy balance and constrain the properties of the unknown UV absorber.

ANGULAR MOMENTUM BALANCE OF THE VENUS ATMOSPHERIC SUPERROTATION IN AND ABOVE THE CLOUD LAYER

M. Takagi[1], M. Imai[2], H. Ando[1], Y. Matsuda[3]
[1] *Faculty of Science, Kyoto Sangyo University*
takagi.masahiro@cc.kyoto-su.ac.jp
[2] *School of Advanced Engineering, Kogakuin University*
[3] *Department of Astronomy and Earth Science, Tokyo Gakugei University*

KEYWORDS:
Venus, atmospheric superrotation, angular momentum balance, meridional circulation, thermal tides, planetary-scale waves, eddy heat flux

INTRODUCTION:
Venus has a rapidly superrotating atmosphere whose global angular velocity greatly exceeds that of the solid planet [1]. Although meridional circulation and thermal tides have long been considered essential for maintaining the superrotation (SR) [2–4], their respective contributions to the angular momentum (AM) balance in and above the cloud layer remain incompletely understood. We investigate the AM balance in the Venusian middle and upper atmosphere based on numerical simulations using the AFES-Venus general circulation model (GCM) [5].

MODEL:
AFES-Venus is a dynamical GCM with simplified physical processes [6]. The horizontal resolution is T42, corresponding to 128×64 grid points. The model atmosphere extends from the surface to 120 km altitude. Solar heating is prescribed based on a recent radiative transfer calculation, while infrared radiative process is simplified by Newtonian cooling. The model was integrated for 51 Earth years from an idealized super-rotating state. We analyzed the final 585 Earth days, during which the simulated atmosphere was in a quasi-equilibrium state. The model reproduces major observed dynamical features of the Venusian atmosphere, including the broad structure of the zonal wind, thermal tides, and planetary-scale waves [6–8].

RESULTS:
The analysis is based on the transformed Eulerian-mean (TEM) framework, which enables the effects of both eddy AM fluxes ($\overline{u'v'}\cos\varphi$ and $\overline{u'w'}\cos\varphi$) and meridional eddy heat flux ($\overline{v'\theta'}$) to be incorporated through the Eliassen-Palm (EP) flux [9]. In the cloud layer, the Eulerian-mean meridional circulation (EMMC) consists of Hadley-like cells at low latitudes and Ferrel-like cells at middle to high latitudes. In contrast, the residual mean meridional circulation (RMMC) is characterized primarily by a single Hadley-like cell extending from the equator to the poles in and above the cloud layer. The RMMC transports net AM upward above approximately 46 km, accelerating the SR above approximately 54 km. Waves produce an opposing downward transport. These contributions nearly balance at each altitude in the quasi-equilibrium state. Thermal tides accelerate the SR at 50–60 km and 67–75 km. In the cloud layer, the contributions of the meridional-circulation mechanism and the thermal-tide mechanism are estimated to be approximately 70 and 30%, respectively.

A regionally integrated AM budget shows that the RMMC transports a substantial amount of AM upward across 54 km at low latitudes and subsequently carries most of it poleward within the 54–73 km layer. Only a relatively small fraction (approximately 15%) of this poleward transport is returned equatorward by waves. Instead, wave-induced downward AM transport at high latitudes is crucial for closing the AM budget. This downward transport is produced mainly by poleward eddy heat flux rather than

by vertical eddy AM flux, indicating that meridional heat transport by waves plays an important role in the AM balance maintaining the simulated SR.

In addition, we will briefly examine the possible contribution of waves with periods shorter than 3 Earth days, which produce a notable poleward eddy heat flux at high latitudes in the cloud layer but have not yet been investigated in detail.

REFERENCES:

[1] Schubert G. et al. Structure and circulation of the Venus atmosphere // J. Geophysical Research. 1980. V. 85. P. 8007–8025. https://doi.org/10.1029/ja085ia13p08007.
[2] Gierasch P. J. Meridional circulation and the maintenance of the Venus atmospheric rotation // J. Atmospheric Sciences. 1975. V. 32. P. 1038–1044. https://doi.org/10.1175/1520-0469(1975)032<1038:mcatmo>2.0.co;2.
[3] Matsuda Y. Dynamics of the four-day circulation in the Venus atmosphere // J. Meteorological Society of Japan. 1980. V. 58. P. 443–470. https://doi.org/10.2151/jmsj1965.58.6_443.
[4] Fels S. B., Lindzen R. S. The interaction of thermally excited gravity waves with mean flow // Geophysical Fluid Dynamics. 1974. V. 6. P. 149–191. https://doi.org/10.1080/03091927409365793.
[5] Takagi M. et al. Angular momentum balance of superrotation in Venus's middle and upper atmosphere simulated by AFES-Venus // J. Geophysical Research: Planets. 2026. V. 131. Article e2025JE009449. https://doi.org/10.1029/2025JE009449.
[6] Suzuki A. et al. A sensitivity study of the thermal tides int he Venusian atmosphere: Structures and dynamical effects on the superrotation // J. Geophysical Research: Planets. 2022. V. 127. Article e2022JE007243. https://doi.org/10.1029/2022JE007243.
[7] Takagi M. et al. A GCM study on the 4-day and 5-day waves in the Venus atmosphere // J. Geophysical Research: Planets. 2022. V. 127. Article e2021JE007164. https://doi.org/10.1029/2021JE007164.
[8] Takagi M. et al. Formation and quasi-periodic variation of equatorial jet caused by planetary-scale waves in the Venusian lower cloud layer // J. Geophysical Research: Planets. 2023. V. 128. Article e2023JE007922. https://doi.org/10.1029/2023JE007922.
[9] Andrews D. G., Holton J. R., Leovy C. B. Middle atmosphere dynamics. Academic Press, 1987.

COMPACT FLUX-FITTING *K*-DISTRIBUTION PARAMETERIZATIONS SUITABLE FOR RADIATION BLOCKS IN VENUS CLIMATE MODELS

M. V. Razumovskiy[1,2], B. A. Fomin[1]
[1] *Moscow Institute of Physics and Technology, Dolgoprudny, Russia*
razumovskii@phystech.edu
[2] *Central Aerological Observatory, Dolgoprudny, Russia,*

KEYWORDS:
Venus, radiative transfer, molecular absorption, flux-fitting *k*-distribution, radiative parameterization; line-by-line modeling; general circulation models

INTRODUCTION:
Radiation schemes in general circulation models (GCMs) connect the state of an atmospheric column with radiative fluxes and the heating/cooling rates that enter the thermodynamic equation. Their computational cost scales with the cost of one column calculation, the number of columns, and the frequency of radiative calls. A line-by-line (LBL) calculation over a high-resolution molecular spectrum cannot be repeated for every column and radiation time step of a three-dimensional Venus model. Consequently, a radiation scheme must be strongly compressed while remaining accurate for spectrum-integrated fluxes and their vertical divergence [1]. This is particularly demanding for the dense, hot CO_2 atmosphere of Venus, whose pressure and temperature vary strongly with altitude. Online self-consistent radiative transfer must represent molecular absorption across a broad range of pressure-temperature conditions, a demanding task because of pressure-broadened line wings and high-temperature hot-band absorption [2, 3]. Accurate representation of the vertical and diurnal heating distribution is dynamically important because cloud-layer thermal tides contribute to the transport of angular momentum and influence the atmospheric superrotation [4]. We present compact parameterizations for radiative transfer in Venus GCMs, achieving substantial spectral compression and reducing the number of solver evaluations per atmospheric column while retaining the prescribed radiative accuracy.

METHOD:
The adopted flux-fitting *k*-distribution approach uses reference LBL radiative outputs as the organizing principle of spectral compression. Unlike a canonical correlated-*k* scheme, it does not explicitly reorder k(ν) or construct a probability distribution in k-space. Additionally, the method does not require the inter-level correlation assumption implied in correlated *k*-distribution schemes. Each spectral band is divided into subsets, and a height-dependent effective absorption profile k*(z) is retrieved for every accepted subset. Fluxes and heating/cooling rates calculated with these profiles are compared directly with the LBL reference. If the prescribed accuracy is not reached, the remaining spectral subset is split again. Thus, each accepted subset adds one *k*-term, and the target radiative accuracy controls the final dimensionality of the parameterization.

Initial absorption coefficients are calculated on the pressure-temperature grid from molecular line data and the selected line-shape and wing models; MARFA is used as the LBL opacity backend [5], including a recent model of the far-wing continuum [3]. The resulting parameterizations contain the effective absorption profiles, band-integrated Planck functions (in the longwave part), and representative spectral points for cloud optical properties and Rayleigh scattering (in the shortwave part). They can therefore be supplied directly to a GCM radiative transfer solver without retaining the original high-resolution spectrum [6]

RESULTS AND CONCLUSIONS:

In the 125–400 nm ultraviolet range, gaseous absorption and absorption by the unknown UV absorber are represented together with Rayleigh scattering and Venus cloud optics by only eight radiative-transfer evaluations. The parameterization was tested for alternative SO_2 and unknown absorber profiles; differences in solar heating rates remain below 1% for solar zenith angles of 0 and 75° [6]. In the shortwave range of 2030–15000 cm^{-1}, the spectrum is represented by 11 intervals and 38 k-terms. For thermal radiation in the 10–6000 cm^{-1} range, a 16-band parameterization for CO_2, H_2O and SO_2 requires 32 radiative-transfer evaluations for an atmospheric column. Validation against the LBL reference model for three representative temperature profiles gives upward-flux errors below 2% below 95 km. Cooling-rate differences are about 1.2 K day^{-1} below 90 km and 0.3 K day^{-1} below 75 km [7]. The number of independent solver calls is one to two orders of magnitude smaller than in typical correlated-*k* implementations for Venus.

Actual wall-clock acceleration within a GCM also depends on the radiative-transfer solver, vertical grid and cloud model, but the number of column solver calls sets the main computational scale. The presented compact height-dependent absorption profiles retain a direct link to reference molecular spectroscopy and reproduce the radiative quantities used by a climate model. The shortwave and longwave constructions therefore provide a consistent route from detailed spectra to reusable radiation-block inputs to allow radiative calls to be scheduled according to physical requirements.

REFERENCES:

[1] Eymet V., Fournier R., Dufresne J.-L., Lebonnois S., Hourdin F., Bullock M. A. Net exchange parameterization of thermal infrared radiative transfer in Venus' atmosphere // J. Geophysical Research: Planets. 2009. V. 114. Article E11008. DOI: 10.1029/2008JE003276.

[2] Lee C., Richardson M. I. A discrete ordinate, multiple scattering, radiative transfer model of the Venus atmosphere from 0.1 to 260 μm // J. Atmospheric Sciences. 2011. V. 68. No. 6. P. 1323–1339. DOI: 10.1175/2011JAS3703.1.

[3] Chaverot G., Turbet M., Tran H. et al. SpeCT: A state-of-the-art tool to calculate correlated-k tables and continua of CO_2-H_2O-N_2 gas mixtures // Astronomy and Astrophysics. 2025. V. 702. Article A137. DOI: 10.1051/0004-6361/202555762.

[4] Lebonnois S., Hourdin F., Eymet V., Crespin A., Fournier R., Forget F. Superrotation of Venus' atmosphere analyzed with a full general circulation model // J. Geophysical Research: Planets. 2010. V. 115. Article E06006. DOI: 10.1029/2009JE003458.

[5] Razumovskiy M.V., Fomin B. A., Astanin D. A. MARFA: An effective line-by-line tool for calculating molecular absorption in planetary atmospheres // J. Quantitative Spectroscopy and Radiative Transfer. 2025. V. 346. Article 109599. DOI: 10.1016/j.jqsrt.2025.109599.

[6] Fomin B. A., Razumovskiy M.V. Effective parameterization of absorption by gaseous species and unknown UV absorber in 125–400 nm region of Venus atmosphere // J. Quantitative Spectroscopy and Radiative Transfer. 2022. V. 286. Article 108201. DOI: 10.1016/j.jqsrt.2022.108201.

[7] Fomin B. A., Razumovskiy M.V. The flux-fitting *k*-distribution technique: An application to thermal infrared absorption in the atmosphere of Venus // J. Quantitative Spectroscopy and Radiative Transfer. 2026. Article 109912. DOI: 10.1016/j.jqsrt.2026.109912.

ELECTRONIC KINETICS AND EMISSIONS OF CARBON MONOXIDE IN DISCHARGES IN CO_2–N_2–CO ATMOSPHERES

A. S. Kirillov[1], V. F. Tarasenko[2], A. N. Panchenko[2]
[1] *Polar Geophysical Institute, Apatity, Murmansk region, Russia*
kirillov@pgia.ru
[2] *Institute of High-Current Electronics, Tomsk, Russia*

KEYWORDS:
carbon monoxide, carbon dioxide, molecular nitrogen, emissions, streamer discharges, atmosphere of Mars

INTRODUCTION:
In recent decades, discharges in the atmospheres of planets and their satellites have attracted the attention of researchers. Experimental modeling of discharges in the atmosphere of Mars is being conducted. The investigation presents experimental results from a study of streamer discharge analogs in a gas mixture corresponding to the atmosphere of Mars.

EXPERIMENTAL AND THEORETICAL RESULTS:
The spectral and optical characteristics of laboratory discharges were recorded, and theoretical estimates of the emission characteristics of CO_2, CO, N_2, and their mixtures were made. The gas mixtures were excited by streamers of plasma diffuse jets, initiated by a pulsed-periodic capacitive discharge. It was found that the emission of CO bands in the wavelength range of 250–900 nm during a pulsed-periodic discharge at low pressures dominates even at low carbon monoxide contents in carbon dioxide.

We pay a special attention to the study of electronically excited CO($b^3\Sigma^+$, v'=0) and CO($B^1\Sigma^+$, v'=0) molecules in the CO_2–N_2–CO atmospheres. Intensities of emissions of the third positive band system

$$CO(b^3\Sigma^+, v') \rightarrow CO(a^3\Pi, v'') + h\nu_{3+}$$

and Angstrom band system

$$CO(B^1\Sigma^+, v') \rightarrow CO(A^1\Pi, v'') + h\nu_{Ang}$$

of CO molecules are calculated and compared with results of experimental measurements. Good agreement of results of theoretical calculation and experimental measurements is obtained.

ACKNOWLEDGMENTS:
The study was carried out within the framework of the State Assignment of the HCEI SB RAS (project FWRM-2026-0008) and within the framework of the State Assignment of the PGI RAS (project FMES-2025-0004).

STUDIES OF THE ATMOSPHERES OF GIANT PLANETS BASED ON DATA OBTAINED AT THE SAO RAS

A. E. Ivanova[1], A. V. Moiseev[1,2], D. G. Evdokimova[1], D. A. Belyaev[1], A. A. Fedorova[1]

[1] *Space Research Institute RAS, Moscow, Russia*
anastasia.ivanova@cosmos.ru

[2] *Special Astrophysical Observatory, Nizhnij Arkhyz, Zelenchukskiy region, Karachai-Cherkessian Republic, Russia*

KEYWORDS:
Jupiter, Uranus, troposphere, clouds, methane, ammonia

INTRODUCTION:

In the atmospheres of giant planets, significant spatial variability is observed in the chemical composition of gases and aerosols, as well as in cloud structure. Spatially resolved spectroscopic observations make it possible to study these variations, as well as their connection to atmospheric circulation and the dynamics of cloud layers [1–4].

In January–March 2025 and July 2026, observations of giant planets were conducted using the SCORPIO-2 focal reducer on the 6-meter BTA telescope at the Special Astronomical Observatory of the Russian Academy of Sciences (SAO RAS) [5]. All observations were conducted in long-slit spectroscopy mode, with the slit oriented perpendicular to the planet's equator; the chosen observational geometry allows for an assessment of the latitudinal distribution of gaseous components in the atmospheres of the giant planets. The wavelength range used (365–1090 nm) covers the main methane and ammonia bands, which are essential for studying the atmospheres of giant planets in the visible and near-infrared ranges. This presentation will provide an overview of the observations.

To interpret the observational data, a model of radiative transfer in a giant planet's atmosphere was developed based on the DISORT radiative transfer method, the HITRAN2024 and ExoMol molecular databases, and various cloud models. The presentation will show the results of analyzing Jupiter's data using this model.

REFERENCES:

[1] Hill S. M., Irwin P. G. J., Alexander C., Rogers J. H. Spatial Variations of Jovian Tropospheric Ammonia via Ground-Based Imaging // AGU. 2024. https://doi.org/10.1029/2024EA003562.

[2] Irwin P. G. J., Hill S. M., Fletcher L. N., Alexander C., Rogers J. H. Clouds and Ammonia in the Atmospheres of Jupiter and Saturn Determined From a Band-Depth Analysis of VLT/MUSE Observations // J. Geophysical Research: Planets. 2024. V. 130. Iss. 1. Article 2024JE008622. 40 p. https://doi.org/10.1029/2024JE008622.

[3] Vdovichenko V. D., Lysenko P. G., Filippov V. A. Absorption variations in the ammonia bands of 645 and 790 nm along the central meridian of Jupiter in 2023 // 15th Moscow Solar System Symp. 2024.

[4] Braude A. S., Irwin P. G. J., Orton G. S., Fletcher L. N. Colour and tropospheric cloud structure of Jupiter from MUSE/VLT: Retrieving a universal chromophore // Icarus. 2020. https://doi.org/10.1016/j.icarus.2019.113589.

[5] Afanasiev V. L., Moiseev A. V. Scorpio on the 6 m Telescope: Current State and Perspectives for Spectroscopy of Galactic and Extragalactic Objects // Baltic Astronomy. 2011. V. 20. P. 363–370.https://doi.org/10.1515/astro-2017-0305.

MARTIAN NEUTRAL ATMOSPHERE FROM THE MESOSPHERE TO CO_2 EXOBASE: A MULTI-MISSION CLIMATOLOGY FROM OCCULTATION EXPERIMENTS

D. A. Belyaev, E. D. Starichenko, D. A. Kossova
Space Research Institute RAS, dbelyaev@cosmos.ru

KEYWORDS:
Martian atmosphere, mesosphere, thermosphere, turbopause, exobase, occultation experiment

INTRODUCTION:
In this work, we study the heights of the middle and upper neutral atmosphere of Mars — the mesosphere (above ~50 km) and the thermosphere (above 100-120 km) up to the exobase for CO_2 molecule (180–220 km). These altitudes contain transition layers: a mesopause of about 80–120 km with a temperature minimum and a turbopause located 10–20 km higher, where the molecular diffusion becomes dominate versus the turbulent one. Variations of the height and temperature of the meso/turbopause, as well as the exobase, are caused by seasonal variability, solar activity, and vertical energy transfer caused by global circulation and atmospheric waves.

In this paper, we present the analysis of vertical profiles of temperature and CO_2 density measured from three occultation experiments by the UV and IR spectrometers: (i) Atmospheric Chemistry Suite (ACS) on board the Trace Gas Orbiter (TGO) of the ExoMars-2016 mission; (ii) Imaging UltraViolet Spectrograph (IUVS) and (iii) Extreme UltravVolet Monitor (EUVM) both on board the Mars Atmosphere and Volatile EvolutioN (MAVEN) mission. The ACS middle-IR channel (ACS-MIR) has been operating in the solar occultation mode at 2.3–4.2 microns since April 2018 up to now. The atmospheric structure is sounded in the strong CO_2 absorption band around 2.7 microns in a wide range of heights, from 10 to 180 km [1]. The MAVEN spacecraft operated in 2015–2025 when IUVS sounded the CO_2 absorption in 130–220 nm at altitudes from 50 to 150 km in the stellar occultation mode [2] and EUVM measured the upper thermospheric CO_2 abundance in 10–20 nm in the solar occultations [3].

The paper shows the results of observations for Martian years (MY) — from MY33 to MY37 by MAVEN and from the middle of MY34 to the end of MY37 by TGO. We show seasonal, local time and latitudinal variations of temperature, density and altitude of the mesopause, turbopause and, partially, exobase. The turbopause zone is determined by comparing the coefficients of molecular (CO_2) and turbulent diffusion under the condition of saturation of atmospheric gravity waves at 80–120 km [4] that are observed in vertical temperature profiles according to ACS data [5].

REFERENCES:
[1] Belyaev D. A. et al. Thermal Structure of the Middle and Upper Atmosphere of Mars from ACS/TGO CO_2 Spectroscopy // J. Geophysical Research: Planets. 2022. V. 127(10). Article e2022JE007286.
[2] Gupta S. et al. Thermal Structure of the Martian Upper Mesosphere/Lower Thermosphere From MAVEN/IUVS Stellar Occultations // J. Geophysical Research: Planets. 2022. V. 127(11). DOI: 10.1029/2022JE007534.
[3] Thiemann E. M. B. et al. Mars Thermospheric Variability Revealed by MAVEN EUVM Solar Occultations: Structure at Aphelion and Perihelion and Response to EUV Forcing // J. Geophysical Research: Planets. 2018. V. 123(9). DOI: 10.1029/2018JE005550.
[4] Kossova D. A. et al. Wave-Induced Eddy Diffusion and the Turbopause Height in the Martian Atmosphere // Solar System Research. 2026. V. 60(24). DOI: 10.1134/S0038094626600186.
[5] Starichenko E. D. et al. Vertical damping of gravity waves evaluated from ACS-TGO solar occultation measurements on Mars // Frontiers in Astronomy and Space Sciences. 2025. V. 12. Article 1672283. DOI: 10.3389/fspas.2025.1672283.

NON-MIGRATING TIDES IN THE MARTIAN MESOSPHERE FROM TEMPERATURE MEASUREMENTS OF TGO AND IUVS/MAVEN

A. Fedorova[1], L. Trompet[2], D. Belyaev [1], J.S. Evans[3], M.A. Lopez-Valverde[4], J. Alday[4], F. Gonzalez-Galindo[4], E. Thiemann[5], S. Gupta[5], S. Jain[5], O. Korablev[1]

[1] *Space Research Institute RAS, Moscow 117997, Russia, fedorova@cosmos.ru*
[2] *Royal Belgian Institute for Space Aeronomy, Brussels, Belgium*
[3] *Computational Physics Inc., Springfield, Virginia, USA*
[4] *Instituto de Astrofisica de Andalucıa, CSIC, Granada, Spain*
[5] *Laboratory for Atmospheric and Space Physics, University of Colorado Boulder, Colorado, USA*

KEYWORDS:
Mars, mesosphere, temperature, tides, ExoMars Trace Gas Orbiter, MAVEN

INTRODUCTION:
The mesosphere, roughly 50–110 km above the surface on Mars, is a transitional atmospheric region where solar radiation, gravity waves, and atmospheric tides interact to shape temperature profiles and composition. But precise temperature measurements in this layer enable insight into energy balance, dynamics and wave propagation, photochemistry and atmospheric composition. The measuring of temperatures in the mesosphere has been challenging. Key missions have progressively filled this gap: the Mars Climate Sounder (MCS) on MRO provided limb observations from the surface to 80 km at 3 AM/PM; SPICAM UV on Mars-Express used stellar occultations to probe the nightside at 70–140 km; and MAVEN's IUVS delivered both dayside and nightside profiles at all local times (30–160 km) [1–3].

The prominent temperature variability in this region takes thermal tides. Classification of tides is typically divided into migrating and nonmigrating groups where the migrating tides are westward traveling Sun-synchronous waves that are forced by zonally uniform solar heating. The non-migrating tides are not Sun synchronous, as they can be eastward and westward propagating with various wavenumbers at periods that are integer fractions of a day [4]. This study focuses on study of non-migrating tides in the mesosphere, using joint observations from TGO spectrometers and MAVEN/IUVS over the same Martian years.

EXPERIMENTS:
We combined data from TGO and MAVEN experiments to study temperature distribution in the mesosphere between 50 and 110 km. TGO includes three spectrometers: ACS NIR, ACS MIR, and NOMAD SO, which operate during solar occultations near the morning and evening terminators. MAVEN IUVS provides day-side limb measurements and stellar occultations at any local time. In this work we used only nightside stellar occultations.

RESULTS:
We investigated non-migrating tide propagation in the mesosphere using the longitudinal temperature distribution within a narrow local time frame. The amplitude of these longitudinal variations fluctuates with height, season, latitude, and local time. To distinguish different tides, we used reconstruction of tides from temperature fields predicted by the General Circulation Model [5]. The first part of our study focused on the height variations of longitudinal variations across different latitude bins, employing TGO datasets. The second part examined local time variations by combining data from ACS NIR with IUVS.

During aphelion in low latitudes, WN-3 (Wave Number 3) and WN-4 dominate, with amplitudes reaching 11K and 9K, respectively. GCM predictions and combined analysis of TGO occultations and IUVS limb observations demonstrate that DE2 (diurnal eastward propagated tide with wavenum-

ber 2) and DE3 is dominated in this season. The model accurately predicts the vertical and latitudinal distribution of these tides but underestimates the amplitude by 1.5–2 times.

In perihelion, WN-2 is dominated by contributions from WN-3, associated with DE1 and DE2, respectively. SE1 and S0 may also contribute, according to GCM predictions. The amplitude is smaller than in aphelion but can reach 8-9K depending on altitude.

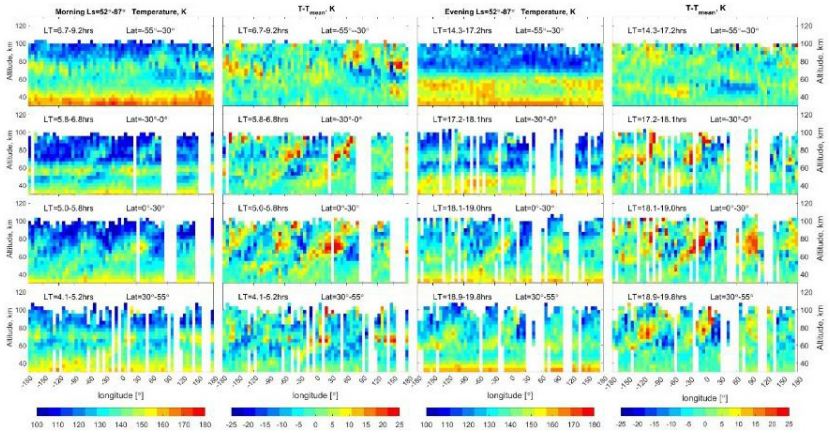


Fig. 1. Longitudinal distribution of temperatures and its deviations from ACS-NIR and NOMAD SO for the morning and evening terminators at Ls=52…87°

ACKNOWLEDGMENTS:

This work was accomplished with the support of the International Space Science Institute as part of ISSI team 23-594 "A Multi-Mission Approach to Close the Gaps in Understanding of the Structure and Variability in the Mars Upper Atmosphere". The IKI team acknowledges financial support from the Russian ministry of science and high education.

REFERENCES:

[1] Guzewich S.D., Talaat E.R., Waugh D.W. Observations of planetary waves and nonmigrating tides by the Mars Climate Sounder // J. Geophysical Research: Planets. 2012. V. 117. Article E03010. https://doi.org/10.1029/2011JE003924.

[2] Withers P., Pratt R., Bertaux J.-L., Montmessin F. Observations of thermal tides in the middle atmosphere of Mars by the SPICAM instrument // J. Geophys. Res. 2011. V. 116. Article E11005. DOI: 10.1029/2011JE003847.

[3] Nakagawa H., Jain S.K., Schneider N.M. et al. A warm layer in the night-side mesosphere of Mars // Geophysical Research Letters. 2020. V. 47. Article e2019GL085646. https://doi.org/10.1029/2019GL085646.

[4] Talaat E.R., Lieberman R.S. Nonmigrating Diurnal Tides in Mesospheric and Lower-Thermospheric Winds and Temperatures // J. Atmospheric Sciences 1999. V. 56 P. 4073–4087. https://doi.org/10.1175/1520-0469(1999)056%253C4073:NDTIMA%253E2.0.CO;2.

[5] Millour E., Forget F., Spiga A. et al. 2024, juillet 3. The Mars Climate Database, MCD version 6.1. EPSC2024. https://doi.org/10.5194/epsc2024-516.

INTERANNUAL VARIATIONS OF THE MARTIAN SEASONAL CYCLE BASED ON DATA FROM THE HEND/ODYSSEY EXPERIMENT

A. E. Romanova, M. L. Litvak, A. B. Sanin
Space Research Institute RAS, Moscow, Russia, nastya-romanova-2019@bk.ru

KEYWORDS:
Mars, neutrons, HEND, CO_2 seasonal cycle, GCR, polar caps, interannual variations

INTRODUCTION:
The analysis is based on 25 years of Mars neutron albedo measurements acquired by the High Energy Neutron Detector (HEND). HEND is a subsystem of Gamma-ray spectrometer suite integrated onboard NASA Mars Odyssey orbiter that is operating on Mars orbit since 2002 [1]. This study summaries the results of observation of seasonal and interannual variability of the CO_2 deposits in the Martian polar regions. The growing and sublimation of Martian seasonal caps is observed as corresponding seasonal variations of neutron flux above Martian polar regions that could be converted into the estimation of column density and mass of CO_2 deposit [2, 3]. Local maxima and minima in the variations of mass of the seasonal CO_2 caps have been studied, and a link to global dust storms has been identified.

SCIENTIFIC INSTRUMENTATION AND METHODS:
HEND provides global mapping of epithermal and high-energy neutron fluxes produced in the subsurface layer (1–2 m) of Mars [1]. Martian neutron and gamma-ray radiation originates from the bombardment of the planet's surface by galactic cosmic ray (GCRs) charge particles, which penetrate through thin Martian atmosphere and interact with primary soil forming nuclei via spallation reaction [1]. Comparing neutron fluxes measured at different energy ranges one can address key HEND objective: to determine the vertical distribution of water ice in the subsurface layer of Mars and create a global map of water abundance in the subsurface of Mars [1, 4]. It was also found that nuclear methods (neutron and gamma-ray spectroscopy) can be used to observe another phenomenon — the global seasonal redistribution of atmospheric CO_2 between Martian poles [2, 3, 5, 6]. In HEND measurements, CO_2 condensation on the surface is manifested by a significant increase in the neutron count rate over the local winter season (Ls=90…180° for the southern hemisphere and Ls=270…360° for the northern hemisphere). The variation in the HEND neutron signal in southern polar region over the Martian year is illustrated in Fig. 1.

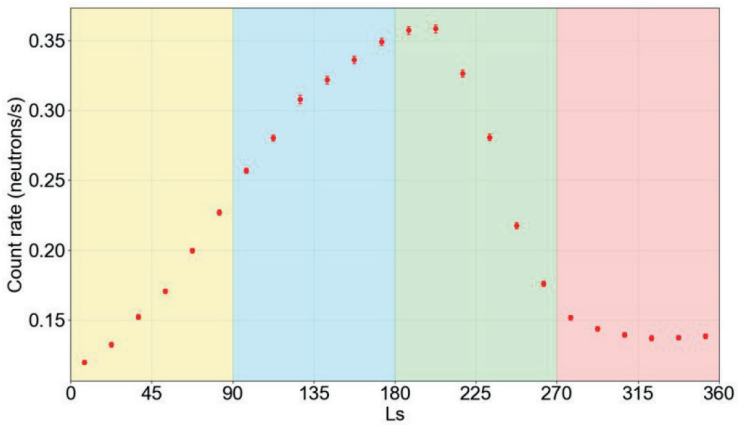


Fig. 1. Neutron count rate measured by the HEND MD detector in the southern polar region. Colored bands indicate the Martian seasons: yellow — autumn, blue — winter, green — spring, and red — summer

The dependence of the HEND neutron signal as a function of solar longitude (Ls) was obtained for 12 successive Martian years. Using numerical simulations, the neutron count rate measured by the HEND detectors was converted into the CO_2 deposit's column density and then into the mass of the whole seasonal cap. The maximum mass of the seasonal CO_2 caps over all period of observation was estimated to be $5.7 \cdot 10^{15}$ kg for the southern polar cap and $3.1 \cdot 10^{15}$ kg for the northern polar cap. It was found that the minimum in the condensed CO_2 mass coincide with episodes of global dust storms. This correlation was tested for the most intense global dust storms observed during the 25-year HEND observation period occurred in Martian Years 25, 28, and 34 [7].

REFERENCES:

[1] Boynton W.V., Feldman W.C., Squyres S.W. et al. Distribution of Hydrogen in the Near Surface of Mars: Evidence for Subsurface Ice Deposits // Science. 2002. V. 297. No. 5578. P. 81–85. DOI: 10.1126/science.1073722.

[2] Mitrofanov I.G., Zuber M.T., Litvak M.L. et al. CO_2 Snow Depth and Subsurface Water-Ice Abundance in the Northern Hemisphere of Mars // Science. 2003. V. 300. No. 5628. P. 2081–2084. DOI: 10.1126/science.1084.

[3] Litvak M.L., Mitrofanov I.G., Kozyrev A.S. et al. Long-term observations of southern winters on Mars: Estimations of column thickness, mass, and volume density of the seasonal CO_2 deposit from HEND/Odyssey data // J. Geophysical Research: Planets. 2007. DOI: 10.1029/2006JE002832.

[4] Litvak M.L., Mitrofanov I.G., Kozyrev A.S. et al. Comparison between Polar Regions of Mars from HEND/Odyssey Data // Icarus. 2006. V. 180. No. 1. P. 23–37. DOI: 10.1016/j.icarus.2005.08.009.

[5] Kelly N.J., Boynton W.V., Kerry K. et al. Seasonal polar carbon dioxide frost on Mars: CO_2 mass and columnar thickness distribution // J. Geophysical Research. 2006. V. 111. No. E3. Article E03S07. DOI: 10.1029/2006JE002678.

[6] Prettyman T.H., Feldman W.C., Titus T.N. Characterization of Mars' seasonal caps using neutron spectroscopy // J. Geophysical Research. 2009. V. 114. No. E8. Article E08005. DOI: 10.1029/2008JE003275.

[7] Smith M.D. THEMIS Observations of the 2018 Mars Global Dust Storm // J. Geophysical Research: Planets. 2019. V. 124. P. 2929–2944. DOI: 10.1029/2019JE006107.

DESTRUCTION OF METHANE BY NEGATIVE IONS IN THE LOWER ATMOSPHERE OF MARS. A POSSIBLE SOLUTION TO THE METHANE PROBLEM

A. K. Pavlov[1], A. A. Gorokhov[2]
[1] *Ioffe Institute, Saint Petersburg 194021, Russia*
anatoli.pavlov@mail.ioffe.ru
[2] *Peter the Great St. Petersburg Polytechnic University*
Saint Petersburg 195251, Russia

KEYWORDS:
Mars, lower atmosphere, methane losses, cosmic rays, discharges, ionization

INTRODUCTION:
This study examines the possibility of a rapid destruction rate for methane in the lower atmosphere of Mars as a solution to a known problem: the discrepancy between methane concentration measurements in the upper atmosphere and the near-surface layer. According to TGO data, the methane content in the upper atmosphere does not exceed 10–100 ppt [1]. In contrast, MSL measurements near the Martian surface indicate a level of ~0.5 ppb, with occasional spikes reaching several ppb. The MSL data also reveal seasonal variations of methane concentration [2]. Standard photochemical models predict a methane lifetime of approximately 300 years, which rules out the possibility of explaining the observed seasonal and spatial variations in methane concentration. Explaining them requires the existence of a rapid methane destruction process with loss rates orders of magnitude higher than those of the photochemical processes expected to operate in the lower atmosphere up to an altitude of several kilometers. Candidate processes include reactions of methane with negative and positive ions generated by the ionization of the lower atmosphere via galactic cosmic rays (GCRs) and by discharges between dust particles in dust devils and dust storms [3]. It has been shown that accounting for ionization caused by GCRs reduces the lifetime of methane molecules by approximately an order of magnitude compared to the standard photochemical lifetime; however, this reduction is insufficient to explain the observed concentration variations. The additional ionization rate in the atmospheric surface layer due to electrical discharges required to explain the observed differences in methane content between the upper and lower Martian atmosphere, as well as the seasonal variations, has been calculated.

REFERENCES:
[1] Korablev O. et al. No detection of methane on Mars from early ExoMars Trace Gas Orbiter observations // Nature. 2019. V. 568. P. 517–520. https://doi.org/10.1038/s41586-019-1096-4.
[2] Webster C. R. et al. Background levels of methane in Mars' atmosphere show strong seasonal variations // Science. 2018. V. 360. P. 1093–1096. http://science.sciencemag.org/.
[3] Chlde B. et al. Detection of triboelectric discharges during dust events on Mars // Nature. 2025. V. 647. P. 865–869. https://doi.org/10.1038/s41586-025-09736-y.

TERRAIN-MODULATED ILLUMINATION AND INCOMING SOLAR RADIATION ON MARS: IMPLICATIONS FOR ATMOSPHERIC SIMULATION MODELS AND MISSION PLANNING

Hanlin Ye, Jinsong Ping
National Astronomical Observatories, Chinese Academy of Sciences, Beijing, China, yehl@radi.ac.cn

KEYWORDS:
Mars, illumination environment, Monte Carlo ray tracing, topographic effects

INTRODUCTION:
The surface illumination environment and incoming solar radiation on Mars play a fundamental role in controlling the Martian surface energy budget. They directly affect surface temperature, atmospheric heating, boundary-layer development, and the exchange of energy between the surface and the atmosphere. In climate modeling, incoming solar radiation is often first determined by orbital geometry and solar position; however, local topography can substantially modify the actual radiation received at the surface through slope, aspect, and terrain-shadowing effects. Studies of terrestrial climate and land-surface processes have shown that whether topographic correction is considered can lead to considerable differences in simulated illumination conditions, especially over regions with complex terrain [1]. Therefore, for Mars, incorporating topographic effects is necessary for a more refined representation of the Martian surface radiation environment. With the development of GoMars [2, 3], China's Mars atmospheric simulation model, improving the description of terrain-modulated radiative processes has become increasingly important.

In addition to its importance for climate modeling, the Martian illumination environment is also a key factor in engineering applications and mission planning. For Mars rovers and landers, solar illumination directly influences power generation, thermal control, and long-term operational safety. Regions with insufficient illumination or strong terrain-induced shadowing may limit rover mobility and reduce the efficiency of solar-energy utilization, whereas areas with stable illumination conditions can provide more favorable environments for surface exploration.

In this study, terrain-modulated Martian illumination and incoming solar radiation were analyzed using the HRSC–MOLA global Martian digital elevation model (DEM) product and a Monte Carlo ray-tracing algorithm [4, 5]. The period from the beginning of Mars Year 17 at 2000-05-30 20:15:13 to the beginning of Mars Year 32 at 2028-08-16 09:48:49 was selected as the main analysis period, covering 15 complete Martian years. Based on this long-term simulation, we investigated the global distribution characteristics of Martian illumination rate and incoming solar radiation, and further quantified the effects of topographic correction on both illumination rate and incoming solar radiation.

RESULTS:
As shown in Fig. 1(a), the multi-year mean illumination rate exhibits a weak hemispheric asymmetry, with higher values in the northern hemisphere than in the southern hemisphere, especially over the northern polar region. This pattern is mainly because the subsolar point remains in the northern hemisphere for a longer period over the course of Mars' elliptical orbit. After considering topographic effects, local terrain signals become identifiable in the illumination-rate distribution, with Olympus Mons clearly visible in Fig. 1(a).

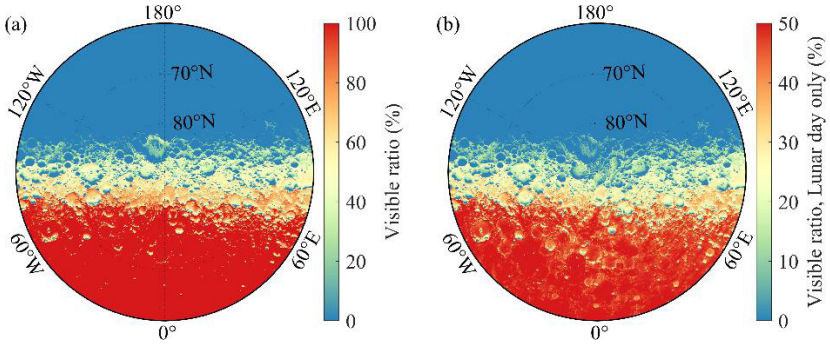


Fig. 1. Global distributions of the multi-year mean Martian illumination rate and incoming solar radiation. (a) Illumination rate, defined as the percentage of illuminated time during the analysis period. (b) Mean incoming solar radiation flux. The results are calculated from Mars Year 17 to Mars Year 32 based on the HRSC–MOLA global Martian DEM product and a Monte Carlo ray-tracing algorithm

Figure 1b shows the global distribution of multi-year mean incoming solar radiation. Unlike the illumination rate, incoming solar radiation presents a much stronger latitudinal gradient, with values in the low- and mid-latitude regions being approximately twice those in the high-latitude regions. Although the subsolar point remains longer in the northern hemisphere, Mars is near aphelion during this period and receives relatively weaker solar radiation, which weakens the hemispheric asymmetry caused by differences in illumination duration. As a result, the multi-year mean incoming solar radiation shows a generally symmetric distribution between the northern and southern hemispheres. After topographic correction, the influence of Martian relief becomes clearly visible, and major topographic features such as Olympus Mons, Ascraeus Mons, and Valles Marineris can be distinguished in Figure 1b.

These results provide a data basis for improving the parameterization of terrain-related radiative processes and incoming radiation in Martian climate models, and also offer scientific support for landing-site selection, energy assessment, and long-term operational safety in future Mars exploration missions.

REFERENCES:

[1] Gu C., Huang A., Li X., Wu Y. Offline correction of CMIP6 HighResMIP simulated surface solar irradiance with 3D sub-grid terrain radiative effects // Geophysical Research Letters. 2024. V. 51. No. 10. Articke e2023GL107737. DOI: 10.1029/2023GL107737.

[2] Dong L., Pu Y., Li Y. et al. A new global open planetary atmospheric model for Mars: GoPlanet-Mars V1 // Chinese Science Bulletin. 2024. V. 69. No. 10. P. 1343–1350. DOI: 10.1360/TB-2023-0699

[3] Liu S., Dong L., Xi X. et al. The fully interactive Martian dust cycle simulations by the GoMars model // Advances in Atmospheric Sciences. 2026. V. 43. No. 3. P. 461–476. DOI: 10.1007/s00376-025-5190-2.

[4] Jaumann R., Neukum G., Behnke T. et al. The high-resolution stereo camera (HRSC) experiment on Mars Express: instrument aspects and experiment conduct from interplanetary cruise through the nominal mission // Planetary and Space Science. 2007. V. 55. No. 7–8. P. 928–952. DOI: 10.1016/j.pss.2006.12.003.

[5] Neukum G., Jaumann R. HRSC: The high resolution stereo camera of Mars Express // Mars Express: The Scientific Payload / ed. by A. Wilson; scientific coordination: A. Chicarro. ESA SP. V. 1240. Noordwijk, Netherlands: ESA Publications Division, 2004. V. 1240. P. 17–35. ISBN 92-9092-556-6.

THE NORTHERN HEMISPHERE STRATOSPHERE IN THE PAST AND FUTURE: A COMPARATIVE ANALYSIS OF TEMPERATURE, VERTICAL VELOCITY, AND HEAT TRANSPORT

T. S. Ermakova[1,2], A. V. Koval[1,2], K. A. Didenko[3,1], E. V. Rocanov[1,4]
[1] *St. Petersburg State University, Saint Petersburg, Russia, taalika@mail.ru*
[2] *Voeikov Main Geophysical Observatory, Saint Petersburg, Russia*
[3] *Pushkov Institute of Terrestrial Magnetism, Ionosphere and Radio Wave Propagation, Troitsk, Russia*
[4] *Davos Physics and Meteorological Observatory/World Radiation Center, Davos, Switzerland*

KEYWORDS:
global atmospheric dynamics, long-term trends; temperature, vertical velocity, heat flux, numerical modelling

ABSTRACT:
The stratosphere is a key component of the climate system, governing the radiative balance, chemical composition, and dynamics of the lower atmosphere. In recent decades, a persistent cooling has been observed in the middle and upper stratosphere, attributed to rising greenhouse gas concentrations, stratospheric ozone depletion, and changes in the Brewer–Dobson circulation. However, the rates of cooling, its seasonal and latitudinal variations, as well as the presence of nonlinear effects, remain subjects of active debate. Of particular interest is the comparative analysis of past observations (the Japanese 55-year Reanalysis, JRA, 1958–2022) and future projections. Numerical simulations were performed using the SOCOL version 4 model. The data were averaged over three ensemble members for each of the two forcing scenarios — SSP2-4.5 and SSP5-8.5 (hereafter SOCOL4 and SOCOL8, respectively, 2025–2089) — enabling an assessment of the evolution of stratospheric processes under different anthropogenic forcing scenarios.

In the present study, three interrelated variables are analyzed: air temperature (as a direct indicator of radiative cooling), vertical velocity (as a diagnostic of the vertical component of the Brewer–Dobson circulation, characterizing the rate of upwelling in the tropical stratosphere and downwelling in polar latitudes), and meridional heat flux (characterizing the efficiency of horizontal energy transport from the tropics to the poles).

For each variable, a comprehensive statistical approach was applied, including:

Linear regression (ordinary least squares) and its non-parametric counterpart — the Mann–Kendall test with Sen's slope estimator — to assess long-term trends and their statistical significance.

Segmented regression (two implementations):

- the maximum likelihood estimation (MLE) method, which optimizes the position of breakpoints and segment parameters;
- the sliding window method with a fixed width of 11 years, which allows for the detection of local changes in trend slope.

The PELT (Pruned Exact Linear Time) algorithm with the Bayesian Information Criterion (BIC) for detecting changes in the mean level of time series.

The CUSUM test (OLS-CUSUM) to check the stability of regression coefficients; a point was considered statistically significant at $p < 0.05$.

The choice of a 11-year window is justified by the need to suppress short-period perturbations (ENSO, volcanic eruptions, sudden stratospheric warmings) while maintaining sensitivity to decadal and longer-term oscillations, including the solar cycle and ozone layer changes. The consistency of re-

sults across methods served as a criterion for the reliability of the identified breakpoints, while the comparison of parametric and non-parametric estimates allowed for the exclusion of artifacts associated with the choice of statistical model.

HISTORICAL PERIOD (JRA, 1958–2022):

In the southern part of the Northern Hemisphere (0–52°N), intense and highly significant cooling was recorded (–0.077 to –0.087 °C/year), with a total magnitude of approximately 5 °C over the 65-year period. In the northern sector (52–87°N), the trends are heterogeneous: December and February show cooling (–0.051 and –0.032 °C/year, respectively), while January exhibits no significant trend. Segmented analysis reveals a single breakpoint in the southern region (1994–2001), followed by a slowdown in cooling by a factor of 1.1–1.5, which is consistent with ozone layer recovery following the Montreal Protocol. In the Arctic, two breakpoints are identified (1973–1984 and 1984–2001), reflecting an oscillatory regime, particularly pronounced in February.

Regarding vertical velocity, a statistically significant increase in upwelling is observed in the southern latitudinal belt during December and January (+0.0004 m/s per year), whereas in the northern region, a weakening of upwelling is found, most pronounced in January (–0.00174 m/s per year). This divergence indicates a reorganization of the Brewer–Dobson circulation with an enhancement of the latitudinal gradient. The PELT algorithm does not detect changes in the mean level, but the sliding window method captures slope changes in 1973–1976 and 1996–2003.

For meridional heat flux, positive trends are observed in the southern region during December and February (+0.04 and +0.03 $K{\cdot}m{\cdot}s^{-1}{\cdot}year^{-1}$, respectively); in the northern region, their magnitude is an order of magnitude higher (December +0.44, January +0.50 $K{\cdot}m{\cdot}s^{-1}{\cdot}year^{-1}$). Both methods (MLE and sliding window) consistently identify periods of structural reorganization: the early 1970s and the mid-2000s, which coincide with stages of abrupt changes in stratospheric circulation.

MODEL SCENARIO SOCOL4 (2025–2089):

Under the SOCOL4 scenario, continued cooling is projected, albeit at a slower rate (–0.04 to –0.05 °C/year), which is approximately half of the observed values. Breakpoints identified in the 2048–2057 period for the southern region indicate a deceleration of cooling; north of this region, February cooling transitions to warming after 2064.

Vertical velocity trends are predominantly linear, with PELT detecting no mean-level shifts. In the southern region, weak negative trends are observed in December and positive trends in January–February; in the north, strengthening of upwelling occurs in December and weakening in January–February. Breakpoints identified by the sliding window method cluster around 2040–2066.

Meridional heat flux trends are positive, except for January in the southern region. The consistency between methods is lower than for JRA, with the best agreement found for February, suggesting a predominantly linear character of changes in this scenario.

MODEL SCENARIO SOCOL8 (2025–2089):

Under the SOCOL8 scenario, cooling is most intense, reaching up to –0.127 °C/year (February, northern region), which is 2–2.5 times higher than in SOCOL4. Three successive points of cooling acceleration are identified (2042–2044, 2056–2058, and 2072–2076), with the rate increasing by 0.02–0.04 °C/year after each breakpoint — a clear indication of a nonlinear threshold response.

Regarding vertical velocity, in the northern part of the Northern Hemisphere, the trend sign reverses after 2051 in January, changing from positive to sharply negative (–0.00208 m/s/year). In February, the CUSUM test confirms the significance of structural breaks in both regions.

For meridional heat flux, maximum growth occurs in February in the southern region (+0.0217 $K{\cdot}m{\cdot}s^{-1}{\cdot}year^{-1}$), and in December in the northern re-

gion (+0.1645 $K \cdot m \cdot s^{-1} \cdot yea^{-1}$), with a negative trend in January. The MLE and sliding window methods demonstrate high consistency for the southern region (2053–2065) and for January in the north (2041–2052).

The comparison of observations and model projections reveals that stratospheric cooling is a persistent trend; however, its intensity, linearity, and the presence of structural breaks depend substantially on the emission scenario. In JRA, two regimes dominate: sustained cooling in the subtropics and highly variable dynamics in the mid- and high latitudes. SOCOL4 exhibits a smooth linear deceleration of cooling, whereas SOCOL8 shows nonlinear acceleration with three distinct breakpoints. Vertical velocity and meridional heat flux demonstrate coherent changes indicative of a reorganization of the Brewer–Dobson circulation, with the most radical shifts projected under the high-emission scenario. The application of a set of complementary statistical methods enhances the reliability of the identified breakpoints and allows for the separation of the climatic signal from natural variability.

ACKNOWLEDGMENTS:
This study is supported by Russian Science Foundation: grant No. 25-47-00122.

THE IMPACT OF SOLAR ACTIVITY ON GLOBAL WAVE PROCESSES IN THE MIDDLE AND UPPER ATMOSPHERE: NUMERICAL MODELING

A. V. Koval[1,2], T. S. Ermakova[1,2,3], K. A. Didenko[1,4]
[1] *S. Petersburg University, Saint Petersburg, Russia, a.v.koval@spbu.ru*
[2] *Russian State Hydrometeorological University, Saint Petersburg, Russia*
[3] *Voeikov Main Geophysical Observatory, Saint Petersburg, Russia*
[4] *Pushkov Institute of Terrestrial Magnetism, Ionosphere, and Radio Wave Propagation, Troitsk, Moscow, Russia*

KEYWORDS:
atmospheric tide, migrating and non-migrating tides, planetary waves, solar activity, wave activity, global atmospheric circulation, numerical modeling

ABSTRACT:
This study examines the global wave dynamics of the middle and upper atmosphere and its sensitivity to changes in direct solar forcing over the 11-year solar activity cycle. Specifically, it examines the amplitudes and phases of solar thermal tides and planetary waves, which have a significant impact on atmospheric dynamics. At the heights of the mesosphere and lower thermosphere (MLT), tides, along with gravity waves, play a major role in shaping the thermodynamic regime of the atmosphere. Solar tides are global-scale oscillations with periods of the solar day (24 hours) and its harmonics (12, 8, and 6 hours), which arise primarily as a result of the absorption of solar radiation by water vapor in the troposphere, ozone in the stratosphere, and oxygen ionization by UV radiation in the thermosphere/ionosphere. Planetary waves are generated in the lower atmosphere due to baroclinic/barotropic instability associated with nonuniform heating of the planet's surface, orographic features, and other factors.

As part of a series of studies dedicated to studying the sensitivity of large-scale wave processes to changes in solar activity (SA), numerical simulations of global atmospheric circulation were conducted using the MUAM nonlinear model of the middle and upper atmosphere. Two ensembles of model simulations were considered, corresponding to high and low SA. The amplitudes of tides and planetary waves were averaged over the corresponding ensembles. The following tides were considered: migrating diurnal and semidiurnal tides with zonal wave numbers of 1 and 2, respectively; non-migrating diurnal and semi-diurnal tides with zonal wave numbers of 2 and 1, respectively; and a non-migrating eastward-propagating diurnal tide with wave number 3. The calculations were performed for the Northern Hemisphere winter season. This allowed us to examine in detail the variability of non-migrating tides: the primary mechanism for generating these tides is the nonlinear interactions of migrating tides with quasi-stationary planetary waves, whose amplitudes are maximized during the winter months, increasing the efficiency of this mechanism. In the MUAM model, tidal generation occurs self-consistently, due to the parameterization of solar heating and nonlinear interactions between gravity waves and planetary waves.

The calculation results showed, in particular, a weakening of the amplitude of the migrating diurnal tide in the 100–150 km altitude range, characteristic of increased solar influence, and an increase at higher altitudes. This effect can be explained by an increase in the vertical temperature gradient in the lower thermosphere, as well as an increase in thermal conductivity, which is proportional to temperature. It hinders the penetration of tides into the thermosphere to greater altitudes with increasing SA. However, at altitudes above 160 km, the effect of increased absorption of direct EUV radiation, which increases with high SA, dominates, and the tidal amplitude at high altitudes with maximum SA increases. Changes in the Eliassen-Palm

(EP) fluxes demonstrate a significant correlation between changes in the vertical propagation of wave activity and changes in the amplitude of the diurnal migrating tide: downward flux increments generally correspond to a weakening of the tide in the 110–150 km range, while upward flux increments correspond to a strengthening of the tide above 150 km. Further analysis of changes in the amplitudes of non-migrating tides revealed a significant dependence on the propagation of stationary planetary waves with zonal numbers 1 and 2 into the thermosphere. For example, above 200 km, the amplitude of the migrating semidiurnal tide in the Northern Hemisphere at high SA increases by a factor of 2-3, while above 150 km in the thermosphere, the amplitude of a stationary planetary wave with zonal number 1 decreases. Taken together, this leads to a complex structure of non-migrating tide amplitude increments. Tidal phases were also considered to analyze the propagation direction.

ACKNOWLEDGMENTS:
This study is supported by Saint Petersburg State University (Project ID 124032000025-1).

ANALYSIS OF EARTH'S POLAR THERMOSPHERE OVERCOOLING DURING GEOMAGNETIC STORMS

G. N. Tsurikov[1], D. V. Bisikalo[2,1], V. I. Shematovich[1], M. S. Berezhnaya[1,3]
[1] *Institute of Astronomy RAS, Moscow, Russia, tsurikov@inasan.ru*
[2] *National Center of Physics and Mathematics, Sarov, Russia*
[3] *Kazan Federal University, Kazan, Russia*

KEYWORDS:
Polar thermosphere, electron precipitation, nitric oxide, thermospheric overcooling

INTRODUCTION:
Intense auroral electron precipitation (with energies up to 30 keV) during strong geomagnetic storms leads to both significant heating of the polar thermosphere [1, 2] (z>90 km) and subsequent cooling (presumably due to the intense formation of nitric oxide molecules and their infrared radiation [3]). In rare cases, thermospheric overcooling is observed when the temperature and density during the storm's recovery phase become lower than before it [4–6]. In [7], we estimated that thermospheric overcooling can occur in the presence of a high-energy fraction in the electron distribution (mean electron kinetic energy for a Maxwellian distribution $E_m \geq 8$ keV, electron energy flux Q_0>1 erg·cm^{-2}·s^{-1}).

In this work, an analysis of geomagnetic storms with overcooling on November 9, 2004, and without it on May 15, 2005 (but with signs of strong cooling, a borderline case) is conducted to refine the theoretically determined electron parameters that trigger thermospheric overcooling. To do this, we used: a) a kinetic model for electron precipitation; b) a chemical model of NO formation in the thermosphere; and c) the average global background atmosphere calculated in [8] for the specified events.

A comparison of the model with NO measurements by the TIMED/SABER satellite for the recovery phase of the November 9, 2004 storm shows [9] that the altitude profiles of NO concentration correspond to electron precipitation with the following parameters: E_m=8 keV, Q_0=2 erg·cm^{-2}·s^{-1}. This result is in good agreement with electron parameter measurements from the DMSP satellites for this event. Electron precipitation into the thermosphere with precisely these parameters can lead to its overcooling, according to theoretical estimates [7]. For the "border" storm of May 15, 2005, the electron parameters were E_m=6 keV, Q_0=2 erg·cm^{-2}·s^{-1}, which is also consistent with theoretical estimates. This allows us to develop an observational criterion for identifying such events.

ACKNOWLEDGMENT:
This work was supported by the Russian Science Foundation (project No. 22-12-00364-p).

REFERENCES:
[1] Wilson G. R., Weimer D. R., Wise J. O., Marcos F. A. Response of the thermosphere to Joule heating and particle precipitation // J. Geophysical Research. 2006. V. 111. Article A10314. DOI: 10.1029/2005JA011274.
[2] Singh V., Gerard J.-C. The thermospheric heating efficiency under electron precipitation conditions // Planetary and Space Science. 1982. V. 30. No. 11. P. 1083–1089. DOI: 10.1016/0032-0633(82)90119-2.
[3] Mlynczak M., Martin-Torres F. J. et al. The natural thermostat of nitric oxide emission at 5.3 μm in the thermosphere observed during the solar storms of April 2002 // Geophysical Research Letters. 2003. V. 30. P. 2100. DOI: 10.1029/2003GL017693.
[4] Knipp D. J., Pette D. V., Kilcommons L. M. et al. Thermospheric nitric oxide response to shock-led storms // Space Weather. 2017. V. 15. P. 325–342. DOI: 10.1002/2016SW001567.
[5] Lei J., Burns A. G., Thayer J. P. et al. Overcooling in the upper thermosphere during the recovery phase of the 2003 October storms // J. Geophysical Research. 2012. V. 117. Atricle A03314. DOI: 10.1029/2011JA016994.

[6] Ranjan A. K., Nailwal D., Sunil Krishna M. V. et al. Evidence of Potential Thermospheric Overcooling During the May 2024 Geomagnetic Superstorm // J. Geophysical Research. 2024. V. 129. DOI: 10.1029/2024JA033148.
[7] Bisikalo D. V., Shematovich V. I., Zhilkin A. G., Tsurikov G. N. On the influence of electron precipitation on the heat balance of the Earth's polar thermosphere // Astronomy Reports. 2026. (In press 2026.)
[8] Scherf M., Krauss S., Tsurikov G., Strasser A. et al. The impact of electron precipitation on Earth's thermospheric NO production and the drag of LEO satellites // Annales Geophysicae. Springer, 2026. V. 44. P. 209–225. DOI: 10.5194/angeo-44-209-2026.
[9] Berezhnaya M., Tsurikov G., Bisikalo D. et al. Analysis of the anomalous phenomenon of overcooling of the polar thermosphere during geomagnetic storms // Astronomy Reports. 2026. (In press 2026.)

TEMPORAL AND SPATIAL CHARACTERISTICS OF SPORADIC CHARGED PARTICLE FLUXES IN THE ORBIT AROUND MARS, AS MEASURED BY THE HEND INSTRUMENT ONBOARD MARS ODYSSEY

S. S. Blazhnova, D. V. Golovin, I. G. Mitrofanov
Space Research Institute RAS, Moscow 117997, Russia
s.blazhnova@np.cosmos.ru

KEYWORDS:
Mars, HEND, magnetosphere, solar wind, MAVEN, solar cycle

ABSTRACT:
The interaction of the variable solar wind with the Martian ionosphere induces complex current systems [1]. These currents control the motion of charged particles and play a key role in both ion acceleration and the formation of the dynamic structure of the ionosphere, which forms the induced magnetosphere of Mars. However, the main feature of the solar wind interaction with Mars is the absence of a global dipole magnetic field. During the planet's evolution, only residual magnetic fields have been preserved to date, with a complex spatial distribution and greatest intensity in the southern hemisphere [2].

In the region of solar wind interaction with the inhomogeneous ionosphere and combined magnetosphere of Mars at an altitude of approximately 400 km above the surface of Mars, according to data from the HEND instrument installed onboard the Mars Odyssey spacecraft [3], sporadic elevated fluxes of charged particles were detected. An analysis of the spatial and temporal distribution revealed that this phenomenon is typically observed in the planet's northern hemisphere and lasts from few days to several months. This effect has a fine temporal structure with a characteristic scale of approximately 1 hour (about half the spacecraft's orbital period). The study also noted a lack of correlation between the global trend in the frequency and intensity of the observing effect and the 11-year solar cycle, but a possible connection with the 22-year Hale cycle. Further observations with the HEND instrument in the coming years will allow us to verify this hypothesis. To study the composition of the fluxes of registered charged particles in near-Martian space, data from the HEND instrument were compared with data from the SEP instrument onboard MAVEN [4] in the same energy range and in the same spatial region.

REFERENCES:
[1] Pan Y. et al. Two distinct current systems in the ionosphere of Mars // Nature Communications. 2024. V. 15. Article 9704. DOI: 10.1038/s41467-024-54073-9.
[2] Boynton W.V. et al. The Mars Odyssey Gamma-Ray Spectrometer Instrument Suite // Space Science Reviews. 2004. V. 110. P. 37–83. DOI: 10.1023/B:SPAC.0000021007.76126.15.
[3] Mitrofanov I. G. et al. Maps of Subsurface Hydrogen from the High Energy Neutron Detector, Mars Odyssey // Science. 2002. V. 297. No. 5578. P. 78–81. DOI: 10.1126/science.1073616.
[4] Larson D. E. et al. The MAVEN Solar Energetic Particle Investigation // Space Science Reviews. 2015. V. 195. No. 1. P. 153–172.

Session 2.
INTERNAL STRUCTURE OF PLANETS AND MOONS (IS)
Oral Session

A PHYSICALLY BASED STRATIFIED MODEL OF THE LUNAR CRUST: COMPARISON WITH AN EXPONENTIAL COMPACTION MODEL

E. V. Kronrod, V. A. Kronrod, O. L. Kuskov
Vernadsky Institute of Geochemistry and Analytical Chemistry RAS
e.kronrod@gmail.com

KEYWORDS:
Moon, lunar crust, megaregolith, porosity, density, GRAIL, impact fragmentation, numerical modeling

INTRODUCTION:
The density and porosity structure of the lunar crust controls the interpretation of gravity data, seismic observations, heat transport, and the thermal evolution of the Moon. Existing models commonly describe porosity reduction with depth using an empirical exponential compaction law [1–3]. Although this approach reproduces the first-order trend inferred from GRAIL, it does not explicitly represent the impact-generated stratification of the crust.

We compare a physically based stratified model with the exponential compaction model using the same physical parameters and observational constraints. The objective is to retain agreement with GRAIL-derived estimates while providing a direct physical interpretation of crustal heterogeneity.

STRATIFIED CRUST MODEL:
The crust is represented as five zones: regolith, upper megaregolith, structurally disturbed crust, fractured crust, and weakly disturbed lower crust. The upper megaregolith is described by a two-level random packing of large fragments and finer material. For a packing porosity of 0.36, the residual structural porosity is approximately 0.13, and the bulk porosity at the top of the megaregolith is related to the intrinsic porosity of the fragments by geometric packing relationships. Consequently, the stratified model is physically applicable for $f_o \geq 0.13$.

The intrinsic porosity of fragment material decreases with lithostatic pressure according to the exponential compaction law. Between depths of 5 and 10 km, the volume fraction of large autochthonous blocks increases, whereas below 10 km the excess structural porosity decays toward the weakly disturbed lower crust. The parameterization is constrained by GRAIL observations, laboratory measurements of lunar rocks [4], and numerical simulations of impact fragmentation [5].

RESULTS AND DISCUSSION:
Calculations were performed for pore-closure pressures P_C=200…300 MPa, grain densities ρ_s=2700…2900 kg·m^{-3}, and porosity at the top of the megaregolith f_o=0.05…0.30; the geometric model was evaluated only for $f_o \geq 0.13$. The best agreement with GRAIL-derived constraints and published porosity-depth profiles is obtained for f_o approximately 0.20–0.25, P_C approximately 200–250 MPa, and ρ_s approximately 2900 kg·m^{-3}.

The stratified and exponential models yield similar volume-weighted mean density and porosity. For realistic parameter combinations, averaging over the whole 40-km crust gives a mean porosity of approximately 4–6%, while substantially higher values characterize the upper 5–10 km. The exponential model describes the smooth first-order compaction trend, whereas the stratified model additionally produces changes in profile slope at the boundaries of the upper megaregolith, structurally disturbed crust, and fractured crust (Fig. 1). This distinction links integrated GRAIL estimates to the physical architecture of the impact-generated crust [1–3, 6].

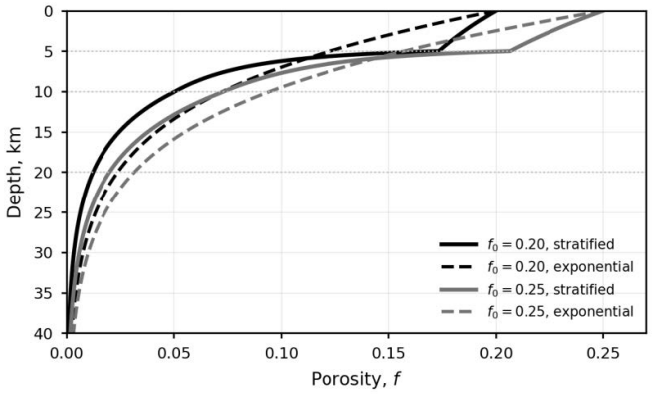


Fig. 1. Porosity profiles predicted by the stratified (solid lines) and exponential (dashed lines) models for P_C=250 MPa and ρ_s=2900 kg·m^{-3}. The parameter f_o is the porosity at the top of the upper megaregolith; horizontal dotted lines mark the principal zone boundaries.

CONCLUSIONS:

1. A physically interpretable five-zone model reproduces the GRAIL-derived density and porosity constraints within its applicability range $f_o \geq 0.13$.
2. The most consistent parameter range is f_o approximately 0.20–0.25, P_C approximately 200–250 MPa, and ρ_s approximately 2900 kg·m^{-3}.
3. The exponential law captures the first-order compaction trend, whereas the stratified model explicitly represents the megaregolith architecture and transitions to deeper, less porous crust.

REFERENCES:

[1] Wieczorek M. A., Neumann G. A., Nimmo F. et al. The crust of the Moon as seen by GRAIL // Science. 2013. V. 339(6120). P. 671–675.
[2] Han S.-C., Schmerr N., Neumann G. A., Holmes S. Global characteristics of porosity and density stratification within the lunar crust from GRAIL gravity and Lunar Orbiter Laser Altimeter topography data // Geophysical Research Letters. 2014. V. 41. P. 1882–1889.
[3] Besserer J., Nimmo F., Wieczorek M. A. et al. GRAIL gravity constraints on the vertical and lateral density structure of the lunar crust // Geophysical Research Letters. 2014. V. 41(16). P. 5771–5777.
[4] Kiefer W. S., Macke R. J., Britt D.T. et al. The density and porosity of lunar rocks // Geophysical Research Letters. 2012. V. 39(7). Article L07201.
[5] Liu T., Wünnemann K., Michael G. 3D-simulation of lunar megaregolith evolution: Quantitative constraints on spatial variation and size of fragments // Earth and Planetary Science Letters. 2022. V. 597. Article 117817.
[6] Wahl D., Wieczorek M. A., Wünnemann K., Oberst J. Crustal porosity of lunar impact basins // J. Geophysical Research: Planets. 2020. V. 125. Article e2019JE006335.

TECTONIC STRESSES IN THE CERBERUS REGION ON MARS ACCORDING TO THE ANALYSIS OF DIGITAL RELIEF MODELS

A.V. Batov[1,2], N.A. Gordeev[1], T.V. Gudkova[1]
[1] *Schmidt Institute of Physics of the Earth, Moscow, Russia, batov@ifz.ru*
[2] *Trapeznikov Institute of Control Sciences, Moscow, Russia*

KEYWORDS:
Mars, tectonic stresses, relief, structural-geomorphological method

INTRODUCTION:
Faults on the planet's surface are a record of the stressed state of the planet's crust and internal dynamics, including changes in the interiors associated with prolonged cooling. The surface of Mars is dotted with numerous thrust faults and wrinkle ridges. The InSight mission showed that Mars is tectonically active, with seismicity similar to intraplate regions on Earth [1]. The nature of seismic activity on Mars is not exactly clear. As on Earth, it is believed that most marsquakes occur as a result of faulting events, which release accumulated stresses inside the planet. The seismic experiment on Mars initiated a number of works to study the morphology of Martian structures that can lead to seismic events [2, 3]. In this work, to study the Cerberus Fossae region, a unique stress study method is used, based on the use of space images, terrain models and topographic maps, developed in [4].

CHARACTERISTICS OF THE STUDY AREA:
Geologically, Cerberus Fossae is younger than 20 Ma, the largest fault network in the Elysium Planitia region, extends ~1200 km along the Martian surface, consists of 5 main parallel faults located 1500 km east of the seismometer, and the faults have a ~ 500-meter vertical displacement. Fault formation and tectonic activity of the region are closely related to the activity of the dominant volcanic region Elysium Planitia, and is characterized by noticeable cracks and faults, the length of which varies from several tens of kilometers to several hundred kilometers. Two main modes of deformation are observed in the region, the structures as a result of stretching are located radially with respect to Elysium Mons; the folds as a result of compression are oriented mainly from north to south, and form separate areas. Cerberus Fossae is a graben system limited by normal faults, in areas between segments and on the eastern tops of grabens, increased stresses are concentrated, potentially leading to the occurrence of marsquakes [5].

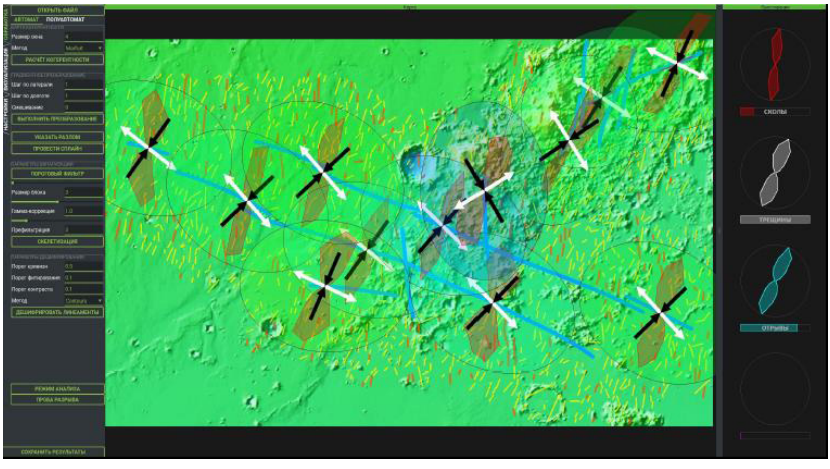


Fig. 1 The map of stress state for the Cerberus Fossae region on Mars

METHOD:
SimSGM software is a specialized tool for automated reconstruction of neotectonic stresses [4]. It uses the structural-geomorphological method of L. A. Sim (SG-method) [6] to analyze digital relief models or satellite images, automatically identifying and statistically processing lineaments - linear elements of the relief that reflect faults and cracks. Based on the orientation of these structures, the program calculates and visualizes the main axes of compression and tension, allowing you to objectively determine the stress field in the surface part of the crust. This method allows us to give qualitative characteristics of the stress state of the studied region and the direction of shear on the faults identified in it based on the analysis of different-scale lineaments.

RESULTS:
For the most part, stresses are developed with orientations of compression axes in the northeastern strike. are divided into two ranks: sub-latitudinal — of the first rank, submeridional — of the second rank.

CONCLUSION:
The structural-geomorphological method was first applied for the Cerberus Fossae region on Mars. Twelve local stress states were reconstructed. A common north-northeast compressive stress field has been identified for a series of north-northwest trending faults and short submeridional faults displacing them. It was obtained that, basically, all faults are displaced by left shifts.

ACKNOWLEDGMENT:
The work was carried out with budgetary funding from the Institute of Physics of the Earth RAS.

REFERENCES:
[1] Banerdt W. B., Smrekar S. E., Banfield D. et al. Initial results from the InSight mission on Mars // Nature Geoscience. 2020. V. 13. C. 183–189.
[2] Perrin C., Jacob A., Lucas A. et al. Geometry and segmentation of Cerberus fossae, Mars: Implications for marsquake properties // J. Geophys. Res.: Planets. 2022. V. 127(1). Article e2021JE007118.
[3] Stähler S. C., Mittelholz A., Perrin C. et al. Tectonics of Cerberus Fossae unveiled by marsquakes // Nature Astronomy. 2022. V. 6(12). P. 1376–1386.
[4] Gordeev N. A., Molchanov A. B. Automation of structural-geomorphological method of reconstruction of shear tectonic stresses L. A. Sim // Geo informatics. 2019. No. 2. P. 25–33 (in Russian).
[5] Jacob A., Plasman M., Perrin C. et al. Seismic sources of insight marsquakes and seismotectonic context of Elysium Planitia, Mars // Tectonophysics. 2022. V. 837. Atricle 229434.
[6] Sim L. A. Study of tectonic stresses by geological indicators (methods, results, recommendations) // Proc. Higher Educational Establishments. Geology and Exploration. 1991. No. 10. P. 3–22 (in Russian).

ON THE DEPENDENCE OF THE VALUE OF THE CHANDLER PERIOD OF MARS ON THE MINERALOGY AND TEMPERATURE OF THE MANTLE

E. A. Kulik[1], T. V. Gudkova[2]
[1] *Moscow Institute of Physics and Technology, kulik.ea@phystech.su*
[2] *Schmidt Institute of Physics of the Earth RAS, gudkova@ifz.ru*

KEYWORDS:
Mars, internal structure of Mars, Chandler Wobble, mineralogy, Andrade rheology, areotherm, Martian mantle

INTRODUCTION:
Information about Martian mantle's composition is based on the content of SNC meteorites (Shergottite-Nakhlite-Chassigny). There are several methods for estimating the mineralogical composition of the Martian interior, which can be denoted as geochemical, isotopic, and geophysical. These approaches are different by calculation's method, but they produce very similar results and have a common base assumption, that SNC meteorites are of Martian origin. This idea was first proposed in [1] and allows to conclude about the weight-based chemical composition of Mars.

In this work, seven chemical models of the mantle were selected to construct test interior models of the planet: DW85 [1], MA79 [2], T13 [3], YM20 [4], LF97 [5], S99 [6], KC08 [7]. The main oxides that account for more than 98% of the mass of the Martian mantle are used as input data. All models are similar to the DW85 model, but they differ slightly in terms of iron content and volatile components.

DISTRIBUTIONS OF MANTLE PARAMETERS:
Mineral composition and temperature (areotherms) are the main parameters of the mantle to be studied. The Perple_X software [8] is used to calculate the phase equilibrium of minerals and obtain the distribution of elastic parameters (density, compressional and shear seismic velocities) in the Martian mantle along chosen areotherms. The areotherms and the content of the main oxides in the mantle serve as an input for this program.

Temperature is one of the parameters of the Martian interior that is still unknown. Variations in temperature profile have an impact on the depth of the mantle's discontinuites, as they affect the conditions of phase equilibrium of minerals and their thermoelastic properties, which leads to variation of seismic velocities. The temperature profiles (three areotherms) are selected from the work [9].

INTEGRAL MODEL PARAMETERS:
For each test model of the internal structure, the integral parameters, the moment of inertia and the Love number k_2, are calculated at the two values of frequency, the solar tide frequency and the frequency of the Chandler Wobble (CW), where the CW period is calculated. The constructed inelastic models of the internal structure of Mars are selected based on their fit to the observed values of the moment of inertia I/MR^2=0.3640±0.0006 and the Love number k_2=0.174±0.008. To account for inelasticity, the Andrade rheology was used.

The formula from [10] is used to calculate the Chandler period:

$$T_W = T_E \left(1 - \frac{(A_c B_c)^{1/2}}{(AB)^{1/2}}\right) \Bigg/ \left(1 - \frac{k}{k_0}\right).$$

Here $T_E = T(\mathrm{ab})^{-1/2}$ is the Eulerian period, A, B are the principal moments of inertia of the planet, A_c, B_c are the principal moments of inertia of the liquid core, k is the Love number, and k_0 is the secular Love number.

RESULTS:

Figure 1 shows how the value of CW period depends on the choice of mineralogical model and areotherm for the selected models. The geochemical models DW85, T13, and YM20 give the lowest values of the Chandler period, while the isotopic models LF97, S99, and the geophysical model KC08 give the highest values of the CW period. At the same time, the variation in temperature and the variation in mineralogical composition give approximately the same spread in the value of CW period — about 1 day. Since, according to [11], the standard deviation in the measurement of the Chandler period is 0.5 days, the period of the Chandler Wobble cannot be used to select the only temperature profile and mineralogy of the planet until the Chandler period of the planet is more accurately determined.

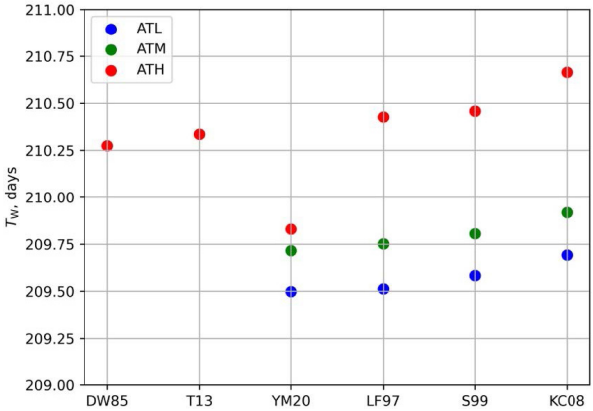


Fig. 1. Dependence of CW period on chemical models and areotherms. Color shows areoterm used

For construction of models the simplified core composition was used: Fe-Ni with some addition of S. However, in real planet, other light elements have a great impact on the behavior of the liquid core. For this reason, we calculated the same interior models with non-zero content of volatiles in the core and compared them with models from Fig. 1.

ACKNOWLEDGMENT:

This work is financially supported by budget funding of Schmidt Institute of Physics of the Earth RAS.

REFERENCES:

[1] Dreibus G., Wanke H. Mars, a volatile-rich planet // Meteoritics. 1985. V. 20. P. 367–381.
[2] Morgan J.W., Anders E. Chemical composition of Mars // Geochimica et Cosmochimica Acta. 1979. V. 43. No. 10. P. 1601–1610. DOI: 10.1016/0016-7037(79)90180-7.
[3] Taylor G.J. The bulk composition of Mars // Geochemistry. 2013. V. 73. No. 4. P. 401–420. DOI: 10.1016/j.chemer.2013.09.006.
[4] Yoshizaki T., McDonough W.F. The composition of Mars // Geochimica et Cosmochimica Acta. 2020. V. 273. P. 137–162. DOI: 10.1016/j.gca.2020.01.011.
[5] Lodders K., Fegley B., Jr. An oxygen isotope model for the composition of Mars // Icarus. 1997. V. 126. No. 2. P. 373–394. DOI: 10.1006/icar.1996.5653.
[6] Sanloup C., Jambon A., Gillet P. A simple chondritic model of Mars // Physics of the Earth and Planetary Interiors. 1999. V. 112. No. 1–2. P. 43–54. DOI: 10.1016/S0031-9201(98)00175-7.
[7] Khan A., Connolly J.A.D. Constraining the composition and thermal state of Mars from inversion of geophysical data // J. Geophysical Research: Planets. 2008. V. 113. No. E7. Article E07003. DOI: 10.1029/2007JE002996.
[8] Connolly J.A.D. Computation of phase equilibria by linear programming: A tool for geodynamic modeling and its application to subduction zone decarbonation // Earth and Planetary Science Letters. 2005. V. 236. No. 1–2. P. 524–541. DOI: 10.1016/J.EPSL.2005.04.033.
[9] Plesa A.-C., Bozdağ E., et al. Seismic velocity variations in a 3D Martian mantle: Implications for the InSight measurements // J. Geophysical Research: Planets. 2021. V. 126. No. 6. Article e2020JE006755. DOI: 10.1029/2020JE006755.

[10] Zharkov V. N., Gudkova T. V. The period and Q of the Chandler Wobble of Mars // Planetary and Space Science. 2009. V. 57. No. 3. P. 288–295. DOI: 10.1016/j.pss.2008.11.010.
[11] Konopliv A. S., Park R. S. et al. Detection of the Chandler Wobble of Mars from orbiting spacecraft // Geophysical Research Letters. 2020. V. 47. No. 21. Article e2020GL090568. DOI: 10.1029/2020GL090568.

TOWARD A GLOBAL MODEL OF THE MARTIAN CRUSTAL MAGNETIC FIELD USING LEGACY ORBITAL MAGNETIC OBSERVATIONS

A. M. Salnikov[1,2], A. V. Batov[1,2], T. V. Gudkova[2], I. E. Stepanova[2]
[1] *Trapeznikov Institute of Control Sciences RAS, Moscow, Russia, salnikov@ipu.ru*
[2] *Schmidt Institute of Physics of the Earth RAS, Moscow, Russia, batov@ifz.ru*

KEYWORDS:
Mars, magnetic field, data selections, global magnetic field model, spherical harmonic analysis

INTRODUCTION:
The orbital magnetic measurements obtained by MGS and MAVEN now form a completed legacy archive for studying the Martian magnetic field. The MGS MAG/ER archive covers observations from 1997 to 2006, while the calibrated MAVEN MAG archive covers observations from 2014 to 2025 [1, 2]. These data differ in altitude, spatial coverage, orbital geometry, temporal distribution, coordinate representation, and level of external magnetic-field disturbance. As a result, they require filtering, regrouping, and construction of consistent selected datasets.

The aim of this work is to assess prepared MGS and MAVEN orbital magnetic datasets and the global models constructed from them. The selected datasets for the three magnetic-field components are considered as an observational basis for a new global model of the Martian crustal magnetic field, with particular attention to data consistency, suitability for global approximation, and model quality.

MAIN RESULTS:
The study is based on an adaptive algorithm developed by the authors for constructing selected datasets and building a global model of the Martian magnetic field from large MGS and MAVEN orbital archives [3]. The algorithm is implemented within the structural-parametric approach and the method of S-approximations, considered as a variant of the method of linear integral representations [4].

The algorithm includes several sequential stages: construction of a computational grid, filtering and regrouping of the initial data, selection of data subsets according to prescribed criteria, field approximation, and analytical continuation to a selected altitude. Its adaptive structure allows the procedure to return to earlier stages and modify filtering, selection, grid, or approximation parameters when intermediate results do not meet the prescribed criteria.

As a first step toward a global model of the Martian crustal magnetic field, consistent orbital magnetic datasets were prepared for the three magnetic-field components: B_r, B_θ, and B_φ. Their quality was assessed using spectral analysis by spherical harmonic degree.

Figure 1 shows an example of a qualitative comparison for the radial component B_r. The power spectrum obtained from the selected orbital observations is compared with spectra of the same component derived from the global models [5, 6] at an altitude of 150 km. This comparison is qualitative because the first spectrum corresponds to selected observational data, whereas the other two spectra correspond to regularized global models. Nevertheless, the selected dataset shows a similar concentration of spectral power and a comparable decrease toward higher spherical harmonic degrees.

The developed algorithm groups large arrays of satellite magnetic measurements near the nodes of a selected computational grid, enabling different global model variants to be constructed, analytically continued to selected altitudes, and evaluated using the proposed approximation method. In this

framework, the completed MGS and MAVEN archive is transformed from a heterogeneous collection of orbital measurements into a physically consistent observational basis for a new global model of the Martian crustal magnetic field.

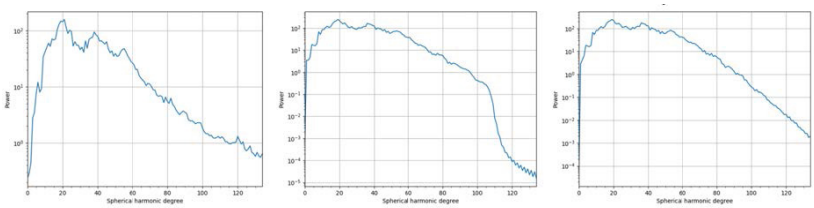


Fig. 1. Power spectra of the radial magnetic field component B_r at an altitude of 150 km. Left: selected orbital magnetic observations used in this work; center: the global model [5]; right: the global model [6]

REFERENCES:

[1] Connerney J. E. P., Mitchell D., Lillis R. J. Mars Global Surveyor MAG/ER Bundle [Dataset]. NASA Planetary Data System, 2024. DOI: 10.17189/y11f-a125.
[2] Connerney J. E. P. MAVEN MAG Calibrated Data Bundle [Dataset]. NASA Planetary Data System, 2026. DOI: 10.17189/1414178.
[3] Salnikov A. M., Batov A. V., Stepanova I. E., Gudkova T. V. On Samples of Satellite Measurement Data for Constructing a Global Model of the Magnetic Field of Mars // Automation and Remote Control. 2024. V. 85. P. 919–930. DOI: 10.1134/S000511792470036X.
[4] Stepanova I. E., Batov A. V., Salnikov A. M., Gudkova T. V. A New Approach to Analytical Modeling of Mars's Magnetic Field // Applied Mathematics in Science and Engineering. 2022. V. 30(1). P. 328–358. DOI: 10.1080/17415977.2021.2018427.
[5] Morschhauser A., Lesur V., Grott M. A spherical harmonic model of the lithospheric magnetic field of Mars // J. Geophysical Research: Planets. 2014. V. 119. P. 1162–1188. DOI: 10.1002/2013JE004555.
[6] Langlais B., Thébault E., Houliez A., Purucker M. E., Lillis R. J. A new model of the crustal magnetic field of Mars using MGS and MAVEN // J. Geophysical Research: Planets. 2019. V. 124. P. 1542–1569. DOI: 10.1029/2018JE005854.

INVERSION RESULTS FOR VENUS' INTERNAL STRUCTURE WITH PROBABILISTIC APPROACH: ELASTIC AND INELASTIC MODELS

I. A. Boronin, T. V. Gudkova
Schmidt Institute of Physics RAS, Moscow 123242, Russia
anarsull23@yandex.ru, gudkova@ifz.ru

KEYWORDS:
Monte-Carlo method, inverse problem, Bayesian statistics, Markov chains, internal structure of the planets, Venus

INTRODUCTION:

Venus is often referred as Earth's twin sister due to their similar sizes, masses and positions in the Solar System. Studying the internal structure of Venus can provide valuable data about its tectonics, the absence of magnetic field, and why the evolutionary pathways of Earth and Venus led to such great differences in surface conditions.

Currently, the observational data available from space missions remain limited, which complicates forward problem of inversion Venus' interior. The Markov chain Monte Carlo (MCMC) algorithm is employed [1, 2] to determine the internal structure of Venus and to obtain probabilistic posterior distributions for both elastic and inelastic models. The rheological model selection (elastic/inelastic) significantly influences the results of probabilistic inversion of interior parameters. This is shown using a three-layer spherically symmetric isotropic model of Venus' internal structure. The MCMC algorithm is applied to obtain posterior probability distributions of the internal structure parameters of Venus by using observation data on mean density, moment of inertia, and Love number. The comparison results are given in the table.

DATA:

We assume that the structure of Venus consists of three layers: a liquid core, a mantle (viscous in the inelastic model), and a crust. For each layer, the model parameters include radius, mean density, viscosity (inelastic model only), and P-wave and S-wave velocities (V_p and V_s). The geodetic observations are as follows: mean radius R=6051.8±1 km, standard gravitational parameter GM = (324858.592±0.006)·10^9 $m^3 \cdot s^{-2}$, mean moment of inertia I/MR^2=0.337±0.024, tidal Love number k_2=0.295±0.066 [3], and mean density ρ=5242.7±2.6 $kg \cdot m^{-3}$. Since the crust contributes only ~0.5% to the total mass of Venus, its parameters are fixed. The core is assumed to be liquid, so the shear wave velocity within it is set to zero.

The Andrade rheology is employed for the inelastic model, which includes complex shear modulus through the complex compliance. The solar tidal period of Venus is T=58.4 days. The viscosity of the mantle is considered for two extreme values — high and low (roughly corresponding to the viscosity of the Earth's lower mantle). As a result, only five out of the twelve model parameters remain free.

SIMULATION RESULTS:

Ten Markov chains were generated, each with a length of 750,000 iterations. More than half of each chain was discarded as burn-in period. After autocorrelation analysis, approximately 4,000 models were collected. The inversion results for the elastic model, as well as for the inelastic model with low and high viscosity values, are presented in Table 1, which shows the posterior probability distributions (1σ) for core radius, mantle and core density. Table 2 lists selected Venus models obtained from the inversion, including their core radius, viscosity, and tidal Love number for both the elastic and inelastic models.

Table 1. Posterior probability distribution (1σ)

Parameter	Elastic	Low Viscosity	High Viscosity
Core radius, km	3251±221	3272±232	3384±246
Core density, kg·m^{-3}	11565^{+921}_{-1198}	11765^{+935}_{-1205}	11200^{+896}_{-1178}
Mantle density, kg·m^{-3}	4032±359	4055±363	4011±352
Viscosity, Pa·s		~10^{21}	~10^{23}

Table 2. Calculated Data for some Venus models

Viscosity, Pa·s	R_c, km	k_2*elastic*	Re(k_2)	Im(k_2)	Δk_2
Low, ×10^{21}	3000	0,2263	0,2529	–0,0101	0,02677
	3100	0,2404	0,2677	–0,0104	0,02754
	3200	0,256	0,2839	–0,0106	0,02806
	3300	0,2727	0,301	–0,0106	0,02845
	3400	0,2909	0,3192	–0,0106	0,02848
	3500	0,3104	0,3383	–0,0104	0,02803
High, ×10^{23}	3000	0,2263	0,2367	–0,0034	0,01046
	3100	0,2404	0,2512	–0,0035	0,01079
	3200	0,256	0,267	–0,0036	0,01099
	3300	0,2727	0,2839	–0,0036	0,01119
	3400	0,2909	0,3022	–0,0036	0,01129
	3500	0,3104	0,3215	–0,0036	0,01112

RESULTS:

The elastic model has systematically lower k_2 values than the inelastic models (by 8–10%, varying across models). High-viscosity mantle models produce a larger core radius (+112 km), lower core density (–565 kg·m^{-3}), and lower mantle density (–44 kg·m^{-3}) compared to low-viscosity models.

ACKNOWLEDGMENT:

The work was carried out with budgetary funding from the Institute of Physics of the Earth RAS.

REFERENCES:

[1] Mosegaard K., Tarantola A., Monte Carlo sampling of solutions to inverse problems // J. Geophys. Res. 1995. V. 100. No. B7. P. 12431–12447.
[2] Xiao C., Li F., Yan J.-G., Hao W.-F., Harada Y., Ye M., Barriot J.-P. Inversion of Venus internal structure based on geodetic data // Research in Astronomy and Astrophysics. 2020. V. 20(8). P. 127–141.
[3] Konopliv A. S., Yoder C. F. Venusian k_2 tidal love number from Magellan and PVO tracking data // Geophysical Research Letters. 1996. V. 23(14). P. 1857–1860.

Session 3.
SURFACES OF PLANETS AND MOONS (SP)
Oral Session

ANCIENT MAGMATISM OF THE EASTERN PART OF THE LUNAR NEARSIDE AS RECORDED IN LUNA-16 SOIL SAMPLE

S. I. Demidova
Vernadsky Institute of Geochemistry and Analytical Chemistry RAS
Moscow, 119991, Russia, demidova.si@yandex.ru

KEYWORDS:
mare basalts, Mg-suite rocks, Luna-16, ancient magmatism

INTRODUCTION:
Luna-16 delivered 101 g of lunar regolith from the north–eastern part of Mare Fecunditatis in 1970. The landing site represents a mare region, where the regolith is dominated by fragments of local basaltic rocks and their derivatives but contains material potentially brought from more distant locations [1]. Here we discuss chemistry, petrology and chronology of rare components of the Luna-16 soil sample which are the products of ancient magmatism (>3.9 Ga) in the lunar crust of the eastern nearside.

RESULTS AND DISCUSSION:
Previous study of seventeenth fragments of Luna-16 samples demonstrated that the regolith of the landing site area contains dominantly basalts with intermediate Ti content and less common very low-Ti (VLT) basalts, both of high-Al composition [2]. The Pb-Pb crystallization age of the main group of basalts is 3590.3±9.4 Ma. This age most likely corresponds to the late episode of volcanism that occupies the most part of the Mare Fecunditatis surface area and occurred during the period of intense mare basalt eruptions between 3.8 and 3.1 Ga [3]. The age of VLT basalts is 3919±27 Ma. These older basalts erupted during the early period of lunar volcanism and may represent the initial underlying basaltic filling of Mare Fecunditatis, at least in some parts of the basin [2]. As being overlaid by younger 3.6 Ga lava flows the older 3.9 Ga age basalts may be considered as cryptovolcanic deposits. They belong to the ancient basalts group (3.9–4.3 Ga) rarely found in both lunar samples (some of Apollo-14 high-Al basalts and Apollo 17 KREEP basalts) and meteorites (high-Al, VLT lunar meteorite Kalahari 009 and basaltic material in Miller Range 13317) [4].

Based on orbital data ancient lunar volcanic deposits, known as cryptomaria were discovered on the lunar surface [5, 6]. They thought to be old (>3.8 Ga) starting erupted during epoch of large impact basins formation [3] and dominated by low-Ti and VLT basalts [7]. Based on gravitational data large volume of cryptovolcanic deposits might exist hidden with overlying material but distinction between cryptomaria and highland Mg-suite rocks is problematic [8].

Rare fragments of highland material were found in Luna-16 sample thought to be sourced by a ~1.5 km fresh crater 30 km southwest of the Luna-16 landing site, or the surrounding highlands area located 100–120 km away [9]. The fragments are represented by spinel troctolites, troctolitic anorthosite, anorthositic norite and dunite. Their mineral chemistry indicates a relation to the primary highland Mg-suite rocks. The studied fragments were subjected to shock nevertheless preserving the relics of a magmatic texture suggesting crystallization from a melt. A single fragment of anorthositic norite has a U-Pb age 3993±66 Ma, which was later disturbed at 413±170 Ma [9]. The younger age most likely reflects an impact event that delivered the fragment to the landing site area. Partial preservation of the primary igneous texture suggests 4.0 Ga age to be a crystallization age of the rock. Nevertheless, there is still a possibility that 4.0 Ga age dates some early impact event. Here we discuss one of the possible scenario of formation of Luna-16 Mg-suite rocks.

As it was previously suggested Mg-suite magmatism was widespread over much of the lunar nearside between 4.30 to 4.36 Ga, thought to represent

a pulse of igneous activity, with uncertainty of younger crystallization ages that makes the duration of the Mg-suite magmatism not clear [10], but the data are scarce. The impact flux of the first billions years was much more intensive, and it is assumed that the role of large impact events is underestimated in the crust-forming processes [11]. Large impact events may produce enormous volumes (>105 km^3) of impact melts which has undergone large-scale igneous differentiation resulted in formation of cumulate stratigraphy (norite – dunite – pyroxenite – (anorthosite)) as modeled for the Orientale basin [11] and South Pole-Aitken (SPA) basin [12]. An important consequence of these model is production of large volumes of melt capable of crystallizing mafic (Mg-suite-like) rock assemblages, that depends on the nature of the target material [11]. There is some evidence that at least some Mg-suite samples may be of impact origin (e.g., [13]). Besides that, study of the Chang'E-6 samples delivered from SPA basin demonstrated that the oldest (~4.25 Ga) impact melt rocks are represented by noritic clasts [14] and observed KREEP enrichment of SPA region is considered as a result of differentiation of giant SPA impact melt pool [15]. Accordingly, the 4.0 Ga date of the Luna-16 Mg-suite also may correspond to a large impact event which resulted in shock-induced melting and following differentiation of an impact melt sheet, that eventually resulted in formation of Mg-suite-like rocks but having much younger age than known Mg-suite rocks. However, an important obstacle to this model is the fact that large amounts of mantle component should be incorporated to produce Mg-suite parental melts and thus some mantle material should appear on the surface and be presented in the lunar samples and meteorites, which is not observed [11, 16].

Thus, the presence of ancient 3.9-4.0 magmatic deposits overlaid by 3.6 Ga basaltic lava flow in close proximity to the Luna-16 landing site area was established based on study of only several fragments of Luna-16 soil sample providing ground truth to understanding the composition and structure of the lunar crust of the eastern nearside.

ACKNOWLEDGMENTS:
This work is a part of the Vernadsky Institute research target.

REFERENCES:

[1] Vinogradov A. P. Preliminary data on lunar ground brought to Earth by Automatic Probe "Luna 16" // Proc. 2nd Lunar Sci Conf. 1971. P. 1–16.
[2] Demidova S., Nemchin A., Merle R. et al. Two episodes of lunar basaltic volcanism in Mare Fecunditatis as revealed by Luna-16 soil samples // Geochimica et Cosmochimica Acta. 2025. V. 394. P. 319–336. DOI: 10.1016/j.gca.2025.02.022.
[3] Hiesinger H., Head J.W., Wolf U. et al. Ages and stratigraphy of lunar mare basalts: a synthesis // Recent Adv. Curr. Res. Issues Lunar Stratigraphy 2011. V. 477. P. 1–51. DOI: 10.1130/2011.2477(01).
[4] Curran N. M., Joy K. H., Snape J. F. et al. The early geological history of the Moon inferred from ancient lunar meteorite Miller Range 13317 // Meteorit. Planet. Sci. 2019. V. 54. P. 1401–1430. DOI: 10.1111/maps.13295.
[5] Whitten J. L., Head J. W. Lunar cryptomaria: Physical characteristics, distribution, and implications for ancient volcanism // Icarus. 2015. V. 247. P. 150–171. DOI: 10.1016/j.icarus.2014.10.030.
[6] Whitten J. L., Head J.W., Lunar cryptomaria: Mineralogy and composition of ancient volcanic deposits // Planet. Space Sci. 2015. V. 106. P. 67–81. DOI: 10.1016/j.pss.2014.11.027.
[7] Lawrence S. J., Hawke B. R., Gillis-Davis J. J. et al. Composition and origin of the Dewar geochemical anomaly // J. Geophys. Res. 2008. V. 113. Article E02001. DOI: 10.1029/2007JE002904.
[8] Sori M. M., Zuber M. T., Head J. W., Kiefer W. S. Gravitational search for cryptovolcanism on the Moon: Evidence for large volumes of early igneous activity // Icarus 2016. V. 273. P. 284–295. DOI: 10.1016/j.icarus.2016.02.009.
[9] Borg L. E., Carlson R. W. The Evolving Chronology of Moon Formation // Annual Review of Earth and Planetary Sciences 2023. V. 51. P. 25–52. DOI: 10.1146/annurev-earth-031621-060538.
[10] Vaughan W., Head J. W., Wilson L., Hess P. C. 2013. Geology and petrology of enormous volumes of impact melt on the Moon: A case study of the Orientale Basin impact melt sea // Icarus 223: 749–765. DOI: 10.1016/j.icarus.2013.01.017.

[11] Vaughan W. M., Head J. W. Impact melt differentiation in the South Pole-Aitken basin: Some observations and speculations // Planetary and Space Science. 2014. V. 91 P. 101–106. DOI: 10.1016/j.pss.2013.12.006.
[12] White L. F., Černok A., Darling J. R. et al. Evidence of extensive lunar crust formation in impact melt sheets 4,330 Myr ago // Nature Astronomy. 2020. V. 4. P. 974–978. DOI: 10.1038/s41550-020-1092-5.
[13] Su B., Chen Y., Wang Z. et al., South Pole- Aitken massive impact 4.25 billion years ago revealed by Chang'e- 6 samples // National Science Review 2025. V. 12. nwaf103. DOI: 10.1093/nsr/nwaf103.
[14] Chen J., Zhang L., Cui Z. et al. KREEP-like lithologies in the South Pole–Aitken basin reworked by the Apollo basin impact at 4.16 Ga // Nature Astronomy 2025. V. 9. P. 1638–1647. DOI: 10.1038/s41550-025-02640-5.
[15] Shearer C. K., Moriarty D. P., Simon S. B. et al. Where Is the Lunar Mantle and Deep Crust at Crisium? A Perspective from the Luna 20 Samples // J. Geophysical Research Planets 2023. V. 128. Article e2022JE007409. DOI: 10.1029/2022JE007409.

THERMAL-CYCLING RESISTANCE OF LUNAR REGOLITH SIMULANT SAMPLES PRODUCED BY SELECTIVE LASER MELTING

A. M. Lysenko[1,2], T. M. Tomilina[1,2], I. G. Mitrofanov[2]
[1] *A. A. Blagonravov Institute for Mechanical Engineering RAS Moscow, Russia, lysenko@imash.ac.ru*
[2] *Space Research Institute RAS, Moscow, Russia*

KEYWORDS:
lunar regolith, selective laser melting, thermal cycling, compressive strength

ABSTRACT:
Lunar regolith is considered a promising in situ resource for the construction of future lunar infrastructure. Selective laser melting (SLM) enables the production of three-dimensional elements directly from regolith without binders [1]. Previous studies have shown that bulk samples with compressive strengths of up to 37 MPa can be produced by SLM from a gabbro-diabase-based lunar regolith simulant [2]. However, the mechanical properties of the manufactured product may change under the influence of constant temperature fluctuations, as has been demonstrated for materials produced from lunar regolith simulants by other methods [3, 4].

The purpose of this study is to experimentally evaluate the effect of cyclic thermal exposure on the compressive strength of samples produced by SLM from a gabbro-diabase-based lunar regolith simulant without binders. Samples were manufactured using a laser 3D printer Concept Laser Mlab Cusing with a maximum laser power of 100 W and a beam diameter of 50 μm, and a laboratory setup with a maximum laser power of 100 W and a beam diameter of 500 μm at average volumetric energy densities ranging from 12 to 19 J/mm^3. The samples were subjected to ten heating–cooling cycles between –70 and +120 °C using an MHX-800 NK climatic chamber and then they were tested for compressive strength. The measured strength values were compared with those of reference samples that had not been exposed to thermal cycling.

After ten thermal cycles, the samples exhibited compressive strengths of 24–38 MPa. The differences between the thermally cycled and reference samples were within the experimental scatter, and no systematic reduction in compressive strength values was observed across the SLM conditions investigated. These results provide evidence for the thermal-cycling resistance of binder-free, laser-melted lunar regolith simulant samples under the investigated conditions and support the potential of SLM for producing construction elements for future lunar infrastructure within the framework of the ISRU strategy.

ACKNOWLEDGMENT:
The study was supported by the Russian Ministry of Science under projects FFGU-2026-0002 and FFWG-2026-0028.

REFERENCES:
[1] Fateri M., Gebhardt A. Process parameters development of selective laser melting of lunar regolith for on-site manufacturing applications // Intern. J. Applied Ceramic Technology. 2015. V. 12. No. 1. P. 46–52. DOI: 10.1111/ijac.12326.
[2] Lysenko A.M., Tomilina T.M., Savvatimova P.R. Peculiarities of SLM technology in melting of natural material — lunar regolith // Engineering and Automation Problems. 2025. No. S4-3. P. 24–33 (in Russian). DOI: 10.52261/02346206_2025_4C3_24.
[3] Grugel R.N. Integrity of sulfur concrete subjected to simulated lunar temperature cycles // Advances in Space Research. 2012. V. 50. No. 9. P. 1294–1299. DOI: 10.1016/j.asr.2012.06.027.
[4] Han W., Zhou Y., Dang F. et al. Spark plasma sintering of HUST-1 lunar regolith simulant and its thermal shock resistance properties // Advances in Space Research. 2024. V. 73. No. 3. P. 1992–2003. DOI: 10.1016/j.asr.2023.11.027.

LOCAL WATER-RICH REGIONS IN THE LUNAR SOUTH POLAR AREA FROM LEND DATA

N. M. Shandrov, A. B. Sanin, I. G. Mitrofanov, M. L. Litvak
Space Research Institute RAS, Moscow, 117997, Russia
shandrov.nik@gmail.com

KEYWORDS:
LEND, Moon, LRO, neutron detector, neutron, water ice, permanently shadowed region

ABSTRACT:
Water ice, presumably present in the polar regions of the Moon, is of considerable interest both for fundamental studies of the origin and evolution of the Earth's natural satellite and for practical applications related to future lunar exploration. The most promising remote-sensing method for determining the hydrogen content in the upper layer of the lunar regolith is orbital neutron sensing, based on measuring the flux of epithermal neutrons generated by the interaction of galactic cosmic rays with the lunar surface material [1]. Since hydrogen is the most efficient neutron moderator, a decrease in the epithermal neutron flux serves as a reliable indicator of enhanced hydrogen abundance and, consequently, of increased water ice concentration [2].

The LEND experiment (Lunar Exploration Neutron Detector), developed at the Space Research Institute of the Russian Academy of Sciences, has been operating since 2009 onboard NASA's Lunar Reconnaissance Orbiter (LRO) spacecraft, performing neutron mapping of the lunar surface [2, 3]. Based on the accumulated LEND data, detailed maps of the epithermal neutron flux distribution and water ice concentration in the lunar polar regions have been produced. Analysis of these maps has demonstrated the existence of extensive regions with enhanced water ice content in the regolith and revealed that the distribution of water ice is considerably more complex than previously assumed. In particular, enhanced water ice concentrations are observed both inside and outside permanently shadowed regions, while many PSRs exhibit no evidence of enhanced water ice content [4].

This work is devoted to the analysis of the water ice distribution map for the lunar south polar region, based on the LEND data. The aim of the study was to develop a systematic approach for identifying local water-rich regions (LWRs), to determine their boundaries, to estimate the average water ice concentration in the regolith, and to investigate the relationship between the location of the identified areas and permanently shadowed regions.

To accomplish these tasks, a new algorithm for identifying LWRs was developed, based on a statistical analysis of the spatial distribution of the epithermal neutron flux measured by collimated detectors of LEND instrument. The proposed algorithm compares the water ice content in the regolith of the candidate region with that of its local drier surroundings, making it possible to identify areas with substantial water reserves.

Application of the developed algorithm to the water ice concentration map of the lunar south polar region made it possible to identify ten local water-rich regions. For each of the identified areas, its location and statistical significance level were determined, and an estimate the average water ice abundance in the regolith were obtained. Comparison of the identified areas with the boundaries of permanently shadowed regions confirmed the previously established conclusion that elevated water ice concentrations can be observed both within and outside permanently shadowed regions and not all shaded regions show signs of water ice in the regolith.

The obtained results can be used in studies of the spatial distribution of water ice on the Moon, in refining models of the formation and evolution of

polar volatiles, and in selecting landing sites for future robotic and crewed missions, as well as potential locations for a future lunar research base.

REFERENCES:

[1] Feldman W. C., Reedy R. C., McKay D. S. Lunar neutron leakage fluxes as a function of composition and hydrogen content // Geophysical Research Letters. 1991. V. 18. Iss. 11. P. 2157–2160.
[2] Mitrofanov I. G., Sanin A. B., Golovin D. V. et al. Experiment LEND of the NASA Lunar Reconnaissance Orbiter for High-Resolution Mapping of Neutron Emission of the Moon // Astrobiology. 2008. V. 8. No. 4. P. 793–804. DOI: 10.1089/ast.2007.0158.
[3] Mitrofanov I. G., Bartels A., Bobrovnitsky Y. I. et al. Lunar Exploration Neutron Detector for the NASA Lunar Reconnaissance Orbiter // Space Science Reviews. 2010. V. 150. P. 183–207. DOI: 10.1007/s11214-009-9608-4.
[4] Sanin A. B., Mitrofanov I. G., Litvak M. L. et al. Hydrogen distribution in the lunar polar regions // Icarus. 2017. V. 283. P. 20–30. DOI: 10.1016/j.icarus.2016.06.002.

RETRIEVING GEOTHERMAL HEAT FLOW OF THE MOON USING ONBOARD PASSIVE MICROWAVE REMOTE SENSING DATA

Z. Meng[1], X. Wang[1], S. Chen[1], X. Zhang[2], J. Ping[3], L. Xiao[4], Y. Zhang[3]
[1] *College of Geoexploration Science and Technology, Jilin University, Changchun, China, mengzg@jlu.edu.cn, wxg24@mails.jlu.edu.cn*
[2] *The State Key Laboratory of Lunar and Planetary Sciences, Macau University of Science and Technology, Macau 999078, China*
[3] *National Astronomical Observatories, CAS, Beijing 100101, China*
[4] *School of Earth Sciences, China University of Geosciences Wuhan 430074, China*

KEYWORDS:
geothermal heat flow, Passive microwave remote sensing, TB simulation, HF retrieval model, geological significance

INTRODUCTION:

Geothermal heat flow (HF), which represents the transfer of energy from the interior of a planet to the surface is critical physical evidence for understanding the thermal state and modeling the thermal evolution of the Moon [1]. The accurate interpretation of HF not only provides insights into key geological questions of the Moon, but also plays a critical role in assessing thermal resources for future lunar exploration and addressing engineering challenges, such as lunar bases construction [2].

Currently, three main approaches are used to evaluate the HF of the Moon: (a) in situ HF experiments, which were done during Apollo 15 and 17 missions; (b) Estimation using heat-producing elements; and (c) Estimation using passive microwave remote sensing data, which is firstly proposed by utilizing ground-based microwave radiometer (MRM) observations and then using the orbital MRM data of the Moon [3–5]. Compared with methods (a) and (b), orbital MRM data provide the most effective ways to retrieve the HF on a global scale. However, the retrieval is severely limited by calibration issue in Chinese Chang'e-2 (CE-2) MRM data and by uncertainties in selecting suitably thermophysical models of the regolith.

To address these issues, we employed an improved TB mapping method to avoid the calibration issue and constructed a new HF retrieval model to estimate HF on a global scale, which were constructed from the brightness temperature TB simulation model and normalized TB (nTB) mapping method with the suitable thermophysical parameters constrained by Apollo in-situ HF experiments and LRO Diviner data. Using this method, the influence of calibration errors is reduced to less than 0.1% on temperature and less than 0.2 $mW{\cdot}m^{-2}$ on the retrieved HF results.

After comparison, the 3.0-GHz TB at night was employed to obtain the HF of the Moon with the constructed HF retrieval model. The retrieved HF values exhibit a wide spatial distribution, ranging from 0 to 66.7 $mW{\cdot}m^{-2}$, with a global average of 18.1 $mW{\cdot}m^{-2}$, coinciding well the previous estimations using other methods. Notably, 85.7% of the values fall within the range of 10–50 $mW{\cdot}m^{-2}$.

Laneuville et al. [6] suggested that radioactive elements are the primary heat-producing elements of the Moon. Then, after comparing the retrieved HF with Th content data from the LP-GRS data, four distinct HF distribution patterns were identified, which are expressed as follows.

1) Regions with high Th and high HF. This agreement further supports the hypothesis that the in-suit HF experiments were likely influenced by the radiogenic elements enriched in the Procellarum KREEP Terrain [7].
2) Regions with high Th but low HF. This pattern hints that the Th contents measure by the LP-GRS instrument can only reflects the heat-produc-

ing elements in the shallow layer of the regolith, which can probably not represent the Th contents across the whole lunar crust.;

3) Regions with low Th and low HF. This pattern provides a suitable sample places to evaluate the mantle HF, which represents an important scientific objective for future lunar exploration.

4) Regions with low Th but high HF. Such pattern probably indicates the localized enrichment of heat-producing elements below the lunar crust that are not detected onboard Gamma ray spectrometer. Interestingly, the existence of the pattern shows a strong correlation with the basins with diameter ranging from 244 to 380 km, deserved to be further studied in future.

These patterns indicate that the distribution of radiogenic heat-producing elements obtained by the LP-GRS data cannot represent the vertical distribution throughout the entire crust. Moreover, these findings highlight the need for further investigation into the scale dependency using additional models and data sources. Due to the limited availability of ground-truth measurements, additional in-situ observations are essential. Future lunar lander missions are expected to provide more thermal data, which will be critical for improving the uncertainty analysis and validation of HF results.

ACKNOWLEDGMENTS:
This work was supported by the National Key Research and Development Program of China under Grant 2021YFA0715104 and the National Natural Science Foundation of China under Grant 42071309.

REFERENCES:

[1] Nagihara S. et al. Improved data reduction algorithm for the needle probe method applied to in-situ thermal conductivity measurements of lunar and planetary regoliths // Planet. Space Sci. 2014. V. 92. P. 49–56.
[2] Siegler M. et al. Lunar Heat Flow: Global Predictions and Reduced Heat Flux // J. Geophys. Res. Planets. 2022. V. 127. No. 9. Article e2022JE007182.
[3] Krotikov V. D., Troitskii V. S. Detecting heat flow from the interior of the moon // Astron. Zhurnal. 1963. V. 40. Article 1076.
[4] Keihm S. J., Langseth M. G. Lunar microwave brightness temperature observations reevaluated in the light of Apollo program findings // Icarus. 1975. V. 24. No. 2. P. 211–230.
[5] Siegler M. A. et al. Remote detection of a lunar granitic batholith at Compton–Belkovich // Nature. 2023. V. 620. No. 7972. P. 116–121.
[6] Keihm S. J. et al. Mapping the lunar heat flow: Methodology and new constraints from recalibrated Chang'E-2 microwave radiometer data // IEEE Trans. Geosci. Remote Sens. 2023. V. 61. P. 1–14.
[7] Laneuville M. et al. Distribution of Radioactive Heat Sources and Thermal History of the Moon // J. Geophys. Res.: Planets. 2018. V. 123. No. 12. P. 3144–3166.
[8] Siegler A., Smrekar S. E. Lunar heat flow: Regional prospective of the Apollo landing sites // J. Geophys. Res.: Planets. 2014. V. 119. No. 1. P. 47–63.

SMALL-SCALE CRATER MORPHOLOGY ON THE MOON

S. S. Krasilnikov[1], B. Wu[1], A. T. Basilevsky[2], Y. Wang[3], Z. Chen[1], W. C. Liu[4], A. S. Krasilnikov[2], O. Turchinskaya[2]

[1] *Research Centre for Deep Space Explorations, The Hong Kong Polytechnic University, Hong Kong, sergey.krasilnikov@polyu.edu.hk*

[2] *Vernadsky Institute of Geochemistry and Analytical Chemistry RAS Moscow, Russia*

[3] *Department of Earth and Space Sciences, Southern University of Science and Technology, China*

[4] *State Key Laboratory of Remote Sensing and Digital Earth, Aerospace Information Research Institute, CAS, China*

KEYWORDS:
The Moon, impact craters, AMA, CSFD

INTRODUCTION:

Craters are the dominant relief elements on the surfaces of airless planetary bodies. Their morphology and distribution provide important constraints on surface formation ages, origins, and geological processes. Absolute model ages (AMAs) of planetary surfaces are commonly derived from statistical analyses of impact-crater size-frequency distributions (CSFDs) [1]. This approach was established several decades ago (e.g., [2, 3]) and remains the principal method for constructing chronologies of planets and satellites. For the Moon, the CSFD curve has been calibrated against absolute radiometric age using samples returned to Earth by the Apollo, Luna, and Chang'e missions. However, CSFD results are strongly influenced by image resolution and by the spatial scale at which crater measurements are performed. Higher-resolution images reveal finer-scale features, including smaller impact craters, which are more readily erased by continuous meteoritic bombardment than larger structures, such as the larger impact craters visible in lower-resolution imagery. Consequently, differences may arise between radiometric ages and crater count ages obtained at different observational scales.

CSFD analysis of craters smaller than 2 km commonly yields ages substantially younger than AMA estimates derived at regional scales. Craters in the 0.2–1 km diameter range have lifetimes sufficiently long for AMA analysis [4], although a correction factor is required. In contrast, craters smaller than 200 m have shorter lifetimes and therefore cannot be reliably used for AMA analysis of geological units. Nevertheless, the morphology and density of these small craters can support age determinations for local crater structures (e.g., [4]). In addition, calibration of the degradation history of such small craters (<200 m) may incorporate boulder size-frequency distribution data and boulder lifetimes [5, 6]. Regional surface inclination also has a significant local influence on the degradation and morphology of craters and boulders [7].

In this study, we examine the morphology of small craters on a subhorizontal surface where secondary craters are expected to have a relatively limited influence. The application of advanced remote sensing data analysis methods enabled characterization of the morphological and morphometrical parameters of craters from their formation through to complete degradation. In addition, the influence of resurfacing processes on slopes was investigated through CSFD calculations.

RESULTS:

Morphology of small craters:

One of the critical parameters in crater formation is excavation depth (de). For the meter-scale craters, the excavation depth remains close to the iconic value de=0.085±0.003D [8], where D is the rim-to-rim diameter. The depth-to-diameter (d/D) ratio for small fresh craters (less than ~30 m in diameter) declines with decreasing crater diameter (e.g., [9]). We used

the d/D ratio to evaluate the degradation stage of small craters based on the classification of [4]. This classification divides craters into three classes (A, B, C) with two sub-classes (AB, BC), where d/D for the A class is 0.33–0.2 (fresh crater), and the C class is <0.08. Our estimation showed the mean value for d/D in the studied region (Schrödinger basin) is 0.04 (0.02 STD) (Fig. 1). Therefore, only 0.5% of craters belong to the fresh crater class (A, AB), and only 6.8% belong to the B, BC classes. This shows a higher percentage of degraded craters than was assumed before [4].

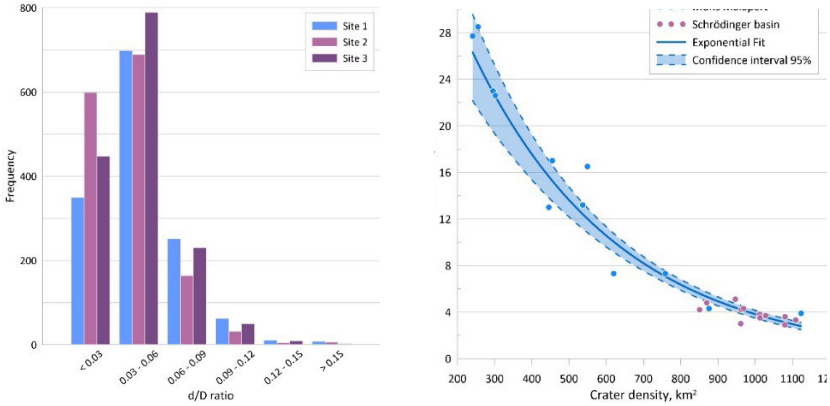


Fig. 1. Left — d/D estimation of small craters on the floor of the Schrödinger basin; right — the density of craters is normalized to one square kilometer for Mons Malapert and the Schrödinger basin

Small craters on the slope:

Slopes influence crater morphology from the initial stage of crater formation, producing asymmetric crater shapes. During the modification stage after impact, gravitational forces exert a strong control on the final crater form. Material from the uphill side slumps into the crater and partially fills it, creating a flatter uphill inner wall and shifting the deepest point toward the downhill wall. Consequently, the alignment of the crater's primary shape becomes evident with increasing slope inclination [7].

In this study, we selected research areas in the foothills and on the slope of Mons Malapert that have uniform slopes and are not significantly affected by secondary cratering. The coefficient of determination for the exponential trendline is relatively high, with an R^2 of 0.92. Furthermore, the low-inclination surface in the Schrödinger basin strengthens the trend, yielding an R2 of 0.95 (see Fig. 1).

ACKNOWLEDGMENTS:

This project is supported by The Hong Kong Polytechnic University Start-up Funding P0052619. Additionally, the work of A.T. Basilevsky, A.S. Krasilnikov, O. Turchinskaya was partly carried out within the state assignment of the Vernadsky Institute of Geochemistry and Analytical Chemistry of the Russian Academy of Sciences (GEOKHI RAS).

REFERENCES:

[1] Neukum G., Ivanov B.A., Hartmann W.K., Cratering records in the inner Solar system in relation to the Lunar reference system // Chronology and Evolution of Mars. Springer: Dordrecht, 2001. pp. 55–86. https://doi.org/10.1007/978-94-017-1035-0_3.

[2] Neukum G., Wise D.U. Mars: A standard crater curve and possible new time scale // Science. 1976. V. 194. P. 1381–1387.

[3] Öpik E.J., The Lunar Surface as an Impact Counter // Mon. Not. R. Astron. Soc. 1960. V. 120. P. 404–411. https://doi.org/10.1093/MNRAS/120.5.404.

[4] Basilevsky A.T. On the evolution rate of small lunar craters // 7th Lunar Scince Conf.. 1976. P. 1005–1020.

[5] Basilevsky A.T., Krasilnikov S.S., Ivanov M.A., Malenkov M.I., Michael G.G., Liu T., Head J.W., Scott D.R., L. Lark. Potential lunar base on Mons Malapert: topographic, geologic and trafficability considerations // Sol. Syst. Res. 2019. 53. 383–398. https://doi.org/10.1134/S0038094619050022.

[6] Li Y., Basilevsky A.T., Xie M., Ip W.H. Correlations between ejecta boulder spatial density of small lunar craters and the crater age // Planet. Space Sci. 2018. V. 162. P. 52–61.
[7] Aschauer J., Kenkmann T., Impact cratering on slopes // Icarus. 2017. V. 290. P. 89–95. https://doi.org/10.1016/J.ICARUS.2017.02.021.
[8] Austin T., Robinson M., Mahanti P. Ejecta Blankets at Small Craters on the Moon // Planet. Sci. J. 2024. V. 5, 114. https://doi.org/10.3847/PSJ/AD3827.
[9] Mahanti P., Robinson M.S., Thompson T.J., Henriksen M.R., Small lunar craters at the Apollo 16 and 17 landing sites — morphology and degradation // Icarus. 2018. V. 299. P. 475–501. https://doi.org/10.1016/j.icarus.2017.08.018.

GEOLOGY OF RIMAE BODE REGION AS PRIORITY SITE CANDIDATE FOR CHINA'S FIRST CREWED LUNAR MISSION

M. Yang[1], J. Huang[1], W. Iqbal[2], L. Wueller[2], C. H. van der Bogert[2], H. Hiesinger[2], S. Mikolajewski[2], M. Xie[3], S. Hu[4], L. Xiao[1,5]

[1] *State Key Laboratory of Geological Processes and Mineral Resources, Hubei Key Laboratory of Planetary Geology and Deep Space Exploration, School of Earth Sciences, China University of Geosciences, Wuhan 430074, China junhuang@cug.edu.cn*

[2] *Institut für Planetologie, Universität Münster, Münster 48149, Germany*

[3] *College of Science, Guilin University of Technology, Guilin 541006, China*

[4] *Institute of Geology and Geophysics, Chinese Academy of Sciences Beijing 100029, China*

[5] *State Key Laboratory of Lunar and Planetary Sciences, Macau University of Science and Technology, Macau 999078, China*

KEYWORDS:
Rimae Bode, Dark Mantle Deposit, Sinus Aestuum, lunar pyroclastic volcanism, mare basalt, sinuous rilles, crewed lunar landing site

INTRODUCTION:
In 2023, China officially unveiled and initiated its crewed lunar exploration program, aiming to land Chinese astronauts on the Moon for the first time by 2030 (https://www.cnsa.gov.cn/n6758823/n6758838/c10355400/content.html). To identify suitable landing sites, candidate regions were assessed in terms of both their scientific value and engineering practicality, a process that progressively reduced the pool from 106 candidates down to 30 prime landing regions [1]. Within this shortlist, the Rimae Bode region stands out as a leading candidate, owing to its high-Ti volcanic deposits, varied lithologies, and favorable geometry for Earth-based observation [1–3].

GEOLOGICAL UNITS:
The Rimae Bode region lies at the lunar mare–highlands boundary, between Sinus Aestuum and Mare Vaporum (Fig. 1a). Within our study area, we distinguish five geological units: a dark mantle deposit (DMD), the mare units of Sinus Aestuum, a network of volcanic rilles including Rimae Bode, and the surrounding highlands (Fig. 1b). The DMD consists of pyroclastic material with relatively low albedo and a thickness of 77–136 m. Sinus Aestuum itself is an ancient impact basin infilled with low-Ti basaltic lavas; these flows reach a maximum thickness of 193–1021 m and yield an absolute model age (AMA) of ~2.96 Ga [4]. The ~4 m-thick regolith in Sinus Aestuum is dominated by local material, with a minor exotic component derived mainly from the Copernicus and Eratosthenes craters. The Rima Bode I mare unit (~3.11 Ga) is marked by sinuous rilles that may have fed the Sinus Aestuum basalts, as suggested by their comparable spectral signatures and AMAs. The Rima Bode II mare unit, in turn, shows high Th and Ti abundances. In addition, we construct a stratigraphic column for eastern Sinus Aestuum (Fig. 1c).

SCIENTIFIC GOALS:
The National Research Council of the National Academies has highlighted the scientific objectives and broader significance of lunar exploration [5]. Building on that report, we define the scientific goals specific to the Rimae Bode region in Table 1. With its wide range of volcanic features, the region offers an exceptional opportunity to address fundamental questions about lunar volcanism. In particular, collecting and returning pyroclastic samples from the DMD unit would substantially refine our understanding of the composition of the deep lunar mantle.

FEASIBLE LANDING SITES:
Guided by this geological framework, we evaluate four prospective landing sites within the traversable terrain (Fig. 1a, b). Together these sites grant

access to a diverse suite of geological samples — including volcanic debris, mare basalts, Copernicus crater ejecta, and high-Th materials — that promises to reveal the geological evolution of the region and to advance our understanding of lunar mantle composition and volcanic processes.

REFERENCES:

[1] Niu R. et al. Scientific Objectives and Suggestions on Landing Site Selection of Manned Lunar Exploration Engineering // Advances in Astronautics Science and Technology. 2024. V. 7. No. 1. P. 37–50. DOI: 10.1007/s42423-024-00153-3.
[2] Van Der Bogert C.H. et al. Science-rich Sites for In Situ Resource Utilization Characterization and End-to-end Demonstration Missions // The Planetary Science J. 2021. V. 2. No. 2. Article 84. DOI: 10.3847/PSJ/abedbb
[3] Hiesinger H. et al. The Rima Bode Region — Candidate for a Future Lunar Landing Site // 52nd Lunar and Planetary Science Conf. 2021. Abstract 1485.
[4] Hiesinger H. et al. The Rima Bode Region — Absolute Model Ages of a Candidate Future Lunar Landing Site // 53rd Lunar and Planetary Science Conf. 2022. Abstract 2169.
[5] National Research Council. The Scientific Context for Exploration of the Moon. Washington, D.C.: National Academies Press, 2007. 120 p. ISBN 0-309-10919-1.

Table 1. Science concepts and goals for the Rimae Bode region, based on the NRC report [5]. Green denotes science goals that can be addressed; red denotes those that cannot

Science goal	a	b	c	d	e
1. Bombardment history of the inner solar system	Test cataclysm hypothesis	Age of South Pole-Aitken	Establish absolute chronology	Recent impact flux	Secondary craters
2. Structure and composition of lunar interior	Thickness/ variability of lunar crust	Stratification of mantle	Size, composition, state of core	Thermal state of interior	N/A
3. Diversity of lunar crustal rocks	Differentiation products	Age, distribution, origin of rocks	Composition of lower crust	Complexity of lunar crust	Extent/ structure of megaregolith
4. Lunar poles and volatiles	State and distribution of volatiles	Source of volatiles	Transport, alteration, loss, processes	Properties of polar regolith	Polar regolith and ancient solar environment
5. Lunar volcanism	Origin/variability of basalts	Age of mare basalts	Range/ extent of pyroclastic deposits	Lunar volcanic flux	N/A
6. Impact processes	Melt sheet differentiation	Structure of multi-ring impact basins	Crater formation	Mixing of local and ejecta material	N/A
7. Regolith processes	Characterize ancient regolith	Physical properties of regolith	regolith modification processes	Rare minerals in regolith	N/A

SOME FEATURES OF CRATER DISTRIBUTION IN THE POLAR REGIONS OF THE MOON

Zh. F. Rodionova[1], N. A. Slodarzh[2], P. V. Litvin[1], E. A. Feoktistova[1]
[1] *Sternberg State Astronomical Institute, Moscow State University Moscow, Russia, marss8@mail.ru*
[2] *Moscow State University of Geodesy and Cartography, Moscow, Russia*

KEYWORDS:
Moon, polar regions, craters, morphometry, crater distribution, DEM, LOLA, CraterTools, ArcGIS, statistical analysis

INTRODUCTION:
Morphometric catalogues of craters with diameters of 10 km and more were compiled for the northern and southern polar regions of the Moon, bounded by latitudes from ±60° to the poles [1, 2]. The source dataset was a digital elevation model based on Lunar Orbiter Laser Altimeter (LOLA) measurements obtained by the Lunar Reconnaissance Orbiter (LRO) spacecraft [3]. The catalogues include crater coordinates, diameters, depths, depth-to-diameter ratios, the maximum and minimum elevations of crater floors and rims, and the inclination angles of the inner and outer slopes. Using ArcGIS Desktop and the CraterTools add-on module, 2,302 craters were digitized and measured in the northern polar region and 1,320 craters in the southern polar region.

Previous studies of these catalogues showed several important features of lunar polar cratering [4–6]. The model ages of the surfaces in both polar regions are close to 4.30±0.02 Ga. The inner slopes of craters in the southern polar region are, on average, steeper than those in the northern polar region. The height differences of crater rims increase with increasing crater diameter. It was also shown that the average depths of craters in the southern polar region are greater than those in the northern region, which may be related to lava filling on the floors of many northern polar craters.

RESULTS AND DISCUSSION:
We analysed the distribution of altitude levels in the northern and southern polar regions of the Moon.

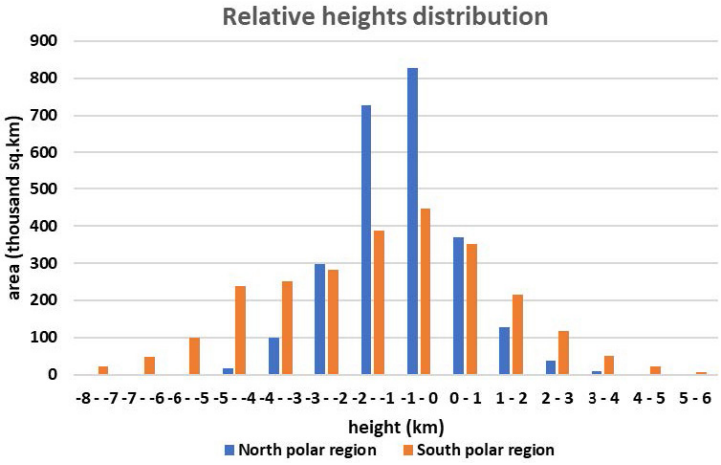


Fig. 1. Distribution of altitude levels in the northern and southern polar regions of the Moon

The relief of the two regions differs noticeably: altitude levels between 0 and –2 km predominate in the northern polar region, whereas levels between +1 and –5 km are more typical of the southern polar region. This difference in hypsometry is consistent with the observed morphometric differences between the crater populations of the two regions.

The crater size-frequency distribution also differs between the northern and southern polar regions. In the northern polar region, craters with diameters of 10–30 km are almost twice as numerous as in the southern polar region. According to the compiled catalogue, the northern polar region contains 1,369 craters with diameters of 10–20 km and 344 craters with diameters of 20–30 km, whereas the southern polar region contains 612 and 230 craters in the same diameter intervals, respectively. For larger craters, this difference becomes less pronounced.

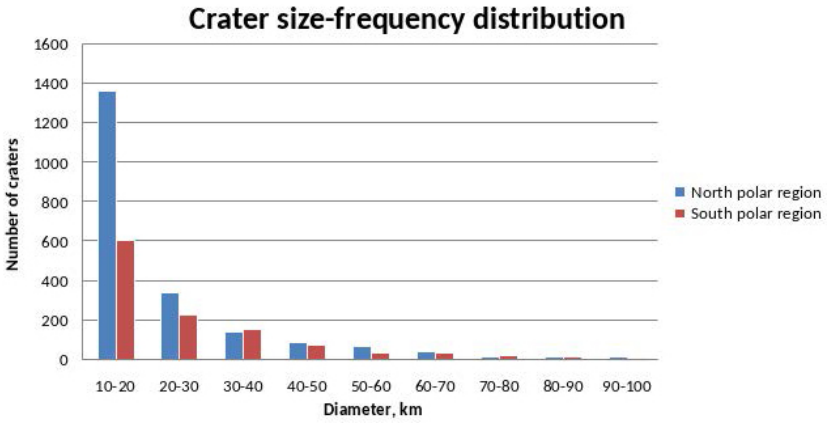


Fig. 2. Crater size-frequency distribution in the northern and southern polar regions of the Moon

Table 1. Crater size-frequency distribution

Diameters, km	North polar region	South polar region
10–20	1369	612
20–30	344	230
30–40	147	158
40–50	95	77
50–60	71	42
60–70	44	36
70–80	20	25
80–90	21	19
90–100	16	13

Special attention was given to 97 craters with diameters greater than 100 km in the northern and southern polar regions. The southern polar region contains six of the largest craters with diameters greater than 300 km, including Poincare, Planck, Schrödinger, and Bailly. In the northern polar region, only one unnamed crater with a diameter of about 337 km belongs to this size group. The largest named crater measured in the southern polar region is Poincare, with a diameter of about 330 km, and one of the deepest is Cabeus, where the difference between rim elevation and floor elevation reaches about 10.1 km.

The distribution of mean crater depths confirms that the southern polar region contains, on average, deeper craters than the northern region. The most noticeable differences occur for craters with diameters of 70–80 km and 90-100 km, where the differences in mean depth reach approximately 0.7 and 1.0 km, respectively [6]. At the same time, the mean depths of craters on the near and far sides of the polar regions are nearly the same, except for some diameter intervals where differences of about 0.5–0.7 km are observed.

CONCLUSION:

The morphometric catalogues of lunar polar craters provide a basis for comparing the structure and evolution of the northern and southern po-

lar regions of the Moon. The northern polar region contains a substantially larger number of small craters, especially in the 10–30 km diameter range. The southern polar region is characterized by a greater number of very large craters, generally steeper inner slopes, and greater average crater depths. These differences indicate that the two polar regions have experienced different local geological conditions, including possible resurfacing and lava filling in parts of the northern polar region. At the same time, crater size-frequency measurements show that the model ages of the surfaces in both polar regions are very close, about 4.3 Ga.

REFERENCES:

[1] Slodarzh N. A., Rodionova Zh. F. Morphometric catalog of craters in the lunar North Polar Region / Department of Lunar and Planetary Research. SAI MSU. 2021. 78 p. https://www.sai.msu.ru/dept/moon/index.html.
[2] Slodarzh N. A., Rodionova Zh. F., Levitskaya T. I. Morphometric catalog of craters in the lunar South Polar Region // Department of Lunar and Planetary Research. SAI MSU. 2020. 46 p. (in Russian). https://www.sai.msu.ru/dept/moon/index.html.
[3] LOLA PDS Data Node. http://imbrium.mit.edu/.
[4] Slodarzh N. A., Rodionova Zh. F. Comparison of the cratering of the north and south polar regions of the Moon // 12th Moscow Solar System Symp.: Abstr. 2021.
[5] Slodarzh N. A., Rodionova Zh. F., Levitskaya T. I. Morphometric features of craters in the southern polar region of the Moon // 13th Moscow Solar System Symp.: Abstr. 2022. pp. 205–207.
[6] Feoktistova E. A., Rodionova Zh. F., Slodarzh N. A. Morphological features of craters in the polar regions of the Moon // 13th Moscow Solar System Symp.: Abstr. of the Moscow. 2022. Article 13MS3-MN-PS-26.

THE DE GERLACH–SHACKLETON CRATER REGION AS A POTENTIAL LANDING SITE FOR FUTURE LUNAR MISSIONS

E. A. Feoktistova, P. V. Litvin, Zh. F. Rodionova
Sternberg Astronomical Institute, Moscow State University
Moscow 119234, Russia, hrulis@yandex.ru

KEYWORDS:
Moon, Polar Regions, landing sites

INTRODUCTION:
The Shackleton and De Gerlach crater region on the Moon is currently being considered by several space agencies as a potential landing site for future landers and a development area for a lunar base. This region attracts researchers' attention because it contains permanently illuminated surface areas, which are essential for solar panel operation, as well as permanently shadowed regions where deposits of various volatile compounds, primarily water ice, may exist. Furthermore, a significant portion of this area lies within a direct line of sight from Earth, which is a critical requirement for ensuring communication with the landing module.

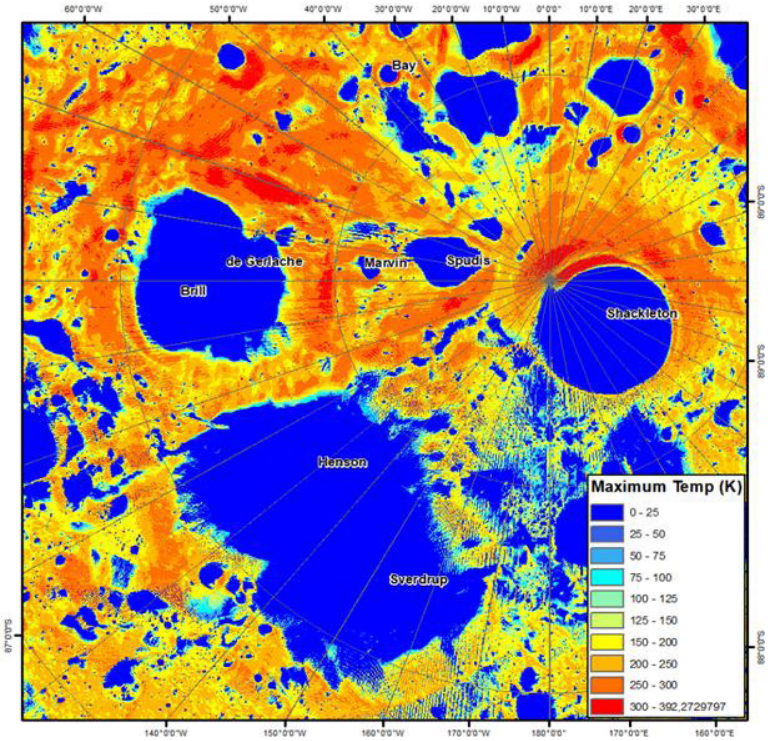


Fig. 1. Distribution of maximum temperatures in the Shackleton and De Gerlach crater region

In 2008, the Indian Moon Impact Probe from the Chandrayaan-1 mission made a hard landing in the area of the Shackleton crater. In the near future, landings of several spacecraft are scheduled in this region: the Chinese Chang'e-7 (in 2026), and the American landers by Intuitive Machines (in 2027–2028) and Blue Origin (in 2028). Under the American Artemis program, astronauts are planned to be deployed to this area. It is also expected that the Russian lander of the Luna-27 mission will be dispatched to this region in 2027.The Shackleton (89.7°S, 129.8°E) and De Gerlach (88.5°S, 88.3°W) craters are located in the immediate vicinity of the lunar

south pole. The Shackleton crater has a diameter of 21 km and a maximum depth of 4.6 km; the De Gerlach crater is situated approximately 30 km from the Shackleton crater and has a diameter of 32.7 km and a maximum depth of 4.1 km. Between the craters, there is a connecting ridge that reaches a height of about 2 km [2] above the surrounding terrain. The ridge consists of four distinct massifs separated by saddles.

To determine the geomorphological parameters of the surface in this region, we used data from the LOLA altimeter onboard the LRO spacecraft with a resolution of 20 m. Based on these data, digital elevation models (DEMs), slope and aspect maps, as well as models of cumulative solar insolation, surface illumination by the Sun, lunar surface temperatures, and visibility from Earth were constructed. Using the obtained data, a surface suitability analysis was performed to identify potential landing sites. The maximum temperature distribution for this area is presented in Fig. 1.

According to the criteria previously defined in several studies, slopes in the potential landing site areas must not exceed 7°, while Earth visibility and solar illumination must be maximized. The locations of the potential landing sites identified in our work are shown in Fig. 2: most of these sites are situated on the rims of the Shackleton and De Gerlach craters (Fig. 2), with some areas located on the ridge between these craters.

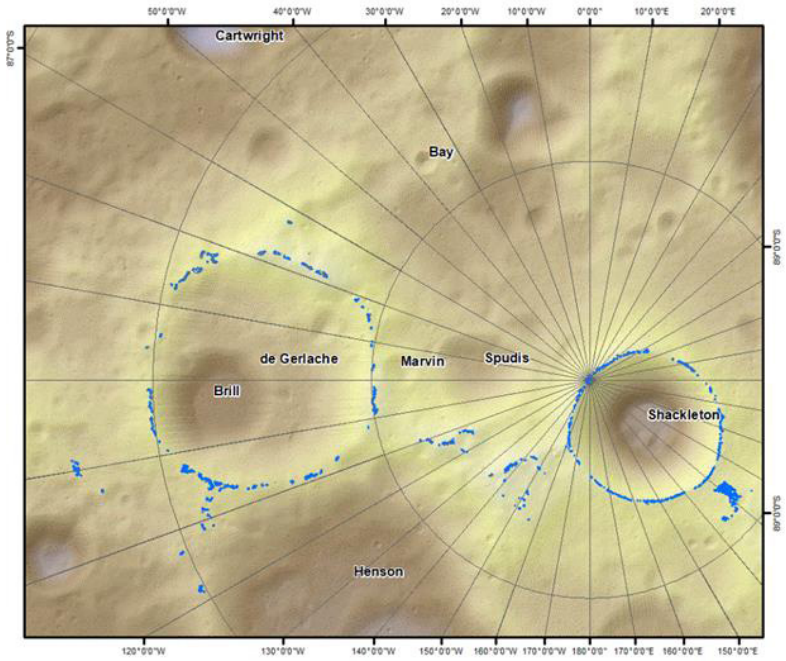


Fig. 2. Locations of surface areas meeting the selection criteria for lander landing sites

REFERENCES:

[1] Leone G., Ahrens C., Korteniemi J., Gasparri D., Kereszturi A., Martynov A., Joutsenvaara J. Sverdrup-Henson crater: A candidate location for the first lunar South Pole settlement // IScience. 2023. V. 26. No. 10.
[2] Boazman S. J. Heather D., Inoue H., Ohtake M. Mapping potential hazards and identifying sampling points within lunar south polar region areas of interest // The Planetary Science J. 2024. V. 5. No. 12. P. 279.
[3] Gawronska A. J., Boazman S. J. Characteristics of the Ridge Crosscut by Shackleton Crater and Implications for Future Sampling Activities at the Lunar South Pole // LPI Contributions. 2025. V. 3090. Article 2886.
[4] Flahaut J., Wöhler C., Berezhnoy A. A., Rommel D., Grumpe A., Feoktistova E. A. et al. // Proc. 7th Lunar Exploration Symposium. 2016. P. 235–245.

DESIGN OF A SMALL-SCALE CAPSULE'S RETURN FROM THE LUNAR SURFACE

O. S. Chernenko, N. A. Eismont, V. A. Zubko
Space Research Institute RAS, Moscow, Russia, o.chernenko@cosmos.ru

KEYWORDS:
Moon, sample return, small-scale capsule, mechanical centrifuge

INTRODUCTION:
Lunar sample return usually requires an ascent stage or another rocket-based system to transfer a payload from the lunar surface onto an Earth-return trajectory. This study considers an alternative concept for small payload masses: direct ballistic return of a small-scale sample capsule after mechanical acceleration on the lunar surface. In this scheme, the capsule performs no active maneuver after release; the required initial velocity is produced by a stationary mechanical system such as a centrifuge or sling. The objective of the study is to assess the principal ballistic feasibility of this sample-return method and to determine lunar surface regions from which a direct transfer to the Earth can be achieved. A capsule mass of about 10–50 kg is considered, corresponding to the delivery of a small amount of lunar material.

SAMPLE RETURN METHOD:
The proposed scheme consists of three main stages. First, the sample capsule is placed at the end of a mechanical centrifuge installed on the lunar surface. During spin-up, the system gives the capsule a velocity sufficient not only to escape the Moon's gravitational field, but also to form the subsequent return trajectory to the Earth. At the moment of release, the capsule velocity is directed along the local horizon, that is, tangentially to the lunar surface. After separation, the capsule performs no active maneuvers and follows a passive ballistic trajectory toward the Earth. In the calculations, arrival at the Earth is detected by crossing the nominal atmospheric boundary at an altitude of 100 km; the atmospheric flight below this altitude is not considered at this stage.

The ballistic problem is reduced to selecting a combination of parameters that places the mechanically accelerated capsule into an acceptable return corridor. These parameters include the location of the site on the lunar surface, the calendar release epoch, the direction of tangential launch, and the velocity excess above the lunar escape velocity. The initial state of the capsule is constructed taking into account the actual position and velocity of the Moon, the orientation of the Moon-fixed coordinate frame, and the motion of the surface point itself. The trajectory is then integrated in the geocentric inertial frame, accounting for the Earth's gravity and perturbations from the Moon and the Sun using ephemerides.

The criterion for a successful return is a descending crossing of the 100 km control altitude above the Earth. In addition, a constraint on the atmospheric entry angle is used for preliminary screening: both excessively shallow trajectories, which are sensitive to errors and may lead to a miss, and clearly steep trajectories, which may cause increased thermal and dynamic loads, are excluded. At this stage, this range is treated only as a ballistic filter for early design. The final admissible atmospheric entry corridor must be refined after specifying the capsule shape, ballistic coefficient, thermal protection system, allowable loads, and atmospheric-flight model.

RESULTS:
A global scan of the lunar surface was performed, and a catalog of feasible locations for the mechanical launch system was constructed. The lunar surface was assumed to be spherical. The catalog contains 933 grid nodes with a 5° spacing. Among them, 721 sites provide an exact descending crossing of the 100 km atmospheric interface, and 652 sites satisfy the preliminary entry-angle constraint. The minimum velocity excess above the lunar escape velocity is 122.66 m/s. The entry velocities of representative solutions

lie in the range of 10.997–11.090 km/s, which is typical for lunar-return trajectories.

The feasible solutions form a connected region on the lunar surface. This region includes low-energy sites near Oceanus Procellarum, a western branch of feasible solutions, several southern options, and a more demanding northern polar scenario. A set of nine representative sites was selected for further analysis. This set includes low-energy solutions, the Chang'e-5 landing site region, the Mairan G crater region, a short-return-time option, and a site associated with the Procellarum KREEP Terrane [1–2].

A calendar analysis was then performed for the selected sites over the 2030–2040 interval. In total, 1323 lunar cycles were tested. For most sites, high-quality launch windows recur with a period close to the sidereal month, and their median width is approximately 6–12 h. The median velocity excess for the main sites is about 145–257 m/s, while the median flight time is approximately 83–159 h. The northern polar scenario was found to be less stable in terms of launch-window recurrence and requires a significantly higher velocity excess. For a capsule mass of 10–50 kg, the payload kinetic energy is approximately 31–302 MJ.

The results confirm the principal ballistic feasibility of direct return of a small-scale sample capsule from the lunar surface using mechanical acceleration. The most promising sites are those combining moderate velocity excess, recurring calendar windows, and proximity to scientifically significant lunar regions. Further work should include the construction of an aerothermodynamic entry corridor, atmospheric-flight modeling, analysis of local lunar topography, assessment of installation conditions, and detailed design of the centrifuge tether system.

REFERENCES:

[1] Chunlai Li, Hao Hu, Meng-Fei Yang et al. Characteristics of the lunar samples returned by the Chang'E-5 mission // National Science Review. 2022. V. 9. No. 2. DOI: 10.1093/nsr/nwae328.

[2] Zelenyi L. M., Shevchenko V. V. Promising Resources of Rare Metals and Rare-Earth Metals in Near-Earth Space // 2nd Intern. Scientific and Practical Conf. "Rare Metals and Materials Based on Them: Technologies, Properties, and Applications" (RedMet-2022). 2022 (in Russian).

DEVELOPMENT OF A LUNAR OBSERVATION SYSTEM FOR THE DETERMINATION OF THE MOON'S ROTATION PARAMETERS

A. O. Andreev[1], N. K. Petrova[1], Y. A. Nefedyev[2], M. V. Sergienko[2]
[1] *Kazan State Power Engineering University, Kazan 420066, Russia andreev.alexey93@gmail.com*
[2] *Kazan Federal University, Kazan 420008, Russia, star1955@mail.ru*

KEYWORDS:
Lunar Observation System, the Moon's Rotation Parameters, Selenodesy

ABSTRACT:
The substantial increase in the volume of high-precision, multi-parameter data acquired by modern spacecraft has significantly stimulated interest in the robotic exploration of the Moon and in future crewed missions to Mars following the establishment of long-term lunar surface bases. Current and planned lunar exploration programs are characterized by unprecedented observational accuracy and the application of diverse measurement techniques. Among the key scientific objectives is the determination of the Moon's rotational parameters [1]. Consequently, new approaches are required to process large volumes of high-precision observational data and to maximize the scientific information extracted from them. The implementation of these advanced space technologies necessitates the deployment of a network of lunar-based telescopes. Decades of Lunar Laser Ranging (LLR) observations have provided an extensive dataset describing the Moon's dynamical behavior [2]. These measurements enable lunar dynamics to be determined with the accuracy required by modern scientific standards, where the uncertainty in the Earth–Moon distance should not exceed one meter and the accuracy of the lunar rotational parameters should reach the milliarcsecond level [3]. Nevertheless, there remains a need for observational techniques that are independent of laser ranging. One promising approach is the deployment of one or more optical telescopes on the lunar surface. By measuring stellar trajectories, such instruments would enable the determination of the Moon's rotational parameters and could subsequently support a wide range of astrophysical and astrometric investigations. This paper presents the results of numerical simulations of observations performed by lunar-based telescopes located at different selenographic latitudes. The sensitivity of the lunar rotational parameters to the observed selenographic coordinates of stars was evaluated. Analysis of the simulation results indicates that the optimal location for such a telescope is at selenographic latitudes between 30° and 45°, where all three physical libration angles (inclination, ascending node, and longitude) can be determined with high efficiency. The paper also proposes practical design concepts for implementing the described experiment and discusses the key technical challenges that will determine the feasibility of deploying a lunar-based optical telescope.

REFERENCES:
[1] Pavlov D., Williams J., Suvorkin V. Determining parameters of Moon's orbital and rotational motion from LLR observations using GRAIL and IERS-recommended models // Celest. Mech. Dyn. Astron. 2016. V. 126. P. 61–88. https://doi.org/10.48550/arXiv.1606.08376.
[2] Petrova N. K., Nefedyev Y. A., Andreev A. O., Zagidullin A. A. Lunar-Based Measurements of the Moon's Physical Libration: Methods and Accuracy Estimate // Astronomy Reports. 2020. V. 64(12). P. 1078–1086. DOI: 10.1134/S1063772920120094.
[3] Williams J., Boggs D. Tides on the Moon: Theory and determination of dissipation // J. Geophys. Res. Planets. 2015. V. 120. P. 689–724. DOI: DOI: 10.1002/2014JE004755.

GEOLOGIC-MORPHOLOGIC ANALYSIS OF MALAPERT MONS ON THE MOON

A. T. Basilevsky[1], A. S. Krasilnikov[1], Yuan Li[2], G. G. Michael[3]
[1] *Vernadsky Institute of Geochemstry and Analytical Chemistry RAS atbas@geokhi.ru, krasilnikov_as@geokhi.ru*
[2] *Suzhou Polytechnic University, Suzhou, China, 91936@jssvc.edu.cn*
[3] *Institute of Geochemistry of Chinese Academy of Sciences, Guiyang, China gregory@mail.gyig.ac.cn*

KEYWORDS:
geologic-morphologic analysis, permanently-shadowed region, PSR, hill-shade image, regolith, water ice

INTRODUCTION:

Polar areas of the Moon are candidates for the construction of a lunar base [1, 2]. Their obvious advantage is the presence of water ice in the regolith of cold traps in permanently-shadowed regions (e.g., [3–5]). Water is a valuable resource for the base crew life particularly as a source of oxygen for life as well as oxygen and hydrogen as fuel components. Besides, polar areas outside the cold traps are rather climatically comfortable because of the absence of very high midday temperatures typical for the majority of lunar regions [6]. Mons Malapert (Fig. 1) is under consideration as a place to build a base in the polar area of the Moon, near the lunar South pole (e.g., [7]), and for the nearer future, as a possible landing site for the Artemis III mission (e.g., [8]).

GEOLOGIC-MORPHOLOGIC DESCRIPTION OF THE STUDY AREA:

Figure 1 shows a hill-shade image of Malapert Mons and its close vicinity as well as the 13 permanently-shadowed regions (PSR) considered in our study.

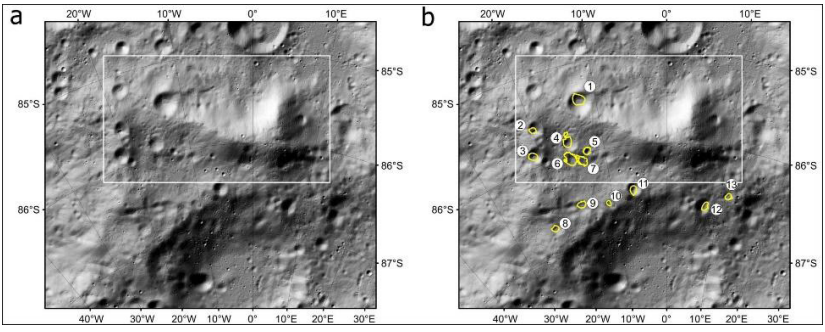


Fig. 1. Hill-shade image of Malapert Mons and its vicinity. White rectangle outlines boundaries of area shown in Fig. 2, while yellow outlines in part b show boundaries of 13 permanently shadowed areas in close vicinity of Malapert Mons

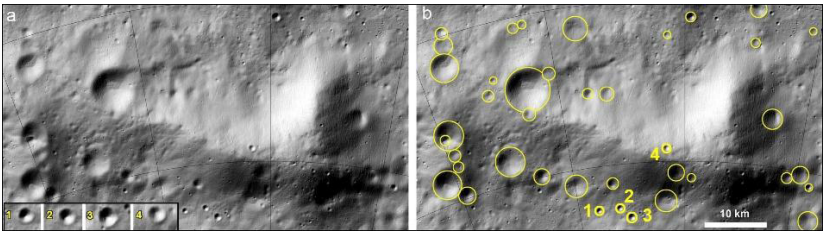


Fig. 2. Hill-shade image of 36·66 km area including Malapert Mons and its close vicinity. Yellow circles show craters larger than 1 km in diameter. Circles with digits nearby show lobate-rimmed craters. Presence of craters of such morphology is usually considered as indication of presence of significant amount of water ice in the target material [10]. The number of mapped craters in this area led to estimation of the absolute model age of this terrain as 4.12 +0.036/-0.039 Ga

It is seen in Fig. 1 that these PSRs are inside craters of ~2 to ~7 km in diameter. Figure 3 shows hill-shade image of Malapert Mons and its close vicinity.

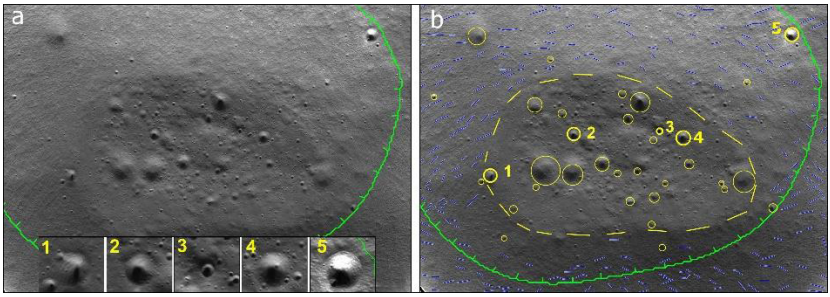


Fig. 3. ShadowCam image of part of PSR-1. Green line is the PSR-1 boundary. Yellow circles in part b of this figure show craters with diameters larger than 45 m. Their quantity led to estimation of the model absolute age of the floor of this crater as The craters numbered from 1 to 5 are those with lobate rims. Their presence in the permanently shadowed area probably suggests the presence of a significant amount of water ice in the floor material [10]. Blue lines show small ridges forming so-called 'elephant-skin' surface texture (e.g., [11, 12]). Dashed yellow line shows the boundary of the sub-horizontal floor of the crater, which contains PSR-1

Figure 3 shows part of a ShadowCam image mosaic of part of PSR-1 located inside a crater with diameter ~7 km.

DISCUSSION AND CONCLUSIONS:

The top of Malapert Mons, due to its selenographic position and altitude, is in permanent visibility from Earth (e.g., [8]), together with the above-mentioned presence of water ice in permanently shadowed regions and rather comfortable mid-day surface temperatures in non-shadowed areas, makes it a very promising location to build a lunar base. Our consideration has shown that in at least one of the permanently shadowed areas, located rather close (~30 km) to the mountain top, there are lobate rimmed craters with diameters from 45 to 123 m (see Fig. 2), usually considered as an indication of the presence of a significant amount of water ice in the target material [10]. Much larger amounts of water ice could be in the floor materials of the large craters Cabeus and Haworth. But their inner slopes are very steep and to reach the water ice deposits may be rather difficult. Our observations showed the unusual presence of craters with diameters of 1,0 to 1,2 km having a morphology reminiscent of the lobate-rimmed type close to the top of the Malapert Mons (see Fig. 3). Our conclusion is that Malapert Mons looks very promising as a place for a lunar base and more studies of this area are necessary.

ACKNOWLEDGMENTS:

Authors are grateful to S. S. Krasilnikov for the help with this study. Work of A. T. Basilevsky and A. S. Krasilnikov was supported by Vernadsky Institute RAS, Russia; work of Yuan Li was supported by Suzhou Polytechnic University, China; and work of G. G. Michael was supported by Institute of Geochemistry of Chinese Academy of Sciences, China.

REFERENCES:

[1] Burke J. D. Merits of lunar polar base location // Lunar Bases and Space Activities of the 21st Century / ed. Mendel W. W. Houston, TX: Lunar Planet. Inst., 1985, P. 77–84.
[2] Zelenyi L., Milestones of the Russian space science program for the decade 2016–2025 // Proc. 7th Moscow Solar System Symposium 7M-S3. Moscow: IKI RAS, 2016. Article 7MS3_OS_01.
[3] Feldman W. C., Maurice S., Binder et al. Fluxes of fast and epithermal neutrons from Lunar Prospector: evidence for water ice at the lunar poles // Science. 1998. V. 281. No. 5382. P. 1496–1500.
[4] Colaprete A., Schultz P., Heldmann J. et al. Detection of water in the LCROSS ejecta plume // Science. 2010. V. 330. P. 463–468.
[5] Sanin A. B., Mitrofanov I. G., Litvak M. L. et al., Hydrogen distribution in the lunar polar regions // Icarus. 2017. V. 283. P. 20–30.

[6] Paige D. A., Siegler M. A., Zhang J. A. et al., Diviner Lunar radiometer observations of cold traps in the Moon's south polar region // Science. 2010. V. 330. P. 479–482. DOI: 10.1126/science.1187726.
[7] Basilevsky A. T., Krasilnikov S. S., Ivanov M. A. et al. Potential lunar base on Mons Malapert: topographic, geologic and trafficability considerations // Solar System Research. 2019. V. 53. No. 5. P. 383–398. DOI: 10.1134/S0038094619050022.
[8] Wueller L., Iqbal W., Frueh T. et al. Geologic history of the Mons Malapert and Mons Mouton regions near the lunar south pole: Basis for future exploration // J. Geophysical Research: Planets. 2025. V. 130. Iss. 10. Article e2025JE009127. https://doi.org/10.1029/2025JE009127.
[9] Basilevsky A. T., Krasilnikov A. S., Li Yuan, Michae G. G. Comparison of the surface morphology of the floors of craters near the pole and at mid-latitudes of the Moon // Solar System Research. 2025. V. 59(63). DOI: 10.1134/S0038094624601671.
[10] Robinson M. S., Mahanti P., Bussey D. B. J. et al. Seeing in the shadows // 55th Lunar and Planet. Sci. Conf. 2024. Article 1669.
[11] Kreslavsky M. A., Bondarenko N. V., Head J. W. Ubiquity of "elephant hide" texture on the Moon // 52nd Lunar and Planet. Sci. Conf. 2021. Article 1826.
[12] Kreslavsky M. A., Zubarev A., Nadezhdina I., Bondarenko N. V., Non-diffusive regolith transport on the Moon // 54th Lunar and Planet. Sci. Conf. 2023. Absrtact 1834.

GEOLOGICAL EXPLORING OF THE MOON: RARE EARTH ELEMENTS

A. V. Gusev
Kazan Federal Uiniversity, Kazan, Russia, agusev33@gmail.com

KEYWORDS:
geological exploration and rare-earth elements on the Moon

INTRODUCTION:

Geological evidence of extensive ejecta deposits from sedimentary basins is observed in the form of plains-like landscapes in the Moon's southern polar region. Water ice and rare-earth elements accumulated in the lunar polar regions are priority targets for lunar exploration due to their significance for both lunar geology and the utilization of extraterrestrial resources [1].

The lunar subsurface can be divided into three units: Unit 1 (down to 12 m) consists of lunar regolith; Unit 2 (depth range of 12–24 m) consists of larger embedded materials; and Unit 3 (depth range of 24–40 m) contains alternating layers of course and fine-grained material. Chinese researchers also estimated the thickness of basaltic units at the Chang'e-5 landing site. The results indicate that at least four magmatic eruptions occurred, with average thicknesses of 230, 70, 4, and 36 m, respectively. Furthermore, studies revealed that the intensity of basaltic eruptions in this area increased significantly approximately 2 billion years ago [2].

Images from the Chang'e-4 (CE-4) mission provide clear information on the subsurface structure, which: 1) consists of highly porous, low-conductivity granular materials and scattered boulders of various sizes; and 2) indicates that the upper boundary of the mare basalt layer lies at a depth greater than 40 m. These results represent the first high-resolution images of lunar ejecta originating from the nearby Finsen crater as well as direct measurements of its thickness and internal structure [3].

Identifying suitable landing sites and determining the origin of sampled or measured surface materials is crucial for future landing missions. The authors mapped over 800 patches of level terrain in the Moon's south polar region, covering a total area of approximately 46,000 km^2. Orbital measurements and analog studies indicate that most of these plains appear to have higher albedo and lower iron content than volcanic mare plains, suggesting an origin linked to debris flows triggered by ejecta from distant impact craters, particularly the Schrödinger basin [4].

The authors' results indicate that the entire lunar south polar region was likely affected by materials from distant basins. The authors recommend these plains as priority landing sites for future research into rare-earth elements in lunar polar regions and the era of early lunar bombardment. Images from CE-4 provide clear information on the subsurface structure, revealing that it: 1) consists primarily of highly porous, low-conductivity granular materials and scattered boulders of various sizes; and 2) suggests the upper boundary of the mare basalt layer lies at depth exceeding 40 m [4].

Examples of subject areas covered include the basaltic volcanism; lunar chemistry; time and motion coordinates; impact-induced space weathering; the lunar environment; geology; geological history; impacts and impact processes; lunar surface processes; theories of origin and evolution; regolith; stratigraphy; tectonic activity; topography; and weathering caused by ionizing radiation from solar winds, solar flares, and cosmic rays [5].

Using samples obtained by the Chang'e-5 lunar probe, Chinese scientists have confirmed that the Moon was volcanically active 2 billion years ago, thereby extending its geological "lifespan" by 1 billion years beyond the previously accepted 3-billion-year mark [5].

Lunar rock samples returned by the Chang'e-6 spacecraft have allowed humanity to touch, for the first time, the ancient memories held within

the Moon's deepest interior. This has not only confirmed the accuracy of hypotheses based on remote sensing but has also revised our understanding of volcanic sources and the depths of impact zones on the far lunar side. New data derived from the Chang'e-6 samples reveal the ages of young lunar mare basalts in detail, documenting the history of volcanic activity on the far side of the Moon [6].

Characterizing landing sites for future lunar crewed missions is key to maximizing the science output. Authors of the article use orbital data to look at the equatorial Rimae Bode region, which is at the mare–highlands boundary and is a high-priority candidate for the upcoming Chinese crewed mission. Authors of the paper identify four distinct geological units: a dark mantle deposit; the Sinus Anestrum mare area; the Rimae Bode unit proper, formed by two distinct areas; and the highlands [7].

The dark mantle deposit is pyroclastic material with relatively low albedo, whose thickness ranges from 77 m to 136 m. Sinus Anestrum is an ancient impact basin filled with low-Ti basaltic lavas with a maximum thickness of 193 m and with a 4-m-thick regolith mostly composed of local materials. Rima Bode I include volcanic rilles that are potential sources for the basalts in Sinus Anestrum, as they share its spectral characteristics, whereas Rima Bode II exhibits high abundances of Th and Ti. Based on this information, authors propose four prospective landing sites in the traversable areas, which provide a range of diverse geological samples, including volcanic debris, mare basalts, Copernicus crater ejecta and high-Th materials [7].

The Encyclopedia of Lunar Science incorporates the latest up-to-date data, definitions, and explanations regarding the many diverse aspects of lunar science. It serves as a highly useful reference for a broad audience extending beyond professional lunar scientists including astronomers, researchers, theorists, practitioners, graduate and undergraduate students, astrophysicists, geologists, and engineers. The book covers all modern fields of lunar science, with entries representing established tertiary-level literature. The content is technically accessible to most upper-level undergraduates and graduate students. As the articles span varying levels of technical complexity, the work will prove valuable to leading experts in the field, graduate students and early-career lunar scientists [8].

REFERENCES:

[1] Tang T., Meng Z. G., Lian Y. et al. Extracting Mare-like Cryptomare Deposits in Cryptomare Regions Based on CE-2 MRM Data Using SVM Method // Remote Sens. 2023. V. 15. Article 2010. https://doi.org/10.3390/rs15082010.
[2] Meng Z. G., Tang T. Q., Dong X. G., Gusev A. Analyzing the microwave thermal emission features of lunar regolith in Chang'E landing sites and its geologic significance. SCIENTIA SINICA Physica // Mechanic and Astronomical. 2023. V. 53. Iss. 3. Article 239609. 17 p. (*chinese*). https://doi.org/10.1360/SSPMA-2022-0303.
[3] Gusev A. V., Meng Z., Ping J. Geological Exploration of the Moon IV: Water and the Mystery of the Early Moon's Thermal Budget // Proc. 57th K. E. Tsiolkovsky Scientific Readings. RAS – RAKTS. Section: "Modern Problems of Rocket and Space Technology". Kazan: RIC "Shkola", 2023. P. 233–248.
[4] Qiao L., Xu L., Head J., Chen J., Zhang Y., Li Bo, Ling Z. Geological evidence for extensive basin ejecta as plains terrains in the Moon's South Polar Region // Nature Communications. 2024. V. 15. Article 5783. 10 p.
[5] Zhao S., Qian Y., Zhao J. Lunar soil maturity of Chang'e-5 samples and its variation with depth // Science Technology. 2026. V. 33. P. 1–33.
[6] Zhang M., Fa W., Jia B. et al. Provenance and evolution of lunar regolith at the Chang'e-6 sampling site // Nature Astronomy. 2025. V. 9. P. 813–823.
[7] Yang M., Huang J. et al. Geology of Rimae Bode region as priority site candidate for China's first crewed lunar mission // Nature Astronomy. 2026. V. 10. P. 644–654.
[8] Encyclopedia of the Moon // World's First High-definition Geologic Atlas of the Moon Unveiled. https://english.cas.cn/head/202405/t20240511_662843.shtml

GEOLOGY OF THE WESTERN PORTION OF NOACHIS TERRA ON MARS

M. F. Ivanov[1], J. W. Head[2], E. S. Cholovskaya[1]
[1] *Vernadsky Institute of Geochemistry and Analytical Chemistry RAS Moscow 119991, Russia, Mikhail_ivanov@brown.edu*
[2] *Brown University, Providence RI, USA*

KEYWORDS:
Mars, phyllosilicates, Nirgal Vallis, regional geology, stratigraphy

INTRODUCTION:
The western portion of Noachis Terra represents a transitional zone at the ESE margin of the Tharsis Rise and is characterized by the presence of numerous volcanic, glacial and fluvial features, the largest of which is Nirgal Vallis. The spectral observations of Mars by the CRISM instrument onboard Mars Reconnaissance Orbiter have revealed numerous outcrops of Fe-Mg phyllosilicates in the western Noachis Terra. The presence in this region of both volcanic and fluvial/glacial landforms suggests that the interaction of lavas and ices may have created favorable conditions for the formation of clay deposits. Alternatively, the phyllosilicate-bearing materials could be linked to an ancient 'warm and wet' climate (e.g., [1, 2]), or to impact processes, either with the formation of hydrothermal systems at large impact basins [3], or with the deposition of hot ejecta [4], or both. In order to assess these hypotheses, we explored the detailed geologic setting and stratigraphy of the study area, compiling a geological map at the scale of 1:300 K, and placing the phyllosilicate deposits in this context.

UNITS AND STRUCTURES:
As we mapped the study area, we defined units in a descriptive manner based on specific morphology of their surfaces. If the morphology is different from the immediate surroundings, it defines a rock unit. No a priori hypotheses underlay the unit definition.

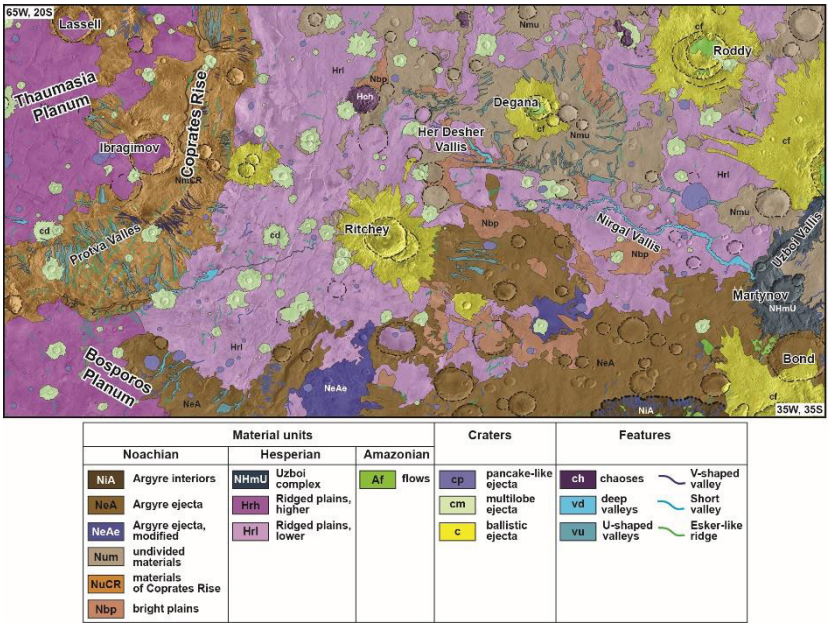


Fig. 1. Geological map of the western Noachis Terra

NOACHIAN UNITS (FIG. 1):
Interiors of the Argyre basin (NiA). This is one of the oldest units seen in the map area and is characterized by a very uneven surface consisting

of large blocks a few kilometers across and smooth deposits in between the blocks. Contiguous ejecta of Argyre (NeA) form the surfaces immediately northward of the basin rim. Degraded ejecta of Argyre (NeAd). The surface of this unit is more degraded with relicts of the smaller (first kilometers) and less degraded larger (tens of kilometers) craters. Noachian materials, undivided (Num). Exposures of this unit occur further northward from Argyre and are characterized by rugged surfaces disturbed by numerous larger craters that are several tens of kilometers across. Bright plains (Nbp) occur in several places of the lower topographic domain. The surface of this unit has a distinctly higher albedo compared with the surrounding units and a smooth to rolling surface texture. The most important characteristic of unit Nbp is that the spectral signature of Fe-Mg phyllosilicates detected by the CRISM instrument is very closely associated with this unit. Thus, it represents outcrops of the clay-bearing materials.

HESPERIAN UNITS (SEE FIG. 1):

Two major units of Hesperian age occur in the map area. These are ridged plains that characterize both the upper (Hrh) and lower (Hrl) topographic domains. The morphology of both units is identical and analogous to ridged plains elsewhere on Mars [5]. Such plains are commonly interpreted as flood volcanic provinces [6].

HESPERIAN FEATURES:

We have mapped specific landforms that do not occur as areally extensive deposits as features. They are mostly of the Hesperian age and include: chaos features on the floor of three craters; sinuous ridges (eskers?) that also occur in the other regions of Mars [7]; V- and U-shaped valleys on the eastern slopes of Coprates Rise; fluvial valleys within the lower topographic domain (unnamed valley, Her Desher Vallis and Nirgal Vallis).

AMAZONIAN UNITS AND FEATURES (SEE FIG. 1):

Landforms of Amazonian age are much less abundant in the map area and are represented by flow-like deposits (AfH) and rays of Hale crater.

DISCUSSION:

Geological settings of the clay-bearing materials in western Noachis Terra: The available CRISM data show that Fe-Mg phyllosilicates represent a significant portion of unit of massive bright plains (Nbp). Its deposits occur as layers up to a few hundred meters thick on the crater walls, as large blocks in ejecta of craters excavating Noachian materials, and as components of bright rays of the Amazonian crater Hale [8]. The phyllosilicates also occur on top of Coprates Rise in areas free of the Hesperian lava plains in association with the ancient materials of Coprates Rise. Such occurrences of the phyllosilicates are not linked to any fluvial/glacial features in the map area and represent a specific component of the undivided Noachian materials (unit Nmu).

The clay-bearing materials also are exposed on the surface of unit Nmu where they form smaller or larger areas with the etched surface. These occurrences of bright plains are common around Her Desher and Nirgal Valles and represent local highs embayed (but not completely covered) by the Hesperian lava plains. Phyllosilicates are exposed as massive layers on the walls of Her Desher Vallis and form the base of an island in the upper portion of the valley. In Nirgal Vallis, the available CRISM images show that the clay-bearing layers in the upper stretches of the valley are beneath the cap of the Hesperian lava plains and come to the surface in the lower portion of the valley, as a component of the Noachian undivided materials.

These settings and relationships of the clay-bearing plains suggest the following: (1) The clay-bearing materials in the map area almost exclusively occur in the pre-Hesperian materials. This means that conditions in the Noachian were favorable for the clay formation. The results of our regional mapping do not provide compelling constraints on the models of the dominance of such conditions during the entire Noachian [1] or their periodic appearance [9, 10]. (2) Western Noachis Terra was a region of widespread clay formation. It extended [11], from Coprates Rise on the West to the Argy-

re basin in the east (~100x500 km). Clays formed both in the highlands of Coprates Rise and in the surrounding lower regions, although occurrences of clays are much more abundant in the lower domain. (3) The Hesperian fluvial/glacial activity does not appear responsible for the formation of clays. The major fluvial systems in the map area (Her Desher, Nirgal) acted as a transport mechanism for older phyllosilicates. Large fluvial systems eastward of our map area (e.g., Margaritifer region) also preferentially transported clay-bearing materials [12–14].

REFERENCES:

[1] Craddock R. A., Lorenz R. D. The changing nature of rainfall during the early history of Mars // Icarus. 2017. V. 293. P. 172–179.
[2] Losekoot A., Balme M. R., Coe A. L., Fawdon P., Davis J. M. Widespread depositional fluvial systems in Noachis Terra, Mars // JGR. 2025. V. 130. Article e2025JE009378.
[3] Newsom H. E., Hagerty J. J., Thorsos I. E. Location and sampling of aqueous and hydrothermal deposits in Martian impact craters // Astrobiology. 2001. V. 1. P. 71–88.
[4] Palumbo A. M., Head J. W. Impact cratering as a cause of climate change, surface alteration, and resurfacing during the early history of Mars // MPS. 2018. V. 53. P. 687–725.
[5] Golombek M. P., Anderson F. S. Zuber M. T. Martian wrinkle ridge topography: Evidence for subsurface faults from MOLA // JGR. 2001. V. 106. P. 23811–23821.
[6] Scott D. H. Tanaka K. L. Geologic map of the western equatorial region of Mars: 1:15,000,000 scale United States Geological Survey Miscellaneous Investigations Series Map 1-1802-A. 1986.
[7] Bernhardt H., Hiesinger H., Reiss D., Ivanov M., Erkeling G. Putative eskers and new insights into glacio-fluvial depositional settings in southern Argyre Planitia, Mars // PSS. 2013. V. 85. P. 261–278.
[8] Jones A. P., McEwen A. S., Tornabene L. L., Baker V. R., Melosh H. J., Berman D. C. A geomorphic analysis of Hale crater, Mars: The effects of impact into ice-rich crust // Icarus. 2011. V. 211. P. 259–272.
[9] Head J. W., Marchant D. R. The climate history of early Mars: insights from the Antarctic McMurdo Dry Valleys hydrologic system // Antarctic Sci. 2014. V. 26(6). P. 774–800.
[10] Wordsworth R. D. The climate of early Mars // AREPS. 2016. V. 44. P. 381–408.
[11] Buczkowski D. L., Seelos K., Murchie S., Seelos F., Malaret E., Hash C. Extensive Phyllosilicate-bearing layer exposed by valley systems in North-West Noachis Terra // LPSC. 2010. Article 1458.
[12] Ehlmann B. L., Mustard J. F., Fassett C. I., Schon S. C., Head J. W., Des Maria D. J., Grant J. A., Murchie S. L. Clay minerals in delta deposits and organic preservation potential on Mars // Nat. Geosci. 2008. V. 1. P. 355–358.
[13] Grant J. A., Irwin R. P., Wilson S. A., Buczkowski D., Siebach K. A lake in Uzboi Vallis and implications for Late Noachian-Early Hesperian climate on Mars // Icarus. 2011. V. 212. P. 110–122.
[14] Thomas R. J., Hynek B. M., Osterloo M. M., Kierein-Young K. S. Widespread exposure of Noachian phyllosilicates in the Margaritifer region of Mars: Implications for paleohydrology and astrobiological detection // JGR. 2017. V. 122. P. 483–500.

GEOLOGICAL SETTINGS OF CLAY MINERALS IN THE WESTERN NOACHIS TERRA, MARS

E. S. Cholovskaia, M. A. Ivanov
Vernadsky Institute of Geochemistry and Analytical Chemistry RAS
Moscow, Russia, cattcholovskaya@yandex.ru, Mikhail_Ivanov@brown.edu

KEYWORDS:
Mars, Noachis Terra, clay, phyllosilicates

INTRODUCTION:
Western Noachis Terra is the one of the places on Mars where numerous outcrops of Fe-Mg phyllosilicates have revealed. Clay minerals can be diagnostic of past climatic conditions on Mars [1, 2]. Various hypotheses have been put forward to explain the formation of phyllosilicates either as the result of the surface weathering in warm and wet conditions [1–3] or(and) in the subsurface due to various processes in cold and dry climate [4]. Our research is aimed at studying the morphological, stratigraphic and mineralogical characteristics of phyllosilicates, which will allow us to suggest the main mechanism that could be responsible for the formation of clay minerals and reconstruct regional climatic conditions in the past.

METHODS:
Geological map of an area (Area 1, centered at 51°W, 22°S) in the western portion of Noachis Terra was compiled using data from the context camera CTX (resolution ~6 m/px). For detailed study of the position of the clay minerals was used high-resolution images from the HiRISE camera (resolution ~0.5 m/px). As the data for studying mineralogical composition of the clay minerals, the MTRDR images from the CRISM spectrometer were used, which contain the full spectral range (IR+VNIR) and have primary adjustments [5]. We analyzed 2 images obtained in the study area using the analysis tool CRISM Analysis Toolkit (CAT), developed for the ENVI software [6]. Summary of the spectral parameters [5, 7] and the spectral ratio method were used for identification and spatial mapping of the spectrally different units.

STUDY AREA:
Based on the previously compiled regional map, areas of interest were identified in which characteristic surface activity (especially fluvial/glacial) was identified for reconstructing the local sequence of geological events and mineralogical features (first of all, the presence of clay minerals, their position and composition). Area 1 is one of these (Fig. 1). There is a small hill of the Noachian age, which is dotted with numerous craters, of which the largest is located in the southwest and has a diameter of 56 km. The Hesperian lava plains surround this hill from the west and south. At the boundary of these units, high-albedo materials form two units, Nha1 and Nha2. Unit Nha1 forms rugged/hummocky/jagged surfaces with noticeable relief, unit Nha2 occur as morphologically smooth areas with lower relief compared with Nha1 and the lack of characteristic polygonal texture. Both units are likely Noachian in age because occur within exposures of the Noachian materials. Nha1 may represent primary deposits that contain clays; Nha2 may represent materials of Nha1 re-distributed by wind.

RESULTS AND DISCUSSION:
There are 2 CRISM images in Area 1, indicating the presence of clay minerals in the study area. Analysis of their spectra confirmed the presence of Fe-Mg phyllosilicates, represented by a mixture of saponite and nontronite (Fig. 2).

The CRISM image 1 shows the mineralogy of the southern edge of a crater (23 km diameter), in the northern portion of the study area in the Noachian deposits. At this place, clay minerals form a deposit exposed in the crater wall near the surface; the apparent thickness the deposit is ~300–350 m. This suggests that the crater has uncovered the pre-crater, near-surface deposits of clay minerals.

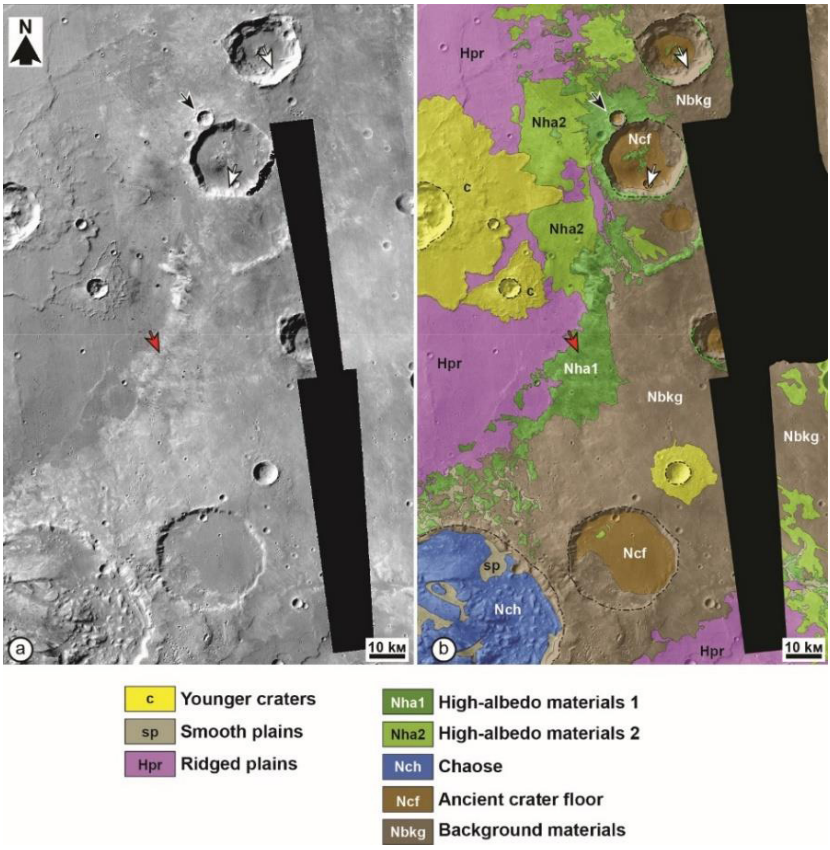


Fig. 1. Geological map of the Area 1 (1:50 000). Red arrow indicates outcrops of clay minerals unrelated to impact structures; black arrow indicates clays in the crater ejecta

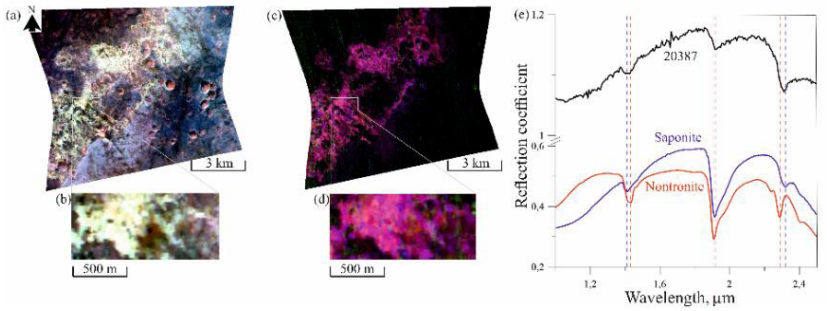


Fig. 2. Results of spectral analysis of the CRISM image 2 (a) pseudocolor image of FRT00020387 obtained with CRISM; (b) enlarged fragment of Fig. 2a; (c) MTRDR CRISM with color coding of spectral parameters (red D2300, green D2200, blue BD1900R2), pink tones — Fe–Mg-phyllosilicates; (d) enlarged fragment of Fig. 2c; (e) final spectrum compared with laboratory spectra

The CRISM image 2 shows the presence of clay minerals in the unit Nha1. Clay-bearing rocks have a lighter phototone relative to the surrounding area. This bright area can be traced almost along the entire exposure of unit Nha1. Individual occurrences of unit Nha1 lie in small depressions, which may indicate that the clay minerals formed in the Noachian period in the subsurface, and later were exposed by a combination of erosion processes. For example, these could be glacial processes since there are no signs of fluvial activity in this area. The outcrop of unit Nha1 is on a shal-

low slope from the Noachian upland to the Hesperian lava plains, therefore the outcrop could represent an area of somewhat enhanced erosion.

CONCLUSION:

Area 1 is a piece of the ancient Noachian upland within the Western Noachis Terra, surrounded by the Hesperian lava plain. Area 1 exhibits several outcrops of clay-bearing materials. One outcrop is within an impact crater and its ejecta. Clays in this occurrence were exposed and excavated during the impact event. The second outcrop forms a lor-relief hill unrelated directly to impact craters. Both outcrops are related to the ancient, Noachian in age, units and clearly predate the emplacement of the Hesperian lava plains. Thus, in the study area, the clay minerals reflect the ancient, Noachian, climate conditions and have not been formed due to the thermal effect of the Hesperian lavas. In the study area, layers of clay minerals formed in the subsurface and are represented by a mixture of saponite and nontronite.

ACKNOWLEDGMENTS:

The work was conducted under financial support of Russian Science Foundation, project No. 25-27-00438, morphological and mineralogical constraints on evolution of climate on Mars on example of Noachian Terra.

REFERENCES:

[1] Bibring J.P., Langevin Y., Gendrin A. et al. Mars surface diversity as revealed by the OMEGA/Mars express observations // Science. 2005. V. 307. No. 5715. P. 1576–1581. DOI: 10.1126/science.1108806.

[2] Poulet F., Bibring J.P., Mustard J.F. et al. Phyllosilicates on Mars and implications for early martian climate // Nature. 2005. V. 438. No. 7068. P. 623–627. DOI: 10.1038/nature04274.

[3] Bish D.L., Carey J.W., Vaniman D.T., Chipera S.J. Stability of hydrous mineral on the martian surface // Icarus. 2003. V. 164. No. 1. P. 96–103. DOI: 10.1016/S0019-1035(03)00140-4.

[4] Ehlmann B.L., Mustard J.F., Murchie S.L. et al. Subsurface water and clay mineral formation during the early history of Mars // Nature. 2011. V. 479. No. 7371. P. 53–60. DOI: 10.1038/nature10582.

[5] Viviano-Beck C.E., Seelos F.P. et al. Revised CRISM spectral parameters and summary products based on the currently detected mineral diversity on Mars // J. Geophysical Research Planets. 2014. V. 119. No. 6. P. 1403–1431. DOI: 10.1002/2014JE004627.

[6] Morgan F., Seelos F.P., Murchie S.L. CAT Tutorial, presented at CRISM // Workshop held in conjunction with the 40th Lunar and Planetary Science Conf. The Woodlands. USA, 2009.

[7] Pelkey S.M., Mustard J.F., Murchie S. L. et al. CRISM multispectral summary products: Parameterizing mineral diversity on Mars from reflectance // J. Geophysical Research Planets. 2007. V. 112. No. 8. DOI: 10.1029/2006JE002831.

LOCAL WATER RICH REGIONS IN THE EQUATORIAL AREA OF MARS BY FREND/TGO DATA

D. V. Golovin, I. G. Mitrofanov, M. L. Litvak, A. B. Sanin, M. V. Djachkova
Space Research Institute RAS, Moscow, 117997, Russia, golovin@np.cosmos.ru

KEYWORDS:
Mars, hydrogen, water, neutron, regolith

ABSTRACT:
FREND is collimated neutron telescope [1] onboard ESA's Trace Gas Orbiter [2]. It is capable to detect hydrogen content in the upper 1 m of regolith with a high spatial resolution less than 200 km. This instrument performs measurements on the 400 km orbit around Mars since April 2018. Such long accumulation time allows decreasing statistical uncertainty of measured neutron flux and improving evaluation of water mass fraction in the soil.

After 8 years of almost continuous neutron observations, we present in this study the results of searching of local water-rich regions (LWRRs) in the equatorial area of Mars. We have found about 10 regions with high statistical significance. These regions were tested using newly developed method witch is able to detect their local most wet part. We have evaluated water content inside LWRRs and surrounded relatively dry areas and theirs sizes. Some most interesting LWRRs were studied in more details taking into account geological context and another datasets (MARSIS radar observations of deep ice [3] and hydrated minerals detections by CRYSM infrared spectrometer [4]) to explain the possible source of the observing water abundance in the Martian subsurface.

REFERENCES:
[1] Mitrofanov I. et al. Fine Resolution Epithermal Neutron Detector (FREND) onboard the ExoMars Trace Gas Orbiter // Space Science Reviews. 2018. V. 214. No. 86.
[2] Vago J. et al. ESA ExoMars program: The next step in exploring Mars // Solar System Research. 2015. V. 49. No. 7.
[3] Carter J. et al. A Mars orbital catalog of aqueous alteration signatures (MOCAAS) // Icarus. 2023. V. 389. Article 115164.
[4] Watters T. R. et al. Evidence of Ice-Rich Layered Deposits in the Medusae Fossae Formation of Mars // Geophysical Research Letters. 2024. V. 51. Article e2023GL105490.

INVESTIGATION OF SEASONAL VARIABILITY IN PASSIVE MEASUREMENTS OF THE DAN INSTRUMENT ONBOARD THE CURIOSITY ROVER

G. A. Baroev[1,2], M. V. Djachkova[1], D. I. Lisov[1], I. G. Mitrofanov[1], M. L. Litvak[1], A. B. Sanin[1]
[1] *Space Research Institute RAS, Moscow, Russia, oritrmaxmen@gmail.com*
[2] *National Research Nuclear University MEPhI, Moscow, Russia*

KEYWORDS:
Mars, DAN instrument, Curiosity rover, passive neutron measurements, seasonal variations, global dust storm, REMS, thermal and epithermal neutrons

ABSTRACT:
The scientific payload of NASA's Curiosity rover includes the Dynamic Albedo of Neutrons (DAN) instrument [1], designed to estimate the hydrogen content in the near-surface layer of the Martian regolith to depths of up to 0.5 m [3, 4]. Variations in the neutron flux detected by DAN in passive mode are primarily governed by changes in the chemical composition of the subsurface [6]. However, non-compositional factors — such as diurnal variations in atmospheric pressure and detector temperature — have also been shown to modulate the passive neutron signal [5]. This work presents the results of an analysis of variations in DAN passive measurements associated with additional factors — seasonal changes on the Martian surface, including the effect of the 2018 global dust storm on the dynamics of the thermal (CTN) and epithermal (CETN) neutron detector readings.

We present the results of an analysis of long-term DAN passive measurements aimed at identifying the factors responsible for variations in the recorded neutron flux. To minimize the influence of geological variability, we analyzed measurements obtained during the rover's long-duration stops, as well as data acquired within a single geological unit but at different seasonal epochs.

The analysis focused on three aspects: (1) the seasonal dependence of the CTN and CETN count rates over the course of a Martian year; (2) the effect of the global dust storm on the dynamics of the surface neutron emission; (3) the correlation of the neutron measurements with meteorological parameters from the Rover Environmental Monitoring Station (REMS) [2].

Statistical analysis of the long-duration-stop data reveals a weak but statistically significant seasonal component in the DAN passive measurements. A comparison of measurements taken within the same geological unit but during different seasons revealed differences in the neutron detector count rates, indicating that the neutron flux is modulated by seasonal processes.

In addition, the global dust storm was found to have affected the recorded parameters. Oppositely directed changes were observed in the CTN and CETN readings: a decrease in the thermal neutron count rate was accompanied by a simultaneous increase in the epithermal neutron count rate. This effect indicates a modification of the neutron energy spectrum under the increased atmospheric density conditions during the dust storm.

REFERENCES:
[1] Mitrofanov I. G., Litvak M. L., Varenikov A. B. et al. Dynamic Albedo of Neutrons (DAN) Experiment Onboard NASA's Mars Science Laboratory // Space Science Reviews. 2012. V. 170. P. 559–582. DOI: 10.1007/s11214-012-9924-y.
[2] Gomez-Elvira J., Armiens C., Castañer L. et al. REMS: The Environmental Sensor Suite for the Mars Science Laboratory Rover // Space Science Reviews. 2012. V. 170(1–4). P. 583–640. DOI: 10.1007/s11214-012-9921-1.
[3] Nikiforov S. Y., Mitrofanov I. G., Litvak M. L. et al. Assessment of water content in Martian subsurface along the traverse of the Curiosity rover based on passive measurements of the DAN instrument // Icarus. 2020. V. 346. Article 113818. DOI: 10.1016/j.icarus.2020.113818.

[4] Mitrofanov I.G., Nikiforov S.Y., Djachkova M.V. et al. Water and chlorine in the Martian subsurface along the 27 km traverse of NASA's Curiosity rover according to DAN measurements: 2. Results for distinct geological regions // J. Geophysical Research: Planets. 2024. V. 129. Iss. 4. Article e2022JE007731. DOI: 10.1029/2022JE007731.
[5] Tate C.G., Moersch J., Jun I. et al. Observed diurnal variations in Mars Science Laboratory Dynamic Albedo of Neutrons passive mode data // Nuclear Instruments and Methods in Physics Research A. 2018. V. 892. P. 70–83. DOI: 10.1016/j.nima.2018.02.100.
[6] Jun I., Mitrofanov I., Kozyrev A. et al. Neutron background environment measured by the Mars Science Laboratory's Dynamic Albedo of Neutrons instrument during the first 100 sols // J. Geophysical Research: Planets. 2013. V. 118. P. 2400–2412. DOI: 10.1002/2013JE004510.

SPICAV IR AND VMC COLLOCATED OBSERVATIONS TO EXPLORE THE VENUS SURFACE PROPERTIES

D. G. Evdokimova[1], D. V. Titov[2,3], N. I. Ignatiev[1], A. A. Fedorova[1], O. I. Korablev[1]

[1] *Space Research Institute RAS, Moscow, Russia, daria.evdokimova@cosmos.ru*
[2] *Leiden University, Leiden, Netherlands*
[3] *Sun Yat-sen University, School of Atmospheric Sciences, Department of Space and Planetary Sciences, Zhuhai, China*

KEYWORDS:
near-infrared transparency windows; radiative transfer; thermal emission; remote sensing

INTRODUCTION:
Venus' surface is enshrouded by a dense CO2 atmosphere and a global cloud layer, which obscures the surface and the lower atmosphere preventing direct remote sensing observations. However, several near-infrared (NIR) atmospheric "transparency windows" near 1 μm allow a fraction of the surface thermal radiation to leak to space [1]. Observations of this weak emission on the planet's night side provide a unique opportunity to investigate surface emissivity and geological properties. Their interpretation requires careful correction of atmospheric absorption and cloud variability [2].

The effective altitude of the observed thermal emission increases with wavelength. Radiation detected in the 1.02-μm transparency window originates almost entirely from the hot surface, whereas the 1.28-μm window primarily probes the lower atmosphere [1].

DATASET:
From 2006 to 2014, the ESA's Venus Express spacecraft orbited Venus. The mission was equipped with the SPICAV (Spectroscopy for Investigation of Characteristics of the Atmosphere of Venus) spectrometer and the Venus Monitoring Camera (VMC). The SPICAV IR channel covered the 0.65–1.7 μm spectral range, sequentially accumulating a spectrum using an acousto-optic tunable filter, a key element of the instrument [3]. VMC included two near-infrared channels, one of which was centered at the 1.02-μm transparency window [4]. Both instruments were designed to address different scientific questions, including investigating thermal emission from the Venus' surface and its deep atmosphere. During the mission, valuable collocated and simultaneous SPICAV IR and VMC measurements were collected. SPICAV IR provided spectral coverage of transparency windows up to 1.3 μm.

METHODS:
The complementary capabilities of the SPICAV IR spectrometer and VMC imager on board Venus Express provide a powerful approach to filtering out variations of the atmospheric absorption and cloud properties from the surface signal in the 1.02-μm transparency window. VMC observations have a broad, regional coverage of the surface thermal emission. Simultaneous and collocated SPICAV IR spectra in the 1.28 μm window, which is mostly insensitive to surface emission, yield a robust characterization of atmospheric absorbers and cloud properties.

A one-dimensional radiative transfer model accounting for multiple scattering and including accurate treatment of spectroscopy was developed to analyze the full set of SPICAV IR spectra in the 1.10-, 1.18-, and 1.28-μm transparency windows [5, 6]. In this work, we adapted this model for the observation of the 1.02-μm transparency window.

RESULT:
The analysis of combined VMC and SPICAV IR datasets enables the separation of atmospheric and surface contributions in the 1.02-μm transparency

window signal. Here we will present preliminary results on the Venus surface emissivity from joint analysis of SPICAV-IR and VMC data using accurate radiative transfer model.

ACKNOWLEDGMENTS:
The authors are very grateful to Dr. Thomas Roatsch and Dr. Klaus-Dieter Matz (DLR, Berlin) for providing the original uncalibrated VMC data.

REFERENCES:

[1] Pollack J.B., Dalton J.B., Grinspoon D. et al. Near-infrared light from Venus' nightside: a spectroscopic analysis // Icarus. 1993. V. 103. No. 1. P. 1–42. DOI: 10.1006/icar.1993.1055.
[2] Kappel D., Arnold G., Haus R. Multi-spectrum retrieval of Venus IR surface emissivity maps from VIRTIS/VEX nightside measurements at Themis Regio // Icarus. 2016. V. 265. P. 42-62. DOI: 10.1016/j.icarus.2015.10.014.
[3] Korablev O., Fedorova A., Bertaux J.-L. et al. SPICAV IR acousto-optic spectrometer experiment on Venus Express // Planetary and Space Science. 2012. V. 65. No. 1. P. 38–57. DOI: 10.1016/j.pss.2012.01.002.
[4] Markiewicz W.J., Titov D.V., Ignatiev N. et al. Venus monitoring camera for Venus Express // Planetary and Space Science. 2007. V. 55. No. 12. P. 1701–1711. DOI: 10.1016/j.pss.2007.01.004.
[5] Evdokimova D., Fedorova A., Ignatiev N. et al. Cloud Opacity Variations from Nighttime Observations in Venus Transparency // Atmosphere. 2025. V. 16. No. 5. Article 572. DOI: 10.3390/ atmos16050572.
[6] Evdokimova D., Fedorova A., Ignatiev N. et al. Near-Surface Water Vapor Content Based on SPICAV IR/VEx Observations in the 1.1 and 1.18 μm Transparency Windows of Venus // Atmosphere. 2025. V. 16. No. 6. Article 726. DOI: 10.3390/ atmos16060726.

EMISSIVITY VARIATIONS OF EXTENSIVE ROCK UNITS ON VENUS FROM THE VMC DATA

M. A. Ivanov[1], D. V. Titov[2], A. T. Basilevsky[1]
[1] *Vernadsky Institute of Geochemistry and Analytical Chemistry RAS Moscow 119991, Russia, Mikhail_ivanov@brown.edu*
[2] *Sun Yat-sen University, Zhuhai, PRC*

KEYWORDS:
Venus, Venus Monitoring camera, Emissivity, Tessera

INTRODUCTION:
The night side images in the 1 micron spectral transparency "window" collected by the VMC instrument onboard of the Venus Express orbiter provide important results on the emissivity of the surficial materials, although with poor resolution (~50 km/pixel) [1, 2]. Relative surface emissivity maps were derived from the VMC night side 1 micron images taking into account atmospheric attenuation and blurring [2]. The emissivity, among other factors, depends upon the iron concentration in materials and, thus, provides the mean for a very broad estimates of the types of materials. For instance, it is believed that non-basaltic, more advanced compositions will have systematically smaller emissivity values because of smaller concentrations of iron. Another important factor affecting the emissivity is temperature, which decreases with elevation. Thus, the highlands are expected to have lower emissivity values [3, 4]. For the materials at about the same elevations, lower emissivity values may suggest lower concentration of iron. In order to estimate the possible composition of different units that make up the surface of Venus, we used the global geological map [5] and collect the emissivity values for the most extensive units such as tessera (t), shield plains (psh), regional plains (rp1), and lobate plains (pl).

DATA AND METHODS:
The most recent release of the emissivity map [6] consists of nine segments, each of 40° wide in longitude (Fig. 1). We co-registered these segments with the geological map and used specific units as areas of sampling to collect the emissivity data. For each unit, we applied sampling by randomly distributed points, the number of which was ~5% of total. So far, we investigated segments 3, 6, and 7.

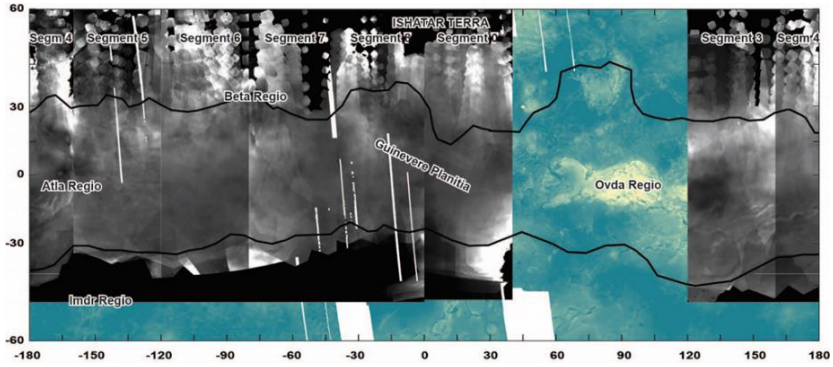


Fig. 1. Segments of the emissivity map overlying global topography. Map in Mercator projection

RESULTS:
Segment 3 is the region of contrasting relief that includes the high-standing eastern portion of Thetis Regio and deep chasmata of the eastern Aphrodite Terra. Segments 6 and 7 are characterized by much more even regional topography. As the first step of our study, we analyzed the correlation between elevation and emissivity. For Segment 3 the correlation is high (r=–0.74); it is moderate/lower for Segment 6 (r=–0.34) and low for

Segment 7 (r=0.06, lack of correlation). Negative correlation indicates that the emissivity decreases with elevation, which is expected due to temperature effect on the emissivity. The high correlation for Segment 3, thus, suggests that the temperature effect on the emissive ability of the surface either was not successfully accounted for or that emissivity really decreases due to temperature dependence. For Segments 6 and 7, the temperature effect plays less important role and we investigated units in these regions.

Tessera massifs in Segments 6 and 7 represent slightly elevated areas and their relative emissivity values vary from ~0.31-0.49 % (Fig. 2). These values are almost completely overlapping with the ranges of emissivity values typical of the plains units such as psh, rp1, and pl. The mean relative emissivity values for t, psh, rp1, and pl are as following: 0.41±0.05, 0.40±0.07, 0.39±0.07, and 0.35±0.04, respectively. None of these units show a trend of changes of the emissivity with the elevation (see Fig. 2).

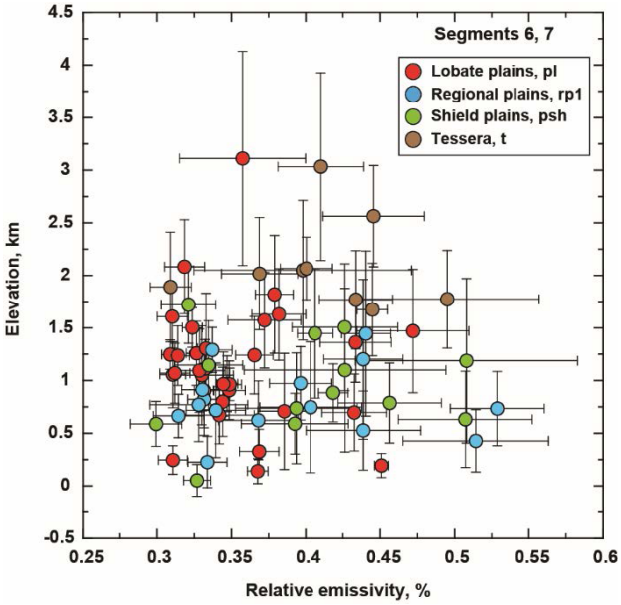


Fig. 2. Elevation vs. emissivity for four studied units in Segments 6 and 7

DISCUSSION/CONCLUSIONS:

Neither all sampling points, nor the mean relative emissivity values for the studied units show any pronounced trend/correlation between elevation and emissivity. Thus, we can safely exclude the elevation/temperature factor from the interpretation. Tessera massifs systematically occur higher that their surroundings; the mean tessera elevation is ~2.09±0.44 km. The plains units are significantly lower; their mean elevations are as follows: psh ~0.95±0.4 km; rp1 ~0.81±0.32 km; pl ~1.14±0.58 km. Despite these differences, tessera is characterized by about the same emissivity values. This means that (1) the ambient temperature in the elevation range of about 1–2 km above the Mean Planetary Radius does not play a significant role in the emissivity variations; (2) tessera in the study region does not differ from the surrounding plains by its emissivity.

Although tessera terrain is considered sometimes as consisting of the non-basaltic, more granite-like materials [7, 8], this interpretation is not supported by the emissivity data (Fig. 2). Both the distribution and mean values of the tessera relative emissivity are not distinguishable from those typical of the plains units, which are believed to be consisted of basaltic lavas.

Shield plains have distinctly different mode of formation compared with regional plains [9] but their emissivity values are almost identical (see Fig. 2). This suggests that the very different mechanisms of the plains formation —

eruptions from shallow and distributed sources for psh and massive lava outpouring and flooding during the emplacement of regional plains — have produced broadly similar materials akin to basalts, which was also suggested by the data from the Venera landers [10, 11].

The youngest lobate plains are characterized by somewhat lower values of relative emissivity (see Fig. 2). The morphology of the flows of lobate plains is indicative of the basaltic composition. The difference in emissivity between lobate plains and shield/regional plains can be due to selective removal of material fractions from the older psh and rp1 units. For example, the lighter, less iron-rich fraction of the plains material could be removed by wind making the composition of the surficial layers more iron-rich and, thus, increasing relative emissivity of the surface of these units. The younger lobate plains may still keep their composition closer to the original one, less affected by the wind erosion.

ACKNOWLEDGMENTS:
The work was conducted under a state order to M. A. Ivanov and A. T. Basilevsky.

REFERENCES:

[1] Baines K. H., Atreya S., Carlson R. W. et al. To the depths of Venus: Exploring the deep atmosphere and surface of our sister world with Venus Express // PSS. 2006. V. 54. P. 1263–1278. DOI: 10.1016/j.pss.2006.04.03.
[2] Markiewicz W., Titiov D. V., Ignatiev N. et al. Venus Monitoring Camera for Venus Express // PSS. 2007. V. 55. P. 1701–1711. DOI: 10.1016/j.pss.2007.01.004.
[3] Klose K. B., Wood J. A., Hashimoto A. Mineral equilibria and the high radar reflectivity of Venus mountaintops // JGR. 1992. V. 97. P. 16252–16370.
[4] Shepard M., Arvidson R., Brackett R., Fegley B. A ferroelectric model for the low emissivity highlands on Venus // GRL. 1994. V. 21 P. 469–472.
[5] Ivanov M. A., Head J. W. Global geological map of Venus // PSS. 2011. V. 59, P. 1559–1600. DOI: 10.1016/j.pss.2011.07.008.
[6] ESA Guest Storage Facility. https://www.cosmos.esa.int/web/psa/psa_gsf.
[7] Nikolaeva O. V. Geochemistry of the Venera 8 Material demonstrates the presence of continental crust on Venus // EMP. 1990. V. 50/51. P. 329–341.
[8] Basilevsky A. T., Shalygin E. V., Titov D. V. et al. Geologic interpretation of the near-infrared images of the surface taken by the Venus Monitoring Camera, Venus Express // Icarus. 2012. V. 217. P. 434–450.
[9] Ivanov M. A., Head J. W. The history of volcanism on Venus // PSS. 2013. V. 84. P. 66–92.
[10] Surkov Yu. A., Barsukov V. L., Moskalyova V. P., Kharyukova A. D., Kemurdzhian A. L. New data on the composition, structure, and properties of Venus rock obtained by Venera 13 and 14 // Proc. 14th LPSC. 1984. Pt. 2. JGR. V. 89. P. B393–B402.
[11] Surkov Yu. A., Moskalyova V. P., Kharyukova A. D., Dudin A. D., Smirnov G. G., Zaitseva S. E. Venus rock composition at the Vega 2 landing site // Proc. 17th LPSC. Pt. 1. JGR. 1986. V. 91. P. E215–E218.

SELECTION OF LANDING SITES OF THE VENERA-D MISSION

M. A. Ivanov[1], V. Zubko[2], N. A. Eismont[2], J. W. Head[3]
[1] *Vernadsky Institute of Geochemistry and Analytical Chemistry RAS Moscow 119991, Russia, Mikhail_ivanov@brown.edu*
[2] *Space research institute RAS, Moscow, 117997, Russia*
[3] *Brown University, Providence RI, USA*

KEYWORDS:
Venus, Venera-D, lander, landing sites, selection criteria

INTRODUCTION:
The Venera-D mission is a part of the Federal space program of Russian Federation. The mission includes a lander the main goals of which are taking the surface panoramas at the landing site and conducting precise chemical analyses of the soil. Accomplishment of these goals requires: (1) selection of a safe place to land and (2) selection of a region of a high scientific value. The ballistic characteristics of the mission (date, trajectory, orbital maneuvers) further constrain selection of the final landing region/site. In this contribution, we describe the safety, scientific, and ballistic criteria for the site selection and propose several places that satisfy these criteria.

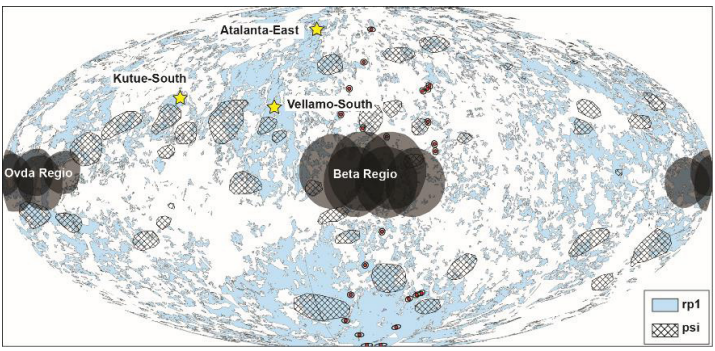


Fig. 1. Dark-gray areas indicate areas unavailable for landing after the gravitational maneuver. Red dots indicate available landing sites in the case of the direct landing

SAFETY CRITERIA:
The strong greenhouse effect on Venus precludes formation of the sedimentary-based geological record that is dominating on Earth. Because of this, practically all landforms on Venus (except infrequent impact craters) are either of tectonic or volcanic origin [1]. The tectonic landforms (terrain, units) include tessera (t), densely lineated plains (pdl), groove belts (gb), ridged plains/ridge and mountain belts (pr/rb/mb) and rift zones (rz) [2]. The surface of these terrains is dominated by numerous structural components (grooves, ridges) that erase morphology of the original materials and form very uneven surfaces with abundant scarps, steep slopes, and rocky aprons. These features of the tectonized terrains make landing on their surface to be extremely risky and the tectonized units are non-appropriate for landing.

Volcanic units (mostly plains) include shield plains (psh), regional plains of two generations (rp1 and rp2), lobate plains (pl), and smooth plains of volcanic (psv) and impact (psi) origin [2]. Volcanic units are significantly less deformed by tectonic structures and, potentially, represent regions appropriate for the safe landing. The exclusions are lobate plains, the upper unit of regional plains (rp2), and smooth volcanic plains. Both lobate plains and unit rp2 are characterized by numerous radar-bright flows, the enhanced backscatter of which suggests their enhanced roughness at the meter-decameter scale. These radar-bright plains likely resemble terrestrial aa-flows that disable safe landing. Volcanic smooth plains usually

form relatively small (tens of kilometers across) flow- and field-like features that commonly occur in tight spatial association with lobate plains. The uncontrolled descent toward these plains can cause landing on lobate plains and destruction of the lander. Among the volcanic units only shield plains, the lower unit of regional plains (rp1) and smooth impact plains represent regions for the safe landing. Both volcanic units cover extensive regions that comprise ~50% of the surface of Venus and unit psi form the radar-dark parabolas associated with younger impact craters and can be many hundreds of kilometers across.

CRITERION OF SCIENTIFIC IMPORTANCE:

This criterion helps to further constraining of regions appropriate for landing. Shield plains are characterized by numerous small (a few kilometers diameter) volcanic constructs that formed above broadly distributed and likely shallow and isolated magma sources [3–5]. Such a mode of emplacement suggests involvement and interference of different processes during formation of shield plains: (1) different degree of differentiation of parent magmas, (2) different degree of contamination of parent magmas by the wall rocks, (3) different frequency of injection of batches of fresh magmas into the magma reservoir, (4) different degree of partial melting in the main reservoir, (5) different degree of mixing of the differentiated and fresh melts. As the result, shield plains will likely have highly variable geochemical characteristics that will not be representative for this unit as a whole.

In contrast to shield plains, the lower unit of regional plains have the same morphology within huge regions [2]. Such a monotonous morphology suggests a uniform mode of origin and, as the result, uniform geochemical characteristics. The mode of formation of unit rp1 suggests that it formed by a lava flooding and chemical composition of its materials may characterize geochemistry of the upper mantle of Venus (e.g., [6, 7]). Because unit rp1 is the most abundant on Venus (it occupies ~35% of the surface) the results of chemical analysis of its materials can be extrapolated globally.

Smooth plains of impact origin form extensive radar-dark parabolas that represent fallout accumulations of fine-grained material elected by an impact event [8]. These materials are very well mixed and form representative sample of the upper crust. Analyses of them may help to solve the long-standing problem of the non-basaltic component of the Venus crust. However, materials of the parabolas can be somewhat altered during their travel through atmosphere and their chemical composition can be shifted relative to the original composition. Fig. 1 shows areas appropriate for the Venera-D landing site selection.

BALLISTIC CONSTRAINTS:

The final scenario of the Venera-D mission includes a gravitational maneuver during one Venusian year [9, 10] and the lander separation after the maneuver. I this scenario, the total area appropriate for landing is much greater comparing with that in the scenario of the lander separation immediately after spacecraft insertion into the orbit around Venus. The forbidden regions for the adopted mission scenario are presented by relatively small areas in Beta Regio and westward of the largest tessera in Ovda Regio (see Fig. 1).

PROPOSED LANDING SITES:

Because the majority of the Venus surface is open for the site selection, one can outline several regions that satisfy both the safety and scientific constraints. At this moment, we have selected three potential landing sites (Fig. 2).

Landing site 1, Kutue-South (33°N, 110°E, see Figs. 1, 2), is within regional plains (rp1) of Niobe Planitia southward of Kutue Tessera. Entire landing circle (300 km diameter) is within morphologically homogenous rp1 unit. Wrinkle ridges and narrow fractures cut the surface of plains within the landing circle. These features, however, comprise a few percent of the total circle area and landing at this place appear to be safe. Materials

of unit rp1 (as well as in all other places) probably formed by melts from the upper mantle of Venus and, thus, have very high scientific priority.

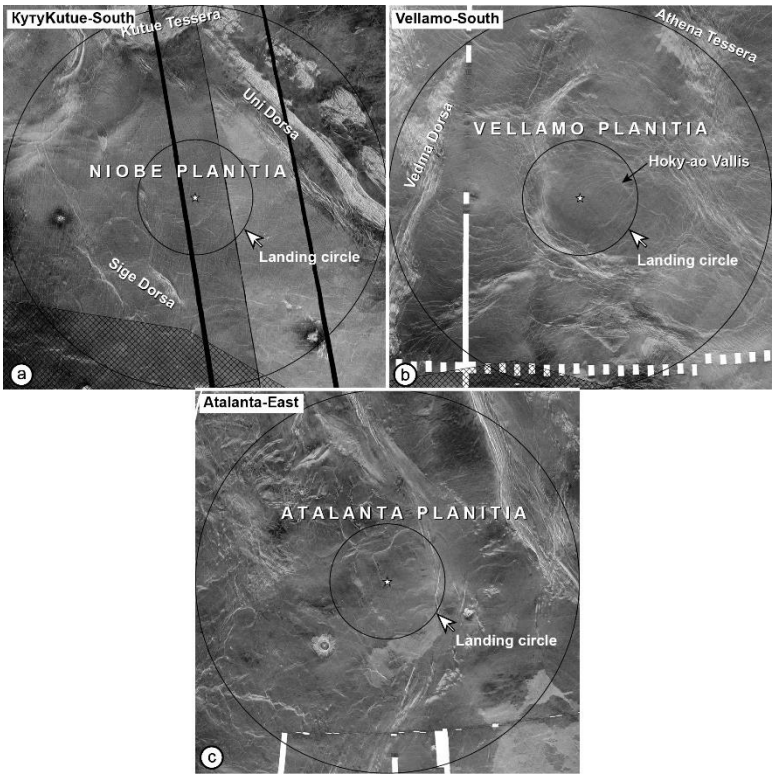


Fig. 2. Proposed landing sites. Stars — landing points; the landing circle is 300 km diameter; the outer circle is 1000 km diameter (illustrates the regional geological setting of the landing sites)

Landing site 2, Vellamo-South (29°N, 164°E, see Figs. 1, 2), is in the southern portion of Vellamo Planitia and practically completely is covered by materials of unit rp1. The most impressive feature of the landing circle is Baltis Vallis, the longest lava channel on Venus, which could by formed by continuous flow of komatiites.

Landing site 3, Atalanta-East (70°N, 137°E, see Figs. 1, 2), is at the eastern edge of a large topographic depression of Atalanta Planitia, the surface of which is almost completely covered by unit rp1.

All three selected sites are within large extensions of the lower unit of regional plains (rp1) and the landing circles include only this unit (see Fig. 2). Because of this, the requirement of knowledge of the exact location of the lander is somewhat softened: the same unit is expected to occur in all points of the landing circles. Nevertheless, determination of the landing site with maximum possible accuracy is still important because the fine-scale variations of texture and structure of the surface of regional plains likely exist but are invisible at the Magellan resolution.

ACKNOWLEDGMENTS:
The work was conducted under a state order to MAI.

REFERENCES:

[1] Barsukov V. L., Basilevsky A. T., Burba G. A. et al. The Geology and geomorphology of the Venus surface as revealed by the radar Images obtained by Venera 15 and 16 // Proc. 16th LPSC. Pt. 2. JGR. 1986. V. 91. P. D378–D398.
[2] Ivanov M. A., Head J. W. Global geological map of Venus // PSS. 2011. V. 59. P. 1559–1600. DOI: 10.1016/j.pss.2011.07.008.

[3] Head J.W., Crumpler L.S., Aubele J.C., Guest J.E., Saunders R.S. Venus volcanism: Classification of volcanic features and structures, associations, and global distribution from Magellan data // JGR. 1992. V. 97. P. 13153–13197.
[4] Guest J.E., Bulmer M.H., Aubele J. et al. Small volcanic edifices and volcanism in the plains of Venus // JGR. 1992. V. 97. P. 15949–15966.
[5] Ivanov M.A., Head J.W. The history of volcanism on Venus // PSS. 2013. V. 84. P. 66–92.
[6] Parmentier E.M., Hess P.C. Chemical differentiation of a convecting planetary interior: Consequences for a one plate planet such as Venus // GRL. 1992. V. 19. P. 2015–2018.
[7] Head J.W., Parmentier E.M., Hess P.C. Venus: Vertical accretion of crust and depleted mantle and implications for geological history and processes // PSS. 1994. V. 42. P. 803–811.
[8] Campbell D.B., Stacy N.J.S., W.I. Newman et al. Magellan observations of extended impact crater related features on the surface of Venus // JGR. 1992. V. 97. P. 16249–16278.
[9] Eismont N., Zubko V., Belyaev A., Fedyaev K., Zasova L., Gorinov D., Simonov A., Nazirov R. Expansion of landing areas on the Venus surface using resonant orbits in the Venera-D project // Acta Astronautica. 2022. V. 197. P. 310–322.
[10] Zubko V.A., Eismont N.A., Fedyaev K.S. Expanding opportunities for landing to Venus: using gravity assist and resonant orbits for orbiter-lander missions // Advances in Space Research. 2025. V. 76. P. 3142–3170. DOI: 10.1016/j.asr.2025.06.052.

SPATIAL DISTRIBUTION AND EVOLUTION OF CORONAE AND LARGE VOLCANOES IN ULFRUN AND BETA REGIONES, VENUS

D. G. Malyshev, M. A. Ivanov
Vernadsky Institute of Geochemistry and Analytical Chemistry RAS
Moscow, Russia, malyshev.danil13@gmail.com

KEYWORDS:
Venus, central-type volcanism, coronae, large volcanoes, rift zones, Ulfrun Regio, Beta Regio, Magellan, stratigraphy

INTRODUCTION:
Coronae and large volcanoes are among the principal expressions of central-type volcanism on Venus and record the interaction between magmatism, tectonic deformation and lithospheric structure. This study compares two northern-hemisphere regions, Ulfrun Regio and Beta Regio, which both contain coronae, large volcanoes and rift structures, but represent different regional geological settings. The aim is to assess how the spatial distribution, morphology, lava-field development and stratigraphic position of volcanic centres vary between a rift-dominated province and a large dome-like volcanic-tectonic rise.

DATA AND METHODS:
The study is based on Magellan synthetic-aperture radar images and topographic data [1, 2], supplemented by published catalogues and regional geological mapping of coronae and large volcanoes [3–7]. The analysis included vector mapping of corona annuli, internal domains, lava flows, large-volcano edifices, lava fields, rift zones and surrounding tectonic structures. To make the two regions comparable, equal observation windows of about 5300·3200 km, with an area of 16.7 million km^2, were used. For each object, the shortest distance to the nearest rift zone was measured both from the centre and from the outer contour. Stratigraphic relationships were interpreted using superposition, cross-cutting, embayment and flooding relationships.

RESULTS:
The main contrast between the regions is spatial. In Ulfrun Regio, 61 coronae and five large volcanoes were identified, giving a total density of approximately 3.95 central volcanic centres per 1 million km^2. In Beta Regio, 24 coronae and five large volcanoes were identified, and the total density is about 1.73 centres per 1 million km^2. Coronae in Ulfrun are strongly associated with rift zones: the median distance from corona centres to rifts is about 39 km, and the median distance from the outer contours is 0 km, indicating frequent intersection with rift structures. Large volcanoes show a similar pattern, with median centre-to-rift and contour-to-rift distances of about 29 and 0 km, respectively. In Beta Regio, the corresponding median distances are much larger: about 394 and 312 km for coronae, and 472 and 437 km for large volcanoes. Thus, central volcanism in Ulfrun is mainly rift-controlled, whereas in Beta it is more weakly tied to the main rift zones and is concentrated in separate volcanic centres.

Morphometric parameters of coronae are broadly comparable in the two regions: the median mean diameter is about 150 km in Ulfrun and 145 km in Beta. However, their morphology and volcanic expression differ. Radial fractures are recorded in 17 of 61 coronae in Ulfrun, but only in two of 24 coronae in Beta, whereas annular structures are common in both regions. Lava flows are associated with 29 coronae in Ulfrun and 14 coronae in Beta. Although the proportion of coronae with lava flows is slightly higher in Beta, the lava fields of Ulfrun coronae are larger: the median area of lava fields related to flow-producing coronae is about 19.4 thousand km^2, compared with 7.5 thousand km^2 in Beta. This suggests a more extensive

volcanic output from Ulfrun coronae and a more localized corona-related volcanism in Beta.

Large volcanoes in both regions show evidence for long-lived magmatic activity, including broad lava fields, summit depressions or calderas, small shield volcanoes and radial graben systems. All large volcanoes in the two regions are associated with lava fields. The total mapped area of lava fields related to large volcanoes is about 1.46 million km^2 in Ulfrun and about 1.00 million km^2 in Beta. Nevertheless, their structural context differs: four of five large volcanoes in Ulfrun are intersected by, or immediately adjacent to, rift structures, whereas in Beta only part of the large-volcano population is directly connected with the main rift zones.

DISCUSSION AND CONCLUSIONS:

Stratigraphic relationships show that both coronae and large volcanoes formed through multiple, partly overlapping tectonic and volcanic episodes. Corona annuli and internal domains commonly represent early stages, whereas lava flows often postdate these elements and embay plains, tectonic structures or older parts of corona complexes. Rift structures may either cut lava flows and corona elements or be partly flooded by younger volcanic materials, which indicates that rifting and volcanism were not strictly sequential but partly contemporaneous. Large volcanoes generally occupy a relatively late position with respect to some coronae and regional plains-tectonic units.

The observed differences are interpreted as the result of contrasting structural control and possibly different crustal/lithospheric conditions. In Ulfrun Regio, rift zones likely enhanced crustal permeability and distributed magma ascent along elongated zones of extension. In Beta Regio, central volcanism developed within a dome-like volcanic-tectonic rise that includes tessera terrains and a more heterogeneous structural framework. As a result, corona-related volcanism is more localized, whereas large volcanoes differ strongly in scale and degree of rift association. The comparison indicates that central-type volcanism on Venus was multi-stage in both regions, but its surface expression was controlled by the regional tectonic setting and by the structure of the crust.

REFERENCES:

[1] Saunders R. S., Spear A. J., Allin P. C. et al. Magellan mission summary // J. Geophysical Research. 1992. V. 97. P. 13067–13090.
[2] Ford J. P., Plaut J. J., Weitz C. M. et al. Guide to Magellan Image Interpretation. JPL Publication 93-24. Pasadena: Jet Propulsion Laboratory, 1993. 148 p.
[3] Stofan E. R., Sharpton V. L., Schubert G. et al. Global distribution and characteristics of coronae and related features on Venus: Implications for origin and relation to mantle processes // J. Geophysical Research. 1992. V. 97. P. 13347–13378.
[4] Ivanov M. A., Head J. W. Global geological map of Venus // Planetary and Space Science. 2011. V. 59. P. 1559–1600.
[5] Hahn R. M., Byrne P. K. A morphological and spatial analysis of volcanoes on Venus // J. Geophysical Research: Planets. 2023. V. 128. Article e2023JE007753.
[6] Gülcher A. J. P., Sabbeth L., Stofan E., Smrekar S. E. Coronae on Venus: An updated global database and insights into morphology, spatial distribution, geological setting, and lithospheric properties // J. Geophysical Research: Planets. 2025. V. 130. No. 5.
[7] Ivanov M. A., Head J. W. Large volcanoes on Venus: Morphology, morphometry, and stratigraphy // Icarus. 2025. V. 429. Article 116404.

RESULTS OF GAMMA-RAY MEASUREMENTS PERFORMED BY THE MGNS INSTRUMENT DURING THE CRUISE PHASE OF THE BEPICOLOMBO MISSION TO MERCURY

V. D. Gubarev[1,2], A. S. Kozyrev[1], I. G. Mitrofanov[1]
[1] *Space Research Institute RAS, Moscow, 117997, Russia, victor.gubarev.2004@mail.ru*
[2] *National Research Nuclear University "MEPhI", Moscow, Russia, 115409*

KEYWORDS:
MGNS, Mercury, BepiColombo, GRS, MESSENGER, elemental composition, gamma-ray, nuclear planetology

ABSTRACT:
The Mercury Gamma-ray and Neutron Spectrometer (MGNS) onboard the Mercury Planetary Orbiter (MPO) of the ESA BepiColombo mission was developed by the Space Research Institute to measure gamma-ray and neutron emission from the surface of Mercury and study its elemental composition. Launched in October 2018, the spacecraft is currently cruising along a heliocentric trajectory that is approaching Mercury's orbit; the cruise phase will continue until November 2026. Before its planned orbital insertion, BepiColombo has completed one Earth flyby, two Venus flybys, and six Mercury flybys.

After the spacecraft's placement into the operational orbit around Mercury in April 2027 and the start of the mapping phase, MGNS will begin measurements of gamma-ray and neutron fluxes produced by interactions of galactic cosmic rays with the upper layer of the Mercurian regolith (to depths of approximately 1–2 m). The instrument will also detect gamma-ray lines produced by naturally radioactive elements. The surface mapping data will be used to determine the elemental composition of Mercury's near-surface layer [1, 2].

This work presents the results of gamma-ray measurements performed by MGNS during the BepiColombo cruise phase to Mercury. A comparison between gamma-ray spectra detected by the MGNS spectrometer based on a $CeBr_3$ scintillation crystal and the background data from the GRS spectrometer on MESSENGER mission, which employed a high-purity germanium detector, is presented [3, 4].

In summary, the initial identification of background gamma-ray lines detected by the MGNS instrument during the cruise phase has been completed, and the energy calibration of the gamma-ray spectrometer has been established. The contribution of the identified background lines to future analyses of Mercury surface gamma-ray measurements was evaluated. The obtained results provide a characterization of the background gamma-ray lines and enable the development of a method for separating the planetary gamma-ray component from the total measured spectrum. These results demonstrate the readiness of the MGNS instrument for the forthcoming Mercury surface mapping phase.

REFERENCES:
[1] Benkhoff J., Murakami G. et al. BepiColombo — Mission Overview and Science Goals // Space Science Reviews. 2021. V. 217. Article 90. DOI: https://doi.org/10.1007/s11214-021-00861-4.
[2] Mitrofanov I. G., Kozyrev A. S. et al. The Mercury Gamma and Neutron Spectrometer (MGNS) on board the Planetary Orbiter of the BepiColombo mission // Planetary and Space Science. 2010. V. 58. P. 116–124. https://doi.org/10.1016/j.pss.2009.01.005.
[3] Kozyrev A. S., Mitrofanov I. G., Owens A. et al. A comparative study of LaBr3(Ce3+) and CeBr3 based gamma-ray spectrometers for planetary remote

sensing applications // Review of Scientific Instruments. 2016. V. 87. No. 8. Article 085112. DOI: 10.1063/1.4958897.
[4] Evans L. G., Peplowski P. N., Rhodes E. A. et al. Major-element abundances on the surface of Mercury: Results from the MESSENGER Gamma-Ray Spectrometer // J. Geophysical Research: Planets. 2012. V. 117. Article E00L07. DOI: https://doi.org/10.1029/2012JE004178.

A UNIFIED APPROACH TO PHOTOMETRIC TRANSFORMATIONS AND CELESTIAL OBJECT COLOR DETERMINATION

A. M. Anpilogov
Pushchino Radio Astronomy Observatory
Astro Space Center, Department of Astronomy
Lebedev Physical Institute RAS, aaskaniy@gmail.com

KEYWORDS:
computational methods, image processing, spectra, photometry, photometric systems, color equation

ABSTRACT:
Photometric measurements are filter-dependent, which hinders the comparative analysis of spectral data. For certain photometric systems, transformation formulas (color equations) are available based on a sample of standard stars; however, these are inapplicable to non-stellar objects (in particular, small Solar System bodies [1]) and unknown for arbitrary pairs of filters. It does not seem reasonable to calculate all possible color equations, since number of optical filters exceeds 11,000 [2]. This work proposes a solution: spectral reconstruction via Tikhonov regularization [3] and the derivation of synthetic photometry. A priori information regarding spectral smoothness is investigated.

The methodology has a wide range of applications: photometry of planets, moons, small bodies, and any other objects with continuum-dominated spectra that differ from standard stars can be converted to any required photometric system. The results of the work include a table of colors and color indices for selected celestial bodies (e.g., spectra from [4] are analyzed). An AstroColor library has been developed for Python, providing the astronomical community with easy access to these methods. For the general public, a GUI wrapper named TrueColorTools is available, which includes an extensive spectral database and phase function models processing.

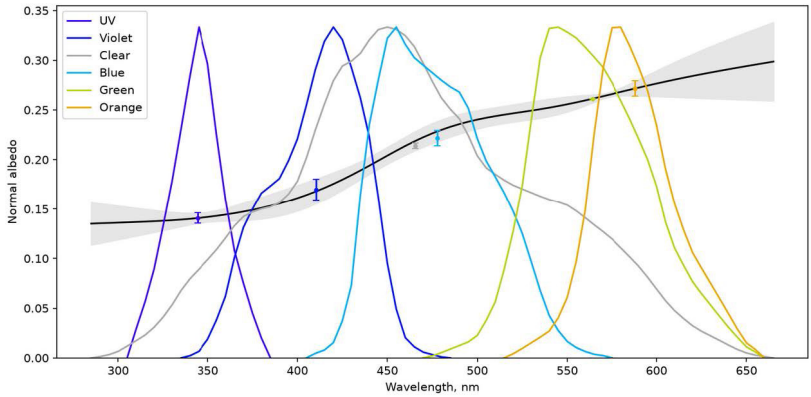


Fig. 1. Application example: reflectance spectrum of Hyperion (black), reconstructed from photometric observations by Voyager spacecraft (ISS NAC) [5]. Filter profiles provided by [2]. "Clear" filter profile depicted gray to distinguish it from the other blue filters. The spectrum does not pass through the points at the effective wavelengths of the filters, as it would if simple interpolation were used. An ill-posed inverse problem has been solved: the convolution with the reconstructed spectrum equals the original values

This approach is also applicable to images captured through filters. As an example, the processing of true-color images from interplanetary spacecraft is examined, where the spectral sensitivity of the human eye is mod-

eled as a filter system. Necessary concepts from colorimetry are introduced, as the procedure is nuanced and subtle [6].

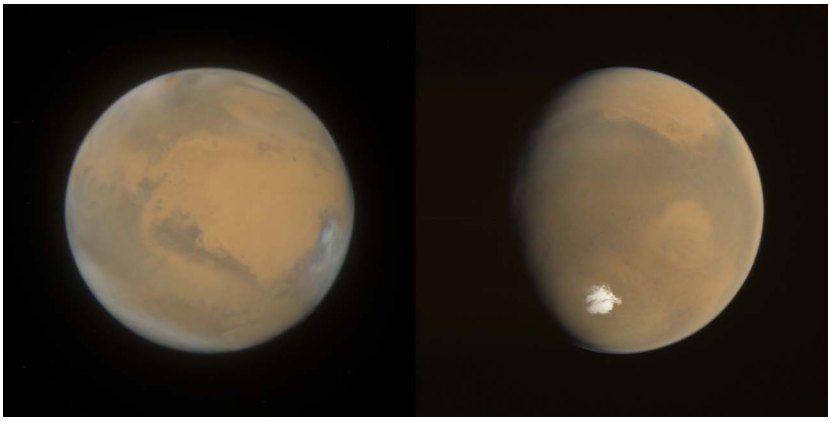


Fig. 2. Images of Mars by Hubble Space Telescope (12. 05.2016) and Psyche spacecraft (16. 05.2026), processed in true colors (sRGB color space, chromatic adaptation for illuminant E white point). The photographs show Sinus Sabaeus, with Arabia Terra above and the South Polar cap below. Image credits: NASA/STScI, NASA/JPL-Caltech/ASU

CODE AND DATA AVAILABILITY:

https://pypi.org/project/astrocolor/

https://github.com/Askaniy/TrueColorTools

REFERENCES:

[1] Kuksenko V., Jevčák P., Sabolová K. et al. Verification of photometric transformations for small Solar System bodies on Main-Belt asteroid color data // EPSC-DPS Joint Meeting 2025. EPSC-DPS2025-126. DOI: 10.5194/epsc-dps2025-126.
[2] Rodrigo C., Solano E. The Spanish Virtual Observatory Filter Profile Service // Contributions to the XIV.0 Scientific Meeting (virtual) of the Spanish Astronomical Soc. 2020. Article 182.
[3] Tikhonov A. N., Goncharskii A. V., Stepanov V.V., Yagola A.G.. Regularization Algorithms and A Priori Information. Moscow: Izd. "Nauka". 1983. 200 p.
[4] Payne A., Villanueva G. L., Kofman V. et al. A Comprehensive Spectroscopic Reference of the Solar System and Its Application to Exoplanet Direct Imaging // The Planetary Science J. 2026. V. 7. No. 2. Article 51. DOI: 10.3847/PSJ/ae2feb.
[5] Thomas P., Veverka J. Hyperion: Analysis of Voyager observations // Icarus. 1985. V. 64. No. 3, P. 414–424. DOI: 10.1016/0019-1035(85)90065-X.
[6] Irwin P.G.J., Dobinson J., James A. et al. Modelling the seasonal cycle of Uranus's colour and magnitude, and comparison with Neptune // Monthly Notices Royal Astron. Soc. 2024. V. 527(4). P. 11521-11538. DOI: 10.1093/mnras/stad3761.

CALCULATION OF RADAR REFLECTIONS FROM RELIEF SURFACES OF CELESTIAL BODIES

Ya. A. Ilyushin[1,2], Zhao Hongli[2]
[1] *V. A. Kotelnikov Institute of Radio Engineering and Electronics RAS Moscow 125009, Russia, ilyushin@phys.msu.ru*
[2] *Lomonosov Moscow State University, Moscow 119992, Russia zhao.h21@physics.msu.ru*

KEYWORDS:
radar reflection, rough surface, celestial bodies, exponential correlation function, Gaussian approximation, synthetic aperture radar, scattering cross section

INTRODUCTION:
Radar remote sensing of the Moon, planets, and small bodies requires computational models that can connect the observed echo with the statistical properties of a relief surface. Direct numerical calculation of electromagnetic reflection from a surface whose horizontal dimensions are much larger than the wavelength remains computationally demanding. For this reason, practical models are usually based on asymptotic approximations, most notably the Kirchhoff approximation, in which the reflected field is represented through integration over a phase screen describing the surface relief [1–3].

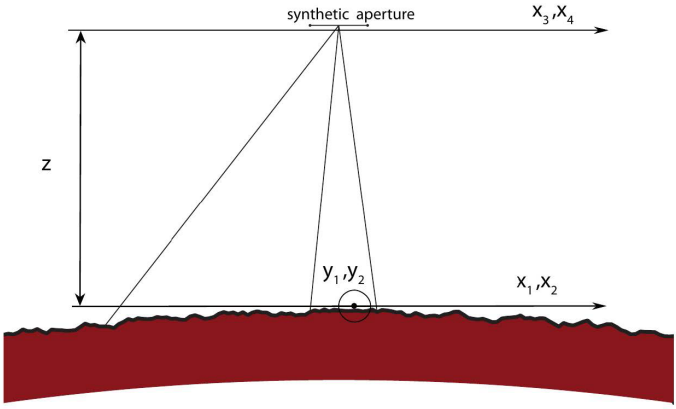


Fig. 1. Schematic geometry of radar sounding of a relief surface with synthetic-aperture reception

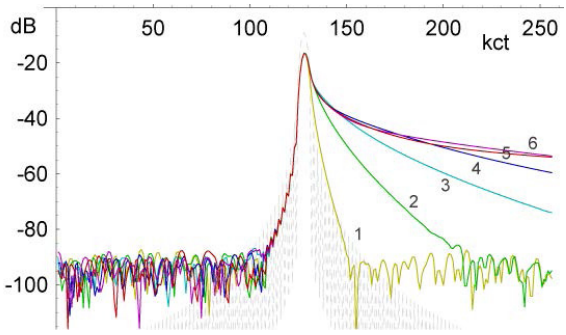


Fig. 2. Linear frequency-modulated radar reflections from a random surface relief (k_0l=100, k_0h=1, k_0z=25 000, β=0.1) for different Gaussian approximations of the exponential correlation function (indicated by numerical labels next to the curves). The dashed curve is the reflection from a flat surface

A persistent difficulty is the choice of a surface-height correlation model. Gaussian correlation functions are convenient because many diffraction integrals and field moments can be written in a closed analytical form. However, radar observations of celestial bodies are often described more successfully by an exponential correlation function, even though this model formally corresponds to an infinite root-mean-square slope and is therefore less convenient for direct analytical treatment [4–7]. The present work develops a computational bridge between these two descriptions.

COMPUTATIONAL APPROACH:

The proposed method approximates the exponential height-correlation function by a finite superposition of Gaussian terms. In dimensionless form, the correlation function can be represented as $C(\rho)=\exp(-\rho/l)$, where l is the correlation length. It is then approximated by a sum of M terms $b_m \exp[-\rho^2/(a_m^2 l^2)]$, with coefficients and scale parameters chosen so that the approximation reproduces the relevant range of spatial scales. This replacement preserves the observationally important exponential model while allowing the use of analytical expressions available for Gaussian-correlated surfaces.

Within the Kirchhoff framework, this approximation makes it possible to calculate radar scattering cross sections and time-dependent radar echoes without fully discretizing the rough surface from first principles. The model is especially useful for simulations of chirp radar signals and synthetic-aperture radar configurations, where the received signal depends both on the angular scattering spectrum and on the time-delay interval over which the surface contribution is significant.

RESULTS AND DISCUSSION:

Calculations performed for exponentially correlated rough surfaces show that the Gaussian-superposition approximation reproduces the known asymptotic laws of diffuse reflection from random surfaces. The comparison provides a consistency check for the numerical procedure and indicates the range of backscattering angles for which the approximation is reliable. Increasing the number of Gaussian terms extends the range of correlation scales and, consequently, the interval of radar time delays that can be modeled with satisfactory accuracy.

For a representative synthetic-aperture radar geometry, the calculated echoes were compared for several Gaussian approximations of the same exponential correlation function. The convergence of these curves toward a common limiting behavior demonstrates that the method can capture the principal contribution of relief scattering to the received signal. A comparison with the reflection from a flat surface separates the effect of surface relief from the purely specular component of the echo.

The approach is not limited to monochromatic plane waves. Because the method is formulated through correlation functions and diffraction integrals, it can be applied to stationary and transient wave fields, finite beams, and different source configurations. This makes it relevant for interpretation of radar reflections from relief surfaces of celestial bodies, where surface statistics, incidence geometry, and signal bandwidth all influence the measured echo.

CONCLUSION:

A practical method is proposed for calculating radar reflections from relief surfaces of celestial bodies whose height statistics are described by an exponential correlation function. By representing this correlation function as a finite sum of Gaussian components, the method combines the empirical relevance of the exponential model with the analytical flexibility of Gaussian-correlated surfaces. The resulting computational scheme can be used for radar cross-section calculations and for modeling chirp and synthetic-aperture radar echoes from statistically rough terrain.

ACKNOWLEDGMENTS:

The work used the equipment of the shared research facilities of the Supercomputing Center of Lomonosov Moscow State University. The study was

carried out within the framework of the state assignment of Lomonosov Moscow State University.

REFERENCES:

[1] Beckmann P., Spizzichino A. The Scattering of Electromagnetic Waves from Rough Surfaces. New York: Macmillan, 1963.
[2] Ogilvy J. A. Theory of Wave Scattering From Random Rough Surfaces. Bristol: Adam Hilger, 1991.
[3] Goodman J. Introduction to Fourier Optics. 2nd ed. New York: McGraw-Hill, 1996.
[4] Hagfors T. Backscattering from an undulating surface with applications to radar returns from the Moon // J. Geophysical Research. 1964. V. 69. No. 18. P. 3779–3784. DOI: 10.1029/JZ069i018p03779.
[5] Sultan-Salem A. K., Tyler G. L. Hagfors' law revisited // J. Geophysical Research: Planets. 2006. V. 111. No. 6. Article E06S07. DOI: 10.1029/2005JE002489.
[6] Johnson J. T., Warnick K. F., Xu P. On the geometrical optics (Hagfors' law) and physical optics approximations for scattering from exponentially correlated surfaces // IEEE Trans. Geoscience and Remote Sensing. 2007. V. 45. No. 8. P. 2619–2629. DOI: 10.1109/TGRS.2007.900682.
[7] Ilyushin Y. A., Zhao H. Calculation of radar reflections from exponentially correlated surfaces // Radiophysics and Quantum Electronics. 2024. V. 67. No. 6.

Session 4.
EXTRASOLAR PLANETS (EP)
Oral Session

USING VENUS AND TERRESTRIAL VOLCANIC ANALOGS TO INTERPRET ROCKY EXOPLANETS

P. D'Incecco[1], J. R. Filiberto[2], C. Ahrens[3,4], G.Andreuzzi[5,6], G. N. Arney[7], C. Badia[1], S. S. Bhiravarasu[8], M. Blackett[9], S. Branca[10], J. Brossier[11], L. Bruzzone[12], R. A. Corsaro[10], R. Cosentino[5,13], G. Covone[14], N. Davidova[15], G. Di Achille[1], G. Di Rico[1], M. Dolci[1], E. Ferroni[1], G. Fiasconaro[16], G. Gallardo i Peres[15,17], J. B. Garvin[7], A. Ghedina[5], D. Gorinov[18], A. Gülcher[19], J. W. Head[20], A. Ivanova[18], S. R. Kane[21], E. Kohler[22], G. Komatsu[23], O. I. Korablev[18], I. López Ruiz-Labranderas[24], J. Lustig-Yaeger[25], N. Mari[26], Ph.J. Mason[15], C. Monaco[10,27], S. Parisini[28], F. Pedichini[6], G. Valentini[1], M. B. Weller[29], L. V. Zasova[18], L. M. Zelenyi[18]

[1] *National Institute for Astrophysics —Astronomical Observatory of Abruzzo, Teramo, Italy, piero.dincecco@inaf.it*
[2] *Astromaterials Research and Exploration Science Division, NASA Johnson Space Center, Houston, TX, USA*
[3] *University of Maryland, College Park, MD, USA*
[4] *Center for Research and Exploration in Space Science and Technology II, NASA Goddard Space Flight Center, Greenbelt, MD, USA*
[5] *Fundación Galileo Galilei — INAF, Telescopio Nazionale Galileo, Breña Baja, La Palma, Spain*
[6] *National Institute for Astrophysics — Osservatorio Astronomico di Roma, Monte Porzio Catone, Italy*
[7] *NASA Goddard Space Flight Center, Greenbelt, MD, USA*
[8] *Space Applications Centre, Indian Space Research Organisation, Ahmedabad, India*
[9] *Centre for Agroecology, Water and Resilience, Coventry University Coventry, UK*
[10] *Istituto Nazionale di Geofisica e Vulcanologia, Osservatorio Etneo — Sezione di Catania, Catania, Italy*
[11] *National Institute for Astrophysics — Institute for Space Astrophysics and Planetology, Rome, Italy*
[12] *Remote Sensing Laboratory, Department of Information Engineering and Computer Science, University of Trento, Trento, Italy*
[13] *National Institute for Astrophysics — Osservatorio Astrofisico di Catania, Catania, Italy*
[14] *Department of Physics Ettore Pancini, Università degli Studi di Napoli Federico II, Naples, Italy*
[15] *Department of Earth Science & Engineering, Imperial College London, London, UK*
[16] *National Institute for Astrophysics — Institute of Space Astrophysics and Cosmic Physics, Palermo, Italy*
[17] *isardSAT S. L., Barcelona, Spain*
[18] *Space Research Institute RAS, Moscow, Russia*
[19] *Earth and Planetary Geodynamics Group, Department of Geosciences, Faculty of Environment and Natural Resources, University of Freiburg, Freiburg, Germany*
[20] *Department of Earth, Environmental and Planetary Sciences, Brown University, Providence, RI, USA*
[21] *Department of Earth and Planetary Sciences, University of California, Riverside, CA, USA*
[22] *Solar System Exploration Division, NASA Goddard Space Flight Center, Greenbelt, MD, USA*
[23] *IRSPS, Università G. d'Annunzio, Pescara, Italy*
[24] *Tecvolrisk Research Group, Departamento de Biología, Geología, Física y Química Inorgánica, Universidad Rey Juan Carlos, Madrid, Spain*
[25] *Space Exploration Sector, Johns Hopkins University Applied Physics Laboratory, Laurel, MD, USA*

[26] *University of Calabria, Rende, Italy*
[27] *Dipartimento di Scienze Biologiche Geologiche e Ambientali, Università di Catania, Catania, Italy*
[28] *National Institute for Astrophysics — Istituto di Radioastronomia, Bologna, Italy*
[29] *Department of Earth and Environmental Sciences, Rensselaer Polytechnic Institute, Troy, New York, USA*

KEYWORDS:
rocky exoplanets, Venus, planetary geology, volcanic analogs, AVENGERS, exoplanet characterization, comparative planetology, surface-atmosphere interactions

INTRODUCTION:
Rocky exoplanets are generally spatially unresolved, so their reflected-light and thermal-emission spectra are integrated over the visible disk. Depending on wavelength and atmospheric opacity, these spectra may include a surface contribution when the atmosphere is sufficiently transparent, together with absorption, emission, and scattering in the atmosphere. Similar disk-integrated observations can arise from planets with different surface materials, atmospheric properties, and evolutionary histories. Geological context helps reduce this ambiguity by linking remote measurements to the processes that form and alter planetary surfaces, and to exchanges between surfaces and atmospheres. The Earth–Venus pair provides a nearby example: the planets are similar in size and are thought to have broadly comparable bulk compositions, yet Venus's dense atmosphere, extreme surface conditions, and volcanic history show how strongly rocky planets can diverge [1].

CONNECTING VENUS AND EXOPLANET OBSERVATIONS:
Past missions to Venus have revealed a complex world, but key links between its atmosphere, surface, interior, and geological evolution remain poorly constrained. Future Venus missions will investigate complementary parts of this system [2–6]. Future exoplanet missions face a different challenge: even nearby rocky worlds will generally remain spatially unresolved [7–10]. The far more detailed view available for Venus can therefore guide the interpretation of disk-integrated exoplanet observations.

FROM TERRESTRIAL ANALOGS TO EXOPLANETS:
The Analogs for Venus' GEologically Recent Surfaces (AVENGERS) initiative connects planetary geology and remote observations of Venus, field and laboratory studies of terrestrial volcanic terrains, and the interpretation of rocky exoplanets [1]. Work at Mount Etna and La Palma provides reference observations and samples of fresh and altered lava flows [1]. Together, these data let us examine how spectral signatures linked to rock type and alteration may appear at an analog site, through the atmosphere of Venus, and in the disk-integrated light of a rocky exoplanet. They also show how alteration can weaken or mask signatures of fresh volcanic materials [1].

FROM MEASUREMENTS TO OBSERVABLES:
The goal is not to infer a surface type from a single measurement. Instead, we test which physically plausible combinations of surfaces and atmospheres can reproduce the observations. Laboratory spectra of terrestrial samples show how strongly reflectance can vary with rock type. Figure 1 compares visible and near-infrared reflectance for selected rocks and minerals and marks the wavelength region containing the Venus nightside surface windows [11]. These measurements provide geological reference cases for interpreting Venus data and testing possible surface contributions to disk-integrated spectra of rocky exoplanets. Observations across several wavelengths can then rule out some surface–atmosphere combinations and guide follow-up work [10, 11].

OUTLOOK:
AVENGERS aims to build geological reference cases for Venus and exoplanets. By connecting Earth-based observations and experiments with Venus data and exoplanet observables, we can identify which interpretations are

robust and where important ambiguities remain. This approach avoids treating every exoVenus as a copy of present-day Venus, or every exoEarth as a copy of present-day Earth, and instead allows for a wider range of geological and atmospheric states.

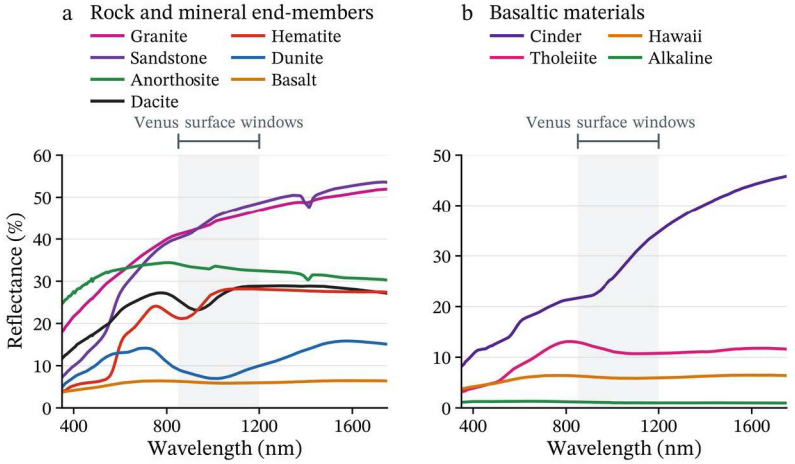


Fig. 1. Visible and near-infrared reflectance spectra of selected rock and mineral end-members (a) and basaltic materials (b), measured at 25 °C. The pale bands mark the 850–1200 nm region containing the Venus nightside surface windows. Adapted from [11]

REFERENCES:

[1] D'Incecco P. et al. The "Analogs for Venus' GEologically Recent Surfaces" (AVENGERS) Initiative: Using Terrestrial Analogs to Study Recent Volcano-Tectonic Activity on Venus and Inform the Characterization of Terrestrial Exoplanets // J. Geophysical Research: Planets. 2025. V. 130. No. 9. Article e2024JE008675. DOI: 10.1029/2024JE008675.

[2] Garvin J.B., Getty S.A., Arney G.N. et al. Revealing the Mysteries of Venus: The DAVINCI Mission // The Planetary Science J. 2022. V. 3. No. 5. Article 117. DOI: 10.3847/PSJ/ac63c2.

[3] Smrekar S.E., Hensley S., Nybakken R. et al. VERITAS (Venus Emissivity, Radio Science, InSAR, Topography, and Spectroscopy): A Discovery Mission // 2022 IEEE Aerospace Conference (AERO). 2022. P. 1–20. DOI: 10.1109/AERO53065.2022.9843269.

[4] Ghail R.C., Wilson C., Galand M. et al. EnVision: taking the pulse of our twin planet // Experimental Astronomy. 2012. V. 33. No. 2–3. P. 337–363. DOI: 10.1007/s10686-011-9244-3.

[5] Gorinov D.A., Zasova L.V., Zelenyi L.M. et al. Venera-D: Scientific Goals and the Mission Architecture // Moscow University Physics Bull. 2025. V. 80. Suppl. 1. P. S445–S448. DOI: 10.3103/S0027134925702078.

[6] Widemann T., Smrekar S.E., Garvin J.B. et al. Venus Evolution Through Time: Key Science Questions, Selected Mission Concepts and Future Investigations // Space Science Reviews. 2023. V. 219. No. 7. Article 56. DOI: 10.1007/s11214-023-00992-w.

[7] Rauer H. et al. The PLATO mission // Experimental Astronomy. 2025. V. 59. No. 3. Article 26. DOI: 10.1007/s10686-025-09985-9.

[8] Tinetti G. et al. A chemical survey of exoplanets with ARIEL // Experimental Astronomy. 2018. V. 46. No. 1. P. 135–209. DOI: 10.1007/s10686-018-9598-x.

[9] Vaughan S.R. et al. Chasing rainbows and ocean glints: Inner working angle constraints for the Habitable Worlds Observatory // Monthly Notices of the Royal Astronomical Society. 2023. V. 524. No. 4. P. 5477–5485. DOI: 10.1093/mnras/stad2127.

[10] Kane S.R. et al. Imaging Venus-like Worlds: Spectral, Polarimetric, and UV Diagnostics for the Habitable Worlds Observatory // Publications of the Astronomical Society of the Pacific. 2026. V. 138. No. 2. Article 024404. DOI: 10.1088/1538-3873/ae417d.

[11] Treiman A.H., Filiberto J., Vander Kaaden K.E. Near-infrared reflectance of rocks at high temperature: Preliminary results and implications for near-infrared emissivity of Venus's surface // The Planetary Science J. 2021. V. 2. No. 2. Article 43. DOI: 10.3847/PSJ/abd546.

DEPENDENCE OF EXOPLANET PROPERTIES ON THEIR LOCATION RELATIVE TO THE HABITABLE ZONE

G. A. Morozov[1,2], E. S. Belenkaya[2]
[1] *Lomonosov Moscow State University, Moscow, Russia*
morozov.ga21@physics.msu.ru
[2] *Skobeltsyn Institute of Nuclear Physics, Lomonosov Moscow State University, Moscow, Russia*

KEYWORDS:
exoplanets, habitable zone, recent Venus, early Mars, runaway greenhouse, moist greenhouse, maximum greenhouse

INTRODUCTION:
The habitable zone (HZ) is the region around a star where liquid water can persist on a planet. This study presents a statistical analysis of the distribution of exoplanet characteristics based on their position relative to the habitable zone. Two models — [1] and [2] —are used to calculate the boundaries of the habitable zone; these models differ in their treatment of planetary mass and the choice of the inner threshold (moist greenhouse effect versus runaway greenhouse effect). Each model calculates conservative and optimistic habitable zones. The proportions of various planet types (super-Earths, mini-Neptunes, gas giants) located within and outside these zones are assessed, and the dependence of these distributions on the host star's temperature is determined. The data used for the calculations were obtained from the NASA Exoplanet Archive [3].

The HZ boundaries were determined based on the effective stellar flux *S*eff as a function of the star's temperature *T*eff and luminosity. For model [1], the classical thresholds of Recent Venus, Moist Greenhouse, Maximum Greenhouse, and Early Mars were used. In model [2], the inner boundary was replaced by the Runaway Greenhouse limit, and the coefficients were interpolated for planetary masses ranging from 0.1 to 5 $M_{\oplus}$. The results showed that only about 3.1–3.4% of all planets lie within the conservative zone, while about 4.9% fall within the optimistic zone. The distribution by radius reveals a distinct pattern: super-Earths and mini-Neptunes ($R_{\oplus}<R<3{,}9R_{\oplus}$) predominate beyond the inner boundary (Recent Venus), whereas gas giants dominate beyond the outer boundary (Early Mars) — a trend linked to observational selection effects. Analysis based on stellar spectral type indicates that the highest concentration of planets within the habitable zone (HZ) occurs around G-type dwarfs (Sun-like stars), even though M-type dwarfs are the most abundant.

REFERENCES:
[1] Kopparapu R. K., Ramirez R., Kasting J. F. et al. Habitable zones around main-sequence stars: New estimates // The Astrophysical J. 2013. V. 765. No. 2. Article 131. DOI: 10.1088/0004-637X/765/2/131.
[2] Kopparapu R. K., Ramirez R., Schottelkotte J. et al. Habitable zones around main-sequence stars: Dependence on planetary mass // The Astrophysical J. Letters. 2014. V. 787. No. 2. Article L29. DOI: 10.1088/2041-8205/787/2/L29.
[3] Akeson R. L., Chen X., Ciardi D. et al. The NASA Exoplanet Archive: Data and Tools for Exoplanet Research // Publications of the Astronomical Society of the Pacific. 2013. V. 125. No. 930. Article 989. DOI: 10.1086/672273.

DEPENDENCES OF THE MASS DISTRIBUTION OF TESS TRANSITING GIANT PLANETS ON PLANETARY ORBITAL PERIODS AND ON HOST STAR MASSES

V. I. Ananyeva, A. V. Tavrov
Space Research Institute RAS, Moscow, Russia, a-lada@yandex.ru

KEYWORDS:
exoplanets, transit, TESS, statistics

INTRODUCTION:
We studied the mass- and the orbital period distributions of transiting giant planets discovered by TESS with the masses of 0.3–13 Jupiter masses and the orbital periods of 0.5–270 days [1]. Obtained distributions were compared with the corresponding distributions of transiting giant planets discovered by Kepler ST and by ground-based surveys. Two observational selection factors were taken into account: the dependence of transit probability on the distance between the planet and its star, and the low efficiency of TESS in detecting long-period planets (P>27.4 days) caused by TESS irregular sampling.

RESULTS:
The mass distribution of giant planets was studied as a function of host star mass. Distributions of planets around stars with masses: $<0.6M_{\odot}$, $0.6–0.8M_{\odot}$, $0.8–1.2M_{\odot}$, and $1.2–1.6M_{\odot}$ were considered. It is shown that the distributions depend significantly on the host star mass. The corrected mass distributions were compared with theoretical predictions obtained through population synthesis [2]. It is shown that the corrected distribution agrees with the theoretical prediction only for the planets orbiting solar-type stars with masses of $(1.0±0.2)M_{\odot}$ (Fig. 1).

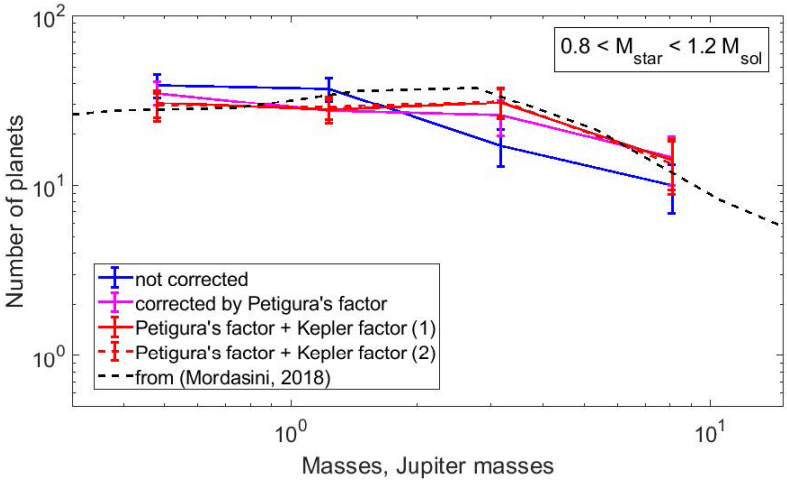


Fig. 1. Mass distribution of giant planets around solar-type stars. The blue line shows the uncorrected (observed) distribution, the magenta line shows the distribution corrected for transit configuration probability (Petigura factor), the red lines show the distribution additionally corrected for TESS observation unevenness (Kepler factor), 2 calculation variants. The black dotted line shows the theoretical distribution prediction from [2]

The mass distribution of giant planets with orbital periods of P<6 days ("hot Jupiters") and planets with periods of 6–270 days was comparatively studied. It is shown that the mass distribution of hot Jupiters qualitatively differs from the distribution of longer-period planets and agrees with the mass distribution of transiting planets discovered by ground-based surveys (Fig. 2).

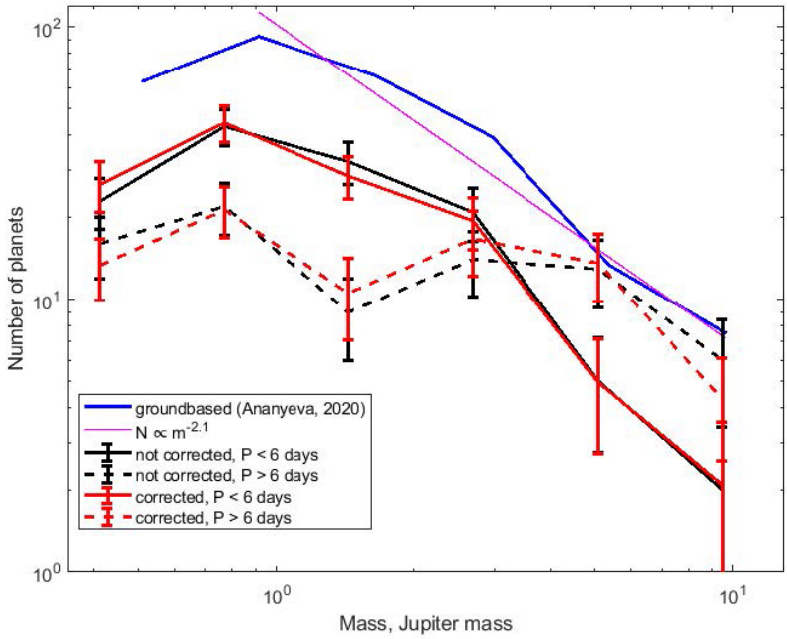


Fig. 2. Mass distribution of short-period (P < 6 days) and long-period (P>6 days) TESS giant planets. The black solid line shows the uncorrected distribution of giant planets with orbital periods shorter than 6 days (hot Jupiters), the red solid line shows the distribution corrected for transit configuration probability. The black dotted line shows the uncorrected distribution of giant planets with orbital periods greater than 6 days, the red dotted line shows the distribution corrected for transit configuration probability. The blue line shows the distribution of hot Jupiters detected by ground-based surveys from [3], the magenta line shows a power law with an exponent of –2.1

REFERENCES:

[1] TESS planets in the NASA Exoplanet Archive: https://exoplanetarchive.ipac.caltech.edu/cgi-bin/TblView/nph-tblView?app=ExoTbls&config=PS&constraint=default_flag=1&constraint=disc_facility+like+%27%25TESS%25%27.

[2] Mordasini Ch., Handbook of Exoplanets / eds. H. J. Deeg, J. A. Belmonte. Cham: Springer, 2018. Artivle 143. ISBN 978-3-319-55332-0. 10.1007/978-3-319-55333-7_143.

[3] Ananyeva V. I., Ivanova A. E., Venkstern A. A. et al. Mass distribution of exoplanets considering some observation selection effects in the transit detection technique // Icarus. 2020. V. 346. Article 113773. DOI: 10.1016/j.icarus.2020.113773.

PHOTOMETRIC OBSERVATIONS OF EXOPLANETS BY THE SAO RAS

A. E. Ivanova[1], O. Y. Yakovlev[2], A. F. Valeev[2], G. G. Valyavin[2]
[1] *Space Research Institute RAS, Moscow, Russia*
anastasia.ivanova@cosmos.ru
[2] *Special Astrophysical Observatory, Nizhnij Arkhyz, Zelenchukskiy region, Karachai-Cherkessian Republic, Russia*

KEYWORDS:
photometry, exoplanet, transit

INTRODUCTION:
As part of the STEP (SAO RAS Transit Exoplanet Program) project, observations of fields 4 and 5 have been conducted since 2024 (fields 1–3 have been previously published and are available [1–3]. The fifth field is notable for its high density of objects, which has yielded a wealth of new data to supplement catalogs of variable stars, white dwarfs, and exoplanet candidates.

In our report, we present the results of the analysis of two new fields for the first time. There will also be an update on the project's current status.

In the future, the existing database will be expanded to include new entries and will be publicly available

REFERENCES:
[1] Yakovlev O.Y. et al. Exoplanet Two-Square Degree Survey With SAO RAS Robotic Facilities // Front. Astron. Space Sci. 2022. https://doi.org/10.3389/fspas.2022.903429.
[2] Yakovlev O.Y. et al. Eight Exoplanet Candidates in SAO Survey // Astrophysical Bull. 2023. https://doi.org/10.1134/S1990341323010108.
[3] Yakovlev O.Y. et al. Catalog of Variable Stars in the WD 0009+501 and GRW +708247 Fields Based on Photometric Survey Data on Transiting Exoplanets // Astrophysical Bull. 2024. https://doi.org/10.1134/S1990341323600400.

COMPARISON OF EXOPLANET CHARACTERISTICS IN SINGLE AND MULTI-STAR SYSTEMS

E. E. Buslaeva[1,2], E. S. Belenkaya[2]
[1] *Lomonosov Moscow State University, Faculty of Physics, Department of Space Physics, Moscow, Russia, buslaeva@physics.msu.ru*
[2] *Skobeltsyn Institute of Nuclear Physics, Lomonosov Moscow State University, Moscow, Russia*

KEYWORDS:
exoplanets, multi-star systems, metallicity, planetary density, planetary radius, Fulton gap, stellar multiplicity

INTRODUCTION:

To date, more than 6,000 exoplanets have been confirmed, with the vast majority orbiting single stars. However, about 860 systems are multiplanetary, hosting two or more planets [1]. This number may be affected by observational biases, as additional small planets or those with long periods often remain undetected. At the same time, most Sun-like stars are thought to form multiple planets, with the Solar System itself being an eight-planet system [2].

Planet formation is believed to occur simultaneously with the host star from a protoplanetary disk [3]. The disk evolves through gravitational instabilities and collisional accretion, forming planetesimals that later grow into either rocky terrestrial planets or gas giants [4]. A key parameter governing this process is the host star's metallicity [Fe/H]. Numerous studies show that stars hosting exoplanets, especially gas giants, are on average more metal-rich than stars without detected planets [5]. High metallicity facilitates the formation of massive rocky cores capable of rapid gas accretion before the disk dissipates [6].

Using data from the NASA Exoplanet Archive, we perform a comparative statistical analysis of exoplanets in single, binary, ternary, and quaternary star systems. Our sample includes several thousand planets in single-star systems, about 300 in binaries, ~50 in triples, and two known quadruple systems (30 Ari B and PH1). We construct two-dimensional heatmaps showing the normalized concentration of planets as a function of density vs. metallicity and radius vs. metallicity.

Our analysis reveals distinct trends. In single and binary systems, the maximum concentration occurs at low densities of about 1–2 $g{\cdot}cm^{-3}$ and near-solar or slightly enhanced metallicities (0.0–0.2 dex), indicating a predominance of icy and gas giants. In triple-star systems, in addition to this giant-planet population, a secondary maximum appears at higher densities of ~4 $g{\cdot}cm^{-3}$ and significantly lower metallicity of about –0.7 dex, suggesting the presence of rocky planets (comparable to Mars with $3.9{\cdot}cm^{-3}$) that may form via an alternative pathway in complex multiple systems. This may indicate that at lower metallicity, more solid material remains in the protoplanetary disk for rocky planet formation.

The radius–metallicity dependence reveals a robust bimodal distribution across all system types: one population of super-Earths/mini-Neptunes with radii of about $2–3R_{\oplus}$ and another of gas giants with radii of about $13–15R_{\oplus}$. Planets with intermediate radii ($4–10R_{\oplus}$) are significantly underrepresented, resembling a "Fulton gap"-like feature at larger scales [7]. A similar separation between super-Earths and mini-Neptunes in terms of radius and composition has been discussed by Morozov and Belenkaya [8], who found that the transition between these two populations occurs around $1.5–2.0R_{\oplus}$, consistent with the Fulton gap, while our results extend this gap-like feature to larger radii ($4–10R_{\oplus}$) in multi-star systems. This gap is consistently observed in single, binary, and triple systems, suggesting a fundamental physical barrier in planet formation or atmospheric evapo-

ration processes. Interestingly, the giant-planet population peaks at higher metallicities (approximately 0.0–0.4 dex), while the small-planet population shifts toward lower metallicities (about –0.6 to –0.1 dex). This supports the scenario where high metallicity favors massive core formation and subsequent gas accretion, whereas in low-metallicity environments, metals are more efficiently used to form dense, rocky planets. The two quadruple-star systems host giant planets with radii of $6.18R_{\oplus}$ and $12.3R_{\oplus}$ around metal-rich stars ([Fe/H]≈+0.2 dex), consistent with this general picture.

REFERENCES:

[1] Fatheddin H.S., Sedighe S. Detecting Multiplanetary Systems with Gravitational Microlensing and the Roman Space Telescope // The Astronomical J. 2023. V. 166. Article 140. DOI: 10.3847/1538-3881/aced8b.
[2] Buslaeva E., Belenkaya E. Characteristics of Multiplanetary Systems with One Host Star // Earth and Planetary Science. 2024. V. 3(2). P. 1–13. DOI: 10.36956/eps.v3i2.1025.
[3] Udry S., Santos N.C. Statistical Properties of Exoplanets // Annu. Rev. Astron. Astrophys. 2007. V. 45. P. 397–439. DOI: 10.1146/annurev.astro.45.051806.110529.
[4] Williams J.P., Cieza L.A. Protoplanetary Disks and Their Evolution // Annu. Rev. Astron. Astrophys. 2011. V. 49. P. 67–117. DOI: 10.1146/annurev-astro-081710-102548.
[5] Fischer D.A., Valenti J. The Planet-Metallicity Correlation // The Astrophysical J. 2005. V. 622. P. 1102–1117. DOI: 10.1086/428383.
[6] Winn J.N., Fabrycky D.C. The Occurrence and Architecture of Exoplanetary Systems // Annu. Rev. Astron. Astrophys. 2015. V. 53. P. 409–447. DOI: 10.1146/annurev-astro-082214-122246.
[7] Fulton B.J., Petigura E.A. The California-Kepler Survey. VII. Precise Planet Radii Leveraging Gaia DR2 Reveal the Stellar Mass Dependence of the Planet Radius Gap // The Astronomical J. 2018. V. 156. No. 6. Article 264. DOI: 10.3847/1538-3881/aae828.
[8] Morozov G.A., Belenkaya E.S. Characteristics of Super-Earths and Mini-Neptunes // Astron. Rep. 2025. V. 69. P. 574–580. DOI: 10.1134/S1063772925701926.

THE SPEKTR-UF SPACE TELESCOPE AS A TOOL FOR STUDYING EXOPLANET ATMOSPHERES

G. N. Tsurikov[1], D. V. Bisikalo[2,1], V. I. Shematovich[1], A. G. Zhilkin[1]
[1] *Institute of Astronomy RAS, Moscow, Russia, tsurikov@inasan.ru*
[2] *National Center of Physics and Mathematics, Sarov, Russia*

KEYWORDS:
Spektr-UF, exoplanets, atmospheres, space weather, biomarkers

INTRODUCTION:
Exoplanetary research occupies a key place in the scientific program of the developed UV (115–310 nm) space telescope Spektr-UF. This telescope is planned to be used to address several particularly pressing issues in exoplanet research, including: a) estimation of space weather parameters around solar-type stars based on observations of the atmospheres of hot exoplanets [1, 2]; b) searching for spectral lines of biosignature molecules in the atmospheres of terrestrial-type exoplanets [3]. This work presents the capabilities of Spektr-UF for addressing these issues.

Interpreting transit absorptions in the atmospheres of hot exoplanets may allow us to estimate space weather parameters (stellar wind and extreme radiation fluxes) around other stars [1, 2]. This work presents estimates of the detection limits for the HI Lyα spectral line (the strongest indicator of interaction between planetary and stellar winds [2]) in the atmospheres of hot exoplanets using Spektr-UF. For this purpose, the results of modeling transit absorptions in this line from [2], as well as the Spektr-UF exposure calculator [4], are used. According to the calculation results, it is shown that the limiting distances for reliable >3σ detection of this spectral line are: a) 20 pc when using a vacuum ultraviolet echelle spectrograph (VUVES, R=50000); b) 150 pc when using a long-slit spectrograph (LSS, R=1000, allows to detect of the integrated absorption in the spectral line). A list of planetary systems with solar-type stars has been compiled for determining space weather parameters using Spektr-UF. This list includes 12 planetary systems for the VUVES spectrograph and 180 exoplanets for the LSS spectrograph. Determining space weather parameters for these planetary systems after the launch of Spektr-UF will enable forecasting of extreme solar events that could impact satellite and civil infrastructure.

An important indicator of biological activity on a terrestrial-type planet is the presence of an N_2-O_2-dominant atmosphere. The search for molecules - indicators of such an atmosphere (potential biomarkers) on exoplanets will be the main issue of the Spektr-UF scientific program. The most promising and reliable biomarker for searches with Spektr-UF is nitric oxide [5]. This study explores the possibility of detecting spectral lines of this molecule (γ-bands, 203–248 nm) in exoplanet atmospheres using Spektr-UF. The obtained results demonstrate that the Spektr-UF LSS spectrograph can detect NO on typical super-Earths and mini-Neptunes located in the habitable zone of G- and early K-type stars that are more active than the Sun. The detection limits for this molecule extend up to 40 pc. A list of 11 exoplanets — candidates for NO detection using the Spektr-UF instrument is presented. Detecting NO on these exoplanets will allow us to identify their N_2-O_2 atmospheres and determine their possible habitability.

ACKNOWLEDGMENTS:
This work was supported by the Russian Science Foundation (project 22-12-00364-p).

REFERENCES:
[1] Shematovich V. I., Shaikhislamov I. F., Zhilkin A. G. et al. Observations of hot exoplanets as a new tool for space weather re-search and forecasting // Physmath. 2023. V. 1. No. 2. P. 20–41 (in Russia). DOI: 10.56304/S2949609823010033.

[2] Shaikhislamov I. F., Shematovich V. I., Tsurikov G. N. et al. Extreme space weather study through observations of hot exoplanets // Physmath. 2025. V. 3. No. 2 (in Russia). DOI: 10.56304/S2949609825020016.
[3] Tsurikov G. N., Bisikalo D. V., Shematovich V. I. et al. Searching for Biomarkers with Spektr-UF Observatory: Nitric Oxide Molecule in Atmospheres of Exoplanets near the Active Host Stars // Astronomy Reports. 2024. V. 68. P. 1406–1422. DOI: 10.1134/S1063772925701355.
[4] Tsurikov G., Sichevsky S., Shmagin V. et al. Planning experiment with the Spektr-UF observatory: the first webversion of exposure time calculator // Proc. SPIE. 2024. V. 13093. 12 p. DOI: 10.1117/12.3020288.
[5] Bisikalo D., Shematovich V., Tsurikov G. Potentially observable biomarkers // Physmath. 2024. V. 2. No. 4. P. 213–252 (in Russia). DOI: 10.56304/S2949609824030078.

PROGRESS IN STELLAR CORONAGRAPHY FOR EXOPLANET IMAGING IN IKI RAS

A.V. Tavrov[1], A.V. Yudaev[1], A.V. Kiselev[1], A.D. Elchev[2]
[1] *Space Research Institute RAS, Moscow, Russia*
tavrov@iki.rssi.ru, yudaev@phystech.edu, kiselev.av@phystech.edu
[2] *National Research University Moscow Power Engineering Institute*
Moscow 111250, Russia, elchev.2004@mail.ru

KEYWORDS:
exoplanet imaging, space telescope, stellar coronagraph, wavefront correction, high-contrast astronomy

INTRODUCTION:

Direct imaging of exoplanets will help to verify exoplanet existence, properties and will remove uncertainties due to advantage of direct to indirect detection. We developed a high-contrast astronomical imaging. In space, without an atmospheric turbulence the quality of optics of telescope and scientific instruments, all limits the ability to observe low-contrast objects such as exoplanets in the vicinity of their host stars. A 2.4-meter diameter space telescope with an adaptive optics is capable to achieve a contrast of 10^8–10^{10}, being sufficient for exoplanet imaging, is the Nancy Roman Telescope (old name WIRST) (https://roman.gsfc.nasa.gov/gallery-technical_data.html), currently scheduled for launch by NASA in 2027.

New algorithms and techniques to estimate the optical field in phase and amplitude in telescope focal plane (after a coronagraph makes dark-field) were specifically developed. Referenced in the technical literature, that method exceeds 50 bibliographic references, just follow to their abbreviations as: EFC — electric field conjugation, PWP — pair-wise probing, SCC — self-coherent camera [1].

The applicability of these innovative techniques forwards our practical interest in connection with the line of optical space telescopes being developed in Russian Federation and, in particular, the potential for use on the mirror diameter 1.7 m Russian orbital telescope named Spektr-UV (WSO-UV) [2].

RESULTS:

Here, we recall the recently proposed *apodization coronagraph* [3], supplemented with adaptive optics functionality, and based on new principles of EFC for active wavefront correction. In comparison with the used onboard Nancy Roman telescope, (with the CGI Lyot coronagraph), we demonstrate the feasibility to use an iterative wavefront reconstruction (correction) technique with rapid convergence using the EFC method in an apodization coronagraph.

A new high-contrast method using the phase apodization of the telescope pupil is combined with the wavefront-correcting EFC technique and is considered aiming to visualize exoplanets in astronomical images. The capabilities of the apodization method in an aberration-free telescope demonstrate a coronagraphic contrast of ~10^{10} in a focal image angular sector exceeding 90°. To cover a circular stellarcentric region, four consecutive measurements with a rotating apodization mask are required.

The proposed apodization coronagraph looks rather simpler than the classical Lyot coronagraph in the number of optical planes and in the design of precision masks and the mathematic algorithm model for EFC, all which are preferable to be implemented in a remote space observatory.

Instead of the use of deformable mirror an SLM is proposed, this spatial light modulator is functional simultaneously for an actively controlled apodization mask and for active wavefront correction to realize the EFC technique. Wavefront measurement is performed by measuring the intensity in the focal plane after the coronagraph.

Our future plans are to set up a physical experiment to rehearse the proposed technique for practical use.

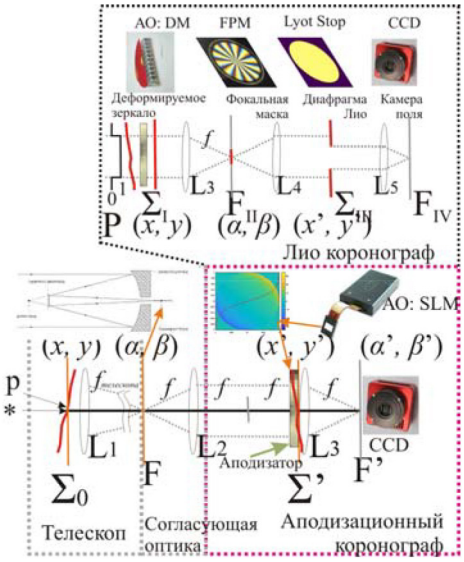


Fig. 1. Optical layout of a telescope with an *apodization coronagraph* (bottom panel) and with a Lyot coronagraph (top panel) for comparison

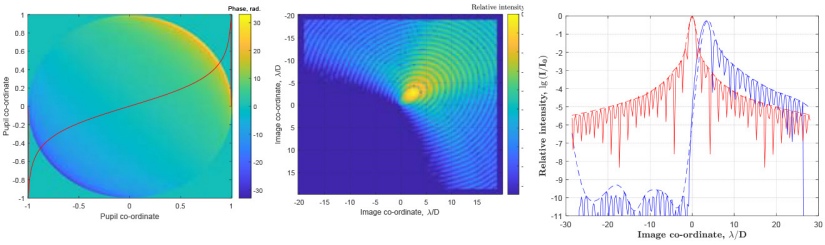


Fig. 2. Apodization coronagraph outline. (left panel): Pupil phase apodization form; (middle panel): Intensity distributions (logarithmic scale) at the focus of a telescope from a point source (PSF) with a coronagraphic apodization; (right panel): diagonal slice (from bottom left to top right), the red line is the PSF without apodization, the blue line is the PSF with apodization, the dotted lines show the envelopes

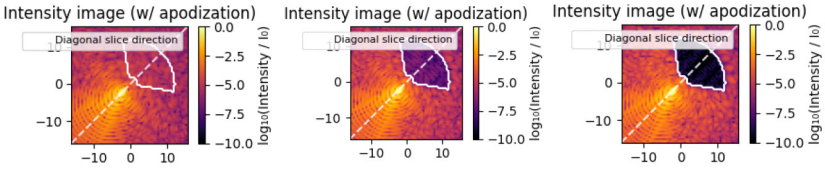


Fig. 3. EFC in dark-zone for pupil phase apodization coronagraph. (left-to-right panels): The iterations numbers of 1,5,30 shows the EFC darkening process inside the desired zone in focal image

REFERENCES:

[1] Potier A., Baudoz P., Galicher R. et al. Comparing focal plane wavefront control techniques: Numerical simulations and laboratory experiments // A&A. 2020. V. 635. Article A192. https://doi.org/10.1051/0004-6361/201937015.
[2] Shustov B. M., Sachkov M. E., Sichevsky S. G. et al. WSO–UV Project: New Touches // Solar System Research. 2021. V. 55. No. 7. P. 677–687. https://doi.org/10.1134/s0038094621070194.
[3] Shulgina I. V., Yudaev A. V., Shashkova I. A. et al. Apodization of the Pupil of a Telescope for Stellar Coronagraphy for the Purpose of Imaging Exoplanets // JETP. 2026. V. 169. No. 1. P. 5–26 (in Russian). https://www.jetp.ras.ru/cgi-bin/dn/r_169_0005.pdf.

IMPROVING EXOPLANETARY MAGNETIC FIELD DETERMINATION VIA ATOMIC ALIGNMENT WITH INHOMOGENEOUS STELLAR SPECTRA

M. Rumenskikh[1,2,3], A. V. Taichenachev[4], M. P. Golubovsky[1,2], S. S. Sharipov[2], I. F. Shaikhislamov[1,2]
[1] *Institute of Astronomy RAS, Moscow, Russia, marina_rumenskikh@mail.ru*
[2] *Institute of Laser Physics SB RAS, Novosibirsk, Russia*
[3] *Pushkov Institute of Terrestrial Magnetism, Ionosphere and Radiowave Propagation RAS, Moscow, Russia*
[4] *Novosibirsk State University, Novosibirsk, Russia*

KEYWORDS:
hot exoplanets, atomic alignment, stellar spectral inhomogeneity, magnetic fields, transit spectroscopy

INTRODUCTION:
One of the most fundamental questions in exoplanetary sciences to date is how to estimate planetary magnetic fields having no possibility to measure them directly. Complex numerical simulations revealed that magnetic fields can significantly shape the atmosphere and its escape [1, 2] with important consequences for available and future observations. Without any information on the planetary magnetic field, the interpretation of transit absorptions by exoplanetary atmospheres is hindered.

From theoretical studies of fine effects of spin-orbital atomic alignment [3], it is known that excitation of transitions by a directed radiation field can lead, through the selective absorption of photons, to a significant anisotropy and a deviation of the relative population of sublevels from the classic statistical weight formula 2J+1. For atmospheres of close-orbit exoplanets, a host star acts as a directed radiation source, potentially changing the relative absorption amplitudes within a multiplet of a given line, producing an observable effect. On the other hand, a global magnetic field also affects the relative absorption amplitudes within the multiplet. This opens an essentially new way of constraining magnetic fields of hot exoplanets by accurate spectrally resolved measurements of absorption by multiplet lines.

METHODOLOGY AND RESULTS:
In the present work, we apply the effective operator formalism to describe transitions in the atomic-ionic medium of the upper exoplanetary atmospheres under the influence of unpolarized, spectrally selective, and spatially anisotropic radiation from the host star. Building upon the theoretical foundations of the atomic alignment method established in [4], we significantly enhance the approach by explicitly accounting for stellar spectral inhomogeneity and its impact on population redistribution. The alignment effect is notably amplified by spectral inhomogeneities overlapping with the exoplanet's absorption lines. Because atomic alignment is proportional to the anisotropic component of the radiation tensor, local peaks or dips in the stellar spectrum induce frequency modulation. Consequently, triplet lines situated on steep spectral gradients become highly sensitive indicators. Specifically, if the stellar flux varies by more than a factor of two across the triplet lines, the population redistribution deviates by over 40% from the equilibrium case. A reduced photon flux at the wavelength of a specific triplet line decreases its transition probability, thereby further increasing the population anisotropy. In this work we report on the method of accurate calculation of fine multiplet structure of suitable lines subjected to directed radiation pumping in presence of a relatively weak magnetic field. We apply the effect to estimate quantitatively its potential to transit absorptions of hot exoplanets. The further development of this method can make a significant contribution to many branches of planetary and atmospheric sciences.

ACKNOWLEDGMENTS:
This work was supported by the RSF projects No. 25-72-10080.

REFERENCES:

[1] Zhilkin A., Bisikalo D. Multi-Component MHD Model of Hot Jupiter Envelopes // Universe. 2021. V. 7(11). Article 422. . DOI: 10.3390/universe7110422.
[2] Khodachenko M. L., Shaikhislamov I. F., Lammer H. The impact of intrinsic magnetic field on the absorption signatures of elements probing the upper atmosphere of HD209458b // Monthly Notices of the Royal Astronomical Society. 2021. V. 507(3). P. 3626–3637. DOI: 10.1093/mnras/stab2366
[3] Varshalovich D. A. Spin states of atoms and molecules in the cosmic medium // Soviet Physics Uspekhi. 1971. V. 13(4). Article 429.
[4] Rumenskikh M., Taichenachev A. V., Shaikhislamov I. F., Yudin V. I., Savintseva E. D. Probing exoplanetary magnetism via atomic alignment effect // Monthly Notices of the Royal Astronomical Society. 2025. V. 541(4). P 2872–2883. DOI: 10.1093/mnras/staf1038.

STRUCTURE OF THE PLANETARY WIND FLOW OF HOT JUPITERS WITH THEIR OWN MAGNETIC FIELD AT DIFFERENT POSITIONS OF THE ALFVÉN CRITICAL SURFACE

R. A. Kislov[1,2], M. S. Rumenskikh[2], I. F. Shaikhislamov[2]
[1] *Pushkov Institute of Terrestrial Magnetism, Ionosphere and Radio Wave Propagation of the Russian Academy of Sciences, Moscow, Russia*
kr-rk@bk.ru
[2] *Institute of Laser Physics SB RAS, Novosibirsk, Russia*

KEYWORDS:
exoplanets, hot jupiters, planetary wind, magnetic field, Alfvén critical surface, MHD

ABSTRACT:
Close-in gas giant exoplanets experience strong stellar irradiation, which can drive intense atmospheric escape and the formation of extended planetary winds. Observations of transit absorptions in He I 2^3S line in several systems revealed helium tails up to 7 planetary radii and fast plasma flows in the upper atmospheres of hot Jupiters. In the presence of a planetary magnetic field, such outflows are governed by magnetohydrodynamic processes and may be crucially compressed by magnetic forces. In star-exoplanet systems, situations are possible when heating and ionization of a hot Jupiter atmosphere leads to the formation of a planetary wind which over flows the Roche lobe. Moreover, spectral line shifts observed in such systems gives evidence of supersonic plasma flows. In plasma flows of this kind, at least two critical points can form in the vicinity of magnetized exoplanet — the sonic and the Alfvén points. Depending on the strength of the magnetic field, the tidal forces, the thermodynamic properties of the atmosphere, different plasma flow solutions are possible depending on the regularization at the critical points. In this work, estimates of the locations of the critical points are presented. It is shown that both a slow subsonic plasma flow regime and a supersonic, super Alfvén regime, can be realized. Moreover, the transition between these regimes can exhibit threshold behavior, as the magnetic field strength at L1 point varies smoothly. The estimates show that atmospheric outflows from hot Jupiters overflowing the Roche lobe can exist in different regimes, including both subsonic and supersonic, super-Alfvénic flows. We demonstrate that a smooth variation of the Alfvén critical surface radius and Alfvén speed may lead to a threshold transition between these regimes. This fact has important implications for the interpretation of observed helium tails and highlights the role of planetary magnetic fields in shaping atmospheric escape and allow to constrain the upper limit of inner magnetic field of exoplanet.

ACKNOWLEDGMENTS:
The study is supported by RSF project № 25-72-10080.

THREE-DIMENSIONAL MODELING OF THE ATOMIC ALIGNMENT EFFECT AS A DIAGNOSTIC OF MAGNETIC FIELDS IN HOT EXOPLANETS

S. S. Sharipov[1], M. S. Rumenskikh[1,2], I. F. Shaikhislamov[1], A. V. Taichenachev[1]
[1] *Institute of Laser Physics SB RAS, Novosibirsk 630090, Russia*
stas.sharipov@mail.ru
[2] *Pushkov Institute of Terrestrial Magnetism, Ionosphere and Radio Wave Propagation RAS, Moscow 142191, Russia*

KEYWORDS:
hot exoplanets, atomic alignment effect, magnetic fields, three-dimensional modeling, magnetohydrodynamics, transit spectroscopy

INTRODUCTION:
The upper atmospheres of hot exoplanets provide unique laboratories for investigating the interaction between intense stellar radiation, plasma flows, and magnetic fields. One of the primary approaches to studying these atmospheres is the analysis of transit absorption spectra, which enables the determination of atmospheric physical properties and the investigation of the processes governing their dynamical evolution. However, the direct detection and characterization of intrinsic exoplanetary magnetic fields remain among the most challenging problems in contemporary astrophysics.

In a recent study [1], a novel method for diagnosing magnetic fields in hot exoplanets was proposed based on the atomic alignment effect [2, 3]. Under the influence of the anisotropic radiation field of the host star, the populations of the magnetic sublevels of long-lived atomic states are redistributed. This redistribution modifies the transition probabilities of individual components within atomic multiplets and consequently alters the relative depths of the corresponding transit absorption lines. It has been demonstrated that the presence of a magnetic field suppresses the atomic alignment effect, implying that the observed intensity ratios of the multiplet components can serve as a diagnostic signature of the planetary magnetic field.

PROBLEM STATEMENT:
In the published model [1], the influence of atomic alignment was incorporated semi-empirically by modifying the statistical weights of the corresponding transitions during the calculation of transit absorption spectra. This approach provided the first quantitative estimate of the magnitude of the effect for several observed exoplanets and demonstrated the feasibility of using atomic alignment as a diagnostic of planetary magnetic fields. However, the adopted model assumed uniform statistical weights throughout the entire atmosphere, whereas atomic alignment is inherently a local process determined by the physical conditions within each computational cell.

According to the theory of atomic alignment, the redistribution of magnetic sublevel populations depends both on the local magnetic field strength and on the angle between the magnetic field vector and the anisotropic radiation field of the host star. Since three-dimensional magnetohydrodynamic models provide the spatial distributions of the magnetic field, density, temperature, and velocity, the statistical weights of atomic transitions should likewise be determined individually for each computational cell.

The objective of the present study is to develop a three-dimensional model of the atomic alignment effect in which the local statistical weights of the atomic magnetic sublevels are calculated directly from the atmospheric parameters obtained through three-dimensional magnetohydrodynamic simulations. The implementation of this approach will, for the first time,

enable a self-consistent calculation of the spatially inhomogeneous atomic alignment effect and allow an assessment of the influence of realistic magnetic field configurations on the formation of transit absorption spectra of hot exoplanets.

METHODOLOGY:

The proposed study builds upon a previously developed three-dimensional magnetohydrodynamic (MHD) model of the upper atmospheres of hot exoplanets "Exo3D" [4], which computes the spatial distributions of density, temperature, flow velocity, and magnetic field. Based on the resulting atmospheric structure, transit absorption spectra are calculated by solving the radiative transfer equation along the observer's lines of sight.

In the present work, the existing spectral synthesis framework is extended to incorporate the spatially varying atomic alignment effect. For each computational cell, the local magnetic field and the system geometry are used to determine the angle between the magnetic field vector and the incident radiation field of the host star. A quantum-mechanical model of atomic alignment [1] is then employed to calculate the local populations of the magnetic sublevels and the corresponding statistical weights of the atomic transitions. These locally determined statistical weights are subsequently used in the calculation of the absorption coefficients, replacing the constant values adopted in the previous implementation.

This approach provides a self-consistent treatment of the spatial variability of the atomic alignment effect and enables a quantitative investigation of how both the strength and the topology of the planetary magnetic field influence the formation of transit absorption spectra.

EXPECTED RESULTS:

The proposed model will, for the first time, enable fully three-dimensional simulations of the atomic alignment effect in the atmospheres of hot exoplanets while accounting for the spatial distribution of the magnetic field. This will make it possible to identify the contributions of different atmospheric regions to the observed spectroscopic signal and to quantify the influence of the local magnetic field geometry on the relative intensities of the multiplet components.

Using the developed model, we will compare the results with those obtained using the previously adopted semi-empirical approach, in which the statistical weights were assumed to be uniform throughout the atmosphere, and determine the range of validity of this approximation. Particular attention will be devoted to investigating different magnetic field configurations, including dipolar, quadrupolar, and more complex topologies, as well as to assessing the sensitivity of the proposed diagnostic method to the magnetic field structure.

The expected results will significantly improve the physical realism of transit absorption spectrum modeling and provide a robust foundation for the interpretation of current and future high-precision spectroscopic observations of hot exoplanets aimed at diagnosing their intrinsic magnetic fields.

ACKNOWLEDGMENTS:

This work was supported by the Russian Science Foundation (RSF) under Grant No. 25-72-10080.

REFERENCES:

[1] Rumenskikh M. S., Taichenachev A. V., Shaikhislamov I. F. et al. Probing exoplanetary magnetism via atomic alignment effect // MNRAS. 2025. V. 541. P. 2872–2883. DOI: 10.1093/mnras/staf1038.

[2] Yan H., Lazarian A. Atomic Alignment and Diagnostics of Magnetic Fields in Diffuse Media // ApJ. 2008. V. 677. P. 1401–1424. DOI: 10.1086/533410.

[3] Varshalovich D. A. Spin states of atoms and molecules in the cosmic medium // Soviet Physics Uspekhi. 1971. V. 13. P. 429–437. DOI: 10.1070/PU1971v013n04ABEH004667.

[4] Shaikhislamov I. F., Miroshnichenko I. B., Sharipov S. S. et al. Aeronomy of the upper atmosphere of KELT-9 b // A&A. 2025. V. 969. Article A211. DOI: 10.1051/0004-6361/202453309.

MAGNETOSPHERE OF THE BROWN DWARF 15 SGE B IN A SYSTEM WITH A SOLAR-TYPE CENTRAL STAR

G. P. Malygin[1,2], E. S. Belenkaya[1]
[1] *Skobeltsyn Institute of Nuclear Physics, Lomonosov Moscow State University, Moscow 119991, Russia, malygin.gp22@physics.msu.ru*
[2] *Lomonosov Moscow State University, Faculty of Physics Moscow 119991, Russia*

KEYWORDS:
brown dwarfs, magnetosphere, paraboloid model, stellar wind, magnetopause

INTRODUCTION:
Brown dwarfs are substellar objects (with mass ~13–80 M_J, where M_J is the mass of Jupiter) intermediate between stars and planets; models of their magnetospheres are still lacking. Here the paraboloid magnetospheric model, developed at SINP MSU for the planets of the Solar System and some exoplanets [1], is applied for the first time to a brown dwarf — 15 Sge b, a companion of a solar-type G0V star, at the moment when it crosses the plane of the stellar magnetic equator at 13.7 AU from the star [2].

The stellar wind of the central star is treated as the solar one, and the flow is super-Alfvénic (Alfven Mach number M_A=11.6) [3]. The equatorial magnetic field of the dwarf, estimated from the empirical scenario for rapidly rotating objects [4], is ≈0.66 kG, consistent with the values obtained from the measurements of radio emission for other brown dwarfs. The pressure balance at the magnetopause yields the model parameters: the substellar magnetopause distance R_1=308R_{bd}, the inner edge of the tail current sheet R_2=216R_{bd}, and the magnetic field at the inner edge of the tail current sheet B_t=2.7 nT, where R_{bd} is the radius of the dwarf. Such extended magnetosphere is a result from the strong magnetic field of the brown dwarf and its large distance from the central star.

REFERENCES:
[1] Belenkaya E. S., Alexeev I. I., Kalegaev V. V. Modeling of the exoplanet HAT-P-11b magnetosphere // Astronomy Reports. 2024. V. 68. P. 39–47. DOI: 10.1134/S1063772924700045.
[2] Crepp J. R., Johnson J. A., Fischer D. A. et al. The Dynamical Mass and Three-Dimensional Orbit of HR7672B: A Benchmark Brown Dwarf with High Eccentricity // ApJ. 2012.
[3] Nichols J. D., Milan S. E. Stellar wind–magnetosphere interaction at exoplanets: computations of auroral radio powers // MNRAS. 2016. V. 461. P. 2353–2366. DOI: 10.1093/mnras/stw1430.
[4] Reiners A., Christensen U. R. A magnetic field evolution scenario for brown dwarfs and giant planets // A&A. 2018. DOI: 10.1051/0004-6361/201014251.

MAGNETOSPHERE OF TAU BOOTIS B IN THE PARABOLOID AND MHD MODELS

A. S. Krotov[1,2], E. S. Belenkaya[2]
[1] *Lomonosov Moscow State University, Faculty of Physics, Moscow, Russia*
a-krotov.2014@mail.ru
[2] Skobeltsyn Institute of Nuclear Physics, Lomonosov Moscow State University, Moscow, Russia

KEYWORDS:
exoplanets, stars, magnetic field, magnetosphere, Alfven Mach number, Alfven wings

INTRODUCTION:

Tau Bootis b was one of the first exoplanets to be discovered. It was discovered by [1] using the radial velocity method. In 2021, using the LOFAR radio telescope, measurements of radio emissions were obtained in the 14–21 and 21–30 MHz frequency bands, which were hypothesized to be associated with the exoplanet's auroral zone [2]. The results of this experiment suggest that planets outside the solar system (in this case, Tau Bootis b) possess their own magnetic field, provided that this radiation does indeed originate from the planet's auroral zone. This assumption also implies that Tau Bootis b possesses a magnetosphere that interacts with the stellar wind from its host star.

Since Tau Bootis b is presumed to be an exoplanet with a magnetic field, studying its magnetosphere and its interaction with the stellar wind is a promising area of research. To better understand the conditions in the space surrounding this exoplanet [3, 4] performed MHD simulations of the environment around Tau Bootis b and its magnetic field using the PLUTO code. We, in turn, will simulate the magnetosphere of this exoplanet using a paraboloid model to compare the results.

REFERENCES:

[1] Butler et al. Three New "51 Pegasi-Type" Planets // The Astrophysical J. 1997. V. 474. No. 2.
[2] Turner et al. The search for radio emission from the exoplanetary systems 55 Cancri, υ Andromedae, and τ Boötis using LOFAR beam-formed observations // Astronomy and Astrophysics. 2021. Article A59. 28 p. 10.1051/0004-6361/20193720.
[3] Elekes F., Saur J. Space environment and magnetospheric Poynting fluxes of the exoplanet τ Boötis b // Astronomy and Astrophysics. 2023. Article A133. https://doi.org/10.1051/0004-6361/202244947.
[4] Evensberget D. et al. An observationally based wind model contemporaneous with the radio detections in τ Boötis // Monthly Notices of the Royal Astronomical Society. 2026. V. 546. Iss. 2.

RESONANCE PROPERTIES OF THE COMPACT FOUR-PLANET SYSTEM KEPLER-51

E. D. Kuznetsov
Ural Federal University, Yekaterinburg, Russia, eduard.kuznetsov@urfu.ru

KEYWORDS:
compact planetary system, mean-motion resonances, dynamic evolution, stability

INTRODUCTION:

The compact three-planet system Kepler-51 was announced in 2013 [1]. Kepler-51 is a $\lesssim$1 Gyr-old Sun-like star hosting three transiting planets with radii $\approx$(6–9)$R_\oplus$ (radii of the Earth) and orbital period ratios close to 1:2:3 (45 days, 85 days, and 130 days for Kepler-51b, c, and d, respectively) detected with Kepler photometry. Transit timing variations measured with past Kepler and Hubble Space Telescope observations have been successfully modeled by considering gravitational interactions between the three transiting planets, yielding low masses and low mean densities ($\lesssim$0.1 g·cm^{-3}) for all three planets.

Authors [2] refined parameters of the Kepler-51 planetary system using data from the TESS space telescope. Authors [3] examined the dynamic evolution of the compact three-planet system Kepler-51 using refined parameters [2]. It is shown that the compact planetary system Kepler-51 is not resonant. Under initial conditions corresponding to the masses and elements of the planets' orbits, determined from observations considering their errors, the evolution of the system is stable and regular over the studied interval of 100 Myr.

Authors [4] reported the discovery of a fourth planet in the Kepler-51 system using the TTV method. They obtained solution, the one in which Kepler-51e is around the 2:1 MMR with Kepler-51d implies low orbital eccentricities ($\lesssim$0.05) and comparable masses ($\sim 5M_\oplus$) for all four planets, as is seen in other compact multi-planet systems. The paper presents two solutions (see [5], Table 6) with different sets of parameters (orbital elements, masses, radii, densities, etc.), called "Outside 2:1" and "Inside 2:1", corresponding to different values of the orbital period of the planet Kepler-51e, near the 2:1 mean motion resonance with the planet Kepler-51d. The Outside 2:1 solution corresponds to $P_e > P_{res}$, the Inside 2:1 solution — $P_e < P_{res}$, where P_{res} is the resonant value of the orbital period of the planet Kepler-51e, corresponding to the 2:1 resonance with the planet Kepler-51d.

In this paper, we will consider the dynamic evolution of the compact four-planetary system Kepler-51 and study stability and resonant property.

METHODS:

We applied an analytical method to estimate the location and width of the resonance zones of mean motion resonances (up to the fourth order inclusive) considering errors in determining the masses of the planets and the eccentricities of their orbits. We used the Analytical-Resonance-Widths script (https://github.com/katvolk/analytical-resonance-widths) [5]. It was found that for most initial conditions there are no low-order resonances in the Kepler-51 system. By varying the period of the outermost planet Kepler-51e within the limits of determination errors, for the set Inside 2:1 was discovered that a narrow range of periods from 255.8 to 256.3 days corresponds to a 3:1 MMR between the second (Kepler-51c) and fourth (Kepler-51e) planets of the system. We performed numerical simulations of the dynamic evolution of the Kepler-51 system to investigate the stability and test the feasibility of a 3:1 resonance between the planets Kepler-51c and Kepler-51e.

Since compact systems, an important factor influencing orbital evolution is tidal interaction. We simulated the evolution of the Kepler-51 system over a time interval of 100 Myr using the Posidonius (https://www.blancocuares-

ma.com/s/posidonius) software [6], which considers tidal interaction. We varied the mass of the star ((0.96±0.05)$M_{\odot}$ [4]) and the masses of the planets (see [4], Table 6) within the limits of determination errors for nominal values of orbital elements. The orbital elements were varied for the nominal masses of the star and planets. The values of the period and eccentricity were varied within the limits of determination errors, the inclinations of the orbits and the longitudes of the ascending nodes were assumed to be equal to zero, and the arguments of the periapsis were assumed to be equal to the nominal values.

Because the Kepler-51 system is young, we chose initial orbital inclinations of zero in our modeling, if the system, which formed from the protoplanetary disk, was initially flat. One of the tasks to be solved was to determine the conditions that would bring the system into a state that would exclude the transit of the outermost known planet, Kepler-51e.

RESULTS AND DISCUSSIONS:

In the first stage, we analyzed how the addition of the fourth outer planet affects the dynamic evolution of the three inner planets. The results of the modeling show that both the inner three-planet part of the system and the full four-planet system maintain a stable evolution of the positional elements of the orbit. The evolution of the longitudes of the ascending nodes and the arguments of the pericenters is regular. The study of the resonance properties of the system shows that pairs of adjacent planets are not in low order MMRs.

An analysis of the dynamic evolution of the system under initial conditions corresponding to a 3:1 resonance between the planets Kepler-51c and Kepler-51e showed that over the studied interval of 100 Myr, the system repeatedly enters resonance and exits resonance. Getting into MMR leads to the fact that in an initially flat system the inclinations of the planets' orbits become non-zero. This property of dynamic evolution can be used to select initial conditions that lead to orbital inclinations of the three inner planets of Kepler-51b, c, and d, excluding the transit of these planets across the disk of the star.

Transits in the Kepler-51 system are possible if the orbital inclinations do not exceed the following limiting values: 1°, 0.67°, 0.43°, and 0.3° for planets Kepler-51b, c, d, and e, respectively. Table 1 shows the maximum values of the orbital inclinations over a 100 Myr resulting from the 3:1 MMR between the planets Kepler-51c and Kepler-51e in an initially flat system, depending on the initial values of the orbital eccentricities for the set Inside 2:1 and P_c=85.3139^d, P_e=255.9^d. We used the minimum and nominal eccentricity values as initial values for the planet Kepler-51c. Since the orbital inclinations of the planets take approximately the same maximum values, Table 1 gives only one maximum inclination value, which characterizes the system.

Table 1. Maximum values of orbital inclinations (Inside 2:1, P_c=85.3139^d, P_e 255.9^d)

e_e	e_c=0.021, deg.	e_c= 0.063, deg.
0.01	0.0007	0.0014
0.02	0.00009	0.0014
0.03	0.00025	0.175
0.04	0.35	0.0006
0.05	2	0.14
0.06	0.0175	0.12
0.07	0.04	0.035
0.08	2	0.8

An analysis of Table 1 shows that for most of the initial eccentricity values considered, the orbital inclinations do not exceed 0.3°, which contradicts the absence of a transit of the outermost planet, Kepler-51e. Perhaps this contradiction can be resolved by increasing the integration interval to 1 Gyr. However, the variant e_c=0.021, e_e=0.04 shows the possibility of ex-

ceeding the 0.3° inclination value for the planet Kepler-51e while maintaining the transit conditions for the three inner planets. Solutions for initial conditions e_e=0.08 *и* e_c=0.021, e_e=0.05 leading to high orbital inclinations do not correspond to the observed transits in the system. The maximum orbital inclinations depend nonlinearly on the initial eccentricity values. This is due to stochastic processes that occur when entering and exiting resonance. The time intervals between resonance captures and the duration of the system's evolution in resonance vary randomly.

CONCLUSIONS:

The compact four-planet system Kepler-51 evolves outside low-order resonances for most initial conditions consistent with values obtained from observations. A 3:1 mean motion resonance is possible in the system between the planets Kepler-51c and Kepler-51e with the orbital period of the planet Kepler-51e in the range from 255.8 to 256.3 days. Resonance causes the orbital inclinations of the planets to increase in an initially flat system.

In the future, it is planned to continue studying the dynamic evolution of the system for resonant and non-resonant initial conditions with non-zero initial values of the orbital inclination of the outermost planet Kepler-51e, corresponding to the condition of the absence of transits of this planet.

ACKNOWLEDGMENTS:

The study was supported by the Russian Ministry of Science and Higher Education via the State Assignment Project FEUZ-2025-0003.

REFERENCES:

[1] Steffen J.H., Fabrycky D.C., Agol E. et al. Transit timing observations from Kepler-VII. Confirmation of 27 planets in 13 multiplanet systems via transit timing variations and orbital stability // Monthly Notices of the Royal Astronomical Society. 2013. V. 428. P. 1077–1087. DOI: 10.1093/mnras/sts090.

[2] Jontof-Hutter D., Dalba P.A., Livingston J.H. TESS observations of Kepler systems with transit timing variations // The Astronomical J. 2022. V. 164. Article 42. DOI: 10.3847/1538-3881/ac7396.

[3] Kuznetsov E.D., Perminov A.S. Study of the dynamical evolution of the compact planetary system Kepler-51 // Solar System Research. 2024. V. 58. No. 5. P. 594–611. DOI: 10.1134/S0038094624700394.

[4] Masuda K., Libby-Roberts J.E., Livingston J.H. et al. A fourth planet in the Kepler-51 system revealed by transit timing variations // The Astronomical J. 2024. V. 168. Article 294. 36 p. DOI: 10.3847/1538-3881/ad83d3.

[5] Volk K., Malhotra R. Dynamical instabilities in systems of multiple short-period planets are likely driven by secular chaos: A case study of Kepler-102 // The Astronomical J. 2020. V. 160. Article 98. 13 p. DOI: 10.3847/1538-3881/aba0b0.

[6] Blanco-Cuaresma S., Bolmont E. Studying tidal effects in planetary systems with Posidonius. A N-body simulator written in Rust // EWASS Special Session 4 (2017): Star-planet interactions (EWASS-SS4-2017). 2017. DOI: 10.5281/zenodo.1095095.

MODELING TRANSIT ABSORPTION IN HI AND HEI LINES AT ATMOSPHERES OF HOT EXOPLANETS FOLLOWING SUPER-FLARE

I. F. Shaikhislamov[1,2,3], I. B. Miroshnichenko[1,3], S. S. Sharipov[1], M. P. Golubovskiy[1,2], M. S. Rumenskikh[1,2], A. G. Berezutskiy[1,2]
[1] *Institute of Laser Physics SB RAS, Novosibirsk, Russia*
Shaikhislamovildar@yandex.ru
[2] *Institute of Astronomy RAS Moscow, Russia*
[3] *Novosibirsk State Technical University, Novosibirsk, Russia*

KEYWORDS:
exoplanets, atmosphere, transit observations, superflare

ABSTRACT:
Hot gas planets rotating in close orbits form a subclass among a very diverse population of exoplanets. They have a unique feature of extensive outflow of the upper atmosphere. Multicomponent and partially ionized matter, heated by intense ionizing radiation of the parent star, flows through the Roche lobe at supersonic speed and collides with the stellar wind plasma. Such dynamics are fundamentally different from the processes in the rarefied exospheres of the planets of the Solar System. Observational evidence for such an outflow of the atmosphere was found for a number of hot Jupiters and warm Neptunes by measuring their transit absorption in the lines of such elements as H, C, O, Mg, Si, Fe. Recently, rich information was provided by the analysis of the transit absorption of exoplanets in the 1083 nm line in the IR range of the metastable helium triplet.

Observations with the Kepler and TESS space telescopes not only detected numerous exoplanets but made a far-reaching discovery of super-flares in Sun-like stars, with energies 4-5 orders of magnitude greater than the most powerful flares observed on the Sun. These data raised the question of the so-called "quiet Sun". The correlation between flare energy and CMEs shows a monotonic pattern for the Sun, but does not allow extrapolation to superflares. Available data for other stars are too limited for reliable conclusions. The rapid progress of exoplanet research is opening up new possibilities for space weather forecasting by developing new methods for obtaining quantitative measurements of CME parameters through transit observations of the response of hot exoplanet atmospheres to the extreme activity of their host stars [1]. The progress in this direction requires upgrading the existing 3D MHD numerical models of atmospheres to include dynamic responses to extremely energetic pulses of radiation and plasma wind, and identifying stars with exoplanets that are the most suitable targets. The first stage of this development should be modeling the response of atmosphere to the pulse of radiation of the superflare [2]. In this work we calculate for the first time the absorption in HI 656.3 nm and HeI 1083 nm lines induced by absorption of superflare radiation.

ACKNOWLEDGMENTS:
The research is supported by RNF project 25-72-10080.

REFERENCES:
[1] Shaikhislamov I. F., Shematovich V. I., Tsurikov G. N., Zhilkin A. G., Savanov I. S., Rumenskikh M. S., Bisikalo D. V. Observations of hot exoplanets as a new tool for space weather research and forecasting // Physmath, 2026. V. 3. No. 2. P. 65–83 (in Russia). DOI: 10.56304/S2949609825020016.
[2] Zhilkin A. G., Gladysheva Y. G., Shematovich V. I., Tsurikov G. N., Bisikalo D. V. Impact of Star Flare Activity on the Structure of the Hydrogen–Helium Upper Atmosphere of Hot Jupiter// Astronomy Reports. 2024. V. 68(9). P. 865–877.

RESIDUAL HYDROGEN-HELIUM ATMOSPHERES OF MINI-NEPTUNES: THE POSSIBILITY OF FORMATION AND STABILITY WITH TAKING INTO ACCOUNT VARIOUS THERMAL LOSS MECHANISMS AND THE INTERIOR COMPOSITION

R. A. Evdokimov[1], V. I. Shematovich[2]
[1] *Rocket and Space Corporation "Energia", Korolev, Moscow Region, Russia*
evdokimovrom@yandex.ru
[2] *Institute of Astronomy RAS, Moscow, Russia*
shematov@inasan.ru

KEYWORDS:
mini-Neptunes, Hyceans, habitable zone, primary atmosphere, thermal dissipation of atmospheres, photoevaporation, core-powered mass-loss, structure of the interior

ABSTRACT:
Among exoplanets, the most promising objects of study, from the point of view of astrobiology, are still Earth-like, rocky exoplanets (sub-, exo-, and super-Earths) located in the classical habitable zone of their parent stars [1]. Nevertheless, the wide variety of exoplanets and planetary systems allows us to consider a number of alternatives, including Hyceans [2] and super-Earths with hydrogen-helium atmospheres at large distances from their parent stars [3, 4]. Hyceans are a hypothetical type of exoplanet possessing a global water ocean and a relatively thin atmosphere of primordial composition. They differ from ordinary mini-Neptunes by the presence of a water surface. The potential habitability of this type of exoplanets, as well as the belonging of a number of known candidates to Hyceans (for example, K2-18b), are widely debated [5–9]. Probably, a strong greenhouse effect in the lower atmospheres of sufficiently massive (several Earth masses) mini-Neptunes close to their parent stars, such as K2-18b, does not allow the existence of a water ocean [9]. Nevertheless, mini-Neptunes in wide orbits are of interest. However, the mass fraction of the primordial atmosphere compatible with the existence of liquid water at the border between the gaseous envelope and the water mantle of a mini-Neptune should be no more than 10^{-5}–10^{-3}, depending on the radiative flux of the parent star, the mass and age of the exoplanet [4, 9, 10]. The probability of the formation of such thin envelopes is relatively low; as a rule, the fraction of the atmosphere is several percent of the mass of a mini-Neptune [4, 11].

In [10], a mechanism was proposed for the formation of residual (thin) gas envelopes of primordial composition around light, water-rich mini-Neptunes (0.5–2$M_\oplus$) in wide orbits around red dwarfs due to the loss of massive atmospheres in the early evolutionary stages. The possibility of a rapid loss of most of the primordial atmosphere under the core-powered mass-loss was considered [12, 13]. It was shown that this mechanism for the formation of potential oceans is most effective for exoplanets around low-mass red dwarfs. Their relatively high luminosity at the initial stage of evolution provides a sufficient equilibrium temperature for the loss of most of the gas envelope. Its further evolution is associated with photoevaporation, the rate of which will decrease with a decrease in the luminosity of the parent star and its activity. Ultimately, the equilibrium temperature of the exoplanet may decrease to values compatible with the existence of an ocean.

The results of calculations for mini-Neptune models of different masses, with different fractions of water in their composition and with different equilibrium temperatures after the formation of host stars of various spec-

tral classes were presented. An assessment was made (based on the conditions at the boundary of the atmosphere and the water mantle) of their belonging to the Hyceans. The stability of the residual gas envelopes was estimated taking into account photoevaporation. However, the issue of the transition between the two main regimes of heat loss of the gas envelopes – core-powered mass-loss and photoevaporation — was not investigated. These modes are competing, and the final mass of the gas envelope depends on the moment of transition, among other parameters [13]. In the present paper, the influence of both loss mechanisms on the formation of thin residual atmospheres of mini-Neptunes is considered, taking into account the possibility of switching between the modes (in accordance with the methodology and criteria presented in [13]). The paper presents the results of calculations (final mass fractions of atmospheres and estimates of their stability over long, geological time intervals) for planets of different masses, with different mass fractions of water and initial primordial atmospheres, at various orbital distances from host stars with different masses. The change in the equilibrium temperature of exoplanets, as well as of the stellar soft X-ray and extreme ultraviolet radiation flux, were taken into account. The role of so-called "enhanced photoevaporation" [13] is investigated: a regime in which the photoevaporation mechanism operates at large radii due to the extention of the atmosphere, “inflated” by the heat flow from the interior of the young exoplanet.

REFERENCES:

[1] Cockell C. S. et al. Habitability: A Review // Astrobiology. 2016.
[2] Madhusudhan, N. et al. Habitability and Biosignatures of Hycean Worlds // ApJ. 2021. V. 918. Article 1.
[3] Pierrehumbert R., Gaidos E. Hydrogen Greenhouse Planets Beyond the Habitable Zone // ApJl 2011. V. 734. Article L13.
[4] Mol Lous M., Helled R., Mordasini Ch. Potential long-term habitable conditions on planets with primordial H–He atmospheres // Nature Astronomy. 2022. V. 6(7). Article 819.
[5] Mitchell E. G., Madhusudhan N. Prospects for biological evolution on Hycean worlds // MNRAS. 2025. V. 538. P. 1653–1662.
[6] Madhusudhan N. et al. The Interior and Atmosphere of the Habitable-zone Exoplanet K2-18b // ApJL. 2020. V. 891. Article L7.
[7] Madhusudhan N. et al. New Constraints on DMS and DMDS in the Atmosphere of K2-18 B from JWST Miri // ApJL. 2025. V. 983. Article L40.
[8] Jordan S., Shorttle O., Quanz S. P. Planetary albedo is limited by the above-cloud atmosphere: Implications for sub-Neptune climate // The Astrophysical J. 2025. V. 993. No. 1.
[9] Innes H., Tsai Sh.-M., Pierrehumbert R.T. The Runaway Greenhouse Effect on Hycean Worlds // ApJ. 2023. V. 953. Article 2.
[10] Evdokimov R. A., Shematovich V. I. // 16-MS^3. 2025.
[11] Owen J. E., Mohanty S. Habitability of terrestrial-mass planets in the HZ of M Dwarfs — I. H/He-dominated atmospheres // Monthly Notices of the Royal Astronomical Society. 2016. V. 459.
[12] Ginzburg S., Schlichting H. E., Sari R. // ApJ. 2016. V. 825. Article 29.
[13] Owen J. E., Schlichting H. E. Mapping out the parameter space for photoevaporation and core-powered mass-loss // MNRAS. 2024. V. 528. P. 1615–1629.

ESTIMATE OF THE INFLUENCE OF INTERIOR COMPOSITION ON THE THERMAL ATMOSPHERIC MASS-LOSS FOR MINI-NEPTUNES

R. A. Evdokimov[1], V. I. Shematovich[2]
[1] *Rocket and Space Corporation "Energia", Korolev, Moscow Region, Russia, evdokimovrom@yandex.ru*
[2] *Institute of Astronomy RAS, Moscow, Russia, shematov@inasan.ru*

KEYWORDS:
mini-Neptunes, thermal dissipation of atmospheres, photoevaporation, core-powered mass-loss, Fulton gap, structure of the interior

ABSTRACT:
Among the most commonly known exoplanets are the so-called mini-Neptunes, with radii ranging from 2 to $4R_\oplus$ and masses ranging from 1 to $10M_\oplus$. According to existing concepts, mini-Neptunes are surrounded by powerful atmospheres of primordial hydrogen-helium composition and represent an intermediate type of exoplanet between super-Earths and ice giants [1]. At sufficiently high equilibrium temperatures (relatively small orbital distances to the parent stars), atmospheric loss should play a significant role in the evolution of mini-Neptunes, which is especially effective in the first millions to tens of millions of years after the formation of the planetary system. It is likely that atmospheric loss explains such features in the observed exoplanet distribution as the Fulton gap [2] and the "hot Neptune desert".

Direct observational evidence of atmospheric loss has now been discovered for some mini-Neptunes, in particular, for TOI-1430 b [3]. Relatively small exoplanets can completely lose their gas envelopes, retaining only dense cores, observed as super-Earths and Earth-like planets with short (up to several tens of days) orbital periods. Thermal loss is considered to be the leading mechanism of atmospheric mass-loss for mini-Neptunes: photoevaporation (caused by heating of the outer layers of the gas envelopes by X-rays and extreme ultraviolet radiation — EUV) [4] and/or core-powered mass-loss (the outer layers are heated by infrared radiation coming from the interior) [5]. Each of these mechanisms has been studied in detail separately, and their combined effect has also been investigated, including the consequences for the parameters of the Fulton gap in parent stars of different spectral classes, as well as the characteristics of the populations of super-Earths and mini-Neptunes [6]. In particular, it was shown that the core-powered mass-loss should dominate for sufficiently hot and "puffy" (with a low average density) exoplanets. As the atmosphere is lost, this mechanism may give a way to photoevaporation. For cooler and denser exoplanets, photoevaporation may dominate initially. In this case, the transition to the core-powered mass-loss regime is possible only due to a decrease in the part of soft X-ray and EUV radiation in the bolometric luminosity of the parent star [6]. The position and depth (reduction in the frequency of occurrence of exoplanets of a given radius) of the Fulton gap, as well as the composition and mass of the residual atmosphere of the mini-Neptune (if it is not completely lost) [6], can significantly depend on the dominant regime of atmospheric loss.

There are various hypotheses about the internal structure of mini-Neptunes. The most widespread hypothesis is that the composition and structure of their interiors is similar to the generally accepted models of ice giants (Uranus and Neptune). In this case, mini-Neptunes, in addition to a powerful hydrogen-helium envelope, should also contain a large amount of water (up to 50–80% of their mass) [1]. However, there are also alternative concepts — on the almost dry interiors of mini-Neptunes and a significantly lower water content in the composition of ice giant's [7]. The composition of the interior determines the radius of the exoplanet's

core for a given mass, the gravity at the boundary of the core, and therefore, all other parameters being equal, the extent of the gaseous envelope and the total radius of the exoplanet. The heat loss rate by the primary atmospheres of mini-Neptunes depends strongly on their radii [8–11]. Also, the transition from the regime of core-powered mass-loss to the photoevaporation one should (all other parameters being equal) depend on this value. At the same time, in previous studies, when modeling this transition, mini-Neptunes with iron-silicate (of terrestrial composition) cores were mainly considered [6]. For fixed values of mass and equilibrium temperature, the radius of the planet was considered as a function of the mass fraction of the atmosphere.

In this paper, we investigate the dependence of the transition between the above-mentioned atmosphere loss regimes for different mass fractions of water contained in the interiors of mini-Neptunes. We consider the calculation results for mini-Neptune models with different masses, equilibrium temperatures, and relative water contents. The calculations were performed for host stars of various spectral classes: we took into account the age of the star at the moment of separation of the exoplanet's atmosphere from the protoplanetary disk, the features of its evolutionary track that affect the change in the equilibrium temperature of the mini-Neptune, and the magnitude of the X-ray and EUV radiation flux. We also present the calculation results for the thoroughly studied mini-Neptune HD207496b [11], and demonstrate the possibility of losing a powerful primary gas envelope both through photoevaporation [11] and core-powered mass-loss in the presence of a significant amount (about 40%) of water [9, 10].

REFERENCES:

[1] Bitsch B. et al. Dry or water world? How the water contents of inner sub-Neptunes constrain giant planet formation and the location of the water ice line // A&A. 2021. V. 649. Article L5.
[2] Fulton B. J. et al. The California-Kepler Survey. III. A Gap in the Radius Distribution of Small Planets // AJ. 2017. V. 154.
[3] Nardiello D. et al. The GAPS Programme at TNG. LXV. Precise density measurement of TOI-1430 b, a young planet with an evaporating atmosphere // A&A. 2025. V. 693. Article A32. 26 p.
[4] Owen J. E., Jackson A. P. Planetary evaporation by UV and X-ray radiation: basic hydrodynamics // MNRAS. 2012. V. 425. Iss. 4. P. 2931–2947. DOI: 10.1111/j.1365-2966.2012.21481.x.
[5] Ginzburg S., Schlichting H. E., Sari R. Super-Earth Atmospheres: Self-consistent Gas Accretion and Retention // ApJ. 2016. V. 825. Iss. 1. Article 29. 12 p. 10.3847/0004-637X/825/1/29.
[6] Owen J. E., Schlichting H. E. Mapping out the parameter space for photoevaporation and core-powered mass-loss // MNRAS 2024. V. 528. P. 1615–1629.
[7] Werlen A. et al. Sub-Neptunes Are Drier than They Seem: Rethinking the Origins of Water-rich Worlds // The Astrophysical J. Letters. 2025. V. 991. No. 1. Article L16. DOI: 10.3847/2041-8213/adff73.
[8] Evdokimov R. A., Shematovich V. I. Evolutionary History of the Atmosphere of the Young Mini-Neptune HD 207496b // Solar System Research. 2025. V. 59. Article 22. 13 p. DOI: 10.1134/S0038094624601579.
[9] Evdokimov R. A., Shematovich V. I. Estimate of Core-Powered Mass-Loss of Primary Atmosphere of the Mini-Neptune (Ocean Planet) HD 207496b // Solar System Research. 2025. V. 59. Article 68.
[10] Evdokimov R. A., Shematovich V. I. Core-Powered Mass-Loss of the Primary Atmospheres of Mini-Neptunes: Influence of Water Content in the Planet Interior and Evolution of the Host Star // Solar System Research. 2026. V. 60. Article 23.
[11] Barros S. C. C. et al. The young mini-Neptune HD 207496b that is either a naked core or on the verge of becoming one // A&A. 2023. V. 673. Article A4.

Session 5.
SOLAR SYSTEM IN THE LAB (SS)
Oral Session

MICROWAVE SINTERING OF LUNAR SOIL ANALOGUE VI-LH1

I. A. Agapkin[1], E. M. Sorokin[1], A. E. Yakovleva[2], E. N. Slyuta[1]
[1] *Vernadsky Institute of Geochemistry and Analytical Chemistry, RAS Moscow, Russia*
[2] *Bauman Moscow State Technical University, Moscow, Russia*

KEYWORDS:
lunar soil analogue, ISRU, lunar base, microwave sintering

INTRODUCTION:
The concept of microwave sintering as a foundational technique for lunar resource utilization—including water, oxygen, and metal extraction — dates back to 1985 [1]. Its primary appeal stems from volumetric heating capabilities and substantially lower power requirements compared to conventional approaches. Among the various processing methods explored to date, microwave sintering is projected to offer the most favorable energy efficiency [2]. This is exemplified by a comparative analysis with selective laser sintering (SLS), where the microwave-based alternative demonstrated a 23% reduction in energy consumption, along with a corresponding decrease in processing duration [3].

SAMPLE:
The experimental feedstock comprised VI-LH1, a lunar soil simulant developed at the GEOKHI RAS laboratory. This material is derived from crushed labradorite and closely replicates the chemical, mineralogical, and granulometric characteristics of highland regolith [4].

EXPERIMENTAL PROCEDURE:
Microwave sintering was performed using a commercial 800 W oven. The VI-LH1 material was milled to a particle size of 100 μm. A 6 g batch was then transferred to a corundum crucible of dimensions 30×20×15 mm. To generate hybrid thermal conditions, the crucible was encapsulated in a ceramic fiber mold lined internally with silicon carbide (Fig. 1) [5].

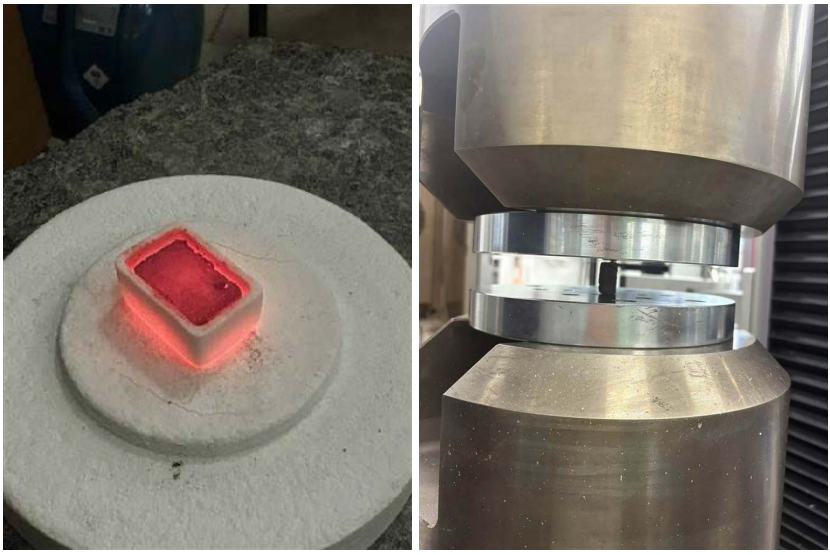


Fig. 1. The sintered specimen within the crucible immediately after microwave sintering (left); uniaxial compressive strength testing of the specimen (right)

RESULTS:
The experimental results demonstrated that a sintering duration of 11.5 minutes was sufficient to fabricate a brick of the specified dimensions. The obtained compressive strength reached 9.44 MPa, which is comparable

to that of M100 grade masonry bricks commonly employed in low-rise construction (up to three stories).

CONCLUSION:

In summary, the compressive strength values obtained in this study are considered satisfactory for the intended application. However, it should be noted that terrestrial building codes and strength requirements may not be directly transferable to lunar conditions, as the reduced gravitational field (approximately 1/6 of Earth's) imposes significantly lower static loads on structural elements [6]. Nevertheless, to fully validate the feasibility of microwave sintering for lunar construction, further experimental investigations are required under conditions that more closely replicate the actual lunar environment, including vacuum, reduced gravity, and extreme thermal cycling.

REFERENCES:

[1] Meek T.T. et al. Microwave processing of lunar materials: Potential applications // Lunar bases and space activities of the 21st century. 1985. Article 479.
[2] Farries K.W. et al. Sintered or melted regolith for lunar construction: state-of-the-art review and future research directions // Construction and Building Materials. 2021. V. 296. Article123627.
[3] Lim S., Anand M. Numerical modelling of the microwave heating behaviour of lunar regolith // Planetary and Space Science. 2019. V. 179. Article 104723.
[4] Mironov D. D. et al. Lunar Highlands Soil Simulant VI-LH1 for Testing Developing In-Situ Technologies and Large-Scale Experiments // 55th Lunar and Planetary Science Conference. 2024. V. 3040. Article 1948.
[5] Liu Z. et al. Sintering of lunar regolith simulants using a domestic microwave: A rapid and energy-efficient strategy for construction material fabrication // J. European Ceramic Society. 2025. V. 45. No. 3. Article 117047.
[6] Caprio L. et al. Determining the feasible conditions for processing lunar regolith simulant via laser powder bed fusion // Additive Manufacturing. 2020. V. 32. Article 101029.

SIMULATION EXPERIMENTS USING POWERFUL PULSED GYROTRONS FOR THE DEPOSITION OF LUNAR DUST ON METAL PLATES

N. N. Skvortsova[1], D. V. Malakhov[1], V. D. Stepakhin[1], E. M. Konchekov[1], L. V. Kolik[1], N. G. Gusein-zade[1], N. S. Akmadullina[1,2], E. V. Voronova[1], O. N. Shishilov[1,3]

[1] *Prokhorov General Physics Institute of the Russian Academy of Sciences Moscow, Russia*

[2] *Baikov Institute of Metallurgy of Russian Academy of Sciences Moscow, Russia*

[3] *MIREA — Russian Technological University, Moscow, Russia*

KEYWORDS:
lunar regolith, simulation experiments, gyrotron discharge, surface modification of stainless steel, tantalum, molybdenum

ABSTRACT:
Clouds of charged dust are continually generated on the Moon by both micrometeorite impacts and human activities, such as spacecraft landings and rover operations, which can loft dust to heights of tens of meters. The detrimental effects of lunar dust are well documented, including its deposition on solar panels, which reduces their efficiency, and its penetration into critical components of different equipment.

We present a new type of simulation experiment developed at the Prokhorov General Physics Institute of the Russian Academy of Sciences to investigate the effects of a levitating cloud of charged particles, generated using a high-power pulsed gyrotron, that simulates levitating lunar regolith dust interacting with metallic surfaces. The experiment is based on the similarity between the physicochemical processes occurring in laboratory experiments with regolith simulants and those taking place on the lunar surface during micrometeorite bombardment [1, 2]. Upon irradiation of the regolith simulant powder with gyrotron-generated microwave pulses, nonlinear physicochemical processes – including particle fragmentation, plasma-chemical chain reactions, and Coulomb-driven particle scattering – develop within the reactor, leading to the formation of a levitating cloud of charged particles [3]. Herein, we report the results of deposition experiments in which charged particles simulating levitating lunar dust were deposited onto stainless steel, tantalum (Ta), and molybdenum (Mo) substrates.

The plasma-chemical experimental setup employing gyrotron-generated microwave radiation has been described in detail elsewhere [4]. Metallic substrates were mounted inside the reactor above the regolith simulant powder. Rectangular substrates measuring 10×40 mm and having a thickness of 0.4 mm were fabricated from 309L stainless steel (ISO 3581), tantalum (Ta), and molybdenum (Mo). Half of the substrates were pretreated using a low-temperature dielectric barrier discharge (DBD) plasma jet [5]. A 0.5–0.7 mm thick layer of regolith simulant powder was spread over the reactor support plate, leaving its upper surface exposed.

A description of the laboratory regolith simulant is given in the patent [6]. The particle size distribution corresponded to the granulometric distribution of lunar regolith. The microwave energy required to initiate chain plasma-chemical reactions in the reactor and generate levitating particle ensembles was 4 kJ, corresponding to a gyrotron pulse duration of 10 ms and a microwave power of 400 kW. The physicochemical processes in the reactor above the regolith powder were initiated 4–6 ms after the leading edge of the gyrotron pulse, while particle ejection and levitation were observed for 300–500 ms (Fig. 1).

The deposition of such particles onto metallic surfaces has been described previously [6, 7]. As an example, Fig. 2 shows the deposition of secondary material derived from the regolith simulant onto stainless steel substrates with and without DBD surface pretreatment after three cycles of the plasma-chemical process. The deposited secondary material consists of spheroidal particles of various sizes. The elemental composition of the deposits on the untreated surface is dominated by components originating from the regolith simulant particles, whereas the DBD-treated surface exhibits a substantial contribution from the underlying stainless steel substrate.

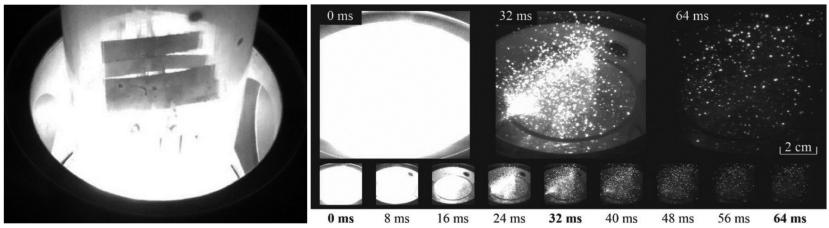


Fig. 1. Left: Photograph of the plates taken 8 ms after the gyrotron was switched off (t=0). Right: Levitating particles observed approximately 30 cm above the regolith surface

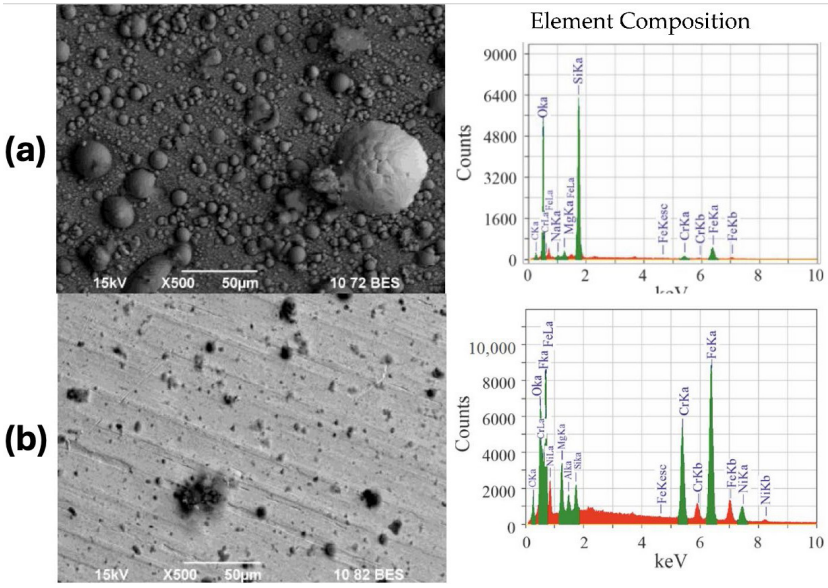


Fig. 2. SEM images of the deposited secondary material (left) and the corresponding elemental composition (right) for untreated (a) and DBD-treated (b) stainless steel plates

REFERENCES:

[1] Popel S.I., Kopnin S.I., Golub' A.P. et al. // Solar System Research. 2013. V. 47. No. 6. P. 419–429. DOI: 10.1134/S0038094613060063.
[2] Popel' S.I., Golub' A.P., Zakharov A.V. et al. // JETP Letters. 2018. V. 108. Iss. 6. P. 356–363, DOI: 10.1134/S0021364018180091.
[3] Skvortsova N.N., Mayorov S.A., Malakhov D.V. et al. // J. Experimental and Theoretical Physics Letters. 2019. V. 109. Iss. 7. P. 441–448. DOI: 10.1134/S0021364019070130.
[4] Sokolov A.S., Akhmadullina N.S., Borzosekov V.D. et al. Plasma-chemical facility for synthesis of micro- and nanoparticles having controlled compositions and structures on the basis of a microwave discharge in the gyrotron radiation // Radiophysics and Quantum Electronics. 2023. V. 65. No. 11. P. 840–854. DOI: 10.1007/s11141-023-10261-z.
[5] Kolik L.V., Kharchev N.K., Borzosekov V.D., Malakhov D.V., Konchekov E.M., Stepakhin V.D., Guzein-zade N.G., Bogachev N.N. Low-Temperature Plasma Generator. Patent RU 181459 U1, 16.07.18.

[6] Skvortsova N.N., Stepakhin V.D. et al. // Materials. 2021. V. 14. DOI: 10.3390/ma14216472.
[7] Skvortsova N.N., Stepakhin V.D., Borzosekov V.D. et al. // Plasma Phys. Rep. 2023. V. 49. Article 120. DOI: 10.31857/S0367292122601394.

EVALUATION OF MID-IR SPECTRA OF NATURAL SILICATES FOR REMOTE SENSING OF THE MOON

S. A. Voropaev[1], A. P. Krivenko[1], V. S. Fedulov[1], N. V. Dushenko[1], A. V. Minaev[1], T. G. Kuzmina[1], Y. Jianguo[2]
[1] *Vernadsky Institute of Geochemistry and Analytical Chemistry RAS Moscow 119991, Russia, voropaev@geokhi.ru*
[2] *State Key Laboratory of Information Engineering in Surveying, Mapping and Remote Sensing, Wuhan University, Wuhan 430070 China*

KEYWORDS:
olivine, pyroxene, anorthite, mid-IR spectra, diffuse reflectance, absorption

INTRODUCTION:
The lack of data on the concentration and chemical composition of olivine (the presumed main mineral of the lunar mantle) in the surface regolith makes it impossible to identify the internal geological structures of the Moon. The point is that the spectral astronomical observations by terrestrial telescopes are limited by the "transparency window" of the Earth's atmosphere. Measurements from orbital spacecraft are free from such limitations, and a number of attempts have been made to use remote sensing of the lunar surface for geological research. For example, the UV/VIS camera on board the Clementine spacecraft had five discrete channels covering the UV/Visible range. Using this camera, a global mapping of the Moon was performed, which made it possible to classify the main rock types [1]. In particular, one of the peaks in the South Pole–Aitken basin and the central peaks in five craters were identified as potentially containing olivine. However, after the launch of the spectral profiler (SP) aboard the Japanese Kagya/Selene lunar satellite, one of the candidates (Tsiolkovsky crater) was classified as containing a mixture of plagioclase and pyroxene, rather than pure olivine [2].

This discovery of SP demonstrated the importance of obtaining and analyzing full reflection spectra in the all possible spectral range, preferably including full IR spectrum. So, the characteristic absorption features of natural silicates in the mid-IR range can be used as a diagnostic tool for olivine and other indicator' minerals when identifying mantle rock outcrops on the lunar surface. For the entire period of operation of Kagya/Selene spacecraft (since November 2007 until June 2009), reflection spectra were obtained using SP for approximately seventy million points (each 0.2–0.5 km in size) in the wavelength range 0.5–2.6 microns with a spectral resolution of 6-8 nm [3]. Based on them, 245 sites potentially rich in olivine were identified, where the absorption band λ~1.05 μm was used as the main diagnostic feature. Most of the spectra for the selected points also showed absorption at λ~0.85, 1.05, and 1.25 microns, but, nevertheless, the characteristic olivine bands were indistinct, which was explained by the presence of plagioclases, pyroxenes with a high Ca content, and mixtures of other minerals.

The purpose of this work is to determine the composition' effect of typical silicates mixtures of the lunar rocks on the resulting IR absorption and reflection spectra in the mid-IR range. For this purpose, natural plagioclases, pyroxenes, and olivine, which are closest to the lunar regolith in chemical composition, were used, as well as numerical modeling.

SAMPLES COLLECTION:
In space research, olivine (orthosilicates with a crystalline structure as $(Mg,Fe)_2[SiO_4]$) is usually detected on extraterrestrial bodies by reflection spectra (for orbital or astronomical observations) or by Raman scattering (for in situ measurements). Both the visible and IR ranges are involved, from near- to far-infrared. Laboratory studies have shown that the mid-IR range contains characteristic lines reflecting the chemical composition of olivine

(Mg, Fe) [4]. Currently, the mid-IR range is little used in remote sensing, but it will be used in research aboard planned orbital stations, including Luna-26.

Anorthite, as a member of plagioclases (crystalline formula $(Ca,Na,K)Al_2[Si_2O_8]$), has a rigid three-dimensional structure which formed by [SiO4] tetrahedra connected by common bridging oxygen atoms. This framework is based on rings of four tetrahedra with alternating tetrahedra with multidirectional vertices. The general features of the IR spectra of feldspars were first studied by Laves and Hafner in 1956, who showed that the degree of ordering of Al and Si affects their absorption lines. Later, Lyon in 1964 compiled a catalog of plagioclase spectra with different chemical compositions, where he noted the characteristic wavelengths. Nash and Salisbury in 1991 showed that the Ca content (minal An) in plagioclases can be determined regardless of the degree of crystallinity using the Christiansen (CF) feature, which is manifested as minimum in the reflection spectra. Recently, Reitze and colleagues investigated the possibility of using spectra in the mid-IR range of crystalline plagioclases with different Al, Si ordering for remote sensing of the Moon, Mercury and other objects of the Solar System in connection with the BepiColombo mission [5].

Augite belongs to the pyroxene group (a single-chain structure of $[SiO_4]$ tetrahedra) common in lunar mare basalts, with the formula $(Ca, Na)(Mg,Fe,Al,Ti)(Si,Al)_2O_6$. The rocks of the lunar upper mantle also contain significant amounts of augite. A recent ChangE-6 mission delivered samples from the South Pole-Aitken (SPA) area where the impact of a huge asteroid penetrated the lunar crust more than 3 billion years ago. Mineralogically, the CE-6 soil consists of 32.6% plagioclase (anorthite and bytownite), 19.7% augite, 10% pigeonite and 3.6% orthopyroxene, and with low content of olivine (0.5%) but high content of amorphous glass (29.4%) [6]. Geochemically, the bulk composition of CE-6 soil is rich in Al_2O_3 (14%) and CaO (12%) but low in FeO (17%), and trace elements of CE-6 soil such as K (~630 ppm), U (0.26 ppm), Th (0.92 ppm) and rare-earth elements are significantly lower than those of the lunar soils within the Procellarum KREEP Terrane. The local SPA basalts are characterized by low-Ti (TiO_2, 5.08%), low-Al (Al_2O_3 9.85%) and low-K (~830 ppm), features suggesting that the CE-6 soil is a mixture of local basalts and non-basaltic ejecta.

METHODS AND RESULTS:

To obtain IR spectra of natural minerals and mixtures, we used a measuring complex: a Fourier spectrometer combined with an optical microscope. The equipment used was from the Simex company (Novosibirsk): FT-801 and MIKRAN-2. Simex supplies a range of additional devices to the main unit, facilitating spectral measurements using various methods. For example, the plug-in for using attenuated total internal reflection (ATR) or the plug-in for double transmission (PRIZ). The main advantage of PRIZ is good transmission spectra for fine powders rolled on a mirrored metal plate. When passing through the sample layer twice, as the radiation reflects off the mirror and moves toward the photodetector, the optical path is doubled. This method is good for obtaining transmission/absorption spectra of bulk natural materials of arbitrary shape and structure (powders, films).

Of particular interest are the IR spectra of natural mixtures of various minerals. The regolith of the Moon is a layer of bedrock ground down by meteorite impacts, ranging in thickness from 2 to 20 m, depending on the age of the region. Since anorthosites and basalts are the main rocks of the lunar crust, the appearance of other minerals against their background is an important diagnostic sign of hidden intrusions and other geological formations. For laboratory studies of natural minerals and mixtures in the form of powders, samples of (ultra)basic plutonic rocks (peridotite, dunite) were used. These provided chemical compositions of minerals (olivine, pyroxenes and plagioclase) and matrices close to lunar basalts and crust. Pure minerals were also investigated to obtain the reference spectra needed for deconvolution.

The mineral powders were mixed in different weight proportions to obtain a mixture with varying total chemical composition of the basic oxides –

SiO_2, MgO, FeO, CaO, Al_2O_3 etc. Some typical IR absorption spectra of natural minerals, obtained on FT-801 by PRIZ, are shown on Fig. 1. The absorption bands shift to lower wave numbers corresponds to a decrease in the vibration frequencies of the heavier parts of the silicate lattice compared to more siliceous. This shift can serve as an important diagnostic feature of the chemical composition of minerals during remote sensing of regolith. Another important difference between the spectra under consideration is the presence of broad water absorption peaks in natural minerals. The band 3500–3700 1/cm corresponds to vibrations (bond stretching) of hydroxyl groups, while the band 1600–1800 1/cm corresponds to deformation vibrations of hydroxyl groups and molecular water sorbed on the surface.

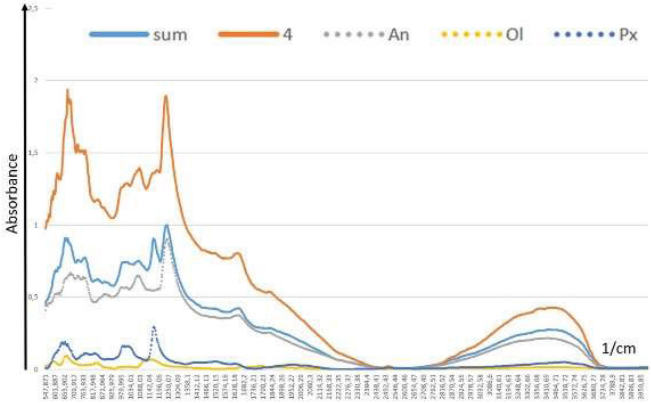


Fig. 1. Absorbance spectra: specific mixture and pure minerals (An — anorthite, Ol — olivine, Aug — augite)

ACKNOWLEDGMENTS:
The study was supported by the Russian Science Foundation grant no. 25-17-00051, https://rscf.ru/project/25- 17-00051/.

REFERENCES:

[1] Tompkins S., Pieters C. Mineralogy of the lunar crust: Results from Clementine // Meteorit. Planet. Sci. 1999. V. 34. No. 1. P. 25–41. DOI: 10.1111/j.1945-5100.1999.tb01729.x.
[2] Matsunaga T. et al. Discoveries on the lithology of lunar crater central peaks by SELENE Spectral Profiler // Geophys. Res. Lett. 2008. V. 35. No. 23. P. L23201–L23206. DOI: 10.1029/2008GL035868.
[3] Yamamoto S. et al. Possible mantle origin of olivine around lunar impact basins detected by SELENE // Nat. Geosci. 2010. V. 3. No. 8. P. 533–536. DOI: 10.1038/ngeo897.
[4] Voropaev S. et al. Evaluation of IR Spectra of Mixtures of Natural Ca-Plagioclases and Olivines for Remote Determination of Composition // Sol. Sys. Res. 2026. V. 60. P. 17-26. DOI: 10.1134/S0038094625601070.
[5] Reitze M. et al. Mid-infrared spectroscopy of crystalline plagioclase feldspar samples with various Al, Si order and implications for remote sensing of Mercury and other terrestrial Solar System objects // Earth Planet. Sci. Lett. 2021. V. 554. P. 116697–116704. DOI: 10.1016/j.epsl.2020.116697.
[6] Li Ch. et al. Nature of the lunar far-side samples returned by the Chang'E-6 mission // National Science Review 11: nwae328, 2024. P. 9–28. DOI: 10.1093/nsr/nwae328.

NEW FRONTIERS IN THE MICROSTRUCTURAL STUDIES OF LUNAR REGOLITH

V. Ia. Shklover[1], M. V. Gerasimov[2]
[1] *Systems for Microscopy and Analysis LLC, Skolkovo, Russia*
shklover@microscop.ru
[2] *Space Research Institute RAS, Moscow, Russia, mgerasim@cosmos.ru*

KEYWORDS:
lunar regolith, microstructural studies, iron nanospheres (Fe^0), correlation X-ray microscopy, electron-ion microscopy, mineralogical mapping, thermal transformation

INTRODUCTION:
The increasing interest in studying lunar soil sample properties necessitates the implementation of new visualization techniques and a comprehensive approach to examining the volumetric internal structure and variability in the elemental composition of regolith samples, enabling the extraction of maximum data from a limited number of unique samples.

To obtain new information and clarify possible processes of mineral transformation and the formation of iron nanospheres, it is necessary to use high-resolution correlation X-ray and electron-ion microscopy.

The key research challenges include the development of single regolith particle sample preparation techniques, 3D visualization of sample structure, determination of elemental composition with micrometre resolution, and automatic mapping of mineral composition.

RESEARCH METHODS:
The research involved the development of sample preparation methods, 3D visualization techniques, and automated mineralogical mapping algorithms. A new research area encompassed in situ experiments in a scanning electron microscope chamber under natural conditions to investigate the deposition of micro- and nanodroplets of water on a solid matrix, along with high-temperature experiments heating samples up to 1,200°C to study the effects of mineral transformation during impact heating and melting. Particular attention was devoted to examining changes in the solid phase resulting from impact and staged thermal transformation of minerals under space vacuum conditions.

RESULTS:
The report presents the results of analyzing two regolith samples (particles) collected by the Luna-20 and Chang'e-5 missions. For the Luna-20 particles, the focus was on developing methodologies for creating 3D models of the particle's structure, whereas the Chang'e-5 sample underwent comprehensive quantitative and morphometric analysis, including the examination of specific objects within the particle, such as iron nanospheres (Fe^0) and void structures. The obtained data enable a detailed description of the structural features of the selected objects, the crystal structure, and the elemental composition of the internal zones, including confirming the presence of Fe^0 both on the surface and within the volume of regolith particles.

PRACTICAL APPLICATION FOR THE EXPLORATION OF THE MOON:
The data obtained can be used to formulate and/or refine hypotheses:

- regarding the transformation of cosmic matter under impact interaction conditions, which will enable better description of microparticle interaction with solid bodies in space in the future;
- concerning the possible causes of charged regolith particle movement in the near-surface layer under solar irradiation in vacuum;
- regarding the formation mechanisms of pores inside regolith particles during various stages of mineral transformation;

- concerning the potential presence and composition of the gas phase in the pore space of regolith particles.

ACKNOWLEDGMENTS:
The authors thank the staff and colleagues of the Geochemistry and IKI RAS for providing the samples for research and for a fruitful discussion of the results.

IMPACT STRUCTURES ON VENUS AS A RESULT OF ASTEROID DESTRUCTION IN THE ATMOSPHERE

V. V. Shuvalov[1], B. A. Ivanov[2]
[1] *M. A. Sadovsky Institute of Geosphere Dynamics RAS, Moscow, Russia*
Shuvalov@idg.ras.ru
[2] *M. A. Sadovsky Institute of Geosphere Dynamics RAS*
boris_a_ivanov@mail.ru

KEYWORDS:
numerical modeling, craters, Venus, asteroids, shock wave, airburst

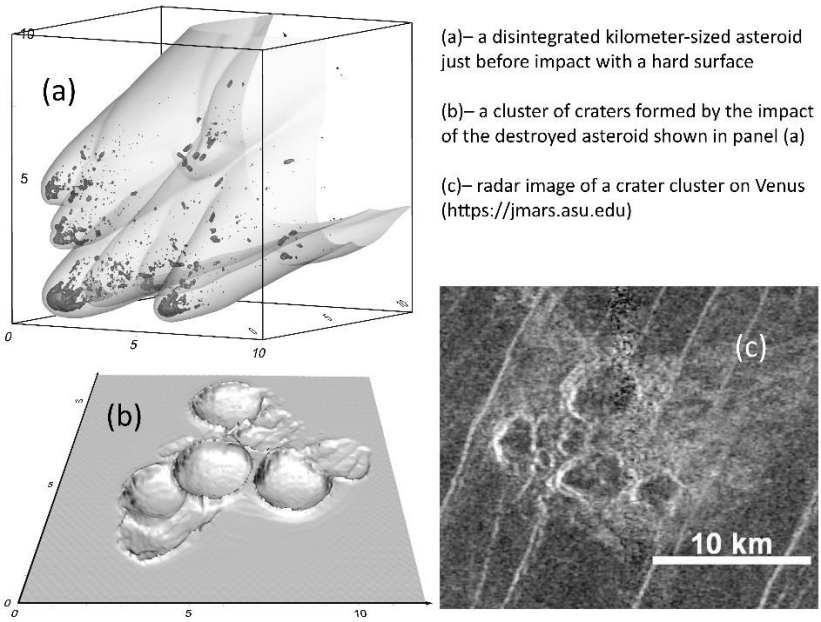
INTRODUCTION:
Venus' thick atmosphere is capable of destroying kilometer-sized bodies such as asteroids, creating various types of traces on the surface. While larger cosmic bodies are able to reach the surface, creating impact craters, smaller bodies effectively transfer the initial kinetic energy into the atmosphere, resulting in an "atmospheric explosion" at some altitude (airburst). In these cases, the most visible marks on the surface of Venus (radar dark and bright splotches) are created by atmospheric shock waves and the flow of gas behind the shock fronts reflected from the solid surface. The transitional sizes of impactors that break up in the atmosphere but reach the surface can produce clusters of craters. In this study we present the results of 3D numerical simulations of the destruction of asteroids in the atmosphere of Venus.

RESULTS OF SIMULATIONS:
Numerical modeling capabilities have increased in recent years, and we can now return to earlier questions with new modeling techniques. To simulate the fall of asteroids on Venus, the model, based on the three-dimensional version of the SOVA program [1], was used. Calculations of deformation, fragmentation and braking carried out using a three-dimensional quasi-fluid model of asteroids in the atmosphere of Venus showed that the axial symmetry used in two-dimensional calculations (and, accordingly, the toroidal shape of fragments after destruction) leads to stronger deceleration of destroyed asteroids. In three-dimensional calculations that are closer to reality, asteroids are decelerated and release energy at lower altitudes than in two-dimensional calculations. It is shown that the structure of a destroyed asteroid before impact on a solid surface, consisting of several large and many small fragments, obtained in three-dimensional calculations, can lead to the formation of crater clusters, previously described for Venus in [2].

In addition to impact craters, images of Venus obtained by the Magellan spacecraft clearly show circular areas (splotches) with sizes from 10 to 100 km, darker or brighter in radar than the surrounding surface [3, 4]. Dark surfaces appear to correspond to smoother surfaces, light surfaces to rougher surfaces. It is believed that the splotches are formed when a shock wave and gas flows generated by an airbust impact the surface. In [4] it is assumed that radar-dark (smoother) surfaces are formed by the severe destruction (sputtering) of rocks located on the surface by the shock wave. However, our calculations of the fall of asteroids with diameters of 0.6–1.0 km at velocities of 20 and 50 km/s on Venus showed that the maximum pressure values in the shock wave propagating along the surface of the planet do not exceed 0.03–0.05 GPa at a velocity of 20 km/s and 0.1 GPa at a velocity of 50 km/s. These values are significantly lower than the 0.2–1 GPa estimated in [4] to be necessary to "spray" rocks onto the surface and reduce its reflectivity.

Another reason for the formation of dark splotches may be thermal radiation generated during a meteor explosion. Our calculations and estimates show that when asteroids with sizes of 0.6–1.0 km impact Venus at velocities of 20 and 50 km/s, a surface layer 1–10 cm thick can evaporate. After

the vapors cool and condense, the fine condensed particles will settle back onto the surface and can make it smoother. There is a mechanism that could significantly increase the thickness of the condensate layer deposited at the impact epicenter. After the asteroid decelerates, a rarefied region forms, filled with hot shock compressed atmospheric gas and asteroid remnants, which begins to rise similarly to the fireball of a strong explosion [5]. The fireball rising results in a flow directed toward the epicenter forms along the surface, which moves the vapors generated by the radiation from the meteor airburst toward the impact epicenter. This mechanism could significantly increase the thickness of the deposited condensate layer beneath the fireball



(a)– a disintegrated kilometer-sized asteroid just before impact with a hard surface

(b)– a cluster of craters formed by the impact of the destroyed asteroid shown in panel (a)

(c)– radar image of a crater cluster on Venus (https://jmars.asu.edu)

Fig. 1.

REFERENCES:

[1] Shuvalov V. V. Multi-dimensional hydrodynamic code SOVA for interfacial flows: Application to thermal layer effect // Shock Waves. 1999. V. 9. No. 6. P. 381–390. DOI: 10.1007/s001930050168.
[2] Herrick R. R., Phillips R. J. Effects of the Venusian atmosphere on incoming meteoroids and the impact crater population // Icarus. 1994. V. 112. No. 1. P. 253–281. DOI: 10.1006/icar.1994.1180.
[3] Schaber G. G., Strom R. G., Moore H. J. et al. Geology and distribution of impact craters on Venus: What are they telling us? // J. Geophys. Res.: Planets. 1992. V. 97. No. E8. P. 13257–13301. DOI: 10.1029/92JE01246.
[4] Zahnle K. J. Airburst origin of dark shadows on Venus // J. Geophys. Res.: Planets. 1992. V. 97. No. E6. P. 10243–10255. DOI: 10.1029/92je00787.
[5] The Effects of Nuclear Weapons // Compil. and ed. S. Glasstone, Ph. J. Dolan. 3rd ed. Washington, DC: United States Department of Defense; United States Department of Energy. 1977. 662 p.

IMPACT EROSION OF OCEAN ON EARLY EARTH

V. V. Svetsov
Sadovsky Institute of Geosphere Dynamics RAS, Moscow, Russia
svetsov@idg.ras.ru

KEYWORDS:
impact, ocean, early Earth, ejecta, water escape, numerical simulation

INTRODUCTION:
Studies of ancient zircons up to 4.4 Gyr old suggest that oceans formed very early in the Earth's history [1–3]. During existence of early oceans, with an intense influx of cosmic objects onto Earth, some water mass could acquire escape velocity. The losses of water by the impacts have not been sufficiently studied. Only in [4] the mass of water ejected into the modern atmosphere at altitudes greater than 16 km was calculated for the impacts of 10-kilometer asteroids at a speed of 20 km/s at an angle of 45° on water basins of various depths. The aim of this work was to conduct numerical simulations of the impacts on oceans in a wider range of parameters, determine the amount of water lost into space and assess the influence of intense asteroid bombardment on the early ocean.

METHOD OF NUMERICAL SIMULATIONS:
Numerical modeling of asteroid impacts was performed in the hydrodynamic approximation using the SOVA method [5] in three-dimensional coordinates, similar to [4], with the difference that spherical coordinates were used. This made it possible to take into account the Earth's spherical shape. During the calculations, the boundaries between materials with different equations of state for the planet, impactor, water, and atmosphere were determined. The asteroid and the ground were assumed to be composed of dunite with a corresponding equation of state. However, the properties of materials of the ground and asteroid have little effect on the ejection of water. The atmosphere consisted of an ideal gas with a scale height of 8 km. The impactors were assumed to be spherical with diameters from 1 to 10 km. At the initial moment of the simulations, the asteroid touched the planet's surface. The thickness of the water layer above the solid surface varied from zero to the diameter of an asteroid.

RESULTS:
A large number of impact variants with several velocities and at different angles α to the Earth's surface were simulated. Figure 1 shows the results of modeling of the impacts of 10-km-diameter asteroids at a velocity of 20 km/s. The relative masses of water that acquire velocities sufficient to overcome the Earth's gravity are shown as functions of the relative ocean depths for several values of α. Angular averaging was performed taking into account the fact that the probability density of an impact at an angle α is equal to sin2α. The maximum values of relative water losses are obtained when the depth of the water basin is about a quarter of the asteroid's diameter, and α~30°. As the relative depth increases above 0.7, the losses become virtually constant. The losses depend significantly on the impact velocity, and at 12 km/s the maximum average water loss is less than 2%.

IMPACT EROSION OF EARLY OCEAN:
Estimates of the possible shallowing of the early ocean were made within the framework of the classical theory of the Earth's formation [6]. It was assumed that at the time when the growing Earth still has to accumulate a certain small percentage p of its current mass to reach its final state, an ocean of depth h exists. The remaining objects in the Earth's feeding zone are distributed by mass according to a power law with an exponent q=11/6, corresponding to a system with intense fragmentation [6]. Water losses were calculated on the basis of equations relating water losses to the growth of the planet mass, using the obtained dependencies of losses on the relative water depth and assuming constant impact velocity V.

The losses are sensitive to p and V. If p=1%, then by the end of the planet's growth an ocean 1 km deep becomes shallower approximately by 50% at V=20 km/s, by 30% at V=15 km/s and by 20% at V=12 km/s. At an initial depth of 300 m, the losses are 75, 50 and 30% respectively. For h=1 km, if p=2%, h decreases by 80, 50 and 35%, and if p=0.5%, by 30, 20 and 10%. The impact erosion of ocean must be taken into account in the water balance of the early Earth in addition to outgassing from the Earth interior and water delivery by water-rich objects.

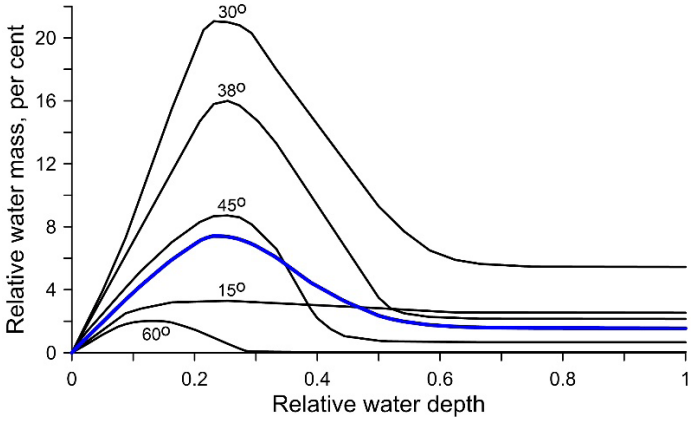


Fig. 1. The ratio of the water mass ejected into space to the impactor mass as a function of the ratio of the ocean depth to the impactor diameter. The values of impact angles are indicated at the curves. The impact velocity is 20 km/s. The blue curve shows the mass of ejected water averaged over angles

ACKNOWLEDGMENTS:
This work was done under the state assignment of the Ministry of Science and Higher Education of the Russian Federation No. 125012200624-5.

REFERENCES:

[1] Wilde S. A., Valley J. W., Peck W. H., Graham C. M. Evidence from detrital zircons for the existence of continental crust and oceans on the Earth 4.4.Gyr ago // Nature. 2001. V. 409. P. 175–178. DOI: 10.1038/35051550.
[2] Peck W. H., Valley J. W., Wilde S. A., Graham C. M. Oxygen isotope ratios and rare earth elements in 3.3 to 4.4 Ga zircons: Ion microprobe evidence for high $\delta^{18}O$ continental crust and oceans in the Early Archean // Geochimica et Cosmochimica Acta. 2001. V. 65. No. 22. P. 4215–4229. DOI: 10.1016/S0016-7037(01)00711-6.
[3] Cameron E. M., Blum T. B., Cavosie J. et al. Evidence for oceans pre-4300 Ma confirmed by preserved igneous compositions in Hadean zircon // American Mineralogist. 2024. V. 109. P. 1670–1681. DOI: 10.2138/am-2023-9180.
[4] Shuvalov V. V. Numerical simulation of material ejection into the atmosphere Induced by oblique Impacts of ten-kilometer-diameter asteroids into the ocean // Izvestiya, Physics of the Solid Earth. 2023. V. 59. P. 452–459. DOI: 10.1134/S1069351323030126.
[5] Shuvalov V. V. Multi-dimensional hydrodynamic code SOVA for interfacial flows: application to the thermal layer effect // Shock Waves. 1999. V. 9. No. 6. P. 381–390. DOI: 10.1007/s001930050168.
[6] Pechernikova G., Vityazev A. Impacts and evolution of early Earth // Catastrophic Events Caused by Cosmic Objects. Dordrecht: Springer, 2008. P. 333–350. ISBN 978-1-4020-6451-7.

MATHEMATICAL MODELING OF A MICROMETEORITE IMPACT

E. M. Sorokin
Vernadsky Institute of Geochemistry and Analytical Chemistry RAS
Moscow 119991, Russia, egorgeohim@ya.ru

KEYWORDS:
micrometeoroid impact, silicate melt, nanophase metallic iron, $npFe^0$, FeO reduction, space weathering, Spheral, M-ANEOS

INTRODUCTION:
Nanophase metallic iron ($npFe^0$) is one of the principal products of space weathering and strongly affects the optical and magnetic properties of lunar regolith [1, 2]. In the author's laser-impact experiments, metallic-iron particles formed within silicate melt without an external hydrogen source [3, 4]. Subsequent microscopy of Luna-20 and Chang'e-5 regolith revealed $npFe^0$ spherules not only on grain surfaces but also inside impact glass. In Chang'e-5 agglutinate glass, chains and clusters of 10-nm to submicrometer spherules contained up to 4.5 wt.% Ni, 6 wt.% P and 8 wt.% S, while mass-balance estimates indicated a surrounding melt feeding zone extending to approximately 3–4 spherule radii. These observations suggest that impact-generated melt itself can be a reaction medium for in situ iron reduction and subsequent nucleation and growth of $npFe^0$. The aim of the present work was therefore to quantify the mass, connected geometry, temperature, pressure, lifetime and energy content of a realistic micrometeoroid-impact melt and to evaluate, as an energetic upper-bound test, whether this reservoir could supply the enthalpy required for FeO reduction in an Fe-bearing silicate analogue. Numerical studies traditionally determine impact melting from peak shock pressure and subsequent release. Calculations for impact velocities of 10–80 km/s showed that the melt zone is commonly flattened rather than spherical [5]. Strength and deformation can substantially increase heating after passage of the shock: inclusion of friction and plastic work reduced the velocity required to melt a mass equal to 10% of the projectile from about 10 to 6 km/s [6], while plastic heating may dominate melt production over approximately 7.5–12.5 km/s depending on rock strength [7]. At higher velocities the process shifts toward vaporization: three-dimensional simulations of a ~30 km/s micrometeoroid impact produced pressures above 100 GPa, temperatures above 10,000 K and almost complete vaporization of the silicate projectile [8]. For porous lunar regolith, ejecta yields extrapolated to porosity 0.9 reached about 20 projectile masses at 90 K and 30 projectile masses at 385 K [9]. Direct three-dimensional calculations at ~100-μm scale that simultaneously resolve multiphase melt, its connected geometry, energy content, vapor and phase-resolved ejecta, and that provide quantitative initial conditions for subsequent redox modeling, remain limited.

MODEL AND CALCULATION CONDITIONS:
The impact was modeled with Spheral using a mesh-free Lagrangian particle method in which moving mass elements carry density, velocity, internal energy and material state. The calculation solved conservation of mass, momentum and internal energy in the general form $d\rho/dt=-\rho\nabla-v$, $dv/dt=\rho^{-1}\nabla\cdot\sigma$ and $du/dt=\rho^{-1}\sigma:\nabla v$, where ρ is density, v is velocity, u is specific internal energy and σ combines pressure with resistance to shape change. Shock dissipation was treated numerically over several particle spacings. The M-ANEOS multiphase thermodynamic model related density and internal energy to pressure, temperature and phase state and distinguished solid, liquid, solid–liquid and condensed–vapor mixtures; liquid and vapor fractions in two-phase states were obtained by the specific-volume lever rule. Pressure-dependent rock strength was included (shear modulus 22.7 GPa, zero-pressure strength 0.60 GPa and limiting strength 3.5 GPa). Calibration calculations showed that shear-driven damage pro-

duced nonphysical damage in molten material, so the final run retained only tensile failure, activated above 100 MPa.

A spherical forsterite projectile 100 μm in diameter impacted a forsterite target normally at 10 km/s. The initial temperature was 296.9 K; the discretized projectile mass was 1.700 μg and kinetic energy 0.08501 J. The target dimensions were 0.75×0.75×0.45 mm. A 5-μm particle spacing gave 2,025,000 target and 4,224 projectile particles, and the evolution was followed to 37 ns. A material element was assigned to the melt domain when its liquid mass fraction was at least 0.05; connected liquid-bearing elements were grouped into clusters, and retained melt was separated from ejecta. Detailed handoffs were analyzed at 25, 30 and 37 ns. In addition to total internal energy, a conservative "superheat" reserve was calculated relative to the M-ANEOS 2163-K reference state, because this energy can in principle be consumed by chemical reactions while the material remains at or above the reference melt temperature. Forsterite was used as a thermodynamic silicate reference; iron chemistry was not solved during the hydrodynamic stage, and FeO reduction was assessed only as a post-processed energetic feasibility test.

RESULTS AND DISCUSSION:

Peak pressure reached 132.3 GPa at 4.75 ns and peak temperature 17,171 K at 9.0 ns, but these are local extrema and do not represent the bulk melt. The liquid reservoir developed much later: maximum target liquid mass and volume, 0.859 μg and $3.14 \cdot 10^{-13}$ m^3 (314 pL), both occurred at 23.5 ns. At 25 ns, 0.836 μg of liquid remained associated with the target; 0.833 μg (99.6% of retained liquid) belonged to one connected cluster with dimensions approximately 198×198×117 μm and an equivalent spherical diameter of 84 μm. The liquid-mass-weighted mean temperature was 3365 K (10–90% range 2156–6007 K), whereas at 30 ns it was still 3081 K (2062–5967 K; median 2279 K). During the same interval the liquid-mass-weighted mean pressure fell from 2.35 to 0.69 GPa, and by 30 ns 68.1% of retained liquid was already below 1 GPa. Thus a large, hot melt reservoir persists after the strongest shock compression has largely relaxed.

Table 1. Key parameters of the final 37-ns, 5-μm calculation

Parameter	Value	Interpretation
Maximum pressure/ temperature	132.3 GPa/17,171 K	Local extrema at 4.75/9.0 ns
Maximum liquid mass/ volume	0.859 μg/314 pL	50.5% projectile mass; 23.5 ns
Retained melt at 25 ns	0.836 μg; 308 pL	99.6% in one connected cluster
Largest retained cluster, 25 ns	0.833 μg; 198×198×117 μm	d_eq=84 μm
Liquid-weighted T, 25/30 ns	3365/3081 K	Medians 2535/2279 K
Melt excess energy, 25/30 ns	2.40/1.58 mJ above 2163 K	4.66/3.29 mJ above cold state
FeO-reduction energy scale, 25/30 ns	0.29/0.22 mJ	10 wt.% FeO analogue; reserve 8.1×/7.1×
Vapor/total ejecta at 30 ns	14.7 ng/3.515 μg	0.87%/207% of projectile mass

The retained melt contained 4.66 mJ of excess internal energy above the initial cold state at 25 ns and 3.29 mJ at 30 ns. More conservatively, the energy above the 2163-K reference state was 2.40 and 1.58 mJ, respectively. To express this reservoir in chemically meaningful terms, $FeO(l) \rightarrow Fe(l) + 1/2\ O_2(g)$ was used as an energetic reference. NIST-JANAF thermochemical functions give a reaction enthalpy of approximately 253 kJ/mol near 3000 K [10]. For a hypothetical silicate containing 10 wt.% FeO, complete reduction of the FeO present in the retained liquid would require only ~0.29 mJ at 25 ns and ~0.22 mJ at 30 ns. The available energy above 2163 K therefore exceeds this stoichiometric enthalpy scale by factors of ~8.1 and ~7.1. This comparison is an energetic feasibility bound rather than a predicted reduc-

tion yield: actual Fe^0 production additionally requires sufficiently reducing oxygen fugacity, oxygen removal from the reacting volume, favorable FeO activity and sufficiently rapid reaction and diffusion kinetics. Vaporization remained secondary to melting at 10 km/s. The target vapor mass increased to 14.7 ng by 30 ns, about 43 times smaller than the retained liquid mass, while total ejecta reached 3.515 μg (2.07 projectile masses). At 37 ns, 0.567 μg of retained liquid still remained, with a liquid-mass-weighted mean temperature of 2654 K; total ejecta reached 5.109 μg and the formal vapor mass 19.1 ng. The later vapor value is less robust because very dilute material first crossed the lower-density boundary of the M-ANEOS table after 30 ns. The dominant high-temperature reservoir relevant to $npFe^0$ formation is therefore the retained silicate melt rather than the vapor plume.

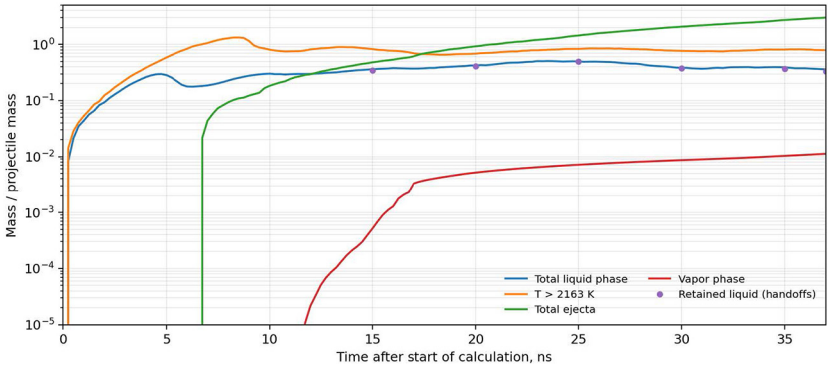


Fig. 1. Evolution of total target liquid, material hotter than 2163 K, ejecta and vapor masses normalized to projectile mass in the final 37-ns calculation. Markers show retained-liquid handoffs; maximum liquid mass occurs at 23.5 ns, while 30 ns is the last strictly EOS-clean handoff

The final 5-μm calculation supersedes the earlier 6.25-μm baseline. No side or bottom boundary disturbance occurred during 37 ns, and the relative total-energy error was $2.9 \cdot 10^{-13}$. All states remained inside the validated M-ANEOS table through 30 ns; at 37 ns only 28 very low-density nodes, with a total mass of 11.3 ng, fell below its 100 kg/m^3 density limit. Consequently, the 25-ns handoff is most representative of the maximum connected melt reservoir, whereas the 30-ns handoff provides the most conservative starting state for subsequent thermo-chemical modeling: 0.633 μg of retained liquid, liquid-weighted mean temperature 3081 K, mean pressure 0.69 GPa and 68.1% of liquid already below 1 GPa.

CONCLUSION:

A 100-μm forsterite projectile impacting at 10 km/s produces a compact, flattened and predominantly retained silicate melt reservoir whose maximum mass (0.859 μg) appears ~14 ns after the temperature maximum. Near its maximum development, one connected ~200-μm-wide melt body contains >0.83 μg of liquid and several millijoules of excess internal energy. Even after substantial pressure release at 30 ns, 0.633 μg remains liquid at a liquid-weighted mean temperature of ~3080 K. A conservative energy-budget comparison shows that, for a hypothetical 10 wt.% FeO-bearing analogue, the melt superheat above 2163 K is about seven times larger than the enthalpy required to reduce all FeO to metallic Fe. Thus the gross thermal-energy budget is sufficient in magnitude and does not by itself preclude $npFe^0$ formation; the actual yield remains controlled by redox conditions, oxygen escape, FeO activity and reaction/diffusion kinetics. The calculated three-dimensional phase, energy, pressure and velocity fields provide physically constrained initial conditions for subsequent chemical-reduction modeling and for quantitative comparison of real micrometeoroid impacts with laser-impact experiments.

REFERENCES:

[1] Hapke B. Space weathering from Mercury to the asteroid belt // J. Geophysical Research. 2001. V. 106(E5). P. 10039–10073. https://doi.org/10.1029/2000JE001338.
[2] Pieters C.M., Noble S.K. Space weathering on airless bodies // J. Geophysical Research: Planets. 2016. V. 121. P. 1865–1884. https://doi.org/10.1002/2016JE005128.
[3] Sorokin E.M., Yakovlev O.I., Sluta E.N., Gerasimov M.V., Zaitsev M.A., Shcherbakov V.D., Ryazantsev K.M., Krasheninnikov S.P. Chemical composition of the nanophase iron ($npFe^0$) obtained in the laser experiment // 54th Lunar and Planetary Science Conference. 2023. Article 2156.
[4] Sorokin E.M., Yakovlev O.I., Sluta E.N., Gerasimov M.V., Zaitsev M.A., Shcherbakov V.D., Ryazantsev K.M., Krasheninnikov S.P. Experimental data on the formation of nanophase iron in the lunar soil // Geochemistry International. 2025. V. 63(2). P. 129–152.
[5] Pierazzo E., Vickery A.M., Melosh H.J. A reevaluation of impact melt production // Icarus. 1997. V. 127. P. 408–423. https://doi.org/10.1006/icar.1997.5713.
[6] Kurosawa K., Genda H. Effects of friction and plastic deformation in shock-comminuted damaged rocks on impact heating // Geophysical Research Letters. 2018. V. 45. P. 620–626. https://doi.org/10.1002/2017GL076285.
[7] Manske L., Wünnemann K., Kurosawa K. Quantification of impact-induced melt production in numerical modeling revisited // J. Geophysical Research: Planets. 2022. V. 127. Article e2022JE007426. https://doi.org/10.1029/2022JE007426.
[8] Hyodo R., Genda H., Madeira G. Pollution resistance of Saturn's ring particles during micrometeoroid impact // Nature Geoscience. 2025. V. 18. P. 44–49. https://doi.org/10.1038/s41561-024-01598-9.
[9] Verkercke S. et al. A thermal origin to the asymmetry of the permanent dust cloud at the Moon // J. Geophysical Research: Planets. 2025. V. 130. Article e2025JE009259. https://doi.org/10.1029/2025JE009259.
[10] Chase Jr., M.W. NIST-JANAF Thermochemical Tables, Fourth Edition // J. Physical and Chemical Reference Data. 1998. Monograph 9. 1951 p.

EXPERIMENTAL MODELING OF THE FORMATION OF THE FUSION CRUST OF STONY METEORITES

E. V. Petrova, V. I. Grokhovsky, A. A. Popov, A. F. Kokorin, G. A. Yakovlev
Ural Federal University, Ekaterinburg 620002, Russia
evgeniya.petrova@urfu.ru

KEYWORDS:
meteorites, fusion crust, ablation, emission spectra, modeling

INTRODUCTION:
Meteoroid ablation during passage through the Earth's atmosphere is accompanied by processes of radiation, mass loss, fragmentation, and the formation of a fusion crust on the fragment surfaces. A review of some aspects of these processes and the structure of the fusion crust is given in [1, 2]. Experimental modeling of meteoroid ablation under atmospheric influence was previously conducted under laboratory conditions using a plasma torch [3–6]. The emission spectra were recorded during the ablation modeling and decoded in [4–6]. The main goal of this study is to investigate the ablation process through experimental modeling. In this series of experiments, we model the final stage of the light trajectory of fireballs on samples of stony meteorite material and compare the recorded emission spectra with the composition of the internal material of the meteorites and the resulting artificial fusion crust.

MATERIALS AND METHODS:
Fragments of ordinary chondrites Chelyabinsk LL5, Tsarev L5, Calama 009 L6, Gandom Berian 011 LL3, and Kainsaz CO3.2 were cut into ~7×7×50 mm bars. Experimental modeling of atmospheric ablation was performed using a setup consisting of a plasmatron with a high-frequency gas discharge in combination with an aerodynamic device for generating gas flows of specified parameters using a Laval nozzle equipped with an optical pyrometer, a CCD camera, and a diffraction grating with 600 lines/mm. The measured spectra were processed using the RSpec program. Polished sections of the samples with the artificial fusion crust were made for optical microscopy (Axiovert 40 MAT) and SEM (Zeiss FE-SEM ΣIGMA VP with EDS X-max 80). Samples of artificial fusion crust, natural fusion crust, and internal meteoritic material were also prepared in powder form. Elemental composition measurements were performed using Perkin Elmer Elan 9000 and Perkin Elmer Optima 2100 DV spectrometers.

RESULTS AND DISCUSSION:
The texture and structure of the artificial fusion crust coincide with natural chondrite crust. The inner and outer layers of the fusion crust are distinguishable: the inner layer has characteristic cracks filled with molten metal and troilite, and the outer layer has vesicles and dendritic crystals, respectively.

The artificial ablation spectra of the chondrites Tsarev L5, Calama 009 L6, Gandom Beryan 011 LL3, and Chelyabinsk LL5 contain lines of Na, Ca, Mg, Cr, and Fe. In the green and yellow (500-590 nm) regions, the spectra have a pattern characteristic of meteoritic material. A similar spectrum is also observed in spectral observations of fireballs, such as the spectrum of the Smalyavichi fireball [7], indicating the relevance of the modeling performed. In the blue region (380–500 nm), more intense lines are observed than in spectral observations of fireballs. This is due to the lack of scattering in the large air gap between the object and the sensor, which is typical for fireball observations.

Chemical analysis of the composition of the artificial and natural fusion crusts shows that the quantitative abundance of elements in the fusion crust varies compared to the composition of the core material. For example, the artificial fusion crust has lower abundances of Na, Mg, Al, Ca, and

Fe compared to the core material. This is consistent with the observation of these lines in the measured spectra during ablation modeling. Furthermore, for example, both the artificial and natural fusion crusts of the Chelyabinsk LL5 chondrite exhibit elevated contents of Sc, Ti, V, Cr, Mn, Cu, Zn, Ga, Zr, Ba, and Pb compared to the internal material of the chondrite and lower contents of Mg, Al, Fe, Ge, and Os.

CONCLUSION:

The plasmatron simulation experiments effectively reproduce the processes occurring during the final stages of a bolide's luminous trajectory. Analysis of the chemical composition and structure of the artificial fusion crust is consistent with the obtained spectral data, the structure of the natural fusion crust preserved in some samples, and the composition and structure of the internal chondritic matter.

ACKNOWLEDGMENTS:

This work was supported by the Ministry of science and higher education of the Russian Federation, the project no. FEUZ-2026-0009.

REFERENCES:

[1] Petrova E.V., Grokhovsky V.I. The Fusion crust of meteorites is the result of changes in the meteoroid material under the influence of atmospheric ablation // Solar System Research. 2026. V. 60, Article 28. https://doi.org/10.1134/S0038094625601239.

[2] Petrova E.V., Grokhovsky V.I, Kartashova A.P. Fusion crust of stony meteorites: From the observation spectrum to the initial meteoroid matter // Icarus. 2026. V. 456. Article 117147. https://doi.org/10.1016/j.icarus.2026.117147

[3] Kopysov A.S., Petrova E.V., Kokorin A.F. Experimental modelling of the fusion crust formation by heating in plasmatron // Meteorit. Planet. Sci. 2018. 53(SI). Article A144. https://doi.org/10.1111/maps.13146.

[4] Loehle S., Zander F., Hermann T. et al. Experimental simulation of meteorite ablation during Earth entry using a plasma wind tunnel // Astrophys. J. 2017. Article 837. https://doi.org/10.3847/1538-4357/aa5cb5.

[5] Helber B., Dias B., Bariselli F. et al. Analysis of meteoroid ablation based on plasma wind-tunnel experiments, surface characterization, and numerical simulations // Astrophys. J., 2019. V. 876. Article 120. https://doi.org/10.3847/1538-4357/ab16f0.

[6] Wang L., Dang L., Yang L.W. et al. Study of iron and stony meteorite ablation based on simulation experiments in an arc heater // Astrophys. J. 2024. V. 962. Article 23. https://doi.org/10.3847/1538-4357/ad063c.

[7] Grokhovsky V.I., Petrova E.V., Yakovlev G.A. et al. Matching of the compositions of chondrites and their fusion crust with the emission spectra of meteoroids // Meteorit. Planet. Sci. 2025. V. 60(SI). Article 5208. https://doi.org/10.1111/maps.70033.

ON ORGANIC COMPOUNDS FORMATION INDUCED BY THE MICROWAVE BREAKDOWN AND PLASMA-DUST CLOUDS GENERATED FROM NITROGEN — CARBON DIOXIDE ATMOSPHERES AND PERIDOTITE

M. A. Zaitsev[1], A. S. Kuzovchikova[1], V. D. Stepakhin[2], V. D. Borzosekov[3], E. M. Sorokin[4], T. E. Gayanova[2], A. A. Letunov[2], E. V. Voronova[2], D. V. Malakhov[2], K. M. Ryazantsev[4], N. N. Skvortsova[2], A. S. Sokolov[2], L. A. Konovalova[5], T. I. Morozova[1], S. M. Kuzovchikov[6], K. V. Naumova[2], M. V. Gerasimov[1]

[1] *Space Research Institute RAS, Moscow 117997, Russia*
mzaitsev@cosmos.ru
[2] *Prokhorov General Physics Institute RAS, Moscow 119991, Russia*
[3] *RUDN University, Moscow, Russia, borzosekov@fpl.gpi.ru*
[4] *Vernadsky Institute of Geochemistry and Analytical Chemistry RAS Moscow, Russia*
[5] *National University of Science and Technology MISIS, Moscow, Russia*
[6] *N. N. Semenov Federal Research Center for Chemical Physics Moscow, Russia*

KEYWORDS:
Organic compounds, OC, abiotic synthesis, plasma-dust clouds, peridotite, chondritic matter simulant, microwave discharge, pyrolysis gas chromatography, mass-spectrometry, Pyr-GC/MS, high-molecular organics

INTRODUCTION:

The abiotic type of complex OC formation from initial inorganic or/and organic substances has been repeatedly showed and approved by different types of model experiments, which simulate different processes on the certain space bodies or in the cosmic medium. Different targets surrounded by model atmospheres, or placed in vacuum, or «persistent containers», were exposed to different energy sources: ultraviolet (UV-) and X-ray irradiation, spark discharges, pulsed laser irradiation, hypervelocity impacts, shock waves, etc. The sources of essential elements for OC formation can be both mineral sample, imitating the regolith or rock of considered space bodies, and surrounded gas medium (if any) containing different combinations of gases that represent actual or hypothetical atmosphere of the space bodies (H_2, N_2, CO, CO_2, NH_3, O_2, CH_4, H_2O, etc.)

One of the main issues of abiotic synthesis is the possible catalytic role determination of the plasma-dust medium in the OC formation. Plasma-dust medium acts as a source of charged particles, UV radiation, radicals, and particles in an excited state. These phenomena significantly increase the number of possible chemical reactions and their rate. Solid particles in plasma regions, where heat fluxes are not sufficient for evaporating or melting them, can act as a heterogeneous catalyst [1].

The experimental method we used for generating plasma–dust clouds involved a discharge initiated by microwave irradiation of powdered samples [2]. It is also necessary to prepare a model starting materials that replicates the physical and mechanical properties and the mineralogical composition of the simulated environment [3, 4]. For that purpose peridotite, consisting of olivines and pyroxenes – the main constituents of stony meteorites [5], was used as a mineral analogue of the matter of stony meteoroids in our experimental simulations of plasma-dust medium conditions.

EXPERIMENTS:

Initial peridotite was crashed and pulverized to a fine powder: first with a steel Abikh's mortar and then – with an agate mortar. A pulverized peridotite sample (200 mg of mass) was subjected to a single microwave pulse of 8 ms duration inside the plasma chemical reactor. The microwave radi-

ation source was a gyrotron of 75 GHz frequency, and 400 kW of power. This power corresponds to an average power density across the beam cross-section of 14 kW·cm^{-2} and a root-mean-square electric field strength of 2.3 kV/cm. We used N_2:CO_2 (5:95 — "carbon-poor" and 50:50 v.v. — "carbon-rich") gas mixtures at 1 atm to create "neutral" types of atmospheres inside the plasma chemical reactor. N_2 and CO_2 were at the same time the main sources of N, C and O essential for OC formation, H_2O from peridotite was the main source of H.

Previous technological experiments with 200 mg of peridotite in argon atmosphere showed successful breakdown. Nevertheless the atmosphere of N_2:CO_2 5:95 v.v. showed the absence of breakdown, so it was decided to use the nickel wire initiator. As it was founded with the high-speed filming, microwave discharge takes too much time to pass through this type of gas medium and reach the solid sample. Therefore, the initiator was placed even closer to the peridotite powder (40 mm) as it is usually placed (80 mm from the powder, on the top of the quartz tube). That increased the time of the discharge action to the peridotite powder.

We used Pyr-GC/MS ("Chromatec-Crystal 5000.2 GC/MSD" analytical complex) to characterize the organics which could form during microwave treatment of peridotite. For that purpose stepwise heating of initial and microwave treated peridotite was conducted at 150, 300, 450, 600 and 800°C under the helium flow. Volatile products of each step were accumulated in a capillary cryogenic trap and then — analyzed with GC/MS.

In order to analyze volatile organics which could form and contain in gas medium we purged the certain part of the gas phase from the plasma chemical reactor through the complex 0.25×3.5" adsorption tubes (filled with "Tenax GR", "Carbotrap B" and "Carbosieve SIII"). The same procedure was also performed before every microwave experiment in the chamber to be sure that there were not any initial organic impurities. The tubes were then treated with the GS/MS analytical complex described above also equipped with a dual stage thermal desorption system.

In order to protect all the exposed materials against contamination with organic substances from the laboratory environment, the preparation of both the chamber and samples for the microwave discharges, as well as the analytical preparation of the irradiated material, was carried out with all necessary precautions.

RESULTS AND THEIR DISCUSSION:

Preliminary characterization of the GC/MS-chromatograms showed that microwave treated peridotite contains only small amounts of high-molecular (soot-like) organics as benzene and toluene – main products of their thermal destruction – comes out from the material only at the temperature of 450°C and above. Also peridotite treated in N_2:CO_2 5:95 v.v. atmosphere gave even more quantities of volatile products of thermal destruction of organics than peridotite treated in N_2:CO_2 5:95 v.v. atmosphere. This effect could be connected with even less speed of the microwave discharge coming through the gas medium contained more carbon dioxide [6].

CONCLUSION:

There was experimentally showed that microwave irradiation of peridotite simulating micrometeoroid induced plasma-dust environment generates high-molecular organics containing carbon from the model N_2:CO_2 atmospheres.

ACKNOWLEDGMENTS:

This work was supported in part by the Russian Science Foundation (project No. 25-22-00505).

REFERENCES:

[1] Tu X., Whitehead J.C., Nozaki T. Plasma catalysis: fundamentals and applications. Springer Series on Atomic, Optical, and Plasma Physics. V. 106. Berlin: Springer, 2019. 348 p.

[2] Batanov G.M., Kossyi I.A. Pulsed microwave discharges in powder mixtures: Status, problems, and prospects // Plasma Phys. Rep. 2015. V. 41. P. 847–857. https://doi.org/10.1134/S1063780X15090020.
[3] Snytnikov V.N. Abiogenic synthesis of prebiotic matter for the Earth's biosphere as a stage of self-organization on an astrophysical and paleontological time scale // Paleontol. J. 2007. V. 41. P. 473–480. https://doi.org/10.1134/S0031030107050012.
[4] Peters S., Semenov D.A., Hochleitner R., Trapp O. Synthesis of prebiotic organics from CO2 by catalysis with meteoritic and volcanic particles // Scientific Reports. 2023. V. 13. Article 6843. https://doi.org/10.1038/s41598-023-33741-8.
[5] Rubin A.E. // Meteoritics and Planetary Science. 1997. V. 32. P. 231–247. DOI: 10.1111/j.1945-5100.1997.tb01262.x.
[6] Artem'ev K. V., Batanov G.M., Berezhetskaya N.K. et al. Parameters of a Subthreshold Microwave Discharge in Air and Carbon Dioxide as a Function of Microwave Field at Different Gas Pressures // Plasma Physics Reports. 2020. V. 46. No. 9. P. 927–935. https://doi.org/10.1134/S1063780X20090019.

SELECTION OF MINERAL SUPPLEMENTS FOR LUNAR REGOLITH SIMULANTS IMPROVING THE CONDITIONS OF MICROWAVE BREAKDOWN AND THE FORMATION OF PLASMA-DUST CLOUDS

A. S. Kuzovchikova[1], V. D. Stepakhin[2], V. D. Borzosekov[3], E. M. Sorokin[4], M. A. Zaitsev[1], T. E. Gayanova[2], V. V. Gudkova[2,3], A. A. Letunov[2], E. V. Voronova[2], D. V. Malakhov[2], Ryazantsev K. M.[4], N. N. Skvortsova[2], A. S. Sokolov[2], E. A. Obraztsova[2,5], T. I. Morozova[1], S. M. Kuzovchikov[6], K. V. Naumova[2], M. V. Gerasimov[1]

[1] *Space Research Institute RAS, Moscow 117997, Russia*
Vasiljek_anna@mail.ru
[2] *Prokhorov General Physics Institute RAS, Moscow 119991, Russia*
[3] *RUDN University, Moscow, Russia*
[4] *Vernadsky Institute of Geochemistry and Analytical Chemistry RAS Moscow, Russia*
[5] *Moscow Institute of Physics and Technology* (*National Research University*) *Dolgoprudny, Russia*
[6] *N. N. Semenov Federal Research Center for Chemical Physics Moscow, Russia*

Keywords:

lunar regolith simulant, microwave discharge, plasma-dust clouds, optical emission spectroscopy, OES, scanning electron microscopy, SEM, X-ray diffraction, XRD, olivine series, pyroxene series, pyrrotite

Introduction:

To investigate the abiotic synthesis of organic compounds occurring within the catalytic environment of plasma–dust clouds, it is necessary to prepare model starting materials that replicate the physical and mechanical properties and the mineralogical composition of the simulated environment [1, 2]. One method for generating plasma–dust clouds involves a discharge initiated by microwave irradiation of powdered mixtures [3]. However, the materials typically employed for this purpose generally lack a sufficient concentration of substances capable of efficiently absorbing microwave radiation to initiate the discharge; consequently, electrical breakdown does not occur and the plasma–dust cloud fails to form. This issue arises, for example, when using mixtures that simulate lunar regolith, which primarily consists of olivines and pyroxenes [4].

The aim of our experimental research is to select mineral components that enhance the microwave absorption capacity of lunar regolith simulants while remaining consistent with the nature of the simulated environment.

EXPERIMENTS:

This paper presents the results of a two-year experimental campaign in which minerals from different classes were tested for their ability to absorb microwave radiation: iron oxides and sulfides, olivine- and pyroxene-series minerals with varying Mg/Fe ratios, and meteoritic materials (ordinary chondrite and iron meteorite). All of these minerals occur in Solar System regoliths, asteroids, and meteoroids. The minerals exhibiting the strongest microwave absorption were planned to be added to lunar regolith simulants in various proportions to determine the minimum mass at which electrical breakdown still occurs and a plasma-dust cloud is formed.

All minerals were preliminarily ground in Abikh and agate mortars to a fine powder. Each sample (mass 200 mg) was subjected to a single microwave pulse of 8 ms duration. The microwave source was a gyrotron (frequency f=75 GHz, power 400 kW). This power corresponds to an average power

density across the beam cross-section of 14 kW·cm^{-2} and a root-mean-square electric field strength of 2.3 kV/cm. An argon atmosphere was used in the plasma-chemical reactor to provide an inert environment. Experiments with the lunar regolith simulant LMS-1D have been conducted previously [5], however, to ensure experimental rigor, it was necessary to perform repeat tests under identical conditions alongside our samples and to use the same mass for all samples.

Table 1. List of samples selected for the experiments and breakdown results

Mineral name or composition of the tested mixture	Chemical formula	Breakdown result
Chrysolite	$(Mg, Fe)_2SiO_4$	Successful, with initiator
Diopside	$CaMgSi_2O_6$	Successful
Chrome-diopside	$CaMgSi_2O_6$	Successful, with initiator
Iron-rich olivine	$(Mg, Fe)_2SiO_4$	Successful, with initiator
Knebelite	$(Mn, Fe)_2SiO_4$	Successful
Hedenbergite	$CaFeSi_2O_6$	Successful, with initiator
Ordinary chondrite from Western Sahara	–	Successful
Magnetite	Fe_3O_4	Successful
Forsterite	$Mg_2[SiO_4]$	Successful
Pyrrhotite	$Fe_{1-x}S$	Successful
NWA 6203 with graphite and silicate inclusions	–	No stable plasma–dust cloud formation
Bronzite	$(Mg, Fe)_2[Si_2O_6]$	Successful
Ilmenite	$FeTiO_3$	Successful
LMS-1D	–	Successful, with initiator
LHS-1D	–	Successful, with initiator

As shown in the table, the strongest microwave (MW) absorption was observed for bronzite, diopside, knebelite, magnetite, forsterite, and pyrrhotite. Ilmenite, although it underwent breakdown without an initiator, performed worse than other minerals such as pyrrhotite and bronzite. For successful breakdown of chrysolite, chrome-diopside, iron-rich olivine and hedenbergite, a nickel initiator was required. The meteorite NWA 6203, containing graphite and silicate inclusions, did not produce a stable plasma-dust cloud. Breakdown and formation of a plasma-dust cloud for the LMS-1D and LHS-1D simulants under these conditions were also achieved only in the presence of an initiator, validating our objective of identifying strongly absorbing minerals to be added to the simulants to enable self-sustained breakdown of the mixtures.

Comparative X-ray diffraction (XRD) analysis of the initial and microwave-irradiated samples revealed no changes in their structural properties. However, scanning electron microscopy (SEM) of polished sections of the samples revealed the formation of nanoscale iron in some pyroxene and olivine samples, as well as characteristic features of recrystallization from a melt with rapid quenching.

The most effective supplements were bronzite and pyrrhotite. These samples exhibited the highest microwave absorption and generated the longest-lived plasma-dust clouds. In subsequent experiments, these minerals were used as additives to the LMS-1D simulant at different mass fractions (10 and 30%). Mixture experiments were conducted under the same conditions as the pure mineral tests. For all mixtures containing bronzite, a nickel initiator was required to achieve breakdown. Pyrrhotite performed better: even a low (10%) pyrrhotite content allowed experiments to be conducted without an initiator.

CONCLUSION:

Testing of minerals from different classes for their ability to absorb microwave radiation showed that pyrrhotite is the most promising supplement for lunar regolith simulants. Even a small addition (10%) of this mineral enables experiments to be performed without a nickel initiator, thereby eliminating the influence of discharges originating on the initiator. Moreover, pyrrhotite is present in small amounts in lunar regolith samples collected by the Apollo missions [6], meaning that its addition does not contradict the nature of the simulated material.

It is noteworthy that within the olivine and pyroxene series, minerals exhibited markedly different responses to microwave radiation; however, no simple systematic trend (e.g., as a function of the Fe/Mg ratio) could be identified. This behavior likely results from the combined action of several factors.

ACKNOWLEDGMENTS:

This work was supported by the Russian Science Foundation (project No. 25-22-00505).

REFERENCES:

[1] Snytnikov V. N. Abiogenic synthesis of prebiotic matter for the Earth's biosphere as a stage of self-organization on an astrophysical and paleontological time scale // Paleontol. J. 2007. V. 41. P. 473–480.

[2] Peters S., Semenov D. A., Hochleitner R., Trapp O. Synthesis of prebiotic organics from CO_2 by catalysis with meteoritic and volcanic particles // Scientific Reports. 2023. V. 13. Article 6843.

[3] Batanov G. M., Kossyi I. A. Pulsed microwave discharges in powder mixtures: Status, problems, and prospects // Plasma Phys. Rep. 2015. V. 41. P. 847–857.

[4] Florensky K. P., Bazilevsky A. T., Nikolaeva O. V. Lunar Soil: Properties and Analogs. Moscow: IGAKh AN SSSR, 1975. 72 p. (in Russian).

[5] Borzosekov V. D., Akhmadullina N. S., Sokolov A. S. et al. Obtaining plasma–dust clouds from meteoritic matter, its analogs and simulants of lunar regolith using microwave discharge // Solar System Research. 2024. V. 58. No. 3. P. 289–314.

[6] Schrader D. L., McCubbin F. M., Juliane Gross J. Sulfides on the Moon: A record of magmatic and impact histories // Geochemistry. 2026., V. 86, Iss. 2, Article126422. https://doi.org/10.1016/j.chemer.2026.126422.

SYNTHESIS OF CARBON NANOTUBES ON METEORITE METAL VIA ALCOHOL DECOMPOSITION

A. S. Bakhmutova[1], G. A. Yakovlev[1,2], V. I. Grokhovsky[1], E. A. Pankrushina[1,2]
[1] *Ural Federal University, Ekaterinburg 620002, Russia, n.s.begun@gmail.com*
[2] *Zavaritsky Institute of Geology and Geochemistry UB RAS Ekaterinburg 620110, Russia*

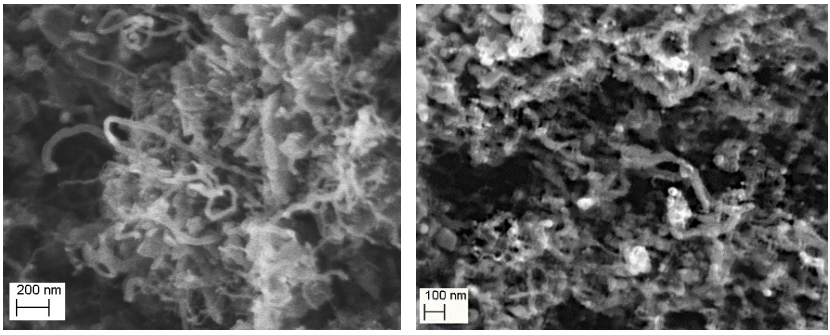
KEYWORDS:
plessite, carbon nanotubes, chemical vapor decomposition, methanol

INTRODUCTION:
It is well established that carbon allotropes found in lunar regolith samples and meteorites exhibit considerable diversity. There are nanodiamonds [1], fullerenes [2], single- and multiwall carbon nanotubes (CNT) [3, 4] among the nanoscale modifications. Various formation mechanisms for these structures have been proposed, grounded in processes that occurred in the early Solar System. The mechanisms underlying the formation of some nanostructures are now largely substantiated [1]. However, the pathway for carbon nanotube synthesis remains a subject of ongoing debate and theoretical conjecture. This study is devoted to synthesis of carbon nanotubes on the meteorite surface via methanol and ethanol decomposition. The chemical vapor deposition (CVD) method was selected, as some researchers have speculated on the possibility of such processes occurring during the formation of certain structures in meteorites [1]. Methanol, one of the most abundant complex organic species in interstellar clouds [5], was chosen as the carbon precursor.

MATERIALS AND METHODS:
The metal parts of the Seymchan pallasite were chosen to be a template of nanotube growth. There were two samples: S11 for the experiment with ethanol and Sm6 for the experiment with methanol. They were prepared using standard metallographic polishing and etching with 1 wt.% nital for 5 minutes. Then several areas were marked on the samples and were analyzed before and after the synthesis of nanomaterials. Extended chemical etching time resulted in an increase of the effective surface area in the plessite zones on the samples surface. We used an ethanol for the experiments since it is well-known method of CNT growth [6], then we used a methanol to simulate CNT growths in extraterrestrial samples. It has been experimentally established that for the synthesis of UHT using methanol a pre-oxidized surface is required, therefore the sample was oxidized: at 600°C, a mixture of distilled water and air was passed into the chamber at 15 kPa for 5 minutes. The CNTs on the samples were synthesized by a pyrolysis of alcohol using the "CVDomna". The metal surface of the samples functioned as both a substrate and a catalyst. The samples were placed into a reaction chamber, then heated to 600°C (S11 sample) or to 550°C (Sm6 sample) temperature at a pressure of 1 kPa. A vapor-gas mixture of ethanol or methanol and air was passed into the reaction chamber for 10 minutes at a linear increase of pressure up to 15 kPa, then they were cooled to 400°C at a pressure of 1 kPa and then cooled under an ambient air. Samples were examined with a Zeiss Axiovert 40 MAT optical microscope and a Zeiss Sigma VP scanning electron microscope equipped with an energy-dispersive X-ray spectroscopy unit. Raman spectra were measured using the LabRam HR Evolution with backscattering geometry. The lateral resolution was 1-2 μm, and the excitation wavelengths were 633 nm.

RESULTS AND DISCUSSION:
Fine-grained plessite was chosen as the main area of study due to its structural complexity. We examined the surface of samples before and after synthesis. On the surface of sample S11, particular attention was paid to the plessite zones. We detected some multiwalled CNTs (MWCNTs) on this

surface after the synthesis. The most probable outer diameter of MWCNTs was 20 nm, accompanied by a considerably high aspect ratio (greater than 50) (Fig. 1a). Raman measurements enable us to conclude that MWCNTs grown on the finer (α+γ) substrate (<0.1 μm, sample S11) possess a more ordered and less defective structure, as evidenced by the higher G1′ band intensity, smaller second-order band widths, and higher aspect ratio (Fig. 2). The narrower linewidth indicates fewer defects, because defects broaden the phonon distribution involved in Raman scattering. Thus, the substrate particle size and the resulting growth environment are key factors determining the structural quality of the MWCNTs.



a) b)

Fig. 1 SEM images of MWCNTs on the surfaces of: a) S11 sample (ethanol precursor); b) Sm6 sample (methanol precursor)

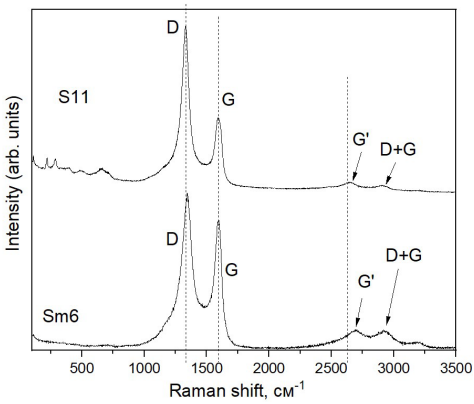


Fig. 2. Raman spectra of MWCNTs on the surface of S11 and Sm6 samples

During the synthesis of MWCNTs on sample S11 using ethanol, simultaneous oxidation of the sample occurred. Raman spectra revealed the presence of hematite in the sample. In contrast, when methanol was used as the carbon precursor, no such oxidation took place, and a series of experiments demonstrated that pre-oxidation of the sample was required prior to the synthesis.

The pre-oxidation of sample Sm6 resulted in the formation of an array of hematite nanowires. On that surface nanomaterials were synthesized. We detected MWCNTs within the plessite zones. The tubes exhibited a curved morphology with an average diameter of 50 nm (Fig. 1b). Encapsulated particles were observed at the tips of the tubes. They are more likely metal particles that suggest a tip-growth catalytic mechanism. The Raman spectra obtained on the surface of Sm6 after the catalytic pyrolysis of methanol contained carbon D and G peaks. The I_D/I_G intensity ratio ($I_D>I_G$) indicates a significant degree of structural disorder [7]. The spectra measured on a plessite surface after the synthesis contained the second-order G′ and D+G band typical to MWCNTs [7] (see Fig. 2).

SUMMARY AND IMPLICATIONS:

In the synthesis experiments conducted on the surface of fine-grained plessite from the Seymchan meteorite, MWCNTs were obtained using both ethanol and methanol as carbon precursors. On sample S11 (ethanol), MWCNTs with a high aspect ratio were produced, and the yield of MWCNTs relative to other carbon forms was also superior to that on sample Sm6 (methanol). Furthermore, synthesis with methanol in our experimental conditions required pre-oxidation. However, from the perspective of modeling the formation processes of MWCNTs in extraterrestrial samples, the experiments with methanol hold greater significance. A low defect density or a high aspect ratio does not characterize carbon nanotubes occurring in natural extraterrestrial specimens, similarly to those synthesized on sample Sm6 in the present study. Therefore, these results offer a plausible mechanism of CNTs formation in extraterrestrial objects, suggesting that transient oxidative and thermal events in space can activate native catalytic sites. Furthermore, our results experimentally support the hypothesis that iron micrometeorites serve as the primary catalysts for the formation of carbon nanostructures similar to those recently observed in lunar regolith [4]. This study demonstrates that intrinsic meteoritic Fe-Ni phases, when activated, can induce complex carbon chemistry under conditions simulating extraterrestrial environments.

ACKNOWLEDGMENTS:

The research funding from the Ministry of Science and Higher Education of the Russian Federation (Ural Fed-eral University Program of Development within the Priority-2030 Program).

REFERENCES:

[1] Fukunaga K., Matsuda J.-I. Vapor-growth carbon and the origin of carbonaceous material in ureilites // Geochemical Journal. 1997. V. 31. P. 263–273.
[2] Becker L., Bunch T.T. Fullerenes, fulleranes and polycyclic aromatic hydrocarbons in the Allende meteorite // Meteoritics and planetary science. 1997. V. 32. No. 4. P. 479–487.
[3] Cruz-Rosas H.I. et al. Multiwall and bamboo-like carbon nanotubes from the Allende chondrite: A probable source of asymmetry // PLoS ONE. 2019. V. 14. No. 7. Article e218750.
[4] Zhang W. et al. Discovery of Naturally Occurring Single-Walled Carbon Nanotubes and Graphitic Carbon on the Far Side of the Moon // Nano Letters. V. 26. Iss. 2. P. 917–925.
[5] Bockelee-Morvan D. et al. The rotational lines of methanol in comets Austin 1990 V and Levy 1990 XX // Astronomy and Astrophysics. 1994. V. 287. P. 647–665.
[6] Begunova A.S. et al. Raman spectroscopy of nanomaterials synthesized on the iron meteorites surfaces // J. Raman Spectroscopy. 2022. V. 53. Iss. 3. P. 472–484.
[7] Antunes E. et al. Comparative Study of First- and Second-Order Raman Spectra of MWCNT at Visible and Infrared Laser Excitation // Carbon. 2006. V. 44. Iss. 11. P. 2202–2211.

MERCURY'S MAGNETOSPHERIC MAGNETIC FIELD AFTER THE SIX BEPICOLOMBO FLYBYS

A. S. Lavrukhin[1], D. V. Nevsky[1,2], I. I. Alexeev[1]
[1] *Skobeltsyn Institute of Nuclear Physics, Lomonosov Moscow State University, Moscow 119991, Russia, lavrukhin@physics.msu.ru*
[2] *Moscow State University, Faculty of Physics, Moscow 119991, Russia*

KEYWORDS:
Mercury, magnetosphere, magnetopause, magnetotail current sheet, BepiColombo, MESSENGER

INTRODUCTION:
BepiColombo spacecraft has completed six flybys of Mercury to date. Three of these flybys are very similar in trajectory to the three MESSENGER flybys it completed before entering Mercury's orbit. As it has been shown in [1], there are problems with magnetometer data onboard BepiColombo, obtained during six flybys. Thus, all the analysis of particles fluxes and magnetosphere state is being conducted without magnetic field data. We use the paraboloid model of Mercury's magnetosphere [2], which has been previously used to analyze the MESSENGER flybys, to estimate the parameters of Mercury's magnetosphere during BepiColombo's flybys.

METHOD:
Using the data on magnetopause crossings obtained with charged particles detectors, we determine the subsolar distance to magnetopause, using technique developed in [3]. Then, we use the "paraboloid" model of Mercury's magnetospheric magnetic field to determine magnetospheric parameters: the magnetospheric stand-off distance, the distance from the planet's center to the inner edge of the tail current sheet, the tail lobe magnetic flux, and the displacement of the tail current sheet relative to the Mercury solar-magnetospheric equatorial plane. Finally, we reconstruct the magnetospheric magnetic field and field lines structure during the six flybys.

REFERENCES:
[1] Constantinescu O. D., Auster H. U., Fischer D. et al. Disturbance-aligned-frame gradiometer technique for removal of spacecraft-generated disturbances from the BepiColombo magnetic field data // Earth, Planets and Space. 2026. V. 78. No. 1.
[2] Alexeev I. I., Belenkaya E. S., Slavin J. A. et al. Ercury's magnetospheric magnetic field after the first two MESSENGER flybys // Icarus. 2010. V. 209. No. 1. Article 2008JA013368.
[3] Nevsky D. V., Lavrukhin A. S., Alexeev I. I. Mercury's Bow Shock and Magnetopause Variations According to MESSENGER Data // Universe. 2024. V. 10. No. 1.

Session 6.
EXOSPHERES OF AIRLESS BODIES (AP)
Oral Session

ABOUT INITIAL CONDITIONS OF EXPANSION OF IMPACT-PRODUCED CLOUDS

A. A. Berezhnoy[1], V. V. Shuvalov[2], G. V. Belov[3], A. E. Ivanova[4], E. A. Feoktistova[1], O. I. Korablev[4]
[1] *Sternberg Astronomical Institute, Moscow State University Moscow 119234, Russia, a_tolok@mail.ru*
[2] *M. A. Sadovsky Institute of Geosphere Dynamics RAS Moscow 119334, Russia*
[3] *Joint Institute for High Temperatures RAS, Moscow 125412, Russia*
[4] *Space Research Institute RAS, Moscow 117997, Russia*

KEYWORDS:
Mercury, exosphere, ejecta, entropy, impact events, condensation

INTRODUCTION:
Initial conditions such as temperature T and pressure p in hot clouds formed during collisions between meteoroids and the Moon/Mercury have significant impact on the quenched chemical composition of hot clouds. For example, increase of initial pressure from 20 to 80 bar at 4000 K leads to condensation of Fe and Mg in hot clouds formed after collisions between CI chondrites and the Moon [1]. It was found that pressure in all regions of the clouds at 4000 K is 13.5 bar for impact velocities equal to 20, 30, and 50 km/s, because the vapor at this temperature begins to condense, and during hydrodynamic simulations the pressure is defined by a phase equilibrium curve in the region of partial condensation [2]. It was also assumed in [1, 2] that impact-produced species have Maxwellian velocity distribution and matters of impactor and target are well mixed in hot clouds. In this abstract an advanced method of estimation of the initial velocity distribution, T_0 and p_0 is discussed.

HYDRODYNAMICS OF IMPACT EVENTS:
Hydrodynamical processes during collisions of meteoroids and Mercury were simulated by numerical studies of vertical collisions between dunite impactors and dunite targets using the SOVA code [3]. Impact-produced clouds were divided into 20–30 fragments, and for each fragment temporal evolution of temperature and pressure was studied. Simulations were performed for impact velocities of 30 and 110 km/s.

Entropy in pure vapor regions of hot clouds is changed between 5200 and 6200 $J \cdot kg^{-1} \cdot K^{-1}$) for 30 km/s impacts and between 5200 and 15000 $J \cdot kg^{-1} \cdot K^{-1}$ for 110 km/s impacts. Velocities of studied fragments were estimated using an approach [4] and exceed 10 km/s for outer regions of cloud formed by 110 km/s impacts. It was also found that during impact events matters of impactor and targets are almost not mixed.

THERMODYNAMICS OF IMPACT-PRODUCED HOT CLOUDS:
Dependence of pressure on entropy at constant temperature for dunite, CI chondrite, and surface of Mercury has been studied using the EQL code [5]. It was obtained that pressure range for dunite at 4000 K is 30–40 and 10^{-4}…40 bar for 30 and 110 km/s impact, respectively. Assuming that entropies of matter of Mercury and dunite are the same during impact events, pressure range for matter of the surface of Mercury at 4000 K is 20–50 and 10^{-5}…50 bar for 30 and 110 km/s impact, respectively. Due to presence of volatile elements for CI chondrites pressures at the same temperature and entropy are much higher than that for dunite and an assumption of the same entropies for dunite and CI chondrite cannot be applied.

DISCUSSION:
Obtained pressure range for 110 km/s impacts is much wider than that found previously [2]. It leads to higher Ca and Al uncondensed fractions in hot clouds.

It is usually assumed that temperature of impact-produced species released to the exosphere is 3000 K and velocity distribution of such species is Max-

wellian [1, 2]. However, observations of Na enrichment in the Hermean exosphere after impacts of meteoroids are better explained if temperature of impact-produced Na atoms is 10000 K [6]. Significant ejecta velocities up to 10–15 km/s can explain presence of such hot impact-produced Na atoms.

CONCLUSIONS:

Method of estimation of initial pressures and temperatures using entropy distribution in hot clouds is proposed. Due to significant non-Maxwellian ejecta velocities Monte Carlo simulations for estimation of surface zenith column densities and number densities of impact-produced species should be performed. Findings of this work can be applied to analysis of BepiColombo mission data [7].

REFERENCES:

[1] Berezhnoy A. A., Belov G. V., Wöhler C. Chemical processes during collisions of meteoroids with the Moon // Planetary and Space Science. 2024. V. 249. Article 105942.
[2] Berezhnoy A. A., Shuvalov V. V., Belov G. V., Ivanova A. E. Evaluation of the effects of meteoroid impacts on properties of the Hermean exosphere // Icarus. 2026. V. 452. Article 117013.
[3] Shuvalov V. V. Multi-dimensional hydrodynamic code SOVA for interfacial 794 flows: application to the thermal layer effect // Shock Waves. 1999. V. 9. P. 381–390.
[4] Shuvalov V. V., Trubetskaya I. A. Numerical simulation of high-velocity ejecta following comet and asteroid impacts: Preliminary results // Solar System Research. 2011. V. 45. Iss. 5. P. 392–401.
[5] Belov G. V. et al. The IVTANTHERMO-online database for thermodynamic properties of individual substances with web interface // J. Phys. Conf. 2018. V. 946. Article 012120.
[6] Cassidy T. A. et al. Detection of large exospheric enhancements at Mercury due to meteoroid impacts // Planet. Sci. J. 2021. V. 2. Article 175.
[7] Yoshikawa I. et al. The Mercury sodium atmospheric spectral imager for the MMO spacecraft of Bepi-Colombo // Planetary and Space Science. 2010. V. 58. P. 224–237.

FURTHER EVIDENCE OF DUST ACTIVITY IN MAIN-BELT ASTEROIDS FROM THEIR REFLECTANCE SPECTRA

V. V. Busarev[1], E. V. Petrova[2], M. P. Shcherbina[3], M. A. Burlak[1], N. P. Ikonnikova[1]

[1] *Sternberg Astronomical Institute6 Lomonosov Moscow State University Moscow, Russia*
busarev@sai.msu.ru

[2] *Space Research Institute RAS, Moscow, Russia*
epetrova@cosmos.ru

[3] *Institute of Astronomy, Russian Academy of Sciences, Moscow, Russia*

KEYWORDS:
asteroids, UBVRI photometry, reflectance spectra, water ice, dust activity, reflectance spectrum modeling

INTRODUCTION:
Our multiband $UBVR_CI_C$ survey observations of asteroids were carried out at the Caucasian Mountain Observatory (CMO) of the MSU SAI (the altitude is 2112 m above sea level) with a CCD camera operating in semi-automatic mode and mounted at the 60-cm RC-600 telescope. From December 2023 to March 2024 and from December 2024 to March 2025, we conducted two series of observations of 39 and 75 main-belt asteroids, respectively, to search for temporarily active objects. To calculate normalized approximated reflectance spectra (NARS) of the asteroids from observational multiband $UBVR_CI_C$ data, we used the similar data for several G-type stars as solar analogs. Additionally, to control the stability of the photometric conditions, standard non-variable stars were observed simultaneously with the asteroids within the same CCD-frame. It should be noted that, in all series of our observations, the successive reflectance spectra of these stars almost coincided.

THE MAIN RESULTS OF OBSERVATIONS:
The surveys included primarily primitive main-belt asteroids moving near perihelion, which ensures their highest subsolar surface temperatures at this time. Such conditions can induce the sublimation of H_2O ice, excavated by recent collisions from beneath the asteroid's surface, and promote the removal of dust by gas flows. We consider short-term changes in the shape of three successive NARS of an asteroid, as well as deviations of the observed shape of NARS from the shape of the normalized reflectance spectrum of the asteroid (if available) in the SMASII database [1], as indicators of asteroid activity. We detected such signs for 210 Isabella, 271 Penthesilea, 372 Palma, 481 Emita, 569 Misa, and 1599 Giomus in the first survey and for 10 Hygiea, 11 Parthenope, 326 Tamara, 495 Eulalia, 973 Aralia, 1182 Ilona, and 1479 Inkeri in the second survey. The results of the second survey also suggest weak activity in asteroids 65 Cybele and 596 Scheila. The measured NARS of these asteroids are presented in Fig. 1 in order of increasing their geometric albedo.

NUMERICAL SIMULATIONS OF REFLECTANCE SPECTRA OF ACTIVE ASTEROIDS:
In our previous works [4–8], we linked the observed changes in the reflectance spectra of a number of asteroids to their short-term sublimation-driven dust activity resulting in the formation of an exosphere around the asteroid. To explain these changes and estimate the properties of particles in the supposed exosphere, we performed numerical simulations of the reflectance spectra of a hypothetical active asteroid (AA) for various (homogeneous spherical and agglomerated) particles in the exosphere and for different values of the optical thickness of the exosphere and the surface albedo. We found that light scattering by particles in the exosphere changes the reflectance spectrum gradient or induces the appearance of unusual spectral features (e.g., [4–8])

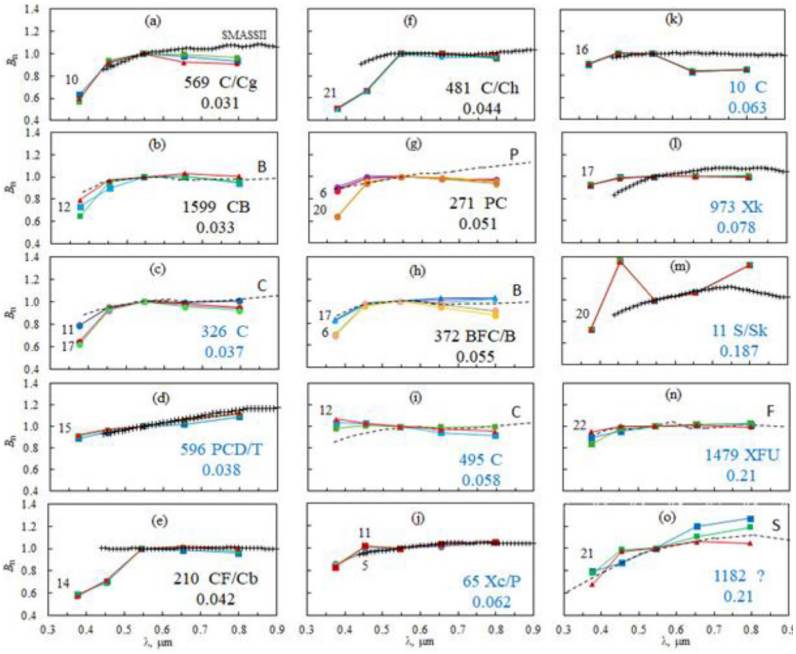


Fig. 1. Three successive NARS (B_n) of each asteroid showing signs of activity during observations in 2023/24 and 2024/25. For each asteroid, the spectral class, geometric albedo (in the lower right corner of each panel), and phase angle of observations (numbers at the short-wavelength end of the graphs), SMASSII [1] spectra measured when the asteroids were inactive, or, if such spectra are not available, approximate averaged spectra of asteroids of the corresponding spectral class (dotted lines) (see [2, 3]) for low-albedo and S-type asteroids, respectively). Asteroid numbers from the first observation series are shown in black, and those from the second in blue

It has been proved that scattering by submicron homogeneous nonabsorbing (or weakly absorbing) particles in the exosphere reduces the positive spectral gradient in the blue range (e.g., Figs. 1d and 1l) and can make it negative (Fig. 1i). However, if the exosphere contains particles absorbing at short wavelengths (e.g., olivine), the positive spectral slope increases (see Fig. 1o). As the optical thickness of the exosphere τ grows, the effect intensifies, but nonlinearly, and at small values of τ it is more noticeable for low-albedo asteroids. Scattering by aggregate particles in the asteroid's exosphere induces a series of extrema in the asteroid's reflectance spectrum, and their positions are determined by the real part of the refractive index and the size of the grains within the aggregates (but not the aggregates themselves) and depends only slightly on their number and the aggregate structure [9, 8].

Comparison of the calculation results with the measured spectra suggests that the presence of maxima at wavelengths shorter than 0.5–0.6 μm (e.g., Figs. 1a, j, k, m) is due to scattering by weakly absorbing particles of complex structure. At the same time, the abrupt drop of B_n at short wavelengths from values corresponding to the reference spectrum (Figs. 1e, f) indicates that, in the exosphere of the AA, there are aggregate particles with the imaginary part of the refractive index increasing with decreasing wavelength (e.g., olivines, refractory organics, and so-called Titan tholins [8]).

One more parameter that can influence the shape of the reflectance spectrum of an AA with the exosphere is the phase angle of observations α. In the 2023/24 and 2024/25 observations, α ranged from 4 to 22°. For observations of the same object, the maximum difference in α was 14° (Fig. 1g). Thus, variations in the shape of the spectra observed at different phase angles may be caused not only by short-term changes in the properties of the exosphere, but also by changes in the phase angle (Figs. 1c, g, h).

CONCLUSIONS:

It should be emphasized that, in general, it is difficult to isolate the effects produced by morphology or composition of particles, variations in the optical thickness of the exosphere, or changes in the phase angle on the shape of the AA reflectance spectrum, since they can overlap in a wide variety of combinations and also depend on the surface albedo. Furthermore, since the exosphere may simultaneously contain particles with different properties, light scattering by them can influence the shape of the AA reflectance spectrum in opposite directions.

Nevertheless, the interpretation of the AA reflectance spectra based on changes in their shape—even at a qualitative level—may provide clues to the nature of AAs and their formation.

REFERENCES:

[1] Bus S., Binzel R. P. SMASS, Phase II. EAR-A-I0028-4-BN0001/SMASSII-V1.0. NASA Planetary Data System, 2003.
[2] Tinaut-Ruano F. et al. Asteroid reflectance spectra from Gaia DR3: Near-UV in primitive asteroids // Astron. and Astrophys. 2024. V. 686. A76. DOI: https://doi.org/10.1051/0004-6361/202348752.
[3] Gaia Collaboration, Galluccio L. et al. Gaia Data Release 3 — Reflectance spectra of Solar System small bodies // Astron. and Astrophys. 2023. V. 674. A35. https://doi.org/10.1051/0004-6361/202243791.
[4] Busarev V. V., Petrova E. V., Irsmambetova T. R. et al. Simultaneous sublimation activity of primitive asteroids including (24) Themis and (449) Hamburga: Spectral signs of an exosphere and the solar activity impact // Icarus. 2021. V. 369. 114634. https://doi.org/10.1016/j.icarus.2021.114634.
[5] Busarev V. V., Petrova E. V. et al. Search for signs of sublimation-driven dust activity of primitive-type asteroids near perihelion // Solar System Research. 2023. V. 57. No. 5. P. 449–466. https://doi.org/10.1134/S0038094623050015.
[6] Busarev V. V., Petrova E. V. et al. An optically thin and thick dust exosphere of active asteroids: Spectral signs and possible formation mechanisms // Solar System Research. 2024. V. 58. No. 3. P. 315–325. https://doi.org/10.1134/S003809462470014X.
[7] Busarev V. V., Petrova E. V. et al. Sublimation-dust activity of primitive type asteroids as a sign of the presence of H2O ice // Solar System Research. 2024. V. 58. No. 6. P. 715–731. https://doi.org/10.1134/S0038094624700503
[8] Petrova E. V., Busarev V. V. On the prospects for estimating the properties of particles in an active asteroid exosphere by features in the UV and visible reflectance spectra // Solar System Research. 2023. V. 57. No. 2. P. 161–174. https://doi.org/10.1134/S0038094623020065.
[9] Tishkovets V. P., Petrova E. V. Spectra of light reflected by aggregate structures of submicron particles // J. Quant. Spectrosc. Radiat. Transfer. 2020. V. 252. Article 107116. https://doi.org/10.1016/j.jqsrt.2020.107116.

SIMULATION EXPERIMENTS ON DEPOSITION OF LMS-1D REGOLITH PARTICLES ON THE SURFACE OF SOLAR PANELS IN GYROTRON DISCHARGE

A. S. Sokolov[1], V. D. Stepakhin[1], T. E. Gayanova[1], A. K. Kozak[1], I. V. Badurin[3], A. A. Lebedev[2], E. A. Obraztsova[1,4], L. V. Kolik[1], N. G. Guseyn-zade[1], N. N. Skvortsova[1]

[1] *Prokhorov General Physics Institute RA, Moscow, Russia, dmc63@yandex.ru*
[2] *JSC "NPP "Kvant", Moscow, Russia*
[3] *National University of Science and Technology MISIS, Moscow, Russia*
[4] *Moscow Institute of Physics and Technology (MIPT), Dolgoprudny, Zhukovsky, Russia*

KEYWORDS:
low-temperature plasma, dust plasma, regolith, gyrotron, microwave discharge, solar panels

INTRODUCTION:

Even at the dawn of the era of studying the Earth' s natural satellite by spacecraft, the question of the properties of its surface was acute. Illustrative examples from the history of the lunar program encourage a detailed study of the behavior of lunar dust, its impact on equipment, and the search for ways to combat the undesirable effects of the unique properties of the lunar soil. Any activity on the lunar surface — whether it is the landing of spacecraft, the movement of astronauts or the operation of lunar rovers — inevitably causes the formation of dust clouds of charged particles rising to a height of tens of meters.

A new type of simulation experiment developed at the Institute of General Physics is presented. To study the effects of a levitating cloud of charged particles created by a powerful pulsed gyrotron on the surface of solar cells, and the results of this work. The experiment is based on the similarity of the processes developing in laboratory experiments with regolith and the processes occurring on the Moon during its bombardment by micrometeorite [1, 2].

Experiments on the effect of regolith on the operation of solar panels are carried out on a plasma chemical stand based on a powerful pulsed gyrotron housed in a cryomagnet [3]. Synthesis directly occurs inside a plasma chemical reactor made in the form of an aluminum cylinder with a set of vertical and horizontal process holes [4]. The design allows experiments to be carried out both at atmospheric pressure (in an air environment) and in a pre-vacuum or an atmosphere of working gases. Inside the reactor there is a quartz container with a powder mixture, as well as holders for installing metal samples or solar panels. The schematic diagram of the experiment is shown in Fig. 1.

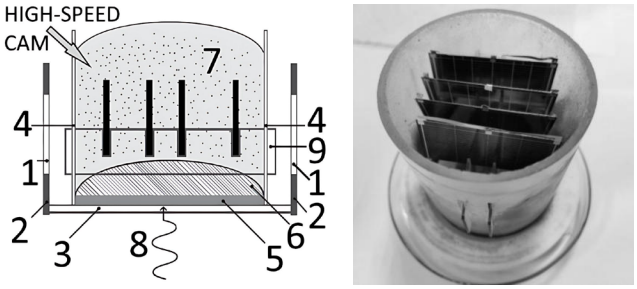


Fig. 1. Scheme of the plasma chemical reactor: 1 — diagnostic quartz windows, 2 — plasma chemical reactor vessel, 3 — quartz bottom of the reactor, 4 — quartz tube, 5 — regolith, 6 — plasma, 7 — plasma chemical reaction zone with flying particles, 8 — microwave radiation, 9 — quartz holder with solar panels

The experiments use the LMS-1D Lunar Mare sample from Exolith, which was created specifically for research related to dust and other tasks requiring the use of ultrafine dust. To stimulate the formation of levitating particles, 10% pure magnesium was added to the mixture, as described in [5].

Under the influence of the microwave radiation of the gyrotron, nonlinear physico-chemical processes are triggered on the regolith, as a result of which a stable cloud of levitating particles is formed. We also used this experimental setup to create a cloud of particles from powder samples that not only repeat the chemical composition of the lunar regolith, but also from the substance of the Tsarev meteorite and ilmenite [5]. The deposition of such particles on metal surfaces has been studied previously [7, 8].

Figure 2 shows photographs of solar panels before and after deposition of charged regolith particles in a plasma chemical reactor.

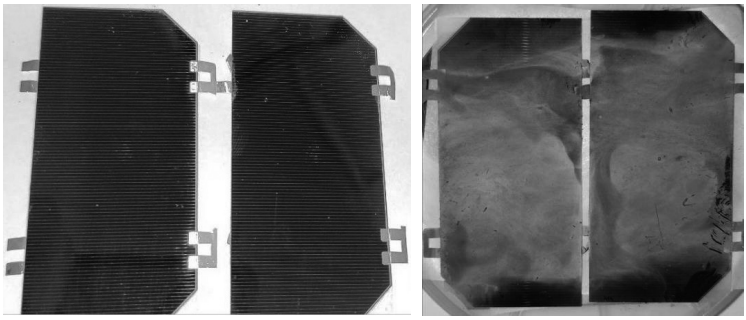


Fig. 2. Clean solar panels (left) and panels with deposited regolith particles (right)

Data analysis shows that solar cells with initially higher efficiency — based on gallium arsenide — show a more intense decrease in efficiency. Silicon batteries, which were initially less efficient, are less susceptible to degradation: their losses after exposure to regolith turned out to be significantly lower than those of gallium arsenide analogues.

The paper presents the results of experiments in which charged particles simulate levitating lunar dust that settles on the surface of solar panels. The regolith particles deposited in this way are characterized by high adhesion to materials and cannot be easily removed by mechanical cleaning methods.

The results obtained allow us to conclude that the developed technique for forming a cloud of charged particles can serve as a model for studying the effect of levitating dust from the lunar exosphere on solar panels and structural materials of spacecraft. This approach is applicable both for preliminary testing of systems before their use in lunar missions, and for the development and testing of effective technologies for cleaning solar panels on the lunar surface.

REFERENCES:

[1] Popel S.I., Kopnin S.I., Golub' A.P. et al. // Solar System Research. 2013. V. 47. No. 6. P. 419–429. DOI: 10.1134/S0038094613060063.
[2] Popel' S.I., Golub' A.P., Zakharov A.V. et al. // J. Experimental and Theoretical Physics Letters. 2018. V. 08. Iss. 6. P. 356–363, DOI: 10.1134/S0021364018180091.
[3] Sokolov A.S., Akhmadullina N.S., Borzosekov V.D. et al. Plasma-chemical facility for synthesis of micro- and nanoparticles having controlled compositions and structures on the basis of a microwave discharge in the gyrotron radiation // Radiophysics and Quantum Electronics. 2023. V. 65. No. 11. P. 840–854. DOI: 10.1007/s11141-023-10261-z.
[4] Batanov G.M., Berezhetskaya N.K., Borzosekov V.D., Kolik L.V., Konchekov E.M., Letunov A.A., Malakhov D.V., Petrov A.E., Sarksyan K.A., Skvortsova N.N., Stepakhin V.D., Kharchev N.K. The plasmachemical reactor on basis of microwave discharge at mixtures of metal-dielectric powders // Advances in Applied Physics. 2013. V. 1. No. 5. P. 564–570 (in Russian).
[5] Skvortsova N.N., Mayorov S.A., Malakhov D.V. et al. // J. Experimental and Theoretical Physics Letters. 2019. V. 109. Iss. 7. P. 441–448. DOI: 10.1134/S0021364019070130.

[6] Borzosekov V.D., Akhmadullina N.S., Sokolov A.S. et al. // Solar System Research. 2024. V. 58. No. 3. P. 290–316. DOI: 10.31857/S0320930X24030049. EDN NEEAJM.
[7] Skvortsova N.N., Stepakhin V.D., Sorokin A.A. et al. // Materials. 2021. V. 14. DOI: 10.3390/ma14216472.
[8] Skvortsova N.N., Stepakhin V.D., Borzosekov V.D. et al. Microwave plasma imitation experiments on deposition of lunar dust on metal plates // Plasma Physics Reports. 2023, V. 49. No. 1. P. 120–128. DOI: 10.31857/S0367292122601394.

LUNAR DUST ACTIVATION PROCESSES: EXPERIMENTAL APPROACH

I. A. Kuznetsov[1], A. V. Zakharov[1], L. M. Zelenyi[1], G. G. Dolnikov[1], I. A. Shashkova[1], A. N. Lyash[1], A. Poroykov[2], S. I. Popel[1], S. A. Bednyakov[1], T. I. Morozova[1]

[1] *Space Research Institute RAS, Moscow, Russia, kia@cosmos.ru*

[2] *National Research University "Moscow Power Engineering Institute" Moscow 111250, Russia*

KEYWORDS:
lunar dust, dust activation, ultraviolet radiation, photoelectric charging, electrostatic dust lofting, regolith simulant, airless bodies, laboratory experiment.

INTRODUCTION:
Solar ultraviolet (UV) radiation is one of the principal factors controlling the charging and dynamics of dust particles on the surfaces of airless bodies. During the Apollo missions, horizon glow and luminous streamers were observed above the lunar surface and were interpreted as possible manifestations of sunlight scattering by electrostatically mobilized dust. Dust particles may acquire electric charge through photoelectron emission induced by solar UV radiation and through interactions with solar-wind plasma. The resulting electrostatic forces can contribute to particle detachment, lofting, and transport.

To investigate these processes under controlled laboratory conditions, we conducted a series of experiments aimed at determining the effects of UV irradiation and external electric fields on the activation and dynamics of regolith dust particles. Lunar regolith simulants with different particle-size characteristics were exposed to UV radiation under vacuum conditions. Dust motion was recorded while the UV intensity and electric-field parameters were varied.

The experiments demonstrated that dust activation begins once threshold irradiation and electrostatic conditions are reached. The boundary conditions corresponding to the onset of particle motion were determined. Additional experimental scenarios were used to simulate transitions between illuminated and shadowed surface conditions. A substantial increase in the dust-particle flux was observed immediately after the UV source was switched off. In another experimental sequence, individual lofting events continued even after both the UV irradiation and the external electric field had been removed. These observations indicate that transient charging, charge relaxation, and redistribution processes may influence dust activity during rapid changes in illumination conditions.

The obtained results contribute to understanding dust activation near the terminator and during illumination–shadow transitions on the Moon and other airless bodies. Such information is important for assessing dust-related risks to scientific instruments, optical surfaces, mechanisms, and future crewed missions. The presentation will describe the experimental setup and measurement procedure, analyse the observed dust-activation regimes, and discuss their possible physical interpretation in the context of lunar surface processes.

APPLICATION OF THE PARTICLE-IN-CELL METHOD TO MODEL ELECTROSTATIC FIELD NEAR AIRLESS BODIES

S. Yu. Kuznetsov[1], V. V. Busarev[2]
[1] *Independent researcher, Moscow, Russia, imarpus@gmail.com*
[2] *Sternberg Astronomical Institute, Lomonosov Moscow University Moscow, Russia, busarev@sai.msu.ru*

KEYWORDS:
numerical methods, surface charging, solar wind, electrostatic, plasma dynamics

INTRODUCTION:
Despite the existence of a number of models describing the dynamics of dust particles in the vicinity of comets and the Moon, the question of the formation and persistence of dusty exospheres around asteroids remains insufficiently studied. The complexity of this problem arises from the interplay of multiple factors: low gravitational forces, photoelectron-induced electrostatic fields, solar radiation pressure, and the solar wind plasma [1]. At the same time, classical analytical methods [2, 3] for calculating the electrostatic field prove to be limited and necessitate the application of numerical approaches.

MATHEMATICAL MODEL:
The Particle-in-Cell (PIC) method [4] is one of the most effective tools for modeling plasma processes. Its essence lies in replacing real particles with a large but finite number of macroparticles, each of which describes the dynamics of an entire ensemble of real electrons or ions. This significantly reduces computational costs while maintaining the physical correctness of the model. The basic idea is a combination of the Lagrangian approach (particle tracking) and the Eulerian approach (field calculation on a grid), which provides a balance between accuracy and computational speed.

Charged particles, in addition to their initial velocity, move in an electromagnetic field due to the Lorentz force. Therefore, for a collisionless, unmagnetized plasma in an electrostatic field, the trajectory of each charged particle is determined by Newton's second law and the Lorentz force:

$$\vec{F} = q(\vec{E} + \mathrm{v} \times \vec{B}).$$

Where v is the velocity of a point charge q, E and B are the electric and magnetic fields, respectively.

Since we neglect the magnetic field in such problems, the electrostatic approximation of Maxwell's equations will be:

Gauss's law	$\nabla \cdot \vec{E} = \rho/\varepsilon_0$
Gauss's law for magnetism	$\nabla \cdot \vec{B} = 0$
Faraday's law	$\nabla \times \vec{E} = 0$
Ampere-Maxwell law	$\nabla \times \vec{B} = 0$

Since $\nabla \times \vec{E} = 0$, then in our case the electric field $\vec{E}$ is calculated through the electric potential φ:

$$\vec{E} = -\nabla\varphi,$$

where φ is the solution to Poisson's equation:

$$\nabla \cdot \vec{E} = -\nabla \cdot \nabla\varphi = -\nabla^2\varphi = \frac{\rho}{\varepsilon_0},$$

which can also be written for a general medium with permittivity ε as:

$$\nabla \cdot (\varepsilon E) = -\nabla \cdot \varepsilon \nabla\varphi = \rho.$$

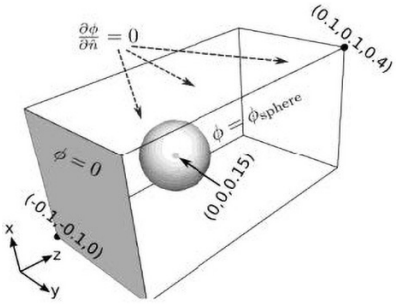


Fig. 1. Computed region

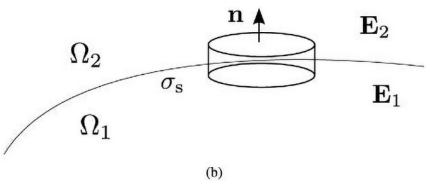


Fig. 2. Electric field near the surface

The problem of the interaction of an asteroid's surface with solar wind plasma can be represented as the interaction of a sphere with the plasma. The method is also demanding on the constructed grid and time step. For the model asteroid, see Figure 1, where the sphere represents the asteroid's surface, and charged particles are directed from the shaded side along the z-axis. The edges of the computational domain represent open boundaries, and the asteroid's surface is the boundary between two environments: the dusty regolith layer and the drifting field of the solar wind plasma flow. Thus, additional internal boundaries (the Dirichlet boundary) arise for the Poisson equation:

$$\varphi(\vec{x}) = \varphi_{sphere} \quad x \in \Omega_{sphere}$$

and at the edges of the calculated region (Neumann boundary):

$$\nabla\varphi \cdot \hat{n} = 0.$$

To save memory on storing particle velocities, we introduce a velocity distribution function. Specifically, we can allow the velocity in each direction to be given by an analytical expression:

$$f_M(\upsilon) = \frac{1}{\sqrt{\pi}\upsilon_{th}} \exp\left(\frac{-(\upsilon-\upsilon_d)^2}{\upsilon_{th}^2}\right).$$

Also known as the Maxwell distribution.

Particles are added to the simulation through a plane perpendicular to the z-axis at a constant rate, such that the constant density of particles added to the simulation is n_0. From the law of conservation of mass, we obtain:

$$\frac{\partial 0n}{\partial t} = -\nabla\cdot(n\vec{\upsilon}).$$

Thus, at the initial moment of time, the incoming flow of particles at the very beginning:

$$\frac{dN}{dt} = n\upsilon_z A_{in}.$$

Here $dN/dt = \dot{N}$ is the number of real particles entering the calculated region through the area A_{in} along the Oz-axis with a velocity υ_z representing the local density n. The number of real particles entering the calculated volume in time Δt: $N = \dot{N}\Delta t$ and the number of simulated macroparticles: $M_f = N/\omega_{mp}$. In this case, M_f is real, so it must be rounded to an integer value. The weight of macroparticles ω_{mp} is a dimensionless quantity.

An object immersed in plasma will collect charged particles on its surface [5]. In addition to plasma currents, other sources, such as photoelectrons and secondary electron emission, also influence the surface potential. This creates a discontinuity in the electric field on the object's surface (Fig. 2). At the interface, the condition for a jump in the electric field flux is as follows:

$$\left[\varepsilon\frac{\partial\varphi}{\partial\mathbf{n}}\right]_{\Gamma} = -\left(\varepsilon_2\mathbf{E}_2 - \varepsilon_1\mathbf{E}_1\right)\cdot\mathbf{n} = -\sigma_s,$$

where the square bracket denotes a jump in the function under consideration, **n** is the unit normal vector from medium 2 to medium 1, and σ_s is the surface potential density.

The surface potential, in turn, influences the current collection at the surface. Thus, an interaction between the plasma and the charged surface is achieved until equilibrium is reached, at which:

$$\sum I\left(\Phi_s\right) = 0,$$

where I is the current collected by the surface.

CONCLUSION:

The application of the Particle-in-Cell method to the problem of interaction between an asteroid's surface and solar wind plasma is considered. Generally, this problem involves the interaction of a sphere with a plasma flow. The Particle-in-Cell method is an effective tool for solving problems of plasma-electrostatic field interaction. Despite computational difficulties, this approach allows for adequate modeling of processes near the surface without atmospheric bodies, where analytical methods are not very effective and have a number of limitations.

REFERENCES:

[1] Kuznetsov S.Y., Busarev V.V. Modeling the Dynamics of Dust Particles in the Gravitational and Electrostatic Fields of a Primitive Asteroid Taking into Account the Sublimation of Water Ice // Moscow Univ. Phys. 80 (Suppl 1). 2025. S414–S418. DOI: 10.3103/S0027134925701358.

[2] Hartzell C. M., Dynamics of 2D electrostatic dust levitation at asteroids // Icarus. 2019. V. 333. Article 234. DOI: 10.1016/j.icarus.2019.05.013

[3] Nitter T., Havnes O. Dynamics of dust in a plasma sheath and injection of dust into the plasma sheath above Moon and asteroidal surfaces // Springer Nature Complete J. 1992. V. 56(7). DOI: 10.1007/bf0005459.

[4] Han D, Wang J. J., He X. Immersed finite element particle-in-cell simulations of plasma charging at the lunar terminator // J. Spacecraft Rockets. 2018. V. 55. No. 6. P. 1490–1497. DOI: 10.2514/1.A34002.

[5] Lund D., He X., Zhang X., Han D. Weak scaling of the parallel immersed-finite-element particle-in-cell (PIFE-PIC) framework with lunar plasma charging simulations // Computational Particle Mechanics. 2022. V. 9. Iss. 6. P. 1279–1291. Doi: 10.1007/s40571-022-00470-0.

Session 7.
ASTROBIOLOGY (AB)
Oral Session

SINGLE-CELL LEVEL MECHANISMS OF TOLERANCE TO EXTREME DESICCATION: HOW A MIDGE CAN FLY TO MARS

O. Gusev[1,2]
[1] *Life Improvement by Future technologies (LIFT) Center, Moscow, Russia*
[2] *Institute of Biochemistry and Genetics of the Ufa Federal Research Center of the Russian Academy of Sciences, Ufa, Russia*

KEYWORDS:
Sleeping chironomid, anhydrobiosis, space radiation, desiccation, gene regulatory network, LEA proteins, trehalose, DNA damage, scRNAseq

ABSTRACT
The capacity of complex multicellular organisms to endure extreme environmental extremes challenges our understanding of the boundaries of life and habitability. The sleeping chironomid, *Polypedilum vanderplanki*, stands out as a premier model for extreme desiccation tolerance — *anhydrobiosis*. In its desiccated state, larvae of this unique insect can survive conditions analogous to the deep space environment, including near-absolute zero temperatures, high-dose ionizing radiation, and vacuum, making it an exceptional subject for astrobiological research.

While the systemic physiological responses of anhydrobiosis are well documented, the precise cellular orchestration enabling this phenomenon has remained elusive. Based on our recent comprehensive analysis of transcriptome data at the single-cell level, we present a high-resolution map of genome regulation driving the desiccation response. By employing single-cell RNA sequencing (scRNA-seq), we deconstructed the specialized roles of distinct cell populations and tissues during the entry into, maintenance of, and recovery from extreme desiccation.

Our findings reveal a highly coordinated, cell-type-specific temporal regulation of protective networks, including the heterogeneous expression of Late Embryogenesis Abundant (LEA) proteins, spatially restricted trehalose synthesis pathways, and localized antioxidative stress responses. We show that survival is not merely a generalized systemic reaction, but a tuned orchestration where specific cellular subsets act as metabolic pacemakers and damage-mitigation centers.

In this talk, I will bridge these single-cell transcriptomic insights with their broader astrobiological implications. We will discuss how the genomic and cellular toolkits of P. vanderplanki can inform the evaluation of the panspermia hypothesis for complex eukaryotes and ultimately, conceptually show how a "midge could fly to Mars".

SURVIVAL OF ARCHAEA AND BACTERIA UNDER OUTER SPACE CONDITIONS OF A POLAR EARTH ORBIT ON THE EXTERIOR OF THE BION-M No. 2 SPACECRAFT

A. A. Guridov[1], S. V. Poddubko[1]
[1] *Institute for Biomedical Problems RAS, Moscow, Russia, gaa1707@mail.ru*

KEYWORDS:
Astrobiology; BION-M No. 2; spaceflight experiment; extremophiles; microbial survival; planetary protection; Enceladus.

INTRODUCTION:
Studying the survival of microorganisms in outer space is one of the primary objectives of experimental astrobiology. This space experiment on microbial survival, named 'Exobiologia,' was conducted aboard the BION-M No. 2 spacecraft, which was launched on August 20, 2025, from the Baikonur Cosmodrome into a polar Earth orbit. The BION-M No. 2 spacecraft is an automated satellite designed to study biological objects in space within Earth's orbit. Unlike space experiments conducted on the ISS and BION-M No. 1, this spacecraft partially exited Earth's magnetosphere; thus, the microorganisms received radiation of a different type and dose compared to previously conducted experiments of this kind [1]. The spacecraft's orbital altitude was approximately 370 km, with a flight duration of 30 days.



Fig. 1. The BION-M No. 2 spacecraft in the assembly facility; containers with scientific hardware for exposing microorganisms in the 'Exobiologia' spaceflight experiment are positioned on the external surface of the satellite [Photo: Oleg Voloshin / IBMP RAS]

METHODOLOGY:
Scientific equipment mounted on the external surface of the spacecraft was utilized for the exposure of the microorganisms. The microorganisms were exposed under several conditions: (A) as thin dry films of desiccated cells on the surface of quartz glasses, (B) as thin dry films of desiccated cells mixed with a Martian regolith simulant on the surface of quartz glasses, (C) as a dried culture on a paper carrier inside small metal containers, and (D) as a dried culture mixed with a Martian regolith simulant inside small metal containers. Exposure conditions for type A and B samples subjected

the microorganisms to all types of stressors characteristic of outer space, including ultraviolet radiation. Exposure conditions for type C and D samples protected the microorganisms from direct ultraviolet radiation; however, all other physical factors of spaceflight were present: vacuum, temperature fluctuations, cosmic radiation, magnetic field variations, and microgravity.

Several species of microorganisms were studied: the spore-forming bacteria *Alkalicoccobacillus gibsonii* and *Bacillus stratosphericus*, the non-spore-forming Gram-positive bacterium *Rubrobacter radiotolerans*, the non-spore-forming Gram-negative bacterium *Methylobacterium radiotolerans*, and the extremely halophilic archaeon *Halorubrum lacusprofundi*. The selection of biological objects for study was based, on the one hand, on their significance as models within astrobiological research, and on the other hand, on their relevance to planetary protection — a set of rules and methodologies for maintaining the microbial cleanliness of spacecraft heading toward other celestial bodies in our Solar System to search for life. The selected microorganisms represent extremophiles based on various types of parameters that combine differently within this list: high radioresistance (*Rubrobacter radiotolerans*, *Methylobacterium radiotolerans*), halophilicity (*Alkalicoccobacillus gibsonii*, *Halorubrum lacusprofundi*), alkaliphilicity (*Alkalicoccobacillus gibsonii*), UV resistance (*Bacillus stratosphericus*, *Rubrobacter radiotolerans*), oligotrophy (*Methylobacterium radiotolerans*, *Halorubrum lacusprofundi*), thermophilicity (*Rubrobacter radiotolerans*), and psychrophilicity (*Halorubrum lacusprofundi*).

RESULTS:

The study of microorganisms' ability to maintain viability after exposure to outer space was conducted by inoculation onto nutrient media specific to each microorganism species and counting the grown colony-forming units post-cultivation. It was revealed that upon exposure to type A conditions, only *B. stratosphericus*, *R. radiotolerans*, and *H. lacusprofundi* survived. Upon exposure to type B conditions, viable cells of all five studied microorganism species — both bacteria and archaea — were detected. However, the ratio of viable cells varied across different species, with *R. radiotolerans* proving to be the most resilient species studied. *R. radiotolerans* does not form endospores (the resting forms extremely resistant to a wide range of diverse stressors, such as those found in *A. gibsonii* and *B. stratosphericus*). This represents a novel and unexpected finding, as it contradicts the previously established fact that only spore-forming bacteria could survive in similar experiments (as demonstrated in space experiments on the FOTON-M satellites using *Bacillus spp*. [2]). Furthermore, in this experiment, all microorganisms survived exposure to type C and D conditions at the same quantitative level as the synchronous Earth control samples stored in the laboratory at room temperature.

CONCLUSION:

Thus, the obtained data indicate a gap in our knowledge regarding how the diverse microbial world can harbor biological species capable of surviving the extremely harsh conditions of outer space, even under the influence of solar UV radiation. Since the selected strains also serve as model objects of analog Earth ecosystems to study the possibility of life on icy moons, the findings on the high survival rate of the psychrophilic extreme haloarchaeon *Halorubrum lacusprofundi* may contribute to the research of Enceladus as a potentially habitable world in our Solar System [3], and also highlight the necessity of strict planetary protection measures for spacecraft heading toward such celestial bodies.

REFERENCES:

[1] Shurshakov V. A., Mitrikas V. G. et al. Modeling the radiation environment in prospective spacecraft orbits. Cosmic Research. 2015. V. 53(5). P. 346–354.
[2] Horneck G., Rettberg P., Reitz G. Protection of Bacterial Spores in Space, a Contribution to the Discussion on Panspermia. Orig Life Evol Biosph. 2001. V. 31. P. 527–547.
[3] MacKenzie S. M. et al. Enceladus Astrobiology, Habitability, and the Origin of Life // Astrobiology. 2021. No. 21(10). P. 1211–1247.

FRAGMENTATION OF LAMBDA PHAGE DRY DNA DURING EXPOSURE OUTSIDE AND INSIDE THE BION-M No. 2 SATELLITE

M. Yu. Karganov[1], M. V. Polyakova[1], A. A. Guridov[2], S. V. Poddubko[2], V. A. Sergunova[3], E. A. Sherstukova[3], I. B. Alchinova[1]

[1] *Institute of General Pathology and Pathophysiology, Moscow, mkarganov@mail.ru*

[2] *Institute of Biomedical Problems of the Russian Academy of Sciences (IBMP RAS), Moscow*

[3] *V. A. Negovsky Research Institute of General Reanimatology, Federal Research and Clinical Center of Intensive Care Medicine and Rehabilitology, Moscow*

KEYWORDS:
cosmic radiation, Lambda phage DNA, restriction analysis, electrophoresis, atomic force microscopy**.**

INTRODUCTION:
The idea of both a longer stay on board spacecraft and an increase in flight distance is becoming more and more realistic. However, it should be borne in mind that the factors affecting the health of the crew that have already been studied for low-Earth orbit may differ from those in conditions of long-range manned space flight. One of the risks for astronauts who find themselves far from the Earth's magnetic belt will be solar and galactic cosmic rays, some of which are heavy and superheavy charged particles.

The purpose of this study was to assess the nature of DNA damage when samples were placed on the outer surface and inside the BION–M No. 2 satellite.

METHODS:
In preparation for placement on the "Exobiofrost" (outer surface) and "Biocont" (inside the satellite), a DNA solution with a concentration of 500 micrograms/ml under aseptic conditions was introduced into sterile plastic micro-samples in the amount of 70 micrograms. The samples were dried overnight under lyophilic conditions and packed. In preparation for placement in the "Exobiology" scientific equipment (outer surface), a DNA solution with a concentration of 500 micrograms/ml under aseptic conditions was applied to clean glasses in an amount of 70 micrograms. The samples were air-dried in a sterile box overnight and packed. The control material, dried and packaged under similar conditions for each experiment, was stored on the Ground in a laboratory. The flight lasted 30 days in a polar orbit at an altitude of 380 km. Passive dosimeters inside the BION–M No. 2 module recorded an integral absorbed dose of 8.2 mGy, which is comparable to the dose measured in the crew cabin of the ISS service module at the current flight altitude of about 420 km (inclination 520) [1]. BION–M No. 2 demonstrated an approximately twofold increase in the contribution of the galactic component of cosmic radiation. The dose outside the lander reached 6 Gy per 30-day flight, and showed a strong dependence on the thickness of the protection (the dose difference on the outer surface reached approximately 300 times). After returning to Earth, the flight samples were dissolved in water, and the DNA concentration in the preparations was evaluated using a NanoDrop 1000 spectrophotometer (Thermo Scientific, USA). The samples were treated with BsuR I and Sse9 I restrictases (SibEnzyme LLC, Russian Federation) at the rate of 10 units of endonuclease per 1 microgram of DNA in a buffer appropriate according to the manufacturer's recommendation. The reaction mixture was incubated for 1 hour at a temperature of 37 °C for BsuR I and 55 °C for Sse9 I. Inactivated for 20 min at 80 °C and 65 °C, respectively. Electrophoretic separation of the fragments obtained after restriction was performed in 1.5 % agarose gel in a TBE buffer, applying 600 ng of DNA to the well. Current parameters I=0.02 A; U=65 V. The time of electrophoresis was 2 h 20 min and 4 h.

The gel was stained with ethidium bromide. The obtained images were processed using GeneTools software (Gene Tools, LLC, USA) and the Microsoft® Excel data analysis package. The size of the area of electrophoretic migration of the visualized fragments was determined based on the pattern of base separation of DNA markers Step 100 Long, Step50 plus and Sky-High (Biolabmix LLC, Russian Federation) deposited in an amount of 600 ng per well, i.e. equivalent to a DNA sample. After drying, the DNA samples were analyzed using an NTEGRA BIO atomic force microscope (NT–MDT SI, Russia). AFM images of dry samples were acquired in air using semi-contact scanning mode and NSG01 cantilevers (NT–MDT SI, Russia) with a nominal tip radius of 10 nm. The scan size ranged from 20×20 μm^2 to 1×1 μm^2, with a resolution of 512 points.

Statistical processing of luminosity data was carried out using the standard Statistica 8 software package (Statsoft Rasa CJSC, Russian Federation). The Mann-Whitney U-test was used. The differences were considered significant at $p<0.05$.

RESULTS AND DISCUSSION:

The data on the graphs is presented as medians. Exposure of samples on glass in outer space ("Exobiology") leads to a decrease in the proportion of large fragments with an increase in the contribution of small ones (Fig. 1a), the differences with the control reach the level of statistical significance. There is a significant decrease in the luminosity of the peak in the 0.07 R_f region (fragments are less than 4000 bp in length, but more than 3000 bp), and the peak in the 0.16 R_f region (2000–2500 bp) decomposes into two less intense luminosities. A significant increase in the peak in the 0.5 R_f region was observed (corresponding to fragment lengths of 600 bp), and the number of fragments smaller than 300 bp increased.

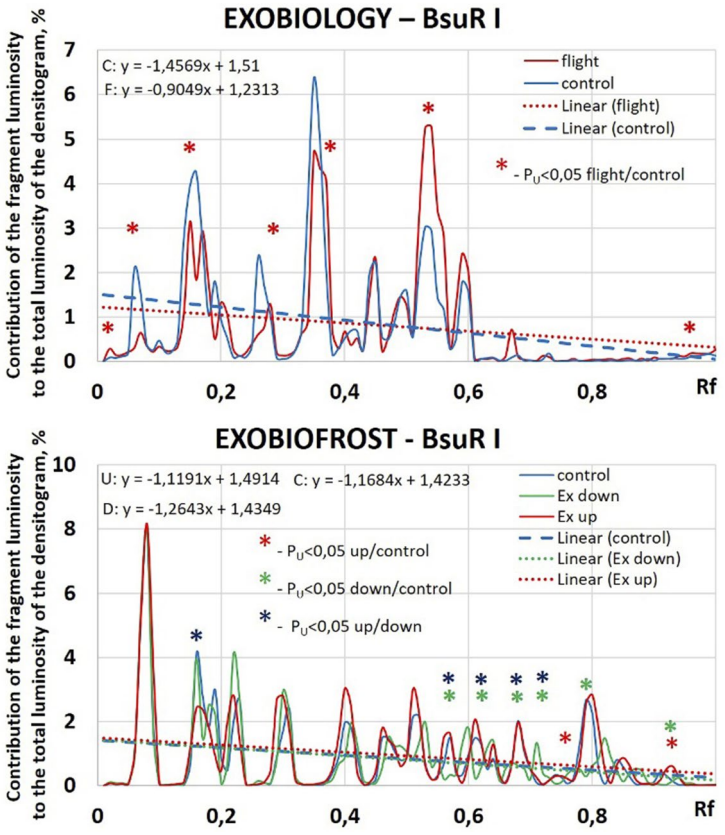


Fig. 1. Densitograms of phage Lambda DNA fragments from samples located on the outer surface of Satellite at Exobiology (a) and Exobiofrost (b)

The samples at "Exobiofrost" were placed in a cylindrical container, which created a situation in which, if a particle entered the lid of the container, the upper samples would take on more energy than the lower ones. In this regard, two groups of samples were compared separately with the control. An increase in the contribution of the average fragments to the luminosity in flight preparations was recorded, in the range from 0.2 to 0.4 R_f (Fig. 1b) these differences did not reach the level of statistical significance. A significant decrease in the luminosity of the 0.57 R_f peak (corresponding to fragment lengths of about 500 bp), as well as a shift of several small peaks in the 0.6–0.8 R_f region on the densitogram of the "lower" samples compared with the "upper" and control samples, turned out to be significant. In the experiment with samples inside the satellite, the main differences between the flight and control samples were concentrated in the region of small fragments from 0.65 R_f onwards (corresponding to fragments less than 400 bp in size). At the same time, the differences between the samples that were in hypomagnetic conditions during flight were shown both when exposed to BsuR I and Sse9 restrictase I. In the case of unshielded flight samples after treatment with Sse9 I restrictase, there were no differences with the control.

Exposure of samples on glasses in outer space ("Exobiology") leads to a decrease in the proportion of large fragments with an increase in the contribution of small ones, which is reflected in the value of the coefficient k of the linear equation of the approximating curve of the densitograms of DNA fragments obtained after electrophoresis of the restricted samples. The differences with the controls reach a level of statistical significance. Slightly less strong differences are seen when Sse9 I restrictase is used to treat samples in an open space container ("Exobiofrost"). Similar, but even less pronounced shifts were recorded when the samples were positioned inside the satellite ("Biocont").

The research method used by us is relatively simple and, as has been shown, informative in analyzing the effects of the space environment on the dried DNA preparation [2]. Its gradual complication, combined with ground-based experiments, will allow us to accumulate the required database on the interaction of fast heavy ions of different nature and energy with a model biological object [3].

REFERENCES:

[1] Andreev-Andrievskiy A. A., Mashkin M. A., Drugova S. V. et al. Bion-M 2 Biosatellite: Multisystem Mouse Responses to 30 Days in High-Latitude Orbit as a Deep-Space Analog // bioRxiv. 2026.05.03.722490. DOI 10.64898/2026. 05.03.722490.
[2] Alchinova I. B., Polyakova M. V., Kharin S. A. et al. Fragmentation of Lambda Phage DNA under the Influence of Cosmic Radiation during Prolonged Exposure in Containers on the Outer Surface of the International Space Station // Bulletin of the Russian Academy of Sciences: Physics. 2026. V. 90. No. 4. P. 610–615. DOI 10.1134/S1062873826700176.
[3] Karganov M. Yu, Alchinova I. B., Polyakova M. V. et al. Stability of dry Phage Lambda DNA irradiated with swift heavy ions // Radiation Physics and Chemistry. 2019. V. 162. P. 194–198. DOI 10.1016/j.radphyschem.2019.04. 048.

The work was carried out within the framework of the state assignment for the Institute of General Pathology and Pathophysiology FGFU-2025-0003 and the Fundamental Scientific Research Program of the RAS (FMFR-2024-0035; FMFR-2024-0036).

PRELIMINARY RESULTS OF GEOHI RAS EXPERIMENTS ABOARD BION-M No. 2

D. D. Barbashin[1,2], A. S. Kuznetsov[2], I. N. Gromyak[1], A. K. Golomidova[2], R. M. Gabdrakhmanov[2], A. D. Efimov[2], E. E. Kulikov[2], A. A. Guridov[4], S. V. Poddubko[4], A. E. Ivanova[3], V. K. Ilyin[4], E. N. Slyuta[1]

[1] *Vernadsky Institute of Geochemistry and Analytical Chemistry RAS Moscow, Russia, barbashin@geokhi.ru;*
[2] *Federal Research Centre of Biotechnology RAS, Moscow, Russia;*
[3] *Lomonosov Moscow State University, Soil Science Faculty, Moscow, Russia;*
[4] *State Scientific Center of Russian Federation — Institute of Biomedical Problems RAS, Moscow, Russia.*

KEYWORDS:
BION–M No. 2, astrobiology, phage induction, bacteriophages, micromycetes, ISRU, soil microbion

INTRODUCTION:
From August 20 to September 19, 2025, a spacecraft of the Bion series performed a flight with multiple experiments on board. We placed five experiments inside it, covering different aspects of astrobiology. The range of objects studied includes: 6 bacteriophage strains and 2 strains of lysogenic *E. coli*, 3 bacterial species, 2 strains of *Aspergillus tubingensis*, and 2 soil samples. Below are the goals and applied significance of all experiments; preliminary data will be presented in the report.

EXPERIMENT ON BACTERIOPHAGE SURVIVAL
Bacteriophages are the most widespread group of biological objects in the biosphere [1]. They are resistant to temperature, osmotic stress, pH [2], and ionizing radiation [3], which makes them important for space biology, astrobiology, and planetary quarantine. However, data on the influence of spaceflight factors on phages are scarce, and their results are fragmentary [4]. Therefore, the aim of this experiment is to study the survival and infectivity of six bacteriophage strains KURISU, *Emesvirus zinderi*, *Lambdavirus lambda, Gamaleyavirus Mimir124, Krischvirus RB49, and Traversvirus tv24B* under near-Earth orbit conditions depending on exposure conditions.

EXPERIMENT ON BACTERIOPHAGE INDUCTION
The stability of the gut microbiota is important for astronaut health. The role of temperate phages and prophages is dual: they maintain the balance of the microflora but can contribute to inflammation. Prophage induction leads to the simultaneous release of mature phage particles and toxins. E. coli, widespread in the normal microbiota but possessing pathogenic potential in some strains, including lysogenic phages with Shiga toxin genes, becomes a complex target for phage therapy. The review by Parfenov and Lukin [5] showed that the *E. coli* K-12 (λ)+ system is sensitive to low doses of radiation, but studies in sealed ampoules could yield false-positive results. The influence of individual flight factors, especially the temperature gradient, remains unclear. The aim is to clarify the effect of the temperature gradient on prophage induction in the model *Lambdavirus lambda* (λ) in the *E. coli* K-12 MG1655 derivative and the clinically significant *Traversvirus tv24B* (phi24B) on strain 4s containing plasmid pWclH.

EXPERIMENT ON BIOLOGICAL LEACHING OF LUNAR REGOLITH ANALOGUE
In the coming decades, crewed missions to the Moon and the creation of a habitable lunar base by 2050 are planned [6], but the task of cost-effectively supplying it with resources remains unresolved, requiring the development of in situ resource utilization (ISRU) technologies. Lunar regolith may become a source of metals and other useful components: nickel, copper, iron, and aluminum are needed for electronics, titanium for rocket and aircraft construction, quartz and rare earth elements for solar panels, magnets, and catalysts, but their delivery from Earth is expensive and limited. Biological leaching (biomining) is considered a promising direction, with

advantages including the low weight of raw materials delivered from Earth and the possibility of autonomous operation at the initial stage of creating the International Lunar Research Station. Aspergillus niger is often used for leaching metals from low-grade and spent ores, and its close relative A. tubingensis has shown efficiency in such processes, making it a promising agent for space biomining. However, for practical application, it is necessary to confirm that the strains remain viable after exposure to vacuum, ionizing radiation, and low temperatures of real spaceflight; targeted studies on the survival of A. tubingensis under such conditions have not been conducted until now.

EXPERIMENT WITH SOIL SAMPLES

The creation of habitable stations on the Moon requires closed life support systems, traditionally based on constructozems [7]. Lunar regolith is toxic, sterile, and devoid of organic matter, so the directed formation of microbial communities capable of transforming toxic compounds and serving as biofertilizers is promising. To manage this, criteria for the functioning of the microbiome are needed, taking into account stress factors, including hypomagnetism. In this work, we studied the influence of the temperature gradient against the background of other spaceflight factors on microbial communities of urban soils (urbanozems) as terrestrial analogues of lunar constructozems. The aim is to assess the survival of the saprotrophic bacterial complex and enterobacteria in urbanozems after a 30-day orbital flight, separating the effects of spaceflight itself and the temperature gradient.

CONCLUSION

The series of experiments is aimed at assessing the resistance limits of prokaryotic and eukaryotic microorganisms, bacteriophages, and soil microbial communities to spaceflight conditions. The obtained data are important for developing planetary protection protocols, biological methods for regolith preparation, space biomining technologies, and ensuring astronaut health. Preliminary results will be presented in the report and article.

REFERENCES:

[1] Clokie M. R. J. et al. Phages in nature // Bacteriophage. 2011. V. 1. No. 1. P. 31–45.
[2] Jończyk E. et al. The influence of external factors on bacteriophages // Folia microbiologica. 2011. V. 56. No. 3. P. 191–200.
[3] Sommer R. et al. Inactivation of bacteriophages in water by means of non-ionizing (UV–253.7 nm) and ionizing (gamma) radiation: a comparative approach // Water Research. 2001. V. 35. No. 13.
[4] Du Toit A. Phage-host dynamics in space: Phage biology // Nature Reviews Microbiology. 2026. P.
[5] Parfenov G. P., Lukin A. A. Results and prospects of microbiological research in space // Space life sciences. 1971. V. 4. No. 1. P. 139–159.
[6] Marov M. Y., Slyuta E. N. Early steps toward the lunar base deployment: Some prospects // Acta Astronautica. 2021. V. 181. P. 28–39.
[7] Prokofyeva T. V. et al. Introduction of soils and soil-like formations of urban territories into the classification of Russian soils // Eurasian Soil Science. 2014. No. 10.

17MS3-AB-05
ORAL

SEQUENTIAL EXPOSURE REVEALS STAGE-SPECIFIC EFFECTS OF SIMULATED MICROGRAVITY AND X-RAY IRRADIATION ON BACILLUS MOJAVENSIS SPORE REVIVAL

S. Chai[1], Y. Wang[1], R. Sun[1], L. Chen[1], H. Ling[1], H. Liu[1], J. Ma[3], L. Liu[2], Y. Fu[1]*

[1] *School of Biological Science and Medical Engineering, Beihang University, Beijing 100083, China (fuyuming@buaa.edu.cn)*

[2] *Department of Radiation Oncology, Beijing Hospital, National Center of Gerontology; Institute of Geriatric Medicine, Chinese Academy of Medical Sciences, Beijing 100730, China*

[3] *China Academy of Space Technology, Beijing 100094, China*

INTRODUCTION:

Planetary protection relies on pre-launch decontamination, yet bacterial endospores may survive sterilization and subsequently encounter low-dose radiation and microgravity during interplanetary transit. Whether these sequential stresses alter spore revival remains unclear. Using Bacillus mojavensis from a spacecraft assembly facility, we exposed spores to graded X-ray doses before recovery under 1 g or simulated microgravity (SMG). Sustained phenotypic divergence emerged primarily during outgrowth: maximum growth rate was jointly influenced by gravity, dose, and their interaction, whereas lag time was associated predominantly with irradiation history. Transcriptomic responses shifted from dose-dominated regulation during germination to coupled gravity-dose interactions during outgrowth, and secondary spores exhibited altered antimicrobial susceptibility. These findings indicate that sequential space-relevant stress reshapes revival in a stage-dependent manner, providing a basis for incorporating exposure history into forward-contamination risk assessment and spacecraft bioburden-control strategies.

EARLY EMBRYOGENESIS IN MICROGRAVITY CONDITIONS — FROM BIOPHYSICS TO SIGNAL PATHWAYS

P. B. Eftimov[1], N. P. Stefanova[1]
[1] *SU St. Kliment Ohridski, Department of Cell and Developmental Biology, 8, Dragan Tsankov str., Sofia, Bulgaria*

KEYWORDS:
embryogenesis, differential adhesion hypothesis, microgravity, signal transduction, alterations.

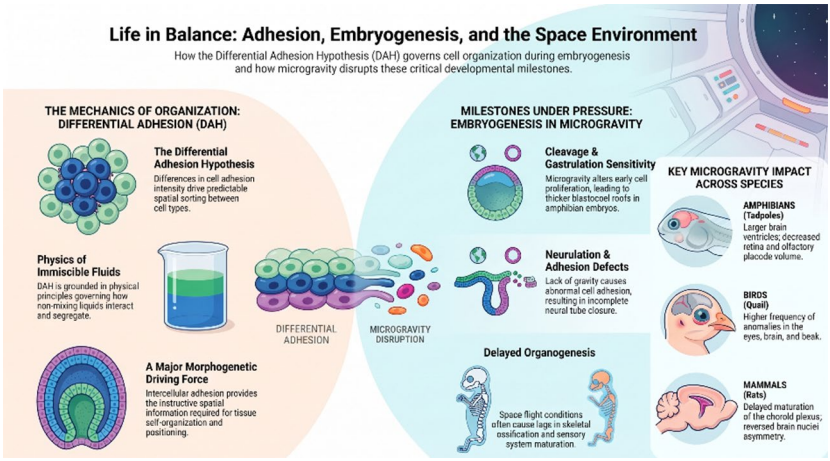
INTRODUCTION:
Early embryogenesis is a highly coordinated process governed by the interplay between physical forces and molecular signaling. During the earliest stages of development, cell sorting, tissue organization, and lineage specification are not driven solely by genetic programs but also by the biophysical properties of cells [1, 2].The Differential Adhesion Hypothesis (DAH) provides a fundamental framework for understanding how cells self-organize according to differences in adhesive strength, minimizing the overall free energy of the developing embryo in a manner analogous to phase separation in liquids [3, 4]. In this context, tissue surface tension emerges as a key mechanical property that reflects the balance between cell-cell adhesion and cortical contractility, contributing to the establishment of embryonic architecture and influencing cell fate decisions [5, 6].

Microgravity represents a unique environment in which the physical cues that normally guide embryonic development are profoundly altered. Although gravity is a relatively weak force at the cellular scale, its indirect effects on fluid dynamics, mechanotransduction, cytoskeletal organization, and mass transport may significantly modify the mechanical landscape experienced by embryonic cells [7, 8]. Changes in cortical tension, adhesion molecule distribution, cytoskeletal dynamics, and extracellular matrix interactions may disrupt the generation and maintenance of tissue surface tension, thereby affecting cell sorting, morphogenesis, and the robustness of developmental patterning [9, 10]

These biomechanical perturbations are expected to interact with conserved signaling pathways that regulate embryonic development, including Wnt/β-catenin, Hippo, Notch, BMP, and TGF-β signaling. Mechanical forces generated through cell adhesion and cytoskeletal tension are increasingly recognized as essential regulators of these pathways, linking the physical state of embryonic tissues to transcriptional programs responsible for lineage commitment [9, 11]. Consequently, microgravity-induced alterations in cellular mechanics may lead to changes in signal transduction, gene expression, and developmental timing, potentially compromising normal embryogenesis [12, 13].

This presentation explores the transition from the biophysical principles governing early embryonic self-organization to the molecular signaling networks that interpret mechanical information. By integrating concepts from developmental biology, mechanobiology, and space life sciences, it discusses how altered gravitational environments may reshape the balance between adhesion, surface tension, and intracellular signaling. Understanding these interactions is essential not only for assessing reproductive and developmental risks during long-duration space missions but also for advancing fundamental knowledge of the physical principles underlying embryonic development on Earth.

GRAPHICAL ABSTRACT:



REFERENCES:

[1] Gilbert S. F. (2014). Developmental Biology (10th ed.). Sinauer Associates.
[2] Lecuit T., Lenne P.-F. (2007). Cell surface mechanics and the control of cell shape, tissue patterns and morphogenesis. Nature Reviews Molecular Cell Biology, 8, 633–644.
[3] Steinberg M. S. (1963). Reconstruction of tissues by dissociated cells. Science, 141, 401–408.
[4] Steinberg M. S. (1970). Does differential adhesion govern self-assembly processes in histogenesis? Journal of Experimental Zoology, 173, 395–433.
[5] Foty R. A., Steinberg M. S. (2005). The differential adhesion hypothesis: a direct evaluation. Developmental Biology, 278, 255–263.
[6] Krieg M. et al. (2008). Tensile forces govern germ-layer organization in zebrafish. Nature Cell Biology, 10, 429–436.
[7] Nickerson C. A. et al. (2004). Low-shear modeled microgravity: a global environmental regulatory signal affecting bacterial gene expression, physiology, and pathogenesis. Journal of Microbiological Methods, 54, 1–11.
[8] Discher D. E., Janmey P., Wang Y.-L. (2005). Tissue cells feel and respond to the stiffness of their substrate. Science, 310, 1139–1143.
[9] Dupont S. et al. (2011). Role of YAP/TAZ in mechanotransduction. Nature, 474, 179–183.
[10] Mammoto T., Ingber D. E. (2010). Mechanical control of tissue and organ development. Development, 137, 1407–1420.
[11] Heisenberg C.-P., Bellaïche Y. (2013). Forces in tissue morphogenesis and patterning. Cell, 153, 948–962.
[12] Lei X. et al. (2018). Effects of simulated microgravity on embryonic stem cells and early development. Stem Cell Research & Therapy, 9, 224.
[13] Ma X. et al. (2022). Spaceflight and simulated microgravity alter mammalian embryonic development: recent advances and future perspectives. NPJ Microgravity, 8, 34.

TARDIGRADE EXTREME STRESS TOLERANCE: IMPLICATIONS FOR RADIATION BIOPHYSICS AND SPACEFLIGHT STUDIES

M. P. Zarubin[1], E. V. Kravchenko[1]
[1] *Dzhelepov Laboratory of Nuclear Problems, Joint Institute for Nuclear Research, Dubna, Russia, mzarubin@jinr.ru*

Tardigrades (phylum *Tardigrada*) exhibit exceptional resilience to diverse physicochemical stresses and are recognized as the most radioresistant animals. Tardigrades have become model organisms for radiation biophysics, spaceflight studies and astrobiology [1], this will reviewed in the report. In these organisms, the distinct effects of various radiation types and dose rates have been characterized. As well in addition to ground-based space-simulation studies (Mars chamber), tardigrades have been deployed aboard space missions including FOTON–M3, Space Shuttle Endeavour (STS–134), Beresheet lunar lander (crashed), International Space Station (ISS, NASA SpaceX–22), and Axiom Space (SpaceX AX–4). The basic biological effects of spaceflight have been validated in tardigrades, moreover they have become the first animals to survive after exposure directly in the outer space environment, including intense solar UV-radiation [2]. This field requires comprehensive genomic and transcriptomic studies of tardigrades exposed to diverse space environments and also an emergence of novel tardigrade-inspired protective technologies is expected. During 2010s, the breakthrough in the research of tardigrades have lead to discoveries of several molecular principles of their extreme resistance including tardigrade-specific disordered proteins (TDPs), which are promising for the development of novel genetic-based protectors. Within the framework of TARDISS project, molecular genetics group at DLNP JINR (Dubna), investigates tardigrade Damage suppressor (Dsup) protein being an effective DNA-protective molecule [3–6]. Our group provided the first demonstration that Dsup protein enhances resistance to oxidative stress and ionizing radiation in *Dsup*-expressing complex animals (*Drosophila melanogaster*), subsequently characterizing effects of Dsup via transcriptome analysis [3]. The structural biology study provided the first characterization of Dsup's molecular features, confirming its classification as an intrinsically disordered protein (IDP) and demonstrating formation of Dsup–DNA fuzzy complex, in which Dsup retains multiple non-rigid conformations [4]. Our recent efforts focus on further *in vivo* and *in vitro* analyses of Dsup's protective mechanism, alongside on the development of applications of Dsup protein as radioprotectors and biomaterial design [3, 5, 6]. Finally, our group have performed space experiment with *Dsup*-expressing and control bacteria used as biosensors of spaceflight exposome (spacecraft/outer space) during polar LEO orbit flight of BION M–2.

REFERENCES

[1] Horikawa D., Kunieda T., Abe W., Watanabe M., Nakahara Y., Yukuhiro F., ..., Okuda, T. 2008. Establishment of a rearing system of the extremotolerant tardigrade *Ramazzottius varieornatus*: a new model animal for astrobiology. *Astrobiology*, 8(3): 549–556. DOI.org/10.1089/ast.2007.0139.
[2] Jönsson K. I., Rabbow E., Schill R. O., Harms-Ringdahl M., Rettberg P. (2008). Tardigrades survive exposure to space in low Earth orbit. *Current biology*, 18(17): R729–R731. DOI.org/10.1016/j.cub.2008.06.048.
[3] Zarubin M., Azorskaya T., Kuldoshina O., Alekseev S., Mitrofanov S., Kravchenko E. 2023. The tardigrade Dsup protein enhances radioresistance in Drosophila melanogaster and acts as an unspecific repressor of transcription. *iScience*. 26(7):106998. DOI.org/10.1016/j.isci.2023.106998.
[4] Zarubin M., Murugova T., Ryzhykau Y., Ivankov O., Uversky V. N., Kravchenko E. 2024. Structural study of the intrinsically disordered tardigrade damage suppressor protein (Dsup) and its complex with DNA. *Sci Rep*. 14(1):22910. DOI.org/10.1038/s41598–024–74335–2.

[5] Zarubin M., Andreev E., Kravchenko E., Pinaeva U., Nechaev A., Apel P. 2024. Developing tardigrade-inspired material: Track membranes functionalized with Dsup protein for cellfree DNA isolation. *Biotechnology Progress*. 40(5): e3478. DOI.org/10.1002/btpr.3478.
[6] Rzyanina A.V., Kravchenko E.V., Zarubin M.P., Mytsin G.V. (2025). Tardigrade Dsup Protein Protects Human Cells during Proton Radiotherapy. *Biochemistry (Moscow), Supplement Series A: Membrane and Cell Biology*. 19(4), 487–490. DOI.org/10.1134/S1990747825700485.

QUESTIONED MICROBIAL COMMUNITIES OF THE SUBGLACIAL ANTARCTIC LAKE VOSTOK WATER FOLLOWING 1st LAKE UNSEALING: RE-EVALUATION OF PREVIOUS FINDS AND DISCOVERING NEW ONES USING NANOPORE SEQUENCING

S. A. Bulat[1,2], E. E. Slepneva[1], A. E. Komissarov[1], A. Ekaykin[3], J–R. Petit[4]
[1] *Petersburg Nuclear Physics Institute of National Research Centre "Kurchatov Institute," Gatchina, Leningrad region,188300, Russia; bulat_sa@pnpi.nrcki.ru*
[2] *Institute of Physics and Technology, Ural Federal University, Ekaterinburg 620002, Russia*
[3] *Arctic Antarctic Research Institute, 199397 Saint-Petersburg, Russia;*
[4] *University Grenoble Alpes, CNRS, IRD, Grenoble INP, IGE, Grenoble, 38402, France*

KEYWORDS:
Antarctica, Lake Vostok, contamination, microbial communities, unclassified finds, extraterrestrial life, subglacial oceans, Jovian's Europa, Saturn's Enceladus, Oxford nanopore sequencing,

INTRODUCTION:
In 2012 it was a breakthrough in subglacial Antarctic Lake Vostok microbiome studies. The 1st lake unsealing happened, and water under pressure entered the borehole and got frozen within with icy clamp frozen on a drill bit. That drill-bit water was collected as clean as possible upon drill recovering and was studied for microbial content using common Sanger sequencing approach. That time and until now in this water-frozen ice the unknow bacterium was discovered — phylotype w123-10 [1, 2]. It proved to be a hitherto-unknown type of bacterium showing less than 86 % sequence similarity to known taxa in GenBank. Its phylogenetic inference was also unsuccessful. Right now, a new attempt was undertaken in trying to classify this phylotype. Nothing has changed — 84–85 % similarity (a bit above family level) with Candidatus *Phycocordibacter aenigmaticus* and Candidatus *Minusculum obligatum* (both associated with microalgae optimized for carbon dioxide sequestration from flue gas [3]). Of uncultured bacterial clones, best fits (96.3 % similarity — genus level) showed clone JQ380240 originating from New Zealand soil and clone KY519816 discovered in lake water sample in Canada (95.3 % similarity — genus level).

Thus, the phylotype w123-10 remained unidentified and unclassified. Objective of the study was re-investigating the same water frozen samples in discovering indigenous microbial community with the focus to re-discover (prove) the phylotype w123-10 using very promising high throughput 4th generation sequencing technology — Oxford nanopore sequencing (Oxford Nanopore Technologies, Nanopore, Oxford, UK).

MATERIAL AND METHODS:
Two samples of frozen water were investigated — one w-1F collected on a site (Vostok station; 5 segments in a 50ml sterile corning tube; delivered by vehicle Fedorov) immediately after drill recovering, and another one w-2Moi (one big segment from the same drill-bit water frozen sample: clean room facilities in a laboratory).

Since that time the gDNA extracted in clean room facilities following strict decontamination protocols [4] has been kept frozen. The gDNA was isolated using MoBio soil DNA isolation kit using sham DNA isolation control (sham). Another control E28 was also implemented (ELGA ultra-clean water used to wash-rinse the ice segment in a laboratory). Nowadays this gDNA has been re-analyzed in PCR in amplifying 16S rRNA bacterial genes, and generated amplicons were sequenced using high throughput nanopore sequencing technology (Next Generation Sequencing 4; Oxford Nanopore

inc., UK). Of 16S rRNA genes the v3-v4 region (about 485 bp in length) was amplified with degenerate 16S rRNA gene targeted primers and generated four amplicons (two controls and two water frozen icy samples) were used to prepare DNA libraries for nanopore sequencing (the MinION–1B device and the R10.4.1 Flow Cell with the Native Barcoding Kit 24 V14 (SQK–NBD114.24)). The reads were basecalled (super-accurate; MinKnow v25.09.16) and classified with Epi2Me software (v5.3.0) through the wf-16s nextflow workflow (v1.2.0) (Oxford Nanopore Technologies). Regarding read sequence comparison for the extraction of similar reads, the global pair-wise alignment of reference vs. tested reads was performed with Bio.Align module from Biopython v1.84 library [5]. Options for alignment were as follows: match — value 2, mismatch penalty — 1, open gap penalty — 2, gap extend penalty -0.5.

RESULTS AND DISCUSSION:

The sequencing was performed in replication (in twice). The results of the first trial are as follows. The combined results will be presented during the event.

In total 82 000 and 71 000 classified reads were obtained for sample w-1F and w-2Moi, correspondingly, and 108 000 and 72 000 classified reads for Sham and Wash water controls, correspondingly. All four samples were very similar in terms of abundance, diversity indices and species richness suggesting no indigenous bacteria in lake water samples. At the phylum level *Proteobacteria* and *Bacteroidota* dominated everywhere. At the species level following extraction of shared reads with controls icy samples showed 19 phylotype/species shared (most confident because of drill-bit frozen water represented one big sample) finds. Amongst them, human(-animal)-associated and soil originating bacteria prevailed (Table 1). Thus, none of lake water originating finds were discovered. It could mean that the water-frozen sample under study could be indigenous bacteria free [6].

Table 1. Classified shared (two samples) findings in drill-bit frozen water of Lake Vostok

No.	Taxa	Status Source PubMed	barcode17 w-1F 82 000 reads	barcode18 w-2Moi 71 000 reads
1	Gammaproteobacteria; Moraxellales; Moraxellaceae; Moraxella osloensis	Human	361	198
2	Firmicutes; Bacilli; Lactobacillales; Streptococcaceae; Streptococcus vestibularis	Human	117	219
3	Gammaproteobacteria; Xanthomonadales; Xanthomonadaceae; Stenotrophomonas maltophilia	Human	212	119
4	Firmicutes; Bacilli; Lactobacillales; Streptococcaceae; Streptococcus chosunense	Human	198	86
5	Gammaproteobacteria; Pseudomonadales; Pseudomonadaceae; Pseudomonas syringae	Human	146	17
6	Firmicutes; Bacilli; Lactobacillales; Streptococcaceae; Streptococcus koreensis	Human — oral	47	12

No.	Taxa	Status Source PubMed	barcode17 w-1F 82 000 reads	barcode18 w-2Moi 71 000 reads
7	Firmicutes; Bacilli; Lactobacillales; Streptococcaceae; Streptococcus oricebi	Animal — oral	26	18
8	Alphaproteobacteria; Sphingomonadales; Sphingomonadaceae; Novosphingobium profundi	Deep-sea seamount	21	20
9	Gammaproteobacteria; Pseudomonadales; Pseudomonadaceae; Pseudomonas alloputida	Env — soil	10	27
10	Firmicutes; Bacilli; Lactobacillales; Streptococcaceae; Streptococcus pantholopis	Animal — feces	19	16
11	Cyanobacteria_Incertae_ sedis; Nostocales; Rivulariaceae; Nunduva fasciculata	Atlantic and Pacific coasts	10	20
12	Firmicutes; Bacilli; Lactobacillales; Streptococcaceae; Streptococcus constellatus	Human — oral	14	9
13	Firmicutes; Bacilli; Lactobacillales; Streptococcaceae; Streptococcus orisratti	Animal — oral	5	12
14	Alphaproteobacteria; Sphingomonadales; Sphingomonadaceae; Sphingobium soli	Soil — rhizosphere	8	9
15	Firmicutes; Bacilli; Lactobacillales; Streptococcaceae; Streptococcus varani	Animal — oral	6	7
16	Betaproteobacteria; Burkholderiales; Oxalobacteraceae; Massilia alkalitolerans	Soil	5	4
17	Alphaproteobacteria; Caulobacterales; Caulobacteraceae; Brevundimonas basaltis	Black sand	5	6
18	Alphaproteobacteria; Sphingomonadales; Sphingomonadaceae; Sphingomonas sanxanigenens	Soil	5	5
19	Sphingobacteriia; Sphingobacteriales; Sphingobacteriaceae; Mucilaginibacter daejeonensis	Rise straw Contaminant [6]	4*	5
20	Unknown; unclassified		413 (0.5 %)	351 (0.5 %)

* — reads with less than three in counts were excluded as non-confident.

At the same time about 0.5 % reads remained unknown (unclassified) — the amount which can hide original finds like phylotype w123–10. Therefore, using w123-10 sequence as a reference unknown reads were searched using a specially designed script for similarity (refer to Methods section). This resulted in finding of several reads with similarity values above 98 %? the phylogenetic Maximum Likelihood tree is presented in Fig. 1. As you can see the phylotype w123-10 is far from any other reads, but cluster (71 % bootstrap support) with a tight group of other unclassified reads which can represent one-two species (did not investigate in depth).

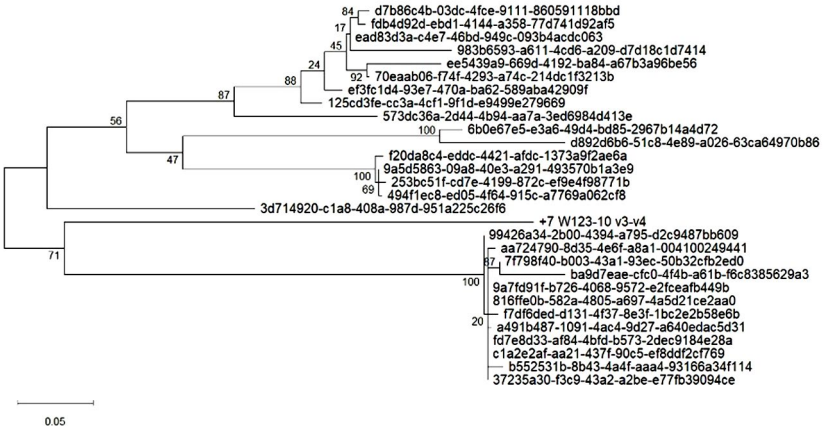


Fig. 1. Phylogenetic assessment (evolution analysis) of unknown phylotype w123-10 within related unclassified reads/species by the Maximum Likelihood method

The phylogeny was inferred using the Maximum Likelihood method and Kimura 2-parameter model of nucleotide substitutions and the tree with the highest log likelihood (–2,876.52) is shown. The percentage of replicate trees in which the associated taxa clustered together, where the number of replicates (108) was determined adaptively, is shown next to the branches. The MP tree had the shortest length among 10 MP tree searches; each performed with a randomly generated starting tree. The evolutionary rate differences among sites were modeled using a discrete Gamma distribution across 5 categories (+*G*, parameter = 3.1992), with 35.08 % of sites deemed evolutionarily invariant (+*I*). The analytical procedure encompassed 29 nucleotide sequences with 439 positions in the final dataset. Evolutionary analyses were conducted in MEGA12 [7]. The scale denotes the number of nucleotide substitutions (%).

CONCLUSION — TAKEAWAY:

1 — Despite of millions reads analyzed no indigenous bacteria were classified-detected in drill-bit frozen lake water meaning the upper most water lake horizon does not contain microbial life (as it suggested before [6]).

2 — the previously discovered unknown unclassified phylotype w123-10 has kept its status.

3 — New unidentified relatives to w123-10 were detected meaning microbial life could thrive in the lake water but does not present in GenBank entries.

PROSPECTS:

Oxford Nanopore sequencing technology has proven to be an efficient tool for recording and proving the microbial content in subglacial Antarctic water reservoirs. The discovery of relatives of the unknown phylotype w123-10 suggests that unique cell populations might reside in faults offshore of the subglacial Lake Vostok. These organisms could provide valuable insights into searching for extraterrestrial life on the icy moons of Jupiter and Saturn.

ACKNOWLEDGEMENT
This research was supported by the Ministry of Science and Higher Education of the Russian Federation, specifically through the Ural Federal University Program of Development under the Priority-2030 Program.

REFERENCES:

[1] Bulat S. A. Microbiology of the subglacial Lake Vostok: first results of borehole-frozen lake water analysis and prospects for searching lake inhabitants. 2016. Phil. Trans. R. Soc. A 374: 20140292. http://dx.doi.org/10.1098/rsta.2014.0292.
[2] Bulat S., Petit J.-R. Vostok, Subglacial Lake. In: Gargaud M. et al. (eds) Encyclopedia of Astrobiology. Springer, Berlin, Heidelberg. 2023. P. 3206–12. https://doi.org/10.1007/978–3-642–27833–4_1765–3_978–3-662–65093–6_1765.
[3] Jonas L., Lee Y.-Y., Bachvaroff T., Hill R.T., Li Y. Erratum for Jonas et al., 'Two novel Patescibacteria: Phycocordibacter aenigmaticus gen. nov. sp. nov. and Minusculum obligatum gen. nov. sp. nov., both associated with microalgae optimized for carbon dioxide sequestration from flue gas'. 2026. mBio 17(4): e00599–26. https://doi.org/10.1128/mbio.00599–26.
[4] Bulat S. A. et al. DNA signature of thermophilic bacteria from the aged accretion ice of Lake Vostok, Antarctica: implications for searching for life in extreme icy environments. 2004. Int J Astrobiology. V. 3. P. 1–12. https://doi.org/10.1017/S1473550404001879.
[5] Cock P. J. A. et al. Biopython: freely available Python tools for computational molecular biology and bioinformatics. 2009. Bioinformatics. V. 25. №. 11. P. 1422. https://doi.org/10.1093/bioinformatics/btp163.
[6] Bulat S. A., Anosova O. I., Tsvetkova A. Yu., Shvetsov A. V. The uppermost water horizon of subglacial Lake Vostok could be microbial DNA-free, as shown by Oxford Nanopore sequencing technology. 2024. Arctic and Antarctic Research. V. 70(Suppl): S97–S107. https://doi.org/10.30758/0555–2648–2024–70(Suppl)-S97–S107.
[7] Kumar S., Stecher G., Suleski M., Sanderford M., Sharma S., Tamura K. Molecular Evolutionary Genetics Analysis version 12 for adaptive and green computing. 2024. Mol Biol Evol 41: 1–9. https://doi.org/10.1093/molbev/msae263.

ASTROBIOLOGICAL RESEARCH AS PART OF THE VENERA-D SPACE MISSION

O. R. Kotsyurbenko[1,2], I. V. Konyukhov[3], D. V. Vilyanen[4], A. B. Rubin[3], S. I. Pogosyan[3]

[1] *GeneXplain GmbH, Wolfenbüttel, Germany*
[2] *Network of Researchers on the Chemical Evolution of Life, Leeds, United Kingdom*
[3] *Lomonosov Moscow State University, Faculty of Biology, Moscow, Russia*
[4] *Institute of Physicochemical and Biological Problems of Soil Science, Russian Academy of Sciences, Pushchino, Russia*

KEYWORDS:
Life on Venus, Biosignatures, Extraterrestrial photosynthesis, "Venera-D".

The Russian Venera-D mission is one of six missions to Venus aimed at a comprehensive study of the planet, including its geology, atmospheric physics and chemistry, and surface structures. However, experiments designed to detect complex organic and potentially biological molecules are included in the research programs of only two missions: "Venera-D" and "Morning Star". The Venera-D astrobiology program offers several key advantages, primarily due to the development of an aerostat designed to fly within Venusian clouds for an extended period at an altitude of 54–56 km — a range identified by astrobiologists as the most suitable for the development of a hypothetical microbial community [1–3]. This research approach is expected to significantly enhance the performance of onboard instruments analyzing the aerosol fraction for potential biomarkers. The aerostat will be equipped with an autofluorescence nephelometer capable of detecting fluorescence across a wide wavelength range; the cloud layer will be illuminated by three or four lasers operating in the UV, visible, and far-red bands, enabling the detection of a broad spectrum of organic and bio-organic molecules should they be present in the clouds. Additionally, the mission plans to use an orbiter module to detect phosphine and identify organic molecules (with masses up to 300 Daltons) during the descent of the probe through the Venusian atmosphere. The mission is currently in the early stages of development, with a launch scheduled for the 2032–2036 timeframe.

REFERENCES:

[1] Kotsyurbenko O. R., Cordova J. A. Jr., Belov A. A., Cheptsov V. S., Khrunyk J., Kolb D., Kryuchkova M. O., Milojevic T., Mogul R., Sasaki S., Slowik G. P., Snytnikov V., Vorobyova E. A. Exobiology of Venus clouds: New insights into habitability through terrestrial models and methods of detection, Astrobiology. 2021. V. 21. No. 10. P. 1186–1205. Https://doi.org/10.1089/ast.2020.2296.
[2] Kotsyurbenko O. R. Search for life on Venus: history of the problem and basic concepts. Solar System Research. 2023. V. 57. No. 3. P. 221–235. DOI: 10.1134/S003809462303005X.
[3] Kotsyurbenko O., Kompanichenko V., Broushkov A., Khrunyk Y., Sorokin V., Skladnev D. Different scenarios for the origin and the subsequent succession of a hypothetical microbial community in the cloud layer of Venus. Astrobiology. 2024. V. 24. No. 423–441. Https://doi.org/10.1089/ast.2022.0117.

SPACE MISSION: FROM DEVELOPING THE BASIC PRINCIPLES OF CREATING HABITABLE PLANETS TO THE SEARCH FOR INTELLIGENT WORLDS

A. N. Safronov[1]
[1] *Obukhov Institute of Atmospheric Physics RAS, safronov_2003@mail.ru*

KEYWORDS:
comet impact, buoyancy theory, thermal nuclear explosion, water origin, natural gas and oil, terrestrial and lunar ores, stellar nucleogenesis, DNA-star, habitability, space mission

INTRODUCTION:

As is well known, the fundamental dilemma of philosophy is the answer to the question: did God or Nature create our world? In this publication, we present a mini-review of the author's series of articles on space exploration. To date, the author has mostly completed research on the development of fundamentally new foundations for nuclear geophysics, astrophysics, and astronomy [1–13]. In addition, individual topics were presented at various conferences; see [14–23]. This series of papers covers a wide range of issues; the overall research framework is shown in Fig. 1.

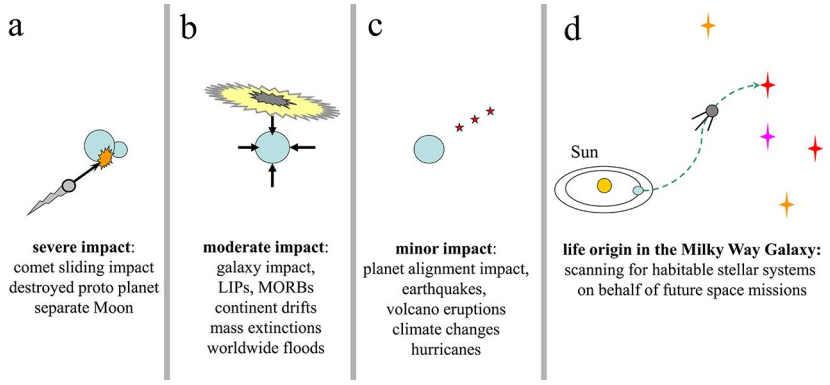


Fig. 1. A diagram explaining the result of strong (A), moderate (B) and minor (C) impacts of various factors on our planet. These factors were studied by the author in the following works: (A) — [1, 7, 8]; (B) — [2]; (C) — [3, 4, 5, 6]. The research series (D) is dedicated to the search for new intelligent worlds. Within the framework of D, the works [9, 10, 11] were published. The work [12] is devoted to the problems of using solar sails in long-range missions

ARCHIMEDES' LAW OF BUOYANCY AND A NEW EARTH'S NUCLEAR REACTOR MODEL:

Research in the field of nuclear geophysics and astrophysics was initiated by the IAEA and Rosatom Corporation after the disaster at the Fukushima nuclear power plant (Japan), which occurred after the devastating earthquake in 2011. Unfortunately, it should be emphasized that neither geophysics nor astrophysics passed the stress test. It is noteworthy that geophysics is the only science about the Earth that does not officially recognize the well-known Archimedes' law. The crisis in geophysics has catastrophic consequences for related fields of science.

Recall that astrophysicists partially recognize the law of buoyancy, but with limitations. Thus, a model of layered structures called the "onion" model is used to describe the processes occurring in massive stars with a mass of more than 8–10 solar masses. We will not dwell on the disadvantages of this model [10], but generalize the law of buoyancy to the distribution of isotopes and apply this law to the isotopes of all existing elements of the periodic table. Thus, the author suggests moving from the classical

mantle-crust structure of the Earth to a plasma layered structure formed by hot nuclear fuel layers and warm layers of decay of nuclear elements. Figuratively speaking, according to this concept, planets should be considered as unformed or cooled stars.

For clarity, in Fig. 2 we present the difference between the model of the Earth's nuclear reactor developed by the author (Fig. 2a) and the previously known model of the Earth's reactor developed by Professor Herndon [24, 25], a well-known pioneer in the field of nuclear geophysics (Fig. 2b), and the traditional model of the Earth's structure (Fig. 2c).

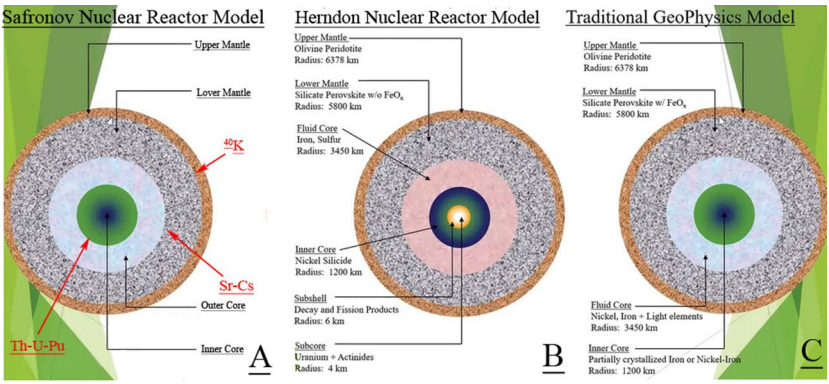


Fig. 2. Comparison of various models of the Earth's structure. (A) — multilayer diagram of the Earth's nuclear reactor proposed by the author; (B) — Herndon's model of the Earth's nuclear reactor. Uranium sank deep into the core and is located at the Earth's center; (C) — traditional geochemical model of the Earth. This figure has been modified. Previously, a similar figure illustrated the difference between the Herndon's model and the traditional Earth model

In [3], it was suggested that the nuclear layer of the ^{40}K isotope, located on the boundary of the upper and lower mantles, is the basis of modern theories of volcanology, seismology, subduction, and continental drift. The study of effusive eruptions provided a clear answer to the question of why light chemical elements, primarily silicon and sulfur compounds, currently predominate in volcanic ash, gases, and lavas. During the constant, quiet combustion of the ^{40}K layer, fragments of the lithospheric crust sink into the ^{40}K zone, where they melt with the dissociation of chemical compounds, and then separate into heavy and light elements. Elements heavier than potassium sink deep into the planet, while elements lighter than potassium float to the surface. The presence of a thermal barrier at the boundary of the upper and lower mantles leads to the formation of shallow convection in the upper mantle. Thus, layers rich in heavy elements are not involved in this process, and volcanic gases, ash, and lavas contain mostly only light elements higher than potassium on the periodic table. This concept also provides a simple explanation of why volcanoes are usually located along subduction zones at a certain distance from them.

TERRESTRIAL AND LUNAR ORES:

The development of the principles of nuclear geophysics and the detailed study of explosive and effusive eruptions answered not only topical issues of volcanology [3], but also gave impetus to the development of related disciplines such as seismology [4], oreogenesis [7], synthesis of water, diamonds, natural gas and oi [8].

Thus, in [7], the theory of ore formation on the Earth and the Moon was developed. It has been shown that ore deposits on Earth and the Moon were mainly formed simultaneously with the separation of the Moon from the protoplanet and the formation of the oldest continents. This happened after the comet hit the surface of the protoplanet at a grazing angle [1]. The time of formation of terrestrial and lunar ores corresponds to the time boundary between the Tonian and Cryogenian periods, ~ 720 million years ago. The formation of terrestrial ores occurred as a result of

the release of medium and heavy chemical elements from the deep layers of the protoplanet, followed by the process of their solidification in old geological faults. We would like to emphasize that only the author of these studies allows planets to collide with comets; other astronomers and astrophysics consider planetary collisions only with asteroids or hypothetical planets such as Thea.

Further in [7] it was noted that the processes of formation of lunar ores proceeded differently on the visible and far sides of the Moon. The far side of the Moon is a single fragment of the protoplanetary lithosphere, so the ores there could have formed mainly due to the overflow of igneous rocks over the edge of the lunar continent. On the visible side of the Moon, due to rapid cooling, ores formed in the constriction region during the drop-liquid separation of the Moon from the proto-Earth. Since the Moon separated at the first stage of liquid-droplet separation, then, unlike the Earth, the amount of water and methane on it is limited. The process of formation of lunar ores is schematically shown in Fig. 3.

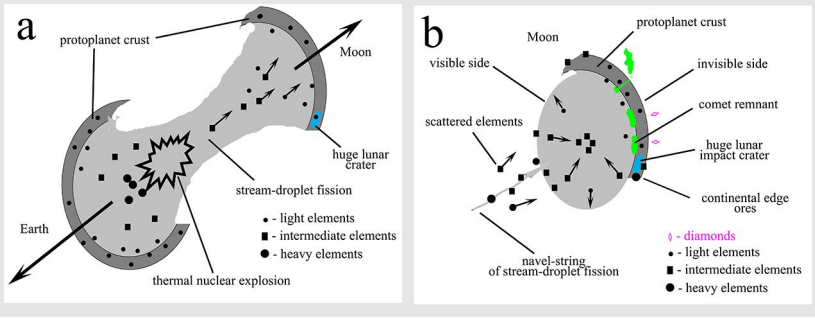


Fig. 3. A diagram illustrating the process of formation of lunar ores. (a) — is a thermal nuclear explosion inside a protoplanet after a collision with a comet. The Moon was formed as a result of droplet separation of the viscous magmatic mass of the protoplanet along with a piece of the protoplanet's crust; (b) — the stage of cooling of the Moon and the formation of lunar ores with separation by atomic weights in accordance with the theory of buoyancy of the elements. The lunar crater formed as a result of a collision with a comet is shown in blue; the gaseous remnants of the comet under the earth's crust are shown in green. The lunar pseudo-volcano erupts a gas plume, which is also colored green, as are the remnants of the comet's matter

In [8], the author investigated the origin of water, natural gas and oil, as well as diamonds. It is shown that diamonds, water, oil, and natural gas on Earth were formed as a result of a thermal nuclear explosion after a comet collided with the surface of a protoplanet, see also [1]. The hypothesis proposed by the author in [8] is the only one explaining the predominance of diamond deposits in the Southern Hemisphere and oil and gas deposits in the Northern Hemisphere. This explains why the spatial distribution of diamond deposits forms pronounced linear or circular spatial clusters. In this paper, two types of diamond deposits and four types of gas and oil deposits are identified. The recommendations on the search for these deposits have been clarified. The process of formation of diamonds, water, natural gas and oil is schematically shown in Fig. 4.

Further in [3, 4, 5], during the study of explosive eruptions and strong earthquakes, it was discovered that there is a connection between the configurations of planets and these natural disasters. It was found that explosive volcanic eruptions and strong earthquakes often occurred under different types of linear planetary alignment. Based on the numerous examples given in [3, 4, 5], it was found that the trigger effect does not depend on the distance between the planets and the mass of the planets, therefore this mechanism was identified as an inertial-gravitational mechanism. Attention was drawn to the fact that the efficiency of the trigger mechanism increases with increasing multiplicity of the ratio of distances between

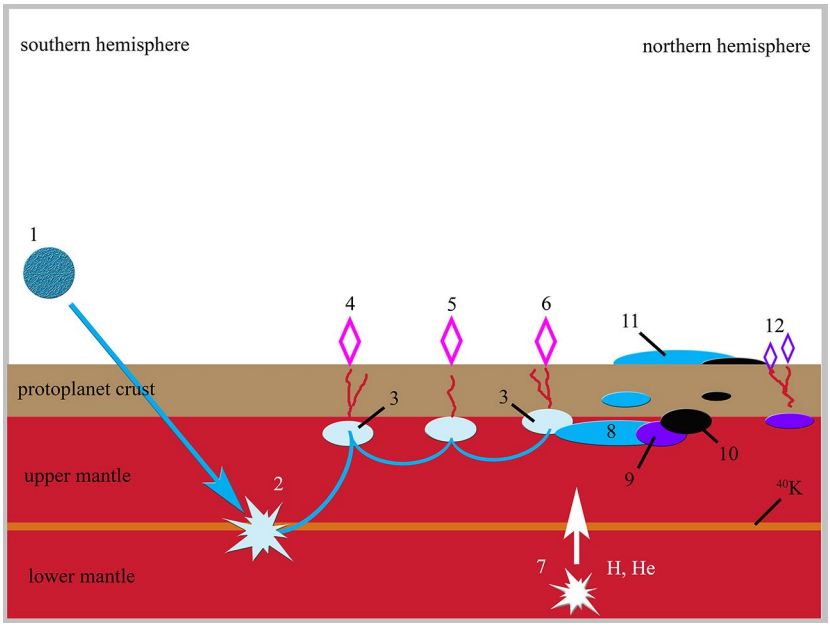


Fig. 4. A diagram illustrating the formation of diamonds in the Southern Hemisphere of the Earth and oil and gas deposits in the Northern Hemisphere. (1) — the collision of a comet with the protoplanet Earth. The comet falls to the surface of the protoplanet at a sliding angle; (2) — the primary explosion of the comet after hitting the ^{40}K nuclear layer; (3) — spasmodic movement of a plasma cloud formed by comet waste products such as CO_2, CO and C; (4–5–6) — diamond deposits. The regular arrangement of diamond deposits is due to the linear and discontinuous movement of cometary derbies.; (7) — secondary deep explosion of the inner nuclear layers of the protoplanet with the release of a large number of different isotopes of hydrogen H, H_2 and helium (He), the creation of the Earth and the separation of the Moon; (8) — synthesis of water (H_2O); (9) — formation of deposits of methane (CH_4); (10) — formation of petroleum deposits; (11) — the release of water and oil onto the surface of the already existing planet Earth; (12) — the formation of a secondary type of diamonds from methane vapor in the Northern Hemisphere.

the planets, as well as with pairwise planetary parallelism, which probably indicates the interference nature of inertial effects. It has been suggested that inertia is a special case of gravity, namely, gravitational self-induction, which, like any self-induction, depends only on the geometry of the problem. From this, based on the principle of Archimedes' planetary lever and Kepler's conjunction, the Third Law of Motion was changed accordingly by adding a few words to the end of the text of the law:

"When one body exerts a force on a second body, the second body exerts a force equal in magnitude and opposite in direction to the force of the first body, in the absence of obstacles on the path between these bodies". (1)

Here are some illustrative examples. The planetary configuration for the well-known climatically significant eruption of Pinatubo in 1991 with an index VEI=6 is shown in Fig. 5a. As is known, after this eruption, the average temperature of the atmosphere decreased by 0.5 °C over the next 1.5–2 years. During the eruption of Pinatubo, the alignment of four planets was observed: Jupiter, Mars, Venus and Earth (J–M-V–E). For comparison, Fig. 5b shows an example of a 4-fold planetary alignment during the M_w7.0 earthquake in California on December 5, 2024. In this case, a planetary alignment was observed between Jupiter, Earth, Mercury, and the Sun (J–E–Mr–Sun).

In [13], the study of planetary configurations observed in 2024 during strong earthquakes of magnitude greater than 7 (M_w7+) continued. Special attention in the study is paid to the processes of graviton formation.

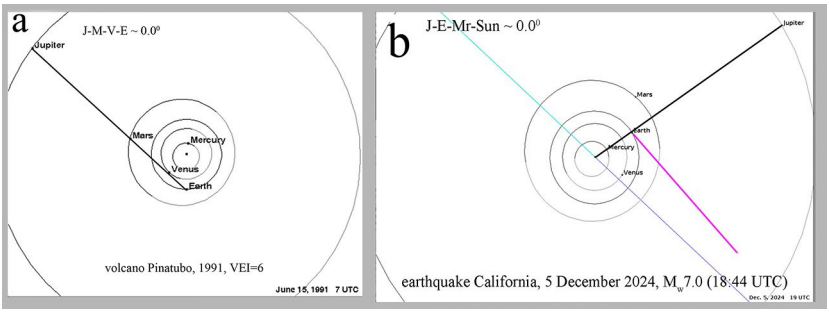


Fig. 5. Examples of planetary configurations that occurred: (a) — during the strongest eruption of Pinatubo in June 1991 with VEI=6, (b) — during the earthquake in California in December 2024 with magnitude of M_w7.0. The planetary alignments are indicated by black lines: (a) — Archimedes' lever; (b) — Kepler binding

It is shown that possible sources of gravitons can be not only planets, but also areas of orbits perturbed by pairwise planetary linearization (planetary coupling). Possible transitions of the graviton of the Solar System from a higher orbit to lower orbits located closer to the Sun, as well as transitions from lower orbits to higher orbits, are noted.

In order to exclude the influence of subduction and the presence of geological activity on Earth on the registration of gravitons in the Solar System, an additional study of seismic activity on Mars was conducted. In [6], we investigated the planetary configuration at the time of the largest marsquake (s1222a) observed by InSight. It is shown that the Solar system has a unique linear configuration formed by Saturn, Mars, Venus, and Mercury (S–M–V–Mr).

The above results significantly enhance the author's work, but the main result of the research in the first part is different. It was shown in [1] that the impact of a comet on the proto-Earth led to the formation of continents, as well as to the formation of seas, oceans, primary atmosphere, and the creation of conditions for the emergence of life on the planet. This part of the study points to the possibility of creating a habitable planet, but it does not answer the question of who created our unique world — God or Nature. On the other hand, there is no doubt that after a certain period of time we will be able to reach the remote stars, so the possibility of creating habitable planets near these stars will already be a purely technical task. In this situation, it is of interest to scan the stars closest to the Solar System for the possibility of an intelligent world on them or the creation of habitable bases on them.

SPACE MISSION TO REMOTE STARS:

The problem of interstellar travels has been of interest to mankind for a long time. After Yuri Gagarin's first flight into space in 1961, the illusion of rapid discovery of interstellar space appeared. Although the 60-year period of cosmonautics development has led to significant achievements in space exploration using satellites and space stations, such research has practically not gone beyond the Solar System. Two important limitations of manned space exploration are: firstly, the lack of new principles and approaches in the development of jet propulsion and, secondly, understanding of the direction of further interstellar missions.

In [9] we focused on studying the possibility of the emergence of life in stellar systems located near the Sun. This study focused on exploring the possibility of life in stellar systems located near the Sun. As it is known, all biological species on Earth have a unique DNA code (Deoxyribonucleic Acid), which determines the entire diversity of biological species. DNA includes the following elements: C, O, N, and P. A new concept of DNA-stars was introduced, in which the spectra of the elements C, O, N, and P were recorded together. The possibility of synthesizing Na, Mg, S, K, Fe, Co, Cu, Zn, Ca, Mn and Mo, which regulate the growth and development of elementary biological forms, is also discussed.

However, these elements are synthesized on different stars. For example, according to the B^2FH model [25], C and N are synthesized during the death of low-mass stars; O, Na, and K are synthesized during the explosion of massive stars; Mn, Fe, Co and Cu are synthesized mainly during the explosion of white dwarfs. The synthesis of different elements on different stars makes it impossible to raise biological forms on these stars.

As mentioned earlier, astrophysics also failed the stress test. It was shown in [9] that these models, such as B^2FH, have several disadvantages. With the exception of the drawback mentioned in [26] regarding the frequency of neutron stars' mergers, firstly, there is no invariance of the distribution of elements in the Solar System; secondly, there is no invariance of elements in neighboring stars; thirdly, there is the absence of enriched stars, in particular, stars consisting entirely of Th and U, and, fourthly, the absence of a significant number of elements in interstellar space. The error is visible even in the name of the Galactic Chemical Evolution (GCE) models, so these models are not Galactic Chemical Transport (GCT) models. Especially for angry opponents, the simplest transfer task from the textbook is shown in Table 1 below. This problem has no solution within the framework of modern astrophysics.

Table 1. A simple task to test GCE models

"The solar reactor is weak and can synthesize mainly hydrogen and helium. According to B^2FH and K^2L models, the thorium can be synthesized in neutron stars (NS), which have a powerful reactor. The closest star system to us is RX J1856.5-3754, which is located at a distance of 167 pc from the Sun. In the Solar System was recorded 1 gram of thorium. How much thorium was produced by the NS donor star?"

Note that the absence of a transport equation in the Galaxy Chemical Evolution (GCE) models such as the B^2FH and K^2L models is just the tip of the iceberg.

Thus, there are four main drawbacks in the theories of B^2FH and K^2L:

- The invariance of element distributions in the Solar System is not recorded;
- Invariance of element distributions on neighborhood stars is also not recorded;
- This is the absence of super-mega-enriched stars, called as donor–stars;
- There is no significant amount of heavy traces in interstellar space.

In this situation, we suggest switching from metallization model, which includes the nuclear fusion process in the donor star and interstellar transfer from donor star to acceptor star [25, 26], to the author's self–enrichment model [9], in which the majority of the elements, which have been found out in the solar system, have been synthesized in our Solar System. Therefore, the theory of the buoyancy of elements and isotopes, developed earlier to describe the processes occurring in the interior of the planet in [1, 2, 3], is generalized to stars. Thus it was assumed in [9] that terrestrial, solar, and ensemble-averaged stellar reactors have a common multilayer structure of K–Sr–Cs–Pb–Th–U.

Based on the chemical compounds, a new method for searching for habitable star systems was developed and 48 DNA-stars in the solar neighborhood were identified, on which life is possible [9,10]. These stars make up only 1.3 % of the total number of 3757 studied stars from the HSC (Hypatia Stellar Catalog, [28]). Recall that the stars, in spectra of which C, N, O, and P values other than zero in their spectra are called DNA–stars. The closest to the Solar System is the DNA-star with the HIP number 15510, which belongs to the G8V class and is located at a distance of 6 PC from the Solar system. Nine DNA-stars have been identified that have the greatest chemical similarity to the solar spectrum. The spatial distribution of these DNA stars is shown in Fig. 6.

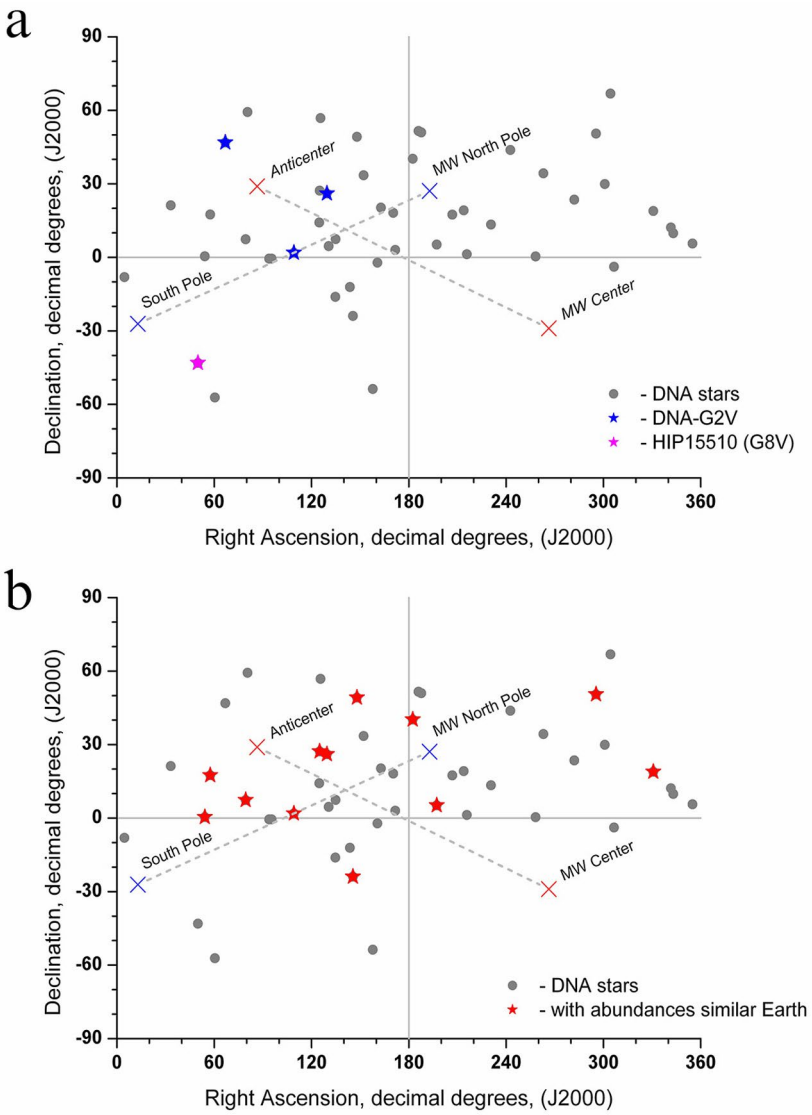


Fig. 6. The spatial distribution of DNA stars (in the spectra of which the elements C, N, O, and P predominate) in the 200 pc neighborhood of the Solar System is shown. In both figures, the 48 DNA stars are highlighted in grey color as a background. In Figure (a): Three blue stars belong to DNA-stars of G2V spectral class (like our Sun). Purple star (HIP15510, G8V class) also belongs to the class of DNA-stars and is closest to our Solar system; (b) — stars that have abundances similar to the Solar system are presented as red stars.

CONCLUSION:

And the last, most important question. Once again, we remind readers of the following. Unfortunately, we have to admit that neither geophysics, astronomy, nor astrophysics passed the stress test. In particular, it was emphasized in [19] that buying one banana in a supermarket calls into question the conduct of such complex and expensive lunar exploration expeditions as Artemida, Chang-E and Luna 25–27, and others, at least within the framework of the tasks currently stated in these missions.

Whether are nuclear astrophysicists losers or cheaters? If the nuclear astrophysicists present themselves as cheaters or gangsters, they should understand that, as in the case of fraud in experiments with geoneutrino, fraud in stellar (thermonuclear) synthesis will sooner or later become public



Fig. 7. Banana equivalent dose (BED) is often correlated with 10^{-7} sievert (0.1 μSv); Potassium-40 (^{40}K) is a long-lived naturally occurring radioactive isotope of potassium with a half-life of 1.251(3) billion years (Ga). Thus, the total lifetime is equal to 2.502 Ga. Please note that the decay time of potassium-40 gives the upper limit of our planet's existence. It follows that 4.5 Ga ago our planet simply did not exist.

knowledge and they will have to deal not with scientists, but with the DOE, NSF, Treasury Department, police (FBI), government, and Congress. However, if they declare themselves losers, then the question of the nomination and the award of author to the Nobel Prize is relevant, please see author's studies [1, 2, 3, 4, 5] about nuclear ^{40}K fuel layer. This nuclear ^{40}K fuel layer is the basis of the new volcanological and seismological theory, the revisions of the theory of subduction and continental drift, the origin of water, oils, ores and diamonds, the Moon-Earth viscous stream-droplet separation, the new elemental buoyant theory of inner structure of planets and stars, and finally, this ^{40}K fuel layer is the milestone of basic principles of creation of habitable planets around stars nearby the Sun, [9].

References

[1] Safronov A. N. The Basic Principles of Creation of Habitable Planets around Stars in the Milky Way Galaxy // International Journal of Astronomy and Astrophysics. 2016. V. 6. P. 512–554. https://doi.org/10.4236/ijaa.2016.64039.
[2] Safronov A. N. A New View of the Mass Extinctions and the Worldwide Floods // International Journal of Geosciences. 2020. V. 11. P. 251–287. https://doi.org/10.4236/ijg.2020.114014.
[3] Safronov A. N. New Theory of Effusive and Explosive Volcanic Eruptions // International Journal of Geosciences, 2022. V.13. No.2 P. 115–137. https://doi.org/10.4236/ijg.2022.132007.
[4] Safronov A. N. Astronomical Triggers as a Cause of Strong Earthquakes // International Journal of Geosciences. 2022. V. 13. P. 793–829. https://doi.org/10.4236/ijg.2022.139040.
[5] Safronov A. N. Kepler's Conjunction for Two Strong Earthquakes in Turkiye in February 2023 // Open Journal of Earthquake Research, 2023. V. 12. P. 27–43. https://doi.org/10.4236/ojer.2023.122002.
[6] Safronov A. N. The End of Einstein's Astronomy: Astronomical Origin for the Largest Marsquake Observed by InSight // HAL preprint. 2024. Hal-04556936. https://hal.science/hal-04556936.
[7] Safronov A. N. Theory of the Origin of Terrestrial and Lunar Ores // International Journal of Geosciences. 2023. V. 14. P. 547–583. https://doi.org/10.4236/ijg.2023.146030.
[8] Safronov A. N. A Few Notes Regarding Origin of Diamonds, Water, Natural Gas and Oil // Open Journal of Geology. 2025. V. 15. P. 309–330. https://doi.org/10.4236/ojg.2025.156015.
[9] Safronov A. N. Life Origin in the Milky Way Galaxy: I. The Stellar Nucleogenesis of Elements Necessary for the Life Origin // Journal of High Energy Physics, Gravitation and Cosmology. 2024. V. 10. P. 647–680. https://doi.org/10.4236/jhepgc.2024.102040.

[10] Safronov A.N. Life Origin in the Milky Way Galaxy: II. Scanning for Habitable Stellar Systems on Behalf of Future Space Missions // Journal of High Energy Physics, Gravitation and Cosmology. 2024. V. 10. P. 681–692. https://doi.org/10.4236/jhepgc.2024.102041.
[11] Safronov A.N. Life Origin in the Milky Way Galaxy: III. Spatial Distribution of Overheated Stars in the Solar Neighborhood // Journal of High Energy Physics, Gravitation and Cosmology. 2024. V. 10. P. 693–709. https://doi.org/10.4236/jhepgc.2024.102042.
[12] Safronov A.N. The Effect of a Monatomic Layer on a Surface on the Transition Radiation // Journal of High Energy Physics, Gravitation and Cosmology. 2024. V. 10. P. 710–723. https://doi.org/10.4236/jhepgc.2024.102043.
[13] Safronov A.N. Pythagoras-Platonic cosmology on the examples of strong earthquakes of 2024 with magnitude greater than M_w7 // HAL Open Science, preprint. 2025. HAL–ID: hal-05010916, https://hal.science/hal-05010916v1.
[14] Сафронов А.Н. Новая теория эксплозивных и эффузивных вулканических извержений // Материалы II Всероссийской научной конференции с международным участием «Современные методы оценки сейсмической опасности и прогноза землетрясений«, посвящается 100-летию академика В. И Кейлис-Борока, 29–30 сентября 2021, ИТПЗ РАН, г. Москва, Россия.
[15] Сафронов А. Н. Поиск обитаемых звездных систем для будущих межзвездных миссий // Материалы Девятнадцатой международной конференции «Современные проблемы дистанционного зондирования Земли из космоса», 15–19 ноября 2021, ИКИ РАН, г. Москва, Россия.
[16] Сафронов А.Н. Галактика Млечного Пути, палеоклимат и массовые вымирания // Материалы Восемнадцатой Всероссийской Открытой конференции с международным участием «Современные проблемы дистанционного зондирования Земли из космоса». 16–20 ноября. 2020. ИКИ РАН, 2020. С. 289. doi:10.21046/18DZZconf-2020a, ISBN 978–5-00015–052–8.
[17] Сафронов А.Н. Новая теория эксплозивных и эффузивных вулканических извержений // XXIII международная конференция «Физико-химические и петрофизические исследования в науках о Земле». Стендовый доклад на секции «Петролого-геофизические подходы построения моделей состава и строения планетарных тел и космохимия». 26–28 сентября 2022 г., Москва, Сборник тезисов докладов. М.: ИГЕМ ЗФР. 2022. С. 238–239. ISBN 978–5-88918–069–9.
[18] Сафронов А.Н. Теория образования земных и лунных руд // Материалы 21-й Международной конференции «Современные проблемы дистанционного зондирования Земли из космоса». Москва, ИКИ РАН, 13–17 ноября 2023 г. https://doi.org/10.21046/21DZZconf-2023a; ISBN 978–5-00015–065–8.
[19] Сафронов А.Н. О кометном происхождении алмазов, воды, природного газа и нефти // Материалы 23-й Международной конференции «Современные проблемы дистанционного зондирования Земли из космоса». 2025. Москва. ИКИ РАН. 10–14 ноября 2025 г. С. 329. https://doi.org/10.21046/23DZZconf-2025a. ISBN 978–5-00015–073–3.
[20] Safronov A.N. Scanning for Habitable Stellar Systems on Behalf of Future Space Missions // Moscow, 2023, Solar system Symposium, 14M–S3, Space Research Institute, Moscow, Russia, October 9–13, 2023. P. 380–384. DOI: 10.21046/14MS3–2023.
[21] Safronov A.N. Theory of the origin of terrestrial and lunar ore // the Fifteenth Moscow Solar System Symposium, 15M–S3, Space Research Institute, Moscow, 21–25 October 2024. P. 220–221. https://doi.org/10.21046/15MS3–2024, ISBN 978–5-00015–068–9.
[22] Сафронов А.Н. Палеоклимат и массовые вымирания // Всероссийская конференция с международным участием, посвященная памяти академика А.М. Обухова, «Турбулентность, динамика атмосферы и климата 2020». 10–12 ноября 2020 г. Сборник тезисов докладов. М.: Физматкнига, 2020. С. 90. ISBN 978-5-89155-340-8.
[23] Сафронов А.Н. Ядерная геофизика как теоретическая основа современной вулканологии и сейсмологии // Вулканизм и связанные с ним процессы. Материалы XXIX ежегодной научной конференции, посвященной Дню вулканолога, 30 марта – 4 апреля 2026 г. Петропавловск-Камчатский: ИВиС ДВО РАН, 2026. С. 212–215. ISBN 978-5-902424-45-1.
[24] Hollenbach D.F., Herndon J.M. Deep-Earth Reactor: Nuclear Fission, Helium, and the Geomagnetic Field // Proceedings of the National Academy of Sciences of the United States of America (PNAS). 2001. V. 98. P. 11085–11090. https://doi.org/10.1073/pnas.201393998.
[25] Herndon J.M. Terracentric Nuclear Fission Georeactor: Background, Basis, Feasibility, Structure, Evidence and Geophysical Implications. // Current Science. 2014. V. 106. P. 528–541.

[26] Burbidge E. M., Burbidge G. R., Fowler W. A.; Hoyle F. Synthesis of the Elements in Stars // Reviews of Modern Physics. 1957. V. 29. P. 547–650. https://doi.org/10.1103/revmodphys.29.547.
[27] Kobayashi C., Karakas A. I., Lugaro M. The Origin of Elements from Carbon to Uranium // the Astrophysical Journal. 2020. V. 900. P. 179. https://doi.org/10.3847/1538–4357/abae65.
[28] Hinkel N. R., Timmes F. X., Youngm P. A., Pagano M. D., Turnbull M. C. Dataset: Stellar Abundances in the Solar Neighborhood: the Hypatia Catalog. 2020. https://www.hypatiacatalog.com/hypatia/default/launch.

LIFE ORIGINATION HYDRATE THEORY: LIVING-MATTER ORIGINATION AND DEVELOPMENT AND POSSIBLE SIGNATURES OF PLANETARY HABITABILITY

E. A. Kadyshevich[1], V. E. Ostrovskii[2]
[1] *Obukhov Institute of Atmospheric Physics RAS, Moscow, Russia; kadyshevich@mail.ru;*
[2] *Karpov Institute of Physical Chemistry, Moscow, Russia, retired; ostrovskii.victor@mail.ru*

KEYWORDS:
Discoveries underlying Life Origination Hydrate Theory, living-matter origination thermodynamic grounds, CH_4-hydrate as living-matter cradle, life-origination mineral sources, natural conditions for living matter origination, DNA natural synthesis, chirality and racemization delay origin in living matter, astrobiology, habitability features available for remote sensing.

INTRODUCTION:
Living matter origination represents one of the most receptive to public interest and most complicated problems of natural history. We consider a number of sub-problems entering into it.

The Life Origination Hydrate Theory (LOH theory), developed by us in 2000–2023, identifies firstly the natural sources, environmental conditions, chemical processes, biophysicochemical principles, and mechanisms underlying the emergence and proliferation of DNA double helixes and the simplest self-replicating living entities. These primitive living entities — first created by Nature at the dawn of its biochemical activity — possessed a set of hereditary traits, such as nucleotide sequence and DNA chain length, as well as the prerequisites for the next stages of evolution.

THE FOUNDATIONS OF THE LIFE ORIGINATION HYDRATE THEORY (LOH THEORY):
The LOH–Theory bears on the following three discoveries made by us:

- DNA and RNA molecules, which are essential and inherent constituents of any living entity, could have formed within a matrix structure of a specific geometry exclusively, and the only mineral matrix structure on the Earth capable of housing any DNA and RNA structural element and each of these molecules as whole is the CH_4-hydrate structure II;
- highly concentrated undisturbed water/functional-polymer systems have, at low temperatures, matrix gas-hydrate structure;
- CH_4-hydrate and NO_3^-– and PO_4^{3-}-ions represent the unique mineral triad necessary and sufficient for synthesis of nucleic acids, amino acids, and proteins on the basis of reactions proceeding with a decrease in free energy.

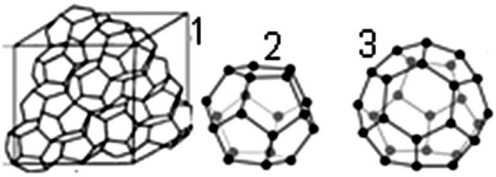


Fig. 1. Crystal lattice of gas-hydrate structure II: 1 — elementary cell formed by 136 H_2O making 16 small and 8 large cavities; 2 — small cavity, pentadodecahedron, d=0.48 nm; 3 — large cavity, hexadecahedron, d=0.69 nm; the vertexes of cavities are O-atoms of water (“hosts”), the length of each edge is the sum of the lengths of the O–H valence bond in a water molecule and H···O hydrogen bond between this and an adjacent water molecule; within the cavities, some molecules or atomic groups (''guests'') are located

In addition, the following sub-problems of living matter origination are solved:

- clarification of the ambient conditions supplying the chemical reactions of the chosen minerals into a multitude of different DNAs with random N-base sequences and clarification of the mechanisms of these reactions;
- revelation of the Earth's regions where the deposits of minerals necessary for living matter origination are located in immediate vicinity to each other;
- clarification of the bio-physico-chemical mechanism of transformation of the multitudes of randomnesses, i.e., of different DNAs, into the multitudes of directednesses, i.e., of the DNA double-strands, each multitude containing identical double-strands capable of vertical transmitting N-base sequences;
- revelation of the possible mechanism of the functional differentiation between simplest plants and animal entities;
- revelation of causes and mechanisms of chirality and racemization delay;
- clarification of the way of transfer of inanimate minerals into the pre-cellular and unicellular living matter having prerequisites for genetic codes formation;
- revelation of signs of the possible life beyond the Earth.

THE MAIN RESULTS OF SOLVING THE ABOVE SUB-PROBLEMS:

(a) The thermodynamic possibility of the following reactions allows syntheses of DNAs, RNAs, and proteins from the mineral triad specified above:

(1) $28.2KNO_3(cr)+38CH_4(g)=C_4H_4N_2O_2(cr)(U)+C_4H_5N_3O(cr)(Cy)+$
$+C_5H_5N_5O(cr)(G)+C_5H_5N_5(cr)(Ad)+4C_5H_{10}O_5(cr)(DR)+28.2\ KOH(cr)+$
$+32.4\ H_2O(lq)+6.6\ N_2(g);$

(2) $29.4KNO_3(cr)+38CH_4(g)=C_4H_4N_2O_2(cr)(U)+C_4H_5N_3O(cr)(Cy)+$
$+C_5H_5N_5O(cr)(G)+C_5H_5N_5(cr)(Ad)+4C_5H_{10}O_5(cr)(DR)+29.4theKOH(cr)+$
$+31.8H_2O(lq)+7.2N_2(g)+1.5O_2(g);$

(3) $23.25KNO_3(cr)+38CH_4(g)=C_4H_4N_2O_2(cr)(U)+C_4H_5N_3O(cr)(Cy)+$
$+C_5H_5N_5O(cr)(G)+C_5H_5N_5(cr)\ (Ad)+4\ C_5H_{10}O_5(cr)\ (DR)+23.25\ KOH(cr)$
$+22.5\ H_2O(lq)+8.25\ NH_3(g).$

For (1), (2), and (3), ΔG^0 (kJ/mol)= –8281, –8121, and –6146, respectively.

The relative contributions of these reactions to conversion of source minerals are determined by kinetic factors only and depend on the ambient conditions.

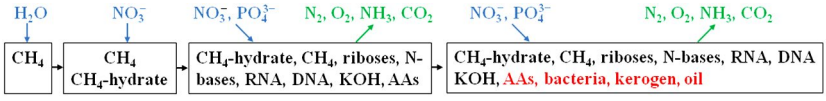


Fig. 2. The living-matter origination history compressed at most

Simplest living entities originated under specified natural conditions within underground and underseabed localizations of the honeycomb CH_4-hydrates from the above-specified mineral triad.

(b) The fact that the number of animal species exceeds the number of plant species by a factor of five to six is explained, and the historical periods, causes, and mechanisms underlying this phenomenon are clarified. It was proven that the possibility of transformation of the random N-base sequences into the ordered ones is caused by the peculiarities of the gas-hydrate matrix and by thermodynamic preferences. The adequate knowledge of the mechanisms behind the life origination and the metabolism evolution is important for far more than just the development of the theory of understanding the world. It is of practical importance for the daily life of human communities and each individual.

For example, it can contribute to the improvement of the methods of detecting and combating various infections, including viral ones, as shown in our recent works.

(c) One of the most important principal scientific results obtained by us lies in the conclusion that the necessary nucleic acids, amino-acids, and proteins could be produced by Nature on the basis of the chosen triad of minerals as a result of thermodynamically conditional chemical reactions, which proceed with a decrease in the Gibbs free energy of the reacting mineral system. Before our works, the opinion about the necessity of external energy for formation of simplest living entities and biologically active substances from minerals had dominated in science.

(d) It is stated on the basis of 3D simulation that the DNA and RNA components and their multi-component fragments are geometrically compatible with the CH_4-hydrate structure II, i.e., the modeled lengths of chemical bonds between DNA (RNA) fragments and of inter-strand H-bonds in the DNA double-helix fragments arranged within gas-hydrate structural cavities coincide well with the lengths of the corresponding bonds measured by X-ray method in DNA (RNA) crystals. This allows for specification of the sources, natural conditions, mechanisms, and succession of the processes that led to the origin of a multitude of multitudes of simplest living entities.

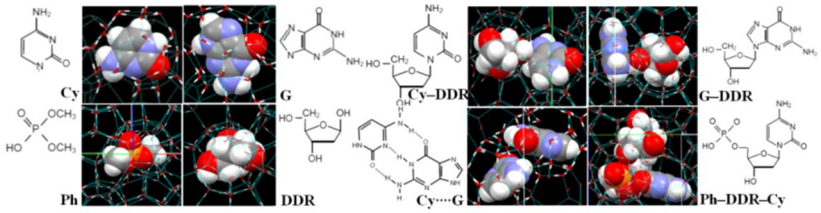


Fig. 3. Scaled arrangement of the DNA fragments in gas-hydrate structure II: cytosine (Cy) and guanine (D) in large cavities, deoxy-D-ribose (DDR) and phosphodiester radical (Ph) in small cavities; Cy in a large cavity DDR in a small cavity; G in a large cavity — DDR in a small cavity; Cy····G pair in two adjacent large cavities; Ph in a small cavity — DDR in a small cavity — Cy in a large cavity. The spheres are the atoms of H (white), O (red), C (gray), N (blue), and P (yellow), the ideal matrix cavities are bounded with H_2O molecules.

(e) The natural conditions of CH_4 activation by nitrate ions are revealed, and it is stated that all chemical reactions that lead to synthesis of nucleic acids, amino-acids, proteins, and other living-matter components from the minerals of the specified triad of natural substances are thermodynamically permissible, i.e., proceed with a decrease in the Gibbs free energy.

(f) The mechanism of differentiation of entities into plants and animals and the cause of the manifold predominance of animals over plants is proposed.

(g) The phenomena of chirality and of racemization delay as applied to different natural substances are explained; the conditions are specified. Chirality is a specific feature of living matter. The mechanism of origination of the phenomenon of chirality of organic substances, in particular, of the biologically active ones, and the cause and mechanism of the racemization delay are first clarified.

(h) The cause of the absence of the Cy(Py)–Ad(Pu), Th(Py)–G(Pu), G(Pu)–Ad(Pu), and Cy(Py)–Th(Py) H-bonds between strands in the DNA double helixes and the selective occurrence of only the Cy(Py)–G(Pu) and Th(Py)–Ad(Pu) H-bonds is revealed; therewith, the cause of unrealizability of the G(Pu)–Ad(Pu) and Cy(Py)–Th(Py) H-bonding is revealed on the basis of three-dimensional simulation and the cause of unrealizability of the Cy(Py)–Ad(Pu) and Th(Py)–G(Pu) H-bonding is revealed on the basis of two-dimensional simulation.

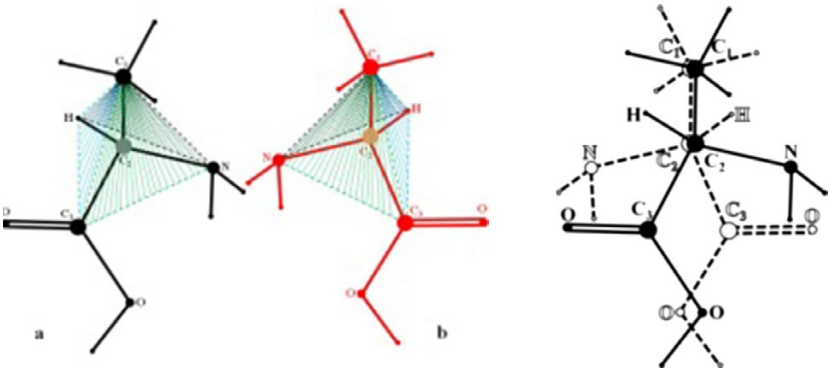


Fig. 4. D-alanine (a) and L-alanine (b) structures; C_1, C_3, H, and N atoms are vertexes of the tetrahedron with the central C_2 atom; HC_1N and HNC_3 facets are located behind the drawing plane; HC_1C_3 and C1NC3 facets are located in front of the drawing plane. Superposition of the D-alanine structure (solid) on the L-alanine structure (dashed); the C_1–C_2 bond projections of these structures on the drawing plane are superimposed. The C_1, C_3, H, and N atoms are vertexes of tetrahedron with the central C_2 atom

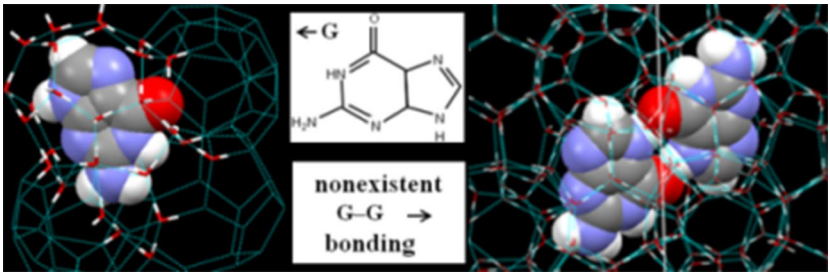


Fig. 5. Illustration of the cause of unrealizability of the Pu–Pu bonding in DNA double helixes (by the example of G); left figure: guanine in a large cavity, right figure: nonexistent G–G dimer going beyond two adjacent large cavities. The Mercury program shows that too many G atoms in the right figure are beyond the large cavity (see the right figure). Py-pyrimidime, Pu-purine; Cy-cytosine, Ad-adenine, Th-thymine, G-guanine.

(i) The living matter simplest elements formation proceeded with O_2 and N_2 emission to the atmosphere. The periods of intense living-matter origination coincided with the periods of stepwise increase in the atmospheric O_2 pressure. The ancient atmosphere transformed to the present O_2/N_2 one.

(j) Signatures of habitable planets are special phenomena considered by us. Population of underground conventional and unconventional (near-surface and deep-seated) CH_4-hydrate localizations with different bacteria, which is proved by analyses of available data, count in favor of the LOH–Theory. The N_2, O_2, NH_3, and CO_2 admixtures in the gases emitting from the CH_4-hydrate localizations count indirectly in favor of the LOH–Theory, because these gases are the side products of living matter synthesis. The LOH–Theory allows the following conclusion. Emissions of gaseous N_2, O_2, H_2O, CO_2, NH_3, and CH_4 in their combinations, solid phosphates and niters in their community, and the underground temperatures of about 270 K could be considered as the markers of the possibility of the life occurrence there.

(k) Based on the LOH Theory and available data, it was shown that CH_4, rather than bacteria, is the primary component of the subsurface CH_4-hydrate deposits (conventional and unconventional). Methane is the primary product; bacteria are formed through the utilization of CH_4 as a source material for living matter creation, while kerogen is the accumulations of its remains.

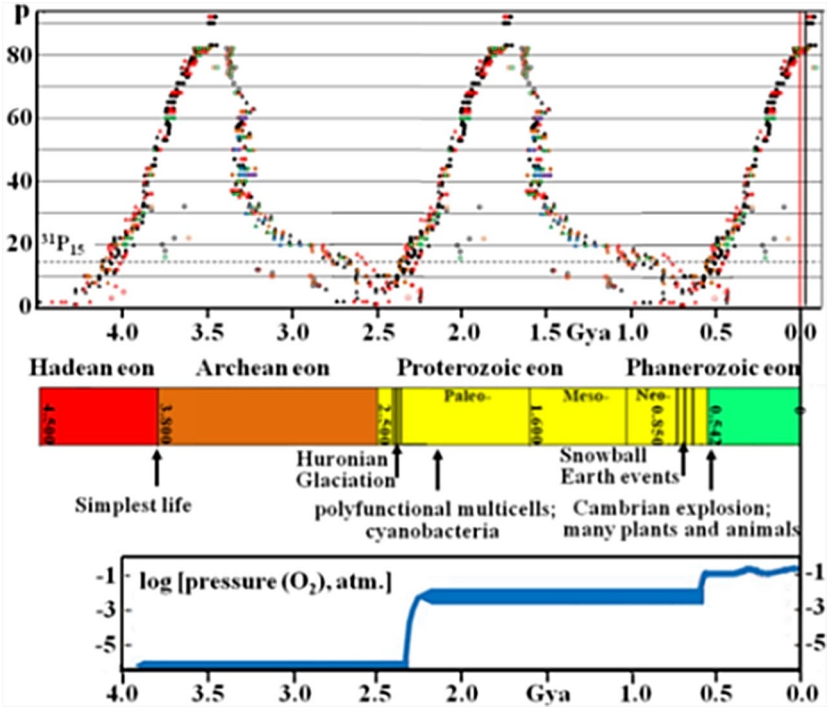


Fig. 6. Milestones of the Sun/Earth-system history (Gya – billion years ago): the upper three-humped scheme describes the past history of the birth of chemical elements in the Sun/Earth system as follows from the PFO-CFO Theory (abscissa is the time, where 0 is the current time, and ordinate P is the proton number in the born elements); the middle scheme describes the paleontological Earth climate history in the same time scale; the lower scheme describes the O_2 pressure variations in the Earth atmosphere with time. The Earth, whose age is estimated at approximately 4.5 Gy, was formed as a result of the explosion of the radiative zone of the star that was the "great grandmother" of the Sun. We are now living in the period marked as zero time and indicated by the red vertical line in the upper subfigure. This figure provides the basis for original and encouraging understanding the history of the today Sun and the phenomena that occurred before and after its formation.

CONCLUSION:

The LOH–Theory can be verified; the principal construction of the apparatus and the methodical grounds are proposed.

Apparently, the LOH–Theory was confirmed by the authors of study, who discovered numerous populations of bacterial microflora in CH_4-containing soil in Sweden, near the boundary of the thawing permafrost layer.

It is worked in the frame of IAP RAS state assignment no. 125020501413–6.

Session 8.
SMALL BODIES INCLUDING SPACE DUST (SB)
Oral Session

NEW PUBLIC DATABASE OF ASTEROID POLARIMETRIC OBSERVATIONS: STRUCTURE, CONTENT, AND SCIENTIFIC APPLICATION

M. P. Shcherbina[1], N. N. Kiselev[2,1]
[1] *Institute of Astronomy RAS, Moscow, mpshcherbina@inasan.ru*
[2] *Crimean Astrophysical Observatory, Nauchny*

KEYWORDS:
asteroids, polarimetry, near-Earth asteroids, database, polarization phase curve, small Solar System bodies

INTRODUCTION:
Polarimetric observations provide one of the most informative remote-sensing techniques for investigating the physical properties of asteroid surfaces. Polarization phase curves contain information on geometric albedo, surface texture, particle size distribution, and light-scattering properties of regolith. Near-Earth asteroids (NEAs) are of particular interest because they can be observed over a much wider range of phase angles than most main-belt asteroids.

Although several thousand asteroid polarimetric measurements have been published over the past decades, these observations remain scattered among numerous articles, catalogs, and observing programs. The Asteroid Polarimetric Database (APD) [1] represents the principal public compilation of such observations. However, its latest public update dates back to 2022, while a considerable amount of new observational material has appeared since then.

The primary goal of the present project is not only to update the available collection of asteroid polarimetric observations, but also to provide a unified research platform that enables efficient search, visualization, selection, and statistical analysis of homogeneous polarimetric datasets.

DATABASE STRUCTURE:
In this work, we present a new public database of asteroid polarimetric observations combining APD data, recent literature sources (2022–2026), and new observations obtained with the 2.6-m telescope of the Crimean Astrophysical Observatory and at telescope Zeiss-2000 of shared research facility "Terskol observatory" of Institute of Astronomy of the Russian Academy of Sciences. At present, the database contains more than 12,000 observations for 572 asteroids obtained at 81 observatories.

The database is implemented as an open-access web resource: https://polarimetry.inasan.ru/ The web application is based on Django and PostgreSQL and has been specifically designed for scientific work with asteroid polarimetric observations rather than simple data storage.

INDIVIDUAL ASTEROID PAGES:
Each asteroid is represented by an automatically generated individual page combining all available information about the object.

Besides the asteroid designation, users can access dynamical classification, asteroid family, Tholen and SMASSII taxonomic classes [2, 3], geometric albedo values collected from external databases, complete bibliographic information, lists of observatories, observational filters, and phase-angle coverage.

The central element of the page is an interactive polarization phase curve combining all available observations of the asteroid. The user may display individual filter groups, export the figure in PNG or SVG formats, and download the complete observational dataset in TXT or CSV formats.

The accompanying observation table contains observation dates, observational bands, phase angles, measured polarization parameters, observatories, and bibliographic references for every individual measurement.

DATA SELECTION AND FILTERING:
One of the principal advantages of the database is its flexible filtering system allowing users to construct observational samples according to scientific objectives rather than manually collecting measurements from numerous publications.

The currently implemented filtering categories are summarized in Table 1.

Table 1. The main filtering categories in the database

Filtering category	Parameters
Object identification	asteroid number
Dynamical class	MBA, NEA, MCA, JT, Centaur
Asteroid families	Flora, Eos, Eunomia, Koronis, Themis, Adeona, etc.
Tholen taxonomy	C, S, X, D, G, B, M, P, etc.
SMASSII taxonomy	C, Ch, Cgh, Sq, Sr, Q, V, K, L, D, etc.
Observational band	U, B, V, R, Rc, R2, I, Ic, J, H, Ks, WR, etc.
Observatory	CrAO, CASLEO, Catalina, Steward, Sanglokh, McDonald, Palomar, etc.

The interactive plots additionally employ visual grouping of observations. Marker shape corresponds to the observational filter group, whereas marker color identifies the original publication. Such visualization considerably facilitates comparison of independent observational datasets and rapid identification of observational gaps.

SCIENTIFIC APPLICATIONS:
The database has already been employed to assemble observational samples of asteroids belonging to different dynamical and taxonomic populations. These samples are currently being used to investigate statistical properties of polarization phase curves and to search for objects exhibiting unusual polarimetric behavior.

The conference presentation will focus on the first scientific results obtained using the database, including statistical trends revealed for different asteroid populations and examples of objects whose polarimetric properties significantly differ from those of their taxonomic counterparts.

The database is intended to become a continuously updated public resource supporting future polarimetric observations and statistical investigations of asteroid surface properties.

REFERENCES:
[1] Lupishko D. F. Asteroid Polarimetric Database // NASA Planetary Data System Small Bodies Node, 2022.
[2] Tholen D. J. Asteroid taxonomy from cluster analysis of photometry: PhD Thesis, University of Arizona, 1984.
[3] Bus S. J., Binzel R. P. Phase II of the Small Main-Belt Asteroid Spectroscopic Survey: A feature-based taxonomy // Icarus. 2002. V. 158. P. 146–177. DOI: 10.1006/icar.2002.6856.

MULTISCALE 3D MODELLING OF TENSION-FRACTURE AND SHEAR DEFORMATION SYSTEMS ON THE SURFACE OF 67P COMET

O. Turchinskaya[2], S. Krasilnikov[2], B. Wu[2], A. Basilevsky[1]
[1] *Vernadsky Institute of Geochemistry and Analytical Chemistry RAS Moscow, Russia, turchinskaya@geokhi.ru*
[2] *Research Centre for Deep Space Explorations, The Hong Kong Polytechnic University, Hong Kong, sergey.krasilnikov@polyu.edu.hk*

KEYWORDS:
comets, 67P, Churyumov–Gerasimenko, Surface processes

INTRODUCTION:
Comet 67P/Churyumov–Gerasimenko is a small bilobate body with a diverse surface morphology. Its surface comprises exposed consolidated terrains, smooth plains, dust-covered units, large-scale depressions, cliffs, talus deposits, boulders, and fracture systems. The distribution of these landforms differs markedly between the northern and southern hemispheres and reflects the combined effects of seasonal insolation, sublimation-driven activity, erosion, material transport, and mass wasting [1].

COMET STRUCTURE:
The bilobate nucleus is interpreted as an accreted body composed of two distinct objects with independently developed layering systems that merged in a gentle, low-velocity collision [2]. Its bilobate geometry is also associated with shape-driven shear deformation and the development of shear-fracture and fault networks on the surface and within the nucleus [3]. Regional structures extending over hundreds of metres and approaching one kilometre in length may preserve evidence of nucleus-scale deformation. At metre and millimetre scales, however, the geometry of tensile fractures is increasingly controlled by local heterogeneities and the mechanical properties of the material.

In this study, we produced a multiscale three-dimensional map of tensile-fracture and shear-deformation systems. Analysis of their spatial distribution and morphometric parameters revealed a predominantly polar orientation of the regional structures and enabled us to estimate the depth of individual fractures, which may reach several tens of metres. Towards smaller scales, the influence of the global nucleus structure becomes less pronounced, whereas local material properties become increasingly important. Consequently, the orientation of metre- and millimetre-scale fractures may deviate substantially from that of the regional structural systems.

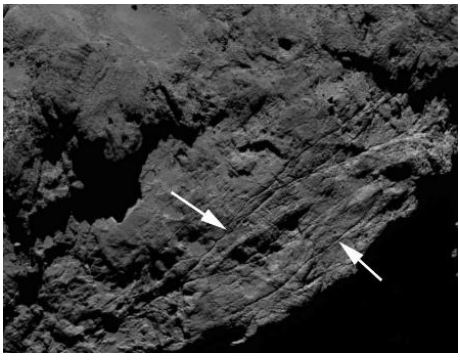


Fig. 1. Crop of NAC image of long hundreds-of-meters-long fractures in the small lobe's southern hemisphere in the Wosret region (N20160127T074441724ID20F22)



Fig. 2. NAC image of polygonal fracture patterns in consolidated materials in the big lobe's northern hemisphere in the Seth/Atum regions (N20160908T232834739ID20F22)

Local polygonal fracture networks are interpreted as thermal-contraction features produced by diurnal and seasonal temperature variations [1, 4]. The obtained morphometric data provide a basis for thermomechanical modelling of crack initiation and propagation in a heterogeneous porous medium subjected to repeated thermal loading.

Our results help to assess the role of fracturing in the mechanical degradation of consolidated cometary material. Fractures create zones of weakness whose continued development may lead to fragmentation, cliff collapse, and the formation of talus deposits and boulders. In addition, the opening of deep fractures may expose volatile-rich material and enhance local gas activity, including short-lived outbursts associated with highly volatile species such as CO and CO_2 [5].

ACKNOWLEDGMENTS:
This project is supported by The Hong Kong Polytechnic University Startup Funding P0052619. Additionally, the work of OT and AB was partly carried out within the state assignment of the Vernadsky Institute of Geochemistry and Analytical Chemistry of the Russian Academy of Sciences (GEOKHI RAS).

REFERENCES:

[1] El-Maarry M. R., Groussin O., Keller H. U. et al. Surface Morphology of Comets and Associated Evolutionary Processes: A Review of Rosetta's Observations of 67P/Churyumov–Gerasimenko // Space Science Reviews. 2019. V. 215. No. 4. Article 36. DOI: 10.1007/s11214-019-0602-1
[2] Massironi M., Simioni E., Marzari F. et al. Two Independent and Primitive Envelopes of the Bilobate Nucleus of Comet 67P // Nature. 2015. V. 526. No. 7573. P. 402–405. DOI: 10.1038/nature15511.
[3] Matonti C., Attree N., Groussin O. et al. Bilobate Comet Morphology and Internal Structure Controlled by Shear Deformation // Nature Geoscience. 2019. V. 12. P. 157–162. DOI: 10.1038/s41561-019-0307-9.
[4] Auger A.-T., Groussin O., Jorda L. et al. Meter-Scale Thermal Contraction Crack Polygons on the Nucleus of Comet 67P/Churyumov–Gerasimenko // Icarus. 2018. V. 301. P. 173–188. DOI: 10.1016/j.icarus.2017.09.037.
[5] Skorov Yu.V., Rezac L., Hartogh P., Basilevsky A.T., Keller H.U. A Model of Short-Lived Outbursts on the 67P from Fractured Terrains // Astronomy and Astrophysics. 2016. V. 593. Article A76. DOI: 10.1051/0004-6361/201628365.

MODELING OF H_2O AND CH_3OH EMISSION LINES IN THE COMA OF A COMET FOR THE SUBMILLIMETER WAVELENGTH RANGE

M. S. Kirsanova[1], E. I. Baranova[2], Ya. N. Pavlyuchenkov [1]
[1] *Institute of Astronomy RAS, kirsanova@inasan.ru*
[2] *Lomonosov Moscow State University, Faculty of Physics*

KEYWORDS:
comets, cometary coma, water, radiative transfer

ABSTRACT:
Water and methanol are among the most common molecules found in the gas surrounding a comet's nucleus. To get ready for future comet observations with the Millimetron space telescope, we need to know how well standard analysis tools will work. In this study, we build a computer model of a comet as it would be seen by Millimetron. Using this model, we simulate water emission lines when they are not in thermal equilibrium. We then take the simulated emission data and analyze it using a common technique called the rotational diagram method, which assumes thermal equilibrium. This lets us compare the physical conditions we put into the model with the conditions an observer would derive from the analysis. We present the results of this numerical test and discuss the limits of both our comet model and the analysis method. We also estimate how long Millimetron would need to observe in order to detect water signals reliably. Finally, we highlight key gaps in current knowledge that make it difficult to fully model the emission from water and methanol [1], especially regarding non-thermal processes and missing input data.

REFERENCES:
[1] Kirsanova M. S., Pavlyuchenkov Ya. N., Olofsson A. O. H., Lerner M., Single-dish observations and non-LTE analysis of CH_3OH, HCN, and CO line emission in the Oort cloud comet C/2017 K2 (PANSTARRS) // MNRAS. 2026. V. 549. Iss. 4. Article stag1086. doi:10.1093/mnras/stag1086.

DUSTY PLASMAS AT COMET NUCLEUS: SPECIFIC DUSTY PLASMA EFFECTS AND INFLUENCE OF DUST PARTICLE CHEMICAL COMPOSITION

S. I. Popel, A. P. Golub', L. M. Zelenyi
Space Research Institute RAS, Moscow 117997, Russia, popel@cosmos.ru

KEYWORDS:
dusty plasmas, comets, anomalous dissipation, strongly-coupled plasma state, plasma-dust crystal, dust particle chemical composition

INTRODUCTION:
Specific effects inherent exclusively to dusty plasma systems that can be realized near comet's nuclei are considered. Particular attention is paid to such physical processes as anomalous dissipation in dusty plasmas and formation of a strongly-coupled state including a plasma-dust crystal. Furthermore, the influence of dust particle chemical composition on dusty plasma properties at comet's nuclei is discussed.

SPECIFIC DUSTY PLASMA EFFECTS:
We discuss specific effects inherent exclusively to dusty plasma systems that can be realized near comet's nuclei. As it is illustrated, anomalous dissipation in dusty plasmas associated with the effect of dust particle charging is important in the context of describing the dynamics of dust particles above the surface of a comet's nucleus. It is shown that for larger comet's nuclei, dust particles move along damped periodic trajectories, whereas above the surface of a smaller nucleus, under certain conditions, the dynamics of dust particles can be aperiodic in nature because of sufficiently strong anomalous dissipation [1].

Another important effect specific to dusty plasma is the possibility of forming a strongly-coupled plasma state and a plasma-dust crystal, which can probably take place in the vicinity of comet nuclei that have a fairly high dust content in their matter. For comets, the formation of dusty plasma regions at altitudes of up to hundreds of meters is possible. For number densities of dust particles near the comet nucleus exceeding values of ~0.1–1 cm^{-3}, the values of the nonideality parameter reach and exceed the critical value for the formation of a plasma-dust crystal, and the parameters of the dusty plasma system, as a rule, correspond to the formation of a body-centered cubic crystal lattice [2] (Fig. 1).

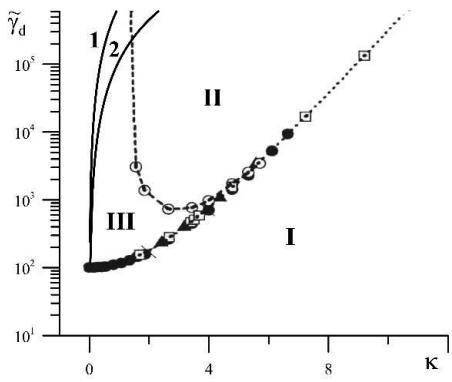


Fig. 1. Phase diagram [1] of Debye systems obtained by numerical simulation. The liquid phase is marked by I. Symbols indicate the boundary between bcc (III) and fcc (II) crystal phases. Lines 1 and 2 characterize the state of the dusty plasma system in the regions of stable equilibrium of dust particles, respectively, for the Churyumov-Gerasimenko comet and the comet described in [3]. is the nonideality parameter, is the so-called structural (lattice) parameter

INFLUENCE OF DUST PARTICLE CHEMICAL COMPOSITION:

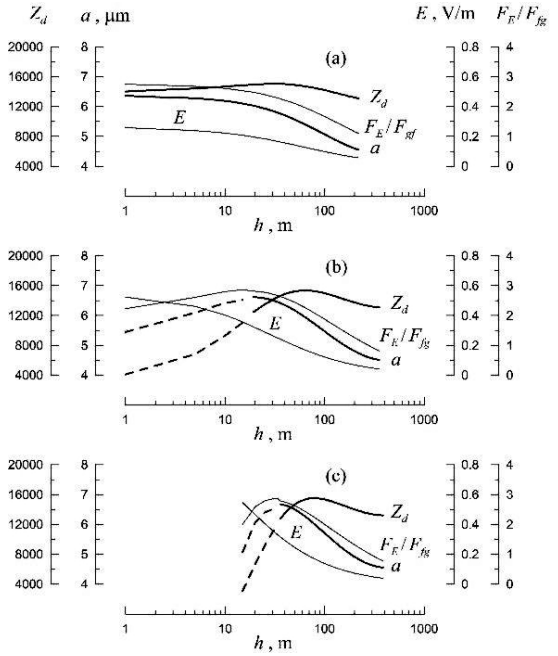


Fig. 2. Size a of silicate dust particles, their charge number Z_d, the ratio of the electrostatic and gas-dynamic forces F_E/F_{fg}, and electric field E as functions of altitude h above the surface of the comet's nucleus for subsolar angles 87° (a), 77° (b), and 0° (c). Calculations [4] were performed for the distance between the comet and the Sun of 5.0 AU. Dashed lines mark the unstable equilibrium positions of dust particles

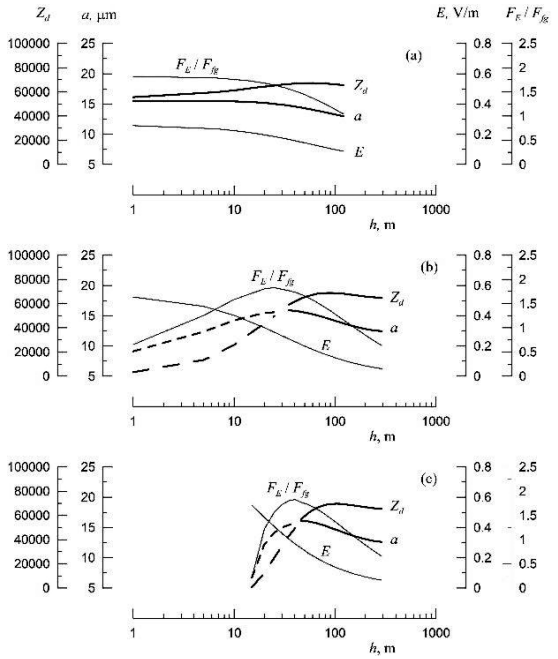


Fig. 3. Size a of water ice dust particles, their charge number Z_d, the ratio of the electrostatic and gas-dynamic forces F_E/F_{fg}, and electric field E as functions of altitude h above the surface of the comet's nucleus for subsolar angles 87° (a), 77° (b), and 0° (c). Calculations were performed for the distance between the comet and the Sun of 5.0 AU. Dashed lines mark the unstable equilibrium positions of dust particles

We consider the influence of dust particle chemical composition on dusty plasma effects near comet's nuclei. We show that the distances from the Sun at which dusty plasma effects manifest for dust particles of different chemical compositions, as well as the altitude range of the region of stable particle equilibrium, differ and depend on the density of the particle material. Figs. 2 and 3 present parameters characterizing the altitude distribution of dust particles, the ratio of the electrostatic force to the force responsible for dust particle entrainment by the gas flow, as well as the electric field above the surface of the comet's nucleus for the case of the comet 67P/Churyumov-Gerasimenko for the situations of silicate and water ice dust particles, respectively.

We discuss also the influence of dust particle chemical composition on specific dusty plasma effects such as the anomalous dissipation, associated with the effect of dust particle charging, as well as the plasma-dust crystal.

ACKNOWLEDGMENTS:
The study was supported by the Russian Science Foundation grant No. 24-12-00064, https://rscf.ru/project/24-12-00064/.

REFERENCES:

[1] Dubinsky A. Yu., Reznichenko Yu. S., Golub' A. P., Popel S. I. On anomalous dissipation in dusty plasma in the vicinity of cometary nuclei and active asteroids // Sol. Syst. Res. 2026. V. 60. Article 12, 7 p. DOI: 10.1134/S003809462560115X.
[2] Popel S. I., Zelenyi L. M. On the possibility of forming a plasma-dust crystal near an atmosphereless celestial body // JETP Lett. 2026. V. 123. No. 9. P. 596–604. DOI: 10.1134/S0021364026600564.
[3] Popel S. I., Golub' A. P., Zelenyi L. M. On dusty plasma processes in the physics of comets // JETP Lett. 2024. V. 120. No. 5. P. 307–314. DOI: 10.1134/S0021364024602653.
[4] Popel S. I., Golub' A. P., Zelenyi L. M. Formation of dusty plasma in the vicinity of comet 67P/Churyumov–Gerasimenko // Plasma Phys. Rep. 2026. V. 52. No. 2. P. 186–197. DOI: 10.1134/S1063780X25604195.

INVESTIGATING THE STRUCTURE, MICROSTRUCTURE AND SHOCK CHARACTERISTICS IN THE LUT DESERT CHONDRITE METEORITE

M. Nastaran[1], A. Kananian[1], A. Rajabi[1], M. Ranjbaran[1], M. Kiani[2]
[1] *School of Geology, College of Science, University of Tehran, Tehran, Iran, maryaaa8754@gmail.com*
[2] *Kian Pars Gemology Institute (KIPA), Tehran, Iran*

KEYWORDS:
meteorites, chondrule, chondrite, petrography

ABSTRACT:
Meteorites provide valuable information about the early solar system and its formation. Earth continuously collects extraterrestrial material ranging from small interplanetary dust particles (IDPs) to larger meteorites. Most meteorites originate from the asteroid belt between Mars and Jupiter, while some may come from comets, planets, and moons. When this material enters Earth's atmosphere, much of it vaporizes due to friction, but the surviving fragments help scientists study the composition and history of their parent bodies [1].

In this study, we examined a chondritic meteorite sample that had previously been identified as a meteorite and was made available to us for further investigation. To examine this sample, we prepared two polished thin sections and one polished mount section. The sample was first examined under a binocular microscope to observe the size, shape, and distribution of the chondrules.

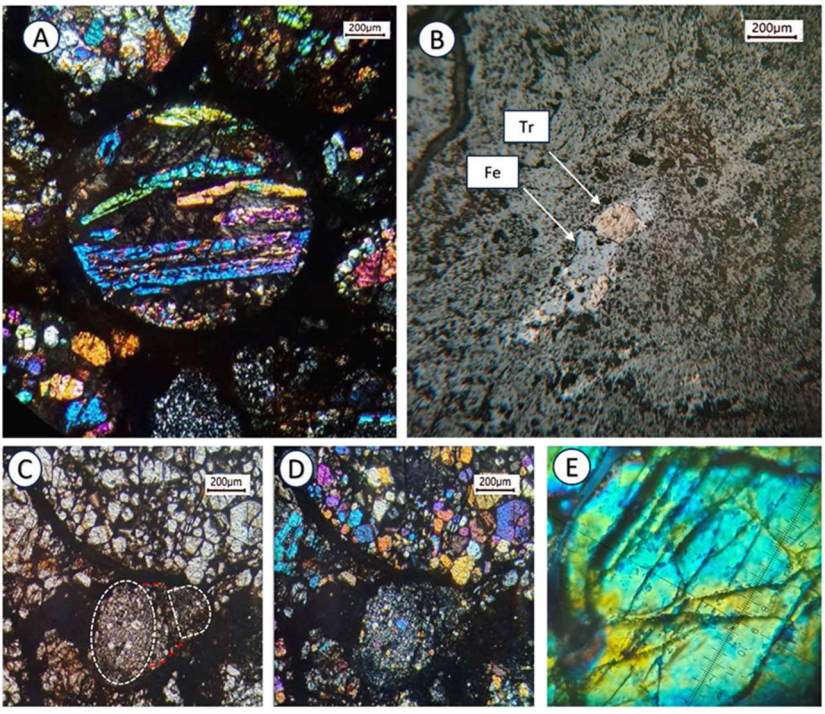


Fig. 1. (A) Barred olivine chondrule in XPL. (B) Presence of iron nickel alloy (Fe, Ni) and troilite (Tr) in the samples (reflected light microscopy). (C) and (D) show a compound chondrule formed by three merged chondrules, which are distinguishable as distinct sections in image (C) under PPL and XPL light. (E) Fluid inclusions in olivine minerals

We then performed petrographic analysis using a microscope equipped with plane-polarized light (PPL), cross-polarized light (XPL), and reflected light. SEM-BSE analysis was carried out to characterize the microstructure and shock features. We also performed laser ablation analysis and Raman spectroscopy.

Our observations revealed a variety of chondrule types and the distribution of metal phases. The analyses identified compound chondrules, barred olivine, barred pyroxene, radial pyroxene, a pair of cryptocrystalline chondrules, and granular olivine-pyroxene chondrules. Each of these chondrule types reflects specific environmental conditions. Radial pyroxene chondrules indicate rapid cooling from a silicate melt droplet and are recognizable by their fan-like (radiating) texture [2]. In addition, we identified calcium-aluminum-rich inclusions (CAIs) within some olivine grains. The abundance of metal phase relative to the chondrules was low, and in terms of distribution, it was located both at the margins and within the chondrules (Fig. 1).

Despite extensive research conducted on meteorites, the precise origin of chondrules remains a subject of debate. Several theories have been proposed, including melting caused by nebular lightning, heating from shock waves, and impact-related processes [3], each of which can, to some extent, account for certain characteristics of chondrules; nevertheless, petrographic evidence continues to serve as a key tool for testing these theories.

REFERENCES:

[1] Rossi A. P., Van Gasselt S. Planetary geology. Cham, Switzerland: Springer International Publishing, 2018.
[2] Rubin A. E. Ordinary Chondrites: The Most Common Meteorites. Cambridge: Cambridge University Press (Cambridge Planetary Science), 2026.
[3] Sears D. W., 2004. The origin of chondrules and chondrites (Vol. 3). Cambridge University Press.

OBSERVATIONS OF SMALL BODIES OF THE SOLAR SYSTEM AT THE TERSKOL AND SANGLOKH OBSERVATORIES

A. Kartashova[1], G. Kokhirova[2], E. Bakanas[1], V. Puzin[1], F. Rakhmatullaeva[2], M. Scherbina[1]
[1] *Institute of Astronomy, Russian Academy of Sciences, Moscow, Russia*
akartashova@inasan.ru
[2] *Institute of Astrophysics, National Academy of Sciences of Tajikistan*
Dushanbe, Tajikistan

KEYWORDS:
asteroids, comets, observations, astrometry, photometry, taxonomy

INTRODUCTION:
Observations of small bodies of the Solar System (asteroids and comets) were carried out in 2025–2026 at the Sanglokh Observatory of the IA NANT (Tajikistan) and the Terskol Observatory of the INASAN (Russia). The program of observations includes asteroids during their closest approaches to Earth and is aimed at solving two key tasks: 1 — developing coordinated observation technology for monitoring potentially dangerous objects and 2 — obtaining comparable astrometric and multicolor photometric data, as well as a preliminary assessment of the taxonomic classification of the studied objects. Simultaneous observations of comets were also conducted.

OBSERVATIONS AND RESULTS:
Observations were conducted during different seasons of the year, which allowed for a significant expansion of the observational program. When forming the observational program, a monthly assessment of the visibility of asteroids from both observatories was carried out (Figs. 1–2).

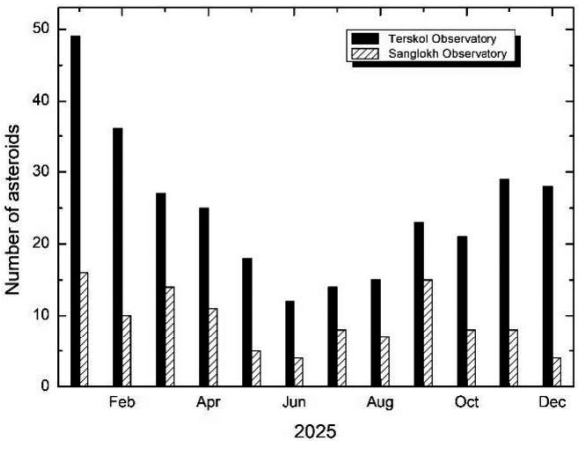


Fig. 1. Number of near-Earth asteroids visible from Terskol Observatory and Sanglokh Observatory in 2025

The magnitudes of the objects, their altitude above the horizon, the duration of the available observational interval, and the capabilities of the telescopes used were taken into account. Modeling showed that the number of objects available for observation changes significantly throughout the year. The use of two telescopes enabled the acquisition of sequential and, in some cases, quasi-simultaneous measurements of the same objects. Thus, the observatories complement each other, increasing the duration and reliability of the observational coverage.

As a result of joint observations of a set of asteroids that come close to Earth and the processing of the obtained data, including standard calibrations, using the Tycho Tracker program [2], astrometric and photometric data for

the studied asteroids were obtained. Based on the combined photometric series obtained with two telescopes, previously published color indices were confirmed, and the asteroids were classified. A color-color diagram (B-V vs. V-R) was used to analyze the results. The asteroids were classified according to the SMASS II taxonomy, and good agreement with the corresponding spectral-class regions was found, confirming the correctness of the applied photometric classification methodology. Some results are shown in Table 1.

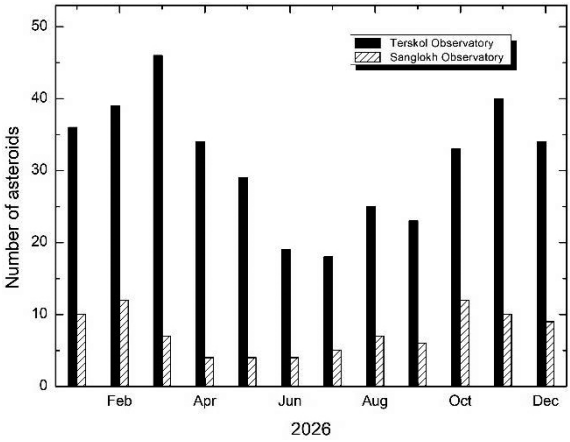


Fig. 2. Number of near-Earth asteroids visible from Terskol Observatory and Sanglokh Observatory in 2026

Table 1. Spectral types of selected near-Earth asteroids according to the SMASS II taxonomy

Name	Spectral type (SMASS II [4])
433 Eros	S
1036 Ganymed	S
1916 Boreas	S
2100 Ra-Shalom	C
138205 (2000 EZ148)	S
442609 (2012 KU42)	S

Observations of selected comets were conducted as well. Their colors, dust production rate (Afρ), absolute magnitude (H), and photometric index (n) were assessed.

CONCLUSION:

The modeling of visibility conditions, together with the implementation of a joint observational program at the Terskol and Sanglokh observatories and the resulting observational data, has demonstrated the effectiveness of the Russian–Tajik observational segment for monitoring and photometric studies of small bodies in the Solar System. Continued simultaneous observations will expand the sample of investigated asteroids, facilitate the compilation of a homogeneous database of their color characteristics, and provide a solid basis for future spectral and physical interpretation of the results.

ACKNOWLEDGMENTS:

This work was supported by the Ministry of Science and Higher Education of the Russian Federation grant No. 075-15-2026-236.

REFERENCES:

[1] Neese C. Asteroid Taxonomy V1.0. urn:nasa:pds:ast_taxonomy::1.0 // NASA Planetary Data System. 2017.
[2] Parrott D. Tycho Tracker: A New Tool to Facilitate the Discovery and Recovery of Asteroids Using Synthetic Tracking and Modern GPU Hardware // J. American Association of Variable Star Observers. 2020. Vol. 48. No. 2. Article 262.

[3] Tedesco E. F. UBV Mean Asteroid Colors V1.0. urn:nasa:pds:compil.ast.ubv-photometry::1.0 // NASA Planetary Data System. 2020.
[4] Bus S. J., Binzel R. P. Phase II of the small main-belt asteroid spectroscopic survey: A feature-based taxonomy // Icarus. 2002. Vol. 158. No. 1. P. 146–177.

CLASSIFICATION OF USG-OBSERVED FIREBALLS

O. P. Popova, D. O. Glazachev
Sadovsky Institute of Geosphere Dynamics, Moscow 119334, Russia
olga@idg.ras.ru

KEYWORDS:
USG-observed fireballs, light curves, classification

INTRODUCTION:
The population and physical properties of near-Earth objects (NEOs) with sizes ranging from a few meters to several tens of meters remain poorly constrained. Objects in this size range are close to the detection limit of current telescopic NEO surveys and enter Earth's atmosphere much less frequently than smaller meteoroids. As a result, only limited information is available on their bulk density, internal structure, and orbital characteristics.

FIREBALL DATA:
Hereafter, USG bolides refer to fireballs detected by U.S. Government satellite sensors and reported in the publicly available USG fireball database. The database provides the date, time, and approximate location of each event, as well as estimates of the radiated and kinetic energies. Recently, light curves for more than 800 USG bolides have also become available. The altitude of maximum brightness is available for approximately half of these events, while entry velocity has been estimated for about one-third, allowing the entry angle and azimuth to be reconstructed. Together, these observations provide a unique data set for investigating meter- and decameter-sized impactors, with the morphology of the light curves offering particularly valuable information on meteoroid fragmentation.

FIREBALL CLASSIFICATION:
The diversity of fireball light curves reflects differences in meteoroid fragmentation behavior, making their classification an important tool for investigating meteoroid properties. Several classification criteria have therefore been proposed based on light-curve morphology, primarily using variations in brightness and the duration of luminous flares. These criteria classify fireball light curves into three principal types: single-primary-maximum events, extended fragmentation, and discrete fragmentation. This classification was applied to all events with known entry velocity. Of these, 87 fireballs (30%) belong to the single-primary-maximum class, 128 (44%) exhibit discrete fragmentation, and the remaining 77 (26%) are characterized by extended fragmentation.

Light curves also provide approximate estimates of meteoroid strength at the time of peak luminosity. The smallest spread in strength is observed for fireballs with a single primary maximum, the great majority of which have estimated strengths between 0.5 and 10 MPa. In contrast, fireballs exhibiting discrete fragmentation show the widest range of strength estimates. Despite this wide range, more than 80% of the estimated strengths still lie between 0.5 and 15 MPa.

ACKNOWLEDGMENTS:
This work was supported by the Ministry of Science and Higher Education of the Russian Federation under State Assignment No. 125012200624-5.

TRAJECTORY DESIGN FOR THE APPLICATION OF EARTH-RESONANT ASTEROIDS IN PLANETARY DEFENSE

O. S. Chernenko, N. A. Eismont, V. A. Zubko, M. V. Pupkov
Space Research Institute RAS, Moscow, Russia, o.chernenko@cosmos.ru

KEYWORDS:
Earth-resonant asteroids, hazardous near-Earth objects, trajectory design, planetary defense

INTRODUCTION:
The deflection of hazardous near-Earth objects is commonly considered in the context of spacecraft-based kinetic impactors, gravity tractors, or other active means of changing the orbit of a target body. An alternative concept is to use a small near-Earth asteroid as a natural impactor. In this scenario, a spacecraft is delivered to the surface of a small asteroid and operates as a propulsion and guidance unit. By applying a controlled impulse to the asteroid, the spacecraft transfers the natural body from its original orbit to an Earth-resonant, or Earth-synchronous, heliocentric orbit. The asteroid impactor then remains in a waiting state until a hazardous object is detected. Once such an object is identified, the spacecraft attached to the asteroid applies an activation impulse that transfers it onto a trajectory leading to an Earth gravity assist. The subsequent Earth gravity assist redirects the asteroid impactor onto an impact trajectory with the hazardous object [1, 2]. Thus, the spacecraft does not act as the main impactor itself; instead, it uses a natural asteroid as a massive kinetic impactor, while the Earth encounter provides additional dynamical amplification. In the present study, possible implementations of this mission profile are demonstrated for several asteroids, including the construction of their waiting orbits and the assessment of the efficiency of hazardous-object deflection via an Earth gravity assist.

TRAJECTORY DESIGN:
The trajectory design is based on the preliminary formation of a reserve of small near-Earth asteroids transferred by spacecraft to Earth-resonant, or Earth-synchronous, heliocentric orbits. In this context, synchronous motion refers to a heliocentric 1:1 resonance with the Earth's orbital period, rather than to a geocentric satellite orbit. Prior to this stage, the accessibility of each candidate asteroid from a low Earth orbit is also assessed. A spacecraft delivered to the asteroid surface can apply a phasing impulse that changes the orbital period of the selected body, or of a captured fragment from the surface, to approximately one Earth year with a moderate characteristic velocity budget. Such resonant trajectories provide regular returns to the Earth's vicinity and allow the asteroid to remain dynamically accessible for many years or even decades. As a result, a small natural body can be maintained in an energetically favorable configuration and later used as a pre-positioned impactor if a hazardous object must be deflected.

The selection of suitable candidates is based on an approach developed for low-energy transfer of small bodies to Earth-resonant orbits. In this approach, orbital geometry, size estimates, transfer accessibility, characteristic velocity budget maps, and resonant-return windows are considered jointly [3]. Once a hazardous object is identified [4], the impactor stored on the waiting orbit is activated by spacecraft impulse and targeted to an Earth flyby. In this case, the Earth encounter acts as a dynamical amplifier: a relatively small preparatory impulse before the encounter, combined with a precise choice of the flyby geometry, can produce a substantially different outgoing heliocentric trajectory.

In the proposed architecture, the asteroid impactor is redirected by the Earth gravity assist toward the hazardous asteroid, while the spacecraft attached to its surface provides the initial activation and, if necessary, small targeting corrections. Thus, the trajectory design procedure links three

stages: energy-efficient placement of a natural body onto an Earth-resonant waiting orbit, long-term resonant storage with repeated access to the Earth's vicinity, and Earth-gravity-assist delivery of the asteroid impactor to the hazardous object.

RESULTS:

The proposed trajectory design procedure was applied to several demonstration planetary-defense scenarios. In one of them, the small near-Earth asteroid 2019 GM1 was used as a natural impactor against a virtual hazardous object generated from the orbit of asteroid 2011 DV. Assuming a geometric albedo of 0.15, the adopted absolute magnitudes (H=27.25) for 2019 GM1 and (H=20.79) for the hazardous object correspond to approximate diameters of 12 m and 239 m, respectively. Therefore, the geometric collision condition requires the distance between the centers of the two bodies to be reduced to about 0.125 km.

The Earth gravity assist was optimized by varying the activation epoch on the waiting orbit, the Earth-encounter epoch, the post-flyby encounter epoch with the hazardous object, the flyby orientation, and the perigee altitude. This made it possible to construct a passive post-flyby trajectory approaching the hazardous object without applying an additional phasing impulse after the Earth encounter.

For 2019 GM1, the impulse required to transfer the asteroid to the waiting orbit was 16.5 m/s, with the possibility of passive residence in an Earth-synchronous region for about 60 years without additional corrections. The required activation impulse was about 189 m/s. The resulting Earth-flyby trajectory had a perigee altitude of about 4000 km, while the relative velocity at the encounter with the hazardous object was approximately 9.1 km/s.

ACKNOWLEDGMENTS:

This study is supported by the Russian Scientific Foundation, project No. 25-79-00042.

REFERENCES:

[1] Eismont N. A., Boyarskii M. N., Ledkov A. A., Nazirov R. R., Dunham D. W., Shustov B. M. On the Possibility of the Guidance of Small Asteroids to Dangerous Celestial Bodies Using the Gravity-Assist Maneuver // Solar System Research. 2013. V. 47. P. 325–333. DOI: 10.1134/S0038094613040102.

[2] Ledkov A. A., Eismont N. A., Boyarskii M. N., Fedyaev K. S., Nazirov R. R. Control of the Motion of Near-Earth Asteroids // Astronomy Letters. 2015. V. 41. P. 67–83. DOI: 10.1134/S1063773715020036.

[3] Chernenko O. S., Eismont N. A., Zubko V. A., Pupkov M. V. Definition of Near-Earth Asteroids and Trajectory Design for Transfer to Earth-Resonant Orbits // Solar System Research. 2026. V. 60. No. 22. DOI: 10.1134/S0038094625601240.

[4] Pupkov M. V., Eismont N. A., Starinova O. L., Fedyaev K. S., Zubko V. A., Chernenko O. S. Designing Halo Orbits Passing through the Trajectories of Near-Earth Asteroids // Solar System Research. 2026. V. 60. No. 29. DOI: 10.1134/S0038094625601379.

ASTEROID ROTATION PERIODS: STATISTICAL ANALYSIS IN THE DIAMETER-SPIN DISTRIBUTION

M. Nastaran[1], A. Poro[2], R. Hosseini[3], M. Najarzadeh[4]
[1] *Faculty of Geology, University of Tehran, 1417935840 Tehran, Iran*
maryaaa8754@gmail.com
[2] *Astronomy Department of the Raderon AI Lab., BC., Burnaby, Canada*
[3] *Department of Earth Sciences and Engineering, Missouri University of Science and Technology, Rolla, MO 65409, USA*
[4] *University of Tehran, 1417935840 Tehran, Iran*

KEYWORDS:
asteroid, data analysis, rotation period

ABSTRACT:
This study examines the rotational characteristics of asteroids through statistical modeling of the diameter–period relationship. A statistical evaluation of the diameter–period relationship was conducted using a dataset of 34,326 asteroids. Clustering identified three main groups, including a dense cluster below the spin barrier, a population of small, fast-rotating asteroids, and a more diffuse group. Geometric and density-based analyses showed that the densest region consists of objects with diameters from 3 to 10 km and rotation periods between 3 and 9 hours, some of which extend beyond the spin barrier. Polynomial modeling demonstrated that a third-degree fit provides the most stable representation of the overall trend without overfitting. Additionally, an empirical lower boundary was identified and proposed, below which no asteroid was found in either the main sample or the selected targets [1].

CONCLUSION:
The investigation of asteroid rotation periods as a function of diameter revealed several consistent and interpretable patterns:

- Clustering analysis identified three well-separated groups of objects in the log diameter–log period space. The largest and densest group is concentrated mostly below the 2.2-hour spin barrier, aligning with the theoretical limit for gravitationally bound, low-cohesion asteroids ([2]). Nonetheless, a fraction of this group appears above the boundary, suggesting a gradual rather than abrupt transition. A second, smaller group consists of fast-rotating asteroids with diameters typically less than 200 meters. The third group includes more dispersed objects with no dominant trend.
- Geometric boundary extraction using the alpha shape method, together with kernel density estimation, provided a detailed representation of the data's spatial structure. The densest concentration of objects was found among asteroids with diameters between 3 and 10 kilometers and rotation periods between 3 and 9 hours. Notably, a portion of this high-density region extends above the 2.2-hour threshold, which may be attributed to measurement uncertainties. These findings suggest that the current understanding of the spin barrier in asteroids may require reevaluation.
- Polynomial modeling of the diameter–period relationship showed that a third-degree polynomial offered an optimal balance between model accuracy and complexity. Higher-order models did not significantly improve the fit and introduced overfitting, especially in sparsely populated regions. Residual analysis confirmed that the cubic model was sufficiently robust for representing the overall trend.

It should be noted that in our clustering analysis, only two physical parameters, diameter and rotation period, were used. The subsequent polynomial fitting was therefore applied as a descriptive tool to outline the empirical boundary of the distribution rather than as a predictive model. Thus,

the present results should be regarded as a statistical characterization of existing data rather than a classification tool for newly discovered asteroids. While in principle DBSCAN could be applied to new data if diameter and period are known, the current framework cannot assign objects based on other features that were not included in the clustering.

- An empirical lower boundary was identified, beneath which no asteroid is present from the dataset. The absence of objects in this region may reflect an inherent constraint on the spin behavior of small asteroids, potentially imposed by internal cohesion, collisional evolution, or observational limitations.
- The observed presence of several asteroids above the nominal spin barrier may be linked to the Yarkovsky-O'Keefe-Radzievskii-Paddack (YORP; [3]) effect. This torque, arising from the anisotropic absorption and re-emission of solar radiation, can gradually alter the spin states of small bodies over timescales of 10^{5}-10^{7} years ([4, 3]). In particular, the YORP effect is capable of both accelerating and decelerating rotation rates, potentially driving some small asteroids beyond the expected spin-barrier threshold. Therefore, the apparent outliers above the barrier in our analysis may not solely represent noise in the data, but could also reflect evolutionary processes induced by YORP. Future studies that couple rotational statistics with dynamical and thermal modeling may help to disentangle the role of YORP in shaping the diameter-period distribution.

REFERENCES:

[1] Nastaran M., Poro A., Hosseini R., Najarzadeh M., Asteroid Rotation Periods: Statistical Analysis in the Diameter-Spin Distribution // Astrophysics. 2025. V. 68. P. 615–621. DOI: 10.1007/s10511-026-09905-5
[2] Pravec P., Harris A. W. et al., Spin rate distribution of small asteroids // Icarus. 2008. V. 197. No. 2. P. 497–504.
[3] Bottke Jr., William F. et al., The Yarkovsky and YORP effects: Implications for asteroid dynamics // Annu. Rev. Earth Planet. Sci. 2006. V. 34. No. 1. P. 157–191.
[4] Rubincam D. P., Radiative spin-up and spin-down of small asteroids // Icarus. 2000. V. 148. No. 1. P. 2–11.

POLARIMETRIC AND PHOTOMETRIC CHARACTERISTICS OF THE INTERSTELLAR COMET 3I/ATLAS: KEY FEATURES

M. Shcherbina[1], N. Kiselev[1,2], M. D. Petrov[2], E. Zhuzhulina[2], N. Karpov[1]
[1] *Institute of Astronomy RAS, Moscow 119017, Russia*
kiselevnn42@gmail.com
[2] *Crimean Astrophysical Observatory, Nauchny 298409, Crimea*

KEYWORDS:
polarimetry, photometry, interstellar objects, comet 3I/ATLAS

INTRODUCTION:
A major achievement in the direct study of small bodies in other planetary systems was the discovery and investigation of the properties of the first interstellar (IS) objects: the asteroid 1I/Oumuamua in 2017 and the comet 2I/Borisov in 2019.The first IS objects demonstrated that this population can be physically diverse. Therefore, the detection of the third IS object, 3I/ATLAS, provided an opportunity to obtain new data about this class of objects.

OBSERVATIONS AND RESULTS:
The purpose of this study was to determine the polarimetric and photometric characteristic of interstellar comet 3I/2025 N1 (ATLAS), and to model the physical properties of particles in its coma. Observations of comet were carried out with the two-channel photoelectric aperture polarimeters "POLSHAKH" at the 2.6-m Shajn telescope of the Crimean Astrophysical Observatory (CrAO) and the 2-m telescope of the shared research facility "Terskol observatory" of Institute of Astronomy of the Russian Academy of Sciences. (PTO). The BVRI broadbands as well as the narrowband cometary filters were used with aperture polarimeters. The imaging observations with the g-sdss and the r-sdss broadband filters, and narrowband cometary filters were also carried out with the SCORPIO-2 at the 6-m BTA telescope of the Special Astrophysical Observatory of the RAS (SAO RAS). All our observations of the comet from November 18, 2025 to January 26, 2026 covered a phase angle range from 30.1 to 0.8°.

OUR FINDINGS ARE THE FOLLOWING:

- comet 3I/ATLAS demonstrated a uniquely high degree of polarization both in the region of the negative polarization branch (in absolute value) and in the positive polarization branch (Fig. 1). The negative polarization branch of comet 3I/ATLAS is highly asymmetric, with P_{min}=−3.01±0.05% at a phase angle α_{min}=5.46±0.05°, an inversion angle α_{inv}=17.6±0.7° and a polarimetric slope h=0.53±0.01%/°. On the positive branch, the polarization of 3I/ATLAS is higher than that of previously observed comets;
- the spectral gradient of polarization ΔP/Δλ is about of (0.004±0.001)%/nm at a phase angle of ~27.7°, which is slightly lower than the gradient (0.008%/nm) for most comets in the Solar system;
- measurements of the comet's reflectivity gradient S' in the wavelength range from the V to the R band, conducted in November 2025, yielded a value of ~4%/1000 Å. In contrast, the blue spectral region exhibits a depression, with $S'(B–V)$=−18.2%/1000Å;
- the colors B – V, V – R, and R – I are ~0.4 mag, and g–r=0.71 mag;
- the parameter $Af\rho$ was measured to be 5461± 70 cm for the r-sdss filter and coma diameter of 22696 km on November 27.083 at heliocentric distance of 1.710au;
- the best fit to the observed phase dependence of the degree of polarization was obtained for the Sh matrix model of conjugate random Gaussian particles with roughness , and a mixture consisting of 95% amorphous carbon, 4.5 % magnesium-rich silicates, and 0.5 % water ice (Fig. 2).

These and other cometary features will be compared with typical properties of Solar System comets.

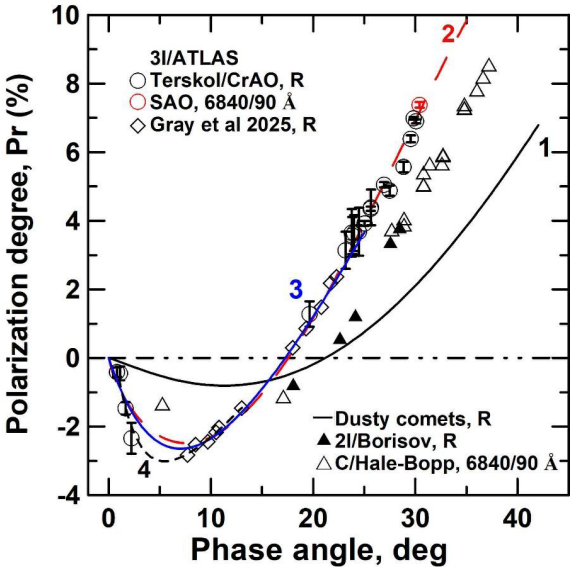


Fig. 1. The phase-angle dependence of polarization for 3I/ATLAS obtained at the 2-m telescope of the PTO and the 2.6-m telescope of the CrAO in the *R* band (open black circles), and at the 6-m BTA SAO in the RC(6840/90Å) filter (red open circle). For comparison the available data for the comet [1] (diamonds) and comets 2I/Borisov [2] (closed triangles) and C/1999O1 (Hale-Bopp) [3] (opened triangles) (many authors from DBCP) is also shown. The solid curve (1) is the synthetic polarization curve of the dusty comets [4]. The red line (2) and blue line (3) are fits data of 3I/ATLAS in the R bands in the range phase angles 0.8–30.1 and 0.8–13° according to trigonometric expression [5] and linear-exponential expression [6], respectively. Line (4) is a 5th-degree polynomial approximation of the data for phase angles between 0.8 and 13°

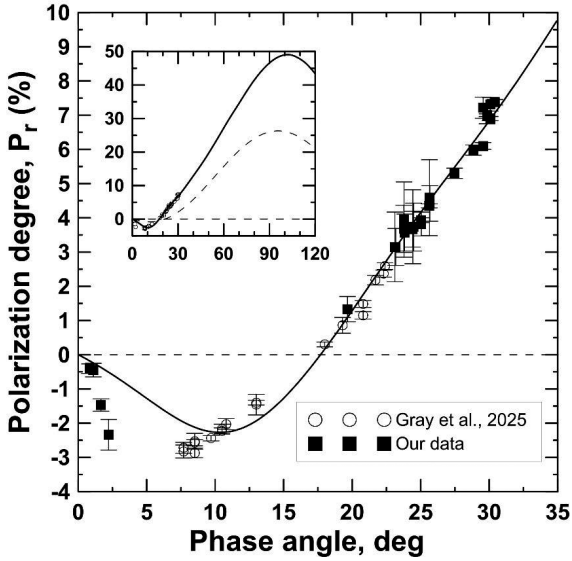


Fig. 2. Phase-angle dependence of the degree of linear polarization for 3I/ATLAS (symbols – observations). The solid line displays the model phase-angle curve of polarization with the following model parameters: 95 percent amorphous carbon, 4.5 percent magnesium-rich silicates, and 0.5 percent water ice. On the inset — a model polarization curve over a wide range of phase angles (solid line) compared to the average curve (dashed line) for comets of the Solar System.

REFERENCES:

[1] Gray Z., Bagnulo S., Borisov G. et al. Extreme Negative Polarization of New Interstellar Comet 3I/ATLAS // ApJ. Letters. 2025 V. 992. Article 9. DOI: 10.3847/2041-8213/ae0c08.
[2] Bagnulo S., Cellino A., Kolokolova L. et al. Unusual polarimetric properties for interstellar comet 2I/Borisov // Nature Communications. 2021. Vol. 12. Artivle 1797. DOI: 10.1038/s41467-021-22000-x.
[3] Kiselev N., Shubina E., Velichko S. et al. Compilation of Comet Polarimetry from Published and Unpublished Sources // NASA Planetary Data System, urn:nasa:pds:compil-comet:polarimetry::1.0. 2017.
[4] Kiselev N. N., Rosenbush V. K., Levasseur-Regourd A-Ch., Kolokolova L. Polarimetry of Stars and Planetary Systems / eds. L. Kolokolova, J. Hough, A-Ch. Levasseur-Regourd. Cambridge: Cambridge University Press, 2015. DOI: 10.1017/CBO9781107358249.022.
[5] Lumme K., Muinonen K. A two-parameter system for linear polarization of some solar system objects // Asteroids, Comets, Meteors 1993. Vol. 810. Article 194.
[6] Muinonen K. et al. Asteroid photometric and polarimetric phase curves: Joint linear-exponential modeling // Meteoritics and Planetary Science. 2009. Vol. 44. No. 12. P. 1937–1946. DOI: 10.1111/j.1945-5100.2009.tb02003.x.

ON DETECTION STRATEGY OF DANGEROUS ASTEROIDS

B. M. Shustov, R. V. Zolotarev, A. S. Shugarov
Institute of astronomy RAS, Moscow, Russia, bshustov@mail.ru

KEYWORDS:
near-Earth asteroids, NEAs detection, NEO problem

ABSTRACT:
In the current formulation of the asteroid and comet hazard (ACH) problem (aka NEO problem) it is considered necessary to detect a sufficiently large number (more than 90% of the total amount) of hazardous bodies that can collide with our planet. A vast majority of these bodies are near-Earth asteroids (NEAs). Based on the analysis of statistical characteristics of the NEA population, it has been shown that, on a practically significant time scale (~1000 years), the main danger is posed by NEAs of size 10–50 m, since they collide with the Earth more often than larger bodies. Consequently, the main practically significant task of counteracting the ACH is to detect such decameter-sized NEAs [1]. They can only be detected in close proximity, at distances of less than 0.05 AU from the Earth. The detection timescale is short, measured in hours (up to one day). This problem is still far from being solved. Larger bodies can be detected with more success. They can be detected at greater distances and, accordingly, the detection timescale is much longer. A rational approach to detecting NEAs has been proposed, the essence of which is that it is necessary to accelerate the development of instruments and methods to detect NEAs in the near zone [2]. This is the most immediate challenge. At the same time, it is also necessary to continue work on searching for larger bodies in the far zone. These detection strategies require different technical means.

REFERENCES:
[1] Shustov B. M. On a Two-Zone Approach to Solving the Problem of Detecting NEAs // Solar System Research, 2025, Vol. 59:98, P. 1–13.
[2] B. M., Zolotarev R. V., and Shcherbina M. P. Characteristics of the Ensemble of Close Potentially Hazardous Asteroids // Astronomy Reports. 2025. Vol. 69. No. 10. P. 1010–1023. DOI: 10.1134/S1063772925702245.

THE SOUTHERN DELTA AQUARIIDS METEOROID STREAM

M. V. Sergienko, Y. A. Nefedyev, A. O. Andreev
Kazan Federal University, Kazan 420008, Russia, maria_sergienko@mail.ru

KEYWORDS:
meteoroids, meteoroid streams, asteroids, small bodies of the Solar system, the orbits evolution, orbital resonances

INTRODUCTION:
A comprehensive model describing the distribution of meteoroid material in near-Earth space has not yet been established. For many meteoroid complexes, the origin and association with a parent comet or asteroid remain uncertain. Therefore, identifying genetic relationships among small Solar System bodies remains an important problem in planetary science. This study investigates the Southern Delta Aquariids meteoroid stream and its possible association with near-Earth asteroids identified using the synthetic method [1, 2]. In addition, the temporal evolution of the orbits of asteroids associated with the meteoroid stream is analyzed over different epochs. A genetic relationship between a meteoroid stream and its parent body is considered plausible only if the parent is an extinct comet that has depleted its volatile material, a comet covered by an insulating dust mantle, or an active asteroid. The Southern Delta Aquariids are active from late July to mid-August, with peak activity occurring around July 29–30. The stream is relatively weak, exhibiting a zenithal hourly rate (ZHR) of approximately 7–8 meteors per hour. Previous studies have suggested an association with comet 96P/Machholz, as well as with comet P/2008 Y12 (SOHO), which has also been classified as a near-Earth asteroid. Other authors have proposed a possible relationship between the stream and the near-Earth asteroid 2003 EH1.

METHODS:
We analyzed the association between the Southern Delta Aquariids meteoroid stream and near-Earth asteroids belonging to the Apollo and Amor groups. To identify potential parent bodies of the meteoroid stream, we applied the authors' synthetic identification method [2]. The selected candidate parent bodies were subsequently examined to assess their mutual dynamical relationships within the identified parent-body group. Furthermore, their long-term orbital evolution was investigated by numerically integrating their orbits both backward and forward in time.

RESULTS:
Application of the synthetic method to investigate relationships among small bodies of the Solar System revealed that the Southern Delta Aquariids meteoroid complex is dynamically associated with comet 96P/Machholz, comet P/2008 Y12 (SOHO), and asteroid (196256) 2003 EH1. Asteroid 2003 EH1 belongs to the Amor group and is characterized by a low albedo and a dark surface. Spectral analyses indicate that it has a carbonaceous composition and is classified as a C-type asteroid, supporting the hypothesis of its cometary origin [3]. Previous studies have investigated the association of the Quadrantids meteoroid stream with comet 96P/Machholz and asteroid 2003 EH1 [4]. Analyses of the dynamical properties of these objects suggest that comet 96P/Machholz and asteroid 2003 EH1 most likely share a common origin. A plausible scenario is the fragmentation of a large parent comet, resulting in the formation of two major fragments. Both the synthetic identification method and long-term dynamical evolution analysis demonstrate that comet 96P/Machholz and asteroid 2003 EH1 are associated with the Southern Delta Aquariids and Quadrantids meteoroid streams. These dynamical relationships provide evidence that the two bodies and the associated meteoroid streams constitute a common asteroid–comet complex, indicating a shared evolutionary origin.

REFERENCES:

[1] Sergienko M.V., Nefedyev Y.A., Andreev A.O. Connection of the sigma-Capricornids meteor shower with Near-Earth asteroids // Meteoritics and Planetary Science. 2024. V. 59. Article A380.
[2] Sergienko M.V., Andreev A.O., Nefedyev Y.A. The modernized synthetic method for searching connections between Near-Earth objects // Meteoritics and Planetary Science. 2024. V. 59. Article A381.
[3] Sicking W. About spectrograms of meteor echoes at different stages of the radiant position of the Quadrantids 2025 — an AI/ML-investigation // eMetN Meteor J. 2025. Vol. 10. No. 2. P.115–119.
[4] Sergienko M.V. et al. Formation of the Quadrantids Meteoroid Complex and Its Connection with Comet 96P/Machholz and Asteroid (196256) 2003 EH1 // LPI Contributions. 2025. V. 3088. Article 5394.

SIZE-FREQUENCY DISTRIBUTIONS OF FRESH IMPACT CLUSTERS IN MARS

E. D. Podobnaya, O. P. Popova, D. O. Glazachev
Sadovsky Institute of Geosphere Dynamics, Moscow 119334, Russia
epodobnaya@idg.ras.ru

KEYWORDS:
Mars, cluster, crater, size-frequency distribution, classification

INTRODUCTION:
Multi-year imaging of the Martian surface with orbital cameras had identified over 1,400 freshly formed dated meteoroid impact sites of meter-scale meteoroids [1, 2]. Over half of the impactors disintegrate in the atmosphere, forming crater clusters. Analysis of recent Martian impact sites provides an opportunity to study the meteoroid population, which is common for both Earth and Mars.

TYPES OF CLUSTERS AND THEIR ANALYSIS:
Previously, three types of fresh Martian clusters (830 impact sites) were identified [3]. The first one includes clusters with one major crater supplemented by some much smaller ones; densely populated clusters correspond to the second type and the final group relates to sparsely populated clusters, which have 2 or more comparable largest craters.

For each identified group, crater size–frequency distributions (SFDs) were constructed for clusters and fitted using two alternative models. The standard power-law fit yields mean exponents of 1.2, 2.0, and 1.5 for groups 1, 2, and 3, respectively, whereas the upper-truncated power-law fit shifts these values to 1.3, 0.9, and 0.6. The exponents derived from both fitting approaches are consistent with maximum likelihood estimations, as well as with fragment size distributions obtained from impact experiments and terrestrial meteorite strewn fields. Analysis of the exponent distributions indicates that the group with a dominating major crater is the most homogeneous and structurally well-defined.

Various statistical tests verify robust, statistically significant differences between the identified groups. These findings suggest that the observed cluster groups may correspond to different types of impactors and/or distinct scenarios of meteoroid fragmentation in the Martian atmosphere.

ACKNOWLEDGMENTS:
This work was carried out within the framework of the state assignment of the Ministry of Science and Higher Education of the Russian Federation No. 125012200624-5.

REFERENCES:
[1] Malin M. C., Edgett K. S. et al. Present-day impact cratering rate and contemporary gully activity on Mars // Science. 2006. V. 314. P. 1573–1577. DOI: 10.1126/science.1135156.
[2] Daubar I. J., Dundas C. M., McEwen A. S., Gao A., Wexler D., Piqueux S., Collins G. S., Miljkovic K., Neidhart T., Eschenfelder J., Bart G. D., Wagstaff K. L., Doran G., Posiolova L., Malin M., Speth G., Susko D., Werynski A. New Craters on Mars: An Updated Catalog // J. Geophysical Research: Planets. 2022. V. 127. No. 7. Article e2021JE007145. House, 2011. 134 p. DOI: 10.1029/2021JE007145.
[3] Podobnaya E., Popova O., Ivanov B., Glazachev D. Classification of Craters Clusters in the Expanded Catalog of Fresh Impact Sites on Mars // Solar System Research. 2025.V. 59. No. 5. Article 46. DOI: 10.1134/S003809462460207X.

ON THE ORIGIN OF THE DISCOVERED 250-KM-RADIUS PLUTINO ATMOSPHERE

G. A. Kucherov[1], A. K. Pavlov[1], A. N. Konstantinov[1,2], A. Y. Merkulova[1]
[1] *Ioffe Institute, Saint Petersburg, Russia, glebkucherov2002@gmail.com*
[2] *Peter the Great Saint Petersburg Polytechnic University Saint Petersburg, Russia*

KEYWORDS:
free radicals, Kuiper belt, trans-Neptunian objects, icy bodies, atmosphere

ABSTRACT:
Recently, an atmosphere was discovered for the first time around the trans-Neptunian object (612533) 2002 XV_{93} [1]. The object's radius is approximately 250 km, and the atmospheric pressure is estimated to be 100–200 nbar. Its distance from the Sun is 37 AU, and the estimated temperature is 40–50 K. The authors suggest that the atmosphere may consist of CO, N_2, and CH_4, which are non-condensable at these temperatures. Due to the body's low mass, the atmosphere should be lost, according to the authors, over a period of only 100–1000 years.

In this work, we propose a possible mechanism that could compensate for the loss of atmospheric gases and maintain the existence of the atmosphere on a much longer timescale. We consider the recombination of radicals accumulated in water ice as a potential energy source, which could lead to the sublimation of volatile gases within the icy body followed by their slow diffusion toward the surface. Preliminary calculations suggest that the proposed mechanism could sustain the atmosphere for one million years or longer.

The process of the long-term accumulation of radicals produced by cosmic ray irradiation and the decay of radionuclides in icy bodies was previously proposed and published in our papers [2–4].

REFERENCES:
[1] Arimatsu K., Yoshida F., Hayamizu T., Takita S., Hosoi K., Ootsubo T., Watanabe J. Detection of an atmosphere on a trans-Neptunian object beyond Pluto // Nature Astronomy. 2026. DOI: 10.1038/s41550-026-02846-1.
[2] Belousov D. V., Pavlov A. K. Cometary outbursts in the Oort cloud // Icarus. 2024. V. 415. No. 116066. DOI: 10.1016/j.icarus.2024.116066.
[3] Pavlov A. K., Kucherov G. A., Merkulova A. Y., Belousov D. V. Accumulation and Recombination of Radicals as an Energy Source for Active Processes in Icy Bodies of the Solar System // Solar System Research. 2025. V. 59. No. 44. DOI: 10.1134/S0038094624601981.
[4] Pavlov A. K., Kucherov G. A., Merkulova A. Y. Possibility of Liquid Water Formation in Icy Bodies Due to the Process of Rapid Recombination of Accumulated Radicals // Solar System Research. 2026. V. 60. No. 27. DOI: 10.1134/S0038094625601355.

MEASURING CRATER MORPHOMETRY ON IRREGULAR BODIES: REFERENCE SURFACES, PROJECTIONS, AND DISTORTION

M. V. Nyrtsov[1], A. I. Sokolov[1], A. E. Zubarev[2], I. E. Nadezhdina[2], M. E. Fleis[3], N. A. Slodarzh[2]

[1] *Lomonosov Moscow State University, Moscow 119991, Russia nyrtsov.maxim@yandex.ru*

[2] *Moscow State University of Geodesy and Cartography (MIIGAiK) Moscow 105064, Russia, n_kozlova@miigaik.ru*

[3] *Institute of Geography RAS, Moscow 119017, Russia, fleis.maria@yandex.ru*

KEYWORDS:
small solar system body, irregular shape, reference surface, triaxial ellipsoid, map projection, distortions in projections, hypsogram, crater morphometry

INTRODUCTION:

There are bodies in the Solar System with irregular shape. To study their relief, it is necessary to measure the morphometric parameters of the craters (area, diameter, etc.). Measurements are often taken from maps or satellite images, which are images on a plane. Thus, the problem of approximating an irregular shape with a reference surface and the problem of transition from this surface to a plane (i.e., a map projection) arise.

The following sources of distortions can be identified when measuring crater characteristics: 1) vectorization errors; 2) distortions in projecting the crater boundary onto the reference surface; 3) distortions in determining the plumb line deviation; 4) distortions of the map projection. When measuring, it is possible to make some corrections to the obtained values for these distortions.

HYPERION (S VII) DATA FOR STUDY:

Saturn's moon Hyperion (S VII) was chosen for the study because of its irregular shape. For small bodies of this kind, the International Astronomical Union (IAU) recommends approximating their shape with a triaxial ellipsoid [1]. Due to the chaotic nature of its rotation, there is an ambiguity in the definition of the coordinate system [2, 3]. Therefore, we applied the parameters of the approximating ellipsoid (a > b > c: 177.6, 128.5, and 105.6 km) and a shape model that we derived [4].

The advantages of using a triaxial ellipsoid instead of a sphere (or spheroid) can be illustrated with a hypsogram of heights distribution. To calculate the hypsogram, we use the shape model of the surface, the method for obtaining geodetic heights relative to a triaxial ellipsoid [5], and formulas for cylindrical projection [6] we derived earlier. The hypsograms of height distribution for Hyperion relative to a best-fit ellipsoid and to a sphere R=141.7 km are presented in Fig. 1.

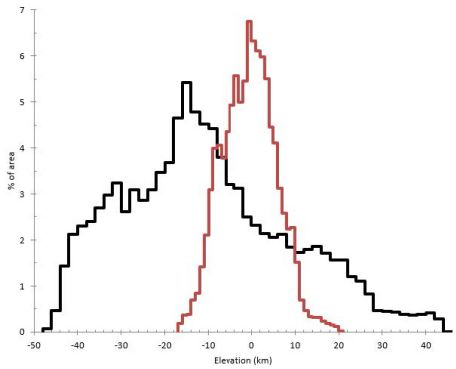


Fig. 1. Hypsogram of height distribution relative to a best-fit ellipsoid (red) and a sphere R=141.7 km (black)

MEASUREMENTS AND CALCULATIONS:
We vectorized 3D shape of 36 craters on the Hyperion's surface. Then we projected this vector data onto two reference surfaces: the best-fit ellipsoid and sphere. To estimate the influence of the reference surface, we measured area and diameter of each crater on the sphere using QGIS software and crater diameters on ellipsoid using original numerical calculations of geodesics. In addition, to estimate the influence of the map projection, we transformed the crater vector data into various triaxial ellipsoid projections and measured these characteristics as well. In all cases, we calculated the distortions as a percentage relative to the "reference" value.

CONCLUSIONS:
When determining crater morphometric characteristics from maps, it is possible to reduce the distortions by choosing proper reference surface and projection. It is preferable to use projections of the triaxial ellipsoid, selected to minimize deviations from the physical surface (best-fit ellipsoid). Calculations show that crater distortions depend on the location of the crater (latitude and longitude) and its dimensions.

ACKNOWLEDGMENTS:
The image data processing and shape study (A.E. Zubarev, I.E. Nadezhdina, N.A. Slodarzh) was performed according to State assignment No. 124071100067-9 (FSFE-2024-0001).

The cartographic part of the study was carried out according to State assignments "Digital technologies and methods of cartography, geoinformatics and remote sensing in geographical research" (A.I. Sokolov, M.V. Nyrtsov) Project No. 121051400061-9 and IG RAS Project No. FMWS-2024-0009 (M.E. Fleis).

REFERENCES:
[1] Archinal B.A., Anton C.H., A'Hearn M.F. et al. Report of the IAU Working Group on Cartographic Coordinates and Rotational Elements: 2015 // Celestial Mechanics and Dynamical Astronomy. 2018. V. 130. No. 22. DOI: 10.1007/s10569-017-9805-5.
[2] Sokolov A.I., Nadezhdina I.E., Nyrtsov M.V., Zubarev A.E., Fleis M.E., Kozlova N.A. Mapping Hyperion in Projections of the Triaxial Ellipsoid Based on a New Reference Network and a Digital Terrain Model // Solar System Research. 2024. V. 58. No. 1. P. 112–121. DOI: 10.1134/S0038094624010106.
[3] Harbison R.A., Thomas P.C., Nicholson P.C. Rotational modeling of Hyperion // Celestial Mechanics and Dynamical Astronomy. 2011. V. 110. No. 1. P. 1–16. DOI: 10.1007/s10569-011-9337-3.
[4] Zubarev A.E., Nadezhdina I.E. Hyperion (S VII): Shape, mosaic and control point network // Icarus. 2025. Vol. 429. Article 116440. DOI: 10.1016/j.icarus.2024.116440.
[5] Sokolov A.I. et al. Investigation and cartographic representation of Hyperion space images photogrammetric processing results // Planetary and Space Science. 2024. Vol. 249. Article 105945. DOI: 10.1016/j.pss.2024.105945.
[6] Fleis M.E., Nyrtsov M.V., Sokolov A.I. Cylindrical projections of triaxial ellipsoid: precise formulae and elliptical integrals // Geodesy and Cartography. 2022. Vol. 982. No. 4. P. 26–38. DOI: 10.22389/0016-7126-2022-982-4-26-38.

MIGRATION OF BODIES FROM THE ZONE OF THE GIANT PLANETS TO THE TERRESTRIAL PLANETS AND THE MOON

S. I. Ipatov
V. I. Vernadsky Institute of Geochemistry and Analytical Chemistry RAS
Moscow, Russia, siipatov@hotmail.com

KEYWORDS:
motion of bodies, giant planets, terrestrial planets, Earth, Moon, Venus, Mars, Mercury, Jupiter, probabilities of collisions

INTRODUCTION:
Migration of bodies during formation of the giant planets was considered in [1]. In calculations presented in [2–6] initial values a_o of semi-major axes of bodies varied from a_{min} to $a_{min}+d_a$, their initial eccentricities equaled to e_o, and initial inclinations equaled to $e_o/2$ rad, the number of bodies with a semi-major axis a was proportional to $a^{1/2}$. In [2] at a_{min}=4.5 AU and a_{max}=12 AU (the zone of Jupiter and Saturn), the probabilities of collisions of bodies with the Earth were about $2 \cdot 10^{-6}$. In [5-6] the values of a_{min} varied with a step d_a=0.1 AU from 3 to 4.9 AU and e_o=0.02 or e_o=0.15.

RESULTS OF CALCULATION:
In the present abstract we discuss the results of calculations for which the values of a_{min} varied with a step d_a=2.5 AU from **2.5 to 40 AU** and e_o=0.05 or e_o=0.3. The initial number of bodies in each calculation variant equaled to N_o=250. The gravitational influence of the Sun and planets (from Venus to Neptune) was taken into account. The package SWIFT [7] was used for integrations. In variants presented in Figs. 1–2, planets were considered as material points. Probabilities of collisions of bodies with planets and the Moon were calculated based on the arrays of orbital elements of migrated bodies [8]. In calculations presented in Table 1, bodies that collided with planets were excluded from integration. In these new variants of calculations, the probabilities of collisions of bodies with planets also were calculated based on arrays of orbital elements (before their collisions obtained in integration). Such probabilities can be small, and for the terrestrial planets often there were no collisions of bodies with planets at integrations. Results of calculations with exclusion of bodies collided with planets better correspond to real evolution than the model of planets as material points. However, no principal differences in probabilities with the terrestrial planets have been found in considered calculations (compare Figs. 1–2 and Table 1).

Fig. 1. Probability of a collision of a body with the Earth multiplied by a million

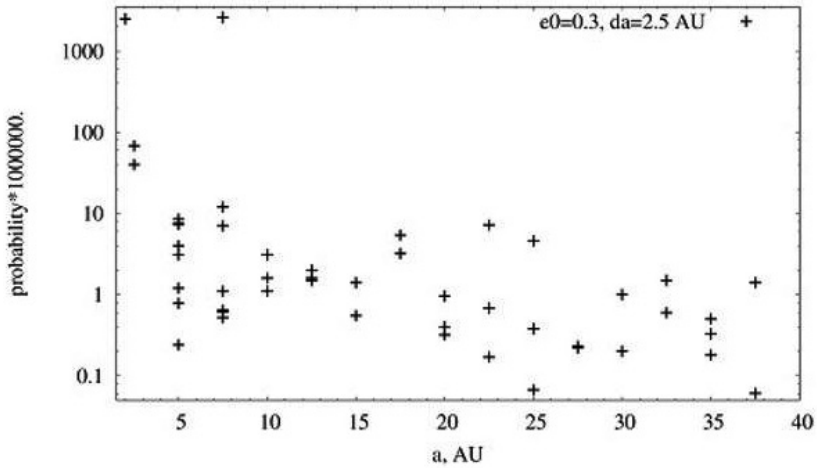


Fig. 2. Probability of a collision of a body with the Earth multiplied by a million

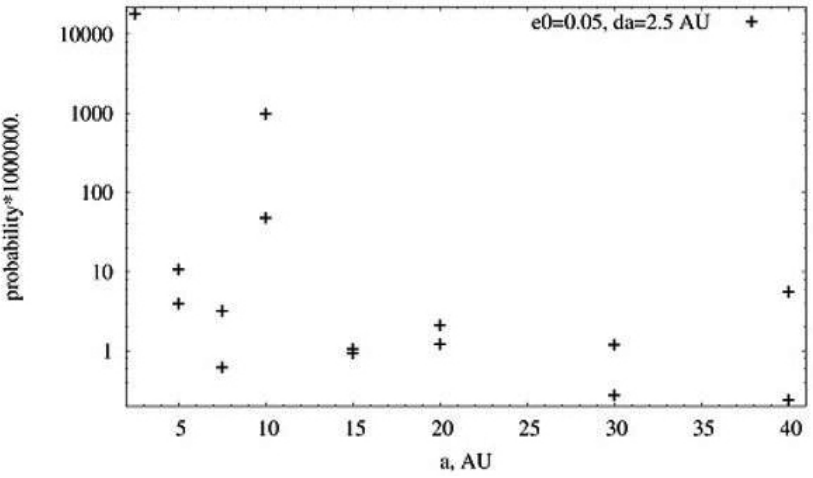


Table 1. Probabilities of collisions of bodies with the terrestrial planets multiplied by a million during time T (T in millions of years). K is the ratio of probabilities of collisions with the Earth and the Moon. N_J is number of collisions of bodies with Jupiter for N_o=250 at integrations, N_{pJ} is number of collisions of bodies with Jupiter for N_o=250 obtained by using analytical formulas. The number of bodies left after T years is presented in the last column

a_{min}	e_o	Earth	K	Mercury	Venus	Mars	N_J	N_{pJ}	T	left
2	0.3	10558	16.6	2761	8481	1690	6	22	10000	5
2.5	0.05	4010	37	540	3974	502	31	21.9	10000	51
2.5	0.3	64.7	17.0	11.4	85.3	33.7	5	25.7	10000	3
5	0.05	6.69	16.5	0.59	5.1	1.2	23	41.2	619	0
5	0.3	0.65	16.7	0.02	0.18	0.4	7	5.97	10.2	0
7.5	0.05	0.54	16.5	0.03	0.35	0.12	6	5.2	474	0
7.5	0.3	2.66	16.6	0.032	2.26	0.56	3	9.08	134	0
10	0.05	10.8	17.2	0.035	2.81	2.05	7	42.6	566	0
10	0.3	1.0	16.6	0.05	0.62	0.26	7	8.6	627	0
12.5	0.05	8.84	16.8	1.24	12.8	1.37	4	13.4	647	0
12.5	0.3	0.22	16.3	0.022	0.20	0.068	6	2.4	151	0
15	0.05	0.38	15.9	0.038	0.31	0.11	3	4.27	1339	0
15	0.3	1.94	16.8	0.037	1.97	0.28	1	2.96	963	0
17.5	0.05	0.84	16.3	0.18	0.067	0.024	2	6.03	3959	1
17.5	0.3	0.057	16.6	0.01	0.41	0.01	3	2.44	862	0
20	0.05	0.99	16.7	0.01	1.12	0.22	2	12.3	3301	1
20	0.3	0.019	16.2	0.029	0.16	0.055	2	2.57	3571	0
22.5	0.05	3.68	16.5	0.041	3.21	0.90	1	12.6	5512	0
22.5	0.3	0.86	15.9	0.056	0.49	0.29	1	1.87	3597	0
25	0.05	0.92	16.6	0.10	1.02	0.13	4	3.8	4285	0
25	0.3	1.074	16.6	0.058	0.76	0.23	2	4.19	10000	1
27.5	0.05	4002	24.0	512	4001	3277	2	16.3	878	0
27.5	0.3	3.10	15.6	0.02	3.06	0.63	4	1.43	2901	0
30	0.05	0.7255	16.8	0.12	0.54	0.14	3	9.23	5000	2
30	0.3	0.59	16.3	0.12	0.51	0.17	3	7.27	2660	0

The values p_E of the probability of a collision of a body with the Earth are on average smaller for greater a_o at $5 \le a_o \le 40$ AU. The values of p_E are about 10^{-6} at a_o about 15-40 a.e. and up to 10^{-5} at $5 \le a_{min} \le 10$ AU. For some values of

a_{min} and e_o the values of p_E calculated for 250 bodies can differ in hundreds of times for calculations with almost the same initial orbits. This difference can be caused by that one body of several thousands of bodies can move in Earth-crossing orbit for millions of years and have much greater probability than for other bodies. For example, larger probabilities of collisions of bodies with the terrestrial planets for the variant of Table 1 at a_{min}=27.5 AU and e_o=0.05 were because one body moved in low eccentricity orbits among the terrestrial planets for a long time. Note that the formulas used in calculations of probabilities of bodies with planets work normally for not small eccentricities of orbits of bodies, but can give larger values if bodies move for a long time in low eccentricity orbits (e.g. in tadpole synodical orbits, as Jupiter's Trojans). In Table 1 number N_J of collisions of bodies with Jupiter for N_o=250 at integrations is often greater than the number N_{pJ} of collisions of bodies with Jupiter obtained by using analytical formulas. However, in three variants of this table, N_{pJ} is smaller that N_J and in a few variants the values of N_{pJ} and N_J are about the same.

The total mass of Earth's oceans is about $2{\cdot}10^{-4}\,m_E$ (where m_E is the mass of the Earth). At $p_E=4{\cdot}10^{-6}$ and the total mass m_Σ of bodies at initial distance from the Sun from 5 to 10 AU equal to $100m_E$, the total mass $m_{\Sigma E}$ collided with the Earth should be $4{\cdot}10^{-4}m_E$. For the zone 10–40 AU at $p_E=1.5{\cdot}10^{-6}$ and $m_\Sigma=100m_E$ we have $m_{\Sigma E}=1.5{\cdot}10^{-4}m_E$. For the zone 3–4 AU at $p_E=10^{-3}$ and $m_\Sigma=10m_E$ we have $m_{\Sigma E}=0.01m_E$. The fraction of water in comets doesn't exceed 33%. Some authors suggest that initial planetesimal could contain more ice (~50%) than present comets. The above estimates show that the total mass of water delivered to the Earth from beyond Jupiter's orbit can be compared with the mass of terrestrial oceans. Though bodies in the region of the outer asteroid belt had smaller total mass and probably had smaller (~10%) fraction of ices than bodies outside Jupiter's orbit, due to greater probabilities of collisions, bodies from the outer asteroid belt could deliver even more water to the Earth than the bodies located outside Jupiter's orbit. Due to decrease of the semi-major axis of Jupiter which ejected planetesimals into hyperbolic orbits, the zone in the asteroid belt with a greater probability of a collision with the Earth moved and included a greater number of planetesimals.

The ratios of total mass of water delivered to Venus and Mercury from the region outside Jupiter's orbit to the masses of the planets were about the same as that for the Earth. In absolute values the total mass of water delivered to Mars was about 3–5 times less than the mass delivered to the Earth. These results testify in favor of ancient oceans on Mars and Venus. The mass of water delivered to the Moon from beyond Jupiter's orbit usually less than that delivered to the Earth by a factor not more than 20. More water vaporized at collisions of bodies with the Moon than with the Earth.

ACKNOWLEDGMENTS:
The studies of delivery of material to the Moon were supported by the Russian Science Foundation, project 25-17-00051. Other studies were carried out under government-financed research project for the Vernadsky Institute.

REFERENCES:

[1] Ipatov S. I. Migration of bodies in the accretion of planets // Solar System Research 1993. V. 27. P. 65–79. https://www.researchgate.net/publication/234281490.
[2] Marov M. Ya., Ipatov S. I. Delivery of water and volatiles to the terrestrial planets and the Moon // Solar System Research. 2018. V. 52. P. 392–400. DOI: 10.1134/S0038094618050052. https://www.researchgate.net/publication/340115418.
[3] Ipatov S.I. Migration of bodies to the Earth from different distances from the Sun // Proc. International Astronomical Union. Vol. 19. Symposium S374. Cambridge University Press, 2025. P. 49–54. DOI: https://doi.org/10.1017/S1743921324000735.
[4] Ipatov S.I. Migration of planetesimals from beyond Mars' orbit to the Earth // 14th Europlanet Science Congress 2020. 21 September – 9 Oct 2020, EPSC2020-71, 2020.https://doi.org/10.5194/epsc2020-71, 5 p.

[5] Ipatov S. I. Migration of planetesimals to the Earth and the Moon from the region of the outer asteroid belt // European Planetary Science Congress 2021. September 13–24, 2021, EPSC2021-100, https://doi.org/10.5194/epsc2021-100.
[6] Ipatov S. I. Formation and evolution of planetary systems (in Russian). 2025. 132 p. ISBN 978-5-6055159-1-3. DOI: 10.17513/np.649. https://dx.doi.org/10.17513/np.649.
[7] Levison H. F., Duncan M. J. The long-term dynamical behavior of short-period comets // Icarus. 1994. V. 108. P. 18–36.
[8] Ipatov S. I., Mather J. C. Migration of Jupiter-family comets and resonant asteroids to near-Earth space // Annals of the New York Academy of Sciences. 2004. V. 1017. P. 46–65. https://doi.org/10.1196/annals.1311.004.

DUST MIGRATION FROM THE OUTER SOLAR SYSTEM UNDER THE INTERSTELLAR GAS CLOUD ENCOUNTER

N. V. Lyashenko[1], A. K. Pavlov[1], V. E. Glebov[2]
[1] *Ioffe Institute, Saint Petersburg, Russia, liashenko@mail.ioffe.ru*
[2] *Peter the Great St. Petersburg Polytechnic University Saint Petersburg, Russia*

KEYWORDS:
interstellar gas cloud, dust migration, outer Solar System, Poynting-Robertson effect, gas drag, orbital evolution, Kuiper Belt

ABSTRACT:
The mechanisms of dust particle generation in the outer Solar System at large heliocentric distances are currently the subject of active debate. According to modern concepts, along with collisional processes, a significant contribution can be made by outburst activity of icy bodies caused by explosive recombination of free radicals accumulated under the influence of galactic cosmic rays [1, 2]. However, the dynamical evolution of such dust particles and their contribution to the observed dust cloud in the outer Solar System have not yet been sufficiently studied.

This paper presents the results of numerical modeling of the orbital evolution of large dust particles (r=10μm) within the range of heliocentric distances from 35 to 500 AU. Integration of the full motion equations was performed taking into account the solar gravity, radiation pressure, the Poynting-Robertson effect [3, 4] and the drag of interstellar neutral gas [5, 6]. Two scenarios were considered: the Solar System passage through an interstellar gas cloud with parameters typical for models of Galactic diffuse clouds (H concentration of 10 atoms/cm^3, flow velocity of 28 km/s, flow inclination angle of 20° to the ecliptic plane) [7, 8] and the dynamics of a dust particle in a modern interstellar medium.

It is shown that in the presence of interstellar gas, its drag becomes the dominant factor determining the long-term evolution of dust orbits in the outer Solar System [5, 6]. While under the Poynting-Robertson effect alone, the timescale for a dust particle to fall from 500 AU to 35 AU is on the order of billions of years [3], the gas drag ensures efficient migration of dust particles from the outer region to the inner Solar System within characteristic time of ~10^5 years [5, 6]. Furthermore, the interaction with interstellar gas cloud fundamentally alters the nature of the motion: the dust particle trajectory undergoes qualitative changes and the key orbital elements – semi-major axis, eccentricity and inclination – exhibit an oscillatory behavior with a period of ~0.5 Myr [9]. Meanwhile, the eccentricity reaches values close to unity, allowing the dust particles to penetrate deep into the inner Solar System [9].

The obtained results indicate that interstellar gas clouds, widely distributed throughout the Galaxy [7, 8], may play a key role in shaping the observed dust cloud in the Kuiper Belt [10, 11]. Our results could explain the absence of the dust density drop with heliocentric distance predicted by standard models in the range of 42–55 AU [12, 13].

REFERENCES:
[1] Pavlov A. K., Kucherov G. A., Merkulova A. Y., Belousov D. V. Accumulation and Recombination of Radicals as an Energy Source for Active Processes in Icy Bodies of the Solar System // Solar System Research. 2025. V. 59. DOI: 10.1134/S0038094624601981.
[2] Belousov D. V., Pavlov A. K. Cometary outbursts in the Oort cloud // Icarus. 2024. V. 415. Article 116066. DOI: 10.1016/j.icarus.2024.116066.
[3] Liou J.-C., Zook H. A. Evolution of Interplanetary Dust Particles in Mean Motion Resonances with Planets // Icarus. 1997. V. 128. No. 2. P. 354–367. DOI: 10.1006/icar.1997.5755.

[4] Burns J. A., Lamy P. L., Soter S. Radiation forces on small particles in the Solar System // Icarus. 1979. V. 40. No. 1. P. 1–48. DOI: 10.1016/0019-1035(79)90050-2.
[5] Scherer K. Drag forces on interplanetary dust grains induced by the interstellar neutral gas // J. Geophysical Research. 2000. V. 105. Iss. A5. P. 10329–10341. DOI: 10.1029/1999JA900343.
[6] Belyaev M., Rafikov R. The dynamics of dust grains in the outer Solar System // The Astrophysical J. 2010. V. 723. No. 2. P. 1718–1735. DOI: 10.1088/0004-637X/723/2/1718.
[7] Ferrière K. M. The interstellar environment of our galaxy // Reviews of Modern Physics. 2001. V. 73. No. 4. P. 1031–1066. DOI: 10.1103/RevModPhys.73.1031.
[8] Draine B. T. Physics of the Interstellar and Intergalactic Medium. Princeton: Princeton University Press, 2011. 576 p. ISBN: 978-0-691-12214-4.
[9] Pástor P., Klačka J., Kómar L. Orbital evolution under the action of fast interstellar gas flow // Monthly Notices of the Royal Astronomical Society. 2011. V. 415. No. 3. P. 2637–2651. DOI: 10.1111/j.1365-2966.2011.18889.x.
[10] Liou J. C., Zook H. A., Dermott S. F. Kuiper Belt dust grains as a source of interplanetary dust particles // Icarus. 1996. V. 124. No. 2. P. 429–440. DOI: 10.1006/icar.1996.0220.
[11] Moro-Martín A., Malhotra R. A Study of the Dynamics of Dust from the Kuiper Belt: Spatial Distribution and Spectral Energy Distribution // The Astronomical J. 2002. V. 124. No. 4. P. 2305–2321. DOI: 10.1086/342849.
[12] Yamamoto S., Mukai T. Dust production by impacts of interstellar dust on Edgeworth–Kuiper Belt objects // Astronomy and Astrophysics. 1998. V. 329. P. 785–791.
[13] Doner A., Horányi M., Bagenal F. et al. New Horizons Venetia Burney Student Dust Counter Observes Higher than Expected Fluxes Approaching 60 au // The Astrophysical J. Letters. 2024. V. 961. No. 2. Article L38. DOI: 10.3847/2041-8213/ad18b0.

DUSTY PLASMA CLOUDS ON VENUS, THE EARTH AND MARS

Yu. S. Reznichenko, S. I. Popel, A. Yu. Dubinskii
Space Research Institute RAS, Moscow 117997, Russia, dvju@yandex.ru

KEYWORDS:
dusty plasma structures, mesospheric clouds, dust particles, condensation, ionosphere, Venus, the Earth, Mars

ABSTRACTS:
Since the late 1990s and early 2000s, considerable attention has been devoted to investigating the dusty plasma structures of planetary ionospheres. For a long time, the primary focus of research was NLC and PMSE of the Earth's ionosphere. Both types of dust formations are recorded in northern and mid-latitudes from mid-May to mid-August. During this time of the year, the temperature in the polar mesosphere drops below 150 K, causing water vapor to become supersaturated, that creates the conditions for dust particle growth due to condensation processes as well as leads to the formation of layered dusty plasma clouds [1, 2].

Similar processes lead to the formation of mesospheric clouds on Mars [3, 4]. The formation of dust clouds in the Martian ionosphere, however, has certain peculiarities associated with the specific structure of the Martian atmosphere. Thus, the main component of the Martian atmosphere is carbon dioxide, so typical Martian mesosphere clouds consist of dry ice particles.

The atmosphere of Venus is currently being actively studied (see, for example, [5, 6]). The temperature regime of the lower Venus ionosphere discovers similarities with the ionosphere of the Earth. Moreover, the main neutral component of the lower ionosphere of Venus, similar to the situation in the ionosphere of Mars, is carbon dioxide [7].

Thus, it is logical to assume that, like the NLC of the Earth's mesosphere and the dusty plasma clouds of the ionosphere of Mars, dusty plasma clouds also exist on Venus. This paper discusses the formation conditions of dusty clouds in the ionosphere of Venus as well as presents a self-consistent model describing ionospheric dusty structures on Venus.

REFERENCES:
[1] Klumov B. A., Morfill G. E., Popel S. I. Formation of structures in a dusty ionosphere // JETP. 2005. V. 100. No. 1. P. 152–164.
[2] Dubinskii A. Yu., Popel S. I. Formation and evolution of dusty plasma structures in the ionosphere // JETP Letters. 2012. V. 96. No. 1. P. 21–26.
[3] Reznichenko Yu. S., Dubinskii A. Yu., Popel S. I. Formation and Evolution of Dusty Plasma Structures in the Ionospheres of the Earth and Mars // Plasma Physics Reports. 2019. V. 45. No. 10. P. 928–935.
[4] Reznichenko Yu. S., Dubinskii A. Yu., Popel S. I. On the Formation of Clouds in the Dusty Ionosphere of Mars // JETP Letters. 2023. V. 117. No. 6. P. 428–434.
[5] Bertaux J.-L. et al. A warm layer in Venus' cryosphere and high-altitude measurements of HF, HCl, H_2O and HDO // Nature. 2007. V. 450. No. 7170. P. 646–649.
[6] Piccialli A. et al. Thermal structure of Venus nightside upper atmosphere measured by stellar occultations with SPICAV/Venus Express // Planetary and Space Science. 2015. V. 113–114. P. 321–335.
[7] Bougher S. W. et al. Neutral Upper Atmosphere and Ionosphere Modeling // Space Sci. Rev. 2008. V. 139. P. 107–141.

MONITORING OF COSMIC DUST FALLOUT IN ANTARCTICA AND GLOBAL DUST EMISSIONS

Y. O. Chetverikov[1], V. F. Ezhov[1], A. A. Ekaykin[2,3], M. S. Glukhov[4], A. S. Loshachenko[5], V. D. Kalganov[5], K. G. Vitovchik[6], O. V. Yakubovich[5,6]

[1] *Petersburg Nuclear Physics Institute named by B. P. Konstantinov of National Research Center "Kurchatov Institute", Gatchina, Russia chetverikov_yo@pnpi.nrcki.ru*
[2] *Arctic and Antarctic Research Institute, Saint Petersburg, Russia*
[3] *Institute of Geography RAS, Moscow, Russia*
[4] *Zavaritsky Institute of Geology and Geochemistry, Ural Branch RAS Yekaterinburg, Russia*
[5] *Saint Petersburg State University, Saint Petersburg, Russia*
[6] *Institute of Precambrian Geology and Geochronology RAS Saint Petersburg, Russia*

KEYWORDS:
cosmic dust, meteor showers, resonant orbits, Vostok station, central Antarctica

ABSTRACT:
Large-scale dynamic phenomena — such as intense meteor showers, meteor airbursts, and volcanic eruptions — release massive volumes of fine dust into the atmosphere. These suspended aerosols alter global sky brightness [1] and produce the sedimentation of metallic spherical particles [2]. Some of these events have a major impact on the Earth's climate [3]. Earth accretes roughly 20–40 thousand tons of cosmic dust annually before atmospheric entry [4], which accounts for approximately 0.0006% of total Earth atmospheric dust.

This work introduces a novel approach to detecting and analyzing global dust emission events primarily attributed to explosive processes resulting from collisions between space objects and Earth [5]. This approach proposes continuous monitoring of atmospheric dust deposition onto the snowpack surface in the ultra-clean environment of Antarctica. The analysis of dust deposits and the determination of correlations between deposit composition and the phenomena responsible for global dust emissions (meteor showers, impacts of large cosmic bodies, volcanic eruptions, large-scale wildfires, dust storms, etc.) will facilitate the identification of distinctive characteristics in the dust's elemental and mineral composition, morphology, and size distribution that are indicative of specific sources. Such an analysis will help quantify the contributions of various sources to global dust emissions on Earth. The collection and analysis of dust particles in Antarctica will provide detailed information on the dynamics of dust transport and deposition processes, as well as their relationship to observable weather phenomena and climate change.

For the 2017 and 2024 collections, the combined data on particle composition, size distribution, and temporal distribution allow us to draw the following conclusions:

- The Mg/Al ratio indicates a multicomponent composition of the collections, which contain comparable proportions of spherules of cosmogenic (>23%) and non-cosmogenic (>43%) origin. A significant proportion of the spherical particles (34%) lack any elemental characteristics that would allow their origin to be determined.
- The crossover point in the 15-μm range was detected in the size distributions of the spherules from both collections, which is a potential indicator of the characteristic particle size of the zodiacal cloud. However, reaching a definitive conclusion requires expanded data collection across various environments, taking into account variations in global

dust levels and the processes that trigger dust fallout from the atmosphere, in order to rule out possible anthropogenic sources, such as volcanic aerosols, engine emissions, etc.

- The increase in the average number of spherules of the 2017 collection (4.2 spherules per day) compared to the 2024 collection (17 spherules per day) may indicate variations in global dust deposition over a timescale of several years. This increase in dust emissions could have been linked to an increase in the flow of cosmic dust as solar activity rose during that period.
- In short-term peaks of spherule fallouts, no temporal evolution of the size distribution is observed, pointing to an abnormally rapid fallout event, likely caused by the ice crystal condensation on particle surfaces in the upper layers of supercooled vapor.
- In the size distribution of particles from the 2017 collection, the increased population in the 3–10 μm range, compared to the 2024 collection, appears as an additional component of the dust flow lacking the noticeably prominent sizes within that range. This is likely due to the fact that changes in upper-atmosphere circulation cause anomalous air mass transport to carry anthropogenic aerosols—including fly ash particles — from temperate to polar latitudes.

The proposed method for monitoring dust deposition in Central Antarctica will, in the long term, help advance our understanding of the processes and characteristics of global dust emissions, as well as its impact on the climate and the environment. Detecting dust emission peaks will make it possible to compile a catalog of peak and periodic changes in dust flux, which will help refine climate models and establish a chronological timescale for global dust deposition.

A comprehensive analysis of fallout time, morphology, mineral and elemental composition can reveal the nature and source of the particles. Collecting and isolating microscopic extraterrestrial dust from Earth will allow scientists to study the composition of known asteroids and comets in terrestrial laboratories.

REFERENCES:

[1] Mane P.B., Mane D.B. Study of aerosol vertical distribution during meteor showers of January 2009 // J. Atmospheric and Solar-Terrestrial Physics. 2021. V. 213. Article 105511.
[2] Ganapathy R. The Tunguska explosion of 1908: Discovery of meteoritic debris near the explosion site and at the South Pole // Science. 1983. V. 220. No. 4602. P. 1158–1161.
[3] Toon O.B. et al. Environmental perturbations caused by the impacts of asteroids and comets // Reviews of Geophysics. 1997. V. 35. No. 1. P. 41–78.
[4] Van Ginneken M. et al. Micrometeorite collections: a review and their current status // Philosophical transactions. Series A, Mathematical, physical, and engineering sciences. 2024. V. 382. No. 2273. Article 20230195.
[5] Chetverikov Y.O. et al. Extraterrestrial dust flux monitoring at Antarctic Vostok station: New collection of extraterrestrial spherules fallen from May to September 2017 // Meteoritics and Planetary Science. 2023. V. 58. No. 6. P. 815–833.

CO-ORBITAL POPULATION OF VENUS: PRESUMED MEMBERS AND THEIR POSSIBLE SECULAR EVOLUTION

N. Adigozalov[1], V.V. Sidorenko[2]
[1] *Moscow Institute of Physics and Technology, Moscow 141701, Russia*
adigozalov@phystech.edu
[2] *Keldysh Institute of Applied Mathematics RAS, Moscow 125047, Russia*
vvsidorenko@list.ru

KEYWORDS:
asteroids, Venus, co-orbital dynamics

INTRODUCTION:
Co-orbital asteroids of Venus are objects moving in 1:1 mean motion resonance with this planet. Their orbital periods are almost exactly equal to the orbital period of Venus (about 224.7 Earth days). However, unlike gravitationally bound satellites, these bodies orbit the Sun along complex trajectories, sometimes ahead of Venus, sometimes behind it, and sometimes crossing its orbit. Currently, about twenty co-orbitals of Venus are known. The first asteroid from this population was discovered in 2004. It was asteroid 2002VE68, later named Zoozwe [1]. Zoozwe is also notable for being the first example of an asteroid moving in a quasi-satellite mode. The population of identified Venus co-orbitals also includes Trojan asteroids and asteroids in complex compound orbits that combine properties of quasi-satellite and Trojan or horseshoe modes (it is noteworthy that no objects in classic horseshoe orbits were detected). An important property of the population of known Venusian co-orbitals is their high eccentricities: the orbits of all objects have e>0.36. This means their orbits are very elongated and reach the distance of Earth's orbit, making them detectable from Earth during favourable visibility windows. So high eccentricities are a manifestation of observational selection, and not some dynamical effect. And we should consider the known population as only "the tip of the iceberg". Modern models (e.g., [2]) predict the existence of a significant undiscovered population of low-eccentricity co-orbitals. Because Venus is close to the Sun, low-eccentricity co-orbitals remain at small solar elongation, making them extremely difficult to detect from Earth.

MAIN DYNAMIC FEATURES OF VENUS CO-ORBITALS:
Known Venus co-orbitals exhibit extremely chaotic behaviour. The secular evolution of their orbits is determined not only by perturbations from Venus, but also by regular close encounters with Earth and Mercury. Semi-analytical models that successfully predict the evolution of the Earth's co-orbitals (e.g., [3]) are less reliable for Venus. Instead, researchers rely on large-scale numerical simulations with clone statistics (e.g., [2]). However, the semi-analytical approach is quite useful in classifying co-orbital motion modes and in analyzing transitions between modes.

To recognize the mode of co-orbital motion, one should consider the behavior of the resonant phase $\varphi = \lambda_A - \lambda_V$ (λ_A and λ_V are the mean longitudes of the asteroid and Venus, respectively). As a model of the system "Sun+Venus+asteroid", the restricted circular three-body problem is used. After averaging over the orbital motions and the proper choice of units, the behavior of the resonant phase can be described by the equation

$$3\frac{d^2\varphi}{dt^2} + \mu\frac{\partial W}{\partial \varphi} = 0\,, \qquad (1)$$

where time t is introduced so that the mean motion of Venus $n_V = 1$, $\mu \ll 1$ is the part of the mass of Venus in the total mass of the system, $W(\varphi, \omega, e, i)$ is the averaged disturbing function.

The expression for the disturbing function averaged taking into account 1:1 resonance of mean motions can be written as

$$W(\varphi,\omega,e,i)=\frac{1}{2\pi}\int_0^{2\pi}\left[\frac{1}{|\mathbf{r}_A(\lambda_A)-\mathbf{r}_V(\lambda_V(\lambda_A,\varphi))|}-(\mathbf{r}_A(\lambda_A),\mathbf{r}_V(\lambda_V(\lambda_A,\varphi))\right]d\lambda_A .$$

Here the vectors $\mathbf{r}_A(\lambda_A)$ and $\mathbf{r}_V(\lambda_V)$ in the integrand define the position of the asteroid and Venus for the corresponding values of their mean longitudes. In the resonant motion under consideration these longitudes are connected by the relation $\lambda_V(\lambda_A)=\lambda_A-\varphi$.

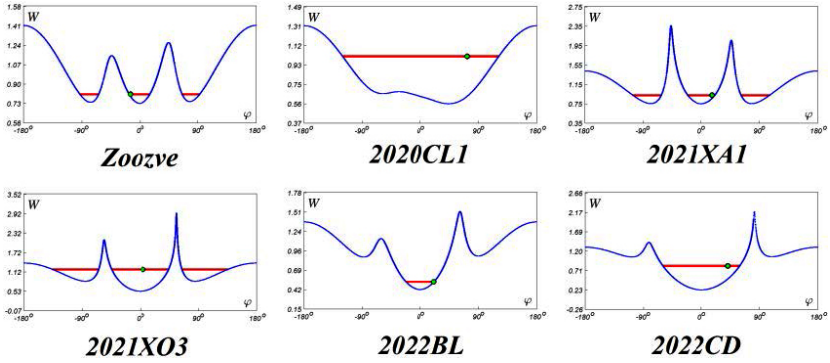


Fig. 1. Averaged disturbing function $\tilde{W}(\varphi,\omega,e,i)$ for Venus quasi-satellies. Here and on other picture the red line indicates the value of the energy integral along the solution of equation (1), corresponding to the observed motion of the asteroid. The dot marks the current value of the resonant phase

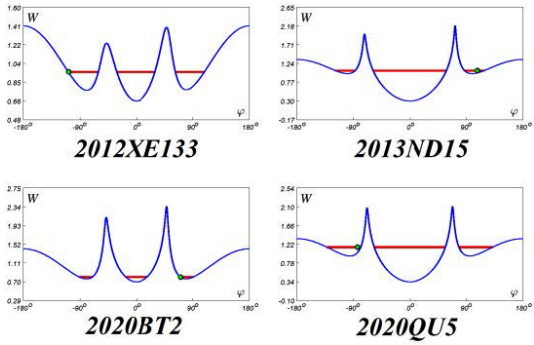


Fig. 2. Averaged disturbing function $\tilde{W}(\varphi,\omega,e,i)$ for Venus Trojans

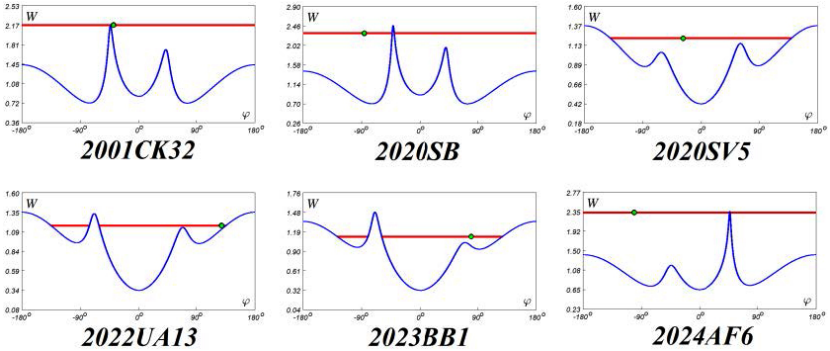


Fig. 3. Averaged disturbing function $\tilde{W}(\varphi,\omega,e,i)$ for Venus co-orbitals in compound orbits

Figs. 1–3 shows the graphs of the averaged disturbing function and the intervals of variation of the resonant phase for known co-orbitals of

Venus. In Fig. 1 one can see 6 quasi-satellites: Zoozve, 2020CL1, 2021XA1, 2021XO3, 2022BL5, 2022CD. In Fig. 2 we presented graphs for 4 Venus Trojans: 2012XE133, 2013ND15, 2020BT2, 2020QU5. Finally, Figure 3 shows graphs for 6 asteroids in compound modes of motion: 2001CK32, 2020SB, 2020SV5, 2022UA13, 2023BB1, 2024AF6. The quasi-satellite mode corresponds to oscillations of the resonant phase around zero. Trojan modes manifest themselves as oscillations around –60 or 60°. In compound modes, the interval of oscillations contains several values of the resonant phase at which *W* has a local minimum.

CONCLUSION:

Venus co-orbitals are not merely a dynamical curiosity but an important, hidden population whose study has both fundamental and applied significance. It is believed that as yet undiscovered low-eccentricity co-orbitals of Venus are responsible for the formation of the dust ring in the vicinity of its orbit [2]. The practical significance of studying Venus's co-orbitals lies in the threat of their collisions with Earth. Due to the difficulties of Earth-based observations, a complete cataloging and observation of Venus's co-orbitals requires space-based observations.

REFERENCES:

[1] Mikkola S., Brasser R., Wiegert P., Innanen K. Asteroid 2002 VE68, a quasi-satellite of Venus // MNRAS. 2004. V. 351. Article L63.
[2] Pokorny P., Kuchner M. Co-orbital asteroids as the source of Venus's zodiacal dust ring // ApJL. 2019. V. 873. Article L16.
[3] Sidorenko V. V., Neishtadt A. I., Artemyev A. V., Zelenyi L. M. Quasi-satellite orbits in the general context of dynamics in the 1:1 mean motion resonance: perturbative treatment // CMDA. 2014. V. 120. Article 131.

Session 9.
PLANETARY MISSIONS AND SCIENTIFIC INSTRUMENTATION (MI)
Oral Session

NEW WINDOW OF EARTH MONITORING FROM LUNAR NORTH POLE

Hanlin Ye, Jinsong Ping
National Astronomical Observatories, Chinese Academy of Sciences
Beijing, China, yehl@radi.ac.cn

KEYWORDS:
lunar north pole, Earth visibility, Earth observation, terrain shadowing, Earth phase, lunar research station

INTRODUCTION:
The lunar polar regions have become primary candidate sites for future lunar exploration and the construction of the International Lunar Research Station (ILRS) [1]. In addition to scientific investigations and in-situ resource utilization, the lunar poles provide a promising platform for long-term Earth observation. Compared with conventional Earth-orbiting satellites, Moon-based observations can provide stable viewing geometry, continuous long-term monitoring, and unique perspectives for studies of the Earth's radiation budget and climate system.

However, the observation capability of sensors deployed in the lunar polar regions remains insufficiently understood. Due to the rugged topography and persistently low solar elevation angles, local terrain can significantly affect both illumination conditions and line-of-sight visibility. Although numerous studies have investigated illumination environments and permanently shadowed regions at the lunar poles [2, 3], few have quantitatively evaluated how terrain-modulated illumination conditions constrain Earth visibility and Earth observation opportunities.

In this study, Earth observation constraints at the lunar north pole were analyzed using the Lunar Orbiter Laser Altimeter (LOLA) digital elevation model (DEM) and the JPL DE440 planetary ephemeris [4, 5]. A terrain model based on a triangulated irregular network (TIN) was constructed from the LOLA DEM, and ray-tracing analysis was performed to determine the visibility of both the Earth and the Sun. The region from 60 to 90°N was selected as the study area. Simulations were conducted at one-hour intervals throughout the year 2026. Based on the resulting visibility database, the Earth visibility fraction, Earth visibility fraction under Lunar day conditions, and visibility statistics for different Earth phases were quantified.

RESULTS:
Figure 1a presents the spatial distribution of the Earth visibility fraction across the lunar north polar region. Owing to the tidal locking of the Earth–Moon system, Earth visibility remains consistently high over most near-side polar areas, with visibility fractions approaching 100%. In contrast, Earth visibility decreases substantially within terrain-depressed regions, particularly at the bottoms of large impact craters where topographic obstruction becomes significant. On the lunar far side, the Earth remains permanently invisible.

Figure 1b shows the Earth visibility fraction under daylight conditions. Compared with the unrestricted visibility results, the visibility fraction is substantially reduced because Earth observation is limited to periods when both Earth visibility and solar illumination are simultaneously available. Over most of the study region, the daylight Earth visibility fraction falls below 50%, while crater interiors exhibit even lower values due to severe terrain shadowing. The maximum daylight visibility fraction reaches only 51.6%, indicating that favorable illumination conditions do not necessarily coincide with optimal Earth visibility.

These results provide quantitative constraints on the observation capability of future Moon-based Earth observation systems and offer scientific support for site selection and operational planning of lunar research stations. Locations with favorable trade-offs between illumination availability and

Earth visibility may represent preferred candidates for future lunar polar Earth-observation facilities.

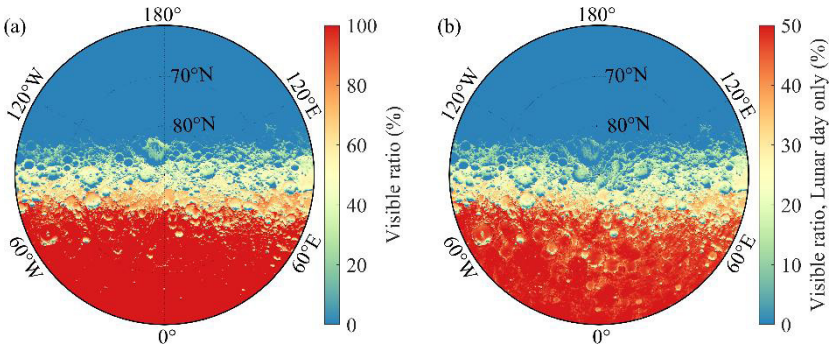


Fig. 1. Spatial distributions of Earth visibility conditions in the lunar north polar region derived from LOLA DEM and JPL DE440 ephemeris data for the year 2026. (a) Earth visibility fraction, defined as the percentage of time during which the Earth is visible from a given location. (b) Earth visibility fraction under Lunar day conditions, defined as the percentage of time during which both the Earth and the Sun are simultaneously visible. Results are calculated for the 60–90°N region using a 0.1° resolution grid and a terrain-based ray-tracing model

REFERENCES:

[1] Pei Z., Liu J., Wang Q. et al. Overview of lunar exploration and international lunar research station // Chin. Sci. Bull. 2020. V. 65(24). P. 2577–2586.
[2] Gläser P., Oberst J., Neumann G. A. et al. Illumination conditions at the lunar poles: Implications for future exploration // Planetary and Space Science. 2018. V. 162. P. 170–178.
[3] Kloos J. L., Moores J. E., Godin P. J. et al. Illumination conditions within permanently shadowed regions at the lunar poles: Implications for in-situ passive remote sensing // Acta Astronautica. 2021. V. 178. P. 432–451.
[4] Smith D. E., Zuber M. T., Jackson G. B. et al. The lunar orbiter laser altimeter investigation on the lunar reconnaissance orbiter mission // Space Science Reviews. 2010. V. 150(1). P. 209–241.
[5] Park R. S., Folkner W. M., Williams J. G. et al. The JPL planetary and lunar ephemerides DE440 and DE441 // The Astronomical J. 2021. V.161(3). Article 105.

LOCATING THE BLUE GHOST M1 LANDER ON THE LUNAR SURFACE USING RADIO INTERFEROMETRIC MEASUREMENTS

E. O. Kazantseva, Yu. S. Bondarenko, D. A. Marshalov
Institute of Applied Astronomy RAS, Saint Petersburg, Russia

KEYWORDS:
VLBI measurements, Blue Ghost M1, lunar lander, Moon, data processing, selenographic coordinates

INTRODUCTION:
The growing number of lunar exploration and development programs places increasing demands on positioning and timing support for current and future missions, particularly for the rapid determination of spacecraft coordinates on the lunar surface. Ground based radio techniques can address this task with sufficient accuracy. This report presents the results of refining the selenographic coordinates of the Blue Ghost M1 (BGM-1) lander using signal time-delay measurements obtained with antennas of the Quasar VLBI Network. The Firefly Aerospace spacecraft successfully landed in Mare Crisium on March 2, 2025. Prior to the onset of the lunar night on March 16, BGM-1 transmitted scientific data to Earth in the S and X bands at frequencies of 2251.1 and 8493.2 MHz, respectively. The spacecraft signals were recorded on March 2, 5, and 15 using the 13.2 m antennas of the Svetloe, Zelenchukskaya, and Badary observatories in left- and right-hand circular polarizations. During the landing phase, Doppler frequency measurements of the signal were performed; during subsequent observations, radio interferometric measurements of the signal arrival delays were carried out. The data processing method previously applied in [1, 2] was further refined. In particular, the FX correlator used for processing was upgraded, enabling delay measurements with an accuracy of 1 ns. This improvement made it possible to determine the coordinates of BGM-1 within an uncertainty area with a radius of 0.9 km.

REFERENCES:
[1] Kazantseva E., Bondarenko Y., Marshalov D., Medvedev Y. Obtaining the Chandrayaan-3 lander coordinates on the lunar surface by the Doppler measurements of the transmitted signal with an Earth-based receiving system // Modern astronomy: from the Early Universe to exoplanets and black holes. SAO RAS. 2024. P. 893–896. DOI: 10.26119/VAK2024.169.
[2] Kazantseva E., Bondarenko Y., Marshalov D. Locating the Blue Ghost M1 Lander on the Lunar Surface Using Radio Interferometric Measurements // Moscow Univ. Phys. Bull. 2025. V. 80 (Suppl 1). S181–S185. DOI: 10.3103/S0027134925701632.

PROPOSED ROUTE FOR A HEAVY SCIENTIFIC ROVER AT THE LUNAR SOUTH POLE: TRAVEL-TIME ASSESSMENT AND PRELIMINARY OPERATIONAL TIMELINE

O. I. Turchinskaya, E. A. Grishakina, E. N. Slyuta
Vernadsky Institute of Geochemistry and Analytical Chemistry RAS, Moscow, Russia, turchinskaya@geokhi.ru

KEYWORDS:
Moon, heavy rover, rout, lunar south pole

ABSTRACT:
The lunar South Pole is a primary target for in situ exploration by a heavy scientific rover. The combination of extended periods of solar illumination, large areas enriched in water-equivalent hydrogen (WEH), which may indicate the presence of water ice in the regolith, and a diverse geological setting makes this region particularly attractive for long-range surface investigations. The proposed route of the Robot-Geologist rover crosses a variety of regional geological units and structures, providing opportunities to identify and characterize rocks of different ages, origins, compositions, and spectral classes, including ancient materials associated with the South Pole–Aitken basin.

The route was designed considering four main criteria: terrain safety, solar illumination, proximity to potential resources, and geological diversity. The study area is characterized by rugged topography, considerable elevation differences, relatively steep slopes, and numerous impact craters. The route was therefore adjusted to the technical capabilities of the rover and, wherever possible, avoids abrupt elevation changes and potentially hazardous terrain (Fig. 1).

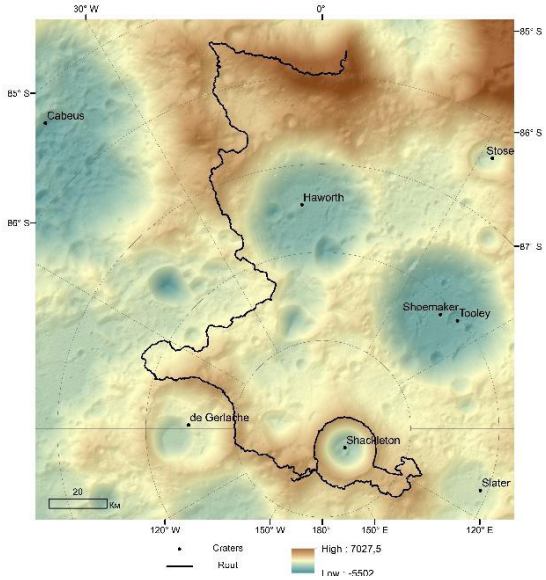


Fig. 1. Hypsometric map of the lunar south polar region with rover route

Surface slopes along the route do not exceed 25°. Approximately two-thirds of its total length crosses the safest terrain, where slopes are below 10°. Solar illumination was treated as another major limiting factor because the rover relies on solar power. Illumination maps were used to identify areas with illuminated-time fractions above 75% and to evaluate sections combining slopes greater than 15° with poor illumination. Most

of the route crosses areas with acceptable illumination and includes several local illumination maxima. However, seven poorly illuminated sections were identified, including one relatively long segment (Fig. 2).

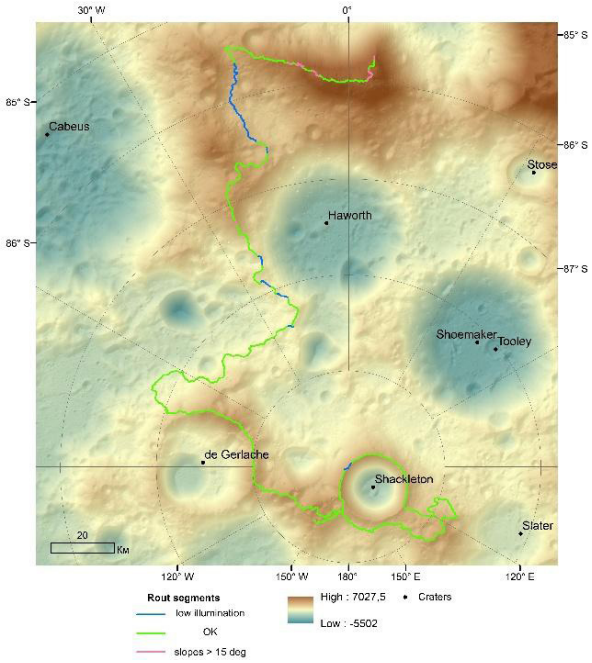


Fig. 2. Route suitability map for the heavy lunar rover

Particular attention was given to locations suitable for drilling, sampling, and geological observations. Thirty-four high-priority scientific sites were selected at contacts between geological units of different ages, within areas showing contrasting WEH values (Fig. 3), and in well-illuminated locations suitable for energy-intensive operations.

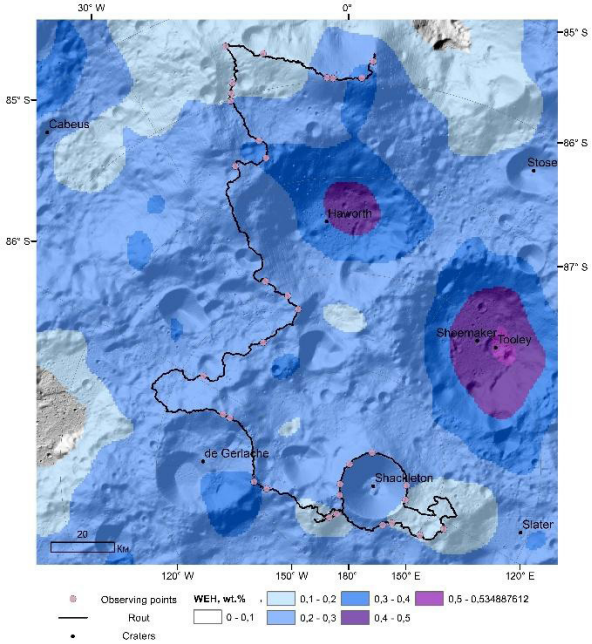


Fig. 3. Observation points in areas with low and WEH content

For the preliminary operational timeline, the route was divided into 2 km segments. Mean slope and illumination were calculated for each segment, while the estimated travel speed was assigned according to terrain slope. Segments with mean slopes of 15–25° or mean illumination below 20% were automatically classified as potentially hazardous or energetically unfavorable.

The total route length is 561.318 km, with an estimated pure driving time of 619.34 hours, or 25.81 Earth days.

A total of 282 sampling locations were placed at 2 km intervals. Assuming that 50 g of regolith is collected at each location, the total sample mass would reach approximately 14.1 kg. The actual mission duration will be longer because the estimate does not include time required for drilling, sampling, in situ analyses, scientific observations, maintenance operations, or waiting for favorable illumination conditions.

ACKNOWLEDGMENTS:
The work was carried out within the state assignment of the Vernadsky Institute of Geochemistry and Analytical Chemistry of the Russian Academy of Sciences (GEOKHI RAS).

LIGHTWEIGHT LUNAR ULTRAVIOLET TELESCOPE (LLUT-150) PROJECT

A. Shugarov[1], D. Weijie[2], M. Sachkov[1], H. Wang[3], J. Wang[3], G. Tsurikov[1]
[1] *Institute of Astronomy RAS, Moscow 119017, Russia, shugarov@inasan.ru*
[2] *Changchun Institute of Optics, Fine Mechanics and Physics, Chinese Academy of Sciences, dengweijie@ciomp.ac.cn*
[3] *National Astronomical Observatory, Chinese Academy of Sciences (NAOC), Beijing 100101, China, wanghj@nao.cas.cn*

KEYWORDS:
UV astronomy, Moon telescope, ILRS, Lightweight SiC design, UV detector

INTRODUCTION:

The Lightweight Lunar Ultraviolet Telescope (LLUT-150) is a cooperative project between the Changchun Institute of Optics, Fine Mechanics and Physics, Chinese Academy of Sciences (CIOMP), the Institute of Astronomy, Russian Academy of Sciences (INASAN), and National Astronomical Observatories of China (NAOC). The goal of the project is to design a compact 10 kg UV-optical telescope capable of operating on a lunar lander or lunar orbiter. The LLUT-150 telescope will be proposed for implementation within the Chinese-Russian cooperation on the Moon exploration program, including the International Lunar Research Station (ILRS), or as an international Chinese-Russian payload on the Russian Luna series missions. INASAN and NAOC are responsible for the scientific justification of the telescope's key technical parameters, while CIOMP is responsible for designing and building the telescope proto-flight model by the end of 2028.

A preliminary telescope design is shown in Fig. 1. The telescope is built on a classical 2-axis fork mount. The electronic unit located aside from the telescope optical assembly. The main LLUT-150 parameters are given below:

A preliminary design of the telescope is presented in Fig. 1. The telescope used a classical 2-axis fork mount, with the electronic unit located separately from the optical assembly. Key parameters of the LLUT-150 are listed below:

Spectral range	115–900 nm
Aperture	150 mm
Detector format	6k×6k pixels
Field of view	2°
Angular resolution	2 arcsec
Image scale	1.2 arcsec pixel^{-1}
Number of scientific filters	9
Telescope tilt angle	–90…+90°
Telescope rotation angle	–180…+180°
Power consumption	15 W
Mass	10 kg

Despite its compactness and simplicity, the LLUT-150 telescope, when operated on a lunar lander module, will be capable of carrying out a reasonably extensive observational program of relatively bright objects and testing new unique observational methods from the Moon.

The technological aspects that can be evaluated and verified by a LLUT-150 Moon-based telescope are:

- Effect of the Moon's dust on astronomical optics.
- Stability of the Moon lander on the lunar regolith at the sub-arcsecond level.
- Experience in conducting astronomical observations under difficult scattered light and thermal conditions during the Moon's day and night.

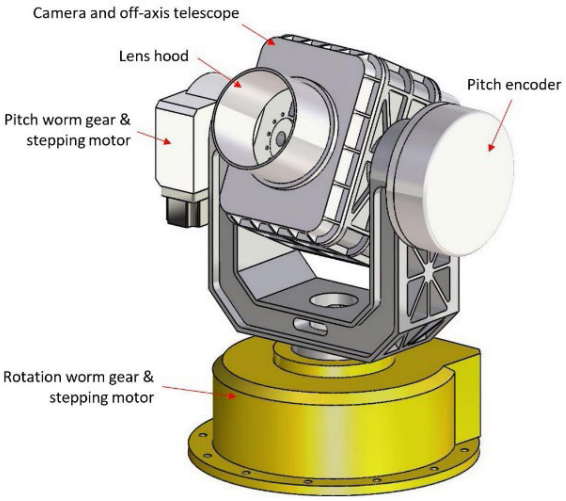


Fig. 1. LLUT150 lunar telescope preliminary design

The LLUT-150 telescope will allow us to probe new unique methods of astronomical observations from the Moon that cannot be done from other orbits close to the Earth:

- Synchronous observation in triangulation mode with Moon- and ground-based telescopes (Moon–Earth baseline) of dangerous asteroids in near-Earth space for faster and more accurate determination of their orbits.
- Observation of asteroids and comets close to the Sun from the Moon.
- Observation of the Earth's exosphere in UV.
- Evaluation of the efficiency of occultation observations by the Moon crater hill.

The LLUT-150 telescope is optimized to operate in the UV range. With limited efficiency, it can address the following solar system and astronomical objectives:

- Transient astronomy and other astrophysical objectives.
- Determination of composition of small bodies approaching the Earth.
- Observation of comets, photoevaporation processes and interaction with the solar wind, including in regions near the Sun.
- Observation of the exospheres and magnetospheres of giant planets.
- Fill the gaps in the GALEX catalog in the region of bright objects.
- Heliosphere monitoring.
- Observations of the Earth's exosphere in preparation for studies of exo-Earths and exoplanets.

The LLUT-150 UV-optical telescope has a compact mirror-based off-axis optical scheme, and it uses CIOMP's experience in designing lightweight optics from SiC material. The telescope is designed to achieve optical quality close to diffraction-limited in the UV range, and all elements are mounted on a thermally stable frame.

A modern CMOS detector GSENSE6060BSI with a small pixel size optimized for UV operation is used. The CMOS detector is not sensitive to local overexposure and has a large dynamic range. Low readout noise will allow obtaining series of frames with subsequent digital stacking to compensate for mount tracking errors and field rotation, and to achieve maximum sensitivity and high dynamic range.

To provide multi-band UV photometry, up to 9 multilayer filters can be placed directly in front of the CMOS detector. This approach avoids the use of moving parts (e.g., a filter wheel) to reduce the weight of the telescope.

During the telescope design, the issue of installing a light baffle will be considered. To reduce contamination of the telescope optics during the descent module's landing on the Moon, a protective telescope cover may be installed. Other methods of protecting the telescope from lunar dust will also be considered for implementation.

The implementation of a 10 kg LLUT-150 telescope will provide valuable experience in conducting astronomical observations from the Moon and will allow us to design future, more ambitious missions, such as the ILRS astronomical UV-optical-IR telescope with a 1 m aperture for the ILRS-5 mission.

REFERENCES:

[1] Zhaoyu Pei, Qiong Wang, Lin Xu et al., Strategic Analysis of Scientific Activities and Study on the Overall Plan of Scientific Operation Platforms Based on the Lunar Research Station // Chinese J. Space Science, 2025, 45(1): P. 1-14., DOI: 10.11728/cjss2025.01.2024-0188.

[2] Shugarov A. S., Sachkov M. E., Wang H, Jiang X The concept of multipurpose compact UV-optical telescope for Lunar lander // INASAN Science Reports. 2025. V. 10. Iss. 5. P. 273–278. DOI: 10.51194/INASAN.2025.10.5.001.

[3] Huijuan Wang, Xuelei Chen, Mikhail Sachkov, Subo Dong et al., A brief introduction to the astronomical research for ILRS // Intern. Workshop on Overall Science Objectives of ILRS. Hefei, China. 2023.

[4] Huijuan Wang, Xiaojun Jiang, Yuanyong Deng et al. Research on methods for site selection for lunar-based UV-Optical-IR astronomical observations // J. Space Science and Experiment. 2024. V. 1(1). P. 33–39. DOI: 10.19963/j.cnki.2097-4302.2024.01.004.

[5] Sachkov M., Shugarov A., Wang H. et al. Wang Toward multiwave-length distributed astronomical observations from the Moon // 16th Moscow Solar System Symp. 16M-S3: Abstr. book. 2025. P. 98–100. DOI: 10.21046/16MS3-2025.

[6] Shugarov A. S., Huijuan Wang, Subo Dong et al. The concept of Lunar-based astrophysical telescope for international lunar research station // Vestnik NPO Lavochkina. 2022. No. 1(55). P. 3–9.

[7] Sachkov M., Shugarov A., Shmagin V., Gómez de Castro A. I. The concept of lunar-based astrophysical telescope for international lunar research station (ILRS) // Proc. SPIE. V. 12181. Space Telescopes and Instrumentation 2022: Ultraviolet to Gamma Ray. 2022. Article 121812V. DOI: 10.1117/12.2629619.

JOINT LUNA DATA CENTRE (JLDC): PROCESSING AND VISUALIZATION OF TOPOGRAPHIC INFORMATION OF THE CELESTIAL BODIES OF THE SOLAR SYSTEM IN PLANETARY DATA GEOPORTAL

A. S. Garov[1], A. E. Zubarev[1], I. E. Nadezhdina[1], N. A. Slodarzh[1,2], N. A. Kozlova[1], I. P. Karachevtseva[1], V. N. Nazarov[2]
[1] *Moscow State University of Geodesy and Cartography (MIIGAiK), MIIGAiK Extraterrestrial Laboratory, Moscow 105064, Russia, mexlab@miigaik.ru*
[2] *Space Research Institute RAS, Moscow, Russia*

KEYWORDS:
Data Centre, Geoportal, Planetary data, Cartography

THE STUDY:
As part of the Russian Federal Space Program, a joint Russian-Chinese Luna Data Centre (JLDC) is being developed. The Russian segment of the JLDC includes several thematic blocks, among them — Cartographic block, which is being created by MIIGAiK. The Cartographic unit is designed to store and organize access to topographic information about the celestial bodies in the Solar System and to provide the following functions:

- Data storage: raw and processed (geo-referenced) planetary data, such as space images and their metadata, as well as navigation information;
- Processing of images of the Moon and planets, including initial geo-referencing based on SPICE navigation data (https://naif.jpl.nasa.gov/naif/), as well as full photogrammetric processing to obtain topographic information (digital elevation models (DEMs) and orthomosaics). For automatic image processing, orthorectification, mosaicking and obtain DEMs, etc. PHOTOMOD (Racurs™) software is used, including the pipeline for processing of image datasets (https://en.racurs.ru/);
- Management and access to spatial planetary data using a web-GIS interface (Geoportal), visualization in 2D with support for map projections and in 3D;
- Support for online morphometric measurements (depth and size of craters, surface slopes, elevation profiles, etc.) using a set of tools for comparative online analysis of topographic data;
- Organization of spatial context at different levels of detail for thematic data from other blocks of the JLDC (archives of Soviet missions to the Moon, Venus, and Mars, cosmic ray research, etc.)

A key function of the Cartographic block of JLDC is providing the basic coordinate-referenced data for celestial bodies, which forms the basis for planetary research for different users. This data complies with international standards and is stored as PDS4 datasets (https://pds.nasa.gov/datastandards/about/). The catalogue structure of the JLDC Cartographic block is organized similar to existing repositories of other space agencies, such as PDS (https://pds.nasa.gov/), PSA (https://psa.esa.int/psa/#/pages/home), and JAXA (https://global.jaxa.jp/), allowing access via standard communication protocols such as http/sftp/sshfs.

An important function of the JLDC Cartographic software is the Geoportal's capabilities for the rapid indexing of metadata from external archives, enabled by standardization based on the PDS4 format and allowing researchers to unify the access to the data from various sources.

ACKNOWLEDGMENTS:
The study was carried out according to the project No. 22257303010410201200570025.

SUMMARY OF 10-YEARS OBSERVATION OF THE RADIATION ENVIRONMENT ONBOARD EXOMARS TGO

J. Semkova[1], R. Koleva[1], K. Krastev[1], Yu. Matviichuk[1], B. Tomov[1], N. Bankov[1], St. Maltchev[1], Ts. Dachev[1], G. Georgiev[1], I. Mitrofanov[2], D. Golovin[2], M. Mokrousov[2], M. Litvak[2], A. Sanin[2], N. Lukyanov[2], V. Benghin[3], V. Shurshakov[3], S. Drobyshev[3]

[1] *Space Research and Technology Institute, Bulgarian Academy of Sciences Sofia, Bulgaria, jsemkova@stil.bas.bg*
[2] *Space Research Institute RAS, Moscow, Russia*
[3] *State Scientific Center of Russian Federation, Institute of Biomedical Problems RAS, Moscow, Russia*

KEYWORDS:
Mars, free space, ExoMars TGO, radiation environment observation, Mars missions, galactic cosmic rays (GCR), solar energetic particles (SEP), solar cycle

INTRODUCTION:
As humans pursue space exploration outside of low Earth orbit, the understanding, monitoring, and forecasting of the radiation environment during the different stages of an exploratory mission becomes increasingly important. Sources of considerable health hazards for manned space missions to Mars are the omnipresent galactic cosmic rays (GCR), sudden solar energetic particle (SEP) events and secondary radiation from the interaction of the primary cosmic rays with the spacecraft structures, Mars atmosphere and surface.

Presented is a summary of 10-years observation of the radiation environment onboard ExoMars TGO by the dosimeter Liulin-MO of FREND instrument [1, 2]. The measurements were taken during the transit to the planet and at Martian orbit.

According the observations at Martian orbit from May 2018 to May 2026, lowest dose equivalent rates for 6-months periods are registered during the start of the decreasing phase, near to the maximum of solar cycle 25 — they are about 1.5–2 times lower that the dose equivalent rates during the other phases of solar cycles 24 and 25. Highest dose equivalent rates are registered around the minimum of solar cycle 24 as a result of the GCR contribution. Particular attention is drawn to the results for the radiation parameters during the most intensive SEP events registered up to the moment during solar cycle 25 — those in October 2021, February 2022, May 2024, and August 2025. These results are compared with the measurements by other missions and instruments located in Mars vicinity during the same periods.

The results show the importance of long-term multi-spacecraft and multi-instrument measurements of the radiation conditions in Mars vicinity. Such measurements will provide the data necessary for the planning of future manned missions to the planet. The data on the observed SEP events add further details regarding the solar activity during solar cycle 25 and is important for subsequent analyses of the solar cosmic rays propagation processes in the heliosphere.

REFERENCES:
[1] Mitrofanov I., Malakhov A., Bakhtin B. et al., 2018. Fine Resolution Epithermal Neutron Detector (FREND) onboard the ExoMars Trace Gas Orbiter // Space Science Reviews. 2018. V. 214. Article 86. https://doi.org/10.1007/s11214-018-0522-5.
[2] Semkova J., Koleva R., Benghin V. et al. Charged particles radiation measurements with Liulin-MO dosimeter of FREND instrument aboard ExoMars Trace Gas Orbiter during the transit and in high elliptic Mars orbit // Icarus. 2018. V. 303. P. 53–66, https://doi.org/10.1016/j.icarus.2017.12.034.

GEANT4-BASED DESIGN OPTIMIZATION AND PERFORMANCE ESTIMATION OF THE SINO-THAI ENERGETIC PHOTON SURVEY (STEPS) COMPACT GAMMA-RAY SPECTROMETER PAYLOAD FOR THE CHINESE SPACE STATION

K. Chaiwongkhot[1], K. Amratisha[1], K. Anuchit[2], Y. Bao[3], S. Chindaratchakul[1], P. Charoenvicha[2], W. Hantrakul[2], X. He[3], P. Jamlongkul[2], P. Kamsing[4], P. Khonsri[2], S. Lu[3], S. Manuthasna[2], P. Muangha[2], T. Panyalert[2], P. Pattarakijwanich[1], Y. Pittayang[2], R. Plumanut[2], K. Pumim[2], K. Puprasit[5], W. Rujopakarn[2], D. Ruffolo[1], W. Mitthumsiri[1], P. Torteeka[2], N. Treesakul[2], J. Xian[3], D. Yang[6], H. Yang[7], B. Zhang[3], N. Zhang[3], H. Zhao[3], J. Zheng[3]

[1] *Mahidol University, Bangkok, Thailand, pha.hikari@gmail.com*
[2] *National Astronomical Research Institute of Thailand* (*Public Organization*), *Chiang Mai, Thailand*
[3] *Changchun Institute of Optics, Fine Mechanics and Physics Chinese Academy of Sciences, Changchun, China*
[4] *Air-Space Control, Optimization, Management Laboratory, Department of Aeronautical Engineering, International Academy of Aviation Industry, King Mongkut's Institute of Technology Ladkrabang, Bangkok, Thailand*
[5] *Chulabhorn Royal Academy, Bangkok, Thailand*
[6] *Jilin University, Changchun, China*
[7] *Institute of Modern Physics, Chinese Academy of Sciences, Lanzhou, China*

KEYWORDS:
gamma-ray spectrometers, solar flares, Geant4 simulation, geometrical acceptance, silicon carbide, sensors, SiC

INTRODUCTION:
The Sino-Thai Energetic Photon Survey (STEPS) is a collaborative space-borne mission designed to deploy a high gamma-ray spectrometer aboard the Chinese Space Station (CSS). Aimed at probing extreme non-thermal emission mechanisms and high-energy particle acceleration dynamics within the heliosphere and extragalactic environments, STEPS features broadband spectral coverage from 50 keV to 100 MeV. This capability effectively mitigates the traditional observational gap between the hard X-ray and high-energy gamma-ray regimes. The payload employs advanced wide-bandgap Silicon Carbide (SiC) semiconductor sensors for high-fidelity hard X-ray spectroscopy, seamlessly integrated with high-Z absorber layers optimized to characterize Compton scattering kinematics and electron-positron pair production events.

In this work, we present the preliminary structural design and the geometrical acceptance estimation of the STEPS payload utilizing comprehensive Monte Carlo simulations within the Geant4 framework. The simulation evaluates the detector's response to primary astrophysical triggers, specifically modeling critical diagnostic spectral signatures of high-energy solar flares — including the 511 keV positron annihilation line, the 2.223 MeV neutron capture line, and the ~67 MeV neutral pion decay continuum—as well as extragalactic gamma-ray bursts (GRBs). We characterize the instrument's effective area, angular dependence, and geometric acceptance across the full multi-decade energy spectrum. Furthermore, we assess the payload's capability to unambiguously isolate solar neutron fluxes from prompt gamma-ray emissions utilizing and characteristic internal neutron capture signatures. These preliminary simulation results validate the instrument architecture, demonstrating that the STEPS configuration meets the rigorous scientific requirements necessary to resolve the precise temporal onset, and structural evolution.

ACKNOWLEDGMENTS:
This presentation is supported by the TSRI Strategic Funding in Scientific and Technology for development of Excellent center In Deep-space exploration Engineering (EXIDE) and Pilot Hub of Talent in Space Scientific Payload Grant No. N35E690062 by National Research Council Thailand.

REFERENCES:

[1] Allison J., Amako K., Apostolakis J. et al. Recent developments in Geant4 // Nuclear Instruments and Methods in Physics Research Section A. 2016. V. 835. P. 186–225. DOI: 10.1016/j.nima.2016.06.125.

MISSION ENVIRONMENT CHARACTERIZATION FOR A GAMMA-RAY DETECTOR PAYLOAD ON THE CHINA SPACE STATION

T. Panyalert[1], P. Torteeka[1], S. Manuthasna[1], X. He[2], K. Chaiwongkhot[3], P. Muangha[1], P. Jamlongkul[1], K. Puprasit[4], K. Anuchit[1], Y. Pittayang[1], P. Khonsri[1], R. Plumanut[1], N. Treesakul[1], W. Hantrakul[1], K. Pumim[1], J. Wannasrn[1], W. Mitthumsiri[3], D. Ruffolo[3], P. Kamsing[5]

[1] *National Astronomical Research Institute of Thailand* (*Public Organization*), *Chiang Mai, Thailand, thanayuth.pa@hotmail.com*
[2] *Changchun Institute of Optics, Fine Mechanics and Physics Chinese Academy of Sciences, Changchun, China*
[3] *Mahidol University, Bangkok, Thailand*
[4] *Chulabhorn Royal Academy, Bangkok, Thailand*
[5] *Air-Space Control, Optimization, Management Laboratory, Department of Aeronautical Engineering, International Academy of Aviation Industry, King Mongkut's Institute of Technology Ladkrabang, Bangkok, Thailand*

KEYWORDS:
gamma-ray detector, china space station, mission environment, observation geometry, radiation environment, South Atlantic Anomaly, orbit propagation, payload operation

INTRODUCTION:

Gamma-ray observations in low Earth orbit are strongly influenced by the orbital environment and operational constraints of the hosting spacecraft. Variations in solar illumination, geomagnetic field intensity, trapped particle radiation, eclipse duration, and spacecraft pointing geometry directly affect detector background, observation efficiency, and instrument operation [1–3]. A comprehensive mission environment assessment is therefore an essential step during the early design phase of space-based gamma-ray payloads. This work presents a mission environment characterization for a conceptual gamma-ray detector payload aboard the China Space Station (CSS) [1]. The objective is to establish a mission analysis framework capable of supporting payload design and operational planning by evaluating the orbital environment, observation geometry, and radiation conditions throughout the mission. The orbital trajectory was propagated from the latest publicly available Two-Line Element (TLE) using the SGP4 propagator [4, 3]. Orbital position, velocity, latitude, longitude, and altitude were subsequently analyzed over an extended mission duration. Observation geometry was evaluated using a nadir-pointing payload configuration to determine the Sun-boresight angle, solar visibility, and field-of-view (FoV) accessibility [2, 3]. Parameter trade-off analyses were further conducted to investigate the influence of payload FoV and allowable gimbal steering on achievable observation opportunities. Mission environmental conditions were characterized through eclipse analysis, geomagnetic field estimation using the International Geomagnetic Reference Field (IGRF) [5], and trapped proton and electron radiation assessment based on the AP9/AE9 radiation models [6]. Regions of weak geomagnetic field associated with the South Atlantic Anomaly (SAA) were identified to estimate science operation constraints arising from elevated charged-particle backgrounds [5, 7].

The analysis provides quantitative metrics including solar visibility, eclipse fraction, SAA occupancy, radiation exposure, and observation availability outside the SAA. The combined results establish a mission-level assessment of operational conditions relevant to gamma-ray observations and identify key environmental factors governing payload performance. The proposed framework offers a practical approach for early-phase mission analysis of gamma-ray instruments operating in low Earth orbit and provides engi-

neering guidance for payload configuration, observation planning, and future scientific mission development aboard the China Space Station.

References:

[1] Wang X., Zhang Q., Wang W. Design and application prospect of China's Tiangong space station // Space: Science and Technology. 2023. V. 3. Article 0035.
[2] Curtis H. D. Orbital mechanics for engineering students. 2019. 692 p.
[3] Vallado D. A. Fundamentals of astrodynamics and applications. 2001. 1007 p.
[4] Hughes S. P. General mission analysis tool (GMAT). No. GSFC-E-DAA-TN29897. 2016.
[5] Alken P., Thébault E., Beggan C. D., Amit H., Aubert J., Baerenzung J., Zhou B. et al. International geomagnetic reference field: The thirteenth generation // Earth, Planets and Space. 2021. V. 73(1). Article 49.
[6] Kruglanski M., Messios N., De Donder E., Gamby E., Calders S., Hetey L., Evans H. Space environment information system (SPENVIS) // EGU General Assembly Conference Abstracts. 2009. Article 7457.
[7] Finlay C. C., Kloss C., Gillet N. Core field changes from eleven years of Swarm satellite observations // Physics of the Earth and Planetary Interiors. 2025. Article 107447.

THE VENERA-D MISSION TO VENUS

L. M. Zelenyi[1], O. I. Korablev[1], D. A. Gorinov[1], L. V. Zasova[1], M. V. Gerasimov[1], N. I. Ignatiev[1], D. S. Rodionov[1], D. V. Strelnikov[1], M. A. Ivanov[2], N. A. Eismont[1], A. Y. Trokhimovsky[1]

[1] *Space Research Institute RAS, Moscow 117997, Russia*
dmitry_gorinov@cosmos.ru

[2] *Vernadsky Institute of Geochemistry and Analytical Chemistry Moscow, Ruaaia*

KEYWORDS:
Venus, mission, spacecraft, orbiter, lander, balloon

INTRODUCTION:

Venera-D is a National Space Project mission to study atmosphere and surface of Venus to resolve the fundamental difference between climate histories of Venus and Earth. The Venera-D mission architecture combines the orbiter, the lander and two airborne balloons to use a complex approach to obtain scientific information about Venus [1].

The Orbiter on the polar orbit is focused on studying thermal structure, dynamics and the composition of the atmosphere (both above and below clouds).

The Lander contains the scientific payload to study the elemental and mineralogical composition of the surface and near subsurface materials, as well as the structure and chemical composition of the atmosphere down to the surface, including the abundances and isotopic ratios of the trace and noble gases, direct chemical analysis of cloud aerosols.

The mission will also include aerial platforms — paired balloons to operate for up to one month at the 53–57 km altitudes. Such modules can provide unique in situ information on the meteorological parameters, composition of the atmosphere, cloud structure, composition and microphysics, nature and distribution of the UV absorber.

The results of the Venera-D project, planned for launch in 2030s, can be complemented by other future Venus missions (Venus Orbiter Mission, VERITAS, DAVINCI and EnVision [2]). A coordination of efforts between missions and their scientific instruments will be crucial to answer the most important fundamental questions about Venus.

REFERENCES:

[1] Gorinov D. A., Zasova L. V., Zelenyi L. M. et al. Venera-D: Scientific goals and the mission architecture // Moscow University Physics Bull. 2025. V. 80. P. S445–S448.

[2] Widemann T., Smrekar S. E., Garvin J. B., Straume-Lindner A. G. et al. Venus Evolution Through Time: Key Science Questions, Selected Mission Concepts and Future Investigations // Space Science Reviews. 2023. V. 219. No. 56.

FEASIBILITY OF USING THE MULTI-ELECTRODE HARMONIZED KINGDON TRAP AS A MASS SPECTROMETER FOR PLANETARY RESEARCH

E. Nikolaev, O. Kharybin, G. Vladimirov, S. Gorbatov, A. Semenov, P. Borisovets, A. Lioznov, Z. Frenkel
Skolkovo Institute of Science and Technology, Moscow, Russia
ennikolaev@gmail.com

KEYWORDS:
mass spectrometer, multi-electrode harmonized Kingdon trap, planetary atmosphere analyses, soil analyses, scientific instrumentation

Introduction:

We have proposed a new type of mass spectrometer for the analysis of gaseous substances, and solid and thermos-desorbed substances. The mass analyzer in this mass spectrometer uses a multi-electrode harmonized Kingdon trap [1–4].

RESULTS:
This trap allows for the ionization of gases to be carried out directly inside the trap, followed by the capture of the resulting ions and their mass analysis, something that is not possible with the most common Kingdon trap with a single internal electrode, known as an orbitrap. Solid substances could be ionized be laser desorption ionization. Ionization inside the trap increases the sensitivity of the device, as it eliminates the need for an ion transport system from the ion source to the analyzer, and allows for a significant simplification of the mass spectrometer, providing opportunities for its miniaturization. Mass spectra are measured in this trap by exciting ions along the trap's internal electrodes with a radiofrequency field and measuring the ion-induced signals in the external electrodes. The analyzer has demonstrated ultra-high resolution (>200,000 at the 28-nominal mass triplet and other multiplets). With the appropriate vacuum system power consumption can be reduced to less than 50 W, and weight to less than 10 kg. Applications of various ionization methods will be discussed. Among them laser desorption ionization, MALDI, field desorption (FD) and field ionization (FI) mass spectrometry. Comparison with mass spectrometers currently used for space research will be provided.

REFERENCES:
[1] Nikolaev E., Sudakov M., Vladimirov G., Velásquez-García L.F., Borisovets P., Fursova A. Multi-electrode Harmonized Kingdon Traps // J. The American Society for Mass Spectrometry. 2018. V. 29. No. 11. P. 2173–2181. https://doi.org/10.1007/s13361-018-2032-9.
[2] Nikolaev E.N., Kharybin O.N., Vladimirov G.N., Gorbatov S.V., Semenov A.S., Lioznov A.V., Borisovets P.Yu. Four-Electrode Kingdon Trap With Equispaced Electrodes: Russian patent. 2023. No. RU 2 806 730 C.
[3] Nikolaev E.N., Kharybin O.N., Vladimirov G.N., Gorbatov S.V., Semenov A.S. Mass Spectrometer With Electron Impact Ionization Based on a Multi-Electrode Harmonized Kingdon Trap: Russian patent. 2023. RU 2 797 722 C1.
[4] Nikolaev E.N., Kharybin O.N., Vladimirov G.N. Multi-Electrode Harmonized Kingdon Trap With Multi-Port Input of Electrons and Ions: Russian patent. 2018. RU 2 818 310 C.

NEPHELOMETERS FOR VENUS: A REVIEW IN THE CONTEXT OF THE UPCOMING VENERA-D MISSION

M. Luginin, I. Kuznetsov[1], A. Lyash[1], G. Dolnikov
Space Research Institute RAS, Moscow, Russia, mikhail.luginin@cosmos.ru

KEYWORDS:
Venus, atmosphere, Venera-D, aerosols, clouds

INTRODUCTION:
Venera-D is a future Russian mission dedicated to the comprehensive exploration of Venus's atmosphere and surface. Currently in its draft design phase, with a planned launch in 2036, the mission comprises an orbiter, a lander, and two baloons, a small one and a big one. Among the scientific payload, both the lander and the smaller baloon are proposed to carry nephelometer instruments designed to investigate Venusian aerosols.

Aerosols play a key role in the climate of Venus. Clouds extend from ~50 to 70 km and completly enshroude the surface of the planet. By absorbing and scattering incoming solar radiation, these particles affect the planet's thermal balance [1] and significantly impact global atmospheric circulation [2]. Furthermore, aerosol particles actively participate in the SO_2 and H_2O cycles—key elements of chemical reactions in the Venusian atmosphere [3]. Although our understanding of the Venus cloud system has advanced considerably over recent decades, a number of fundamental questions remain unresolved.

In this work, we will give a brief review of previous investigations, with particular focus on in-situ aerosol measurements. We then outline open scientific problems and describe the current design of the nephelometer payload proposed for the Venera-D mission.

REFERENCES:
[1] Limaye S.S., Grassi D., Mahieux A., Migliorini A., Tellmann S., Titov D. Venus Atmospheric Thermal Structure and Radiative Balance. 2018. https://doi.org/10.1007/s11214-018-0525-2.
[2] Sánchez-Lavega A., Lebonnois S., Imamura T., Read P., Luz D. The Atmospheric Dynamics of Venus. 2017. https://doi.org/10.1007/s11214-017-0389-x.
[3] Marcq E., Mills F.P., Parkinson C.D., Carine A. Composition and Chemistry of the Neutral Atmosphere of Venus. 2018. https://doi.org/10.1007/s11214-017-0438-5,

INFRARED STUDIES OF THE VENUSIAN ATMOSPHERE USING THE VIKA AND VIRAL INSTRUMENTS

A. Trokhimovskiy, O. I. Korablev, A. S. Patrakeev, D. A. Belyaev, A. A. Fedorova
Space Research Institute RAS, Moscow, Russia, trokh@cosmos.ru

KEYWORDS:
Venus atmosphere, minor species, solar occultation, infrared spectroscopy

INTRODUCTION:

Infrared spectroscopy is one of the most effective methods for studying the composition, structure, and dynamics of the Venusian atmosphere – from the lower atmosphere and cloud layer to the mesosphere and thermosphere. This work presents two complementary infrared instruments being developed at the Space Research Institute of the Russian Academy of Sciences (IKI RAS) for future orbital studies of Venus: the Venus Infrared Kit for Atmospheric studies (VIKA), proposed for the Russian mission Venera-D (planned launch year after 2033), and the Venus InfraRed Atmospheric Linker (VIRAL) for the Indian mission Venus Orbiter Mission (planned launch year 2028).

The VIRAL experiment is designed to operate exclusively in solar occultation mode, covering the 2.2-4.2 μm range with high spectral resolution. The VIKA instrument will comprise two spectral channels: VIKA-SW, operating in the 1.0–1.6 μm range, and VIKA-LW, designed for measurements in the 2.3–4.3 μm range. VIKA-SW will enable nadir observations of both the day and night sides, with particular emphasis on studying the D/H isotopic ratio as an indicator of possible volcanic activity. VIKA-SW will also operate in solar occultation mode, enabling the study of water vapor and its isotopologues, CO, and other constituents in the lower and middle atmosphere, as well as the structure and variability of the cloud layer. VIKA-LW, like VIRAL, will operate only in solar occultation mode.

The concept of atmospheric sounding in solar occultation mode builds upon the scientific approach of the SOIR experiment aboard Venus Express, while the hardware implementation draws largely on the technological heritage of the infrared channels ACS-MIR and NIR from the ExoMars TGO mission. The high spectral resolution and sensitivity of VIKA and VIRAL will enable precise measurements of the composition and temperature of the above-cloud atmosphere at altitudes ranging from the upper cloud boundary to the mesosphere and lower thermosphere. The spectral range includes absorption bands of CO_2, H_2O and HDO, CO, SO_2, OCS, HCl, HF, PH_3, and other minor atmospheric constituents.

The preparation of these instruments and the conduct of space-based experiments continues a long-standing line of infrared studies of Venus initiated by the VIRTIS, SPICAV, and SOIR experiments, opening new opportunities for comprehensive investigations of the present-day Venusian atmosphere and its evolution.

MICROCOMB-BASED MID-INFRARED DUAL-COMB SPECTROSCOPY WITH GHZ RESOLUTION

Zhiquan Yuan
Tsinghua University, Beijing, China, yuanzq@tsinghua.edu.cn

KEYWORDS:
microcavity, microcomb, dual-comb spectroscopy, difference-frequency generation, mid-infrared, integrated photonics

INTRODUCTION:
Microcomb based dual-comb spectroscopy of methane in the mid-infrared is demonstrated with GHz resolution. This fine resolution is enabled by generating spectrally densified mid-infrared combs via interleaved difference-frequency-generation. Methane and ethane spectra are measured over intervals as short as 0.5 ms, and tuning of spectral resolution on demand is demonstrated.

POSTER SESSION

DETECTION LIMITS OF TRACE GAS CONSTITUENTS IN VENUS MESOSPHERE MODELED FOR A SOLAR OCCULTATION EXPERIMENT IN THE INFRARED

A. D. Sviachko[1,2], D. A. Belyaev[2], A. Trokhimovskiy[2], A. A. Fedorova[2], A. S. Patrakeev[2], O. I. Korablev[2]
[1] *National Research University "Higher School of Economics", Moscow, Russia, adsvechko@edu.hse.ru*
[2] *Space Research Institute RAS, Moscow, Russia*

KEYWORDS:
Venus mesosphere, atmospheric absorption, solar occultation, IR spectroscopy, sulfur dioxide, hydrogen sulfide, phosphine, detection limits

INTRODUCTION:

The mesosphere of Venus hosts a complex photochemical system where trace gas constituents play a critical role in shaping the chemical structure of the sulfur-bearing cloud layer. Understanding the abundance and distribution of those minor species is essential for constraining photochemical models, characterizing atmospheric dynamics, and identifying potential signatures of active geological processes.

Among the most diagnostically valuable trace gases are sulfur compounds, particularly sulfur dioxide (SO_2) and hydrogen sulfide (H_2S). The abundance of SO_2 above the clouds is governed by photochemistry, transport, and vertical mixing, and its variations are considered as a possible indicator of volcanic activity [1, 2]. H_2S serves as a tracer of non-equilibrium chemical processes and may also be linked to deep atmospheric sources.

Vertical profiles of SO_2 in the Venus overcloud atmosphere were first obtained by the SPICAV and SOIR solar occultation experiments onboard the Venus Express orbiter in 2006–2014 [1, 3]. SPICAV-SOIR revealed two layers of enhanced SO_2 at 65–80 km and 85–105 km with mixing ratios of 100–300 ppb [3]. Significant uncertainties up to 50–70% in the SOIR data at the planet's cloud top of 65-75 km, made the interpretation for gaseous variability complicate [2, 3]. For H_2S, reliable observational constraints remain scarce.

In recent years, phosphine (PH_3) has emerged as a molecule of considerable interest due to its potential role in unexpected bio-chemical pathways in the Venusian atmosphere. This interest was sparked by reports of its possible detection in the cloud decks using ground-based JCMT/ALMA observations [4]. However, subsequent independent analyses yielded conflicting results, with inferred mixing ratios ranging from 1–20 ppb to complete non-detection [5, 6]. The question of phosphine's detectability remains open and requires more sensitive observations.

The planned VIRAL experiment (Venus InfraRed Atmospheric gases Linker) for the Indian Venus Orbiter Mission, based on solar occultation with a high-resolution echelle spectrometer, is expected to provide significantly improved sensitivity to minor atmospheric constituents [7]. This work presents an assessment of the detection limits for SO_2, H_2S, and PH_3 in the Venus mesosphere under the conditions of the VIRAL experiment. The input parameters include the spectral resolution and noise characteristics of the spectrometer, as well as the vertical profiles of temperature, CO_2 concentration, and pressure in the planetary mesosphere. Based on these data, and accounting for the line broadening parameters of molecular absorption in the CO_2 atmosphere, atmospheric transmission spectra are modeled, and the inverse problem of estimating the detection limits is solved.

METHOD:

The VIRAL experiment is based on the solar occultation method. The atmospheric transmittance $T(\nu, z)$ at wavenumber ν and tangent height z is determined as:

$$T(\nu,z) = F(\nu,z)/F_0(\nu) = \exp\left[-\tau_{mol}(\nu,z) - \tau_{aerosol}\right],$$

where $F(\nu,z)$ is the spectrum at tangent height z, $F_0(\nu)$ is the solar spectrum above the atmosphere, τ_{mol} is the molecular optical depth, and $\tau_{aerosol}$ is the aerosol optical depth. The optical depth is determined by integrating the extinction coefficient along the line of sight:

$$\tau_{mol}(\nu,z) = \int \chi(\nu,l)\,\mathrm{d}l,$$

The extinction coefficient, in turn, is the sum of contributions from individual gas components:

$$\chi(\nu,z) = \sum_x \sigma_x(\nu,T,p) n_x(z),$$

where $\sigma_x(\nu,T,p)$ is the absorption cross-section of species x, and $n_x(z)$ is its number density.

For calculations in a spherically symmetric atmosphere, it was divided into concentric homogeneous layers. The optical depth is computed using the Abel matrix, and the system of linear equations is solved sequentially from the upper layers downward (the "onion peeling" method) [8]. Absorption was calculated line-by-line using the HITRAN2024 database [9]. The absorption cross-section was computed as the sum of contributions from individual lines with the Voigt profile, accounting for Doppler and collision broadening:

$$\sigma_x(\nu,T,p) = \textstyle\sum_k S_k(T) f_k(\nu - \nu_{0k}, T, p),$$

where $S_k(T)$ is the line intensity, f_k is the Voigt line profile, and ν_{0k} is the line center frequency. Line broadening was calculated for a CO_2 medium. Vertical profiles of temperature and pressure were taken from the VIRA (Venus International Reference Atmosphere) model [10]. Aerosol extinction was included using averaged SOIR data [3]. The ACE-FTS solar atlas [11] was used as the reference solar spectrum and was multiplied by the calculated transmission spectrum when modeling the radiation transmitted through the atmosphere.

The instrument parameters used in the simulations are following: spectral range 2.3–4.3 μm, resolving power ~23,000, 640-pixel detector array with 0.05 cm^{-1} spectral width per pixel and with signal recording of 16-bit ADC [7]. Synthetic spectra were convolved with a Gaussian instrumental function ($\Delta\nu$=0.1 cm^{-1}). Noise was estimated for signal levels of $1{\cdot}10^6$, $5{\cdot}10^6$, and $1{\cdot}10^7$ ADU, assuming Poisson statistics. These signal levels are expected given the ADC bit depth and accumulation of multiple frames with ~1 ms exposure.

The detection limit for the gases was determined by comparing synthetic transmittance spectra of a pure CO_2 atmosphere and spectra of a CO_2 mixture with the gas under study. As a quantitative criterion, a reduced chi-squared function was used, computed over selected spectral windows:

$$\chi^2_{red} = \frac{1}{N_{pix}} \sum_{j=1}^{N_{pix}} \left[T_{CO_2}(\nu_j) - T_{mixture}(\nu_j)\right]^2 \Big/ \sigma_j^2,$$

where N_{pix} is the total number of spectral points, T_{CO_2} and $T_{mixture}$ are the transmission spectra, and σ_j is the measurement error in the j-th channel from Poisson statistics. A statistically significant difference was defined as $\chi^2 \geq 1.0$. The minimum gas concentration that met this criterion was taken as the detection limit.

RESULTS:

Synthetic solar occultation spectra were calculated for SO_2, H_2S, and PH_3, accounting for the VIRAL instrument parameters. For each molecule, spectral intervals with relatively weak CO_2 absorption and maximum contrast of the target lines were selected, ensuring the best visibility of the molecular features on a background of abundant carbon dioxide's spectral lines.

Using the detection criterion, vertical profiles of minimum detectable concentrations were constructed for three signal accumulation levels (Fig. 1). The lowest detection limits are achieved near the upper cloud boundary (68–72 km), where target gas concentrations are still relatively high and aerosol extinction is not yet prohibitive.

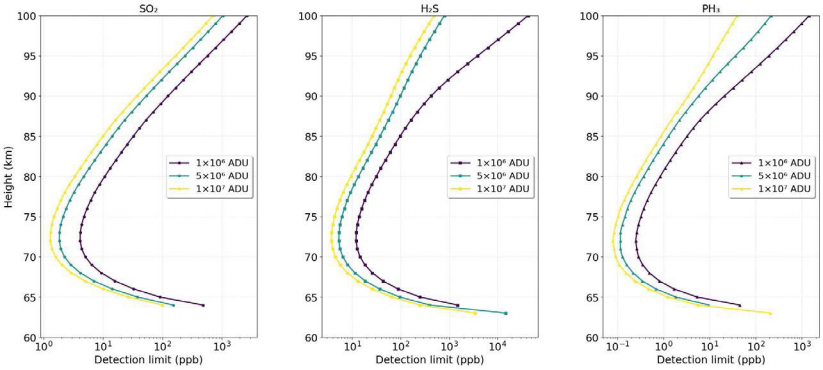


Fig. 1. Vertical profiles of detection limits (in parts per billion (ppb)) for SO_2, H_2S, and PH_3 above Venus's clouds at different accumulated signal levels ($1{\cdot}10^6$, $5{\cdot}10^6$, and $1{\cdot}10^7$ ADU).

For an expected signal level of $1{\cdot}10^6$ ADU, the minimum detectable mixing ratios at 72 km are 4.11 ppb for SO_2, 12.01 ppb for H_2S, and 0.25 ppb for PH_3. As the signal level increases to $5{\cdot}10^6$ ADU, these limits improve to 1.83, 5.30, and 0.12 ppb, respectively. At the highest simulated level of $1{\cdot}10^7$ ADU, the detection limits reach 1.30 ppb for SO_2, 3.74 ppb for H_2S, and 0.08 ppb for PH_3. The higher limits for H_2S compared to SO_2 and PH_3 are due to its lower line intensities and stronger overlap with CO_2 lines in the selected spectral ranges.

For comparison, expected SO_2 concentrations in this altitude range are 50–500 ppb, while upper limits for H_2S are below 23 ppb, and for PH_3 the expected upper limits are below 1 ppb. The derived detection limits for these gases under study are thus well below expected values.

CONCLUSION:

We have modeled solar occultation spectra for the planned VIRAL experiment and assessed detection limits for SO_2, H_2S, and PH_3 in the Venus mesosphere. The calculations used a line-by-line approach with the HITRAN 2024 database, incorporating Venus atmospheric conditions and instrument characteristics, including the spectral range, resolving power, and expected signal levels.

The results indicate that VIRAL should be capable for detecting SO_2 at its expected abundance levels. For H_2S, the derived detection limit is below currently expected upper constraints, suggesting that the experiment may provide useful observational data. For PH_3, the predicted detection limit suggests that the instrument's capabilities may be sufficient to contribute meaningful constraints on its presence, potentially helping to clarify the current uncertainties. These findings provide a basis for optimizing observation parameters and for future interpretation of VIRAL measurements.

REFERENCES:

[1] Belyaev D., Korablev O., Fedorova A. et al. First observations of SO2 above Venus' clouds by means of Solar Occultation in the Infrared // J. Geophysical Research. 2008. V. 113. Article E00B25. DOI: 10.1029/2008JE003143.

[2] Mahieux A., Vandaele A.C., Bougher S.W. et al. Update of the Venus density and temperature profiles at the terminator measured by SOIR on board Venus Express // Icarus. 2015. V. 261. P. 157–168. DOI: 10.1016/j.pss.2015.02.002.
[3] Belyaev D., Montmessin F., Bertaux J.-L. et al. Vertical profiling of SO_2 and SO above Venus' clouds by SPICAV/SOIR solar occultations // Icarus. 2012. V. 217. No. 2. P. 740–751. DOI: 10.1016/j.icarus.2011.09.025.
[4] Greaves J.S., Richards A.M.S., Bains W. et al. Phosphine gas in the cloud decks of Venus // Nature Astronomy. 2021. V. 5. P. 655–664. DOI: 10.1038/s41550-020-1174-4.
[5] Villanueva G.L., Cordiner M., Irwin P.G.J. et al. No evidence of phosphine in the atmosphere of Venus from independent analyses // Nature Astronomy. 2021. V. 5. P. 631–635. DOI: 10.1038/s41550-021-01422-z.
[6] Trompet L., Robert S., Mahieux A. et al. Phosphine in Venus' atmosphere: Detection attempts and upper limits above the cloud top assessed from the SOIR/VEx spectra // Astronomy and Astrophysics. 2021. V. 645. Article L4. DOI: 10.1051/0004-6361/202039932.
[7] Patrakeev A., Trokhimovskiy A., Korablev O. et al. The Venus infrared atmospheric gases linker instrument concept for solar occultation studies of Venus atmosphere composition and structure onboard the Venus Orbiter Mission of the Indian Space Research Organization // Proc. SPIE. V. 12138. Optics, Photonics and Digital Technologies for Imaging Applications VII. 2022. Article 1213810. DOI: 10.1117/12.2632371.
[8] Krasnopolsky V.A. Photochemistry of the Atmospheres of Mars and Venus. Berlin: Springer-Verlag, 1986. 334 p. ISBN: 0387153365.
[9] Mahieux A., Vandaele A.C., Robert S. et al. Densities and temperatures in the Venus mesosphere and lower thermosphere retrieved from SOIR on board Venus Express: Carbon dioxide measurements at the Venus terminator // J. Geophysical Research: Planets. 2010. V. 115. Article E12014. DOI: 10.1029/2010JE003589.
[10] Gordon I.E., Rothman L.S., Hargreaves R.J. et al. The HITRAN2024 molecular spectroscopic database // J. Quantitative Spectroscopy and Radiative Transfer. 2026. V. 277. Article 107949. DOI: 10.1016/j.jqsrt.2026.109807.
[11] Zasova L.V., Moroz V.I., Linkin V.M. et al. Structure of the Venus atmosphere // Planetary and Space Science. 2006. V. 54. No. 13–14. P. 1352–1359. DOI: 10.1016/0273-1177(95)00254-C.
[12] Hase F., Wallace L., McLeod S.D. et al. The ACE-FTS atlas of the infrared solar spectrum // J. Quantitative Spectroscopy and Radiative Transfer. 2010. V. 111. No. 4. P. 521–528. DOI: 10.1016/j.jqsrt.2009.10.020.

HYDROGEN DENSITY FIELD AT THE ALTITUDE OF THE METEOR NO. 2-4 SPACECRAFT IN JANUARY 2025

A. V. Tertyshnikov
Regional Budgetary Institution "Novgorod Regional Veterinary Laboratory", Novgorod, Russia
atert@mail.ru atert@mail.ru
Institute of Applied Geophysics, Moscow

KEYWORDS:
upper atmosphere, ion, hydrogen, measurements, mass spectrometer, maps, density, climate, morphology, field

ABSTRACT:
The complex morphology of the geocorona (Earth's hydrogen layer) glow in extreme ultraviolet light under the influence of solar storms, since December 2025 is recorded in images from the L1 point of the Carruthers Geocorona Observatory (launched September 24, 2025, NASA). The hydrogen concentration at the lower boundary of the geocorona at the base of the exosphere (exobase) is recorded by the Meteor No. 2-4 spacecraft in sun-synchronous orbit at an altitude of approximately 832 km. At this altitude, the hydrogen density corresponds to the H^+ ion density. The measurements utilize radio frequency selection [1] based on the technical solution [2, 3].

To analyze the instrumental measurements, daily average H^+ and He^+ ion concentration fields were reconstructed. To interpolate the data into nodes of a regular geographic grid, a spherical function series expansion of all daily density measurements for each ion and the LSQR (Least Squares, QR) algorithm were used. It is similar to the conjugate gradient method for solving sparse systems of linear equations.

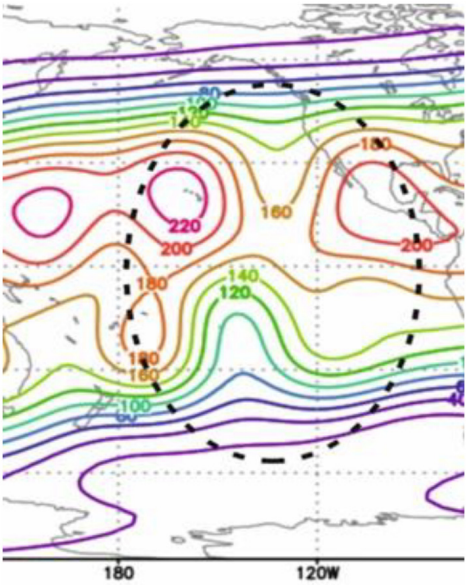


Fig. 1. Average concentration of H^+ ions in units of conventional current for the second half of January 2025. The saddle is highlighted with an oval

Reconstructed H^+ ion concentration maps reveal structures of varying scales, from planetary to regional. The inhomogeneous structure of Earth's hydrogen ring above the magnetic equator confirms the nonspherical glow in geocorona images. The saddle-shaped structure over the Pacific Ocean is

a planetary feature of the H+ ion concentration distribution (Fig. 1). The formation of the saddle region is associated with the "fountain effect" during changes in the Earth's magnetic field under the Pacific Ocean, discovered in [4].

A statistical model of the concentration of the diagnosed ions also revealed anomalous features in the morphological variations of the reconstructed fields. These features are believed to be responsible for the active influence of space weather on the state of the geospheres.

ACKNOWLEDGMENTS:
The author thanks PhD in Agricultural Sciences Sergei Gennadievich Gubin and Tatyana Mikhailovna Aksyutenko for helpful discussions and assistance with this work.

REFERENCES:

[1] *Tertyshnikov A. V.* The Beginning of the 25th Cycle of Solar Activity in Variations of the Oxygen Ion Density in the Orbit of the Meteor Spacecraft // Cosmic Research. 2025. V. 63. P. 276–283. http://doi.org/10.1134/S0010952525601380.
[2] *Tertyshnikov A. V.* Space mass spectrometer. Patent No. 2726186 for application No. 2019121111/20(041262) in the FIPS register dated July 5, 2019.
[3] *Tertyshnikov A. V.* Method for determining the onset of the solar activity cycle. Patent. Application: 2023135791, Dec. 27, 2023. Bulletin No. 21.
[4] *Madsen F. D., Howard I., Brown W. J. Whaler K. A.* Principal component analysis of the 2010 reversal of core-surface flow beneath the Pacific Ocean // J. Studies of Earth's Deep Interior. 2026. V. 2. http://doi:10.46298/jsedi.17268.

SPECTRAL OBSERVATIONS OF TITAN AND SATURN IN 2024

V. D. Vdovichenko[1], S. K. Salamakhin[1], A. M. Karimov[1], S. M. Rakhmatulla[2]
[1] *V. G. Fesenkov Astrophisical Institute, Almaty, Kazakhstan*
sergey_ks2002@mail.ru
[2] *Woosong University Kazakhstan*

KEYWORDS:
Titan, Saturn, troposphere, methane, absorption, aerosol

INTRODUCTION:

Titan is the largest moon of Saturn with a dense nitrogen-methane atmosphere (~1.5 bar at the surface). Methane plays a key role in the energy balance and chemical evolution of the atmosphere, participating in the evaporation-condensation-precipitation cycle and forming stable surface reservoirs of hydrocarbons.

Photochemical processes in the upper atmosphere lead to the formation of complex hydrocarbons and an aerosol layer from a mixture of various organic copolymers (tolins) formed in the atmosphere from simple organic compounds such as methane and ethane under the influence of ultraviolet radiation from the Sun, which determines the spectral properties of reflected solar radiation.

Spectrophotometry in the visible and near-infrared ranges (600–950 nm) allows for the probing of different levels of the Titanian atmosphere through methane absorption bands of varying intensity.

Weak bands are formed in deeper layers, while strong bands probe the upper layers of the atmosphere.

The following diagnostic absorption bands are used for observations (Table 1):

Table 1. Methane absorption bands studied and their formation levels according to [1]

λ (nm)	The nature of the strip	Pressure (bar)
619	weak	~1–1,5
727	strong	~0,5–1
790	moderate	~0,2–0,6
861	strong	~0,5–1
889	very strong	~0,05–0,2

OBSERVATION CONDITIONS, PROCESSING METHODS, AND RESULTS:

Spectral observations of Titan and Saturn in parallel were performed on 12/06/2024 and 12/11/2024 at the observatory of the V. G. Fesenkov Astrophysical Institute (Almaty, 1450 m above sea level) using an SGS diffraction spectrograph with an ST-7XE CCD camera mounted in the focus of the 0.6-meter Cassegrain RC-600 telescope.

The CCD matrix has The size is 765×510 pixels. The spectrograph's dispersion is 0.43 nm/pixel. The spatial scale is 4.18 pixels per arcsecond.

17 spectra of Titan were obtained with an exposure of 300 seconds, and 13 spectra of Saturn were obtained with an exposure of 120 seconds, with the spectrograph's slit oriented along the equator. This orientation of the spectrograph's slit allowed for the simultaneous acquisition of:

- spectra of the planet's equator, free from the influence of the ring,
- spectra of the "ears" of Saturn's rings, which were used as a solar reference.

The best-quality spectra were used for processing. In total, 8 spectra of Titan and 5 spectra of the center of Saturn's disk and the "ears" of its rings were

processed. Additionally, the night sky background was recorded for each object spectrum. Subtracting the background from the spectra of Titan and Saturn eliminated the influence of scattered night sky light around the object and in the spectrometer, as well as the dark current of the ST7 CCD array. This procedure was particularly necessary for reliably recording the intensity in the region of the strong 889 nm absorption band, which is located near the sensitivity limit of the ST7 CCD array.

The selected exposures provided for the center of the Saturn disk the accumulation of 50000–55000 pulses in the continuous spectrum and 2000–2500 at the center of the deepest methane absorption band 886 nm. With a background noise track, outside the main spectrum of 50–60 pulses along the entire spectrogram, this provided a signal-to-noise ratio of 1000 in the continuous spectrum 600 nm and 40 in the methane absorption band 886 nm. For Titan, the signal-to-noise ratio was 200 in the continuous spectrum at 600 nm and 10 in the deep absorption band at 889 nm.

After subtracting the background, the spectra were normalized to the maximum and averaged.

Then, the spectra of Titan and Saturn were divided by the ring spectrum. This ratio served the following purposes. It compensated for Fraunhofer lines and telluric absorption bands. Moreover, the ratio to the ring spectrum gave an additional advantage in that the spectra of Titan and Saturn were taken at an equatorial distance, which completely compensated for the telluric bands without additional adjustment.

In addition, this ratio compensated for the strong decrease in solar radiation intensity in the long-wavelength part of the spectrum and the spectral sensitivity of the CCD array.

Figure 1 shows a comparison of the Titan spectrum in the 600–950 nm range from our measurements (1) and from Karkoschka (1994) (2), which demonstrates a good match.

The "clean" spectra of the center of the Saturn and Titan disks, which show the features of the methane absorption band profiles, are presented in Fig. 2.

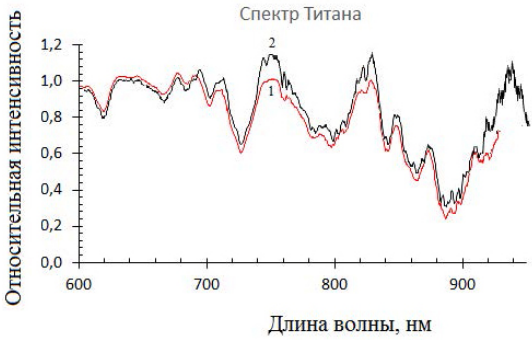


Fig. 1. Titan spectrum in the 600–950 nm region. 1 — observations of the authors, 2 — according to Karkoschka [2]

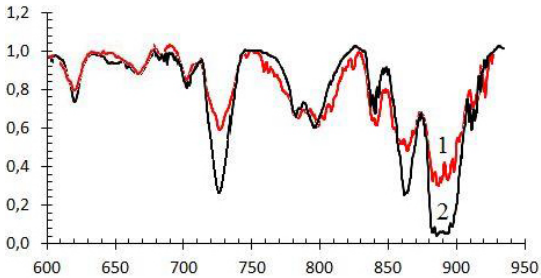


Fig. 2. Spectra of Titan (1) and the center of Saturn's disk (2)

In search of features in the spectrum of Titan, we decided to compare it with the spectrum of the center of the Saturn disk.

Table 2 shows the depths of Ru in the centers of the methane absorption bands on Titan and the center of the Saturn disk.

Table 2. Central depths of the CH4 absorption bands on Titan and for the center of the Saturn disk

λ (nm)	Titan Ru	±%	Saturn Ru	±%
619	0,18	2,5	0,25	1,5
727	0,42	4,0	0,73	2
790	0,35	5,0	0,30–0,40	3
861	0,50	6,0	0,74	3
889	0,70	7,0	0,95	3–5

We would like to draw your attention to the following three points:

1. The weak methane band at 619 nm and the moderate band at 790 nm, which are formed in the deep layers of the atmosphere (~0.5–3 bar), are similar in intensity to those on Saturn, while the stronger CH4 bands at 727 nm, 861 nm, and 889 nm, which are formed in the upper troposphere (<0.5 bar), are significantly weaker.
2. The continuous spectrum reflectivity curves of Titan and the center of Saturn's disk differ significantly.

This can be clearly seen in Figure 3, where the spectra of Titan are compared to the spectrum of Saturn.

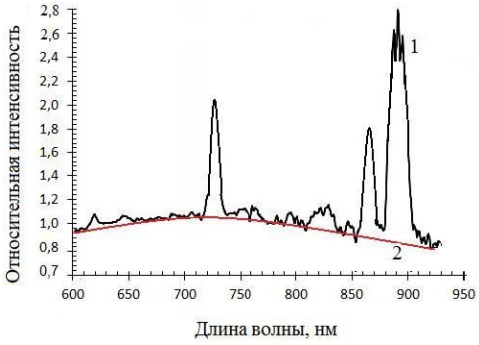


Fig. 3. Ratio of the initial spectra of Titan to the spectrum of the center of the Saturn disk. 1 — ratio of the methane absorption band profiles of Titan to Saturn, 2 — ratio by the level of the continuous spectrum

Such features in the 600–1000 nm continuous spectrum region indicate that the scattering aerosol differs not only in size, but also in chemical composition and volume scattering coefficient. However, quantitative estimates could be made using absolute measurements based on standard stars and subsequent comparison with model calculations. Unfortunately, our spectrometer design does not allow for this.

3. The methane 727 nm band profiles differ between Titan and Saturn, indicating differences in the vertical distribution of methane and the structure of the aerosol.
    - The profiles are similar in the wings of the band, which are formed in deeper layers.
    - In the central part of the absorption band, Titan exhibits a "kink" in the profile, which appears to indicate a sharp boundary between the cloud layer and the upper, thin atmosphere where methane is frozen out (Fig. 4).

However, it cannot be excluded that the fact that for Titan the spectrum was taken integrally for the whole disk without taking into account the change in the intensity of the absorption bands to the edge.

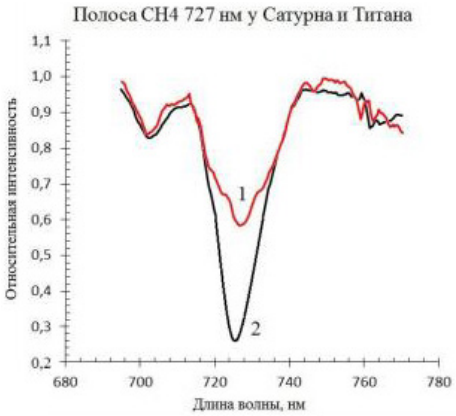


Fig. 4. Comparison of the CH4 727 nm absorption band profiles of Titan (1) and Saturn (2)

We have carried out a comparative analysis of the observation results with the dynamic models of the Titan atmosphere obtained earlier by us [3–5], taking into account vertical transport, turbulent diffusion and microphysics of the aerosol.

In total, ten models of cloudiness were calculated in the process of its development with time.

The parameters of all models are listed in Table 3.

Table 3. Values of the variable model parameters

No. option	***k*, cm^2/c**	***w*, cm/c**	**X_{CH4}**
1	10^6	5	0.01
2	10^6	10	0.028
3	10^7	10	0.01
4	10^7	5	0.028
5	10^6	5	0.046
6	10^6	10	0.064
7	10^7	10	0.046
8	10^6	5	0.082
9	10^6	10	0.10
10	10^7	5	0.10

where: *w* — vertical ascent velocity cm/s; *k* — coefficient of turbulent diffusion cm^2·s^{-1}; CH_4 — methane content

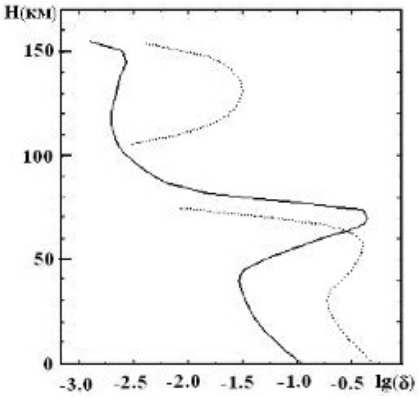


Fig. 5. Vertical distribution of the methane condensate content for model 2 — solid line and for model 10 — dotted line. See the text for model parameters

All calculated scenarios show quite complex profiles of Titan's cloud struc As a typical example, Fig. 5 shows the result of calculating the δ profile, which is the specific content of the condensed part of methane (methane content) with altitude, for values of the vertical ascent rate w=10 cm/s, the turbulent diffusion coefficient k=10^6 cm^2/s, and the methane content X_{CH4}=0.028 (model 2, solid curve), and for w=5 cm/s, k=10^7 cm^2/s, and X_{CH4}=0.1 (model 10, dotted curve).

ture, which are determined by both the thermal and dynamic structure of its atmosphere.

The best fit to the observed spectra for the assumed stratification of Titan's clouds is achieved with model 2, which produces a stratified cloud-aerosol structure (fog→main cloud layer→upper haze) with vertical rise velocity w=10 cm/s, turbulent diffusion coefficient k=10^6 cm^2/s, and methane content CH_4=0.028.

The weakening of strong methane bands is consistent with the decrease in methane gas in the upper troposphere due to freezing.

CONCLUSIONS

1. Spectrophotometric observations of Titan and Saturn in the 600–950 nm range with high signal-to-noise ratio were conducted.
2. The weak 619 nm and moderate 790 nm bands are similar in intensity for both bodies, while the strong 727, 861, and 889 nm bands are systematically weakened on Titan.
3. Differences in methane band profiles are revealed, indicating a complex stratification of Titan's atmosphere, different from that of Saturn.
4. The spectral continuum of Titan differs from that of Saturn as a result of the difference in the microphysical properties of the aerosol.
5. Comparison with dynamic models allows us to estimate the parameters of the atmosphere: the turbulent diffusion coefficient k~106…107 cm^2/s, the vertical transport velocity w=5…10 cm/s, and the volume fraction of methane 3–6%.
6. The joint analysis of depths, band profiles, and the continuum is an effective tool for diagnosing the vertical structure of Titan's atmosphere.

ACKNOWLEDGMENTS:

The work is carried out within the framework of the Project No. BR31714731 "Fundamental research in observational and theoretical astrophysics", financed by the Ministry of Science and Higher Educational of the Republic of Kazakhstan.

REFERENCES:

[1] Niemann H. B. et al. The abundances of constituents of Titan's atmosphere from the GCMS instrument on the Huygens probe // Nature. 2005. V. 438. P. 779–784.
[2] Karkoschka E. Spectrophotometry of the jovian planets and Titan at 300–1000 nm wavelength // Icarus. 1994. V. 111. P. 174–192. https://pds-atmospheres.nmsu.edu/planetary_datasets/titan_infrared.html
[3] Vdovichenko V. D., Kirienko G. A. Exploration of Jupiter, Mars, Titan and Vesta. LAP LAMBERT Academic Publishing, 2013. 386 p. (in Russian). ISBN: 978-3-659-51391-6.
[4] Ibragimov K. Yu. Numerical Modeling of Stratiform Cloudiness in the Atmospheres of Giant Planets. Alma-Ata, 1990. 239 c. (in Russian).
[1] Ibragimov K.Yu., Kirienko G. A., Vdovichenko V. D. On the possible cloud structure of Titan // Academic Scientific J. Computer Science. 2003. No. 4. P. 54–57. (in Russian).

FEATURES OF METHANE AND AMMONIA ABSORPTION ALONG JUPITER'S CENTRAL MERIDIAN AND IN THE GREAT RED SPOT IN 2014–2024

V. D. Vdovichenko[1], S. K. Salamakhin[1], A. M. Karimov[1], S. M. Rakhmatulla[2]
[1] *V. G. Fesenkov Astrophysical Institute, Almaty, Kazakhstan*
sergey_ks2002@mail.ru
[2] *Woosong University Kazakhstan*

KEYWORDS:
Jupiter, Great Red Spot, troposphere, methane, ammonia, absorption

INTRODUCTION:

Spectrophotometric observations of Jupiter in the visible and near-infrared (IR) spectral ranges are widely used to study the vertical structure of clouds and the distribution of gases in the upper troposphere. Of particular interest are the methane and ammonia absorption bands in the 600–950 nm range, which are sensitive to the altitude of cloud tops and the optical properties of aerosols.

The Juno mission has shown that the GRS has a complex vertical structure and extends to a considerable depth into the troposphere, raising the question of the mechanisms responsible for its stability [1].

Ground-based observations over a broad spectral range, from the ultraviolet to the radio domain, are becoming a key tool for systematic monitoring of the evolution of the GRS.

This paper presents the results of spectral studies of variations in molecular methane and ammonia absorption in the 600–950 nm range along the central meridian during the passage of the Great Red Spot across it, based on observations obtained in 2014, 2016, 2017, 2018, 2020, 2023, and 2024.

OBSERVATIONAL CONDITIONS, DATA PROCESSING METHODS, AND MAIN RESULTS:

Our spectral observations were carried out near Jupiter's opposition at the observatory of the V.G. Fesenkov Astrophysical Institute. The highest-quality spectrograms were selected for processing. The criteria for selecting spectrograms, the improved methodology, and the program used to process the observational data are described in [2].

Figures 1 and 2 show the temporal variations in the brightness of the GRS during 2014–2024 at the center of the deep 889 nm methane absorption band when the GRS crossed the central meridian. For clarity of comparison, variations at other latitudes are not shown in Fig. 1. They will be presented in Fig. 3. It can clearly be seen that during the period from 2014 to 2024, the relative brightness of the Spot decreased by a factor of 1.4. The spectrogram cross-section in the 889 nm CH_4 band also shows a well-defined increase in brightness in the polar regions due to high-altitude aerosol haze, which serves as an indicator of the good quality of Jupiter images at the times of observation. The same brightening, in the form of polar "caps", can regularly be seen in high-quality images of Jupiter in the 889 nm methane band posted on the ALPOJapan website (https://alpo-j.sakura.ne.jp/index_e).

It should be noted that the trend we identified toward a decrease in the relative brightness of the Spot and an increase in the equivalent width in the deep 889 nm methane absorption band, as well as similar variations in the 790 nm ammonia band, are not regular but indicate a time-dependent trend, particularly pronounced in 2023 and 2024.

An analysis of Hubble Space Telescope data for the period 2015–2021 [3] showed that the most significant changes in the GRS region are associated

with variations in tropospheric and stratospheric haze, with their vertical distribution changing from year to year rather than showing a persistent downward trend, which is consistent with the results of our observations.

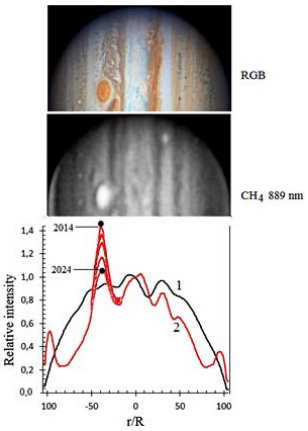


Fig. 1. Brightness distributions along the central meridian in 2014. 1 — in the continuum at 635 nm, 2 — at the center of the 889 nm CH_4 absorption band. The curves are normalized to the center of the disk. Variations in the brightness of the GRS over the period 2014–2024 are shown separately

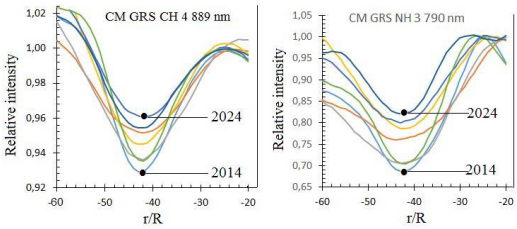


Fig. 2. Temporal range of changes in absorption in the GRS region in the 889 nm methane absorption band and the 790 nm ammonia band. The data are normalized to the region adjacent to the northern boundary of the GRS

For a more detailed comparison of variations in the intensities of the absorption bands, we used variations in their equivalent widths.

Figure 3 below presents, by year:

- Variations in brightness along the central meridian in the 635 nm continuum and at the center of the 889 nm CH_4 absorption band (upper graph);
- Variations along the central meridian in the equivalent widths of six methane absorption bands (middle graph). For clarity, the curves are evenly shifted along the ordinate axis;
- Variations along the central meridian in the equivalent widths of two ammonia absorption bands (lower graph).

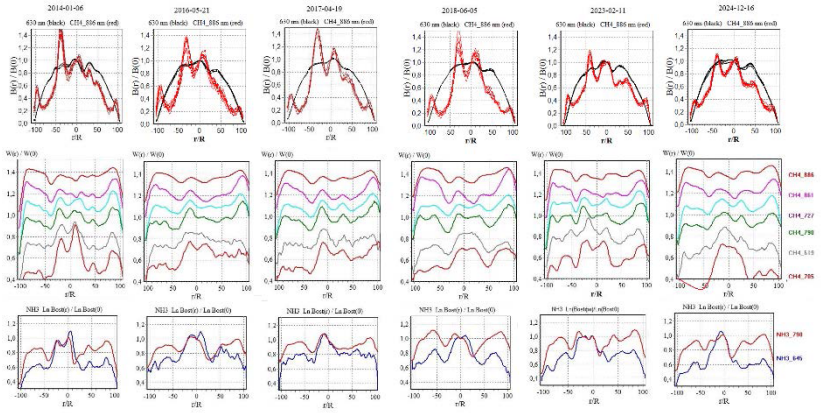


Fig. 3. Meridional variations in brightness and in the equivalent widths of methane and ammonia absorption bands. Explanations are given in the text

From the upper graph, the changes in the brightness of the GRS from year to year can be traced. The main changes occurred in 2023 and 2024, when the brightness of the GRS decreased from 1.5 to almost 1 relative to the bright equatorial zone (EZ).

From the series of graphs in the middle, it can be noted that:

Within each observing season, weak differences are preserved in the meridional variations of the equivalent widths of the strong and moderate methane absorption bands at 727, 790, 861, and 889 nm, which are formed in the upper part of the troposphere at pressure levels from 0.15 to 0.7 bar. In the deeper layers, from 0.8 to 1.5 bar, where the weak absorption bands at 619 nm and especially 703 nm are formed, the absorption variations differ significantly from those in the upper layers. Apparently, this is caused by differences in the stratification and density of the lower cloud layers composed of NH_3 and NH_4SH, as well as the deeper NH_3+H_3O layers, and by the thickness of the gaseous gap between them.

The lower series of graphs in Fig. 3 demonstrates variations in absorption in the ammonia bands. A systematic increase in absorption in the equatorial region and an ammonia deficit at higher latitudes are clearly noticeable. This is particularly well manifested in the weak 645 nm ammonia absorption band at a level of ~0.6–0.8 bar, corresponding to the transition zone between the upper NH_3 clouds and the NH_4SH layer. Of particular note is the previously identified persistent sharp weakening of absorption at the boundary between the bright equatorial zone (EZ) and the dark North Equatorial Belt (NEB) [4].

ACKNOWLEDGMENTS:
The work was carried out within the framework of Program No. BR31714731, "Fundamental Research in Observational and Theoretical Astrophysics," funded by the Ministry of Science and Higher Education of the Republic of Kazakhstan.

REFERENCES:

[1] Wong M. H. et al. Evolution of the Great Red Spot observed by Hubble Space Telescope // AJ. 2020. V. 159. Article 234. DOI: 10.3847/1538-3881/ab8d35.
[2] Vdovichenko V. D. Methodological aspects of the study of ammonia-methane absorption variations in the atmosphere of Jupiter // 15th Moscow Solar System Symp. 2024. P. 138–141.
[3] Anguiano-Arteaga A. et al. Temporal Variations in Vertical Cloud Structure of Jupiter's Great Red Spot, Its Surroundings and Oval BA From HST/WFC3 Imaging // J. Geophys. Res. Planets. 2023. V. 128. Article e2022JE007427. DOI: 10.1029/2022JE007427.
[4] Vdovichenko V. D., Karimov A. M., Lysenko P. G., Teifel V. G., Filippov V. A., Kharitonova G. A. Some Characteristic Features of Latitudinal Variations in Methane and Ammonia Absorption on Jupiter // Solar System Research. 2025. V. 59. P. 57–68.

INFLUENCE OF THE REDISTRIBUTION OF AEROSOLS IN ALTITUDE WITHIN THE RADIATIVE TRANSFER PROBLEM IN THE NIR BANDS OF CO_2 AND CO MOLECULES UNDER BREAKDOWN OF VIBRATIONAL LTE IN THE DAYTIME MARTIAN ATMOSPHERE

V. P. Ogibalov
Admiral Makarov State University of Maritime and Inland Shipping, St. Petersburg 198035, Russia
Department of Atmospheric Physics, St. Petersburg State University, St. Petersburg-Petrodvorets198504, Russia, vpo563@yandex.ru

KEYWORDS:
radiative transfer, infrared molecular bands, vibrational non-LTE, carbon dioxide, Martian atmosphere, aerosol extinction

INTRODUCTION:
Since the Martian atmosphere is sufficiently rarified already at the surface, the breakdown of the local thermodynamic equilibrium (LTE) over the vibrational degrees of freedom of these molecules (vibrational non-LTE) for the CO_2 and CO molecules starts in the daytime from the troposphere. As the Mars lower atmosphere is dusty, the scattering of infrared solar radiation by aerosols should affect the vibrational state populations of these molecules.

The first attempt to estimate the aerosol scattering effect on the populations of vibrational states of molecules was made in the papers [1–2] using the transport approximation. The more realistic Henyey-Greenstein phase function for Martian aerosols and first results of modeling the radiative transfer under non-LTE conditions in the CO_2 and CO bands in the wavelength range of 1–5 μm, taking into account the radiation scattering by aerosols were presented in [3]. The present study is a continuation of the papers [3].

MODEL:
To explore qualitatively the effects on the values of the non-equilibrium populations of the CO_2 and CO molecules when accounting for the aerosol scattering of radiation, the simple model of aerosols in the Martian atmosphere from the study [3] has been supplemented. The vertical profile of concentration of the aerosol particles was assumed to be exponential with the height scale H_a. The concentration of aerosols at the surface of Mars is determined by the value τ_a of the total optical depth of the Martian aerosol. The phase function of aerosol particles is supposed to be of Henyey-Greenstein type with parameter g.

The models of the Martian atmosphere and its aerosoll redistribution in altitude is completely corresponded to that described in [3].

RESULTS AND DISCUSSION:
Main effect of aerosols on population distribution:
The effect of aerosols on vibrational state population manifests itself as an increase in population above a certain altitudinal level with a pressure p_0 and its decrease below this level (Figs. 1–2).

Numerical experiments have shown that the pressure p_0 corresponds to heights at which the optical path length of direct solar radiation, due to the combined effect of molecular absorption of radiation and aerosol extinction, reaches the magnitudes of an order of 1. An increase in the numerical density of aerosols at any height while maintaining the type of altitude distribution of aerosols, determined by H_a in the model used, leads to an

increase in the aerosol optical depth τ_a. Therefore, the pressure p_0 decreases with increasing τ_a (Fig. 1). Some bands does not show the aerosol effect in a near-surface layer: the greater the optical thickness τ_b, the thicker this layer.

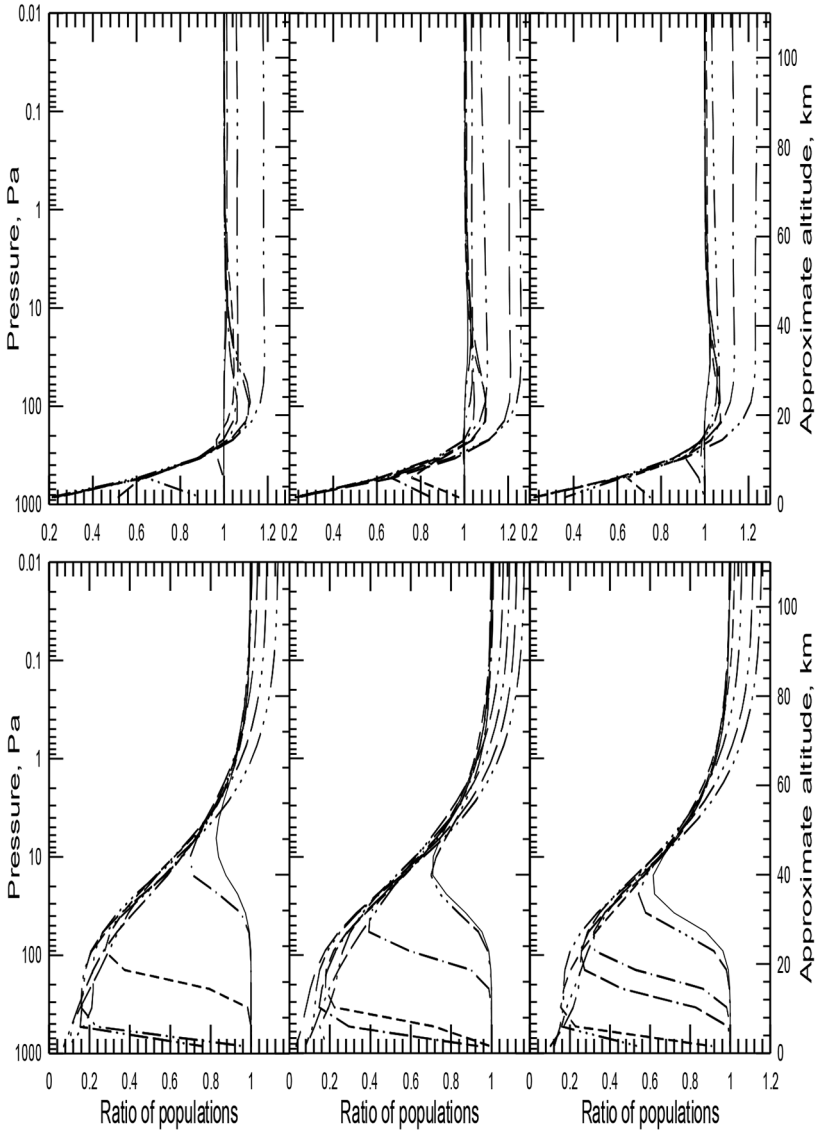


Fig. 1. The ratio of the vibrational state population obtained with taking account of radiation scattering by aerosols to the population calculated in the neglect of this scattering for τ_a=2, Λ=0.95, g=0.63. Top panels: H_a=7 km, SZA=60°; bottom panels: H_a=11.5 km, SZA=85°. The curves of the left panels present the vibrational states, transitions from which form the $^{12}C^{16}O_2$ bands at 4.3 (solid), 2.7 (dotted-dashed), 2.0 (dashed), 1.6 (a dash with two dots), 1.4 (two dashes with two dots), 1.3 (two dashes with three dots), 1.2 (two dashes with a dot), and 1.05 μm (a dash with three dots). The curves of the middle panels present the same, but for the $^{13}C^{16}O_2$ bands at 4.3 (solid), 2.7 (dotted-dashed), 2.0 (dashed), 1.6 (a dash with two dots), and 1.4 μm (two dashes with two dots) and the $^{12}C^{16}O$ bands at 4.7 (two dashes with three dots), 2.3 (two dashes with a dot), 1.6 (a dash with three dots), and 1.2 μm (long dashed). The curves of the right panels present the same, but for the $^{16}O^{12}C^{18}O$ bands at 4.3 (solid), 2.7 (dotted-dashed), 2.0 (dashed), 1.6 (a dash with two dots), and 1.4 μm (two dashes with two dots) and the $^{16}O^{12}C^{17}O$ bands at 4.3 (two dashes with three dots), 2.7 (two dashes with a dot), and 2.0 μm (a dash with three dots).

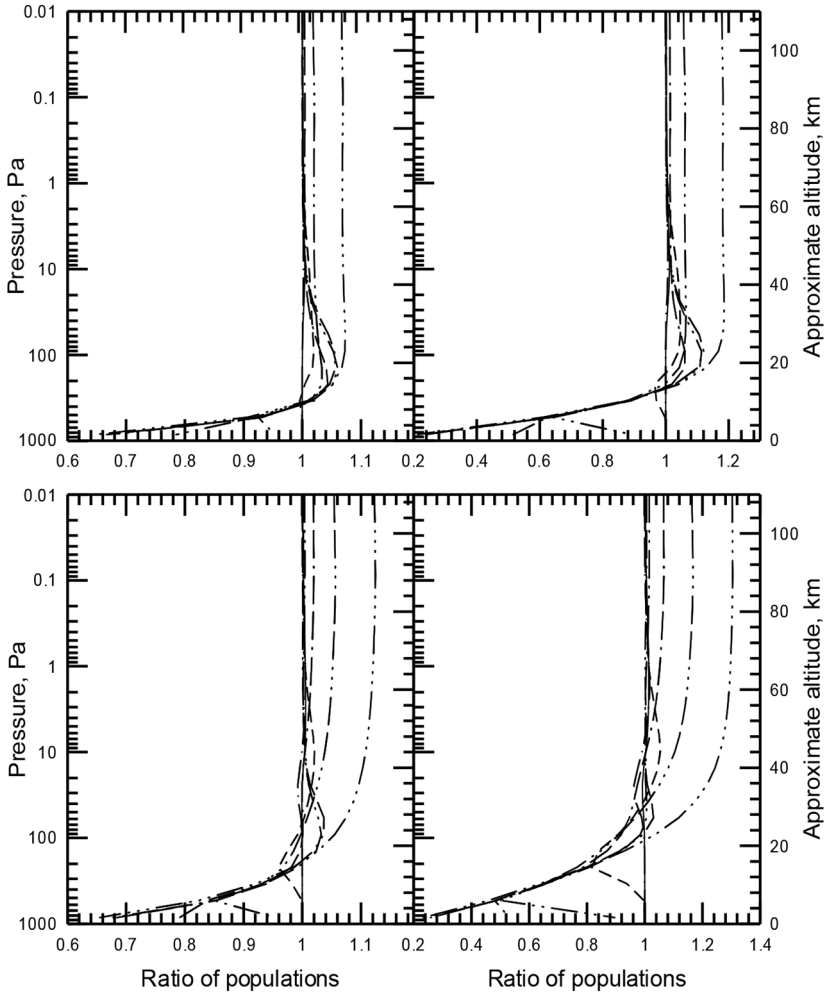


Fig. 2. The ratio of the vibrational state population obtained with taking account of radiation scattering by aerosols to the population calculated in the neglect of scattering for Λ=0.95, g=0.63, SZA=60°. Left panels: τ_a=0.5; right panels: τ_a=2. Top panels: H_a=7 km; bottom panels: H_a=11.5 km. The curves present the vibrational states, transitions from which form the $^{12}C^{16}O_2$ bands at 4.3 (solid), 2.7 (dotted-dashed), 2.0 (dashed), 1.6 (a dash with two dots), 1.4 (two dashes with two dots), 1.3 (two dashes with three dots), 1.2 (two dashes with a dot), and 1.05 μm (a dash with three dots). The scale of horizontal axis is different for different panels.

Dependence on the optical thickness of band:
The effect of aerosols on vibrational state populations depends mainly upon the band optical thickness, τ_b, determined as the product of the optical thickness of the Martian atmosphere in the center of the strongest line of band on the relative abundance of isotopologue.

For isotopologue $^{12}C^{16}O_2$, the values of τ_b are of an order of the magnitudes $2.5{\cdot}10^8$, $2.5{\cdot}10^6$, $4{\cdot}10^4$, $5{\cdot}10^2$, $1.5{\cdot}10^3$, $1{\cdot}10^2$, 30, and 2 for the bands at the wavelengths 4.3, 2.7, 2.0, 1.6, 1.4, 1.3, 1.2, and 1.05 μm, respectively. As expected, the aerosol effect is stronger, the smaller τ_b, and the pressure p_0 tends to decrease with increasing τ_b (see Figs. 1–2). The same conclusion has been previously otained in [1]. The population can increase by ~30% for $p<p_0$, and it can decrease by an order of magnitude for $p>p_0$. The effect of radiation scattered by aerosols turns out to be significant only for relatively weak bands. The aerosol effect for relatively strong bands is manifested only in the population decrease over a certain range of heights.

The probability of molecule excitation due to photon absorption at altitudes with $p<p_0$ depends on the magnitude of the flux of photons scattered by aerosols below the altitude under consideration and reflected from the surface, and having reached this altitude. The greater τ_b and the less p, the less photons reaching a considered altitude and exciting molecules.

Dependence on the redistribution of aerosols in altitude:
The more H_a, the higher the aerosol spread above the planetary surface. The pressure p_0 decreases with increasing H_a for all the bands (see Fig. 2). For $p<p_0$, the effect of the H_a variation on vibrational state population depends on the band optical thickness τ_b. The increase of H_a results in population rise in the whole layer with $p<p_0$ for the weakest bands, such as the $^{12}C^{16}O_2$ bands at 1.3, 1.2, and 1.05 μm. However, for the 'medium strength' bands (such as the $^{12}C^{16}O_2$ bands at 2.0, 1.6, and 1.4 μm), for which the aerosol effect is population rise only in some layer, the increase of H_a results in population reduction caused by the p_0 decrease.

CONCLUSIONS:
The paper presents the results of modeling the radiative transfer under non-LTE conditions in the CO_2 and CO bands in the wavelength range of 1–5 μm, taking into account the radiation scattering by aerosols. The populations were studied depending on the optical thickness both of the aerosol layer and of the bands, the vertical distribution of aerosols, the solar zenith angle, and the aerosol parameters describing the scattering and absorption of radiation.The weaker the band, the stronger the aerosol effect on a population. This effect manifests as an increase and a decrease in population above and below a certain altitude level, respectively.

REFERENCES:
[1] Ogibalov V. P. Radiative Transfer in the near-infrared CO_2 bands taking account of continuum absorption by aerosol particles in the Martian atmosphere // Vestnik of St. Peterburg Univ. (Series 4). 2008. V. 3. P. 27–36.
[2] Ogibalov V. P. Non-equilibrium radiation in the infrared bands of the CO_2 and CO molecules in the planetary atmospheres (in the application to Mars) // Proc. SPIE. V. 10466. Part 1: 23-rd Intern. Symp. Atmospheric and Ocean Optics: Atmospheric Physics. Irkutsk, Russia, 2017. P. 1–14. DOI: 10/1117/12.2292238.
[3] Ogibalov V. P. Radiative transfer in the NIR bands of CO_2 AND CO molecules under breakdown of vibrational LTE in the daytime Martian atmosphere. Effect of radiation absorption by aerosols on vibrational state populations // The Sixteenth Moscow Solar System Symposium 16M-S3. October 20–24, 2025. M.: IKI RAS. 2025. P. 72–78. DOI: 10.21046/16MS3-2025.

METHOD FOR SOLUTION OF THE RADIATIVE TRANSFER PROBLEM IN THE ROVIBRATIONAL BANDS OF THE CO_2 AND CO MOLECULES UNDER BREAKDOWN OF VIBRATIONAL LTE IN THE MARTIAN ATMOSPHERE WITH TAKING ACCOUNT OF RADIATION EXTINCTION BY AEROSOLS

V. P. Ogibalov
Admiral Makarov State University of Maritime and Inland Shipping, St. Petersburg 198035, Russia
Department of Atmospheric Physics, St. Petersburg State University, St. Petersburg-Petrodvorets198504, Russia, Keywords:

radiative transfer, molecular bands, non-LTE, carbon dioxide, planetary atmospheres, Mars, aerosol extinction

INTRODUCTION:

The troposphere of Mars, as a rule, is dusty, and the dust can be raised to ~50 km. Thus, the radiation transfer in the above bands under the breakdown of the local thermodynamic equilibrium (LTE) over the vibrational degrees of freedom of these molecules (vibrational non-LTE) in the daytime Martian atmosphere should be considered taking into account the radiation scattering by aerosols.

The first attempt to estimate the aerosol effect on the populations of vibrational states of molecules was made in the papers [1–2] using the so-called transport approximation for single scattering phase function. These studies have shown that aerosol scattering can significantly change the populations. However, the papers [1–2] did not present a comprehensive study of the aerosol scattering effect on the populations of vibrational states of the CO_2 and CO molecules.

So, the method of solution of the radiative transfer problem with utilizing the more realistic phase function (e.g. of the Henyey-Greenstein type) was necessary to be realized.

METHODOLOGY:

The necessity of taking into account the vibrational non-LTE in the Martian atmosphere means that when considering the problem of radiation transfer (RT) in the rovibrational bands of the CO_2 and CO molecules one needs to solve together: (1) the system of the steady-state equations (SEE) system, which express the equality of the total population and de-population rates of the accounted within the model processes for each molecular vibrational state; and (2) the radiative transfer equation (RTE), which relates the radiation field at a given height to the vibrational state populations at all altitudes in the planetary atmosphere. As a result, one can calculate the non-equilibrium values of the populations of the vibrational states, which are connected by both the R-V radiative transitions and the vibrational-vibrational (V-V) and vibrational-translational (V-T) processes of vibrational energy exchange during collisions.

Let us consider a Maxwellian gas mixture in a planetary atmosphere consisting of different gases. Their quantum energy levels are enumerated throughout the entire mixture by the index *l* which denotes the set of vibrational and rotational quantum numbers identifying a given rovibrational level of the gas. Each energy level is characterized by its statistical weight g_l, excitation energy E_l and population n_l. We abbreviate the energy relations $E_l < E_{l'}$ and $E_l > E_{l'}$ by $l < l'$ and $l > l'$, respectively.

We consider the case of a plane-parallel atmosphere. In this case, for each frequency-angle point (μ, ν), where ν is a frequency, $\mu = Cos\theta$ and θ is

the zenith angle of the direction of radiation propagation, the vertical profile of the specific intensity $I(z,\mu,\nu)$ of the proper atmospheric radiation is determined when solving the radiative transfer equation

$$\mu\frac{\partial I(z,\mu,\nu)}{\partial z} = -\chi(z,\nu)I(z,\mu,\nu) + \eta(z,\mu,\nu) \quad (1)$$

at zero boundary conditions. The values in the formula (1) represent the total emissivity $\eta(z,\mu,\nu)$

$$\eta(z,\mu,\nu) = \sum_{l>l'}\eta_{ll'}(z,\nu) + \eta_c(z,\mu,\nu), \quad (2)$$

and the total opacity

$$\chi(z,\nu) = \sum_{l>l}\chi_{ll'}(z,\nu) + \chi_c(z,\nu). \quad (3)$$

The radiative properties of gas being considered are completely characterized by the spectral line emissivity $\eta_{ll'}(z,\nu)$ and the spectral line opacity f $\chi_{ll'}(z,\nu)$ or each pair of levels connected by a radiative line transition. If the macroscopic velocity field can be neglected, these quantities do not depend on μ. For $l > l'$ they are given by expressions

$$\eta_{ll'}(z,\nu) = \frac{h\nu_{ll'}}{4\pi}n_l(z)A_{ll'}\phi_{ll'}(z,\nu), \quad (4)$$

$$\chi_{ll'}(z,\nu) = \frac{h\nu_{ll'}}{4\pi}[n_{l'}(z)B_{l'l} + n_l(z)B_{ll'}]\phi_{ll'}(z,\nu), \quad (5)$$

where is the line center frequency; $A_{ll'}$, $B_{ll'}$ and $B_{l'l}$ are the Einstein coefficients and $\phi_{ll'}(z,\nu)$ is the line profile function normalized such that $\int d\nu\,\phi_{ll'}(z,\nu) = 1$. In the model we adopted the Voight line profile with the Voight parameter depending on altitude.

The last terms $\eta_c(z,\mu,\nu)$ and $\chi_c(z,\nu)$ of the right-hand sides in formulas (2) and (3) represent the emissivity and opacity of the background continuum, respectively. It is known from the theory of radiation transfer in spectral lines of the atomic multiplets that the presence of absorption in the continuum spectrum significantly affects onto the process of transfer of radiation in the wings of the spectral lines, because in this case the values of the total opacity and emissivity do not decrease to zero in the far wings of the spectral lines.

The advantage of the present study in comparison to the previous ones consists in that we treat the values of $\eta_c(z,\mu,\nu)$ and $\chi_c(z,\nu)$ to take into account for the interaction of the radiation at the frequencies of the gas spectral lines with the aerosol particles. The extinction of the radiation intensity in the planetary atmosphere due to the processes of scattering and absorption of radiation by aerosols is described by the volume coefficients $\sigma_{sca}(z,\nu)$ and $\sigma_{abs}(z,\nu)$ of scattering and absorption, respectively:

$$\chi_c(z,\nu) = \sigma_{sca}(z,\nu) + \sigma_{abs}(z,\nu). \quad (6)$$

The contribution to the radiation intensity by changing the direction of propagation of photons due to scattering on aerosol particles, and due to their thermal emission is described by the volume coefficient of emissivity

$$\eta_c(z,\mu,\nu) = \sigma_{sca}(z,\nu)\int_{4\pi}I(z,\mu',\nu)p(Cos\gamma)d\omega' + \sigma_{abs}(z,\nu)B_\nu\left(T_{kin}(z)\right), \quad (7)$$

where $p(Cos\gamma)$ is the phase function (normalized to unity) for scattering angle γ; ω is the solid angle about the direction, characterized by zenith angle $\theta = arccos\,\mu$ and azimuth angle ϕ; $B_\nu\left(T_{kin}(z)\right)$ is the Planck function for the kinetic temperature $T_{kin}(z)$.

CALCULATION METHOD:

The phase function of aerosol particles $p(Cos\gamma)$ is supposed to be of Henyey-Greenstein type with parameter *g*. The models of the Martian atmosphere and its aerosoll redistribution in altitude is completely corresponded to that described in [3].

The method of taking into account all types of line overlapping was developed in [4] for the transitions that form the 15 μm CO_2 band. In this study, it is extended to all the NIR bands of CO_2 and CO.

The solution of the steady-state equations is obtained using the accelerated lambda iteration method. An iterative scheme is used to solve the RTE (1), which is based on the formal solution of this equation. The radiation terms in the RTE are discretized in terms of optical depth and direction. The resulting system of linear algebraic equations is solved using the Gauss-Seidel single-step iteration method. When calculating the radiation terms in the SSEs, the downward radiation intensity is first calculated from one node of the altitude grid to the next node from the top of the atmosphere to the surface. Then, taking into account the reflection of downward radiation from the surface, the upward radiation intensity is calculated from node to node in the opposite direction.

The idea is to organize internal iterative cycles in solving the RTE, during which already the source function, which includes as a term the integral over all solid angles from the product of the scattering phase function on the radiation intensity, is realized into correspondence with the populations of the CO_2 molecules of the vibrational states obtained during the previous ALI-iteration. On average, 2-4 such internal iterations (with a maximum of 6) were required to achieve a relative residual of 10^{-5}. Since the values of the non-equilibrium populations of the CO_2 molecule's vibrational states are determined during the solution of the SSE system, this approach allows for accurate estimates of the effect of the radiation scattering by aerosols.

The results of the numerical experiments are analyzed in [3].

CONCLUSIONS:

The main results are as follows.

1. An original iterative algorithm was developed, which made it possible to take into account the reflection of radiation in the CO_2 bands by the planet's surface, and estimates of the influence of this process on the populations of excited vibrational states of the CO_2 molecule were obtained.

2. It has been generalized two classical cases that are traditionally considered separately in the theory of radiation transport (monochromatic radiation scattering with direction redistribution and radiation scattering in spectral lines with frequency redistribution), derived equations, and formulated the problem of radiation transfer in the spectral lines of the R-V bands of CO_2 under condition of the vibrational non-LTE, taking into account the processes of absorption and scattering of radiation by aerosols in the continuous spectrum.

REFERENCES:

[1] Ogibalov V. P. Radiative Transfer in the near-infrared CO_2 bands taking account of continuum absorption by aerosol particles in the Martian atmosphere // Vestnik of St. Peterburg Univ. (Series 4). 2008. V. 3, P. 27–36.

[2] Ogibalov V. P. Non-equilibrium radiation in the infrared bands of the CO_2 and CO molecules in the planetary atmospheres (in the application to Mars) // Proc. SPIE. V. 10466. Part 1: 23-rd Intern Symp Atmospheric and Ocean Optics: Atmospheric Physics. Irkutsk, Russia, 03-07 July 2017. 2017. P. 1–14. DOI:10/1117/12.2292238.

[3] Ogibalov V. P. Radiative transfer in the NIR bands of CO_2 AND CO molecules under breakdown of vibrational LTE in the daytime Martian atmosphere. Effect of radiation absorption by aerosols on vibrational state populations // The Sixteenth Moscow Solar System Symposium 16M-S3. M.: IKI RAS. 2025. P. 72–78. DOI: 10.21046/16MS3-2025.

[4] Ogibalov V. P., Shved G. M. An improved optical model for the non-LTE problem for the CO_2 molecule in the atmosphere of Mars: Nighttime populations of vibrational states and the rate of radiative cooling of the atmosphere // Solar Syst. Res. 2003. V. 37. No. 1. P. 23–33.

SEARCH FOR SEISMIC ACTIVITY ON VENUS BY PRESSURE PERTURBATIONS IN THE ATMOSPHERE

T. V. Gudkova[1], I. E. Stepanova[1], A. V. Batov[1,2]
[1] *Schmidt Institute of Physics of the Earth, Moscow, Russia, gudkova@ifz.ru*
[2] *Trapeznikov Institute of Control Sciences, Moscow, Russia*

KEYWORDS:
Venus, seismic event, infrasound waves, linear integral representations, pressure fields, analytical continuation

INTRODUCTION:
The available observation data do not impose strict restrictions on the interiors of Venus and there is a wide range of internal structure models that differ in the thickness of the crust, mantle and core size. The complexity of conducting seismic studies on Venus is determined by the conditions on its surface (temperature 750 K and pressure 93 atm). Unconventional ways of studying its seismic activity are proposed: registration of perturbations from seismic signals in the atmosphere and ionosphere of the planet by orbiters, for this, special methods are being developed [1, 2]. The concept of detecting seismic infrasound by pressure sensors on balloon platforms on Earth has been carefully studied over the past decade [3]. In this work, we are testing the use of the method of linear integral representations [4-6] to find equivalent sources of a seismic event in the interiors of Venus using a synthetic signal of pressure perturbations in the atmosphere.

NUMERICAL MODELLING:
If the planet is represented as a half-space, then the mathematical statement of the problem can be written in Cartesian coordinates, which greatly simplifies calculations. In this work, all variational settings will be studied in the Cartesian coordinate system. Let us have a vertically heterogeneous environment. The model represents two subsystems (two half spaces). In the first (subsurface) medium bounded by a free surface, there is some source of a seismic event that leads to vertical surface movements. The wave propagates in a direction parallel to the surface of the planet. The vertical motion of the surface causes atmospheric fluctuations. In the second medium (planet atmosphere), due to vibrations of the lower boundary, acoustic waves arise, which propagate upward at infrasonic speed, and are recorded at a given height. Infrasound signals are a scaled reflection of the vertical displacement velocity of the surface below the sensor.

To test the method used in this work and create a synthetic database of parameters, the data of coseismic displacements of the Earth's crust of the northeastern outskirts of the Eurasian continent, initiated by the catastrophic Tohoku earthquake on March 11, 2011, which were obtained in [7], are used as the starting material. The data used covers the territory defined by 160 points within latitudes from 23 to 54° N and longitudes from 97 to 153° E.

Modeling is carried out under certain assumptions. In this work, we do not take into account the attenuation of the acoustic wave. Estimates of the effect of attenuation on acoustic waves were carried out in [1], in which it was noted that infrasonic signals generated by seismic waves below 1 Hz are weakly attenuated. Considering that the attenuation of the acoustic wave is insignificant, to simulate the amplitudes of pressure perturbations caused by vertical displacement of the surface, we use the formula from [1]:

$$DP = \rho(z_b)c(z_b)\sqrt{\frac{\rho(0)}{\rho(z_b)}}\left(\frac{\tilde{}\,\pi \quad ^{-6}A_d}{T_s}\right),$$

where A_d (in μm) – vertical displacement of the surface for the period T_s, $\rho(z_b)$ and $c(z_b)$ — density and speed of sound at altitude z_b in the atmosphere, respectively.

Let's generate a synthetic signal at an altitude of 50 km for a period of 10 s. The density on the surface and in the atmosphere at an altitude of 50 km is assumed to be 65 and 1.3 kg/m^3, respectively. The speed of sound is 426 and 310 m/s, respectively.

Since the surface temperature on Venus is high, it is believed that the thickness of the seismogenic layer on Venus is not more than 30 km, due to a less deep transition of the viscous-brittle state in the crust. Therefore, mainly shallow quakes are expected. Therefore, we will look for sources of the seismic event at depths of 5–30 km.

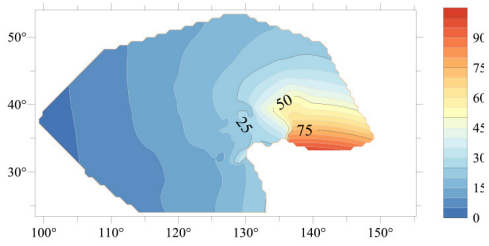


Fig. 1. Pressure perturbations amplitudes at an altitude of 50 km (synthetic data, Pa)

According to synthetic data of the pressure amplitude field at an altitude of 50 km from the planet's surface, we restore the distribution of seismic signal sources at depths from 10 to 30 km. Values of pressure amplitudes near the surface of Venus (see Fig. 2) are calculated from the obtained distribution of equivalent sources in the field of pressure, and then the procedure for determining new equivalent seismic sources is carried out from the data on pressure at the surface.

The amplitudes of pressure perturbations at a given altitude were found using a stationary S-approximation. The approximation quality index was $1.3 \cdot 10^{-8}$ for the set consisting of 160 points.

The pressure field was analytically continued down to a level of 5 km, and further to the surface of Venus, with a seismic source located at the depth of 20 km. The results are shown in Fig.2.

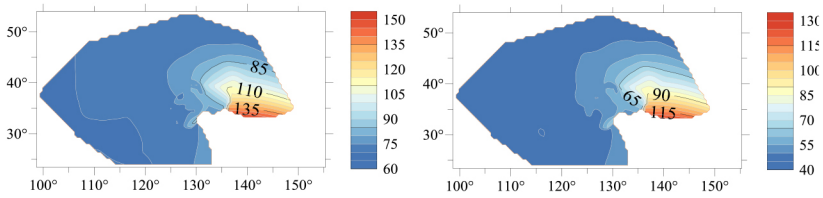


Fig. 2. Pressure field (Pa) continued down to the surface of Venus (left) and to a level of 5 km (right)

Further, the field of pressure amplitudes was analytically continued up to the level where the initial amplitudes data were set (Fig. 3). As can be seen from the comparison of Fig. 2 and 3, the relative error of recovery of the initial pressure field is 10–15 percent.

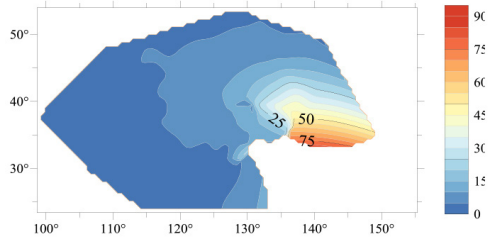


Fig. 3. Pressure field (Pa) obtained by analytical continuation from the surface up to the level of 50 km.

CONCLUSION:

Numerical modeling was carried out to determine the equivalent sources of the seismic event in the interiors of Venus using a synthetic signal of the amplitudes of pressure perturbations in the atmosphere. For this, a version of linear integral representations method was used to solve the inverse problem of restoring wave potential sources in the local version. Results of mathematical experiment on finding of analytical extension of field of synthetic pressure amplitudes are given. The study showed the applicability of the method used. The approximation quality indicator is equal to $1.3 \cdot 10^{-8}$ or a set of 160 points.

ACKNOWLEDGMENTS:

The work was carried out with budgetary funding from the Institute of Physics of the Earth RAS.

REFERENCES:

[1] Garcia R. F., van Zelst I., Kawamura T. et al. Seismic wave detectability on Venus using ground deformation sensors, infrasound sensors on balloons and airglow imagers // Earth Space Sci. 2024. V. 11. Article e2024EA003670. DOI: 10.1029/2024EA003670.

[2] Brissaud Q., Kong C., Froment M. et al. Aerial and space-borne seismology on Venus: Viability and design implications for future missions // Earth Space Sci. 2026. V. 13. Article e2025EA004541. Doi:10.1029/2025EA004541.

[3] Krishnamoorthy S., Bowman D. C. A "floatilla" of airborne seismometers for Venus // Geophys. Res. Lett. 2023. V. 50(2). Article e2022GL100978. https://doi.org/10.1029/2022GL100978.

[4] Strakhov V. N., Stepanova I. E. The S-approximation method and its application to gravity problems // Izv. Phys. Solid Earth. 2002. V. 38(2). P. 91–107. EDN: LHLKQT.

[5] Raevskiy D. N., Stepanova I. E. On the solution of inverse problems of gravimetry by the modified method of S-approximations // Izv. Phys. Solid Earth. 2015. V. 51. P. 207–218. https://doi.org/10.1134/S1069351315020081.

[6] Stepanova I. E., Kolotov I. I., Yagola A. G. et al. On the uniqueness of discrete gravity and magnetic potentials // Comput. Math. Math. Phys. 2025. V. 65. P. 603–617. https://doi.org/doi:10.1134/S0965542524702130

[7] Shestakov N.V., Gerasimenko M.D., Kishkina A.K. et al. Methodology of coseismic displacements combination obtained by data stemming from heterogeneous geodetic networks: On the example of the great 2011 Tohoku earthquake, Mw 9.1 // Geodyn. Tectonophys. 2024. V. 15(1). Article 0736. DOI: 10.5800/GT-2024-15-1-0736.

DETERMINATION OF THE MIXING FACTOR OF LOCAL AND FOREIGN MATERIAL IN THE LANGRENUS, CAVALERIUS AND THEOPHILUS CRATER EJECTA

A. S. Krasilnikov, M. A. Ivanov
Vernadsky Institute of Geochemistry and Analytical Chemistry RAS Moscow, Russia, krasilnikov_as@geokhi.ru

KEYWORDS:
The Moon, Langrenus, Cavalerius, Theophilus, rays, ejecta, mixing factor

INTRODUCTION:
Determining the material mixing factor when impact crater ejecta are formed, is one of the main tasks, the solution of which will help to clarify our knowledge of the distribution of material on the Moon. Understanding of this distribution allows constraining on interpretation of the composition of the samples of lunar regolith returned to Earth and provides information on the composition and origin of certain ejecta. However, the existing models of ejecta emplacement and their mixing differ greatly, and therefore the material mixing factor needs to be studied in more details with the help of modern high-resolution and multicomponent data.

MIXING FACTOR OF LOCAL AND FOREIGN MATERIALS:
The existing models of the changes of ejecta thickness do not take into account the mixing of ejecta material with the underlying regolith. The approximation of the mixing problem was proposed by [1], where they presented the results of studies of evaluation of volume ratio of the local regolith to material of ejecta (μ factor), based on a series of experiments and studies of secondary craters on the Moon:

$$\mu = 0.0183R^{0.87}, \quad (1)$$

where *R* — distance from the middle of the crater radius to the point where μ is estimated.

In their work, Petro and Pieters [2] compared mixing model of Oberbeck et al. [1] with the geochemical and petrographic features of the Apollo 16 soil and determined that the mixing factor μ calculated from formula (1) should be reduced by about a factor of two.

ESTIMATION OF THE MIXING FACTOR BY THE DATA ON FEO AND OLIVINE CONTENT IN THE RAYS OF CRATERS LANGRENUS, CAVALERIUS, AND THEOPHILUS:
At this moment, we don't know if the model by [1] or its modification by [2] correctly describe the ejecta mixing. In order to address this problem from a geochemical/mineralogical point of view, we estimated the distribution of iron oxide and olivine in the rays of craters Langrenus, Cavalerius and Theophilus using data of the Clementine mission.

These craters have been selected because of the following reasons:

(1) they are located at the border of the mare and the highlands, and part of their rays are clearly visible on the dark and smooth mare surface;

(2) the ages of the Langrenus and Cavalerius craters are close to the ages of the neighboring maria, which minimizes the factor of the mechanical disturbance of the regolith in the ray formation. The age of the Langrenus crater, 3.41 Ga, almost coincides with the age of the surface of Mare Fecunditatis in the region where the rays are visible, 3.45 Ga [3]. The age of the Cavalerius crater is ~3.2 Ga [4], and the age of the Oceanus Procellarum nearby is 3.18 Ga [5].

In our study, were used only those rays that lie on the smooth mare. Within each of them, were have selected randomly distributed points, at which the model iron oxide and olivine contents were determined. The obtained data form clear trends of increasing of the local (mare) material defined by

FeO and olivine (Ol) components as the distance from the center of the crater increases (Fig. 1). From Langrenus rays, trends are approximated by the following linear functions:

$$FeO = 2.47 \cdot 10^{-5} R + 9.33, \quad (2)$$

$$Ol = 8.99 \cdot 10^{-8} R + 0.03, \quad (3)$$

where R — distance from the crater center in meters.

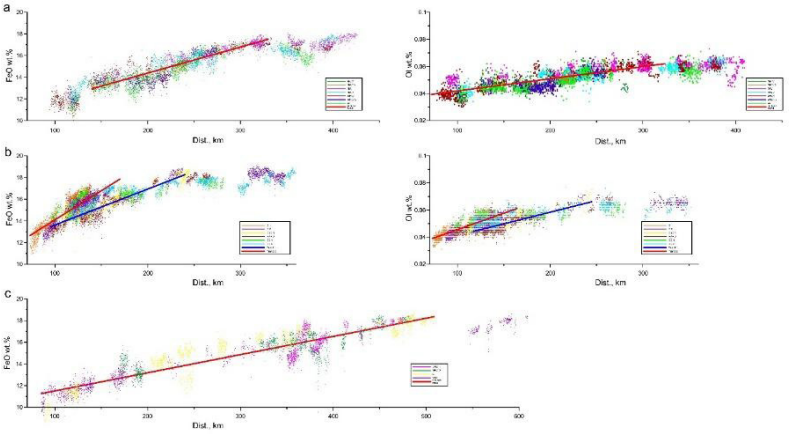


Fig. 1. Variations of the amount of iron oxide and olivine in the rays of the Langrenus (a), Cavalerius (b) and Theophilus (c) craters as a function of the distance from the center centers

At the distance of about three diameters of the Langrenus crater (~300 km), both trends are flattening and no increase in iron oxide and olivine content in the rays is observed. We consider the increase in iron oxide as a result of the mixing of two end members: mare material with an average FeO content of 17.5 wt.%, and highland materials with an average FeO content of 5.5 wt.%. The determined function (2) shows that immediately after the zone of continuous ejecta at a distance of ~150 km from the center of the crater, the content of iron oxide is ~13.16 wt.%, which, at the adopted contents of iron oxide in the end-members, corresponds to a mix of ~36 and 64% of the highland and mare components, respectively. At a distance of 330 km, where the horizontal part of the trend begins, the iron oxide content is estimated to be ~17.5 wt.%, which corresponds to almost 100% of the mare component.

The obtained dependence (2) allows us to propose a formula for estimating the proportion of foreign/local material (L/F) in the range of distances from the zone of contiguous ejecta (~100 km) to the zone where the rays fade out (~300 km):

$$L/F = (2.1 D^{0.49}) \cdot 10^{-3}, \quad (4)$$

where D — distance from the crater center in kilometers.

The olivine content of the rays of the Langrenus crater was considered in a similar way and the following formula was obtained:

$$L/F = (7.2 D^{0.8}) \cdot 10^{-5}. \quad (5)$$

Iron oxide and olivine contents were also determined for rays from the Cavalerius crater. Their contents form two trends, the first of which is confined to the east-southeast rays and the second is related to the southeast rays. Presumably, the formation of these two trends is related to an oblique impact, which caused an asymmetric ejecta distribution. The resulting relationships can be described by the following formulas:

$$FeO = 3.31 \cdot 10^{-5} R + 10.32, \quad \text{(trend 1)} \ (6)$$

$$FeO = 5.59 \cdot 10^{-5} R + 8.43, \quad \text{(trend 2)} \ (7)$$

$$OI = 1.71 \cdot 10^{-7} R + 0.03, \quad \text{(trend 1) (8)}$$

$$OI = 2.43 \cdot 10^{-7} R + 0.02. \quad \text{(trend 2) (9)}$$

As in the case of the Langrenus crater, formulas were obtained for determining of the mixing ratio in the rays of the Cavalerius crater:

$$L/F = (3.9D^{0.6}) \cdot 10^{-4}, \quad \text{(FeO, trend 1) (10)}$$

$$L/F = (4.3D) \cdot 10^{-5}, \quad \text{(OI, trend 1) (11)}$$

$$L/F = (4.2D^{0.8}) \cdot 10^{-5}, \quad \text{(FeO, trend 2) (12)}$$

$$L/F = (6.4D) \cdot 10^{-6}, \quad \text{(OI, trend 2) (13)}$$

For the rays of Theophilus crater, only the iron oxide content was determined and only in rays on the surface of Mare Tranquillitatis because the surface of Mare Nectaris contains a large amount of ejecta from other craters. This resulted in the following dependence of the iron oxide content in the crater rays on distance:

$$FeO = 1.68 \cdot 10^{-5} R + 9.83. \quad (14)$$

The obtained formulas (4-5, 10-14) describe the transportation and mixing of the ray-forming, fine-grained fraction of the crater ejecta that compose a significant portion of the crater redistributed material and represent foreign materials in the samples of lunar regolith. Being compared with the formulas derived by Oberbeck et al. [1] and Petro and Pieters [2], most of the obtained dependencies are closer to the values of the Petro-Pieters [2] corrections. The values obtained from the analysis of the rays of the crater Theophilus stand out most strongly. Presumably, this is due to the large difference in age between the imbrian surface of the Mare Tranquilitatis(~3.4–3.8, [6]) and this crater of the Eratosthenian age (1.1–3.2, [7]).

REFERENCES:

[1] Oberbeck V. R., Hörz F., Morrison R. H., Quaide W. L., Gault D. E. On the origin of the lunar smooth-plains // The Moon. 1975. V. 12. P. 19–54.
[2] Petro N. E., Pieters C. M. Modeling the provenance of the Apollo 16 regolith // J. Geophysical Research. 2006. V. 111. Iss. E9. P. 1–13.
[3] Ivanov M. A., Head J. W., Hiesinger H. New insights into the regional and local geological context of the Luna 16 landing site // Icarus. 2023. V. 400. Article 115579.
[4] Hood L. L. The enigma of lunar magnetism // EOS. 1981. V. 62. P. 161–163.
[5] Stöffler D., Ryder G. Stratigraphy and isotope ages of lunar geologic units: Chronological standard for the inner solar system // Planetary and Space Science. 2001. V. 49. P. 1509–1527.
[6] Hiesinger H., Jaumann R., Neukum G., Head J. W. Ages of Mare basalts on the lunar nearside // J. Geophysical Research. 2000. V. 105. P. 29,239–29,275.
[7] Wilhelms D. E. The geologic history of the Moon // USGS Numbered Ser. Prof. Pap. 1987. V. 1348. Article 302.

MORPHOLOGY AND TOPOGRAPHIC CONFIGURATION OF THE PALLACOPAS VALLIS FLUVIAL SYSTEM, MARS: PRELIMINARY RESULTS

A. S. Vozisov[1], M. A. Ivanov[2]
[1] *Lomonosov Moscow State University, Moscow, Russia*
owlcartful@gmail.com
[2] *Vernadsky Institute of Geochemistry and Analytical Chemistry RAS*

KEYWORDS:
Mars, Argyre basin, Pallacopas Vallis, hydrology, morphology

INTRODUCTION:
The Argyre basin is one of the largest impact structures on Mars likely formed ~4 Ga ago [1, 2]. Since that time the basin plays an important role in distribution and re-distribution of water on Mars [3–5]. The basin certainly received waters from several prominent valleys at the eastern and southern sites and the floor of the basin contained a glacier or a series of glaciers [Bernhardt]. Was the basin overflowed at some moment in its history? Did it serve as a transient reservoir in the proposed global system of water re-distribution from the southern hemisphere to the northern plains [3 ,4]? Or, alternatively, did the basin serve as final reservoir accommodated waters and prevented their flow further to the North [5]? Important components of these problems are morphology and hydrologic histories of the major inlets to the basin. One of these is Pallacopas Vallis and in this contribution we report the results of our photogeological investigation of this valley.

DATA AND METHODS:
The photogeological analysis was conducted with the help of images of different resolution. We used the THEMIS daytime and HRSC images for the outlining and refinement of the most prominent features at the eastern edge of the Argyre basin. For key areas, we use the higher-resolution CTX images to verify the nature of the mapped features and determination of their relative ages. We did not conduct yet crater size-frequency measurements to determine the absolute model ages of units in the study area. The critically important topographic data have been collected from the MOLA measurements.

RESULTS:

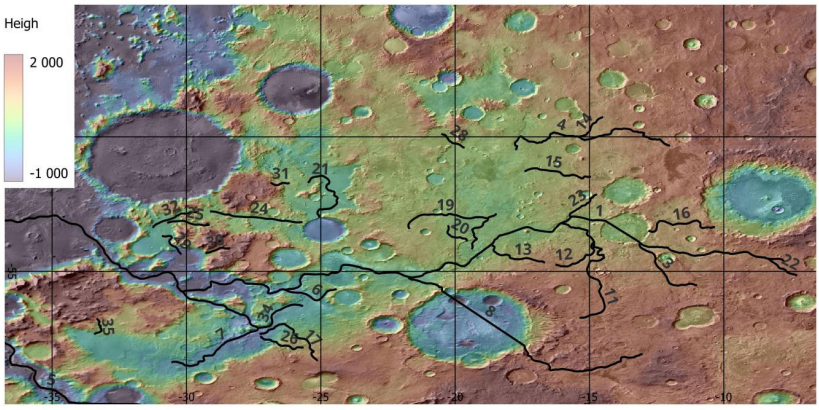


Fig. 1. Pallacopas Vallis system. Numbers is a designations of valleys

Within the study area, we have mapped a number of valleys that apparently form a complex system of Pallacopas Vallis (see Fig. 1). For these valleys we note the position of the thalweg, their planforms, the presence or absence

of longitudinal ridges, terrace-like features, kataracts, and the other features that may characterize the fluvial regimes in the valleys.

In total, within the Pallacopas Vallis system we have mapped 30 individual valleys (Fig. 2), they are oriented radially relative to Argyre. In the northern portion of this system, there is a complex of valleys, Frento Vallis (valleys 4, 14, 15) that gently descent toward the Pallacopas Vallis system. Most of the valleys have non-gradational longitudinal profile, sometimes with steps and/or peaks along the thalweg. In their upper stretches, many valleys have longitudinal ridges that likely represent eskers. The deepest incisions of the valleys are observed near Argyre where they sometime look as deep canyons. In several places some of the valleys cross impact craters and leave no traces on the crater floors.

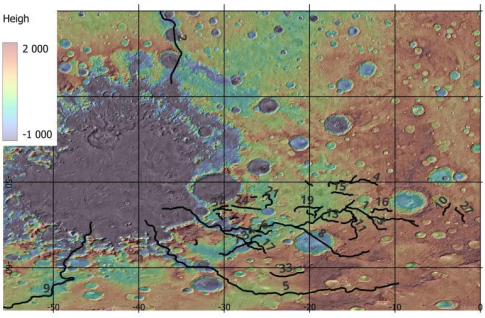


Fig. 2. The main Argyre fluvial systems

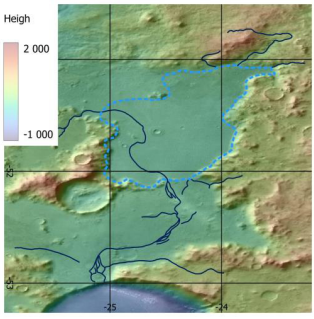


Fig 3. System #21

Valley system #21 (Fig. 3):
The main channel of this system enters an impact crater at 25°W, 53.3°S. However, there is no noticeable features suggesting enhanced erosion regime as the channel crosses the crater rim (e.g., a deep incision). The upper stretches of the main valley cross a topographic depression with flat floor and leveled topography. Edges of the depression often represent short and steeper slopes separating the depression from the mountainous surroundings.

SUMMARY:
The Pallacopas Vallis system is a branching system, although the number of individual valleys is small comparing with terrestrial systems. Because all valleys have non-gradational profiles, the entire system can be classified as an immature system. The presence of eskers and the uphill direction of some valley segments suggest that the system was (at least partly) covered by ice sheets and some valleys (or pats of them) formed by sub-ice flows. Some of the craters that are crossed by valleys likely represented open lakes filled with water during the formation of the Pallacopas Vallis fluvial system.

The source of the system #21 was probably related to the flat-floored depression (Fig. 3) and water from the source flowed toward the unnamed crater. The lack of deep incision at the place where the main valley enters the crater indicate the high-standing level of erosion and, thus, suggests that the crater was filled either by ice or water.

Valley #2 at the northern rim of Argyre (Fig. 2) is significantly higher than the lower stretches of Pallacopas Vallis. This portion of the valley represent a prominent canyon and the same topographic position and morphology characterize the lower stretches of two other large valleys entering Argyre, Surius and Dzigai Valles. All these valleys have been considered as fluvial systems that have caused overfilling of the Argyre basin and its emptying through Valley #2 [3, 4]. such an interpretation is poorly (if at all) consistent with the topographical and morphological characteristics of Pallacopas Vallis. The longitudinal profiles of the Pallacopas channels suggest that this was an immature, short-lived, fluvial system. However, its lower stretches represent prominent canyon, the formation of which require a low erosional level, the maximum elevation of which is equal to the endpoint of

the Pallacopas canyon. The beginning of Valley #2 is ~1.5 km higher than the canyon endpoint and, thus, waters of Pallacopas Vallis could not participate in the overfilling of the Argyre basin. The same reasoning can be applied to the other two major fluvial systems entering Argyre and it appears to be highly likely that neither Surius nor Dzigai Valles have contributed enough water to fill Argyre.

REFERENCES:

[1] Werner S.C., The early Martian evolution-Constraints from basin formation ages // Icarus. 2008. V. 195. Iss. 1. P. 45–60. DOI: 10.1016/j.icarus.2007.12.008, 2008.

[2] Frey H.V., Ages of very large impact basins on Mars: Implications for the late heavy bombardment in the inner solar system // Geophysical Research Letters. 2008. V. 35. Article L13203. DOI: 10.1029/2008GL033515.

[3] Parker T.J., Clifford S.M., Banerdt W.B., Argyre Planitia and the Mars global hydrologic cycle // 31st Lunar and Planetary Science Conf. 2000. V. 31. Article 2033.

[4] Parker T.J., Grant J.A., Anderson F.S., Banerdt W.B. From the South Pole to the Northern Plains: The Argyre Planitia story // 6th Intern. Conf. Mars. LPI Contrib. 1164. Lunar and Planet. Inst., Houston, Tex., 2003. Article 3274.

[5] Hiesinger H., Head J.W. Topography and morphology of the Argyre Basin, Mars: implications for its geologic and hydrologic history // Planetary and Space Science. 2002. V. 50. No. 10–11. P. 939–981, DOI: 10.1016/S0032-0633(02)00054-5, 2002.

RADIO SCIENCE EXPERIMENT ON LUNA-26 ORBITER, METHODS AND ACCURACY OF GRAVITATION FIELD MEASUREMENTS

A. S. Kosov, R. E. Borovsky, R. S. Kalandadze, L. S. Roshkov, V. S. Roshkov
Space Research Institute RAS, Moscow 117997, Russia, akosov@cosmos.ru

KEYWORDS:
Moon, radio-science, Ka-band, mm-waves, receiver, gravitational field, mascon

INTRODUCTION:
Radio science experiment on Luna-26 orbiter implies gravitation field variation measurements by Doppler shift of reference signal sending from Ground station [1]. Figure 1 shows layout of the experiment.

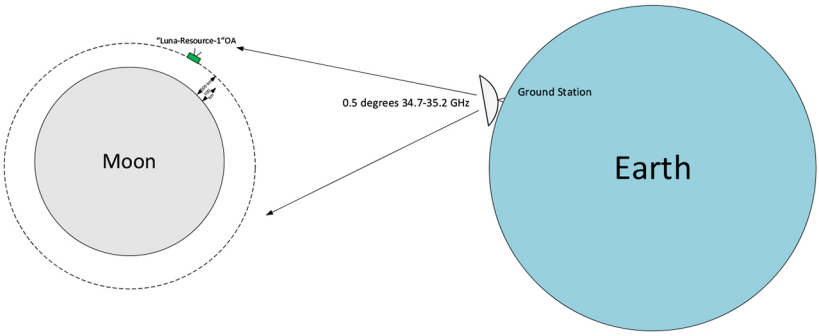


Fig. 1. Layout of the experiment

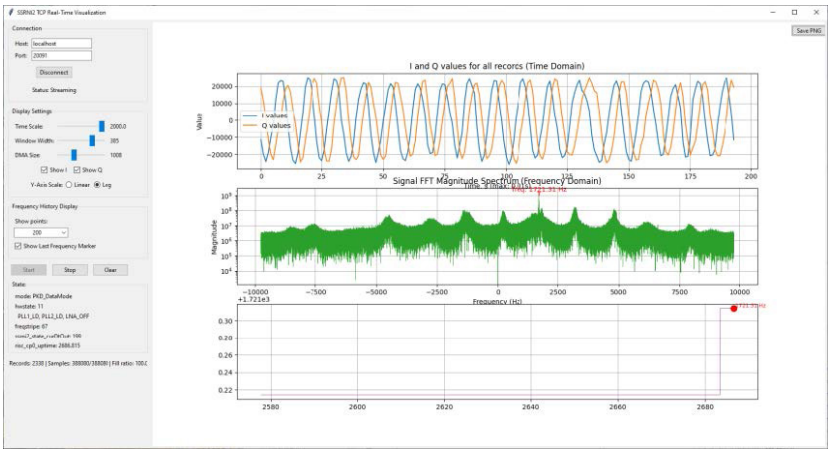


Fig. 2 — Results of instrument laboratory testing

Value of gravitation on Moon varies according to 162,5 ± 0,5 cm·s^{-2}, where 162,5 cm·s^{-2}— mean value of gravity acceleration; variation ±0,5 cm·s^{-2}. The objectives of the experiment are to measure the value of gravity with accuracy better when 0.01 cm·s^{-2} and to create the map of gravitation field strength on Moon's visible side with special resolution about 10 km.

The experiment will be conduct at frequency band 34.7–35.2 GHz. To measure acceleration strength with accuracy better when 0.01 cm/s^2 the accuracy of frequency measurement should be better than 0.01 Hz with integration time 10 s.

Results of laboratory instrument testing are shown on Fig. 2. During testing the reference signal at 34801 MHz was send to the instrument. The instrument converts frequency to low domain, digitizes and sends information to PC. Scientific information was treated by PC program. Data in time and frequency domains is shown. Bottom graph shows measured frequency.

The graph confirms that the accuracy of frequency measurement is better than 0,01 Hz under integration time 10 s.

CONCLUSIONS:

The radio science experiment onboard Luna-26 orbiter allows to measure the anomaly of near side Luna gravitation strength with accuracy better than 0.01 $cm \cdot s^{-2}$ and special resolution about 10 km.

REFERENCES:

[1] Kosov A. S., Roshkov L. S., Roshkov V. S. Ground Station for Radio Science Experiment with Ka-band Receiver (PKD) onboard of Luna-26 orbiter // 16MS3 Symp.: Abstr. Book. 2025.
[2] Kosov A. S., Roshkov L. S., Roshkov V. S. Moon's gravity field investigation by PKD instrument deployed on Luna-26 Orbiter // 15MS3 Symp.: Abstr. Book. 2024.

MULTIPARAMETER HARMONIC MODEL OF ASTEROID RYUGU USING DATA FROM THE "HAYABUSA2" SPACE MISSION

Y. A. Nefedyev[1], E. N. Ahmedshina[1], A. O. Andreev[2], M. V. Sergienko[1]
[1] *Kazan Federal University, Kazan 420008, Russia, star1955@mail.ru*
[2] *Kazan State Power Engineering University, Kazan 420066, Russia andreev.alexey93@gmail.com*

KEYWORDS:
asteroid Ryugu, modern space missions, multiparameter harmonic modeling

ABSTRACT
In this study, we investigated the surface structural characteristics of asteroid (162173) Ryugu. It is believed to contain the primordial material of the Solar System [1]. As it turned out, the surface of Ryugu is covered with rocks ranging in size from a decimeter to a meter, without deposits of fine-grained material. The asteroid experienced a previous period of strong solar heating caused by changes in its orbit [2]. During the implementation of the Japanese space mission "Hayabusa-2" a soil sample was collected from this asteroid, and organic molecules were found in the analyzed samples returned to Earth. In our work, an analysis of the optical data obtained by the Hayabusa-2 mission was carried out, and self-similar regions and distribution on the minor planet were determined based on harmonic modeling and fractal geometry methods. The theoretical conclusions proposed in the work [3] for the asteroid Bennu were confirmed, that in the case of Ryugu, at negative latitudes, the emission of particles from the surface of the minor planet occurs, followed by their return back to the asteroid in the form of an additional accumulation of matter in the equatorial region, which forms the observed bulge. Spectral-fractal analysis also showed that the resulting artifacts are explained by the fact that, under the influence of solar radiation, a stable spectrum of orbits of particles emitted by Ryugu is formed, which explains its diamond-shaped form, as in the case of Bennu. An original methodology was developed to examine airless small bodies of the Solar System, enabling the analysis of the spatial heterogeneity of their surface morphology. The conducted analysis revealed the presence of self-similar regions whose formation is associated with the action of similar evolutionary processes that governed the development of the asteroid's surface and internal structural features. The proposed methodology can be adapted for investigating the formation and evolutionary processes of other airless small bodies within the Solar System.

REFERENCES:
[1] Jaumann R., Schmitz N., Ho T.-M., Schröder S. E., Images from the surface of asteroid Ryugu show rocks similar to carbonaceous chondrite meteorites // Science. 2019. V. 365(6455). P. 817–820. DOI: 10.1126/science.aaw8627.
[2] Morota T., Sugita S., Cho Y., Kanamaru M. et al. Sample collection from asteroid (162173) Ryugu by Hayabusa2: Implications for surface evolution // Science. 2020. V. 368(6491). P. 654–659. DOI: 10.1126/science.aaz6306.
[3] McMahon J.W., Scheeres D.J., Chesley S.R. et al. Dynamical Evolution of Simulated Particles Ejected From Asteroid Bennu // J. Geophysical Research: Planets. 2019. V. 125. Article JE006229. DOI: 10.1029/2019JE006229.

LUNAR NEAR-SURFACE RADAR SOUNDING USING BALLISTIC HOPPER TRAJECTORIES

Changqing Ding, Fanyi Liu, Yihang Ding, Ge Dong
School of Aerospace Engineering, Tsinghua University, Beijing, China
dcq23@mails.tsinghua.edu.cn, dongge@tsinghua.edu.cn

KEYWORDS:
Lunar exploration, near-surface sounding, ballistic hopper, lunar regolith, synthetic aperture radar, subsurface tomography

INTRODUCTION:
High-resolution characterization of the lunar near subsurface is important for geological investigation, resource prospecting, and the selection of future exploration sites. Lunar penetrating radar has demonstrated its capability for investigating regolith structures and buried geological features during previous lunar missions [1, 2]. However, conventional rover-based observations are constrained by surface mobility, particularly in rough terrain, crater interiors, and permanently shadowed regions. Ballistic hoppers provide an alternative mobility concept for lunar exploration and may enable radar observations over regions that are difficult to access using conventional surface vehicles [3, 4].

METHODOLOGY:
This study investigates a lunar near-surface sounding concept using a ballistic hopper carrying a radar payload. Radar echoes acquired continuously along the hopping trajectory are synthesized to form a curved synthetic aperture. For a single hop, image reconstruction is performed using a backprojection approach that directly accounts for the nonlinear trajectory. Because the electromagnetic wave propagates across the vacuum–regolith interface, the propagation time is calculated by considering the dielectric properties of the lunar regolith and the corresponding refraction effect [5, 6]. For three-dimensional subsurface tomography, two multi-hop acquisition geometries are considered: sequential laterally displaced trajectories for systematic area coverage and intersecting trajectories for targeted observations of complex terrain.

RESULTS:
Numerical simulations demonstrate accurate focusing of subsurface point targets along a parabolic trajectory. The proposed multi-hop geometries also provide sufficient spatial diversity for three-dimensional reconstruction of distributed target positions. In addition, the feasibility of curved-trajectory synthetic aperture radar imaging is examined using a terrestrial experimental system. A 13–18 GHz MIMO radar and a controlled relative-motion platform are used to emulate the parabolic observation geometry. Metallic targets are successfully reconstructed with well-focused contours, confirming the capability of backprojection reconstruction for nonlinear trajectories.

CONCLUSIONS:
The results indicate that ballistic hopping can simultaneously provide terrain mobility and synthetic-aperture diversity for lunar subsurface radar observations. Compared with conventional rover-based surveys, the proposed concept may extend near-surface sounding to rough or otherwise inaccessible lunar regions. Multi-hop measurements further provide a potential pathway toward high-resolution subsurface tomography, making hopper-borne radar a promising concept for future lunar geological investigation and resource exploration.

REFERENCES:
[1] Su Y., Fang G., Feng J. et al. The preliminary results of lunar penetrating radar on board the Chinese Chang'E-3 rover // Proc. 15th Intern. Conf. Ground Penetrating Radar (GPR). 2014. DOI: 10.1109/ICGPR.2014.6970584.

[2] Zhang L. et al. A flat-bottomed buried crater and paleo-layered structures revealed at the Von Kármán Crater using Lunar Penetrating Radar // The Astrophysical J. Letters. 2024. V. 978. Article L2. DOI: 10.3847/2041-8213/ad9a4f.
[3] Middleton A., Paschall S., Cohanim B. Small lunar lander/hopper performance analysis // Proc. IEEE Aerospace Conf. 2010. DOI: 10.1109/AERO.2010.5446728.
[4] Yoshimitsu T. et al. Small hopping robot for lunar exploration // Proc. 74th Intern. Astronautical Congress (IAC). 2023. Article IAC-23-A3.2B.13.
[5] Dong Z., Fang G., Zhao D. et al. Dielectric properties of lunar subsurface materials // Geophysical Research Letters. 2020. V. 47. Article e2020GL089264.DOI: 10.1029/2020GL089264.
[6] Góes J. A., Lukin K. A., Oré G., Hernandez-Figueroa H. E. Refraction effect in SAR processing for focused subsurface tomography // Proc. SBMO/IEEE MTT-S Intern. Microwave and Optoelectronics Conf. (IMOC). 2023. DOI: 10.1109/IMOC57131.2023.10379707.

GROUND-BASED SPECTROSCOPIC DETECTION OF JUPITER-LIKE PLANETS ORBITING CONTACT BINARY STARS: MINIMUM INSTRUMENTAL REQUIREMENTS AND OBSERVATIONAL CONSTRAINTS

D. Rahbarmah
The National Organization for Development of Exceptional Talents (*SAMPAD*)
Iran, atilaporo@bsnp.info

KEYWORDS:
exoplanets, binary systems

ABSTRACT:
The spectroscopic detection of Jupiter-like planets orbiting contact binary stars remains one of the most demanding challenges in exoplanet research. The rapid rotation of contact binaries, severe rotational broadening of spectral lines, magnetic activity, and the composite spectra of both stellar components substantially limit the radial velocity precision achievable with conventional ground-based techniques [1]. Defining the minimum instrumental and observational requirements is therefore essential for assessing the feasibility of future radial velocity surveys targeting these systems.

A practical observational framework is presented to establish the minimum specifications required for the ground-based spectroscopic detection of Jupiter-like planets around contact binary stars. Considering the expected radial velocity amplitudes produced by planetary companions together with the intrinsic properties of W UMa-type systems, the analysis indicates that observations should employ a thermally stabilized high-resolution echelle spectrograph with a resolving power of approximately R=80,000…120,000, capable of delivering a long-term radial velocity precision better than 20 $m \cdot s^{-1}$. Reliable orbital solutions are expected to require spectra with signal-to-noise ratios exceeding 150 per resolution element, obtained using telescopes with primary mirror diameters of at least 4 m, while 6–8 m class facilities are expected to provide substantially improved performance for fainter targets. Because Jupiter-like planets in relatively wide circumbinary orbits are expected to produce the largest radial velocity signatures, reliable detection is expected to require spectroscopic monitoring spanning at least one complete planetary orbital cycle, which will typically correspond to 3–10 years of regular observations, depending on the orbital period of the companion.

Target selection is expected to play a decisive role in maximizing detection efficiency. Priority should be given to relatively bright contact binary systems ($V \lesssim 12$ mag) with well-determined orbital ephemerides, low levels of magnetic activity, and no significant evidence of active mass transfer or additional stellar companions capable of introducing long-term radial velocity variations. Observations should be conducted at high-altitude observatories offering excellent atmospheric stability and consistently good seeing conditions in order to minimize systematic errors and maximize the long-term stability of radial velocity measurements.

These instrumental and observational requirements provide a realistic baseline for future ground-based radial velocity searches for Jupiter-like planets orbiting contact binary stars. Under these conditions, Jupiter-like planets with relatively long orbital periods are expected to represent the most accessible targets for spectroscopic detection, whereas lower-mass planets are likely to remain beyond the sensitivity limits of current ground-based high-resolution spectroscopic facilities.

REFERENCE:

[1] Poro A., Paki E., Alicavus F., Michel R., Detailed Investigation of a W UMa Contact Binary with an Ultralow Mass Ratio and a Third Body as a Potential Merger Candidate // The Astrophysical J. 2026. V. 998. No. 1. Article108. DOI: 10.3847/1538-4357/ae3375.

SEARCHING FOR CIRCUMBINARY PLANETS AROUND CONTACT BINARY STARS: METHODOLOGY, CHALLENGES, AND DETECTION LIMITS

A. Rakian
The National Organization for Development of Exceptional Talents (*SAMPAD*)
Iran, atilap1981@gmail.com

KEYWORDS:
exoplanet, detection, binary system

ABSTRACT:
The search for circumbinary planets around contact binary stars remains one of the least explored topics in exoplanetary research. Although eclipse timing variations (ETVs) constitute a powerful indirect technique for detecting distant companions, their interpretation in contact binaries is complicated by several astrophysical processes capable of producing timing signatures similar to those expected from planetary companions. Establishing a robust methodology is therefore essential for distinguishing genuine planetary signals from other sources of orbital period variations.

A systematic framework based on eclipse timing analysis is outlined, beginning with the construction of high-quality O–C diagrams using long-term eclipse timing measurements collected from ground-based observations, space missions, and archival databases [1]. The analysis subsequently evaluates the Light-Travel Time (LTT) effect while accounting for alternative mechanisms, including magnetic activity cycles, mass transfer, angular momentum loss, secular orbital period evolution, and the presence of additional stellar companions. The combination of these diagnostics provides a more reliable assessment of potential circumbinary planet candidates and reduces the likelihood of false-positive detections.

The practical detection limits imposed by timing precision, observational baseline, and orbital configuration are also considered. Under current observational capabilities, eclipse timing analyses are expected to be most sensitive to massive circumbinary companions, including Jupiter-mass planets and low-mass brown dwarfs in relatively wide orbits, whereas lower-mass planets generally remain beyond the detection threshold.

This methodological framework provides a consistent strategy for future circumbinary planet searches around contact binary stars and establishes a foundation for improving the reliability of candidate identification through comprehensive evaluation of competing physical mechanisms [2].

REFERENCES:

[1] Poro A., Paki E., Alicavus F., Michel R., Detailed Investigation of a W UMa Contact Binary with an Ultralow Mass Ratio and a Third Body as a Potential Merger Candidate // The Astrophysical J. 2026. V. 998. N. 1. Article .108. DOI: 10.3847/1538-4357/ae3375.

[2] Bahraminasr M., Jafarzadeh S. J., Montazeri F., Poro A., Sarabi S., Evaluating the effect of four unknown parameters included in a latitudinal energy balance model on the habitability of exoplanets // Open Astronomy. 2020. V. 29. N. 1. P. 231–250.

COMPARISON OF THE METAL STRUCTURE IN THE MESOSIDERITES CATALINA 500 (A3) AND VACA MUERTA (B1)

E. V. Brusnitsyna[1], V. I. Grokhovsky[1], G. A. Yakovlev[1,2], E. A. Biryukova[1]
[1] *Institute of Physics and Technology, Ural Federal University Ekaterinburg 620002, Russia, jeka_bru@list.ru*
[2] *A. N. Zavaritsky Institute of Geology and Geochemistry UrB RAS Ekaterinburg 620110, Russia*

KEYWORDS:
meteorites, mesosiderites, Vaca Muerta, Catalina 500, Widmanstätten structure, cloudy zone, taenite, kamacite, tetrataenite

INTRODUCTION:
Mesosiderites are breccias consisting of variably sized silicate rock and metal fragments bound together by a silicate matrix. The silicates comprise igneous rock fragments showing different degrees of metamorphism [1]. The metal component is composed of Fe–Ni–Co alloys with variable composition, structure, and morphology. Classification is based on silicate composition (groups A, B, C) and metamorphic grade (petrologic types 0–4) [1–3].

EXPERIMENTAL:
Two mesosiderite fragments—Catalina 500 (group A1) and Vaca Muerta (group B3) — both found in the Chilean desert, were examined in this study. Samples were prepared using standard metallographic methods and etched with a 3% solution of HNO_3 in ethanol. Structure analyses were conducted using an Axiovert 40 MAT optical microscope and a ZEISS ΣIGMA VP scanning electron microscope with EDS.

RESULTS AND DISCUSSION:
Vaca Muerta contains more plagioclase and is less metamorphosed, whereas Catalina 500 is pyroxene-rich and shows higher shock metamorphism. The metal portion in both consists of kamacite (α-Fe(Ni,Co); 4–7.5 wt.% Ni) and taenite (γ-Fe(Ni,Co); 30–50 wt.% Ni). Both mesosiderites display high-Ni taenite particles with an "M-shaped" Ni profile. The bright rim around taenite is tetrataenite (ordered γ'-FeNi, 48–50 wt.% Ni), followed by a nanoscale cloudy zone (γ' + α) where Ni decreases from 48 to 30 wt.% with increasing distance from the rim. In Catalina 500, the cloudy zone is heterogeneous: some taenite grains contain coalesced tetrataenite particles, like those observed in the Seymchan pallasite after heating at 500 °C for 6 hours [4]. Well-preserved cloudy zones with high-Ni particles are also present.

The average particle size within the cloudy zone and the corresponding cooling rates (determined following [5]) are as follows: Vaca Muerta — 368 nm, 0,37 K/Myr; Catalina 500 — 254 nm, 0,9 K/Myr. Both samples contain troilite (FeS), occurring either as isolated grains or in association with metal. In Catalina 500, iron oxides are observed around metal grains and along cracks, which likely resulted from terrestrial weathering. In Vaca Muerta, a Widmanstätten structure is preserved in numerous metal grains.

CONCLUSIONS:
The metal grain structures differ between the two mesosiderites. The Widmanstätten pattern is absent in Catalina 500. The cloudy zone is preserved in both samples; however, Catalina 500 shows evidence of heating and partial dissolution of this zone in some metal grains. The metal phase in Vaca Muerta appears to have undergone less intensive thermal and shock metamorphism compared to that in Catalina 500, which may point to different conditions of material formation.

ACKNOWLEDGMENTS:
This work was supported by the Ministry of science and higher education of the Russian Federation, the project no FEUZ-2026-0009.

REFERENCES:

[1] Floran R. J. Silicate petrography, classification, and origin of the mesosiderites: Review and new observations // Proc. 9th Lunar and Planetary Science Conf. 1978. P. 1053–1081.
[2] Powell B. N. Petrology and chemistry of mesosiderites — I. Textures and composition of nickel-iron // Geochimica et Cosmochimica Acta. 1969. V. 33. No. 7. P. 789–810. DOI: 10.1016/0016-7037(69)90027-1.
[3] Kimura M., Sugiura N., Yamaguchi A., Ichimura K. The most primitive mesosiderite Northwest Africa 1878, subgroup 0 // Meteoritics and Planetary Science. 2020. V. 55. No. 5. P. 1116–1127. DOI: 10.1111/maps.
[4] Brusnitsyna E. V., Yakovlev G. A., Muftakhetdinova R. F., Grokhovsky V. I. Disappearance temperature of the cloudy zone structure in the Seymchan meteorite (PMG) // Meteoritics & Planetary Science. 2025. V. 60. Suppl. 1. Article A5251. DOI: 10.1111/maps.70033.
[5] Goldstein J. I., Scott E. R. D., Chabot N. L. Iron meteorites: Crystallization, thermal history, parent bodies, and origin // Chemie der Erde. 2009. V. 69. No. 4. P. 293–325. DOI: 10.1016/j.chemer.2009.01.002.

LABORATORY SIMULATION OF IONS AND NEUTRAL PARTICLES INTERACTION WITH DIFFERENT MATERIALS

D. A. Moiseenko, D. N. Limareva, A. I. Petukh, A. A. Matukhin
Space Research Institute RAS, Moscow, Russia

KEYWORDS:
ion scattering, plasma interaction with regolith, solar wind, energetic neutral atoms

INTRODUCTION:
The study of the processes of space plasma interaction of with various surfaces has great scientific importance for investigation of environment of different objects of Solar system. Moreover, processes and effects of plasma and energetic neutral atoms interaction with targets has practical importance for designing scientific instruments or spacecrafts. An example of the interaction of plasma with objects of the solar system is the reflection of the solar wind from the surface of the Moon - up to 20% of the solar wind protons can be reflected in the form of energetic neutral atoms. Detecting the flow of neutral atoms will allow us to study the properties of the surface depending on the structure, topography, and angle of illumination by the solar wind, solve the problems of localization of magnetic anomalies, and investigate the boundaries of these regions depending on the changing conditions of space plasma. Additionally, the processes of ion neutralization during interaction with a target can be used in ion mass analyzers in time-of-flight schemes.

ABSTRACT:
The paper presents the results of a study of the processes of scattering and reflection of ions and neutral atoms on targets made of various metals and with different surface treatments.

The targets were exposed under the flux of ions with different masses. During the experiment energies of ion flux has been changed in diapason ranging from 500 to 3000 eV.

During the experiment, the angle of exposition of the targets was varied, and the angular distributions of the particles, such as ions and neutral atoms, produced by the interaction of the initial beam with the targets, were recorded.

The data obtained from the experiment allowed us to assess the impact of the target structure and material on the processes of reflection and scattering of ions of various masses and energies, determine the expected trajectories of neutral atoms and ions, and evaluate the energy distribution of secondary and scattered particles.

The results of this study provide valuable insights for the design and modeling of instruments that utilize the conversion of ions into neutral atoms or the ionization of energetic neutral atoms.

Also evolution of this study will allow to simulate the processes of solar wind interaction with regolith in laboratory environment.

ON THE DYNAMIC STRENGTH OF METEORITES

R. F. Muftakhetdinova[1], S. V. Razorenov[2], A. S. Savinykh[2], G. V. Garkushin[2], I. V. Khomskaya[3], V. I. Grokhovsky[1]
[1] *Institute of Physics and Technology, Ural Federal University Ekaterinburg 620002, Russia, gizrozka91@bk.ru*
[2] *Federal Research Center of Problems of Chemical Physics and Medicinal Chemistry RAS, Chernogolovka 142432, Russia*
[3] *Mikheev Institute of Metal Physics, Ural Branch RAS Ekaterinburg 620108, Russia*

KEYWORDS:
meteorites, spall strength, high-speed deformation, shock waves

INTRODUCTION:
This work presents the results of a series of experiments on high-velocity shock-wave loading of meteoritic materials and an investigation of their strength properties. The objects of study comprised two fundamentally different types of meteorites: iron meteorites (Chinga, Sikhote-Alin, Seymchan, Dronino) and stony chondrites (Tsarev L5, Calama 009 L6, Chelyabinsk LL5, and Kainsaz CO3.2). The primary objective of the work was to determine the critical fracture stresses (spall strength) and the parameters of the elastic–plastic transition (Hugoniot elastic limit) for these materials under short-pulse loading conditions, with pressure amplitudes ranging from 0.5 to 11 GPa and strain rates on the order of 10^4–10^5 s^{-1}.

RESULTS AND DISCUSSION:
The experiments were conducted using a 50-mm-caliber pneumatic launcher. The deformation and fracture processes were recorded by means of a VISAR laser Doppler interferometer with nanosecond temporal resolution, which enabled the acquisition of complete velocity profiles for the free or impact surface of the specimens. Analysis of these profiles allowed determination of the elastic precursor amplitude, maximum compression stress, decay rate of the release wave, and spall pulse parameters. On this basis, the Hugoniot elastic limit (σ_{HEL}) and spall strength (σ_{sp}) were calculated using the acoustic approximation and the shock adiabat equation [1].

It has been demonstrated that the behavior of iron meteorites under shock compression is generally typical of metals and alloys: a two-wave configuration comprising an elastic precursor and a plastic wave is observed, while spall fracture exhibits features characteristic of metallic materials. The highest Hugoniot elastic limit ($\sigma_{HEL}\approx$1.6 GPa) was recorded for Sikhote-Alin meteorite samples, which is attributed to the high defect density and the presence of Neumann bands. The maximum spall strength (3.92–4.03 GPa) was measured for the ataxite Chinga, a value comparable to the strength level of high-strength structural steels. The Seymchan and Dronino meteorites exhibited lower values ($\sigma_{sp}\approx$2.5–3.1 GPa), with the Dronino samples showing a pronounced influence of internal defects and oxidation traces, which led to premature fracture and loss of surface reflectivity. It has been shown that an increase in shock compression intensity from 5.5 to 11 GPa does not lead to a substantial increase in the spall strength of iron meteorites, indicating that the strength properties reach saturation within this loading range. A comparative analysis with commercial N6 steel, which has a similar chemical composition, revealed that the spall strength of the meteorites is at the same level, and heat treatment of the steel alters its strength by only 10–15%. This finding confirms that thermal effects during atmospheric passage have an insignificant influence on the bulk properties of meteoritic material [1].

In the case of stony meteorites (chondrites), the situation is fundamentally different. These materials are highly heterogeneous, composite-like media composed of a silicate matrix, chondrules, metallic grains, sulfides, phosphides, and various types of discontinuities. Their spall strength varies by

more than an order of magnitude—from 20 MPa for the Chelyabinsk meteorite (light lithology) to 310 MPa for the carbonaceous chondrite Kainsaz. For the Tsarev and Calama 009 samples, the values range from 50 to 100 MPa. Such a wide scatter is explained by differences in the degree of cracking, porosity, size and type of chondrules, as well as the presence of shock-melt zones and secondary alterations. It is important to note that in the elastic deformation regime (at pressures up to 0.6–0.7 GPa), the spall strength of chondrites is higher than when the elastic limit is exceeded and plastic deformation develops, with fracture occurring at lower tensile stresses. This indicates a brittle fracture mode for stony meteorites, similar to that of rocks and ceramics. For comparison, experiments were conducted on pyroxenite — a mineral close in composition to the main phases of chondrites. Its spall strength in the elastic region was 65±15 MPa, which is close to the values for the Tsarev and Calama 009 meteorites but considerably lower than for Kainsaz. It has been demonstrated that even at low shock-wave amplitudes (below 1 GPa), stony meteorites undergo irreversible structural changes, a factor that must be taken into account when predicting their fragmentation in the atmosphere and during impacts [2, 3].

Of particular interest is the comparison of the obtained data with the challenges of counteracting asteroid–comet hazards. Many scenarios for the deflection or fragmentation of hazardous celestial bodies rely on explosive or kinetic impacts, the effectiveness of which critically depends on the material strength under high-velocity loading. The present results indicate that iron meteorites possess strength comparable to that of terrestrial steels, and their fragmentation would require significant energy expenditure. In contrast, stony chondrites are relatively weak objects prone to brittle fracture even at stresses of several tens of megapascals. However, the high internal heterogeneity of chondrites renders their behavior difficult to predict, necessitating further statistical studies on a larger number of samples

In conclusion, it should be noted that this work constitutes the first comprehensive comparative analysis of the dynamic strength of both iron and stony meteorites over a wide range of pressures and strain rates. The quantitative data obtained can be used for the validation of numerical models of meteoroid fragmentation, refinement of atmospheric break-up criteria, and evaluation of the effectiveness of various Earth defense strategies

REFERENCES:

[1] Razorenov S.V., Savinykh A.S., Garkushin G.V. et al. Spall strength and dynamic elastic limit of iron meteorites // Technical Physics. 2024. V. 69. No. 6. P. 803–809. DOI: 10.61011/TP.2024.06.58822.87-24.

[2] Borovička J., Spurný P., Shrbený L. Fragmentation of meteoroids in the atmosphere // The Astronomical J. 2020. V. 160. No. 42. P. 1–12. DOI: 10.3847/1538-3881/ab9608.

[3] Petrov D.V., Shubin O.N., Nogin V.N., Simonenko V.A. Asteroid Hazard from the Viewpoint of Weapon Physicists. Snezhinsk: RFYaTs–VNIITF Publishing House, 2023. 488 p. ISBN: 978-5-902700-50-4 (in Russian).

CONCENTRATED SOLAR-SIMULATED SINTERING OF LUNAR SOIL ANALOGUE VI-LH1

I. A. Agapkin[1], M. V. Khudorozhko[2], V. V. Khomenko[2]
[1] *Vernadsky Institute of Geochemistry and Analytical Chemistry RAS*
15331533@mail.ru
[2] *Bauman Moscow State Technical University*

KEYWORDS:
lunar soil analogue, ISRU, lunar highlands, solar sintering, lunar base

INTRODUCTION:
As early as the first lunar missions, solar radiation was considered by researchers as a virtually inexhaustible energy source for in-situ resource utilization (ISRU) on the Moon. The primary advantage of solar sintering lies in its directness and independence from complex electrical networks, as it utilizes concentrated natural light to fuse regolith particles [1]. Potentially, this method could become one of the most sustainable among all investigated technologies for constructing lunar bases, requiring only optical concentrators instead of power-consuming generators. For example, compared to conventional microwave sintering, solar sintering relies entirely on renewable energy and is suitable for large-scale surface hardening, although it is significantly affected by day-night cycles.

SAMPLE:
The experiments were conducted using VI-LH1, a lunar soil simulant developed at the GEOKHI RAS laboratory. This material is composed of crushed labradorite and closely matches the chemical-mineralogical and granulometric characteristics of highland lunar regolith [2].

EXPERIMENTAL PROCEDURE:
The experiment was conducted using a concentrated radiative-heating rig based on an array of ellipsoidal-reflector halogen lamps (USHIO, 150 W each), configured in three tiers for a total of 30 lamps and 6 kW of electrical power (boostable to 7 kW), producing a mean incident flux of 45.3 W/cm^2 and a radiative-equilibrium temperature of 1681 K. The VI-LH1 highland simulant was loaded into a corundum crucible and compacted by vibration and mechanical tapping to achieve natural packing without applied pressure. The crucible was seated in an Al_2O_3-SiO_2 thermal-insulation block (150×150×100 mm, pre-calcined at 1500°C), allowing cylindrical specimens up to 50 mm in diameter or rectangular specimens of 30×20×15 mm to be produced. Heating followed a closed-loop PID-controlled profile: a ramp of 500 K per 30 s to 1500 K, an isothermal hold for 20-30 min, and controlled cooling at 500 K per 30 s down to 500 K, with temperature continuously monitored by type K/B thermocouples and cross-checked with a SATIR D300 infrared camera.

RESULTS:
The resulting samples were investigated by optical microscopy and scanning electron microscopy (Fig. 1). Observations revealed a graded, three-zone structure through the specimen height: a nearly continuous, fully fused layer at the top (closest to the incident radiation), an intermediate zone with extensive grain fusion and largely obliterated grain boundaries, and a coarser-grained base region where solid-state sintering dominates. Large closed pores up to several millimeters across were observed, increasing in size with sintering temperature, most likely due to gas evolution from the melt and air entrapped during powder compaction.

The test results show a mean compressive strength of 12.4 MPa, which is equivalent to the M125 grade for fired construction brick (according to GOST 530-2012) [4]. Thermophysical characterization gave a thermal conductivity of 0.51 W·m·K^{-1}), a coefficient of thermal expansion of 2.41·10^{-6}°C^{-1}, and

a total hemispherical emissivity of 0.88–0.98, all comparable to or exceeding the corresponding values for conventional fired brick.

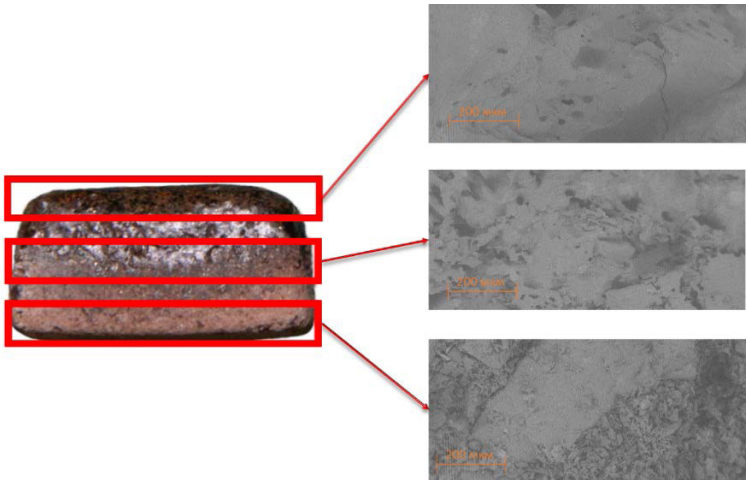


Fig. 1. Microstructure images of sintered lunar soil analogue sample.

CONCLUSION:

Preliminary estimates indicate that concentrated radiative sintering under these experimental conditions is capable of producing mechanically sound monolithic material without any applied pressure or binder, with a five-fold improvement in compressive strength over previously reported xenon-solar-simulator 3D-printed lunar bricks. However, the pronounced height-wise structural gradient observed in the sintered specimens remains the principal source of scatter in the mechanical data and the main remaining opportunity for improvement.

The next stage of research will focus on reducing the thermal gradient across the specimen thickness by refining the lamp configuration and heating profile, and on extending the present bulk-sintering approach to a moving-beam, layer-by-layer configuration. Further work will also include sintering under vacuum conditions, since all experiments reported here were performed in air, as well as testing on a larger sample population to reduce the statistical uncertainty associated with the observed structural gradient.

REFERENCES:

[1] Meurisse A. et al. Solar 3D printing of lunar regolith // Acta Astronautica. 2018. V. 152. P. 800–810.
[2] Mironov D. D. et al. Lunar Highlands Soil Simulant VI-LH1 for Testing Developing in-Situ Technologies and Large-Scale Experiments // 55th Lunar and Planetary Science Conference. 2024. V. 3040. Article 1948.
[3] Khudorozhko M.V., Prosuntsov P.V. Method for selecting the parameters of the working area of a concentrated radiation heating installation // Thermal processes in engineering. 2024. V. 16. No. 12. P. 547–558.
[4] GOST 530-2012 Ceramic brick and stone. General specifications. Standartinform, 2013. 32 p.

STUDY OF COMET 3I/ATLAS

A. Q. Vodniza, L. L. Chaves
University of Narino Observatory, Pasto, Colombia
aquijanov@gmail.com, leonardochaves83@gmail.com

KEYWORDS:
3I/Atlas, University of Narino Observatory, hyperbolic orbit, interstellar comet, thick disk of the Milky Way, orbital parameters, light curve

INTRODUCTION:

On July 1, 2025, the "ATLAS" system discovered a celestial body moving at high speed (60 kilometers per second) and following a hyperbolic orbit. "Its orbit is strongly hyperbolic, with eccentricity e=6.143, inclination i=175.1° and perihelion at q=1.357 au (solution reference JPL#21, data arc from 2025 May 22 to 2025 July 28)" [1]. These parameters indicated that it was an object originating from another solar system. To date, only three interstellar visitor objects have been discovered: Oumuamua (2017), Borisov (2019), and 3I/ATLAS. "The presence of interstellar objects in the solar system allows us to research matter created beyond the boundaries of our planetary system" [2]. From the Astronomical Observatory of the University of Nariño, just a few days after the discovery, we began monitoring 3I/ATLAS and continued until October 2/2025, when the comet was no longer observable from Earth. We resumed observations starting on November 8/2025 at dawn, after its perihelion passage. 3I/ATLAS may have originated in the thick disk of the Milky Way, where the oldest stars are found, and its age is estimated to be around 10 billion years — much older than our Sun. 3I/ATLAS is a comet with its own characteristics, some of them quite different from those of comets in our solar system, which is expected given its origin in a very distant region. For example, 3I/ATLAS showed cometary activity at a large distance of 4 AU. "The comets Borisov and ATLAS have both shown cometary activity at distances in which water sublimation is inefficient, suggesting that their activity must be powered by the sublimation of a nonwater substance like CO or CO2" [3]. Gases such as CO_2, CO, and H_2O, among other components, have been detected in its coma. In solar system comets, the proportion of water vapor is usually much higher than that of CO_2, which contrasts with what has been found in 3I/ATLAS. The nucleus of 3I/ATLAS may have a diameter of approximately 5 kilometers. It also has a rotation period of about 16.79±0.23 hours [4].

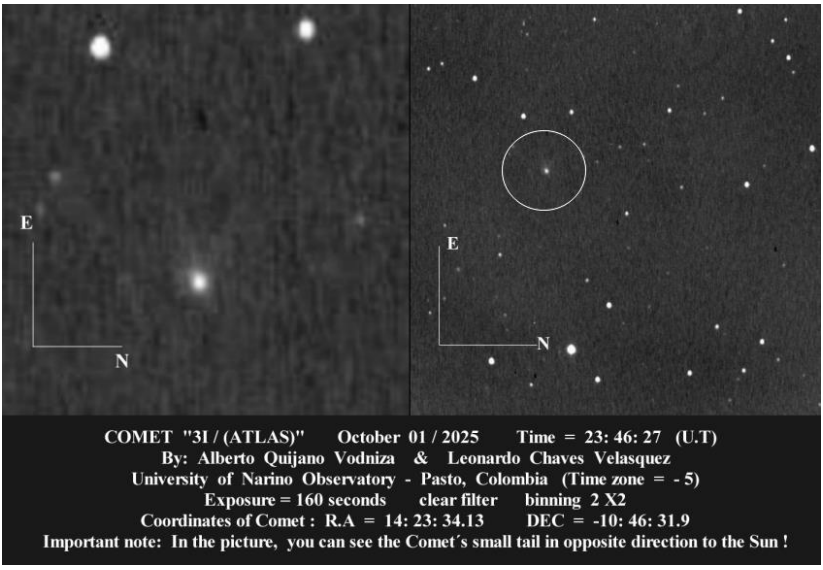


Fig. 1. Photo of the comet on October 1, 2025

"Over the three epochs of Tianwen-1 observations from 2025 September 30 to October 3, 3I showed a dust tail changing from a fan shape to a more elongated curving shape, centered near the antisunward direction. This morphological change was due to the change in the observing perspective of about 34° over the four days. The coma extends to about 10″ in the sunward direction" [5]. We also observed this phenomenon from our observatory (Fig 1).

During its approach to the Sun, and because it was on the opposite side of our star, it was not visible from ground-based observatories; however, it was observed by space telescopes and by robotic probes located on Mars.

METHODOLOGY:

The pictures were captured with the following equipment from our Observatory: CGE PRO 1400 CELESTRON (f/11 Schmidt-Cassegrain Telescope) and STL-1001 SBIG camera. The data were sent to Mars.

RESULTS:

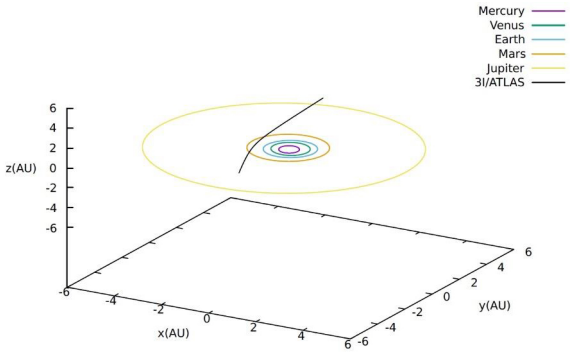


Fig. 2: Comet's orbit

N o t e : We worked until December 17, 2025. Figure 3 shows a photo taken on November 11, 2025.

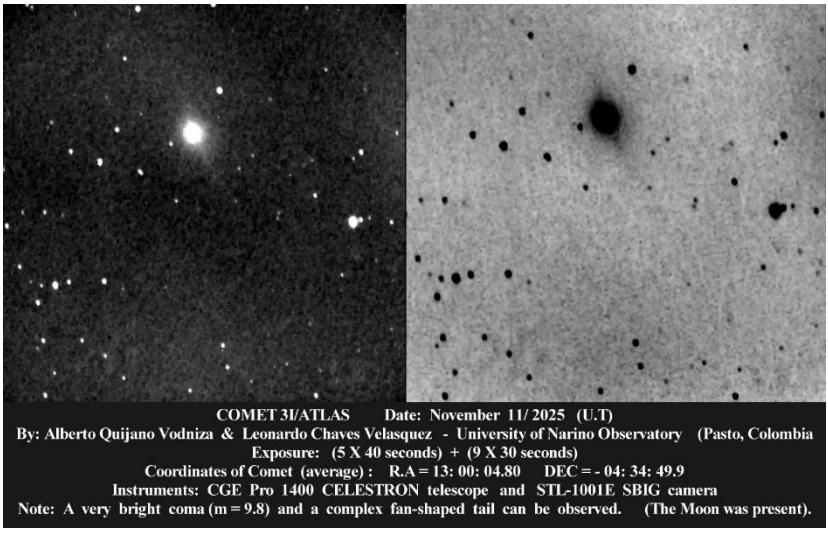


Fig. 3. Photo of the comet on November 11, 2025

The following orbital parameters were obtained: eccentricity=6.14666±0.00311, orbital inclination=175.11381±0.00059°, longitude of the ascending node=322.1412±0.0034°, argument of perihelion=128.017±0.015°, perihelion distance=1.35752±0.00047 A.U. The parameters were calculated based on 40 observations (Aug.06 to Dec.08/2025) with mean residual=0.26 arc seconds. The light curve was

also obtained. Taking into account the orbital parameters, the comet's approaches to several celestial bodies were calculated: Mars: 0.193661 AU (2025-10-03), Sun: 1.356441 AU (2025-10-29), Venus: 0.649443 AU (2025-11-03), Earth: 1.797606 AU (2025-12-19), Jupiter: 0.358547 AU (2026-03-16).

REFERENCES:

[1] Jewitt D. et al. Hubble Space Telescope Observations of the Interstellar Interloper 3I/ATLAS // The Astrophysical J. Letters. 2025. V. 990. No. 1. P. 1–8. DOI: 10.3847/2041-8213/adf8d8.
[2] Wesołowski M. et al. Photometric Analysis of the Interstellar Comet 3I/ATLAS During its Pre-perihelion Period // Publications of the Astronomical Society of the Pacific. 2026. V. 138. No. 2. P. 1–8. DOI: 10.1088/1538-3873/ae3eb5.
[3] Kareta Th. et al. Near-discovery Observations of Interstellar Comet 3I/ATLAS with the NASA Infrared Telescope Facility // The Astrophysical J. Letters. 2025. V. 990. No. 2. P. 5–6. DOI: 10.3847/2041-8213/adfbdf.
[4] de la Fuente Marcos R. et al. Assessing interstellar comet 3I/ATLAS with the 10.4m Gran Telescopio Canarias and the Two-meter Twin Telescope // Astronomy and Astrophysics. 2025. V. 700. No. L9. P. 1–7. https://doi.org/10.1051/0004-6361/202556439.
[5] Xin R. et al. Interstellar Object 3I/ATLAS Observed from Mars by China's Tianwen-1 Spacecraft // The Astrophysical J. Letters. 2026. V. 1003. No. 1. P. 9–10. DOI: 10.3847/2041-8213/ae61b3.

DUST PARTICLE CHARGING IN JOVIAN MAGNETOSPHERIC PLASMAS

S. I. Kopnin, S. I. Popel
Space Research Institute RAS, Moscow 117997, Russia, kopnin@cosmos.ru

KEYWORDS:
dusty plasma, photoelectric effect, charging of dust particles, kappa electron distribution

ABSTRACT:
There are regions in Jovian magnetosphere which are filled by dust particles. Among such regions there are those of Jupiter's rings. Dusty plasmas in this region and their properties are discussed. The results of calculations are presented as dependencies of dust particle charges on sizes of dusts under the conditions of different parts of Jovian magnetosphere. It is shown that in Jupiter's relatively dense and hot magnetospheric plasma, even in the presence of the photoelectric effect, dust particles acquire negative charges. It should be noted that under conditions where a kappa electron distribution is realized, higher negative charges of dust particles can be expected compared to the case where electrons are distributed according to Maxwellian distribution. These high charges can be explained by the presence of a "heavy" tail in the kappa distribution with a fairly large fraction of high-energy particles. It can also be noted that in the case of a power-law distribution over electron velocities, the equilibrium is established during quite long time.

PHYSICAL CHARACTERIZATION OF NEAR-EARTH ASTEROID (163899) 2003 SD220 FROM BISTATIC RADAR OBSERVATIONS

Yu. S. Bondarenko, D. A. Marshalov
Institute of Applied Astronomy RAS, Saint Petersburg, Russia
bondarenko@iaaras.ru

KEYWORDS:
near-Earth asteroids, Radar observations, Range-Doppler image

INTRODUCTION:
Asteroid 2003 SD220 was discovered on 2003 September 29 by the Lowell Observatory Near-Earth-Object Search (LONEOS) at Anderson Mesa Station. This Aten class near-Earth asteroid (NEA) is classified as a "Potentially Hazardous Asteroid" by the Minor Planet Center. Photometry reported by B. Warner [1] indicates a slow rotation period of 285±5 h and a light-curve amplitude of about 2 magnitudes, suggesting that this object is very elongated.

We have already eavesdropped the Goldstone radar echoes from 2003 SD220 during its close approach to the Earth in December 2018 using 32-m radio telescopes (RT-32) in Zelenchukskaya and Svetloe Observatory [2]. Obtained echo power spectra revealed that the asteroid is elongated with a length of at least 2.7 km. Our estimates of the circular polarization ratio and radar albedo were 0.22 and 0.17 suggesting an S-class NEA. The next close approach of 2003 SD220 to Earth within 0.0363 au (14.1 lunar distances) occurred on 2021 December 17. At that time, we also had the opportunity to join the bistatic radar observations of 2003 SD220 in cooperation with the Goldstone planetary radar. Here we present radar observations of 2003 SD220 and a physical characterization derived from 2021 radar data.

RADAR OBSERVATIONS AND RESULTS:
We observed 2003 SD220 on 2021 December 4, 9, and 21 using Goldstone 70-m radar (DSS-14) to transmit and 32-m radio telescope (RT-32) in Badary observatory to receive echoes from the asteroid. December 4 and 9, DSS-14 transmitted continuous wave (CW) signal at fixed frequency of 8560 MHz and December 21 DSS-14 used a linear frequency modulation with the bandwidth of 20 MHz. As a result, we obtained CW echo power spectra for both December 4 and 9 observation sessions as well as Range-Doppler radar image of asteroid 2003 SD220 for December 21.

The broadening of the obtained spectra corresponds to an asteroid of at least 570 meters on December 4 and at least 1140 meters on December 9, assuming that its rotation period is 285 h. These results characterize an object with a noticeably elongated shape, which is consistent with radar observations of 2018. By integrating the CW spectra, we obtained a radar albedo of 0.22, suggesting C- or S-class NEA with a less radar bright surface than other asteroids [3]. We also estimated the circular polarization ratio to be 0.16, which indicates that the surface of 2003 SD220 at decimeter scales is lower than that for the majority of NEAs with known circular polarization ratios [4].

The Range-Doppler radar image of asteroid 2003 SD220 obtained on December 21 is shown in Fig. 1. In this image radar illumination is from the top, the vertical axis shows range, increases towards the bottom, and the horizontal axis shows Doppler frequency, increases to the right. For the used modulation parameters, the range resolution of the obtained radar image is about 7.5 m per pixel. The resolution along the Doppler frequency axis was determined by the 500 seconds integration time of the echo signal and corresponds to 0.02 Hz. The image is normalized so that the noise has a zero mean and a standard deviation of one. The visible range extent of the asteroid in the radar image is about 800×2500 m, confirming the asteroid's elongated shape. The image also clearly shows the asteroid's fairly

smooth surface, without any characteristic irregularities, and the absence of large piles and individual boulder fragments. Obtained results contribute to a better understanding of the physical properties, surface structure, and compositional class of 2003 SD220, which is essential for assessing its potential impact hazard and for planning future exploration missions.

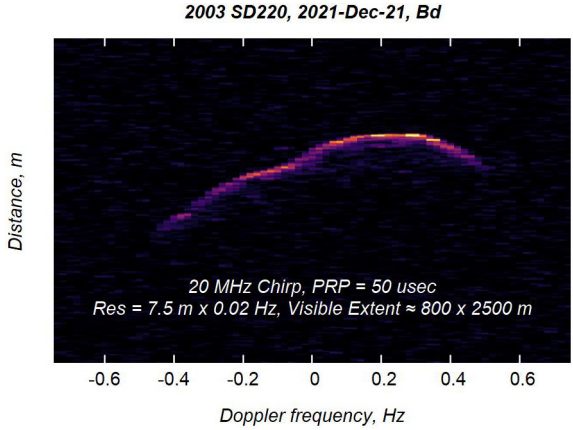


Fig. 1. Range-Doppler radar image of asteroid 2003 SD220 obtained from bistatic observations using the DSS-14 radar in Goldstone and the RT-32 radio telescope at the Badary Observatory on 2021 December 21

ACKNOWLEDGMENTS:
We thank L. A. Benner, S. Naidu, M. Brozovic and the technical staff at Goldstone for their assistance in conducting radar observations of the 2003 SD220.

REFERENCES:
[1] Warner B. D. Near-Earth asteroid lightcurve analysis at CS3-Palmer Divide Station: 2015 October-December // Minor Planet Bull. 2016. V. 43. P. 143–154.
[2] Bondarenko Yu.S., Marshalov D. A., Vavilov D. E., Medvedev Yu.D. Radar observations of near-Earth asteroid 2003 SD220 // EPSC Abstracts. 2019. V. 13. EPSC-DPS2019-554-1.
[3] Margi C., Nolan M. C., Ostro S. J., Giorgini J. D. A radar survey of main-belt asteroids: Arecibo observations of 55 objects during 1999–2003 // Icarus. 2007. V. 186. P. 126–151. DOI: 10.1016/j.icarus.2006.08.018.
[4] Benner L. A., Ostro S. J., Margi C., Nolan M. C. et. al. Near-Earth asteroid surface roughness depends on compositional class // Icarus. 2008. V. 198. P. 294–304. DOI: 10.1016/j.icarus.2008.06.010.

PHOTOMETRIC OBSERVATIONS OF COMET C/2022 N2 (PANSTARRS)

E. S. Bakanas[1], G. I. Kokhirova[2], V. V. Emel'yanenko[1], A. P. Kartashova[1], V. B. Puzin[1], F. J. Rakhmatullaeva[2], S. A. Naroenkov[1]
[1] *Institute of Astronomy RAS (INASAN), Moscow, Russia, oterma@yandex.ru*
[2] *Institute of Astrophysics of the National Academy of Sciences of Tajikistan, Dushanbe, Tajikistan*

KEYWORDS:
distant comets, C/2022 N2 (PANSTARRS), BVRI photometry, light curves, colour indices, Afρ, dust production

INTRODUCTION:
Photometric observations of distant comets are important for studying the mechanisms of cometary activity at large heliocentric distances, where water-ice sublimation does not yet play a dominant role, while the contribution of hypervolatile species and dust becomes particularly significant. Homogeneous observational series obtained with several instruments and reduced to a common photometric system make it possible to compare the evolution of brightness, colour characteristics and dust activity of individual objects, including distant comets.

Comet C/2022 N2 (PANSTARRS) is of particular interest because it was already active at a very large heliocentric distance. Discovery images obtained with the 1.8-m Pan-STARRS2 telescope on 4 July 2022 showed a condensed coma and a straight 3″ tail when the comet was about 9.5 au from the Sun, and prediscovery detections extend back to 2 June 2022 [1, 2]. The comet moves on a near-parabolic orbit with a perihelion distance of q=3.83 au (perihelion on 31 July 2025), and the JPL orbital solution includes a non-gravitational acceleration modelled with a CO-driven activity law [3]. Thus the comet shows activity over a wide range of heliocentric distances, from ~9.5 au at discovery to ~4 au after perihelion, i.e. largely beyond the zone where water-ice sublimation is efficient.

OBSERVATIONS AND DATA REDUCTION:
We present results of multicolour CCD photometry of the long-period comet C/2022 N2 (PANSTARRS) obtained on 11 nights between September 2025 and January 2026 at three observatories: Sanglokh Observatory, the Kislovodsk Mountain Astronomical Station of INASAN and the Core Shared Research Facility "Terskol Observatory" of INASAN. The observations in the BVRI filters of the Johnson–Cousins system cover heliocentric distances of 3.84–4.06 au and phase angles from 14.3° to 2.6° on both sides of opposition. The data were reduced using the comet module of the ASTREA software package developed by the authors. The package maintains a unified registry of FITS frames and observing nights for all observatories, which ensures homogeneous processing of data obtained with different telescopes. Its comet module includes tools for analysing the structure of the coma and tail and for fitting phase curves. The colour indices and the dust production parameter Afρ were estimated. At r≈3.8 au, Afρ in the R band is several hundred centimetres (approximately 400–1000 cm for $\rho \approx (1\ldots2)\cdot10^4$ km, not corrected for the phase angle), which is comparable to the values reported for other active distant comets at r≈4…5 au [4–6] and indicates noticeable dust activity of the comet.

DISCUSSION:
To date, comet C/2022 N2 (PANSTARRS) has been mentioned mainly in brief discovery announcements [1, 2] and observational databases, without a detailed photometric analysis. The results are of interest both for characterising the comet itself and for placing it in the context of other objects: they expand the sample of photometrically studied distant comets and allow its activity parameters, colour indices and dust production to be compared with those of other small bodies of the Solar System.

ACKNOWLEDGMENTS:
This work was supported by the Ministry of Science and Higher Education of the Russian Federation, grant No. 075-15-2026-236.

REFERENCES:

[1] Weryk R., Nakano S. Comet C/2022 N2 (PANSTARRS) // Central Bureau Electronic Telegrams. 2022. No. 5148 / ed. Green D.W.E. https://tamkin3.eps.harvard.edu/iau/cbet/005100/CBET005148.txt.
[2] Minor Planet Center. MPEC 2022-N48: Comet C/2022 N2 (PANSTARRS) // Minor Planet Electronic Circulars. 2022, 8 July. https://minorplanetcenter.net/mpec/K22/K22N48.html.
[3] JPL Small-Body Database Lookup. C/2022 N2 (PANSTARRS), orbital solution JPL#96. 2026. https://ssd.jpl.nasa.gov/tools/sbdb_lookup.html#/?sstr=C/2022%20N2.
[4] Kulyk I., Rousselot P., Korsun P. P., Afanasiev V. L., Sergeev A. V., Velichko S. F. Physical activity of the selected nearly isotropic comets with perihelia at large heliocentric distance // Astronomy and Astrophysics. 2018. V. 611. Article A32. DOI: 10.1051/0004-6361/201731529.
[5] Ivanova O. et al. Photometry, spectroscopy, and polarimetry of distant comet C/2014 A4 (SONEAR) // Astronomy and Astrophysics. 2019. V. 626. article A26. DOI: 10.1051/0004-6361/201935077.
[6] Ivanova O., Luk'yanyk I., Moreno F., Bauer J. M., Rosenbush V. Photometry and spectroscopy of distant comet C/2014 N3 (NEOWISE) // Astronomy and Astrophysics. 2025. V. 697. Article A188. DOI: 10.1051/0004-6361/202453286.

HARDWARE–SOFTWARE COMPLEX OF THE CHECK-OUT EQUIPMENT FOR GROUND TESTING OF THE SAMPLING DEVICE OF THE LUNA-27 LUNAR LANDER

E. O. Tarasov[1,2], M. I. Mokrousov[1], A. A. Anikin[1]
[1] *Space Research Institute RAS, Moscow 117997, Russia*
taras_buulba@vk.com
[2] *National Research Nuclear University "MEPhI"* (*NRNU MEPhI*)
Moscow 115409, Russia

KEYWORDS:
Luna-27, sampling device, lunar regolith, check-out equipment, ground testing, control unit, operator software, telemetry

ABSTRACT:
The development of spaceflight hardware necessarily includes a stage of ground experimental verification, during which the electrical, functional, and information characteristics of a flight instrument are demonstrated to comply with the established technical requirements prior to its installation on the spacecraft. This stage is of particular importance because, once the instrument has been integrated into the spacecraft, direct access to its individual circuits and subsystems becomes severely limited; their operability must therefore be confirmed in advance on a dedicated test bench. Such verification is performed by means of specialized check-out equipment, which reproduces the electrical and information interfaces normally provided by the onboard systems and ensures reliable registration of the test progress.

The present work addresses this problem for the sampling device (SD) of the Luna-27 (Luna-Resurs-1) lander — a key element of the Russian lunar exploration program aimed at studying the surface and the near-surface layer of the lunar regolith in the south polar region of the Moon [1]. The sampling device is intended for the acquisition of lunar regolith samples and their delivery to the onboard analytical instruments [2]. To support its ground test campaign, dedicated check-out equipment (CE) has been developed at the Space Research Institute of the Russian Academy of Sciences.

The check-out equipment constitutes a unified software-controlled complex built around a control unit, programmable power supplies, and operator software. It provides electrical powering of the device under test, simulation of command actions of the onboard systems, command and telemetry exchange with the SD electronics unit, monitoring of the onboard temperature sensors, control of the heater circuits, and time-tagged recording of all test events. The control unit hardware implements the measurement and switching functions of the complex, while the operator software integrates the control of all test bench components into a single operator workstation, providing command generation, telemetry acquisition and display, real-time visualization of the measured parameters, and registration of the test data in a form suitable for subsequent analysis.

DEVELOPMENT OF FUNGAL BIOTECHNOLOGIES FOR LUNAR EXPLORATION

D. D. Barbashin, A. R. Belolipetskaya, I. N. Gromyak, E. N. Slyuta
Vernadsky Institute of Geochemistry and Analytical Chemistry RAS, Moscow, Russia, turchinskaya@geokhi.ru

KEYWORDS:
in situ resource utilization, ISRU, bioleaching, mycotecture, biocomposites, space biotechnology

ABSTRACT:
Human exploration of the Moon and the establishment of a permanent lunar base will require efficient technologies for in situ resource utilization (ISRU). The transportation of construction materials and industrial resources from Earth remains economically and logistically challenging, making local resource processing a key objective of future lunar missions.

This work considers two complementary biotechnology approaches based on filamentous fungi. The first is the biological extraction of valuable elements from lunar regolith (bioleaching), which could provide access to iron, aluminum, titanium, rare-earth elements, and other strategic resources. The second is the production of mycelium-based biocomposites ("mycotecture"), where fungal mycelium acts as a natural binder for regolith particles, enabling the fabrication of lightweight construction materials directly on the lunar surface.

Both approaches share common methodological principles, including the delivery of fungal spores from Earth, cultivation under controlled conditions, and interaction with lunar regolith simulants. Their combination offers the possibility of partially unified biotechnological infrastructure for future lunar bases, including common cultivation systems, bioreactors, and experimental validation protocols.

Current research is focused on selecting candidate fungal strains with high bioleaching potential and the ability to colonize mineral substrates while maintaining biological safety. Particular attention is paid to Aspergillus tubingensis, whose close relative, A. niger, is widely used in terrestrial bioleaching technologies. Future studies will evaluate fungal growth on lunar regolith simulants, survival under simulated space environmental factors, adhesion to mineral particles, and the mechanical properties of mycelium-based biocomposites.

The proposed integrated biotechnology platform may contribute to reducing the mass and cost of resource supply for future lunar infrastructure and represents a promising direction for sustainable ISRU systems supporting long-term human presence on the Moon.

THE VAMP EXPERIMENT: MAGNETIC FIELD MEASUREMENTS ONBOARD THE VENUS-D ORBITER

S. V. Kulikov[1], A. A. Skalsky[1], M.Yu. Korensky[2], A. F. Zarutskiy[2], V. A. Stiagkin[2]

[1] *Space Research Institute RAS, Moscow, Russia, sv_kulikov@cosmos.ru*

[2] *Physical Instrumentation Center of the Institute of General Physics RAS Moscow, Troitsk, Russia, miklekor@pic.troitsk.ru*

KEYWORDS:
Venus, induced magnetosphere, ionosphere, magnetic ropes, fluxgate magnetometer

ABSTRACT:
Venus, as a planet with no intrinsic magnetic field, presents a pure case of direct interaction between the planetary ionosphere/atmosphere and the solar wind. The so-called "induced magnetosphere" of Venus is built by interplanetary magnetic field lines draping around the planet, penetrating into the ionosphere, then slipping to the Venusian nightside and forming the magnetic wake.

Magnetic field measurements carried out onboard spacecraft orbiting Venus aim to investigate the physical nature of specific regions and boundaries in the Venusian environment (foreshock, bow shock, magnetosheath, ionopause, and the neutral sheet in the wake). The magnetic holes and ropes inherent to the induced magnetosphere are of prime interest.

Magnetic field observations deep within the ionosphere will allow the investigation of whistler waves, which possibly originate from electrical discharges in the planetary atmosphere.

The magnetic field experiment (VAMP) proposed for installation onboard the Venus-D orbiter, consists of two fluxgate magnetometers. Both instruments allow measurements of the magnetic field vector (with each component at ±1000 nT) with a resolution of 128 vectors/s. The prototype is shown in the figure below.



Fig. 1. Prototype of the VAMP instrument: the LPMS-LG magnetometer designed for a Lunar orbiter

FEASIBILITY OF REACHING EXTREME TRANS NEPTUNIAN OBJECTS USING MULTI-PLANET GRAVITY ASSISTS

Zubko V. A., Sukhanov A. A., Fedyaev K. S., Eismont N. A., Belyaev A. A.
Space Research Institute RAS, Moscow 117997, Russia, v.zubko@cosmos.ru

KEYWORDS:
Sedna, mission architecture, trajectory optimization, multiple gravity assists

INTRODUCTION:
Exploring extreme trans-Neptunian objects (ETNOs) such as Sedna is critical for understanding the early dynamical evolution of the Solar System. However, direct transfers to these objects cannot be realized using current launch capabilities due to extreme distances (>75 AU) to the objects as well as their long orbital periods. This study investigates the possibility of sending a small (≤250 kg) separable probe to ETNOs using inner- and outer-planet gravity assists, deployed as a piggyback payload on a flagship outer-planet mission. The total flight time is limited by 30 years, and the ΔV budget is constrained to values compatible with current launch vehicles and onboard propulsion systems.

METHODS:
Transfer trajectories are computed using the patched-conic approximation with JPL DE430 ephemerides. The analysis covers direct transfers, Venus–Earth–Earth–Jupiter and Venus–Earth–Earth–Jupiter–Neptune gravity-assist sequences (EVEEJ and EVEEJN, respectively), the Solar Oberth manoeuvre, and multi-target scenarios with a separable probe. Repeatability of launch windows is estimated from the synodic periods of the relevant outer-planet alignments. The radiation environment during close Jupiter flybys is modelled with SPENVIS to define shielding requirements, and the operational lifetime of radioisotope thermoelectric generators sets a 50-year mission limit. Target ETNOs are selected from the JPL Small-Body Database based on constraints on perihelion distance, semi-major axis, absolute magnitude, and mean anomaly.

RESULTS:
The EVEEJ and EVEEJN schemes significantly reduce the required ΔV compared with direct transfers. For a launch in 2039, a trajectory to Sedna requires a total ΔV of ~4.5 km/s and a time of flight of 27.2 years (Table 1). The same window provides access to several other ETNOs, including 2012 VP_{113} and 2013 SY_{99}, with ΔV values between 3.98 and 4.93 km/s (Table 1). Multi-target mission scenarios are shown to be feasible using a probe separation impulse of ≤0.5 km/s. Radiation modelling indicates that an aluminium shield 5–10 mm thick could limit the total ionising dose to below 100 krad for Jupiter flyby altitudes greater than $5R_J$.

Table 1. Optimal trajectories to selected ETNOs using the EVEEJ scheme (the 2039–2040 launch window)

Object	TOF (yr)	Launch date	Total ΔV (km/s)	Jupiter flyby altitude (km)
Sedna	27.2	19.09.2039	4.500	93610
2012 VP_{113}	24.0	15.09.2039	4.930	19476
2013 SY_{99}	19.3	29.07.2039	4.040	5072
2013 FT_{28}	27.2	28.12.2040	3.978	262199

CONCLUSIONS:
The analysis indicates that a dedicated flyby of Sedna or another sednoid could be achieved within 30 years using Venus–Earth–Earth–Jupiter gravity assists, with a total ΔV of approximately 4–5 km/s. The 2039 launch window appears particularly favourable for several high-perihelion trans-Neptunian objects. A small separable probe could be integrated into planned

missions such as Neptune Odyssey or IHP-2, with limited additional mission complexity, enabling a potential first close exploration of a sednoid. The radiation environment at Jupiter necessitates dedicated shielding provisions consistent with current spacecraft design practice, and ^{238}Pu RTGs are expected to provide sufficient power over the required 50-year mission duration. Future work should refine the trajectories with full ephemeris optimization and further assess aerogravity-assist potential.

LOW-ENERGY MULTI-ASTEROID MISSIONS USING RESONANT ORBITS, VENUS GRAVITY ASSISTS AND SPLIT-PROBE DEPLOYMENT

Zubko V. A., Pupkov M. V., Chernenko O. S., Fedyaev K. S., Eismont N. A.
Space Research Institute RAS, Moscow 117997, Russia, v.zubko@cosmos.ru

KEYWORDS:
resonant orbit, gravity assist maneuver, Venus, space mission, asteroids exploration

INTRODUCTION:
Asteroid exploration is central to understanding Solar System formation, ensuring planetary defence, and resource prospecting. A single launch capable of visiting multiple asteroids substantially increases scientific return per mission, but traditional direct-transfer trajectories require large propellant budgets. We present a mission design framework that exploits a Venus gravity assist not only to reduce launch energy but also to deploy multiple small probes during the planetary approach. By taking advantage of the shared incoming hyperbolic excess velocity and the geometry of resonant heliocentric orbits, the separation impulses are reduced to the order of metres per second, enabling a single carrier to survey several asteroids with negligible additional propellant cost. The approach is supported by a fast two-stage procedure of candidate pre-selection that identifies a set of asteroids reachable from a single resonant arc.

METHODS:
The trajectory design is formulated as a two-stage optimization problem. First, an analytical minimum orbit intersection distance (AMOID) scan over the resonant-orbit manifold rapidly screens thousands of asteroids — for example, Potentially Hazardous Asteroids (PHAs) — and selects those approaching the post-flyby trajectory within a prescribed threshold. Second, a global-local optimiser minimises the total velocity increment Δv (which includes a launch impulse, deep-space corrections, and asteroid-encounter manoeuvres) while satisfying gravity-assist turn-angle constraints derived from the minimum allowable value of a flyby altitude at Venus.

The proposed mission employs a split-probe architecture (Fig. 1). Following the Earth–Venus transfer, the carrier releases probes along the incoming asymptote prior to periapsis passage, at distances sufficiently large to limit the required separation impulses. All probes share the incoming hyperbolic excess velocity $\bar{v}_\infty^-$; each probe is directed to a certain asteroid by imparting a small separation impulse Δv_{sep}, computed from the difference between the required outgoing asymptotes. A parametric study shows that for a typical Earth–Venus transfer with $v_\infty \approx 5$ km/s, Δv_{sep} falls below 0.1 km/s if the separation occurs at distances beyond 10×10^6 km. We consider a total mission objective function as a total characteristic velocity required for the carrier releasing *M* probes at the first Venus flyby. This function can be written as

$$J = \Delta v_0 + \Delta v_{\pi,\mathrm{Venus}} + \sum_i \left(\Delta v_{\mathrm{sep},i} + \Delta v_{\mathrm{ast},i} + \Delta v_{\pi,i} \right),$$

where Δv_0 is the Earth-departure impulse (shared across all probes), Δv_π, accounts for any powered correction at the carrier's Venus flyby, and $\Delta v_{sep,i}$, $\Delta v_{ast,i}$, $\Delta v_{\pi,i}$ are, respectively, the separation, asteroid-encounter, and Venus-return impulses for the *i*-th probe. The two-stage pre-selection ensures that only feasible asteroid candidates are passed to the optimiser, reducing computational cost by more than three orders of magnitude relative to a brute-force Lambert scan.

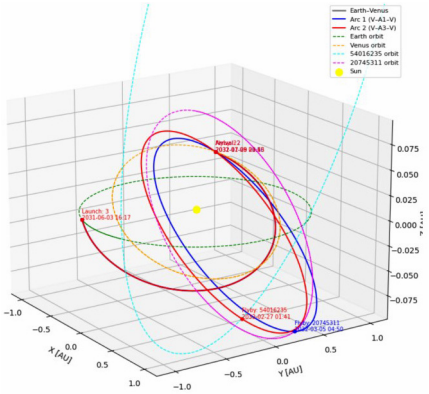


Fig. 1: Heliocentric trajectory of the split-probe mission. The carrier releases two probes after the Venus flyby; each probe visits a distinct PHA and returns to Venus.

RESULTS:

The methodology is demonstrated using a 2031 Venus launch window. A single carrier departs Earth, performs a Venus flyby, and releases two probes along the incoming approach trajectory. The probes are directed to asteroids 20745311 (2002 HP11) and 54016235 (2020 FR1), respectively; both probes return to Venus after the encounters. The complete mission timeline is given in Table 1 and the trajectory is presented in Fig. 1. The total mission cost Δv is 3.688 km/s, with the Earth-departure burn constituting the dominant contribution; probe separation requires less than 0.6 m/s per probe, confirming that the split-probe architecture imposes a negligible propellant penalty. The pre-selection algorithm identified the asteroid pair from a catalogue of 2500 PHAs in under one minute on a standard workstation.

Table 1. Optimal split-probe mission for the 2031 Venus window

	Launch	E–V leg	Probe 1	Probe 2
Date/Duration	2031-06-03, 13:57	176.3d	90.4*d* (to asteroid)/134.4*d* (to Venus)	94.6*d* (to asteroid)/130.2*d* (to Venus)
Target (SPKID)	–	–	20745311	54016235
Total Δ*v*			3.688 km/s	

The same two-stage framework can generate more extended tours. For reference, a 4.8-year mission achieving seven asteroid flybys with a launch Δ*v* of 3.581 km/s (total 3.802 km/s) was obtained when probes are not separated but the carrier chains multiple Venus resonances. Therefore, the split-probe concept represents a natural extension of the resonant-arc architecture: it trades a marginal increase in total Δ*v* for a multiplicative increase in the number of asteroids visited per launch.

CONCLUSIONS:

The split-probe Venus gravity-assist architecture provides an effective mission design approach for Solar System exploration: a single launch can survey multiple asteroids by releasing independent probes at the first planetary encounter, with separation costs at the meter-per-second level. The combination of fast AMOID pre-selection and global-local optimisation makes the design systematic and computationally tractable. The generated reference trajectories are suitable for preliminary mission analysis and can be adapted to study specific asteroid populations, including Venus co-orbitals and PHAs.

ACKNOWLEDGMENTS:

Vladislav Zubko is receiving funding from the Russian Scientific Foundation, project No. 25-79-00042.

LOW-ALTITUDE RAPID TERRAIN EXPLORATION: A PORTABLE JETPACK PLATFORM WITH ADAPTIVE PROPULSION CONTROL

Jiangchao Yuan, Ge Dong
School of Aerospace Engineering, Tsinghua University, Beijing, China
yuanjc24@mails.tsinghua.edu.cn

KEYWORDS:
terrain exploration, portable jetpack, micro-turbojet engine, adaptive control, flight dynamics

ABSTRACT:
Low-altitude portable flight systems are of critical importance for earth exploration missions, offering transformative potential for rapid terrain surveying, geological mapping, and environmental monitoring in areas that are difficult to access by ground vehicles or foot travel. This paper presents the design, mathematical modeling, and adaptive control of a jetpack-type platform intended for such terrestrial exploration tasks, with emphasis on its twin-micro-turbojet propulsion system.

A nonlinear component-level model of the micro-turbojet engine is established in MATLAB/Simulink, capturing the steady-state and transient thermodynamic behavior of the inlet, compressor, combustor, turbine, and exhaust nozzle. The common working equations are solved iteratively using the Newton-Raphson [1] and improved Euler methods[2], yielding both steady-state and dynamic models that describe the engine's internal working characteristics across a wide speed range.

To overcome the significant nonlinearity and parameter variation inherent in small turbojet engines, two adaptive control strategies: single-neuron adaptive PID [3] (SNA-PID) and Lyapunov-based model-reference adaptive control [4] (MRAC) are implemented and compared against classical incremental digital PID. Simulation results demonstrate that both adaptive schemes substantially improve command-tracking performance in terms of rise time, settling time, and overshoot elimination. Notably, the SNA-PID controller exhibits superior transient response and self-tuning capability throughout the entire speed envelope, outperforming both classical PID and MRAC.

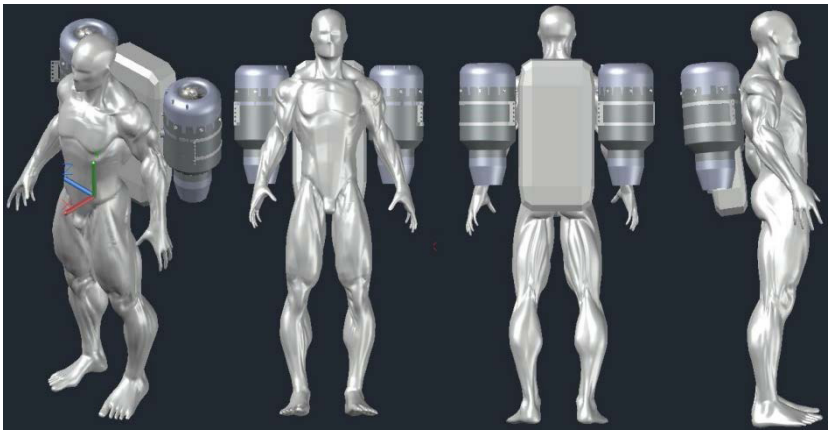


Fig. 1. General arrangement sketch of the portable jetpack platform (isometric, front, rear, and left views)

Furthermore, a three-degree-of-freedom point-mass flight dynamics model of the integrated operator-platform system is derived, incorporat-

ing thrust, gravity, and aerodynamic drag. The model is validated through fourth-order Runge-Kutta numerical integration [5], successfully reproducing representative maneuvers including turning and steady circling. The results confirm that the proposed propulsion control architecture, combined with body-attitude modulation, enables stable and maneuverable low-altitude flight.

Although the jetpack platform was originally designed for terrestrial atmospheric conditions, the feasibility of extending the control algorithms and framework to future space platform operating in planetary analog sites is discussed. Meanwhile, the backpack architecture allows the integration of lightweight scientific instrumentation for low-altitude environmental sensing, such as multispectral cameras or gas sensors, positioning the platform as a flexible testbed for both earth exploration and space exploration.

REFERENCES:

[1] Ly S., Pho K. H., Pan S. H. et al. Newton-Raphson Method: Overview and Applications // Advances in Decision Sciences. 2024. V. 28. No. 3. P. 1–26.
[2] Biswas B. N., Chatterjee S., Mukherjee S. P. et al. A discussion on Euler method: A review // Electronic J. Mathematical Analysis and Applications. 2013. V. 1. No. 2. P. 2090–2792.
[3] Chen X. J., Hong D. Q. Research on single neuron adaptive PID controller // Applied Mechanics and Materials. 2014. V. 651. P. 826–830.
[4] Wang J. Q., Zhang W. C., Hu Z. Z. Model-based nonlinear control of aeroengines. Berlin: Springer, 2022. ISBN 978-981-16-4452-8.
[5] Gao X. G., Li B., Wan K. F. et al. Hangkong junyong feixingqi daolun (Introduction to Military Aerospace Vehicles). 2nd ed. Xi'an.: Northwestern Polytechnical University Press, 2022 (in Chinese).

PRELIMINARY GEANT4 SIMULATION STUDY OF GAMMA-RAY RESPONSES IN LUNAR ENVIRONMENT USING THE MATCH DETECTOR ONBOARD CHANG'E-7 ORBITER

P. Jamlongkul[1], K. Chaiwongkhot[2], K. Puprasit[4], P. Muangha[1], T. Panyalert[1], P. Torteeka[1], S. Manuthasna[1], D. Ruffolo[2], W. Mitthumsiri[2], P. Khonsri[1], Y. Pittayang[1], K. Anuchit[1], W. Sophonamphonsucha[1], K. Amratisha[2], S. Burom[5], S. Chindaratchakul[2], W. Hantrakul[1], J. Lakronwat[2], R. Plumanut[1], K. Pumim[1], N. Treesakul[1], J. Wannasorn[1], P. Pattarakijwanich[2], P. Kamsing[6], X. He[7], N. Zhang[7], J. Zheng[7], B. Zhang[7], D. Yang[8], H. Yang[9], J. Xian[7], Y. Bao[7], S. Lu[7], H. Zhao[7], S. Zhang[3]

[1] *National Astronomical Research Institute of Thailand* (*Public Organization*), *Chiang Mai, Thailand, paparin_ja@outlook.com*
[2] *Mahidol University, Bangkok, Thailand*
[3] *National Space Science Center, Chinese Academy of Sciences, Beijing, China*
[4] *Chulabhorn Royal Academy, Bangkok, Thailand*
[5] *Chulalongkorn University, Bangkok, Thailand*
[6] *Air-Space Control, Optimization, Management Laboratory, Department of Aeronautical Engineering, International Academy of Aviation Industry, King Mongkut's Institute of Technology Ladkrabang, Bangkok, Thailand*
[7] *Changchun Institute of Optics, Fine Mechanics and Physics, Chinese Academy of Sciences, Changchun, China*
[8] *Jilin University, Changchun, China*
[9] *Institute of Modern Physics, Chinese Academy of Sciences, Lanzhou, China*

KEYWORDS:
gamma ray, lunar environment, Chang'E-7 orbiter, MATCH payload, BGO, Geant4

INTRODUCTION:

The Chang'E-7 Moon Aiming Thai-Chinese Hodoscope (CE-7 MATCH) payload is designed to measure high-energy charged particles in lunar orbit and the lunar albedo environment, including protons, electrons, and alpha particles [1,2]. The MATCH detector stack consists of plastic scintillator layers, double-sided silicon strip detectors (DSSDs), and bismuth germanate (BGO, $Bi_4Ge_3O_{12}$) crystal scintillators, supporting charged-particle identification and deposited-energy measurement using the ΔE–E technique. In this configuration, the front DSSD layers measure the initial energy loss and provide tracking information, while the BGO crystal scintillators act as residual-energy detectors or calorimeter layers. Owing to its high density, high effective atomic number, and short radiation length, BGO is suitable for compact calorimeter applications and efficient detection of gamma rays and high-energy particles. These properties also allow gamma-ray interactions and electromagnetic showers to be localized within a compact crystal volume [3]. This work presents a preliminary Geant4 simulation study of gamma-ray interactions with the CE-7 MATCH detector as an initial step toward supporting future post-analysis of MATCH data. The main purpose of this study is to establish a simulation-based reference for understanding the detector response to incident gamma rays over selected energy ranges. The simulation results are intended to provide preliminary information for evaluating possible gamma-ray-related responses in the lunar environment, including solar gamma-ray flares and albedo gamma rays from the lunar surface, which may be considered in future analyses of MATCH observations.

ACKNOWLEDGMENTS:
This presentation is supported by the TSRI Strategic Funding in Scientific and Technology for development of Excellent center In Deep-space explo-

ration Engineering (EXIDE) and Pilot Hub of Talent in Space Scientific Payload Grant No. N35E690062 by National Research Council Thailand.

REFERENCES:

[1] Panyalert T., Manuthasna S., Torteeka P. et al. Signal Calibration and Energy Resolution Optimization of a Double-Sided Silicon Strip Detector for Lunar-Based Particle Detection // IEEE Sensors Letters. 2025. V. 9. Iss. 7. No. 99. P. 1–4. DOI: 10.1109/LSENS.2025.3580433.
[2] Panyalert T., Manuthasna S., Torteeka P. et al. Ground software architecture for a lunar particle detector: Implementation with a double-sided silicon strip detector // Advances in Space Research. 2026. V. 77. No. 8. P. 8492–8509. DOI: 10.1016/j.asr.2025.09.089.
[3] Grynyov B., Ryzhikov V., Kim J.K., Jae M. Scintillator Crystals, Radiation Detectors and Instruments on Their Base. Kharkiv: Institute for Single Crystals, 2004. 376 p.

SIMULATION OF THE ALIGN PAYLOAD FOR CHANG'E-8: NEUTRON-GAMMA DISCRIMINATION AND BACKGROUND EFFECTS FROM A RADIOISOTOPE HEATER UNITS

Pradiphat Muangha[1], Koth Amratisha[2], Kanatip Anuchit[1], Sunruthai Burom[3], Kullapha Chaiwongkhot[2], Sarawit Chindaratchakul[2], Shen Guohong[4], Wutthiphat Hantrakul[1], Donghui Hou[3], Paparin Jamlongkul[1], Pakorn Khonsri[1], Jidapa Lakronwat[2], Shariff Manuthasna[1], Warit Mitthumsiri[2], Thanayuth Panyalert[1], Yaowarat Pittayang[1], Ratchanonth Plumanut[1], Kanyapak Pumim[1], Kunlanan Puprasit[5], David Ruffolo[2], Woradon Sophonamphonsucha[1], Peerapong Torteeka[1], Natthapong Treesakul[1], Shenyi Zhang[4]

[1] *National Astronomical Research Institute of Thailand Chiang Mai, Thailand, pradiphat@narit.or.th, Muangha.P@gmail.com*
[2] *Mahidol University, Bangkok, Thailand*
[3] *Chulalongkorn University Bangkok, Thailand*
[4] *National Space Science Center, Chinese Academy of Sciences, Beijing, China*
[5] *Chulabhorn Royal Academy, Bangkok, Thailand*

KEYWORDS:
International Lunar Research Station, ILRS, Chang'e-8 mission, albedo neutrons, albedo protons, gamma-rays, Geant4 simulation, Galactic Cosmic Rays, GCRs, Solar Energetic Particles, SEPs

INTRODUCTION:

The near-surface environment of the moon presents a highly complex, mixed radiation field dominated by the continuous flux of Galactic cosmic rays (GCRs) and solar energetic particles (SEPs). As these primary energetic particles bombard the lunar regolith, they initiate nuclear cascades that generate a continuous upward flux of secondary albedo protons, albedo neutrons, and gamma-rays [1]. Characterizing these multi-species surface emissions across varying solar activities is essential for study local surface and subsurface compositions, as well as evaluating radiation risks for future long-duration human operations under the International Lunar Research Station (ILRS).

To address this, we present the conceptual design of multi-species albedo particle detector developed as the Assessing Lunar Ion-Generated Neutrons (ALIGN) payload for the Chang'e-8 lander. This detector is specifically designed to measure both charged and neutral particles. In this work, we primary focus on Geant4 toolkit simulations [2] of optimize instrumental technical for achieving a clean of discrimination between secondary lunar neutrons and ambient gamma-rays. An operational challenge addressed in this simulation work is the background radiation profile introduced by the lander's onboard Radioisotope Heater Units (RHUs), which are expected to be fueled by Plutonium-238 (Pu-238) [3, 4]. This localized thermal management system continuously emits a significant background of neutrons that threatens to contaminate the lunar albedo signatures.

To mitigate these background effects, our simulation framework evaluates the efficacy of localized radiation shielding optimized specifically for the RHU source. We assess various shielding geometries, arrangements, and material compositions to maximize the attenuation of the leakage flux before it reaches the active sensor head. The simulation establishes crucial performance benchmarks, including geometric factors, energy deposition profiles, and cross-contamination rejection ratios for neutral particles. Ultimately, these results demonstrate a viable path to isolate true lunar albedo protons, neutrons, and gamma-rays from both environmental cosmic rays and onboard spacecraft noise, providing a robust calibration and shielding

baseline for the successful scientific deployment of the ALIGN payload on the lunar surface.

ACKNOWLEDGMENTS:
This work was supported by the TSRI Strategic Funding in Science and Technology for the development of the Center of Excellence in Deep-Space Exploration Engineering (EXIDE) and the Pilot Hub of Talent in Space Scientific Payloads under Grant No. N35E690062 by the National Research Council of Thailand (NRCT).

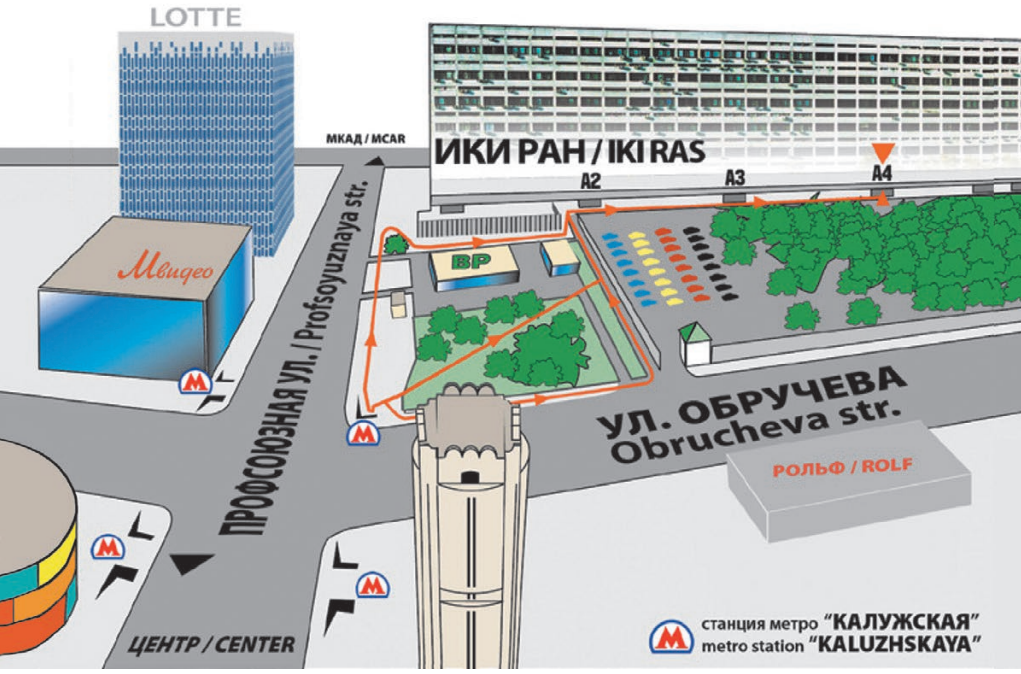
REFERENCES:

[1] McCord T. B. et al. Sources and physical processes responsible for OH/H2O in the lunar soil as revealed by the Moon Mineralogy Mapper (M3) // J. Geophysical Research (Planets). 2011. V. 116, ArticleE00G05.
[2] Agostinelli S. et al. Geant4 — a simulation toolkit // Nuclear Instruments and Methods in Physics Research Section A: Accelerators, Spectrometers, Detectors and Associated Equipment, 2003, V. 506, No. 3, P. 250–303. DOI: 10.1016/S0168-9002(03)01368-8.
[3] Taherzadeh M. Neutron Radiation Characteristics of Plutonium Dioxide Fuel: Jet Propulsion Laboratory Technical Report 32-1555. Pasadena: California Institute of Technology, 1972. 16 p.
[4] Chen H., Zhang Y., Zhang C., Chen H., Xiang Q., Zeng J., Hu G., Liu Y. Characterization of 238PuO2 neutron and gamma radiation based on the latest nuclear databases // Radiation Physics and Chemistry. 2025. V. 232. Article 112659. DOI: 10.1016/j.radphyschem.2025.112659.

INFORMATION

address:
Space Researh Institute (IKI)
Profsoyuznaya street 84/32
post code 117997
metro station: Kaluzhskaya
Moscow, Russia





ИКИ РАН

площадь академика Келдыша
метро «Калужская», первый вагон из центра, по тоннелю – прямо,
по второму поперечному тоннелю – направо, выход на площадь,
далее по стрелкам на схеме

IKI RAS

You should get off at "Kalyzhskaya" metro station using the southern exit.
After leaving a station lobby through glass doors you should go straight
to the end of the tunnel, then take right and use the stairs to get to the surface.
From this point you may follow either arrow on this map

MOSCOW METRO SCHEME



REGISTRATION AND INFORMATION DESK

location: IKI, entrance A-4
time:

12 October, 9:00–18:00
13–15 October, 10:00–18:00
16 October, 10:00–16:00

ORAL SESSIONS

location:

- IKI conference hall, second floor
  October 12 Opening session, Atmospheres of planets session
  October 13 Surfaces of planets and moons session
  October 14 Solar System in the lab session,
  Exospheres of airless bodies session
  October 15 Small Bodies including space dust session
  October 16 Scientific meetings

- IKI exhibition hall, ground floor
  October 12 Internal structure of planets and moons session
  October 13 Extrasolar planets session
  October 14 Astrobiology session
  October 15 Planetary missions and scientific instrumentation session

POSTER SESSION FOR ALL SESSIONS

location:

- IKI exhibition hall, ground floor
  12 October, 18:30–20:30
  14 October, 18:00–20:00

COFFEE BREAKS, WELCOME PARTY, RECEPTION

location:

- IKI exhibition hall, ground floor

INTERNET ACCESS AND WIFI

there is Internet access in and near the conference hall

SOCIAL PROGRAM

	BOLSHOI THEATRE	OPERETTA THEATRE	HELIKON THEATRE *Stravinsky Hall*	STANISLAVSKY AND NEMIROVICH-DANCHENKO MUSICAL THEATER	NOVAYA OPERA	MOSCOW INTERNATIONAL HOUSE OF MUSIC *Svetlanov hall*	KREMLIN PALACE
12.10					**19.00** **Anna Karenina** *Ivanov music theatre performance*		
13.10	**15.00** **Rigoletto** *historic stage* *opera*	**19.00** **Anna Karenina** *Music performance*					**19.00** **The classics of Russian ballet.** *Mikhail Lavrovsky*
14.10	**19.00** **Rigoletto** *historic stage* *opera*	**19.00** **Anna Karenina** *Music performance*					**19.00** **“Songs from the heart”**
15.10	**19.00** **Rigoletto** *historic stage* *opera*	**19.00** **Anna Karenina** *Music performance*	**19.00** **Aida** *Opera*		**19.00** **Rigoletto** *Opera*	**19.00** **Wagner and Tchaikovsky. “The Valkyrie” and “Swan Lake”**	**19.00** **Christina. Solo concert “River of Friendship”**
16.10	**19.00** **Carmen suite** **Divertissement** **One-act ballets**	**19.00** **Anna Karenina** *Music performance*	**19.00** **Aida** *Opera*	**19.00** **Cherry Garden. Garden cherry** *Ballet*	**19.00** **Rigoletto** *Opera*	**19.00** **“Symphony of Time: The Era of the 90s”**	
17.10	**12.00, 19.00** **Carmen suite** **Divertissement** **One-act ballets** *New stage*	**14.00, 19.00** **Anna Karenina** *Music performance*	**19.00** **Aida** *Opera*	**19.00** **Cherry Garden. Garden cherry** *Ballet*	**20.00** **Tristan and Izolda** *Consert-suita*	**17.00** **Relaxation in the big city. Russian Philharmonic** **19.00** **Crazy dances with Fabio Mastrangelo**	**18.00** **Gala concert “My Russia, My Family”**
18.10	**14.00** **Carmen suite** **Divertissement** **One-act ballets** *New stage*	**14.00, 19.00** **Anna Karenina** *Music performance*	**16.00** **Aida** *Opera*	**14.00. 19.00** **Cherry Garden. Garden cherry** *Ballet*	**18.00** **Boris Godunov** *Music drama*	**14.00** **Energy Classic. Orchestra “Russian Philharmonic”**	**16.00** **“The Little Flower.”** *A performance by the Kremlin Ballet Theatre.* **17.00** **«Notre-Dame de Paris» «Opera XXI»** *small hall*

https://bolshoi.ru	БОЛЬШОЙ ТЕАТР, BOLSHOI THEATRE
https://mosoperetta.ru	ТЕАТР ОПЕРЕТТЫ, OPERETTA THEATRE
https://www.helikon.ru	ГЕЛИКОН-ОПЕРА, HELIKON THEATRE
https://www.stanmus.ru	МУЗЫКАЛЬНЫЙ ТЕАТР ИМ. К.С. СТАНИСЛАВСКОГО И ВЛ. НЕМИРОВИЧА-ДАНЧЕНКО, STANISLAVSKY AND NEMIROVICH-DANCHENKO MUSICAL THEATER
https://novayaopera.ru	НОВАЯ ОПЕРА, NOVAYA OPERA
https://www.mmdm.ru	МОСКОВСКИЙ МЕЖДУНАРОДНЫЙ ДОМ МУЗЫКИ, MOSCOW INTERNATIONAL HOUSE OF MUSIC
https://kremlinpalace.org	ГОСУДАРСТВЕННЫЙ КРЕМЛЁВСКИЙ ДВОРЕЦ, KREMLIN PALACE

LUNCH POINTS NEAREST TO IKI



1. **ИНСТИТУТ КОСМИЧЕСКИХ ИССЛЕДОВАНИЙ РАН**,
   ул. Профсоюзная, 84/32,
   столовая, 1 этаж, секция А3
   SPACE RESEARCH INSTITUTE,
   Profsoyuznaya street, 84/32,
   Food center, Ground Floor, Section A3
2. **ТЦ «КАЛУЖСКИЙ»**,
   ул. Профсоюзная, 61А,
   зона ресторанов, 2 этаж
   “KALUZHSKIY” Market Center,
   Profsoyuznaya Street, 61A,
   2 Floor
3. **КАФЕ «АНДЕРСОН»**,
   ул. Обручева, 30/1
   CAFÉ “ANDERSON”,
   Obrucheva street, 30/1
4. **ИНСТИТУТ ПРИКЛАДНОЙ МАТЕМАТИКИ РАН,**
   ул. Профсоюзная 84/32,
   столовая, 1 этаж
   INSTITUTE OF APPLIED MATHEMATICS,
   Profsoyuznaya street 84/32,
   Food center, Ground Floor



